Radboud Repository

Radboud University Nijmegen

PDF hosted at the Radboud Repository of the Radboud University Nijmegen

The following full text is a publisher's version.

For additional information about this publication click this link.
https://repository.ubn.ru.nl/handle/2066/236411

Please be advised that this information was generated on 2021-11-26 and may be subject to change.

# Tales of the uncommon

## massive binary stars and gravitational-wave sources

Jakub Klencki

# Tales of the uncommon:
# massive binary stars and gravitational-wave sources

**Jakub Andrzej Klencki**

# Tales of the uncommon: massive binary stars and gravitational-wave sources

**Proefschrift**

ter verkrijging van de graad van doctor
aan de Radboud Universiteit Nijmegen
op gezag van de rector magnificus prof. dr. J.H.J.M. van Krieken,
volgens besluit van het college voor promoties
in het openbaar te verdedigen op
dinsdag 28 september 2021
om 10.30 uur precies

door

**Jakub Andrzej Klencki**

geboren op 1 juli 1993
te Łódź, Polen

| | | |
|---|---|---|
| Promotor: | Prof. dr. G. A. Nelemans | |
| Copromotoren: | Dr. A. Istrate | |
| | Dr. O. R. Pols | |
| Manuscriptcommissie: | Prof. dr. B. Krishnan | |
| | Prof. dr. I. Mandel | Monash University, Australië |
| | Prof. dr. S. E. de Mink | Max Planck Institüt für Astrophysik, Duitsland |
| | Dr. F. Schneider | Universität Heidelberg, Duitsland |
| | Prof. dr. F. W. M. Verbunt | |

© 2021, Jakub Klencki
Tales of the uncommon: massive binary stars and gravitational-wave sources
Thesis, Radboud University Nijmegen
Cover & pagemarker: Martyna Chruślińska

ISBN: 978-94-6421-461-1

# Contents


**1 Introduction** **1**

1.1 Live fast, die young: massive stars . . . 1
1.1.1 Massive stars in the Universe . . . 1
1.1.2 Evolutionary cycle and remnants of massive stars . . . 3
1.1.3 Massive stars are rarely single . . . 5
1.2 Black-hole X-ray binaries and gravitational-wave sources . . . 7
1.2.1 Black hole X-ray binaries . . . 8
1.2.2 Compact-object binaries as gravitational-wave sources . . . 10
1.3 Evolution of massive binary stars: theory . . . 13
1.3.1 Mass transfer and its stability . . . 13
1.3.2 Effect of stable mass transfer on the binary orbit . . . 16
1.3.3 Unstable mass transfer: common-envelope evolution . . . 17
1.3.4 Other processes affecting the binary orbit . . . 18
1.3.5 Computations in stellar and binary evolution . . . 19
1.4 Formation puzzles of black-hole binaries . . . 21
1.4.1 Black-hole X-ray binaries . . . 21
1.4.2 The many formation scenarios for DCO mergers . . . 22
1.4.3 How important is low-metallicity for progenitors of binary BH mergers? . . . 24
1.5 This thesis . . . 26

**2 Black-hole X-ray binaries from fly-by encounters** **31**

2.1 Introduction . . . 32
2.2 Dynamical interactions as source of X-ray binaries . . . 33
2.2.1 LMXB formation scenario of MP2016 . . . 33
2.2.2 Dynamical interactions in the field . . . 36
2.3 Population synthesis modeling . . . 37
2.3.1 General approach . . . 37
2.3.2 Pre-BH stage – binary evolution modeling . . . 38
2.3.3 Post-BH stage – stellar encounters modeling . . . 40

2.4 Results . . . 44
2.4.1 An exemplary evolutionary route . . . 44
2.4.2 Evolution of orbital parameters . . . 46
2.4.3 The population of LMXBs . . . 48
2.5 Discussion . . . 50
2.5.1 Lifetime of LMXBs . . . 51
2.5.2 Mass function of the fly-bys . . . 51
2.5.3 BH natal kicks . . . 52
2.5.4 Ultra-wide systems – comparison with MP2016 . . . 53
2.6 Conclusions . . . 55

**3 Initial binary parameters for binary BH and NS mergers 59**
3.1 Introduction . . . 60
3.2 Initial distributions . . . 64
3.2.1 Inter-correlated initial binary parameters . . . 64
3.2.2 IMF and its dependence on metallicity . . . 68
3.3 Computational method . . . 69
3.3.1 Physical assumptions – the StarTrack code . . . 69
3.3.2 Cosmological calculations of the merger rates . . . 70
3.3.3 Calculations of predictions for the LIGO/Virgo detectors . . . 71
3.3.4 Differences with respect to Belczynski et al. (2016b) and Belczynski et al. (2016a) . . . 72
3.4 Results . . . 72
3.4.1 Birth properties of compact binary mergers . . . 72
3.4.2 Formation of compact binary mergers across metallicity . . . 78
3.5 Merger rates and LIGO/Virgo predictions . . . 79
3.5.1 Source-frame merger rate density . . . 79
3.5.2 LIGO/Virgo detection rates . . . 81
3.5.3 Metallicity distribution of BH-BH progenitors . . . 82
3.6 Discussion . . . 83
3.6.1 Understanding the impact of the new initial distributions . . . 83
3.6.2 Small impact of a top-heavy IMF . . . 84
3.6.3 Population synthesis on cosmological scales . . . 85
3.6.4 Comparison with LIGO/Virgo detection rates and other studies . . . 87
3.7 Summary . . . 88
3.A Conversion coefficients between SFR and IMFs . . . 90
3.B Local star formation rate at metallicities $Z < 0.1\ Z_{\odot}$ . . . 91

**4 Effective spins of binary BH mergers 95**
4.1 Introduction . . . 96
4.2 Model . . . 99

4.2.1 Natal Black Hole Spin . . . 99
4.2.2 Black Hole Spin Misalignment . . . 102
4.2.3 Black Hole Masses . . . 103
4.2.4 Black Hole Accretion Model . . . 105
4.2.5 Tidal Interactions . . . 109
4.2.6 Cosmic Star Formation History and Metallicity Evolution . . . 111
4.2.7 Calculations . . . 114
4.3 Results . . . 118
4.3.1 Binary Evolution of BH-BH Mergers . . . 118
4.3.2 Merger Rate Density and Detection Rate . . . 122
4.3.3 BH Masses . . . 128
4.3.4 BH-BH Effective Spins . . . 132
4.4 Discussion . . . 138
4.4.1 Angular Momentum Transport in Massive Stars . . . 138
4.4.2 Using Single Stellar Models in Binary Simulations . . . 141
4.4.3 BH-BH/BH-NS/NS-NS Merger Rate Densities . . . 142
4.4.4 BH Masses . . . 147
4.4.5 BH-BH Effective Spins . . . 149
4.4.6 Origin of LIGO/Virgo BHs . . . 152
4.5 Conclusions . . . 154
4.A Appendix . . . 157
4.A.1 Geneva Stellar Models . . . 157
4.A.2 MESA Stellar Models . . . 161
4.A.3 CO Core Mass versus BH Mass . . . 165
4.A.4 Making GW170104 . . . 167
4.A.5 The Effective Spin Parameter: $\chi_{\rm eff}$ . . . 168
4.A.6 NS Spins . . . 169
4.A.7 Binary Evolution Calculations . . . 172
4.A.8 Detectabilty of Mergers in Gravitational Waves . . . 177
4.A.9 BH-NS merger rate limits from the ongoing O3 run . . . 177

**5 Metallicity and the onset of mass transfer 181**
5.1 Introduction . . . 182
5.2 Stellar models: physical ingredients . . . 184
5.3 Results . . . 185
5.3.1 Stellar tracks and radius evolution of massive stars . . . 185
5.3.2 Binary parameter ranges for different donor types . . . 188
5.3.3 Model variations . . . 191
5.3.4 Convective envelope donors . . . 193
5.4 Comparison with observations: clues for post-MS expansion . . . 195

5.4.1 SMC-like metallicity ($Z = 0.2\ Z_\odot$) . . . 196
5.4.2 Solar metallicity . . . 200
5.5 Discussion . . . 202
5.5.1 Why does the size of massive HG stars decrease with metallicity? . . . 202
5.5.2 How robust is the trend with the metallicity? . . . 203
5.5.3 WR stars formed through binary interactions . . . 203
5.5.4 Mass transfer evolution and slow envelope stripping . . . 204
5.5.5 Late cases of RLOF: progenitors of type II supernovae, long GRBs, and binary BH mergers? . . . 205
5.6 Conclusions . . . 206
5.A Density inversions, MLT++, and the HD limit . . . 208
5.B Internal mixing during the Hertzprung gap phase . . . 209
5.C Additional HR diagrams . . . 212

**6 Common-envelope evolution in BH binaries 215**
6.1 Introduction . . . 216
6.2 The model . . . 218
6.2.1 Stellar models of massive giants . . . 218
6.2.2 Conditions for mass-transfer instability . . . 219
6.2.3 Energy budget criterion for a successful CE ejection . . . 221
6.2.4 Model summary: the "optimistic" choice of assumptions . . . 224
6.3 Results . . . 224
6.3.1 The envelope binding energy: impact of the outer convective layer . . . 224
6.3.2 Common-envelope ejectability in BBH merger progenitors . . . 226
6.3.3 It has to be cool: tight link between the CE donors and red supergiants . . . 232
6.3.4 A detailed look at the structure and the binding energy of convective-envelope giants . . . 235
6.4 Discussion . . . 240
6.4.1 How robust is the prediction that CE evolution in BH binaries requires RSG donors? . . . 240
6.4.2 Upper luminosity limit of RSGs: indication of a maximum mass beyond which the CE channel does not operate? . . . 242
6.4.3 Implications for population synthesis and merger rates of compact binaries 244
6.4.4 Tidal spin-up in close BH-WR binaries . . . 246
6.4.5 Common-envelope ejection in BH-LMXB progenitors . . . 247
6.4.6 Alternative scenario: partial envelope ejection followed by stable mass transfer . . . 249
6.5 Conclusions . . . 251
6.A Common-envelope binding energy parameter fits . . . 253
6.B Numerical robustness of models . . . 254

6.B.1 The setup . . . 254
6.B.2 Numerical robustness: envelope binding energies . . . 255
6.B.3 Numerical robustness: detailed internal structure . . . 258
6.B.4 Numerical robustness: HR diagram at $Z = 0.2\ Z_\odot$ . . . 259
6.C Additional figures . . . 260

**7 Stable mass transfer evolution from massive donors 263**
7.1 Introduction . . . 264
7.2 Method: binary stellar evolution models . . . 266
7.2.1 Physical ingredients: single and binary evolution . . . 266
7.2.2 Initial parameter space and stopping conditions . . . 268
7.3 Results . . . 269
7.3.1 Nuclear-timescale mass transfer and partial envelope stripping . . . 269
7.3.2 Parameter space for nuclear-timescale mass transfer . . . 275
7.3.3 Formation and properties of partially-stripped stars in detached binaries . 277
7.4 Why partially stripped? Radial response of stars to mass loss . . . 282
7.5 Discussion . . . 286
7.5.1 The importance of post-MS expansion and its uncertainty due to mixing . 286
7.5.2 The case of stellar-accretor binaries . . . 288
7.5.3 Increased accretion efficiency in low-Z binaries? . . . 288
7.5.4 Core-He burning primaries in the HR diagram . . . 289
7.5.5 Fewer stripped and WR stars from interacting binaries at low-Z? . . . 293
7.5.6 Implications for explodability and SN progenitors . . . 295
7.5.7 Implications for ultra-luminous X-ray sources . . . 296
7.6 Summary . . . 297
7.A Additional figures . . . 299

**8 Summary 303**

**9 Samenvatting 309**

**Bibliography 319**

**About the author 341**

**Acknowledgments 343**

**Research Data Management 347**

*To Martyna*

*”Astronomy compels the soul to look upwards*
*and leads us from this world to another.”*

Plato

# Chapter 1

# Introduction

*"Shooting stars never stop*
*Even when they reach the top*
*There goes a supernova*
*What a pushover, yeah"*
*Frankie Goes to Hollywood*

## 1.1 Live fast, die young: massive stars

### 1.1.1 Massive stars in the Universe

The Sun is the basis of all the life on Earth. It is our relentless engine, an uninterruptible power supply that never ceases to provide Earth with energy – and it has been doing so for the last five billion years. For many starting science enthusiasts it might seem almost absurd that an object could be so bright for so long when its main source of power is simply to connect four Hs together, that is to fuse four hydrogen atoms into helium.[1] As all good things come to an end, so the life of the Sun will. Luckily for us, not for another several billion years: there is still plenty of time to come up with a plan.

The Sun is a star, one of tens of billions of stars in our Galaxy, and the basic principles behind any star are the same. The gravity is trying to pull all the matter inwards towards a collapse but the in-fall is prevented by various counteracting forces, of which the most important ones are the pressure of gas and radiation. We call this state a hydrostatic equilibrium. The gas is constantly heated by the nuclear fusion in the center, which replaces the energy lost from the stellar surface in the form of radiation and kinetic outflows: a thermal equilibrium is maintained. A tiny part of the energy emitted from the surface reaches the Earth, so that a civilization could develop and wonder about all those things.

[1] More senior science enthusiasts are better used to shocking revelations.

Even though their basic principles are the same, two stars can greatly differ from one another in terms of their size, luminosity, temperature, life expectancy and many other factors. The single most important characteristic of a star, that will largely determine the other properties, is its initial mass. The Sun is a relatively low-mass star: although its least massive 'colleagues' have only about 8% of the Solar mass (the minimum mass required for a star to sustain hydrogen fusion as the main energy source), the most massive stars in the nearby Universe are significantly heavier, reaching at least 150 times the Solar mass ($M_\odot$) and likely beyond (Crowther et al., 2010). Those that have at least $8\,M_\odot$ or so are referred to as massive stars. Their defining characteristic is that at the end of their lives, massive stars collapse to form neutron stars (NSs) or black holes (BHs), as I will describe in Sec. 1.2.

The more massive a star the less common it is, as the initial mass distribution of stars can be approximated with a power-law: $p(M) \propto M^{-2.3}$ (Salpeter, 1955). As a result, in every 10,000 stars that are formed, only about 25 will be more massive than $8\,M_\odot$. In addition to being rarely born, massive stars die very young: with higher temperatures and densities in their cores, massive stars are much quicker to process all the fuel available for nuclear fusion compared to low-mass stars such as the Sun. The total stellar lifetime scales approximately as $\propto M^{-2.8}$, $M$ being the mass of a star (Kippenhahn & Weigert, 1990). For example, while a Solar-like star takes 10 billion years to run out of fuel, the life of a massive star lasts for about a few million to a few tens of millions of years. One can then realize that massive stars truly are a rarity in an average stellar population or galaxy. Yet, despite being so few in numbers, massive stars play a pivotal role in various areas of astrophysics. They are extremely luminous, with individual stars reaching even $10^7$ times the luminosity of the Sun (Crowther et al., 2010), and can dominate the light emission from star-forming galaxies (especially in ultraviolet wavelengths). Massive stars have much higher surface temperatures than low-mass stars. Thanks to that their spectra peak at shorter wavelengths and are the primary source of stellar-origin ionizing photons. In fact, it is thought that it was the first massive stars that reionized the Universe after the Dark Ages (Yoshida et al., 2007; Greif et al., 2010; Hirano et al., 2015)

Massive stars are characterized by strong outflows of material (winds) from the surface, which for most of their lifetime are driven by radiation pressure on spectral lines and accelerated to supersonic velocities (Vink et al., 2000). The mass loss can further be enhanced through pulsations and violent eruptions (Smith, 2014). Copious amounts of ejected matter blast through the surrounding medium, providing kinetic feedback and seeding turbulence (Mac Low & Klessen, 2004). Over the course of their lifetime, in stellar winds alone a massive star can lose more than half of its initial mass back into the galaxy in which it formed. Part of this material has already been enriched in elements synthesised in stellar interiors, providing metals for the formation of next generations of stars and planets.

In fact, the metallicity of a massive star (i.e. the initial abundance of elements heavier than helium, typically not larger than $0.02-0.03$), in particular the abundance of iron strongly influences the efficiency of line-driven winds (Vink et al., 2001; Vink & de Koter, 2005). The higher the metallicity, the more metal nuclei with multiple atomic levels are available for photon scatterings –

and therefore the more efficient the wind acceleration and the higher the mass-loss through winds. While high-metallicity massive stars are predicted to lose their entire hydrogen-rich envelopes as a result of stellar winds alone (Conti, 1975; Maeder & Meynet, 1994), their low-metallicity counterparts might barely be affected by mass loss during their entire evolution (Vink et al., 2021).

Perhaps the most important role that massive stars play in the Universe takes place in the 'final breath' of their lives, a supernova explosion, as I will discuss in the next section.

### 1.1.2 EVOLUTIONARY CYCLE AND REMNANTS OF MASSIVE STARS

The initial composition of stars is mostly hydrogen ($\sim 70\%$) and helium ($\sim 30\%$), with possibly small addition of heavier elements (metals) that over time becomes larger with every next generation of stars ($\sim 1.5\%$ in the case of Sun). For most of its lifetime ($\sim 90\%$), a massive star is powered by the fusion of hydrogen into helium (i.e. hydrogen burning) during a phase called the main sequence. Once the hydrogen fuel runs out, the helium core contracts until the temperature and density in the center are high enough for the fusion of helium $^4$He into carbon $^{12}$C in the so-called 3-$\alpha$ chain of reactions. At the same time, some of the newly synthesised $^{12}$C nuclei interact with $^4$He to form oxygen $^{16}$O. As a result, at the end of the core-He burning phase the central part of a star is a carbon-oxygen core surrounded by a helium shell and further out by a hydrogen-helium envelope.

In massive stars, the carbon-oxygen core is massive enough to allow for a further sequence of advanced burning stages, with the key phases being subsequently the burning of carbon, neon, oxygen, and silicon. The evolution through advanced burning is very fast (less than 1% of the total lifetime, e.g. Woosley et al., 1995). The end product is an onion-like structure of a star with an iron core in the center and gradually lighter elements in the surrounding shells. The cycle stops because a fusion of iron would consume more energy than it can produce.

And the end of each burning stage, when the fueling element is exhausted and the energy production in the center stops, the star loses its thermal equilibrium and its structure needs to change. The core contracts until the ignition of the next element. The outer envelope, on the other hand, much larger than the core to begin with, tends to expand even more in the so-called 'mirror' effect. This transition can be especially dramatic after the end of the core-H burning phase, when some massive stars increase in size by about two orders of magnitude (from $\sim$10 to $\sim$1000 $R_\odot$, $R_\odot$ being the Solar radius) and become red supergiants. From the end of carbon burning and beyond, further contractions of the core no longer affect the global size of the star as the timescale on which the outer envelope would readjust its structure is longer than the remaining lifetime of the core.

Once the iron core is formed and there are no further burning stages to support the structure, the star begins to collapse. The increase in temperature and density in the center leads to photodisintegration of the heavy nuclei into gradually lighter elements. This decreases the radiation pressure and speeds up the gravitational collapse. Protons begin to capture electrons to form neutrons and neutrinos: the matter becomes extremely neutron rich and neutrinos carry most of the energy released from the gravitational collapse. Neutrons obey the Pauli exclusion principle

and their degenerate pressure is what stops the collapse. A compact remnant forms (proto-NS) with a radius of a few tens of kilometers and mass between $\sim 1.2$ and $2.5\,M_\odot$. The layers in-falling from above hit and bounce off the degenerate center and a shock wave forms (e.g. Janka, 2017). If the inner layers together with neutrinos can overcome the collapse of the remaining outer part of the star and the shock can break through the in-falling layers then the result is a supernova explosion. Otherwise, the in-fall resumes until the degenerate neutrons in the center are unable to sustain the pressure and the entire star (except for the escaping neutrinos) collapses into a BH (Fryer & Kalogera, 2001) – an object with a surface gravity so strong that not even light can escape it.

In the case of a supernova explosion the final remnant is generally thought to be a NS, with most of the remaining matter being ejected to the interstellar medium with velocities reaching thousands kilometers per second. An intermediate outcome might also be possible, that is a supernova explosion in which part of the initial ejecta remains bound and ultimately falls back onto the compact remnant to cause a delayed collapse into a BH (Fryer, 1999) In general, the more massive the star the more likely it is to end its life as a BH rather than a NS. The usually quoted threshold for the initial mass above which stars are predicted to form BHs is around 20-25 $M_\odot$ (Fryer et al., 2012). Their remnants are sometimes referred to as stellar-mass black holes, to distinguish them from supermassive BHs found in the centers of galaxies. Stellar-mass BHs can have masses from a few to a few tens of Solar masses.

Both NSs and BHs can receive a velocity kick on formation (a 'natal' kick), ranging from tens to hundreds of km/s (Hobbs et al., 2005; Repetto et al., 2017; Verbunt et al., 2017). Observational evidence for natal kicks comes from measurements of velocities of radio pulsars and (BH) X-ray binaries in the Milky Way. The origin of the kick is poorly understood but likely has to do with asymmetries in the supernova ejecta (Janka, 2013).

A supernova explosion – the final breath in the life of a massive star – is where the uniqueness of massive stars and their special role in the Universe really shines[2]. Neutrons and alpha particles produced in the center of a collapsing star are captured by the nuclei in the layers above leading to nucleosynthesis of new heavy elements (in particular of the iron group, e.g. Timmes et al., 1995). In fact, the exceptionally high density of neutrons (a very rare occurrence anywhere else in the Universe) also makes r-process nucleosynthesis possible in some supernovae (Kobayashi et al., 2020), i.e. a sequence of neutron captures that occur in quick succession before the unstable nuclei they produce experience a $\beta$-decay. Products of all these nuclear reactions are then ejected in a supernova explosion and distributed all over the host stellar cluster (and possibly galaxy). Besides the enrichment of the interstellar medium with heavy elements, supernovae provide strong kinetic feedback to the surrounding gas in star-forming regions where massive stars live their lives.

Unfortunately, details of the advanced evolutionary stages, the pre-collapse structure of the core, and the collapse itself are far from being understood (Janka et al., 2016). BHs and NSs are the living witnesses of those events, and although massive stars live short lives and suffer violent deaths, their remnants are forever, giving us insights into the past populations of massive stars all

[2]Literally: supernovae can be brighter than entire galaxies!

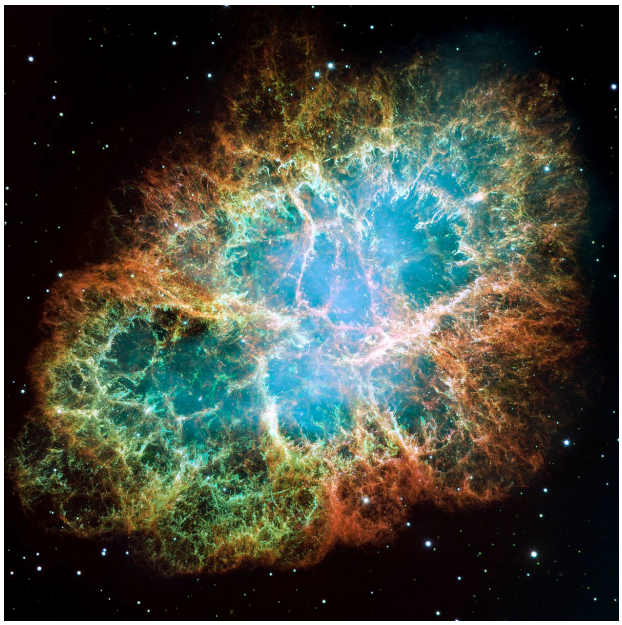

FIGURE 1.1: The Crab Nebula viewed by the Hubble telescope. It is a supernova remnant, formed as a result of explosion of a massive star. It was observed by Chinese astronomers in 1054 AD. Credit: NASA, ESA.

throughout Cosmic History. They are, however, difficult to detect, especially BHs as they do not emit any significant amount of light on their own. In Sec. 1.2, I will discuss various ways which such dark remnants can be discovered.

### 1.1.3 MASSIVE STARS ARE RARELY SINGLE

One of the major breakthroughs in the massive star community in the recent years was the realization that it is rare for massive stars to evolve as single, unperturbed objects. The vast majority are formed in pairs (binaries) or even higher order systems such as triples or quadruples (Sana et al., 2013; Moe & Di Stefano, 2017). In most binary systems, the orbital separation is small compared to the sizes that massive stars achieve during their evolution (especially when they become red supergiants). As a result, most massive stars (~70%) will at some point overflow their wells of gravitational potential (the so-called Roche lobes) and strongly interact with their companions by transferring mass and angular momentum (Sana et al., 2012).

A mass transfer interaction can become dynamically unstable, leading to a spiral-in and a merger of two stars in a spectacular transient event (such as luminous red novae; Tylenda et al., 2011). Products of stellar mergers may be some of the most massive and luminous stars in stellar populations (McCrea, 1964; Schneider et al., 2015), lead to a peculiar class of supernovae (including the most recent naked-eye supernova SN 1987A, see Podsiadlowski et al., 1990), and have been proposed as the origin of strong magnetic fields in stars (Ferrario et al., 2009; Schneider et al., 2019). But the mass transfer can also proceed in a slow and stable way, without destroying the binary. Even in that case, it has dramatic consequences for the basic properties of both stars. A

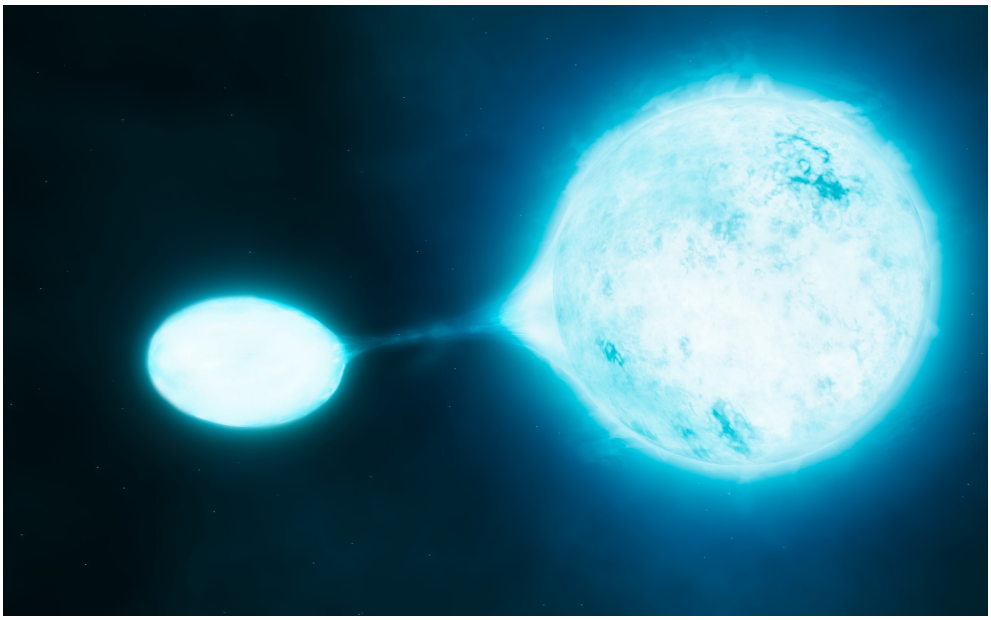

FIGURE 1.2: Artist's impression of mass transfer in a main-sequence binary with a 20 $M_\odot$ and 15 $M_\odot$ massive-star components. The mass gainer (left) is spun up by accretion, which leads to a significant oblateness. Credit: ESO/M. Kornmesser/S.E. de Mink.

giant star transferring mass to its companion in an interacting binary is thought to quickly become stripped of its hydrogen-rich envelope (which is usually more than half of its mass), thus revealing a hot helium core (Paczyński, 1971; van den Heuvel, 1975; Podsiadlowski et al., 1992)[3]. This affects its further evolution, leading to systematically different pre-collapse core structures of massive stripped stars (Woosley & Weaver, 1995; Laplace et al., 2021; Schneider et al., 2021) and a class of hydrogen-free supernova explosions (type Ib and Ic). Stripped stars, being hotter than normal hydrogen-rich stars, may also be an important source of ionizing photons at later times after a burst of star formation (Götberg et al., 2018, 2020).

The companion star, on the other hand, which gains mass as a result of mass transfer, may become rejuvenated when the fresh hydrogen fuel is transported inwards towards the burning core (Hellings, 1983; Braun & Langer, 1995; Dray & Tout, 2007). Rejuvenation prolongs the lifetime of a mass gainer and makes it look younger than it really is. Depending on how much of the mass transferred from the Roche lobe of the mass-losing star (the donor) can be accreted by the mass-gaining companion (the accretor), products of stable mass transfer may be among the most massive stars in a population (similarly to stellar mergers). Matter that instead of being accreted by the companion is ejected from the binary systems will enrich the interstellar medium with products of nuclear burning from the donor interior (e.g. helium, nitrogen, sodium, aluminium; de Mink et al., 2009b)[4]. In addition, accretor stars are quickly spun-up to even critical rotation velocities (when the centrifugal force together with the radiation pressure are equal to surface gravity, see

[3]Although in chapter VII we show that this is not always the case in metal-poor environments

[4]Unlike the supernova ejecta, matter lost as a result of mass transfer will be slow (tens of kilometers per second) and therefore could be retained in environments such as stellar clusters.

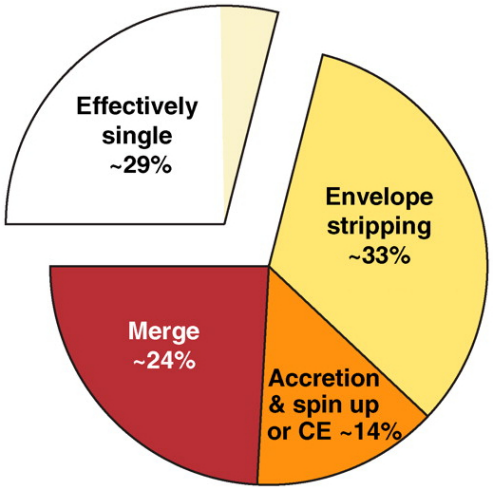


Figure 1.3: Schematic representation of the relative importance of different mass-transfer interaction processes in a population of massive stars (O-type, $\gtrsim 16\,M_\odot$). Only $\sim 30\%$ of massive stars live their lives unaffected by mass transfer (mostly in very wide binaries or higher order systems). Figure adapted from Sana et al. (2012).

Packet, 1981). This process likely produces the fastest spinning stars known (Pols et al., 1991; de Mink et al., 2014).

Arguably, the most exciting consequence of stars living in close systems is the enormous range of possible evolutionary scenarios. Many of those lead to rare energetic phenomena and uncommon outcomes that are outside the regime of single-stellar evolution. Last but not least, binary evolution raises the possibility of a strong interaction between a compact object and a living star (X-ray binaries) or another compact object (gravitational-wave sources), thus offering us the best chance to study the remnants of massive stars. Understanding the formation of such systems from binary stars is the main subject of this thesis. In Sec. 1.2, I provide an overview of the current observational results on stellar-mass BHs. In Sec. 1.3, I introduce the essentials of binary evolution theory. Sec. 1.4 describes the current challenges and open questions related to the formation of BH binaries. Sec. 1.5 outlines the main chapters of the thesis in which we tackle those puzzles.

## 1.2 Black-hole X-ray binaries and gravitational-wave sources

Black holes do not emit any light on their own and we cannot observe them directly in electromagnetic waves[5], which makes their detection a challenging task. There is, however, a number of indirect methods which rely on probing their gravitational field. For instance, in the case of supermassive BHs, a long-time monitoring campaign of the movement of stars within the innermost arcsecond of the Galactic center has allowed astronomers to weigh the central invisible

[5]Besides the theoretical Hawking radiation.

mass and conclude that it is consistent with a BH of about four million Solar masses (a spectacular discovery awarded with a Nobel Prize in 2020, see Ghez et al., 2005, 2008; Genzel et al., 2010). In a recent breakthrough achievement, a global network of radio telescopes working together as a very-long baseline interferometer known as the Event Horizon Telescope has been able to resolve the signature of an event horizon in the photon field around the supermassive BH in the center of M87 (a result otherwise known as taking a picture of a shadow of a BH; Event Horizon Telescope Collaboration et al., 2019).

In the case of stellar-mass BHs, their presence in a binary system may be revealed through measurements of the orbital movement of the companion star. One strategy to hunt such systems is the use of large-scale spectroscopic surveys such as APOGEE or LAMOST to search for signatures of binarity in the spectra of BH companions (several BH candidates have been reported this way, see Thompson et al., 2019; Liu et al., 2019; Rivinius et al., 2020). Alternatively, especially in the case of wide binaries, a presence of an invisible BH in a binary could be revealed through precise orbital astrometry of the companion, for example obtained by the Gaia satellite (Breivik et al., 2017; Wiktorowicz et al., 2020). Another detection method is the use of gravitational microlensing: a well-defined temporary brightening of a star due to light bending by a stellar-mass BH located on the line of sight (Paczynski, 1986). The uniqueness of gravitational microlensing is that it could lead to a discovery of a single BH (which evade detection through other methods). Theoretical models estimate that even a 100 million of such isolated BHs could be present in the Milky Way (e.g. Wiktorowicz et al., 2019). Although light curves of microlensing events found by surveys such as OGLE are fitted with great accuracy, mass of the invisible (dark) lens is measured with large error bars. This is due to a degenerate effect played by two of the unknown parameters: the microlensing parallax and the relative proper motion. As a result, most of the candidate BH lenses are also consistent with sub-solar mass objects (Wyrzykowski et al., 2016). On the other hand, Wyrzykowski & Mandel (2020) showed that the combined distribution of the dark lens masses is continuous in the mass range between $2\,M_\odot$ and $5\,M_\odot$, disfavoring claims for a the so-called 'mass gap' of dark remnant masses in that range.

Most commonly though, a stellar-mass BH is detected either in the X-rays, as the accretor in an X-ray binary system, or in gravitational waves, as a component of a compact object merger event. I describe these two types of systems and the observed populations below.

### 1.2.1 BLACK HOLE X-RAY BINARIES

Accretion in a mass-transferring binary system with a BH- or a NS-accretor proceeds through an accretion disk. Through frictional heating, gas in the central part of the disk becomes extremely hot ($10^5$ – $10^6$ K) and the system is a bright X-ray source: an X-ray binary (Shakura & Sunyaev, 1973). Searches for the X-ray signature of an accretion disk have led to a discovery of tens of stellar-mass BHs or BH candidates in the Milky Way and a handful of extragalactic systems (Remillard & McClintock, 2006; Corral-Santana et al., 2016).

A smoking-gun evidence that an X-ray binary system is hosting a BH rather than a NS (or a

white dwarf) comes from a constraint that the accretor is more massive than $\sim 3\,\mathrm{M}_\odot$ (the upper mass limit of a NS). Mass measurements in X-ray binaries are obtained by tracking the orbital movement of the companion star (e.g. Casares et al., 1992). Observationally derived quantities – the semi-amplitude of the radial velocity of the companion projected onto the line of sight ($K_c$) and the orbital period $P_{\rm orb}$ – can be related to the mass of the compact-object accretor ($M_{\rm acc}$), the mass of the donor ($M_{\rm don}$), and the inclination ($i$) of the orbit via the so-called mass function $f(M)$ (see the review by Casares & Jonker, 2014):

$$f(M) = \frac{P_{\rm orb} K_c^3}{2\pi G} = \frac{M_{\rm acc}^3 \sin^3 i}{(M_{\rm acc} + M_{\rm don})^2} \quad . \tag{1.1}$$

Note that even if the inclination and the mass ratio $q = M_{\rm don}/M_{\rm acc}$ are unknown, the mass function places a lower limit on the accretor mass. In some systems the inclination can be determined via light-curve fitting to the ellipsoidal modulations in the optical flux arising from the fact that the donor star is tidally distorted. The mass ratio, on the other hand, can be determined by measuring the rotational broadening of the absorption lines in the donor spectrum ($V_{\rm rot;eq} \sin i$) which, under the assumption that the donor is synchronised with the orbit, relates to $K_c$ only via a function of $q$.

The combined determination of $f(M)$, $q$, and $\sin i$ allows one to obtain the accretor mass as a so-called dynamical mass measurement. Currently, around 20 BH accretors have been confirmed dynamically in X-ray binaries in the Milky Way, with a few more extragalactic sources (Corral-Santana et al., 2016; Tetarenko et al., 2016b). BH X-ray binaries are short-period systems (typically $P_{\rm orb} < 10$ day). The majority are classified as BH low-mass X-ray binaries (BH-LMXBs), i.e. the companion is a low-mass star ($< 2\,\mathrm{M}_\odot$), with the companion mass distribution peaked at around $0.6\,\mathrm{M}_\odot$. Based on the sensitivity of X-ray monitoring surveys, it was estimated that the total number of BH-LMXBs in the Milky Way is about $10^3 - 10^4$ (Romani, 1998; Corral-Santana et al., 2016) or possibly even larger (Tetarenko et al., 2016a). Notably, these two properties – the number of sources and the companion mass distribution – cannot be simultaneously recovered by current theoretical models of binary evolution (Wiktorowicz et al., 2014; Li, 2015), although see Wang et al. (2016). I will return to the formation puzzle of BH-LMXBs in Sec. 1.4.

Apart from BH-LMXBs, several BH X-ray binaries with high-mass companions are known. Unlike in the case of BH-LMXBs, the accretion disk in high-mass X-ray binaries (HMXBs) may be 'wind-fed', i.e. formed as a result of accretion of the gas that is continuously ejected from the surface of the massive companion as a strong stellar wind. Noteworthy, while BH-LMXBs are thought to be long-lived sources (with lifetimes counted in Gyr), BH-HMXB are short-lived due to short lifetimes of massive stars (of the order of $\sim 10$ Myr).

BH binaries serve as an excellent test-bed for our understanding of massive stellar and binary evolution, in particular scenarios involving a mass-transfer interaction. Taking the population of BH-LMXBs as an example, that fact that a low-mass main-sequence star with a radius of $\sim 1\,\mathrm{R}_\odot$ is overflowing its Roche lobe implies that the binary separation is of the order of a few $\mathrm{R}_\odot$. This is much less than the size that a massive star – the BH progenitor – achieves during its evolution,

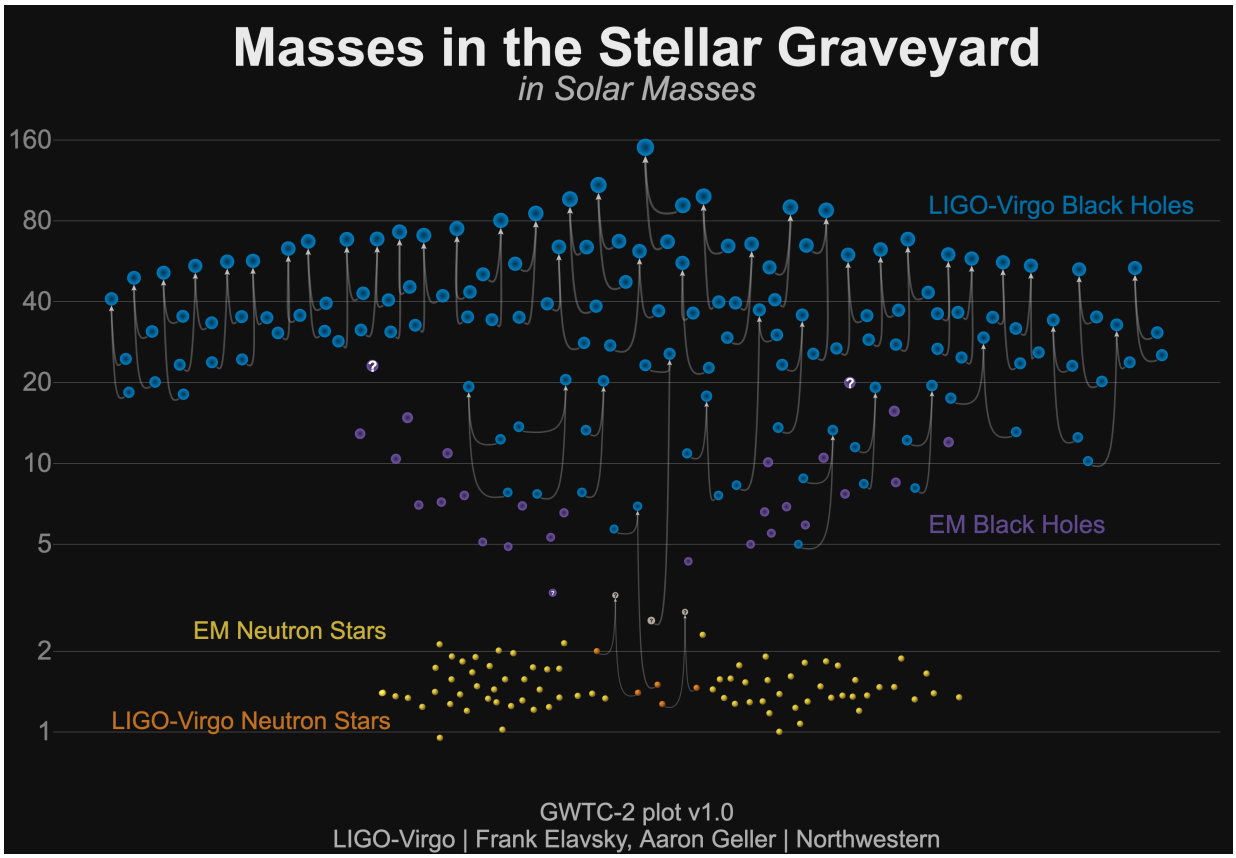


FIGURE 1.4: Masses of all the compact binaries detected by LIGO/Virgo, with BHs in blue and NSs in orange. Also shown are stellar-mass BHs (from BH X-ray binaries, purple) and NSs (yellow) discovered with electromagnetic observations. Credit: LIGO/Virgo/Northwestern Univ./Frank Elavsky/Aaron Geller.

meaning that at some point in the past the binary separation must have been substantially reduced. One candidate process that could be responsible for this orbital shrinkage is the highly uncertain common-envelope evolution, which I will introduce in Sec. 1.3. In addition, BH binaries are perhaps the most direct probes of the highly-uncertain BH formation process, allowing us to constrain how much of the progenitor mass was ejected during a BH formation or whether BHs (similarly to NSs) receive a significant velocity 'kick' upon formation (Nelemans et al., 1999; Repetto & Nelemans, 2015; Repetto et al., 2017). The dynamically-derived masses of BHs in X-ray binaries range from about $\sim 5$ to $25\,M_\odot$. More massive stellar-mass BHs are found among the merging binary BHs detected in GW, as I will discuss below.

### 1.2.2 COMPACT-OBJECT BINARIES AS GRAVITATIONAL-WAVE SOURCES

Within general relativity, any two masses orbiting each other emit GW. The waves carry energy at the expense of the orbital energy, which causes a gradual decrease of the binary separation. If there are no other processes that would counteract the shrinking of the binary, the emission of GW will eventually lead to a merger of the two bodies. The shrinkage of a binary orbit due to GW

emission was confirmed empirically through precise pulse timing in a pulsar-NS binary system (the Hulse-Taylor pulsar; Hulse & Taylor, 1975; Taylor & Weisberg, 1982) – an achievement that earned the Noble prize in physics for Russell Hulse and Joseph Taylor, Jr., awarded in 1993.

The GW luminosity of a binary system $L_{\rm GW}$ with a circular orbit can be expressed as (Kokkotas, 2008):

$$L_{\rm GW} = \frac{32}{5}\frac{G^4}{c^5}\frac{M^3\mu^2}{a^5} \quad , \tag{1.2}$$

where $M = M_1 + M_2$ is the total mass, $\mu = M_1 M_2/M$ is the reduced mass ($M_1$ and $M_2$ being the component masses), and $a$ is the binary separation. Seeing as $L_{\rm GW} \propto a^{-5}$, the GW signal is the strongest at the final stages of the inspiral and during the merger event itself. The assumption of a Keplerian orbit is no longer valid at that point but we can still use Eqn. 1.2 to estimate how the GW luminosity of a merger scales with the mass $M$ and radius $R$ of the merging bodies. Taking $a \propto R$ and $\mu \propto M$, we find $L_{\rm GW} \propto (M/R)^5$. The strongest GW signal (in terms of GW luminosity) is thus emitted at a coalescence of the most compact objects: NSs and BH. I will refer to merging binaries in which both of the components are either a NS or a BH as merging double compact objects (DCOs). It is worth to point out that what is actually measured by GW detectors is the GW amplitude (strain, $h(t)$), not the energy flux. The time-dependent amplitude of the GW signal scales as $h(t) \propto \mathcal{M}^{5/3} f_{\rm GW}(t)^{2/3}$, where $\mathcal{M} = (M_1 M_2)^{3/5}/(M_1 + M_2)^{1/5}$ is the chirp mass and $f_{\rm GW}(t)$ is the GW frequency (twice the orbital frequency of the system; Sathyaprakash & Schutz, 2009).

The strength of GW emission by a binary systems is a strong function of the binary separation ($L_{\rm GW} \propto a^{-5}$ in Eqn. 1.2). As a result, also the timescale on which the GW emission leads to a merger ($\tau_{\rm merg}$) depends strongly on the binary separation. In the case of a circular binary with parameters $M_1$, $M_2$, and $a$ this timescale can be expressed as (Peters, 1964):

$$\tau_{\rm merg;circ} = \frac{5c^5}{256G^3}\frac{a^4}{M_1 M_2 (M_1 + M_2)} \quad . \tag{1.3}$$

From Eqn. 1.3 one can estimate the upper limit for the separation of a given DCO binary so that it can merge within the age of the Universe (the Hubble time $t_{\rm Hubble}$). Taking $\tau_{\rm merg;circ} < t_{\rm Hubble} \approx 14$ Gyr, a circular binary NS system with $M_1 = M_2 = 1.4\,{\rm M}_\odot$ needs to have a separation $a \lesssim 4.75\,{\rm R}_\odot$. A circular binary BH system with $M_1 = M_2 = 20\,{\rm M}_\odot$ requires a separation $a \lesssim 35\,{\rm R}_\odot$. Similarly to the case of short-period BH X-ray binaries, such orbital separations are much smaller than the sizes that massive stars – BH and NS progenitors – achieve during their evolutionary cycle. Any scenario for the formation of DCO mergers has to be able to produce very close binaries. I will introduce the main formation channels for close DCO systems in Sec. 1.4.

**Gravitational-wave detections of DCO mergers**

The year 2015 witnesses one of the greatest achievements in the history of experimental physics. On September 14, 2015 the two interferometers of the Advanced Laser Interferometer Gravitational-wave Observatory (aLIGO; LIGO Scientific Collaboration et al., 2015), in an observing run by the LIGO/Virgo collaboration, detected the first GW signature of a binary BH

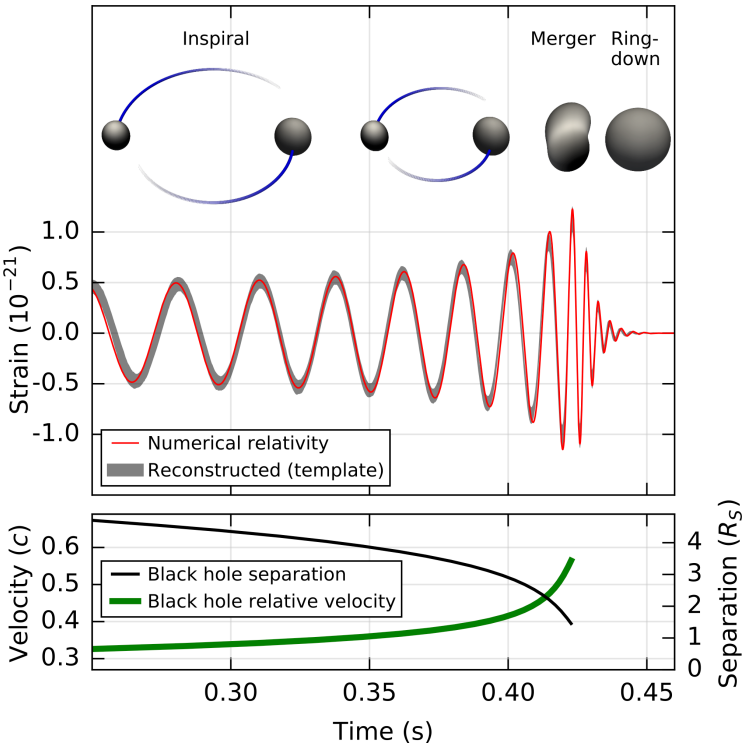


FIGURE 1.5: The first GW detection from a binary BH merger: GW150914. Top: Reconstructed gravitational-wave strain amplitude projected onto the LIGO Hanford interferometer compared to a numerical relativity waveform for a system with parameters consistent with those recovered from GW15091 (solid line). Inset images show numerical relativity models of the BH horizons as the BHs coalescence. Bottom: BH separation in units of Schwazschild radii ($R_S = 2GM/c^2$) and the effective relative velocity in units of $c$. Figure adapted from Abbott et al. (2016b).

coalescence, an event dubbed GW150914 (Abbott et al., 2016b). This outstanding achievement was a culmination of decades of work of thousands of researches and engineers from all across the world. A Nobel prize in physics was awarded to three of them in 2017: Rainer Weiss, Kip Thorne, and Barry Barish. The modern era of GW astronomy has started.

Six years and two and a half observing runs later, through the joint efforts of the LIGO and Virgo collaborations, we now have a total of 47 GW events detected so far (Abbott et al., 2020a): 44 confident binary BH events, two binary NS mergers, and a NS-BH merger candidate (which may also be a binary BH event). Results from the second half of the third observing run are expected to appear later this year. From the detections so far, a truly exceptional event was the first binary NS merger observed in August 2017, GW170817 (Abbott et al., 2017a). It was the only event so far with a robustly associated electromagnetic counterpart, a kilonova transient and a short gamma ray burst (GRB; Abbott et al., 2017e). The GW170817 event and its counterpart confirmed various theoretical predictions for the course and outcome of a binary NS merger, their role in r-process nucleosynthesis, and association with short GRBs, as well as triggered a number of new questions (e.g. peculiar jet structure, unexpected host galaxy). The follow-up observational campaign, which was launched immediately after the GW signal and the short GRB detection,

spanned all across the electromagnetic wavelength spectrum in a combined effort of more than three thousand astronomers.

The masses of the component BHs in the first detected GW event (GW150914) were measured to be $36^{+5}_{-4}\,M_\odot$ and $29^{+4}_{-4}\,M_\odot$. Such massive BHs had not been observed in any of the known BH binary systems. Subsequent detections of binary BH mergers revealed that GW150914 was not an isolated case: many of the binary BH mergers observed in GW consist of BHs with masses above $25-30\,M_\odot$, see Fig. 1.4. This has led to a suggestion that the massive binary BH mergers may predominantly originate from metal-poor environments, i.e. galaxies in which stars had been forming with a lower content of metals compared to the Sun and most of the other stars in the Milky Way and nearby galaxies (Belczynski et al., 2016b; Abbott et al., 2016c). The lower the metallicity of a massive stars, the weaker the mass loss through line-driven stellar winds. Consequently, a low-metallicity massive star will have retained more mass at the core-collapse stage compared to a high-metallicity star with stronger winds, and as a result can form a more massive BH. Understanding what were the metallicities of the progenitors of the DCO merger events gives us a clue as to what were the types of galaxies where the DCO systems had formed and at what redshifts (e.g. Chruslinska & Nelemans, 2019a). I will come back to this point in Sec. 1.4.

The signal measured by GW detectors depends primarily on the chirp mass $\mathcal{M}$ introduced above. A few other parameters of the system can also be estimated from higher order effects (alas less accurately; Sathyaprakash & Schutz, 2009). These include the total mass, the mass ratio, as well as the effective spin parameter $\chi_{\rm eff}$ defined as

$$\chi_{\rm eff} = \frac{M_1 a_{\rm spin;1}\cos(\theta_1) + M_2 a_{\rm spin;2}\cos(\theta_2)}{M_1 + M_2} \quad . \tag{1.4}$$

In the above formula, $a_{\rm spin;1,2}$ are the spin magnitudes and $\theta_{1,2}$ are the angles between the spin directions and the orbital angular momentum vector. Interestingly, the effective spin values of the binary BH mergers detected by LIGO/Virgo appear to be clustered around 0 (Abbott et al., 2021). In chapter IV we will study this observation in the context of formation of DCO mergers from massive binary stars.

## 1.3 Evolution of massive binary stars: theory

### 1.3.1 Mass transfer and its stability

In the classical, Newtonian limit, two stars in a binary system orbit each other moving on Keplerian orbits. In the corotating frame of reference, the effective potential of a binary system is determined by the masses of the two components (the gravitational term) as well as the centrifugal force arising from the orbital motion. The resulting equipotential surfaces are illustrated in Fig. 1.6. Locations of the Lagrangian points are also shown, i.e. the local extrema of the effective potential where the gravity and centrifugal force balance each other. The thick line defines the two Roche lobes of the binary components, connected through the L1 Lagrangian point. A useful quantity is the Roche lobe radius $R_{\rm RL}$, which is defined by the condition that $(4/3)\pi R^3_{\rm RL}$ equals the volume of the space

enclosed by the Roche lobe. The Roche lobe radius depends on the mass ratio ($q$) and separation ($a$) between the binary components. A fitting formula for $R_{\rm RL}$ was provided by Eggleton (1983):

$$R_{\rm RL} = a \, \frac{0.49q^{2/3}}{0.6q^{2/3} + \ln(1 + q^{1/3})} \quad , \tag{1.5}$$

where for $q = M_1/M_2$. The above formula gives the Roche lobe of the binary component with mass $M_1$. As long as each star remains within its respective Roche lobe (i.e. $R < R_{\rm RL}$), the binary is in a so-called detached stage.

In the majority of massive binary systems, expansion of stars due to their evolution will at some point lead to a situation when their radius becomes greater than $R_{\rm RL}$, which is referred to as Roche-lobe overflow. The star (donor) then begins to transfer mass through the L1 point into the Roche lobe of its companion (accretor). The rate at which mass is transferred (mass-transfer rate, usually in units of $M_\odot$ per year) depends on how quickly the donor star re-expands with respect to its Roche lobe to replenish the mass that has been lost from the surface. A useful quantity is $\zeta_{\rm RL} = d\log \mathrm{R_{RL}}/d\log \mathrm{M_1}$, which describes the change of the Roche lobe radius of the donor star (of mass $M_1$) as a result of mass transfer (parameterized by a change in $M_1$, note that $d\log \mathrm{M_1}$ is negative). It takes into account the effect of mass exchange on the orbital separation and on the mass ratio, and can be expressed analytically with a few extra parameters describing the fate of the matter that is transferred through L1 (e.g. how much is accreted by the companion, what the angular momentum is of the non-accreted matter), see Eqn. 16.25-26 in Tauris & van den Heuvel (2006)

The response of the donor's radius can be written similarly as $\zeta_{\rm don} = d\log \mathrm{R_1}/d\log \mathrm{M_1}$. The timescale and stability of mass transfer will depend on the comparison between $\zeta_{\rm don}$ and $\zeta_{\rm RL}$. It is useful to consider the value of $\zeta_{\rm don}$ on different timescales associated with changes in the donor's structure. A star that has lost some mass is perturbed out of both thermal and hydrostatic equilibrium. First, it will regain hydrostatic equilibrium on a dynamical timescale (about $\sim$ 1 day to $\sim$ 10 yr, depending on the mass and radius of a massive star), adjusting its radius according to $\zeta_{\rm don;dyn}$. On a longer thermal timescale (typically $\sim 10^3 - 10^5$ yr for massive stars), it will regain thermal equilibrium and change its radius according to $\zeta_{\rm don;th}$.

The condition $\zeta_{\rm don;dyn} < \zeta_{\rm RL}$ means that the Roche lobe size is decreasing with respect to the donor size on a short dynamical timescale, i.e. the donor star continues to rapidly increase in size with respect to its Roche lobe. Such a situation is dynamically unstable and leads to unstable mass transfer evolution which I will describe in Sec. 1.3.3.

If $\zeta_{\rm don;dyn} \geq \zeta_{\rm RL}$ but $\zeta_{\rm don;th} < \zeta_{\rm RL}$ then the mass transfer is stable on the dynamical timescale and begins to proceed on the thermal timescale of the donor, with the rate typically in the range of $\sim 10^{-4} - 10^{-2}\,\mathrm{M_\odot\,yr^{-1}}$. The donor is still gradually increasing in size with respect to its Roche lobe (which is accompanied by a rise in the mass transfer rate) but much more slowly. Whether the situation will remain stable for the entire mass transfer duration or the donor will eventually overflow its Roche lobe past the point of no return (possibly up to the L2/L3 Lagrangian points) causing a steep rise in the mass transfer rate and a dynamical instability after all, depends on various factors such as the mass ratio (e.g. Ge et al., 2010; Pavlovskii & Ivanova, 2015)

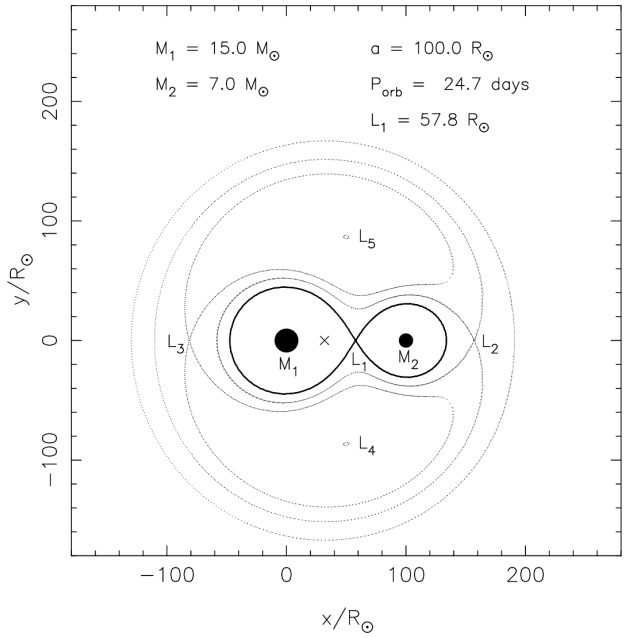


FIGURE 1.6: A cross-section in the orbital plane of a binary system. Lines indicate equipotential surfaces. Masses are marked as 'M1' and 'M2', Lagrangian points as 'L1' through to 'L5'. The center of mass is indicated with a cross. The thick curve crossing through L1 is defining the Roche lobes of the two components. Figure adapted from Tauris & van den Heuvel (2006).

The case of $\zeta_{\rm don;th} \geq \zeta_{\rm RL}$ is when the donor star shrinks with respect to its Roche lobe even on the thermal timescale. The mass transfer rate is then determined by the rate of the donor expansion as a result of its normal evolution. This case is referred to as nuclear-timescale mass transfer and for massive stars proceeds with a rate typically in the range of $\sim 10^{-7} - 10^{-5}\,{\rm M}_\odot\,{\rm yr}^{-1}$.

**Cases of mass transfer**

How stable mass transfer proceeds will largely depend on when in the lifetime of the donor star is the interaction initiated. The case of Roche-lobe overflow from a donor that is still a main-sequence star is referred to as case A mass transfer (Kippenhahn & Weigert, 1967). It was found to consist of two stages: first a short thermal-timescale mass exchange, followed by a long nuclear-timescale mass transfer phase (e.g. Pols, 1994; Wellstein et al., 2001). Case A mass transfer more or less continues until the end of the main-sequence evolution of the donor, at which point the star begins to rapidly expand in the transition to become a giant. This increases the mass transfer rate and quickly strips the remaining hydrogen-rich envelope from the donor, leaving behind a naked helium core and a detached binary.

Stable mass transfer initiated by a post-main sequence massive giant, on the other hand, is thought to proceed on the thermal-timescale and quickly strip (nearly) the entire hydrogen-rich envelope of the donor star (within $\lesssim 10^4$ yr, e.g. Paczyński, 1967; van den Heuvel, 1975; Vanbeveren, 1982; Podsiadlowski et al., 1992; Verbunt, 1993; Vanbeveren et al., 1998). The remaining lifetime of the stripped donor depends on how late in its post-main sequence evolution the mass transfer was started. As we will show in this thesis (chapter VII), this textbook view of

post-main sequence mass transfer evolution is no longer true in the case of low-metallicity massive stars.

### 1.3.2 EFFECT OF STABLE MASS TRANSFER ON THE BINARY ORBIT

The orbital angular momentum of a binary system is given by:

$$J_{\rm orb} = M_1 M_2 \left( \frac{Ga(1-e^2)}{M} \right)^{1/2} \quad , \tag{1.6}$$

where $M = M_1 + M_2$ is the total mass, $a$ is the separation, and $e$ is the eccentricity. Mass-transferring binary systems are thought to be efficiently circularized by the tidal torques and so typically $e \approx 0$. We can first consider a case when all the mass that is transferred through L1 becomes accreted by the accretor ($dM_1 = -dM_2$, $M_1$ being the donor mass), i.e. the total mass $M$ is conserved. This case is referred to as fully conservative mass transfer. In most binary systems, the orbital angular momentum is much greater than the angular momentum of stars. We can thus approximate $J_{\rm orb}$ as being constant. This means that over the course of a mass transfer phase the factor $M_1 M_2 \sqrt{a}$ has to remain constant too. Based on this condition one can see that binary systems in which the donor is more massive than the accretor ($M_1 > M_2$) will begin to shrink as a result of mass transfer (decreasing $a$). This trend may reverse once a sufficient amount of mass has been transferred to the companion so that $M_2$ becomes larger than $M_1$. In addition, the more unequal the mass ratio the more significant the change in the $M_1 M_2$ factor as well as the associated effect on the orbital separation. Although we have made several simplifications, this already illustrates that for $M_1 > M_2$, the larger the value of the mass ratio $q = M_1/M_2$, the more quickly the Roche lobe of the donor shrinks as a result of mass exchange, and therefore the more likely it is that the mass transfer will become dynamically unstable. This is why the criterion for mass transfer stability in a binary is sometimes simply given by a critical mass ratio above which the mass transfer would become unstable.

A fully-conservative mass transfer is the most simple case. In practice, in many situations a significant fraction of the matter transferred through L1 will not be accreted by the companion (sometimes even $\sim 100\%$, a so-called fully non-conservative case). The non-accreted matter becomes ejected from the system as is characterized by some specific angular momentum (i.e. per unit of mass, $l_{\rm ej}$). The value of $l_{\rm ej}$ is often assumed to be the same as the specific angular momentum of the accretor in its orbital movement. This assumption is well justified in the case when the matter is ejected from the close proximity of the accretor (for instance from its surface or from the inner layers of an accretion disk) and is ejected with a high velocity so that it quickly loses synchronization with the orbit (and does not exchange any more angular momentum). In practice, $l_{\rm ej}$ may often be greater than that, especially when the amount of mass ejected from the system is significant or the accretor's Roche lobe becomes fully filled with matter which then starts to leave the system through the L2 point (MacLeod & Loeb, 2020a). These processes remain highly uncertain. The larger the $l_{\rm ej}$ the more angular momentum leaves the binary, which works towards decreasing the separation. Coupled with the fact that the accretion efficiency is typically also very

uncertain (and treated as a free parameter), this means that the net quantitative effect of a stable mass transfer phase on the binary separation is quite uncertain (which leaves a certain amount of freedom in various binary evolution scenarios). As a rule of thumb though, if the initial mass ratio is large ($q \gtrsim 3$) then a mass transfer interaction can lead to a significant shrinkage of the orbit. I will come back to this point when introducing the stable mass transfer formation channel for binary BH mergers. On the other hand, if the initial mass ratio is close to unity, the mass transfer will likely cause the orbit to expand.

### 1.3.3 Unstable mass transfer: common-envelope evolution

As described in Sec. 1.3.1, the expansion of the donor star with respect to its Roche lobe may become a runaway process occurring on the dynamical timescale. It was proposed by Paczynski (1976); van den Heuvel (1976) that such a rapid expansion of the donor's envelope would cause it to lose synchronization with the binary orbit and eventually engulf the entire binary system. This is the beginning of what we call common-envelope evolution (Ivanova et al., 2013b). The companion, now moving through the gaseous medium of the common envelope, experiences a drag force which causes it to spiral-in deeper and deeper into the shared envelope originating from the giant donor. This process can lead to a dramatic shrinkage of the separation between the binary components: the size of envelope itself can span orders of magnitude (e.g. from $\sim 1\,\mathrm{R}_\odot$ near the helium core up to several thousand $R_\odot$ at the surface), so there is a long way for the companion to spiral in. The energy generated by the in-spiral is at least partly dissipated into the common envelope. If this energy input is large enough to unbind the envelope and eject it from the system then the in-spiral can stop and the binary survives the common-envelope phase. The result is a short-period system (with separation smaller by even two orders of magnitude compared to the pre-common-envelope state). If part of the envelope remains bound and cannot be ejected then the in-spiral continues and leads to a merger between the companion and the core of the giant donor.[6] The drastic reduction in the orbital separation is the key stage in various binary evolution scenarios involving a common-envelope phase. I will describe two of such scenarios in Sec. 1.4.

It is easy to see that the common-envelope evolution is extremely challenging to model in detail. Apart from the huge range in length scales, various common-envelope phases may be occurring on different timescales: ranging from the dynamical in-spiral (tens of days to tens of years) to the initial phase until the loss of co-rotation or late stages of the in-spiral just before the envelope ejection (both could take hundreds of years or even more). As a result, only a small number of cases of common-envelope evolution have so far been modelled with 3D hydrodynamic simulations, mostly in the regime of low- and intermediate-mass stars (Nandez et al., 2015; Nandez & Ivanova, 2016; Ohlmann et al., 2016; Clayton et al., 2017; Sand et al., 2020), although see Ricker et al. (2019); Law-Smith et al. (2020).

[6] If the donor is not a giant but still a main-sequence star then dynamically unstable mass transfer most likely always leads to a merger.

Due to this complexity of a common-envelope phase, its outcome in evolutionary scenarios is instead often predicted based on a simple energy formalism (van den Heuvel, 1976; Tutukov & Yungelson, 1979; Iben & Tutukov, 1984; Webbink, 1984). The amount of energy needed to unbind the envelope $E_{\rm bind}$ is equated to the energy input from the orbital in-spiral (written as the change in the orbital energy $\Delta E_{\rm orb}$) multiplied by an efficiency parameter $\alpha_{\rm CE}$: $E_{\rm bind} \approx \alpha_{\rm CE}\Delta E_{\rm orb}$. Knowing that the orbital energy of masses $m_1$, $m_2$ orbiting each other at separation $a$ is $E_{\rm orb} = Gm_1m_2/(2a)$, we can write:

$$E_{\rm bind} = \alpha_{\rm CE}\left(-\frac{GM_1M_2}{2a_{\rm ini}} + \frac{GM_{\rm core}M_2}{2a_{\rm f}}\right) \quad , \tag{1.7}$$

where $M_1$ is the mass of the donor, $M_{\rm core}$ is the mass of its core (that remains after the envelope ejection), $M_2$ is the companion mass, $a_{\rm ini}$ is the initial and $a_{\rm f}$ the final separation. The case when the final separation is such that any of the binary components is larger than their Roche lobe is interpreted as a merger (i.e. not enough energy is released to unbind to envelope). Otherwise, Eqn. 1.7 is used to estimate the resulting post-common envelope separation in a surviving binary. The $\alpha_{\rm CE}$ parameter was introduced to account for the fact that not all the energy input from the in-spiral can be used to unbind the envelope (e.g. due to energy loss in the form of radiation). As such, it would take a value between 0 and 1. In theory, due to additional energy sources such as energy from accretion of mass by the companion or energy from recombination of ions in the expanding envelope, $\alpha_{\rm CE}$ could in some cases take values above 1 (Ivanova et al., 2013b). The envelope binding energy $E_{\rm bind}$, on the other hand, is calculated based on detailed stellar models and the internal envelope structure of the donor star. Chapter VI of this thesis is devoted to $E_{\rm bind}$ calculations in the case of massive supergiants and common-envelope evolution in BH binaries.

### 1.3.4 OTHER PROCESSES AFFECTING THE BINARY ORBIT

Apart from mass transfer, there are a number of other processes that will affect the orbit of a binary system. I will briefly mention those relevant for this thesis.

Stars in a binary system are also affected by tidal interactions. Tides exchange angular momentum between the stars and the orbit until the binary is fully circularized and the rotation of both components is synchronized with the orbital period.[7] As a result, tidal interactions will usually spin up a star (e.g. a slowly-rotating star in a short-period binary) but in some cases can also cause it to slow down (e.g. rapidly-rotating stars that were spun up by accretion). The strength of tides acting on a star is a strong function of the size of that star compared to the orbital separation $R/a$, making the tides most efficient for stars that nearly fill their Roche lobes (e.g. Zahn, 1992). In particular, mass-transferring systems are expected to be quickly circularized and synchronized by tides.

The orbital dynamics are affected by the loss of mass through stellar wind from any of the binary components. This is typically modeled by assuming that the wind leaves the system with a high velocity and carries the specific angular momentum corresponding to the surface of the mass-losing star. Usually, mass loss through stellar winds leads to an increase in the orbital

[7]Systems in which the tides are strong enough to maintaining that state are referred to as being tidally locked.

separation. A notable exception are tidally-locked systems which experience magnetic braking. In that case the stellar wind is anchored to the magnetic field lines of the star and is forced to corotate out to a larger radii, thus carrying a larger amount of angular momentum and strongly braking the rotation of the star (Verbunt & Zwaan, 1981). Tidal locking ensures that the angular momentum lost in the wind is replaced by that from the orbit, causing the separation to decrease. Magnetic braking is thought to only be efficient in stars with sufficiently strong magnetic fields (e.g. low-mass stars with convective envelopes).

Sometimes, one of the binary components can experience a sudden ejection of a substantial amount of mass during its evolution, in particular during a supernova explosion. Similar to the steady mass loss through winds, a sudden mass loss perturbs the binary orbit. In fact, if the ejected amount is larger than half of the binary mass, the system is completely disrupted. As mentioned in Sec. 1.1, formation of a BH or a NS can also be associated with a velocity kick received by a newly formed compact object (natal kick), ranging from tens to hundreds of km/s, which affects the orbit and often results in a disruption of the binary (or in rare cases can safe the system from being disrupted by mass loss).

In the case of very close binaries with a compact object (for example BH LMXB systems or DCO binaries), the binary orbit is also affected by the emission of GW. This process leads to a decrease of eccentricity as well as of binary separation.

### 1.3.5 Computations in stellar and binary evolution

Four stellar structure equations describes the hydrostatic equilibrium, mass conservation, energy transport (via radiation), and energy conservation. Together with an equation of state and a set of equations describing changes in the abundance (one per isotope), this set of highly non-linear coupled differential equation can be used to numerically 'solve' a star. The equations contain a large number of parameters that are computed separately and tabulated as input data for stellar codes (e.g. opacity tables, atomic data, equations of state, nuclear reaction networks).

In 1D stellar evolution codes, a star is represented by a one-dimensional mesh of layers: going from the center to the surface. For a typical number of layers per star in modern codes ($\sim 10^3 - 10^4$) and a number of isotopes included in the computation ranging from $\sim$ 20 to 200 (depending on complexity of the considered problem), obtaining a solution for the stellar structure (i.e. an evolutionary step) requires solving $10^4 - 10^6$ non-linear ordinary differential equations. Luckily, this task is not outside the regime of well-established numerical methods and the computational power of modern computers. A full evolutionary cycle of a star may then be computed as a series of $\sim 10^4 - 10^5$ evolutionary steps. One might ask: if this is possible then why is the evolution of stars not a fully solved problem? The method described above simply provides a series of solutions that are hydrostatic. It does not account for a number of processes that are dynamical in nature or can only be accurately treated in more than one dimension, such as turbulence and convection, rotationally-induced instabilities in a differentially-rotating star, or outbursts and eruptions. These and other processes, vital for the evolution and properties of stars, are included in 1D stellar codes

based on a number of simplifications or parametric prescriptions, which need to be calibrated (most importantly by observations). The same is true for all the processes related to binary evolution, such as mass transfer evolution or tidal torques, the implementation of which in 1D stellar codes naturally requires approximations. In addition to these intrinsic limitations of the method, computation of stellar models even in one dimension remains numerically challenging in a number of specific but important cases (for instance, models of radiation-dominated envelopes of the most luminous stars or computations of very high mass transfer rates in interacting binary systems). It is worth noting that although 3D models of stars exist, their computational expense is so large that they are still a long way away from replacing the 1D approach in various areas of stellar astrophysics.

An alternative approach to detailed 1D stellar-evolution codes described above are rapid binary-evolution codes. Instead of solving the stellar structure equations, such codes model stellar evolution by relying on analytical fits to pre-computed evolutionary sequences of stars of different masses and metallicities. In each evolutionary step, a star is described simply by a number of its global properties such as the mass, radius, temperature, angular momentum, age, the current burning stage, and so on. All the relevant stellar and binary evolution processes – such as stellar winds, mass transfer stability and evolution, core collapse and compact object formation, or common-envelope evolution (and many others) – are modeled using simple parametric prescriptions or approximations guided by the results from dedicated detailed studies. The rapid method, although containing many simplifications, allows one to compute the evolution of tens of millions of binary stars and to create a population model (which is referred to as population synthesis). The computation of so many models is necessary to cover the parameter space of all the possible initial binary configurations: different primary masses, mass ratios, orbital periods, eccentricities, and metallicities. Detailed binary evolution models from 1D stellar codes exploring this entire parameter space and all the evolutionary stages (e.g. not just the main sequence) are still unavailable. In this thesis we make a use of both a rapid binary-evolution code (chapters II-IV) as well as a detailed 1D stellar-evolution code (chapters V-VII). In the next section, I will introduce the most important challenges and open questions that were studied in the thesis.

Notably, one of the ingredients of the population-synthesis method are initial distributions of the above-mentioned binary parameters, needed to assign probabilistic weights to the computed models (for instance, in a real population massive binaries are formed much more rarely than low-mass stars). In Sec. 1.1, I introduced the initial mass function. Similarly, astronomers have empirically derived initial distributions of orbital periods, eccentricities, and mass ratios with which the binary systems are formed. For a long time, these distributions were treated as independent from each other: even though evidence for inter-correlation existed, a quantitative calibration was missing. This has changed thanks to Moe & Di Stefano (2017) who analysed more than 20 surveys of massive binary stars and corrected their results for selection effects and other biases. They combined the data into a homogeneous sample, to which they were able to fit analytic functions that account for various inter-correlations between the initial binary parameters. In chapter III, we will investigate the effect of these findings on the predicted population of DCO mergers.

## 1.4 Formation puzzles of black-hole binaries

### 1.4.1 Black-hole X-ray binaries

As introduced in Sec. 1.2, the majority of BHs with dynamical mass measurements reside in X-ray binaries with low-mass main-sequence companions ($< 2\,M_\odot$) and short-period orbits ($\lesssim 1$ day): BH-LMXBs. Such systems are expected to originate from binaries with a massive primary star $M \gtrsim 20 - 25\,M_\odot$ (a BH progenitor; Fryer et al., 2012) and a low-mass companion ($< 2\,M_\odot$). Given a small separation at the BH-LMXB stage, the binary must have interacted through mass transfer in the past. The commonly-accepted evolutionary scenario (e.g. Verbunt, 1993) dictates that the massive primary expands in radius during its evolution and overflows its Roche-lobe. The mass transfer that commences is dynamically unstable due to an extremely unequal mass ratio of the system. A common-envelope evolution seems unavoidable: it is at that stage of the scenario that the binary separation is significantly reduced down to a few $R_\odot$. The small separation is then maintained until the BH-LMXB stage and allows the main-sequence companion to overflow its Roche lobe and start transferring mass onto the BH. Notably, for this scenario to be effective, a non-negligible fraction of BHs needs to be formed with very small natal kicks.

The above common-envelope scenario was first suggested more than 30 years ago as an explanation of the origin of the A0620-00 BH X-ray binary (de Kool et al., 1987). In the case of BH-LMXB, however, the scenario has several flaws. First, many authors pointed out that the dynamical inspiral of a low-mass star in the common envelope originating from a massive BH progenitor does not provide enough energy to eject the envelope (Portegies Zwart et al., 1997; Kalogera, 1999; Podsiadlowski et al., 2003; Yungelson & Lasota, 2008). A merger could only have been avoided for apparently unphysically large values of the $\alpha_{\rm CE}$ parameter reaching even a few tens for some BH-LMXB systems (e.g. Yungelson & Lasota, 2008). Several modifications to the common-envelope energy formalism have been proposed to resolve this issue (for a recent review, see Li, 2015), e.g. additional energy source from the nuclear-burning in deep envelope layers (Podsiadlowski et al., 2010) or an alternative core-envelope boundary that would allow for a lower binding energy of the envelope (Tauris & Dewi, 2001). The modified common-envelope scenarios, however, fail to reproduce the companion mass distribution that in the observed systems peaks at around $0.6\,M_\odot$ (Wiktorowicz et al., 2014). Several alternative scenarios have been proposed, none of which seems to be able to reproduce all of the characteristics of the BH-LMXB population. For example, Justham et al. (2006) suggested that BH-LMXB could originate from systems with intermediate-mass secondaries (usually of $\sim 5\,M_\odot$), which would help to overcome the common-envelope ejection problem. However, among other inconsistencies, this scenario is in tension with the effective temperatures of the donor stars. More exotic scenarios tend to struggle to reproduce the total number of BH-LMXBs in the Milky Way (estimated at around $10^3 - 10^4$ based on wide-field X-ray surveys).

In chapter II we investigated the recently proposed scenario for the formation of BH-LMXBs from wide BH binaries perturbed by repeated fly-by encounters in the Galactic field. In chapter VI, on the other hand, we revisit the discussion of common-envelope ejection in the context of

BH-LMXBs, showing cases in which it could be possible with $\alpha_{\rm CE}$ below 1.

Besides the intriguing formation puzzle of BH-LMXBs, perhaps even more strongly connected with this thesis are BH X-ray binaries with high-mass donor stars (BH-HMXBs), which are a centerpiece of various evolutionary scenarios of massive binary systems. In a few BH-HMXBs (e.g. Cyg X-3 or NGC300 X-1) the companion has already lost its hydrogen-rich envelope and is a massive helium star: a Wolf-Rayet (WR) star. Such systems might be the most immediate progenitors of close BH and BH-NS binaries: gravitational-wave (GW) sources (Bulik et al., 2011; Belczynski et al., 2013). In particular, it was suggested that in BH-WR binaries with sufficiently close orbits (the exact separation threshold being rather uncertain) tidal forces could be strong enough to synchronize the WR star with the short-period orbit, thus making it a fast rotator (Kushnir et al., 2016; Zaldarriaga et al., 2018). Assuming that this angular momentum could be preserved during the collapse into a BH, the secondary BH formed in such systems could potentially be fast rotating, with implications on the effective spin values measured in GW (Hotokezaka & Piran, 2017b; Qin et al., 2018, , see also chapter IV). As we discuss in chapter VI, it is important to properly take the duration of the BH-WR stage into account in those considerations (which, as we will demonstrate in this thesis, can strongly depend on metallicity). It is interesting to point out that the measurements of BH spins in BH-HMXBs, although rather uncertain, appear to be significantly larger than the low spin values suggested by the small effective spins of the binary BH merger population (Miller & Miller, 2015). This discrepancy could be explained by somewhat different evolutionary paths leading to BH-HMXBs and binary BH mergers (Qin et al., 2019) Finally, BH X-ray binaries with preferentially inclined orbits and intermediate- or high-mass donors are likely to appear as ultra-luminous X-ray sources (ULXs; Kaaret et al., 2017). Thanks to their high X-ray luminosity ($L_X > 10^{39}$ erg/s), ULXs can be found up to distances of tens of Mpc across a spectrum of different galaxy types, surviving as a test-bed of the effect of environment and the host metallicity on mass transfer evolution in massive binary systems (Walton et al., 2011; Swartz et al., 2011a; Kovlakas et al., 2020) It should be noted, however, that the nature of the accretor in most ULXs is unknown (whether a NS, a stellar-mass BH, or an intermediate-mass BH with $M > 100\,{\rm M}_\odot$).

### 1.4.2 THE MANY FORMATION SCENARIOS FOR DCO MERGERS

As discussed in Sec. 1.2, the separation between the two compact objects that will merge due to GW emission within a time shorter than the age of the Universe is much smaller than the radii reached by their massive star progenitors during their evolution. Unless the strong radial expansion of stars can somehow be avoided, binary systems that form the observable DCO mergers need to be tightened by some process during their evolution. Alternatively, DCO mergers may originate from two stars that evolved separately and only encountered each other after having collapsed to form a BH or a NS. Two fundamentally different ideas for the origin of DCO mergers distinguish between the isolatad binary evolution and dynamical formation channels. Many variations of these two scenarios have been proposed in the literature. Below, I will characterise their main versions.

**Isolated binary evolution**

The most commonly discussed version of the isolated binary evolution channel involves the evolution of an initially wide binary systems that is eventually tightened by mass transfer at the stage when the first compact object has already been formed. In the classical version of the channel, the orbital shrinkage is achieved through a common-envelope evolution resulting from dynamically unstable mass transfer (Tutukov & Yungelson, 1993; Portegies Zwart & Yungelson, 1998; Belczynski et al., 2002; Voss & Tauris, 2003; Belczynski et al., 2016b; Eldridge & Stanway, 2016), similarly to the formation of BH-LMXBs outlined earlier. After the common-envelope phase, the binary is a short-period system comprised of a compact object (NS or a BH) and a helium star of a few $R_\odot$ in size. The separation problem is thus solved. The common-envelope channel is among the most prominent formation channels discussed in the literature. It is widely considered to be the dominant channel for the formation of binary NS mergers. However, in chapter VI we will show that its efficiency in the case of binary BH mergers has most likely been severely overestimated (see also Marchant et al., 2021) . Moreover, it was proposed that a merging binary BH system could also be formed through stable mass-transfer evolution, without the need for a common-envelope phase (van den Heuvel et al., 2017). The stable mass transfer channel makes use of the fact that non-conservative mass transfer from a donor that is a few times more massive than the accretor can also lead to a significant shrinkage of the orbit (as discussed in Sec. 1.3).

In the so-called chemically-homogeneous evolution channel (de Mink & Mandel, 2016; Mandel & de Mink, 2016; Marchant et al., 2016), a binary BH merger originates from two massive, low-metallicity stars that are born in a binary system with an already small separation. In very close binaries the stars are synchronized with the orbital period due to tidal interactions and therefore fast rotating. Rapid rotation in leads to enhanced mixing of the the elements in stellar interiors (e.g. Maeder, 1987; Zahn, 1992). In sufficiently massive stars (BH progenitors), rotational mixing can distribute the produce of nuclear burning in the center throughout the entire star so efficiently that the star evolves as a chemically homogeneous object. Such stars can remain compact during their evolution, avoiding a Roche-lobe overflow despite living in close binaries. The low metallicity is required because at high metallicity, strong wind mass loss would lead to an expansion of the orbit and a loss of tidal synchronization. Without the tidal spin-up, stars would slow down the rotation, suppressing the chemically-homogeneous evolution (de Mink et al., 2009a).

**Dynamical formation channels**

Most stars and stellar systems in the Universe (binaries, triples, etc.) live their lives in sparsely populated regions, where dynamical encounters with other stars and stellar systems are extremely rare and in most cases insignificant. There are, however, much denser environments in which dynamical interactions are common. Examples include central regions of galaxies (nuclear star clusters), globular clusters, and young massive star clusters.

A series of dynamical encounters in dense stellar clusters may be an efficient way of forming binary BH mergers, with authors finding a contribution to the overall binary BH merger detection rate comparable to that of the classical binary evolution channel (e.g. Rodriguez et al., 2016a;

Fragione & Kocsis, 2018; Rodriguez et al., 2018b; Mapelli et al., 2021). Dynamical evolution in clusters is not expected to produce many merging NS binaries (Belczynski et al., 2018; Zevin et al., 2019; Ye et al., 2020)

Dynamical binary BH merger formation may be significantly enhanced in the presence of gas, for instance in the disks of active galactic nuclei (AGN) found around central regions of some galaxies (McKernan et al., 2012, 2014).The torque from the disk causes BHs to migrate within the disk towards the so-called migration traps, where they can encounter other BHs at relatively low velocities. This allows for the efficient formation of new or hardening of the existing binaries. The efficiency of the AGN disk channel is highly uncertain (McKernan et al., 2018).

Merging DCOs can also form due to a combination of binary interactions and dynamical processes, for instance by evolving in triple or higher-order systems (e.g. Antonini et al., 2017b; Hamers & Thompson, 2019).

**The challenge of disentangling the formation channels**

As outlined above, many formation channels for DCO mergers have been proposed in the literature, especially in the case of binary BHs. The population of GW sources detected by the LIGO/Virgo likely contains a mixture of systems formed through different channels. Single exceptional events might be showing characteristics favoring or disfavoring a particular formation scenario. For instance, the most massive event observed to date (GW150921), with the primary mass measured to be above $65\,M_\odot$ at 99% credibility, is a challenging system to explain by isolated binary evolution scenarios (Abbott et al., 2020c). In general though, we are currently unable to identify which channels dominate the formation of DCO mergers. This largely due to enormous uncertainties in theoretical scenarios and the predicted rates and properties of GW sources they could produce. Building a better understanding of massive star and binary evolution, the central theme of this thesis, is one of the key steps in alleviating the situation and making the full use of GW astronomy in the future. Of particular interest is the role of low metallicity in the formation of binary BH mergers, which I will describe below.

### 1.4.3 How important is low-metallicity for progenitors of binary BH mergers?

The BH masses in the first detected binary BH merger GW150914 ($\sim 25-40\,M_\odot$) were above the BH masses measured in all the known BH X-ray binaries ($\lesssim 20-25\,M_\odot$, mostly $< 10\,M_\odot$). As mentioned in Sec. 1.2, this has led to a suggestion that the GW150914 event may have occurred in a metal-poor galaxy, where the low-metallicity of the progenitor stars had led to the formation of BHs more massive than those found in the Milky Way and in the local Universe (where the BH X-ray binaries are). Apart from GW150914, many of the subsequent GW events were mergers of BHs of $\sim 20\,M_\odot$ and more (see Fig. 1.4). A question arises whether metal-poor environments is where most the observed binary BH mergers originate (Chruslinska et al., 2019; Chruslinska & Nelemans, 2019a). It should be noted that there is a strong bias towards more massive BHs in

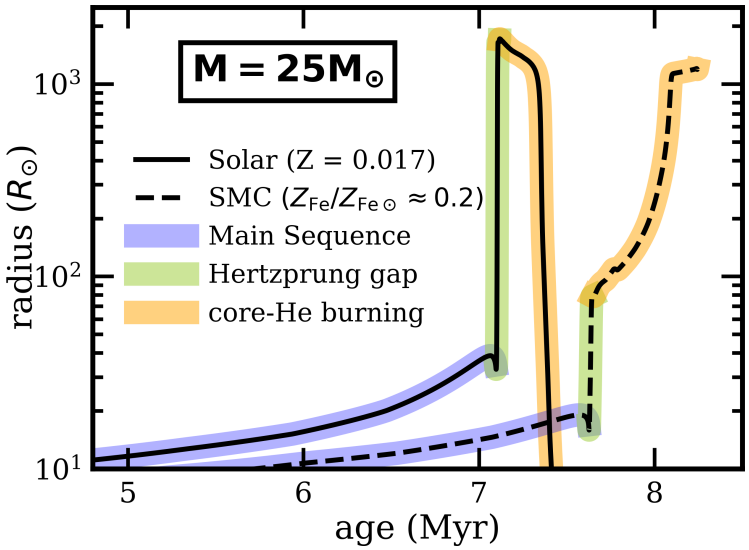


Figure 1.7: Radius evolution of 25 $M_\odot$ single stellar models computed at high (Solar) metallicity (solid line) and a low-metallicity, characteristic of the Small Magellanic Cloud (dashed line). Colors indicate the main evolutionary stages.

the detected sample due to their stronger GW signal. Based on the detections so far, the intrinsic primary BH mass distribution could roughly be fitted with a broken power-law $p(M_1) \propto M_1^{-\alpha}$ with $\alpha \approx 1.5$ below $M_1 \approx 40\,M_\odot$ and $\alpha \approx 5.6$ above (with large uncertainties and tentative evidence for more complex features in the $M_1$ distribution; Abbott et al., 2021).

Prior to the GW150914 discovery, it was already suggested that massive binary evolution at low metallicity could produce merging binary BHs more frequently compared to that at high (~ Solar) metallicity, i.e. even without taking the detection bias into account (Belczynski et al., 2010b). The higher formation efficiency of binary BH mergers from low-metallicity binaries was also reproduced in a number of more recent results (Giacobbo et al., 2018; Chruslinska et al., 2019; Neijssel et al., 2019), including our work presented in chapter III. There are two main reasons for this metallicity effect. Firstly, evolution at low metallicity is thought to have weaker stellar winds which leads to more massive cores at the end of stellar lives. These are more likely to collapse directly to form a BH rather than explode in a supernova and experience a natal kick that could disrupt the binary, according to the most commonly used prescription in the literature (Fryer et al., 2012). This would lead to a higher survival rate of low-metallicity binaries after the first BH formation (when in the standard common-envelope scenario the orbit is still wide and easy to disrupt).

Secondly, metallicity affects the way in which a massive star expands in radius after the end of the main sequence (Brunish & Truran, 1982; Baraffe & El Eid, 1991). This is illustrated in Fig. 1.7, where as a function of age, I plot the radius of a 25 $M_\odot$ star at high, Solar metallicity (solid line) as well as at low-metallicity, characteristic of the Small Magellanic Cloud (dashed line). As the colors indicate, a high-metallicity star experiences an episode of very significant expansion right after the end of the main sequence, in the transition to the core-helium burning phase (the

so-called Hertzprung gap). In a binary system, this is often when such a star would overflow its Roche lobe and start transferring mass to its companion. Low-metallicity massive stars, on the other hand, tend to expand much less before the onset of core-helium burning and continue to expand up to the red-supergiant size ($R \sim 1000\,\mathrm{R}_\odot$) during this stage, as illustrated in Fig. 1.7. This dramatically increases the chance for a mass transfer interaction with a core-helium burning donor. Belczynski et al. (2010b) argues that a common-envelope phase initiated by such a star has a much better chance of survival than in the case of a Hertzprung-gap donor (the later often being assumed to always result in stellar mergers). In addition, in various population-synthesis models (including ours in chapters II and III), mass transfer from a core-helium burning giant is assumed to be more prone to develop a dynamical instability and a common envelope in the first place. As a result, the differences in the post-main sequence expansion of massive stars of different metallicities illustrated in Fig. 1.7 have led to claims for a significantly higher efficiency of the common-envelope formation channel of BH binaries at low metallicity.[8] In the last three chapters of this thesis, we will scrutinize the way in which metallicity affects mass transfer evolution in massive binaries and the above-mentioned assumptions in particular. We will show that, most likely, the preference for low-metallicity has been severely overestimated in most population models for binary BH mergers from common-envelope evolution.

## 1.5 THIS THESIS

This thesis is devoted to two main subjects. The first is a study of massive binary evolution pathways leading to the formation of BH X-ray binaries and GW sources (binary BH and NS mergers). The second, motivated by the suggestion that most binary BH mergers originate from metal-poor environments, is a detailed investigation of the effect of metallicity on the evolution of massive stars in binary systems (in particular when they evolve through phases of mass transfer). The work is computational in nature. In chapters II-IV, we make a use of a rapid binary-evolution code StarTrack that relies on analytic approximations of stellar evolution and allows one to explore the full parameter space. In chapters V-VII, we perform detailed stellar-evolution computations with the MESA code, which solves the stellar-structure equations and accounts for additional processes such as chemical mixing or rotation.

In chapter II, in an attempt to tackle the long-standing formation puzzle of BH-LMXB systems, we take on a poorly studied topic of binary evolution coupled with stellar system dynamics. Motivated by Michaely & Perets (2016), we investigate how frequently random fly-by encounters in the Milky Way disk could perturb orbits of ultra-wide BH binaries ($a \gtrsim 500$ astronomical units) up to very high eccentricities ($e > 0.99$), at which point tidal interactions at the pericenter passage could circularize the orbit producing a close BH system with a low-mass main-sequence companion: a BH-LMXB progenitor. To this end, we modify the StarTrack rapid binary-evolution code (Belczynski et al., 2008a) to include the effect of random dynamical three-body interactions

[8] In the mass range for NS formation the post-main sequence expansion is less dependent on metallicity.

on the orbital parameters. Combined with a simple Milky Way model, we estimate the size and properties of the population of BH-LMXB candidates formed through the scenario proposed by Michaely & Perets (2016). We discuss the viability of the considered channel in resolving the BH-LMXB formation challenges.

In chapter III, prompted by the revolutionary discovery of GW sources, we study the formation of binary BH and NS mergers as products of isolated binary evolution. Specifically, we investigate the effect of inter-correlations between the initial binary parameters (unaccounted for in previous studies) on the formation efficiency of different types of merging DCOs and their predicted detection rate with the LIGO/Virgo interferometers. To do so, we build a binary population model with the StarTrack code and combine it with a simple model for the Cosmic star formation history. In addition, we consider the effect of variations in the initial-mass function while accordingly adjusting the Cosmic star formation rate. We discuss the implications on the predicted rates of the LIGO/Virgo GW sources.

In chapter IV, motivated by the low values of effective spins of all the ten binary BH mergers reported at the end of the second observing run of the LIGO/Virgo collaboration, we investigate the range of effective spin distributions predicted by the common-envelope formation scenario. To this end, we employ the StarTrack code to create a series of population models of GW sources. We consider three different prescriptions for the initial BH spin values (motivated by results from detailed stellar models with various assumptions on the internal angular momentum transport in massive stars) as well as explore several variations in the key assumptions of the population-synthesis method. We discuss the results in the context of distinguishing between different formation channels of binary BH mergers.

In chapter V, stimulated by the supposed importance of stellar evolution at low-metallicity in the formation of binary BH mergers, we investigate the effect of metallicity on the radial expansion of massive stars and, consequently, at which point in their evolution they would initiate mass transfer when in binary systems. We compute extensive grids of detailed models of single massive stars across a range of metallicities (from 100% down to 1% of the Solar metallicity) and masses (from $10\,M_\odot$ to $80\,M_\odot$). We use the MESA stellar-evolution code (Paxton et al., 2011), varying several assumptions known to affect the post-main sequence expansion of massive stars. We constrain the models by comparing the number of blue, yellow, and red supergiants they predict with the observed samples in the Milky Way and in the Small Magellanic Cloud. We discuss the implications of our findings in the context of various binary evolution scenarios.

In chapter VI, we set out to decipher which massive binary systems can evolve through and survive a common-envelope phase postulated as one of the two main channels for the formation of GW sources that are being detected by the LIGO/Virgo interferometers. We employ the MESA stellar-evolution code to carry out extensive modeling of internal structures of supergiants at different metallicities. We calculate the binding energies of their envelopes, studying the role played by metallicity and the outer convective zone that develops during the red supergiant stage. Based on the obtained binding energies, we predict the outcome of a common-envelope evolution (whether survival or a merger) in massive binaries with a BH companion across a grid of different

masses, orbital periods, and metallicities. We discuss the results in the context of the formation of GW sources and BH-LMXBs.

In chapter VII, we continue our investigations of the effect of metallicity on the evolution of massive binary systems, in particular through phases of post-main sequence mass transfer. To this end, with the MESA stellar-evolution code, we compute grids of detailed binary models at three different metallicities (Solar and that of Large and Small Magellanic Clouds), spanning a wide range of orbital periods (from $\sim$ 3 to 5000 days) and primary masses (from 10 $M_\odot$ to 36-53 $M_\odot$, depending on metallicity). We discuss our results in the context of binary interaction products in stellar populations of different metallicities, pre-supernovae structures of massive stars, and BH X-ray binary populations.

# Chapter 2

# Dynamical formation of black hole low-mass X-ray binaries in the field: an alternative to the common envelope

J. Klencki, G. Wiktorowicz, W. Gladysz & K. Belczynski

*MNRAS, volume 469, 3088, (2017)*

**Abstract**

Very wide binaries (> 500 AU) are subject to numerous encounters with flying-by stars in the Galactic field and can be perturbated into highly eccentric orbits ($e \sim 0.99$). For such systems the tidal interactions at close pericenter passages can lead to orbit circularization and possibly mass transfer, consequently producing X-Ray binaries without the need for common envelope. We test this scenario for the case of Black Hole Low-Mass X-Ray Binaries (BH LMXBs) by performing a population synthesis with numerical treatment of random stellar encounters. We test various models for the threshold pericenter distance under which the tidal forces cause circularization. We estimate that fly-by interactions can produce a current population of ~ 60–220 BH LMXBs in the Galactic field. The results are sensitive to the assumptions on the tidal circularization efficiency and the BH natal kick, since zero to very small kick velocities of several km/s are required for the wide systems to survive the BH formation (~60% of the cases in our simulations). We show that the most likely donors are low-mass stars (< 1 $M_\odot$; at the onset of mass transfer) as observed in the population of known sources (~ 20). However, the low number of systems formed along this route is in tension with the most recent observational estimate of the number of dormant BH LMXBs in the Galaxy $10^4$–$10^8$ (Tetarenko et al., 2016b). If indeed the numbers are so high, alternative formation channels of BHs with low-mass donors need to be identified.

## 2.1 INTRODUCTION

There are currently 19 Galactic X-ray binary systems in which black holes (BHs) have been confirmed dynamically, with a few more extragalactic sources observed (Remillard & McClintock, 2006; Casares & Jonker, 2014; Wiktorowicz et al., 2014; Tetarenko et al., 2016c). They are all close binaries (with the majority of orbital periods $P_{\rm orb} < 1$ day), for which a mass transfer occurs and an accretion disc is formed around the black hole and is responsible for the X-ray activity (Shakura & Sunyaev 1973; Lasota 2015). 16 of these systems possess companion stars of relatively low mass ($< 2\,M_\odot$), with the distribution peaking at around $0.6\,M_\odot$ and the spectral types ranging from A2V to M1V – they are classified as low-mass X-ray binaries (LMXBs). All known BH LMXBs are transient X-ray sources, exhibiting occasional outbursts with their brightness increasing by 3-5 orders of magnitude, which are attributed to disc instability (e.g. Lasota, 2001).

The BH LMXBs are most commonly thought to originate from primordial binaries of a black hole progenitor ($M_{\rm a} > 20 - 25\,M_\odot$, e.g. Fryer et al., 2012) and a much less massive main sequence (MS) secondary ($M_{\rm b} < 2\,M_\odot$) although evolution starting with intermediate mass secondaries was also proposed (Justham et al., 2006; Chen & Li, 2006). As the primary expands during its evolution it is expected to fill its Roche lobe and launch a dynamically unstable mass transfer, initiating the common envelope (CE) phase (Paczynski, 1976). As a result of this short-lived evolutionary stage the separation between the components decreases significantly, which ultimately leads to a later mass transfer from the low-mass star onto the black hole and prolonged X-ray activity. The formation of a black hole from a Zero-Age Main-Sequence (ZAMS) star takes less than 10 Myr. In such a time the low-mass secondary is still at the beginning of the MS (or even still during pre-MS contraction; Ivanova, 2006) and is expected to remain a MS star for the next 2.5–10 Gyr.

This now considered standard scenario was first suggested nearly 30 years ago to explain the origin of the A0620-00 black hole X-ray binary (de Kool et al., 1987). Since then, however, multiple studies have pointed out flaws of this conception in the particular case of BH LMXBs, suggesting that it is difficult for a binary of a massive giant and a much less massive companion to eject the CE at the expense of its orbital energy (e.g. Podsiadlowski et al., 2003). Thus, unless abnormally high values of the CE ejection efficiency are adopted (Yungelson & Lasota, 2008), the system is most likely to merge. In an attempt to justify such increased efficiency several modified CE models were proposed (see Li 2015 and references therein). Population synthesis studies have recently shown, however, that CE models in their current state fail to reproduce the distribution of donor mass of the observed BH LMXBs (Wiktorowicz et al. 2014; Wang et al. 2016), implying the need for either a more significant adjustment of the CE modeling or an alternative formation scenario to be considered.

Recently Michaely & Perets 2016 (hereafter MP2016) suggested that LMXBs (including those with black holes) could originate from very wide binaries ($a > 1000$ AU) that undergo a series of subsequent fly-by interactions with stars of the Galactic field. The authors predict that some of these wide systems should be excited into orbits of very high eccentricity, eventually circularized by tidal effects at pericenter. This essentially transforms a wide binary into a compact one, playing

a similar role to the CE phase in the standard scenario.

Dynamical formation of LMXBs is definitely not a new concept when it comes to dense stellar environments, such as globular clusters, where gravitational interactions and tidal captures take place most often (Clark 1975; Fabian et al. 1975). In fact, it appears that the formation channel of X-ray binaries through dynamical processes is very efficient, as $\sim 10\%$ of all LMXBs is being found in globular clusters, which contain only about $\sim 0.1\%$ of all stars in the Galaxy (Irwin, 2005) (note that these are all X-ray binaries with a neutron star as the accretor as all known BH LMXBs reside outside globular clusters). Similar processes should be effective also in the most dense, central regions of galaxies. This was confirmed by Voss & Gilfanov (2007) who carried out Monte Carlo simulations of a binary population in the bulge of M31, applying the FEWBODY code (Fregeau et al., 2004) to numerically simulate random dynamical interactions with passing by stars.

A similar study, however, has never been done for the Galactic disc, where all of the known BH LMXBs reside (Li, 2015). Although the disc is typically considered to not be dense enough for stellar encounters to play an important role, dynamic interactions do become significant for wide binaries with naturally larger cross-sections (e.g. Bahcall et al. 1985). It is even predicted that very wide binaries should be the primary source of stellar collisions in the Milky Way (Kaib & Raymond, 2014), thanks to similar excitations to highly eccentric orbits as considered by MP2016 in their scenario for LMXBs formation.

Here we perform a population synthesis study on the dynamical formation of BH LMXBs from primordial binaries in the Galactic disc. We focus only on binaries with a black hole as their primary and a MS star as their secondary, as the origins of these systems remain most mysterious (MS companions are also most frequent among observed systems, as $\sim 75\%$ of donors are low-mass dwarf stars, Corral-Santana et al., 2016).

The paper is organized as follows: in section 2 we describe the MP2016 scenario, as well as introduce our modeling of dynamic interactions and tidal circularization. In section 3 we describe our population synthesis approach and utilized computer codes. In section 4 we present and discuss our results. We conclude in section 5.

## 2.2 Dynamical interactions as source of X-ray binaries

### 2.2.1 LMXB formation scenario of MP2016

The scenario for the dynamical formation of a LMXB is explained in details in MP2016, with an analytical description for the probability of the MS companion being tidally captured by the BH in a BH-MS system due to an interaction with a field star given therein. Here we briefly present the main points as well as provide a model for integrating dynamical interactions into binary population synthesis, essentially substituting the approximate analytical approach of MP2016 with the numerical treatment of stellar encounters.

Let us consider a wide binary ($a > 1000$AU) of a stellar BH and a companion MS star. Its large cross-section makes it subject to random short duration interactions with flying-by field stars. Such

encounters affect the system's angular momentum and energy, thus changing its orbital parameters. MP2016 predict that it is possible for a binary to be perturbated into a very highly eccentric orbit ($e \approx 1$), for which the distance between components at pericenter ($d_{\rm per} = a(1-e)$) can be very small. They define a threshold distance $d_{\rm tidal}$ between components, at which tidal effects become strong enough to cause circularization of the orbit – a wide, eccentric BH-MS system fulfilling $d_{\rm per} < d_{\rm tidal}$ is thus transformed by tidal forces into a close, circular BH-MS binary. Such a system is subject to processes which may further decrease its separation (e.g. magnetic braking, gravitational waves radiation) leading to mass transfer and consequent formation of a LMXB.

Estimating the value of $d_{\rm tidal}$ for a given binary is a complicated problem since our understanding of tides and energy dissipation mechanisms remains very uncertain. For their model MP2016 adapted results obtained by Kaib & Raymond (2014) who in the regime of dynamic tides investigated timescales of circularization due to energy dissipation at pericenter passages for equal mass MS-MS wide eccentric binary systems. They conclude that circularization becomes significant (i.e. energy dissipated during single pericenter passage is comparable with the entire orbital energy) for $d_{\rm tidal} \approx 5R_{\rm mean}$, where $R_{\rm mean}$ is a mean radius of the binary components – in the case of a BH-MS system $R_{\rm mean} = 0.5\,R_*$, where $R_*$ is the radius of the MS secondary. This result is in agreement with prescription developed by Portegies Zwart & Verbunt (1996) stating that circularization occurs immediately if the stellar radius of one component is larger than 0.2 of the distance between binary components at periastron. In order to adopt the result of Kaib & Raymond (2014) to a binary of unequal masses MP2016 apply an additional factor of mass ratio $1/q = M_{\rm BH}/M_*$:

$$d_{\rm tidal_MP} = 2.5 \;\; R_* \, \frac{M_{\rm BH}}{M_*} = 2.5 \;\; R_* \, \frac{1}{q}, \tag{2.1}$$

where $M_{\rm BH}$ and $M_*$ are masses of BH and MS respectively. Adding the term $1/q$ alone is a very simplified approach to stellar mass scaling (as it does not take into account changes of stellar radius or inner structure), which can be often justified in problems we have poor understanding of, such as tidal interactions. However, according to relation (1) the ratio $d_{\rm tidal}/R_*$ grows very big for small values of $q$ expected in the case of potential BH LMXBs progenitors, as a typical mass of a stellar Galactic BH is around 7–8$M_\odot$ and the MS companion is a low-mass star, often $< 1M_\odot$ (Casares & Jonker, 2014). We find this behavior rather controversial and decide to additionally consider models which are less dependent on the components mass ratio, for which the threshold distance between binary components $d_{\rm tidal}$ is estimated based on the ratio $\alpha$ of MS radius and the size of its Roche Lobe (Roche Lobe filling factor), i.e.:

$$R_* = \alpha \; R_{\rm RL} = \alpha \;\; q_{\rm RL} \;\; d_{\rm tidal} \tag{2.2}$$

where $q_{\rm RL}$ can be approximated with the formula of Eggleton (1983):

$$q_{\rm RL} = \frac{0.49 q^{2/3}}{0.6 q^{2/3} + \ln(1 + q^{1/3})} \tag{2.3}$$

This yields the condition for $d_{\rm tidal}$ to be:

$$d_{\rm tidal} = \alpha^{-1} \;\; R_* \;\; q_{\rm RL}^{-1} \tag{2.4}$$

In our population synthesis we test one model following relation 2.1 proposed by MP2016 as well as three models corresponding to values $\alpha = 0.2$ (very optimistic), $\alpha = 0.5$ (optimistic) and $\alpha = 0.8$ (most realistic) in relation (4). Fig. 2.1 shows a comparison of $d_{\rm tidal}$ vs $q$ relation in each of these cases. The expected range of $q$ for LMXBs is about $q < 0.25$.

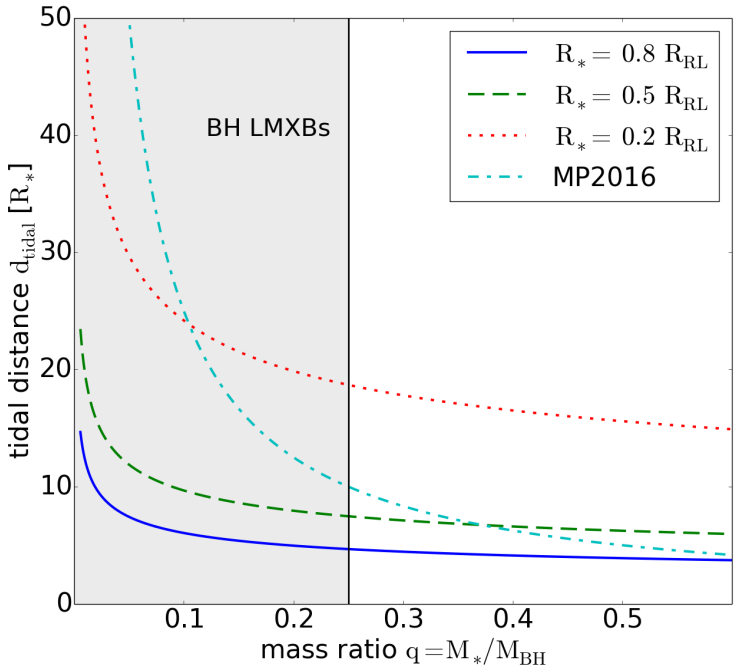


FIGURE 2.1: Comparison of 4 different models for the tidal distance $d_{\rm tidal}$ between components in a BH-MS binary, at which we assume tidal circularization becomes significant. $d_{\rm tidal}$ is expressed in the unit of radius of the MS component $R_*$. The first 3 models are based on the minimal required Roche Lobe filling factor $\alpha$, i.e.: $R_* = \alpha R_{\rm RL}$, with the values $\alpha = 0.8$ (most realistic), $\alpha = 0.5$ (optimistic) and $\alpha = 0.2$ (very optimistic). The last model is following relation 2.1 proposed by MP2016.

For a mass ratio $q = 0.2$ the size of a MS secondary Roche Lobe is approximately equal to 0.25 the distance between binary components (i.e. $R_{\rm RL} \approx 0.25\ d_{\rm tidal}$). This means that for $q \gtrsim 0.2$ the model with $\alpha = 0.8$ (i.e. $R_* = 0.8\ R_{\rm RL}$ required for circularization) is roughly corresponding to the prescription for immediate circularization $R_* = 0.2\ d_{\rm tidal}$ given by Portegies Zwart & Verbunt (1996) and supported by Kaib & Raymond (2014). For lower mass ratios, however, especially in our optimistic models, the threshold pericenter distance required for tidal circularization corresponds to $R_* < 0.2\ d_{\rm tidal}$. In such case the timescale of circularization could be significantly longer, possibly even a few Gyr.

To illustrate this we simulated the evolution of orbital parameters ($a$,$e$) of an exemplary wide and eccentric BH-MS binary from our population synthesis modeling using the STARTRACK binary evolution code (Belczynski et al., 2002, 2008a, detailed description in section 2.3.2) – see figure 2.2. STARTRACK calculates tidal evolution in the equilibrium-tide, weak-friction approximation of Zahn (1989), using Portegies Zwart & Verbunt (1996) prescription for immediate tidal circularization. The system of interest consists of a 8.3 $M_\odot$ BH and a 0.87 $M_\odot$ secondary MS of radius $R_* = 0.78\ R_\odot$. The starting semi-major axis was $a = 390$ AU, whereas the value of eccentricity was set such that for each model the exact threshold condition for circularization was satisfied ($e$ between 0.99978 and 0.999946 across the models). For such a low mass ratio $q = 0.87/8.3 \approx 0.1$ the condition $R_* = 0.2\ d_{\rm tidal}$ is never fulfilled, thus circularization does not occur instantaneously as calculated in STARTRACK. In fact, as figure 2.2 shows, only in models

with $\alpha = 0.5$ and $\alpha = 0.8$ the orbital size decreased quickly enough and full circularization was complete in under 10 Gyr. Even though the model with $\alpha = 0.2$ and the one adopted from MP2016 are thus proven to be extremely optimistic in the tidal regime of Zahn (1989), we decide to test them regardless in order to investigate how the efficiency of dynamical formation channel for BH LMXB could be affected by exceptionally strong tidal forces.

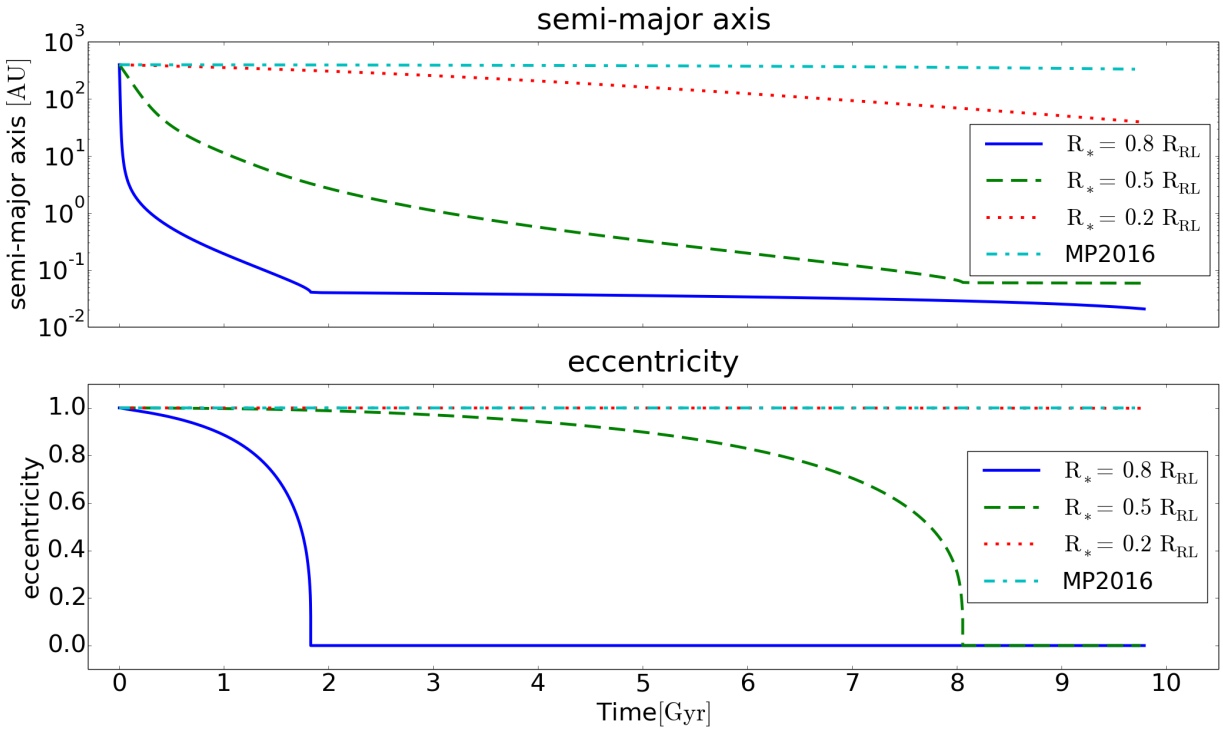


FIGURE 2.2: Evolution of orbital parameters as calculated by STARTRACK of a wide and eccentric BH-MS binary (initial parameters: $a_0 \approx 400$ AU and $e_0 \gtrsim 0.999$) fulfilling threshold condition for tidal circularization in 4 of our tested models. The binary components masses were $M_{BH} = 8.3\ M_\odot$ and $M_{MS} = 0.87\ M_\odot$, the MS star radius was $R_* = 0.78\ R_\odot$ at the beginning, evolving up to $0.79\ R_\odot$ at 2 Gyr and $0.85\ R_\odot$ at 8 Gyr. The value of eccentricity was set such for each model that the exact threshold condition for circularization was satisfied ($e$ between 0.99978 and 0.999946 across the models).

### 2.2.2 DYNAMICAL INTERACTIONS IN THE FIELD

In this study we investigate a simplified scenario in which wide binaries encounter only single stars, i.e. we assume the binary fraction of passing by stars equal to zero and only consider binary-single interactions. Let us consider a binary of masses $M_1$, $M_2$ and a semi-major axis $a$, located in the Milky Way at position $\vec{r}$ and moving with velocity $\vec{v}$. With its position in the Galaxy we can associate a value of local stellar number density $n_*$ and a local distribution of stellar velocities $f(\vec{v_*})$. The expected number of encounters in a time frame $\Delta t$ with stars passing by within distance $b_{\max}$ from such binary can be expressed as:

$$N(\Delta t) = n_*\ \Delta t\ \pi b_{\max}^2 \int |\vec{v_*} - \vec{v}|\ f(\vec{v_*})\ d\vec{v_*} \tag{2.5}$$

We define mean free time $t_{MF}$ as a mean time between stellar encounters for such a binary, which is equal to:

$$t_{\rm MF} = \frac{\Delta t}{N(\Delta t)} \tag{2.6}$$

The value of $b_{\rm max}$ was chosen as $b_{\rm max} = 5a$ because for larger impact parameters the eccentricity changes induced by a fly-by are negligible ($\delta e/e \ll 1$; Fregeau et al., 2004; Heggie & Rasio, 1996). It is worth noticing here that the rate of encounters ($t_{\rm MF}^{-1}$) is greater not only for wider binaries ($t_{\rm MF}^{-1} \propto a^2$) but it also increases for systems moving with velocity significantly different from the local mean velocity of passing-by stars.

Mean free time is a useful quantity for Monte Carlo simulations of a binary evolution. Upon each time step $\delta t \ll t_{\rm MF}$ we randomize whether or not a flying-by field star was encountered during this time, with the probability of such event equal to $\delta t/t_{\rm MF}$. If a star was encountered, we draw its relative velocity $\vec{v_{\rm rel}} = \vec{v_*} - \vec{v}$ from the local distribution of velocity $f(\vec{v_*})$, whereas its mass $M_{\rm single}$ is drawn from the Initial Mass Function (IMF). We use the Milky Way velocity distribution based on observational results of the Sloan Digital Sky Survey (SDSS, Bond et al., 2010, see section 2.3.3.1 for more details) and the IMF of Kroupa et al. (1993) with the power-law exponent modified to $-2.3$ for the stars of mass $\mathrm{M} > 1.0\,\mathrm{M}_\odot$, as recently adjusted by Sana et al. (2012).

Another important quantity describing a binary-single interaction is impact parameter $b$. Due to effect of gravitational focusing, the cross-section for two masses $M_{\rm binary}$ and $M_{\rm single}$ passing with relative speed $v_{\rm rel}$ within an impact parameter $b$ from each other is given by the conservation of energy and momentum (e.g. Voss & Gilfanov, 2007):

$$\sigma(b, v_{\rm rel}) = \pi b^2 \left(1 + \frac{2G(M_{\rm binary} + M_{\rm single})}{b\, v_{\rm rel}^2}\right) \tag{2.7}$$

Knowing $v_{\rm rel}$ and $M_{\rm single}$ we draw $b$ from the following distribution, obtained simply as a differential of the cross section 2.7 normalized to $b \in [0, b_{max}]$:

$$f(b, v_{\rm rel}) = \frac{1}{\sigma(b_{\rm max}, v_{\rm rel})} \frac{\partial \sigma(b, v_{\rm rel})}{\partial b} \tag{2.8}$$

## 2.3 Population synthesis modeling

### 2.3.1 General approach

Our intention is to provide a realistic approach to the problem of dynamical interactions of wide binaries and single stars in the Galactic field. We combine realistic initial conditions for stars and binaries, invoke relevant binary processes (BH formation with its potential effects on binary orbits) and apply a wide range of criteria on the key issue: tidal circularization of hyper-eccentric binaries. Investigating the effect of three-body encounters on a system evolution is a computationally heavy task, since for every wide system one can expect on the order of thousands of dynamical

interactions during its several Gyr long evolution, each of those needed to be simulated individually. To simplify the computations and focus on the most important factors for LMXBs formation in the MP2016 scenario we have split each binary evolution into two subsequent evolutionary stages: pre and post BH formation from the massive primary (hereafter denoted as the "pre-BH" and the "post-BH" stage).

The pre-BH stage begins with a zero-age binary and ends once the primary has ended its evolution and formed a BH. Since it only lasts for up to 10 Myr (progenitors of stellar BHs evolve very quickly) we assume no dynamical interactions taking place during this stage. Even though for a very wide binary ($a \sim 10^4$AU) it is possible to obtain mean free time between interactions of the order of Myr it is unlikely that a single encounter will change orbital parameters in a significant way, thus affecting the pre-BH evolution. This could happen if the encountered star was an exceptionally massive object of at least few solar masses (see Sec. 2.4.1 for discussion of this matter in the case of BH-MS systems). However, due to the combined effects of stellar evolution and the IMF being shifted towards lower masses, the majority ($> 90\%$, see discussion in Sec. 2.5.2) of field object are low-mass stars or white dwarfs ($M \lesssim 2\mathrm{M}_\odot$). On the other hand, internal binary evolution during this stage is very dynamic and thus the main focus of our simulations.

The post-BH stage begins with a newly-formed BH-MS binary and lasts until the present Galactic age. The primary factor affecting a wide binary evolution during such a long period is the influence of dynamic interactions with fly-bys. This stage is to last several Gyr on average, the exact length depending on the moment of a binary birth, thus multiple encounters with passing-by stars are expected and have to be accounted for. Their frequency depends on the local conditions in the Galaxy (i.e. stellar number density, velocity distribution), thus the evolution of a binary position in the Milky Way potential has to be calculated as well.

### 2.3.2 PRE-BH STAGE – BINARY EVOLUTION MODELING

We employ the STARTRACK binary population synthesis code to generate a population of BH-MS binaries. The code was created based on single stellar models adopted from Hurley et al. (2000) with special attention being given to massive stars and compact objects. A detailed description of STARTRACK can be found in (Belczynski et al., 2002) and (Belczynski et al., 2008a). Factors especially important for the evolution leading to wide BH-MS binaries have recently been updated, including the addition of new prescription for wind mass loss as well as the implementation of convection driven, neutrino enhanced supernova engines with rapid explosion development (Dominik et al., 2012; Belczynski et al., 2012b). For BHs natal kicks during supernova explosion we adopt Maxwellian distribution of kicks with $\sigma = 265\,\mathrm{km\,s^{-1}}$ (as for neutron stars, see Hobbs et al. 2005), with the value of the kick being lowered proportionally to amount of material falling back onto the BH (Fryer et al., 2012; Belczynski et al., 2016b). As a result the natal kicks for BHs are often negligible or very small . However, even in the case of no natal kick each system evolving into BH-MS is given an additional velocity of $\sim 10 - 20$ km s$^{-1}$ due to Blaauw kick (Blaauw, 1961), which is associated solely with the mass loss of the primary during BH formation.

For massive primaries we have chosen the mass range 19–150 $M_\odot$, to ensure a BH formation, whereas for secondaries a corresponding 0.08 $M_\odot$–$M_{primary}$ range. We adopt the initial parameters distributions from Sana et al. (2012), implied from the spectroscopic measurements of massive O-type stars. These include: the IMF for the primary proposed by Kroupa et al. (1993) with the power-low exponent modified to −2.3 for the stars of mass $M > 1.0\,M_\odot$, binary mass ratio $q = M_b/M_a$ flat distribution (as also obtained by Kobulnicky et al., 2006), eccentricity distribution $f(e) \propto e^{-0.42}$ in range [0.0, 1.0] and period distribution $f(P) \propto \log(P/day)^{-0.55}$ in range [0.15, 5.5]. Note that spectroscopic measurements can only reliably detect binary systems of orbital periods up to $\log(P/day) \lesssim 3.5$. However, basing on recent interferometric observations of Galactic massive stars by Sana et al. (2014), probing binaries of separations up to ∼ 200 AU, we expand the period distribution up to $\log(P/day) \lesssim 5.5$ (similarly to de Mink & Belczynski (2015a); Belczynski et al. (2016b) and other population synthesis works).

Such initial conditions result in widest binaries having separations of about ∼ 400 AU. Meanwhile some companions to massive stars are visually detected on even much wider orbits, of the order of thousands AU, thanks to lucky imaging (Peter et al., 2012) and space-based observations (Caballero-Nieves et al., 2014; Aldoretta et al., 2015). However, these observations also reveal that many of such ultra-wide systems with massive stars are in fact triples. In a recent work Moe & Di Stefano (2017) analyzed results of more than twenty surveys and concluded that companions to massive stars with orbital periods of $\log(P/day) \gtrsim 5.5$ are essentially tertiary components in hierarchical triples. For such systems the dynamics during close pericenter passages of the wide component would be much more complex, making them unlikely progenitors of X-ray systems in the MP2016 scenario – see Sec. 3.1.4 of MP2016 for details. We thus consider $\log(P/day) = 5.5$ to be a reasonable upper cutoff of the orbital period of our starting binaries.

We have evolved $4.5 \times 10^7$ binaries starting from ZAMS, with stellar formation history (SFH) assumed constant throughout the whole Milky Way age $t_{disc} = 10$ Gyr. Given SFR = $3.5 M_\odot yr^{-1}$ and binary rate $f = 0.5$ our sample corresponds to about 94% of the binaries with $M_a \geq 19 M_\odot$ in the Galactic disc population, so only a mild scaling was needed (i.e. the numbers of BH LMXB we eventually obtain across all our models are on average $1.0/0.94 \approx 1.06$ times the numbers of actual BH LMXB systems in our simulations). We adopt Solar metallicity (Z = 0.02 Villante et al., 2014) to all stars in the Galactic disk that we evolve.

Additionally, in order to be able to do a straightforward comparison with the results of MP2016, we also evolved $1.215 \times 10^7$ ultra-wide binaries with initial periods of $\log(P/day)$ from range [5.5, 8.5] and $f(P) \propto \log(P/day)^{-0.55}$ (keeping Sana et al. (2012) distributions for other initial binary parameters). Note that due to likely triple nature of systems this wide (Moe & Di Stefano, 2017) we exclude them from our main results and only address in the discussion (7.5).

An exemplary BH-MS candidate for future dynamically formed BH LMXB in our simulations was born at ZAMS as a MS-MS system of 29 $M_\odot$ primary and 0.75 $M_\odot$ secondary, with orbital parameters $a = 92$ AU and $e = 0.51$. As a core helium burning giant the primary expands up to a radius ∼ 1730 $R_\odot \approx 8$ AU. However, since the separation between components is very high, the giant does not fill its Roche lobe and no mass transfer occurs (in particular there is no CE

phase). The primary loses the majority of its mass due to stellar winds, which in turn increases the semi-major axis. Throughout the pre-BH evolution the primary reduces its mass down to $\sim 8.8$ $M_\odot$ and eventually becomes a naked helium star. At this stage the semi-major axis has been increased up to $a = 290$ AU, whereas the secondary mass and the orbit eccentricity remain unchanged. At around 6.8 Myr since ZAMS the primary evolves into a BH through a core-collapse supernova. No direct natal kick has been given to BH since all expelled material fell back onto it. Neutrino emission reduces its mass down to the final $M_{BH} \sim 7.9$ $M_\odot$, however, the associated Blaauw kick gives the binary only a negligible velocity of 0.03 km $s^{-1}$. The post-BH formation orbital parameters are $a = 306$ AU and $e = 0.47$.

It should be noted here that in our simulations we also evolve systems with much shorter separations $a < 10$ AU at ZAMS. During evolution as helium burning giant the massive primary in such binaries expands overflowing its Roche lobe and leading to the CE phase. In the vast majority of our systems this leads to a merger, as it is very difficult for a low-mass secondary to eject a massive envelope created by his companion (e.g. Wiktorowicz et al., 2014). The few systems which have undergone and survived the CE phase were all close binaries with separations of the order of a few AU. Due to their small cross-sections for stellar encounters they did not pay any role in the dynamical formation channel we investigated.

### 2.3.3 POST-BH STAGE – STELLAR ENCOUNTERS MODELING

All successfully formed BH-MS binaries are made subject to dynamical interactions during the long post-BH evolutionary stage. Similarly to the pre-BH stage and STARTRACK code regime, we take Monte Carlo approach to model random stellar encounters.

In this study we limit ourselves to BH-MS X-ray binaries only, which means that we require the secondary star to remain at the main sequence for the whole duration of the post-BH stage and to not evolve onto the giant branch until the present day. This limitation essentially favors the study towards less-massive companions (as they stay on the MS the longest), which are not only more numerous but, more importantly, are subject to larger perturbations from flying-by stars due to their lower orbital energy, thus being more likely to form an LMXB through the MP2016 scenario. It is worth pointing out here that the majority of donors in observed BH LMXBs are low-mass MS dwarfs (Li, 2015).

The big advantage of restricting ourselves to MS companions only is that low-mass MS stars evolve very slowly, without changing their mass or radius in a significant manner. This allows us to assume no stellar evolution throughout the post-BH stage. Same assumption can be made when it comes to interactions between binary components – such as tidal forces (eg. Zahn, 1989), mass transfer, gravitational waves emission (Peters, 1964) or magnetic braking (eg. Rappaport et al., 1983). In the case of binaries comprised of a stellar BH and a low-mass MS companion those effects only become important for systems with separations of a few solar radii. Meanwhile, encounters with field stars become relevant for binaries with semi-major axes of at least 10–100 AU (due to their cross section), which is a few orders of magnitude more. Of course once a condition

for tidal circularization is fulfilled and a wide and eccentric BH-MS binary becomes a compact and circular system with a separation of a few solar radii then the above-mentioned effects become significant again. However, the evolutionary fate of systems post tidal circularization is subject to large uncertainties (see the discussion in Sec. 2.3.3.3) and we do not model it in this study.

#### 2.3.3.1 Binary dynamics evolution

Each system is first assigned with a certain position inside the disc, as well as given its disc velocity drawn from the local velocity distribution, which is added to the velocity acquired during its pre-BH stage evolution (*i.e.* due to Blaauw kick plus potentially non-zero natal kick). For the Milky Way disc model we have adopted distributions fitted to the observational results of SDSS survey: the stellar number density distribution from Jurić et al. (2008) and stellar velocity distributions from the kinematics study of Bond et al. (2010).

Following Gilmore & Reid (1983) we model the disc as a sum of two exponential components (the "thin" and the "thick" disc) allowing for different scale lengths ($L_{\rm thin}$ and $L_{\rm thick}$) and heights ($H_{\rm thin}$ and $H_{\rm thick}$) for each component.

$$\rho_D(r,z) = \rho_D(r,z;L_{\rm thin},H_{\rm thin}) + f\,\rho_D(r,z;L_{\rm thick},H_{\rm thick}) \tag{2.9}$$

where

$$\rho_D(r,z;L,H) = \rho_D(r_\odot,0)e^{\frac{r_\odot}{L}}\exp\left(-\frac{r}{L}-\frac{z+z_\odot}{H}\right) \tag{2.10}$$

We adopt bias corrected scales of Jurić et al. (2008): $L_{\rm thin} = 2600\,{\rm pc}$, $H_{\rm thin} = 300\,{\rm pc}$ for the thin disc and $L_{\rm thick} = 3600\,{\rm pc}$, $H_{\rm thick} = 900\,{\rm pc}$ for the thick one. The less massive thick disc is normalized to $f = 0.12$ with respect to thin disc, normalized to 1.0. We constrain the size of the disc with $|z_{\rm max}| = 4000\,{\rm pc}$, $r_{\rm min} = 3000\,{\rm pc}$ and $r_{\rm max} = 15000\,{\rm pc}$, thus staying outside of the influence of central bulge, for which the results of SDSS are uncertain due to high blending. For the value of stellar number density in the Sun neighborhood we adopt $\rho_D(r_\odot,0) = 0.005\,{\rm ly}^{-3}$.

For the velocity distribution of disc stars we adopt the results of Bond et al. (2010). They model the distribution of rotational velocities as a sum of two Gaussians, first normalized to the factor of 0.75 and second to 0.25. At the disc plane ($z = 0\,{\rm pc}$) mean value and dispersion of the first Gaussian are $\mu_\phi = -194\ {\rm km\ s^{-1}}$ and $\sigma_\phi = 12\ {\rm km\ s^{-1}}$ respectively, whereas the second Gaussian is given with $\mu_\phi = -228\ {\rm km\ s^{-1}}$ and $\sigma_\phi = 34\ {\rm km\ s^{-1}}$. Distributions of radial and vertical to the disc velocities are described with a single Gaussian only, for which the mean value = 0 km s$^{-1}$ in both cases. Dispersions at the disc plane are given as $\sigma_r = 40\ {\rm km\ s^{-1}}$ and $\sigma_z = 25\ {\rm km\ s^{-1}}$. For all the distributions the values of dispersions increase slowly with distance from the disc $|z|$.

Each binary is moving through the Galaxy subject to its Galactic potential. We have made use of the Galactic potential description of Flynn et al. (1996), where the total potential is modeled by the sum of potentials of three standard components: the dark halo $\Phi_H$, the central component $\Phi_C$ and the disc $\Phi_D$. The dark halo potential is given in a spherical form:

$$\Phi_H \propto V_H^2 \ln(r^2 + r_0^2) \tag{2.11}$$

where $r^2 = x^2 + y^2 + x^2$ and $r_0 = 8.5$ kpc, $V_H = 220$ km s$^{-1}$. The spherical component potential is modeled by two separate components:

$$\Phi_C \propto -\frac{M_{C_1}}{\sqrt{r^2 + r_{C_1}^2}} - \frac{M_{C_2}}{\sqrt{r^2 + r_{C_2}^2}} \tag{2.12}$$

where $M_{C_1} = 3 \times 10^9$ M$_\odot$ is the mass of bulge/stellar-halo, $M_{C_2} = 1.6 \times 10^{10}$ M$_\odot$ is the mass of the most central component, $r_{C_1} = 2.7$ kpc and $r_{C_2} = 0.42$ kpc. The disc potential, on the other hand, is modeled by the sum of three Miyamoto-Nagai potentials (Miyamoto & Nagai, 1975):

$$\Phi_D = \Phi_{D_1} + \Phi_{D_2} + \Phi_{D_3} \tag{2.13}$$

where:

$$\Phi_{D_n} \propto -\frac{M_{D_n}}{\sqrt{\rho^2 + (a_n + \sqrt{z^2 + b^2})^2}} \qquad n = 1, 2, 3 \tag{2.14}$$

where $\rho^2 = x^2 + y^2$, mass-like parameters of subsequent disc components are $M_{D_1} = 6.6 \times 10^{10}$ M$_\odot$, $M_{D_2} = -2.9 \times 10^{10}$ M$_\odot$, $M_{D_3} = 3.3 \times 10^9$ M$_\odot$ and the values of other parameters are $a_1 = 5.81$ kpc, $a_2 = 17.43$ kpc, $a_3 = 34.86$ kpc and $b = 0.3$ kpc.

We evolve each binary position and velocity in the Galactic potential implementing Verlet's integration algorithm (Verlet, 1967), applicable for Newtonian equations of motion (often referred to as Velocity Verlet algorithm).

#### 2.3.3.2 ENCOUNTERS WITH FLY-BYS

We model random encounters with passing-by stars utilizing the mean-free time $t_{\rm MF}$ quantity introduced in Section 2.2.2. We apply adaptive time step $\delta t$, dependent of the expected frequency of interactions for a given binary, limited to not exceed 1000 yr to guarantee smooth dynamics evolution:

$$\delta t = \min(0.1\ t_{\rm MF}\ ;\ 1000{\rm yr}) \tag{2.15}$$

Every hundred time steps of a binary dynamics evolution the value of $t_{\rm MF}$ is updated to correspond to the changing local conditions (*i.e.* stellar number density and velocity distribution). It is also updated after each dynamical interaction.

Upon each time step $\delta t$ we randomize whether or not a flying-by field star was encountered during this time, with the probability of it equal to $\delta t / t_{MF}$. If a star was encountered, we draw three main parameters describing such event – encountered star mass $M_{\rm single}$, its relative velocity to the binary $\vec{v_{\rm rel}}$ and impact parameter $b$ – following procedure described in Section 2.2.2. Subsequently, we employ FEWBODY code (Fregeau et al., 2004) to simulate the interaction and obtain resulting system parameters. FEWBODY uses the 8th-order Runge-Kutta Prince-Dormand integration method with adaptive time step to solve N-body problems for small, few body systems (N < 10). It offers a suitable toolkit for binary-single scattering experiments – it numerically integrates orbits of stars during their interaction, terminates the computations once the result is unambiguous and classifies

the resulting configuration. Apart from $M_{\rm single}$, $\vec{v_{\rm rel}}$ and $b$ each encounter is described by four additional parameters, which we draw from a flat distribution: mean anomaly $\xi$ of the binary and three angles defining the direction of a flying-by star movement with respect to the system's orbit.

Once an encounter is completed we check whether or not the resulting orbit satisfies the condition for tidal circularization, i.e. whether $d_{\rm per} < d_{\rm tidal}$. If it does we keep monitoring its state until periastron is reached (i.e. $\xi = 0.$) which for very wide and eccentric orbits is roughly where tidal forces become significant. For a wide binary of $a \sim 10^4$ AU it is possible to encounter third bodies at frequency comparable to its orbital period – thus, the fulfilled condition for tidal circularization might not remain satisfied up until the periastron is reached as subsequent interactions could potentially violate it.

#### 2.3.3.3 Tidal circularization

Eventually, once the periastron is reached and $d_{\rm per} < d_{\rm tidal}$ remains satisfied, the evolution of the binary orbit becomes very complicated, as the amount of energy dissipated during a single periastron passage depends on tidally induced stellar oscillations and is very much a matter of debate. If the timescale for dissipation of such oscillations' energy is short and a significant fraction of energy is thermalized during one orbital period (as argued by Kumar & Goodman, 1996), the orbit becomes circularized quickly, with its size being reduced considerably already at the first pericenter passage. Such scenario is also supported by the results of Kaib & Raymond (2014), who investigate periastron passages of wide, eccentric binaries in the regime of Press & Teukolsky (1977) and Lee & Ostriker (1986) tidal modeling, and show that for pericenter separation of the order of 5 stellar radii the tidal circularization proceeds quickly, with pericenter distance remaining nearly constant (*i.e.* $a \simeq d_{\rm per}$)

This simplified picture of tidal circularization becomes very complicated when we take into consideration that energy dissipated from tidally induced oscillations affects the internal structure of a tidally affected star (Ray et al., 1987). If the timescale of such process is too short, the heated star may expand and create a common envelope or even lead to a merger (Podsiadlowski, 1996). If, on the other hand, the energy dissipation is ineffective, the orbit may become subject to quasi-periodic fluctuations, significantly extending the circularization process (Mardling, 1995). In this work, however, we assume (similarly to Voss & Gilfanov, 2007) that all binaries for which the pericenter is reached and $d_{\rm per} < d_{\rm tidal}$ is satisfied become circularized within one orbital period and $a \simeq d_{\rm per}$.

It should be noted here, that due to dynamic interactions some wide binaries can be excited into extremely wide orbits of $a \sim 10^5$AU and eventually disrupted, resulting in an observable plateau in $f(a)$ distribution (Poveda et al., 2007). Such wide binaries are subject to exceptionally frequent stellar encounters, thus require a challenging amount of computational time. In order to address this issue we place an upper limit for a binary size $a_{\rm max} = 10^5$AU, at which we consider it certain to be disrupted and do not evolve it any further. In the discussion we show that this limitation does not effect our predictions (see Sec. 2.5.4).

Before we move on to discuss the results we should clearly state an important simplification

we make: similarly to MP2016 and other authors, we assume that *all* tidally circularized systems become X-ray binaries (LMXBs precisely, as they all turn out to have low-mass companions). In reality, the evolution of a tidally circularized binary may not always lead to a mass transfer and X-ray activity. This is not only due to the uncertainties concerning the influence of tidal heating on the MS stellar structure (as discussed in details earlier in this section), but also due to the fact that even after circularization, once the binary components are very close to each other, the MS secondary may not fill its Roche Lobe just yet and it may take even several Gyr for a mass transfer to be launched (an exemplary time period obtained by Wiktorowicz et al., 2014, for a system of $\sim$ 7–10 $M_\odot$ BH and $\sim$ 1–1.2 $M_\odot$ secondary MS, reducing separation from 8 $R_\odot$ to 5 $R_\odot$ and initializing mass transfer, is $\sim$ 4 Gyr ). However, our typical separations after circularization are rather small ($a \approx 3 - 7$ $R_\odot$ for nearly all the of systems in $\alpha = 0.5$ and $\alpha = 0.8$ models and $a \approx 3 - 10$ $R_\odot$ in the majority of cases in other models) and we expect that combined effects of magnetic braking and gravitational waves emission will allow for a significant orbital decay in a lifetime of a binary leading to LMXB phase in majority of our systems.

## 2.4 RESULTS

For the scope of this section we will denote the moment just after the BH formation as Zero Age (ZA) for BH-MS binaries. Out of $4.5 \times 10^7$ systems at the beginning of pre-BH stage about $\sim$ 27.5% survive until ZA for BH-MS, with only $\sim$ 1.12% of those having companions expected to remain on MS until present day. Thus, the ZA BH-MS population of interest consists of roughly 138,500 systems, with the majority of secondaries being low-mass ($< 2M_\odot$) MS stars due to their longer living expectancy. A typical semi-major axis for ZA BH-MS population lies in range 100–1000 AU, whereas the distribution of eccentricities covers full range 0–1, peaking at $e \sim 0.1$.

### 2.4.1 AN EXEMPLARY EVOLUTIONARY ROUTE

In order to illustrate characteristic features of evolution leading to dynamical formation of LMXBs we take a closer look at the evolutionary path of an exemplary binary which have become an LMXB out of a Galactic disk BH-MS binary through dynamics and tidal circularization. Note that this is the very same binary that served as an example when describing the details of typical pre-BH evolution in Sec. 2.3.2. Here we continue its journey towards tidal circularization, starting from a newly formed ZA BH-MS system comprising of a $\sim 7.9\,M_\odot$ BH and a $\sim 0.75\,M_\odot$ MS companion, having orbital parameters a = 306 AU and e = 0.47. The system has been assigned a Galactic velocity $\vec{v}$, drawn from the local stellar velocity distribution, which with respect to the mean local velocity $\vec{v_*}$ was $|\vec{v_{\rm rel}}| = |\vec{v_*} - \vec{v}| = 75\,{\rm km/s}$. Since the BH was created with no direct natal kick and the Blaauw kick was very small, the system's velocity deviation $\vec{v_{\rm rel}}$ is only caused by dispersion of the Galactic velocity distribution.

Then, during a $\sim$ 7.6 Gyr long period of evolution stretching from the BH formation to the binary tidal circularization, the system was subject to around 5,000 stellar encounters, affecting its

orbital parameters and eventually leading to very high eccentricity and very small distance between companions at periastron. At the moment of tidal circularization the binary orbital parameters were $a \approx 1730\,\mathrm{AU}$ and $e \approx 0.99999$, corresponding to separation at pericenter $d_{\mathrm{per}} \approx 3.8\,\mathrm{R}_{\odot}$ and companion filling its Roche Lobe in 89% (radius-wise), which is sufficient for circularization in all our models.

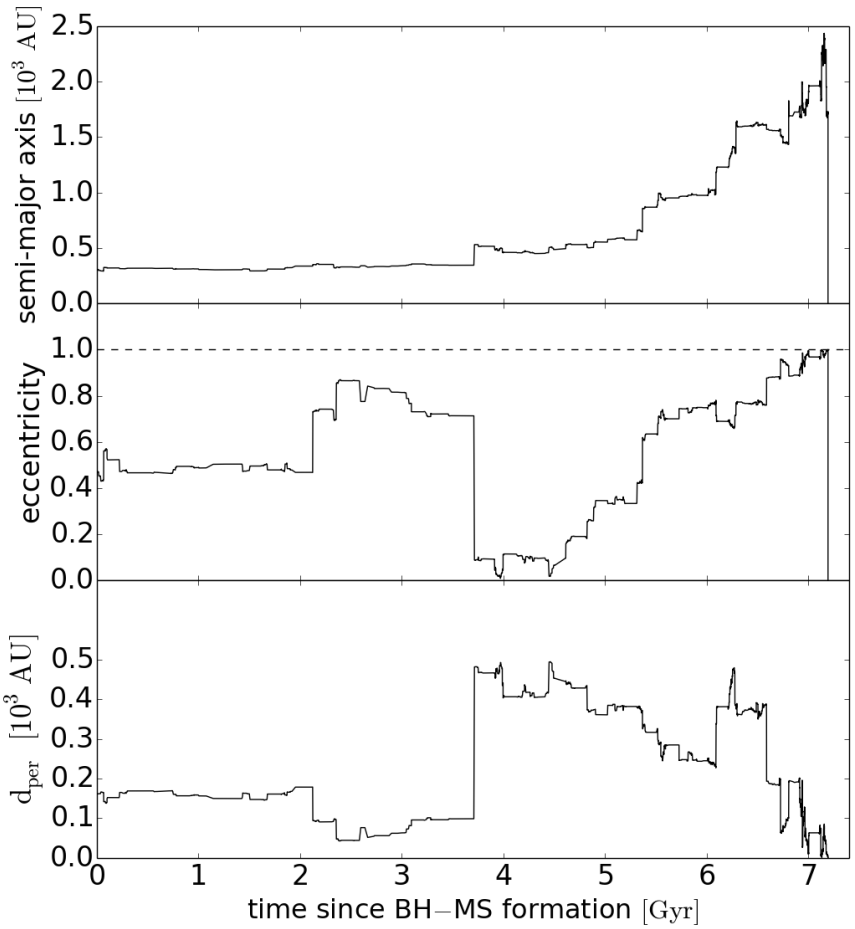


FIGURE 2.3: Detailed evolution of orbital parameters $a$ and $e$, as well as distance at pericenter $\mathrm{d_{per}} = \mathrm{a}(1-\mathrm{e})$ for an exemplary, typical binary that have undergone tidal circularization (noticeable as a rapid decrease of both semi-major axis and eccentricity at the very end of evolution). This particular system was subject to over 5,000 stellar encounters, most of them occurring during second half of its evolution. The binary was subject to several major changes of orbital parameters due to encounters with exceptionally massive fly-bys. For instance, the most significant change of eccentricity from 0.71 to 0.09 at around 3.7 Gyr (coupled with semi-major axis increase from 345 AU to 530 AU) was caused by an interaction with a $\sim 4.5\,\mathrm{M}_{\odot}$ star, whereas the mean mass of fly-bys in our simulations is $\sim 0.62\,\mathrm{M}_{\odot}$. Additionally, the encountered star was passing by with a relatively low speed of $\sim 45$ km s$^{-1}$ with respect to the binary (the mean relative speed of all fly-bys being $\sim 125$ km s$^{-1}$), which granted an exceptionally long time of gravitational interaction.

Figure 2.3 shows detailed evolution of the binary orbital parameters $a$ and $e$, as well as the pericenter separation $d_{\mathrm{per}}$. Even though the binary was affected by more than 5,000 encounters

altogether the vast majority of interactions had very little effect on its orbit, with only few inducing significant changes of orbital parameters. The average mass of passing-by stars in the only 10 encounters during which the orbital energy was changed by more than 10 % was $\sim 13.5\,M_\odot$, whereas the average mass of all stars encountered by the binary was $\sim 0.62\,M_\odot$. In fact, it is very typical for the majority of dynamically formed LMXBs in our simulations that the dynamic evolution of a binary is mainly dependent on a few key encounters with, on average, exceptionally massive fly-bys. This is connected to the fact that, on average, the amplitude of a velocity kick induced by a fly-by to one binary component with respect to the other can be analytically estimated as proportional to the fly-by's mass (e.g. Hills, 1981), i.e.:

$$\langle \Delta V \rangle = \frac{3aGM_{\mathrm{fly-by}}}{v_{\mathrm{rel}} b^2} \tag{2.16}$$

where a is semi-major axis of the binary, $M_{\mathrm{fly-by}}$ is mass of the fly-by, b is the impact parameter and $v_{\mathrm{rel}}$ is the fly-by's velocity, relative to mass center of the binary. This suggests that the local stellar mass distribution has influence on the timescale of evolution through dynamical interactions and therefore the effectiveness of LMXBs' dynamical formation channel. We discuss it further in Sec. 2.5.2.

### 2.4.2 EVOLUTION OF ORBITAL PARAMETERS

The evolution of orbital parameters at figure 2.3 also illustrates a general trend of steadily increasing semi-major axis. This is an average regularity for all of our evolutionary paths leading towards tidal circularization, which is shown in table 2.1, where we compare some basic characteristics of binaries which have evolved to undergo a circularization with same characteristics of the whole BH-MS population. We choose parameters which are influenced by stellar iterations: the deviation of a binary velocity $\bar{v}$ from mean local stellar velocity $\bar{v}_*$, as well as the values of orbital parameters $a$ and $e$. We analyze those parameters at two moments of time: at ZA for BH-MS systems (i.e. just after the BH formation) and at the beginning of tidal circularization (CIRC).

Due to stellar encounters the semi-major axes of future BH LMXBs tend to be gradually increasing, with their typical values at the moment of circularization being a few times higher than at ZA. This, paired with extremely high eccentricities induced by encountered fly-bys ($e \gtrsim 0.9999$), makes the orbit of a typical binary at circularization very wide and almost linear (i.e. degenerate ellipse). Such increase of a semi-major axis, very characteristic for our population of systems to undergo tidal circularization, makes a binary subject to more frequent stellar encounters as wider systems have naturally larger cross-sections (see relation 2.5 for which $b_{\max} \propto a$). This also explains the slight bias towards wider ZA BH-MS systems in the population of future BH LMXBs – for each of our models the majority of systems to undergo tidal circularization had ZA separations falling in range 200 – 750 AU, whereas the corresponding most common range for the entire BH-MS population was around 100 – 600 AU.

According to relation 2.5 systems with higher velocity deviations from typical field stars velocities are subject to more frequent interactions with fly-bys. Our results show that they are thus

| model | $\lvert\bar{v} - \bar{v}_*\rvert$ [km/s] | | semi − major axis [$10^3$AU] | | eccentricity | |
|---|---|---|---|---|---|---|
| | ZA | CIRC | ZA | CIRC | ZA | CIRC |
| MP2016 | $68 \pm {}^{42}_{27}$ | $73 \pm {}^{43}_{32}$ | $0.42 \pm {}^{0.39}_{0.23}$ | $1.38 \pm {}^{7.32}_{1.0}$ | $0.32 \pm {}^{0.38}_{0.21}$ | $\gtrsim 0.9999$ |
| 0.2 Roche | $67 \pm {}^{40}_{26}$ | $74 \pm {}^{42}_{33}$ | $0.42 \pm {}^{0.35}_{0.23}$ | $1.41 \pm {}^{7.19}_{1.01}$ | $0.32 \pm {}^{0.39}_{0.21}$ | $\gtrsim 0.9999$ |
| 0.5 Roche | $71 \pm {}^{37}_{28}$ | $78 \pm {}^{44}_{36}$ | $0.41 \pm {}^{0.35}_{0.21}$ | $1.35 \pm {}^{6.41}_{1.03}$ | $0.34 \pm {}^{0.38}_{0.24}$ | $\gtrsim 0.9999$ |
| 0.8 Roche | $70 \pm {}^{39}_{26}$ | $77 \pm {}^{32}_{33}$ | $0.40 \pm {}^{0.35}_{0.20}$ | $1.14 \pm {}^{3.69}_{0.75}$ | $0.38 \pm {}^{0.34}_{0.28}$ | $\gtrsim 0.9999$ |
| all Zero Age BH-MS binaries | $46 \pm {}^{29}_{21}$ | - | $0.28 \pm {}^{0.35}_{0.17}$ | - | $0.20 \pm {}^{0.34}_{0.11}$ | - |

Table 2.1: The comparison of median values of characteristic binary parameters between the Zero Age (ZA) and the moment of tidal circularization (CIRC), drawn for the population of binaries that have undergone circularization. Also compared with median values of these parameters for the whole ZA BH-MS population. Subsequent columns correspond to median values of: deviation of a binary velocity $\bar{v}$ from mean local stellar velocity $\bar{v}_*$, semi-major axis $a$ and eccentricity $e$. Ranges corresponding to 68% of all systems (i.e. $1\sigma$) are given for each quantity except the eccentricity at the moment of tidal circularization (rightmost column), for which all the systems satisfy $e \gtrsim 0.9999$.

more predisposed to be tidally circularized, as the typical values of velocity deviations for future LMXBs (falling in range $\sim 40 - 110$ km s$^{-1}$) are significantly higher then velocity deviations for the entire BH-MS population ($\sim 25 - 75$ km s$^{-1}$). However, only a negligible $< 1\%$ of all our BH LMXB systems have been given a non-zero natal kick during BH formation – their distinctly high velocities have been drawn from the Galactic velocity distribution due to its dispersion. In general, the effect that potentially higher BH natal kicks could have on the effectiveness of the dynamical formation channel is unclear. On the one hand higher kicks could potentially lead to formation of more BH-MS systems moving through the Galaxy with exceptionally high velocities, likely subjects of numerous stellar encounters. On the other hand, stronger kicks could significantly lower the number of binary systems surviving BH formation in the first place. We further discuss the later effect in Sec. 2.5.3.

### 2.4.3 THE POPULATION OF LMXBS

Table 2.2 compares the numbers of LMXBs ($N_{LMXB}$) formed dynamically in 4 tested models for tidal circularization threshold distance, as well as the values of donor mass $M_{MS}$, also compared with the whole ZA BH-MS population, the mean times between ZA and circularization ($t_{evol}$, which is roughly mean age of circularized binaries) and finally the mean numbers of interactions (NOI) which had occurred by the time circularization was achieved.

The amount of dynamically formed LMXBs decreases for different models from $\sim 220$ for the MP2016 condition for circularization down to $\sim 65$ in a model, where circularization occurs only when secondary fills at least 80 % of its Roche Lobe (radius-wise). This corresponds to the fact that for subsequent models the conditions for circularization becomes more and more stringent for low values of mass ratios $q \lesssim 0.25$ expected in BH-low mass MS binaries – see the comparison of $d_{\rm tidal}$ vs mass ratio $q$ relations at figure 2.1.

The differences between $d_{\rm tidal}(q)$ relation for subsequent models are also reflected in corresponding differences between the shape of companion mass function (CMF) of a resulting population of dynamically formed BH LMXBs (see figure 2.4). For MP2016 and 0.2 Roche Lobe models, where the values of $d_{\rm tidal}$ are significantly higher for low mass ratios, so that circularization becomes easier for less massive stars, the shape of CMF responds respectively.

For comparison we also plot the CMF of observed Galactic BH LMXB systems. One set of data was taken from table 1 of Wiktorowicz et al. (2014) whereas alternative values come from table 13 of Tetarenko et al. (2016c) (the differences mainly arise from that fact that Tetarenko et al. (2016c) applies BH masses argued by Kreidberg et al. (2012)). Most of the companions with measured masses are found in range 0.1–1.0 $M_\odot$, which is consistent with our findings. However, a more robust comparison with the observed distribution (i.e. one taking into account its shape for $M < 1\ M_\odot$) is beyond the scope of this paper, as it would require modeling of the actual LMXB phase and mass transfer rates. Also note that the sample of systems with measured companion masses is still very small ($\sim$20) and the masses themselves may be subject to systematic errors (Kreidberg et al., 2012).

| model | $N_{LMXB}$ | $M_{MS}$ [$M_\odot$] | $t_{evol}$ [Gyr] | NOI [$10^3$] |
|---|---|---|---|---|
| MP2016 | 219 | $0.64 \pm {}^{0.44}_{0.42}$ | $1.6 \pm {}^{2.9}_{1.3}$ | $1.5 \pm {}^{4.3}_{1.1}$ |
| 0.2 Roche | 189 | $0.81 \pm {}^{0.44}_{0.50}$ | $1.5 \pm {}^{3.0}_{1.3}$ | $1.6 \pm {}^{5.3}_{1.1}$ |
| 0.5 Roche | 104 | $0.85 \pm {}^{0.42}_{0.47}$ | $1.4 \pm {}^{3.4}_{1.1}$ | $1.5 \pm {}^{6.2}_{1.0}$ |
| 0.8 Roche | 64 | $0.81 \pm {}^{0.49}_{0.44}$ | $1.6 \pm {}^{4.3}_{1.2}$ | $1.6 \pm {}^{7.0}_{1.0}$ |
| all Zero Age BH-MS binaries | - | $0.81 \pm {}^{0.83}_{0.51}$ | - | - |

Table 2.2: Comparison of dynamically formed LMXBs for different tidal circularization models. Subsequent columns correspond to: the number of formed LMXBs ($N_{LMXB}$) and the median values of the mass of MS companion $M_{MS}$, the time between BH-MS formation and circularization ($t_{evol}$) and the number of interactions (NOI) which occurred before circularization. Ranges corresponding to 68% of all systems (i.e. $1\sigma$) are given. Subsequent rows correspond to different models. The very final row corresponds to the entire BH-MS population at ZA.

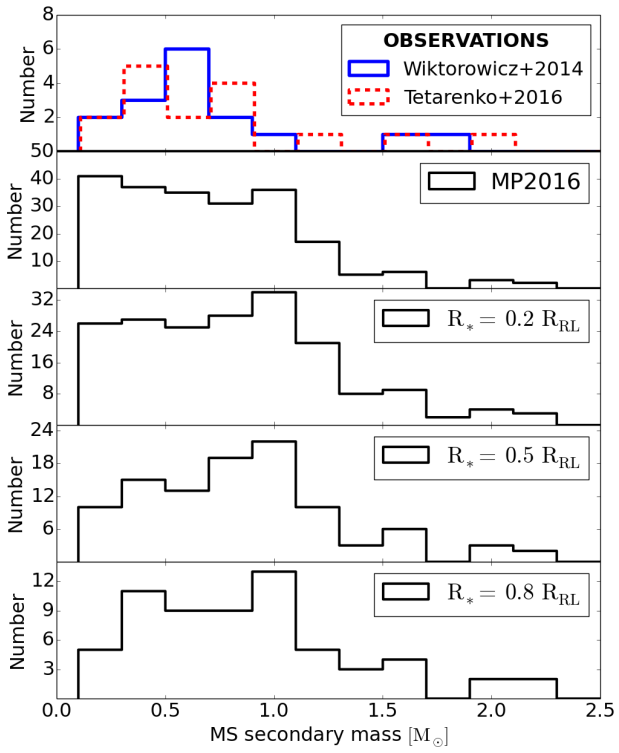


FIGURE 2.4: The comparison of companion mass function of tidally circularized systems for all our models as well as the observed population of Galactic BH LMXB systems (data taken from table 1 of Wiktorowicz et al. (2014), alternative values come from table 13 of Tetarenko et al. (2016c)). Shape of each distribution is strictly connected to the shape of $d_{\rm tidal}(q)$ relation in a given model, favoring less massive companions for models with significantly higher $d_{\rm tidal}$ values for low mass ratios. It is worth noticing that in all models the majority of companions lie within the range 0–1 $M_\odot$, which is consistent with observations. However, a robust comparison would require modeling of the mass transfer phase (see text).

We wish to mention that the observed CMF is in tension with the results of population synthesis of LMXBs through CE evolution for various CE energy binding parameters proposed up to date (Wiktorowicz et al., 2014), as they generally result in a distribution peaking strongly around 1.0 $M_\odot$ with a possible smaller peak around 0.2–0.3 $M_\odot$. Similar results were obtained by Wang et al. (2016), although it seems that a better agreement with observations could potentially be obtained if BH were formed in failed SN (Kochanek, 2014) rather than through material fallback (Fryer et al., 2012). In the meantime channels involving intermediate mass donors (Justham et al., 2006; Chen & Li, 2006) are also inconsistent with observations as they predict donor spectral types which are too hot to explain the observed temperatures of companion stars in BH LMXBs.

## 2.5 DISCUSSION

Table 2.2 shows that the number of LMXB candidates is strongly dependent on the assumption on pericenter distance required for the tidal circularization, varying by a factor of $\approx 3.5$ across our models. In fact, even our most pessimistic model may be too optimistic, as strong tidal interactions at pericenter may not always lead to circularization of the orbit (see Podsiadlowski (1996); Mardling (1995) and the brief discussion in Sec. 2.3.3.3).

In the following text we point out the main assumptions of our analysis and discuss their significance.

### 2.5.1 Lifetime of LMXBs

Because the process of tidal circularization is still uncertain, both in terms of the timescale and the final outcome (see Sec. 2.3.3.3), we do not attempt to model the evolution of our systems once they fulfill our condition for tidal circularization. Instead we simply assume that each of such systems will have enough time to become an X-ray binary and it contributes to the final numbers of LMXB systems in table 2.2.

In particular we do not model the actual phase of X-ray activity and do not account for its finite duration. This leads to an overestimation of the number of LMXBs in our predictions. For instance, if we assume that it typically takes up to 2 Gyr for a system to start its X-ray phase once it fulfills the condition for tidal circularization and that the duration of the following LMXB phase is about 1 Gyr we find that only about 20% of the systems given in table 2.2 can be observable as X-ray binaries at present time. Because the typical mass transfer rates from low-mass MS donors discussed in the literature are of the order of $\sim 10^{-10}\,\mathrm{M}_\odot\,\mathrm{yr}^{-1}$ (King, 1988; Verbunt, 1993), which corresponds to LMXB lifetimes of about several Gyr, the actual fraction of observable systems is likely higher – somewhere between 20% and 100%.

### 2.5.2 Mass function of the fly-bys

The analyses of the evolution of orbital parameters due to interactions with passing-by stars (Sec. 2.4.1) reveals that the most significant changes are, on average, induced by massive fly-bys of at least several solar masses. This suggests that the local stellar mass function (SMF) has influence on the timescale of evolution through dynamical interactions and therefore the effectiveness of LMXBs' dynamical formation channel. The SMF of the Milky Way disc is generally unknown, as there is no reliable way of constraining the population of Galactic dark objects such as single black holes (although there is some hope in the possibility of observing microlensing events Wyrzykowski et al., 2016). In this study we simply derive masses of flying-by stars from the IMF of Kroupa et al. (1993) with the power-law exponent modified to $-2.3$ for the stars of mass $\mathrm{M} > 1.0\,\mathrm{M}_\odot$, as recently adjusted by Sana et al. (2012). In reality though the SMF should be shifted towards lower masses compared to the IMF, since giant stars evolve and lose mass very quickly. Thus, even though we do not account for binary and higher order fly-bys, our approach still likely overestimates the frequency of interactions with massive systems. For comparison, if we employ StarTrack for single star evolution, assume the above-mentioned IMF, constant star formation rate of 10 Gyr, 50% binary fraction and that the average binary mass is $\sim 1.5$ the average single star mass (coming from flat mass ratio distribution) we obtain the present SMF which returns massive fly-bys (of at least 5 Solar masses) $\sim 3.5$ times less often than the IMF we used. If we now assume that only encounters with such massive objects play any role in evolution of orbital parameters, in which case the times between BH-MS formation and circularization of our systems would be 3.5 times longer, we find that only about $\sim 40\%$ of LMXB candidates in table 2.2 would have enough time to become circularized (i.e. $N_{\mathrm{LMXB}}$ reduced by a factor of $\sim 2.5$), irrespective of the model of tidal circularization. Such assumption is pessimistic since encounters

with less massive fly-bys can also have an effect on the binary orbit given the impact parameter b is low (see equation 2.16).

### 2.5.3 BH NATAL KICKS

Because wide BH-MS binaries have relatively low orbital energy and can be easily disrupted, the natal kicks play a crutial role in their formation. Unfortunately, the BH natal kicks are still poorly understood (eg. Repetto & Nelemans, 2015). They are generally thought to be caused by two main processes: asymmetries in the SN ejecta (when the BH is believed to be formed via fallback onto the proto-NS, see Fryer & Kalogera 2001; Zhang et al. 2008) or asymmetries in neutrino flux (also possible during direct collapse and BH formation without SN, although it might require strong magnetic fields – see Janka 2013 for the recent review). In either case the assumption of linear momentum conservation yields BH natal kicks reduced with respect to those of NS: $V_{BH\,NK} \sim (M_{NS}/M_{BH})V_{NS\,NK}$. This simple picture implies BH natal kicks decreasing with BH mass, which is in agreement with the observations of Galactic BH X-ray binaries (although natal kick velocities independent of BH mass cannot be ruled out yet Belczynski et al., 2016c). It might be challenged, however, by the spacial distribution of known systems in the Milky Way, which seems consistent with BH gaining similar velocities to NS rather than similar momentum (Repetto et al., 2012), although Mandel 2016 argues that with a more careful approach and within uncertainties no BH kicks larger than 100 km/s are required to explain all observed systems. While natal kicks seem necessary for some binaries to reach the large distances above the Galactic plane at which they are observed, the positions of several systems can be explained with no natal kick whatsoever (Repetto & Nelemans, 2015). This could correspond to the case in which a BH is formed directly from a massive star with no associated SN, no mass loss and no asymmetry in neutrino emission.

We have employed the asymmetric mass ejection model for the BH natal kicks in combination with the rapid supernova model for BH mass (Fryer et al., 2012). This results in magnitude of the kick decreasing with BH mass (with no natal kicks for most massive BHs). This is consistent with above-mentioned observations as well as with current LIGO limits on merger rates of BH-BH binaries (Belczynski et al., 2016b). However, we note that models with moderate BH natal kicks ($\sim 100 - 200$ km/s) are *also* consistent with all those observations and limits (Belczynski et al., 2016c). Because the wide BH-MS systems evolve from wide MS-MS binaries ($a \gtrsim 100$ AU) there is no mass transfer between companions. The BHs in these systems evolve from non-interacting stars following single stellar evolution with BH mass set by the initial star mass, metallicity and our adopted wind mass loss and supernova model. For Sana et al. (2012) IMF the rapid SN model results in about 56% of BHs receiving zero natal kicks (direct collapse), while for the rest 44% the amount of material falling back is always bigger than 62% corresponding to $\sigma_{NK} \lesssim 100\,\mathrm{km/s}$. Characteristic orbital velocity $V_{orb} \sim \sqrt{G(M_a + M_b)/a}$ for our systems at the moment of BH formation ($M_a \sim 10\,M_\odot$, $M_b \sim 1\,M_\odot$, $a \sim 300$ AU) is $V_{orb} \sim 6\,\mathrm{km/s}$. This indicates that unless the BH natal kick is very small, such systems are likely to be disrupted (which indeed is the

case for almost all of the 44% of our BHs which do not form in direct collapse). In fact, only about 10% and about 30% of the BH LMXB candidates from table 2.2 would survive the BH formation if NKs were drawn from a Maxwellian with $\sigma_{NK} = 10$ km/s or even only $\sigma_{NK} = 5$ km/s, respectively. Comparison of different BH NK models is beyond the scope of this study but it seems necessary that a significant fraction (in our case ∼56%, direct BH formation) of BHs is born with zero to negligible NK of a few km/s in order to produce a large enough population of wide BH-MS systems, so that some of them may be circularized thanks to stellar encounters and become LMXBs.

### 2.5.4 Ultra-wide systems – comparison with MP2016

As discussed in Sec. 2.3.2, the multiplicity of systems with massive stars has been found to increase with separation (eg. Sana et al., 2014; Aldoretta et al., 2015). In particular Moe & Di Stefano (2017) reports that ZAMS companions to massive stars on orbits with periods $\log(P/\mathrm{day}) \gtrsim 5.5$ are essentially tertiary components in hierarchical *triples*, which makes them unlikely progenitors of BH LMXBs through dynamical scenario tested in this study (see Sec. 3.1.4 of MP2016). For that reason we set $\log(P/\mathrm{day}) = 5.5$ as the upper limit on the initial binary periods, which results in $a_{\mathrm{MS-MS}} \lesssim 10^{2.5}$ AU for the MS-MS binaries and $a_{\mathrm{BH-MS}} \lesssim 10^{3}$ AU for BH-MS systems just after the BH formation. On the contrary, MP2016 only consider BH-MS binaries with $10^3\mathrm{AU} < a < 3 \times 10^4\mathrm{AU}$, for which they predict the dynamical scenario to be most likely. Thus, for the sake of comparison with their result, we have simulated a sample of additional $1.215 \times 10^7$ *binaries* with periods at ZAMS between $\log(P/\mathrm{day}) = 5.5$ and 8.5, which we denote as "ultra-wide systems" to differentiate from our main sample – the "wide systems". For the rest of this section we also assume MP2016 condition for tidal circularization.

MP2016 predict that the probability of a dynamical interaction causing tidal capture and circularization is the highest for $a_{\mathrm{crit}} \approx 1.3 \times 10^4\mathrm{AU}$ (see their Fig.1). In order to compare this prediction with our simulations we combine BH LMXB candidates from both populations, wide and ultra-wide systems, and plot their semi-major axes at the moment just before the final interaction, after which the MP2016 condition for tidal circularization is fulfilled (see figure 2.5 top panel). We indeed find that the distribution has its maximum at around $10^4$ AU, which is in good agreement with MP2016 estimation. Note that our upper cut-off at $10^5$ AU on the binary separation above which we stop following its evolution (marked with vertical line in the plot) is at the falling end of the distribution, so only few BH LMXB candidates were lost by introducing it.

In the figure 2.5 we also plot the distributions of semi-major axes at previous stages of the systems evolution: at ZA for BH-MS binaries and finally at ZAMS. Since both the stellar evolution of BH progenitor (see Sec. 2.3.2) and dynamical interactions during the BH-MS phase (see Sec. 2.4.2) tend to increase the binary semi-major axes, subsequent distributions in the plot are more and more shifted towards lower values. Note that the entire range of BH-MS separations $10^3\mathrm{AU} < a < 3 \times 10^4\mathrm{AU}$ considered by MP2016 (marked as dashed region) is covered. In the middle panel we also plot the semi-major axes distribution of all our BH-MS systems, from both

wide and ultra-wide samples (the red, dotted curve with separate label on the right-hand side). In range from $10^{2.5}$ to $10^{4.5}$ AU it turns out to be relatively flat. This means that the MP2016 dynamical scenario is most effective for BH-MS systems of separations between 2000 and 6000 AU, corresponding to the maximum of the distribution of BH LMXB candidate separations at ZA for BH-MS stage.

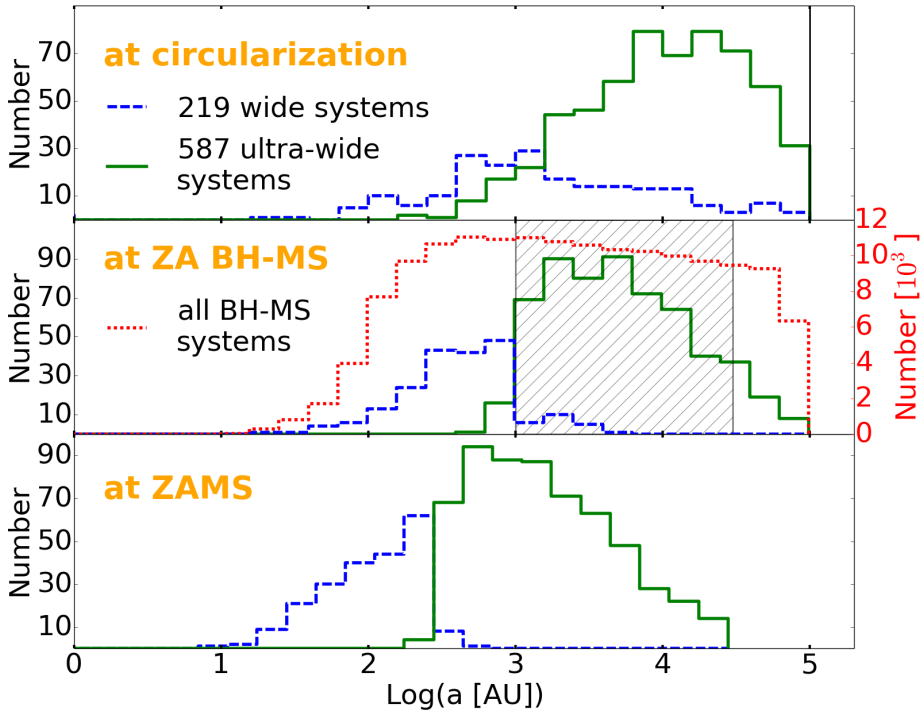


FIGURE 2.5: Distribution of semi-major axes for BH LMXB candidates from both wide and ultra-wide samples at three different stages: at the moment just before the final interaction, after which the MP2016 condition for tidal circularization is fulfilled (top panel), at the moment of BH formation (middle panel) and at ZAMS (bottom panel). Wide systems are those which contribute to our main results (Sec. 7.3) while the population of ultra-wide systems is an additional sample calculated to make a comparison with MP2016. In the middle panel we also plot the semi-major axes distribution of all our BH-MS systems, from both wide and ultra-wide samples (note the separate label on the right-hand side). Dashed region in the center panel marks limits on separation for BH-MS systems assumed in MP2016. Vertical line at $a = 10^5$ AU in the upper panel corresponds to our limit for a binary separation. The presence of maxima has been predicted by MP2016 and is in agreement with their estimates (see text).

For the MP2016 model of tidal circularization there are 587 BH LMXB candidates in our sample of ultra-wide binaries and 219 among wide systems, giving 806 in total. Thus, the addition of ultra-wide systems increased predictions by a factor of about $\sim 3.7$ (note that this factor is roughly the same for other models as well). In order to compare these numbers with MP2016 results we need to adjust a few assumptions. Firstly, MP2016 only consider BH-MS systems with separation between $10^3$ and $3 \times 10^4$ AU, which results in 546 BH LMXB candidates from our samples. They also assume an LMXB lifetime of 1 Gyr, which reduces this number down to 138 binaries, as well as a distribution of initial mass ratios $f(q) \sim q^{-0.5}$ (Duchêne & Kraus, 2013),

which is shifted towards lower $q$ with respect to the flat distribution we adopt. If we assume that BH LMXBs only originate from systems with $q_{\rm ZAMS} \lesssim 0.05$ (masses of BH progenitors are over 20 $M_\odot$ at ZAMS, while MS companions are mostly low-mass stars of M < 1M$_\odot$) this gives us scaling factor of $\sim 4.5$ and finally we obtain 621 BH LMXB candidates for MP2016 conditions. The only remaining difference is in the BH natal kicks. MP2016 estimate the number of BH LMXBs to be $N_{\rm LMXB} \approx 1200$ assuming no NKs for BH and only $N_{\rm LMXB} \approx 60$ for NKs drawn from $\sigma_{BH;NK} = 19$ km/s (see their Table 3). As we discuss in Sec. 2.5.3 our model is somewhere in between (56% of BHs receiving no NK), and we expect that if 100% of our BHs received no NK the number of BH LMXB candidates from our simulations would be around 1100, which is in very good agreement with MP2016 prediction for that favorable case (around 1200 systems). However, we would like to emphasis that this number is also based on three other optimistic assumptions: (i) the MP2016 condition for tidal circularization (more conservative models we tested give around 2–3.5 times less BH LMXB candidates), (ii) the assumption that mass transfer will be launched in all tidally circularized systems, leading to LMXB phase in each case (this might not always be the case, see Ray et al. 1987 and Sec. 2.3.3.3) and finally (iii) the assumption that primordial binaries with massive BH progenitors are also born on ultra-wide orbits with periods of up to log(P/day) = 8.5, while observations suggest that most of systems this wide are in fact hierarchical triples (Moe & Di Stefano, 2017). A more conservative limit on initial period log(P/day) = 5.5 results in about 3.7 less BH LMXB candidates.

We wish to mention that formation channels of LMXBs from triple star systems, although beyond the scope of this study, were also proposed. Most notably, orbits of inner binaries in hierarchical triples in which the outer companion is on a highly inclined orbit could be driven into high eccentricities through the eccentric Lidov-Kozai effect (see Naoz 2016 for the recent review) and form LMXBs this way. Recently Naoz et al. (2016) It was also suggested that exotic binaries such as LMXBs could originate from dynamically destabilized triples (Perets & Kratter, 2012).

On a final note, notice that some ultra-wide BH-MS progenitors face the danger of being disrupted during their pre-BH evolution due to extensive wind mass-loss (Johnston et al., 2012). In the Vink et al. (2011) model of stellar winds a massive star ($\gtrsim 22$ M$_\odot$) with Solar metallicity loses more than half of its mass in just a fraction of a Myr during the core helium burning phase. This means that the binaries with low-mass secondaries ($\lesssim 2$ M$_\odot$) and semi-major axes of more than about $10^4$ AU will lose over half of their mass through winds in less than one orbital period, which may lead to their disruption (see appendix B of Toonen et al. 2017, also Veras et al. 2011 for the somewhat similar case of exoplanets orbiting AGB stars).

## 2.6 Conclusions

We have performed the first population synthesis study on dynamical formation of BH LMXBs from primordial binaries in the Galactic field. Starting from a population of $4.5 \times 10^7$ primordial binaries with massive ($> 19$M$_\odot$) primaries of periods of up to log(P/day) = 5.5, we utilize the StarTrack binary population synthesis code to produce a population of BH-MS binaries.

Subsequently, we distribute them in the Milky Way disc following stellar density distribution and evolve their positions in the Galactic potential. Throughout this long evolutionary stage we account for random encounters with field stars and simulate results of such dynamical interaction using FEWBODY toolkit. We model tidal circularization of highly eccentric systems at periastron by applying a threshold distance $d_{\rm tidal}$, at which tidal forces become significant and are able to fully circularize the system. We test four models, each with a different prescription for the value of $d_{\rm tidal}$: one suggested by MP2016 in their analytical approach and three more based on the ratio $\alpha$ of MS secondary radius to its Roche Lobe: $\alpha = 0.2$, $\alpha = 0.5$ and $\alpha = 0.8$ (Roche Lobe filling factor). Additionally, we have evolved a sample of $1.215 \times 10^7$ "ultra-wide" binaries with initial periods between log(P/day) = 5.5 and 8.5 (corresponding to BH-MS systems forming with separations of about $10^3 - 10^5$ AU). Note, however, that systems this wide containing massive primaries are most likely triples (Moe & Di Stefano, 2017).

We arrive at the following conclusions:

1. **The number of BH LMXBs:** we find that dynamical formation of LMXBs from primordial binaries in the Galactic field can lead to a population of $\sim$ 60–220 BH LMXBs, depending on the model of tidal circularization. This number could possibly be higher by a factor of about 4.5 if the distribution of initial mass ratios was $f(q) \sim q^{-0.5}$ (Duchêne & Kraus, 2013), instead of the flat distribution we adopted. In the same time though, we do not account for the finite duration of the LMXB phase and we simplistically assume initial mass function for the mass function of flying-by field stars. Both those assumption lead to an overestimation in the number of BH LMXB candidates, possibly be a factor of 5 and 2.5 respectively (see Sec. 2.5.1 and 2.5.2).

   Our resulting population is most likely a small fraction of the expected total number of BH LMXBs in the Milky Way, as the estimates based on observational surveys typically span over the range of $10^2$–$10^4$ systems (e.g. Romani 1998; Corral-Santana et al. 2016), whereas the recent discovery of the first candidate for quiescent BH LMXB outside of a globular cluster by Tetarenko et al. (2016b) indicates, that quiescence BH LMXB may be even more abundant in the Galaxy than previously thought, rising the estimate of the total number of BH LMXBs up to $10^4$–$10^8$. Our results are based on a simple treatment of tidal circularization during sufficiently close periastron passages, where we assume that mass transfer will be launched in all tidally circularized systems, leading to a LMXB formation in each case, which, in reality, might not always be the case (Ray et al., 1987). Thus, our estimates serve more as upper limits and we consider it unlikely that a more detailed study could obtain a much bigger population of $\sim 10^4$ dynamically formed BH LMXBs. Our results rather indicate that the dynamical formation channel is only responsible for a small fraction of all the Galactic sources – unless the population of wide BH-MS binaries is much larger than we considered. Possible additional sources of such systems include ultra-wide primordial binaries with massive BH progenitors (with orbital periods beyond the limit log(P/day) = 5.5 we assumed), which could increase the number of dynamically formed BH LMXBs by a factor of about 3.5–4 (see Sec. 2.5.4), as well as the cluster-dispersal scenario

in which a massive object (such as a stellar BH) tidally captures a low-mass star on a wide orbit following a dispersal of their host cluster (Perets & Kouwenhoven, 2012). Another possibility for dynamical formation of LMXBs are channels involving triple star systems (eg. Perets & Kratter, 2012; Naoz et al., 2016).

2. **Important factors :** We find that wide ($\gtrsim$ 200 AU), fast moving BH-MS binaries ($40 - 110$ km s$^{-1}$ relative to local Galactic velocity) are most likely candidates for dynamical formation of BH LMXBs. For such systems the frequency of stellar encounters is sufficient (on average several thousand interactions during a few Gyr evolution), so that it is possible for their orbits to be perturbated into highly eccentric states and then circularized by tidal forces at close pericenter passages. In principle, the dynamical scenario would most efficient for systems with separations between 2000 and 6000, although the existence of BH-MS binaries this wide is uncertain (see Sec.2.5.4). Note that high velocities of our systems are solely associated with dispersion of the Galactic velocity distribution, as the natal kicks of BHs in the surviving binaries in our simulations were either very small (a few km/s) or negligible. In fact, we find that the dynamical scenario quickly becomes ineffective with increasing magnitude of BH natal kicks as only about 10% of our BH LMXB candidates could survive BH formation with kicks drawn from an Maxwellian distribution with $\sigma_{NK} = 10$ km/s (see Sec. 2.5.3). Even though higher kick velocities could potentially produce fast-moving systems with respect to the surrounding stars, giving chance for more stellar encounters and working in favor of the dynamical scenario, we consider this effect to be of secondary importance.

   We also show that the effectiveness of dynamical formation channel is largely dependent on the effectiveness of tidal circularization, which is very much a matter of debate. A detailed treatment of tidal forces would narrow the constraints on the number of formed BH LMXBs.

   We find that a typical evolutionary path leading towards a highly eccentric binary is dominated by only a handful ($\sim 10$) of truly significant interactions (i.e. orbital energy changing by more than 10 %), even though the total number of encounters is usually of the order of several thousands. These few key interactions are, on average, with exceptionally massive fly-bys (often $> 10$ M$_\odot$).

3. **Companion mass function:** we find that the distribution of donor masses in dynamically formed BH LMXB systems is very sensitive to changes of the condition for tidal circularization at close pericenter passage, which is still a poorly understood and difficult to model process. Thus, a more detailed treatment of tidal forces is required to conclude about the exact shape of the CMF in dynamically formed BH LMXB population. We do show, however, that in general the most likely companions are low-mass stars of M $< 1$ M$_\odot$ with the distribution peaking at around $\sim 0.9$ M$_\odot$ in all our models based on the Roche Lobe filling factor (see table 2.2 and figure 2.4). Since we do not simulate the mass transfer itself, in reality the donor masses in dynamically formed BH LMXBs should be even smaller. This result is

in agreement with the observed population of BH LMXBs for which donor masses span mostly in range 0.1–1.0 $M_\odot$, peaking at around $\sim 0.6\ M_\odot$ (see Wiktorowicz et al. (2014) and Fig. 2.4).

**ACKNOWLEDGEMENTS**

We are grateful to the anonymous referee for careful reading of the manuscript and very helpful remarks. We would like to thank Serena Repetto for useful comments and discussion. We would also like to thank thousands of Universe@Home users who have provided their personal computers for our simulations. Authors acknowledge support from the Polish NCN grant Sonata Bis 2 (DEC-2012/07/E/ST9/01360), the Polish NCN grant OPUS (2015/19/B/ST9/01099) and the Polish NCN grant OPUS (2015/19/B/ST9/03188).

# Chapter 3

# Impact of inter-correlated initial binary parameters on double black hole and neutron star mergers

J. Klencki, M. Moe, W. Gladysz, M. Chruslinska, D. E. Holz & K. Belczynski

*Astronomy & Astrophysics, volume 619, A77, (2018)*

**Abstract**

The distributions of the initial main-sequence binary parameters are one of the key ingredients in obtaining evolutionary predictions for compact binary (BH-BH / BH-NS / NS-NS) merger rates. Until now, such calculations were done under the assumption that initial binary parameter distributions were independent. For the first time, we implement empirically derived inter-correlated distributions of initial binary parameters primary mass ($M_1$), mass ratio ($q$), orbital period ($P$), and eccentricity ($e$).

Unexpectedly, the introduction of inter-correlated initial binary parameters leads to only a small decrease in the predicted merger rates by a factor of $\lesssim 2-3$ relative to the previously used non-correlated initial distributions. The formation of compact object mergers in the isolated classical binary evolution favours initial binaries with stars of comparable masses ($q \approx 0.5-1$) at intermediate orbital periods ($\log P$ (days) $= 2-4$). New distributions slightly shift the mass ratios towards lower values with respect to the previously used flat $q$ distribution, which is the dominant effect decreasing the rates. New orbital periods ($\sim 1.3$ more initial systems within $\log P$ (days) $= 2-4$), together with new eccentricities (higher), only negligibly increase the number of progenitors of compact binary mergers.

Additionally, we discuss the uncertainty of merger rate predictions associated with possible variations of the massive-star initial mass function (IMF). We argue that evolutionary calculations should be normalized to a star formation rate (SFR) that

is obtained from the observed amount of UV light at wavelength 1500Å (an SFR indicator). In this case, contrary to recent reports, the uncertainty of the IMF does not affect the rates by more than a factor of $\sim 2$. Any change to the IMF slope for massive stars requires a change of SFR in a way that counteracts the impact of IMF variations on compact object merger rates. In contrast, we suggest that the uncertainty in cosmic SFR at low metallicity can be a significant factor at play.

## 3.1 INTRODUCTION

The Laser Interferometer Gravitational-wave Observatory (LIGO) began its first upgraded observational run (O1) in September 2015; the first ever detection of a gravitational wave signal from a binary black hole (BH-BH) coalescence came shortly afterwards: i.e. GW150914 (Abbott et al., 2016b,c). Since then, four additional BH-BH mergers and, most recently, a double neutron star (NS-NS) merger, were detected and reported to the community: i.e. GW151226 (BH-BH, Abbott et al., 2016a), GW170104 (BH-BH, Abbott et al., 2017b), GW170608 (BH-BH, Abbott et al., 2017c), GW170814 (BH-BH, Abbott et al., 2017d), and GW170817 (NS-NS, Abbott et al., 2017a). The last three events were observed during the second observational run (O2); the Advanced Virgo detector (Acernese et al., 2015) joined the run on August 1, 2017 and contributed to the analysis of GW170814 and GW170817.

The LIGO discovery marks the beginning of the gravitational-wave era. Detections of the coalescence signals from compact binary mergers (CBM) are of utmost astrophysical significance as, among other applications, they will constrain potential formation scenarios, stellar evolution models, and other assumptions associated with theoretical predictions (e.g. Stevenson et al., 2015; O'Shaughnessy et al., 2017a; Barrett et al., 2018). Various formation scenarios for CBM have been proposed. Those most widely discussed include the isolated binary evolution channel involving a common envelope (CE) phase (Eldridge & Stanway, 2016; Belczynski et al., 2016b; Chruslinska et al., 2018; Mapelli et al., 2017; Giacobbo et al., 2018; Stevenson et al., 2017b) or stable mass transfer (van den Heuvel et al., 2017), isolated evolution of field triples (eg. Antonini & Rasio, 2016), dynamical evolution in dense stellar environments such as globular clusters (GCs; Rodriguez et al., 2016b,a; Askar et al., 2017; Park et al., 2017), nuclear star clusters (Miller & Lauburg, 2009; Antonini & Rasio, 2016) or even discs of active galactic nuclei (Stone et al., 2017)), and the formation of compact objects in very close and tidally locked binaries through chemically homogeneous evolution (de Mink & Mandel, 2016; Mandel & de Mink, 2016; Marchant et al., 2016). We note that while it is still possible to distinguish between different types of mergers (i.e. BH-BH, BH-NS, or NS-NS) in a model-independent way (Mandel et al., 2015, 2017) using their gravitational-wave signatures, we still lack a reliable way to determine the formation channel of an observed merger. This is especially true in case of the LIGO/Virgo NS-NS merger (Belczynski et al., 2018). In the case of BH-BH mergers there is some hope connected to the measurement of the BH-BH spin-orbit misalignments (Stevenson et al., 2017b; Farr et al., 2017, 2018b), although this may not work if the BH spins are intrinsically very small (Belczynski et al., 2020b).

Regardless of the formation scenario, the theoretical predictions for the compact binary merger rates are burdened with significant uncertainties due to numerous assumptions and models with poorly constrained parameters, for example the infamous CE phase (Dominik et al., 2012) or the BH/NS natal kicks (Repetto & Nelemans, 2015; Belczynski et al., 2016c)). One of the key ingredients in the calculations are the initial conditions for the simulations: the birth properties of stellar clusters in the case of dynamical scenarios and the characteristics of primordial binaries in the case of isolated binary evolution channels.

Recently, de Mink & Belczynski (2015b) incorporated the updated primordial binary parameter distributions obtained by Sana et al. (2012) from spectroscopic measurements of massive O-type stars in very young ($\sim$ 2 Myr) open star clusters and associations. The updated distributions included a much stronger bias towards close binary orbits with respect to the previously adopted Öpik's law, i.e. a flat in logarithm distribution (Öpik, 1924; Abt, 1983). Intuitively, this change should favour interacting binaries (including those undergoing the CE phase) and possibly cause a notable increase in merger rates. However, de Mink & Belczynski (2015b) found only a very small increase of less than a factor of 2. This is because the distributions obtained by Sana et al. (2012) also show a heavy bias towards low eccentricities with respect to the thermal-equilibrium distribution of Heggie (1975); this distribution results in a nearly unchanged distribution of periastron separations, which is the essential separation regulating the onset of mass transfer.

The sample of binaries observed by Sana et al. (2012) suffers from a significant limitation: it is restricted to systems with $\log P$ (days) $< 3.5$ (spectroscopically detectable binaries) and dominated by very short-period orbits with P $< 20$ days (hence the huge fraction of circularized systems). Since the BH-BH mergers can originate from primordial binaries of up to $\log$ P $\sim 5.5$ (de Mink & Belczynski, 2015b) the binary parameter distributions obtained by Sana et al. (2012) need to be extrapolated to longer periods, which automatically assumes no intrinsic correlations between parameters. However, the joint probability density function cannot be decomposed into independent distribution functions of the individual parameters, i.e. $f(M_1, q, P, e) \neq f(M_1)f(q)f(P)f(e)$. Observational studies have hinted at probable correlations (Abt et al., 1990; Duchêne & Kraus, 2013), but hitherto the selection biases have been too large to accurately quantify the intrinsic interrelations. Recently, Moe & Di Stefano (2017) (hereafter MD17) analysed more than 20 surveys of massive binary stars, corrected for their respective selection effects, combined the data in a homogeneous manner, and fit analytic functions to the corrected distributions. These authors confirm that many of the physical binary star parameters are indeed correlated at a statistically significant level.

de Mink & Belczynski (2015b) concluded that the most significant variations of merger rates associated with the initial parameters are due to uncertainties of the initial mass function (IMF) power-law slope for massive stars (merger rates going up and down by a factor of six in the case of BH-BH). Cosmological calculations of the BH-BH merger rates (e.g. Dominik et al., 2013, 2015; Belczynski et al., 2016b; Kruckow et al., 2018; Mapelli et al., 2017) are performed based on the assumption of a universal IMF across the cosmic time. Often assumed is a so-called "canonical" IMF, which is a multi-part power-law distribution $dN/dM = \xi(M) \propto M^{-\alpha_i}$, where $\alpha_1 = 1.3$

for $M/M_\odot \in [0.08, 0.5]$ and $\alpha_2 = \alpha_3 = 2.3$ for $M/M_\odot \in [0.5, 1.0]$ and $[1.0, 150.0]$, respectively (Kroupa, 2001).

Although clear evidence for strong IMF variations with environmental conditions is still lacking, there are a growing number of results hinting at departures from the IMF universality (see reviews by Bastian et al., 2010; Kroupa et al., 2013). Notably, a recent spectroscopic survey of massive stars in the 30 Doradus star-forming region in the Large Magellanic Cloud has led to a discovery of an excess of stars with masses above 30 $M_\odot$ with respect to the canonical IMF (Schneider et al., 2018); the best-fitted single power-law exponent for $M > 1\ M_\odot$ is $\alpha_3 = 1.90^{+0.37}_{-0.26}$ (although see a technical comment on the data analysis from Farr & Mandel, 2018, suggesting somewhat larger values for $\alpha_3$).

The unknowns associated with the massive-star IMF are often considered to be one of the significant contributors to uncertainty of compact binary merger rates calculated based on population synthesis. In this work, we argue that by normalizing the simulated stellar population to the total amount of far-UV light that it emits, rather than to its total mass, one can significantly reduce the uncertainty associated with possible variations of the IMF slope in different environments; see Sect. 3.6.2. As an example of such a variation and its impact on merger rate calculations, we study in detail the case of a possible correlation between the massive-star IMF slope and metallicity Z.

With the exception of above-mentioned results of Schneider et al. (2018), numerous observations of OB associations and clusters in the Local Group did not reveal any significant deviations from the canonical IMF slope for massive stars $\alpha_3 \approx 2.3$ (Massey, 2003). These included surveys of the Milky Way ($Z \approx Z_\odot = 0.02$; Daflon & Cunha, 2004) [1], the Small Magellanic Cloud ($Z \approx 0.004$; Korn et al., 2000) and the Large Magellanic Cloud ($Z \approx 0.008$; Korn et al., 2000), indicating that for $Z \geq 0.004$ ([Fe/H] $\gtrsim -0.7$) the high-mass end of IMF does not significantly depend on metallicity. Moe & Di Stefano (2013) showed that the same is true for the parameters of close binaries with massive stars. Even at solar metallicity, the discs of massive protostars are already highly prone to gravitational instability and fragmentation, explaining why the close binary fraction of massive stars is so large (Kratter & Matzner, 2006; Kratter et al., 2008, 2010; Moe & Di Stefano, 2017). Further reducing the metallicity can therefore only marginally increase the close binary fraction of massive stars (Tanaka & Omukai, 2014; Moe et al., 2018). However, as we show, the vast majority of BH-BH mergers evolving from the CE channel are expected to originate from $Z < 0.004$ environments, for which there is no direct observational evidence for the persistence of the canonical IMF.

From a theoretical point of view, both the Jeans-mass formalism (Jeans, 1902; Larson, 1998; Bate & Bonnell, 2005; Bonnell et al., 2006) and the model of stellar formation as a self-regulated balance between the rate of accretion from the proto-stellar envelope and the radiative feedback from the forming star (Adams & Fatuzzo, 1996) predict that at a certain sufficiently low metallicity the IMF becomes top heavy [2]. In the first case, the prediction comes from the fact that the Jeans mass has to be larger at lower Z owing to less effective cooling of the proto-stellar cloud

[1] throughout this study, we adopt $Z_\odot = 0.02$ (Villante et al., 2014)

[2] an IMF shifted towards higher stellar masses with respect to the canonical IMF, i.e. $\alpha_3 < 2.3$

($M_J \propto \rho^{-1/2} T^{3/2}$). The radiative feedback, on the other hand, is also metallicity dependent since photons couple less effectively to gas of lower metallicity. Hydrodynamical simulations of the formation of Population III stars ($Z/Z_\odot < 10^{-6}$) demonstrate that the first generation of stars were almost exclusively massive OB-type main-sequence (MS) stars (Bromm et al., 1999; Yoshida et al., 2006; Clark et al., 2011). However, by redshift $z \approx 10$, the mean metallicity of actively forming stars was $Z/Z_\odot \approx 10^{-3}$ (Tornatore et al., 2007; Madau & Dickinson, 2014). For such Population II stars with intermediate metallicities, the IMF is expected to be only moderately top heavy compared to the canonical IMF (Fang & Cen, 2004; Daigne et al., 2006; Greif et al., 2008).

From the observational side, there is indirect evidence for top-heavy IMF variations at cosmological times. The relative paucity of metal-poor G-dwarf stars in the Milky Way (the so-called G-dwarf problem; Pagel, 1989) can be explained by applying an IMF, which is increasingly deficient in low-mass stars the earlier the star formation took place (Larson, 1998). By modelling the abundances of Lyman-break and submillimetre galaxies in the ΛCDM cosmology, Baugh et al. (2005) found that the observations can be reproduced only if some episodes of star formation with a top-heavy IMF were also present in addition to the canonical IMF. Nagashima et al. (2005) used the same model with two modes of star formation to explain the elemental abundances in the intracluster medium of galaxy clusters. Wilkins et al. (2008) pointed out that the local stellar mass density is significantly lower than the value obtained from integrating the cosmic star formation history with a Salpeter IMF (single slope, $\alpha = 2.35$; Salpeter, 1955). At low redshifts ($z < 0.5$) they manage to match the observations using a slightly top-heavy ($\alpha_3 = 2.15$) IMF. For higher redshifts, however, Wilkins et al. (2008) argued that no universal IMF can reproduce the measured stellar mass densities.

The only quantitative calibration of the relation between the high-mass IMF and metallicity obtained thus far has been made possible thanks to the observations of some GCs in the Milky Way. Djorgovski et al. (1993) noticed that the higher metallicity GCs tend to have a bottom-light present day mass function (i.e. a deficit of low-mass stars). De Marchi et al. (2007) later found that these GCs are also the least concentrated sources in their observed sample. Such a trend contradicts basic cluster evolution theory – GCs are expected to be losing low-mass stars from their outer regions owing to their collapse into dense, highly concentrated clusters. An explanation was put forth by Marks et al. (2008), who proposed that low-mass stars could be unbound from mass-segregated GCs during expulsion of their residual gas. This introduces a dependence on metallicity, since the process of gas expulsion is expected to be enhanced in metal-rich environments (Marks & Kroupa, 2010). Finally, Marks et al. (2012) concluded that in order to provide enough radiative feedback to expel the residual gas and match the characteristics of the observed GCs, their IMF had to be top heavy with the value of $\alpha_3$ decreasing with cluster metallicity.

It should be noted, however, that the model of residual gas expulsion applied by Marks et al. (2012) relies on simplified assumptions concerning the radiative feedback. First, the amount of energy deposited from stars into the ISM is fitted to stellar models of only three different masses (35, 60, and 85 $M_\odot$; Baumgardt et al., 2008), and second there is no metallicity dependence. Additionally, Marks et al. (2012) assumed that the energy needed for residual gas removal is

provided by the stellar winds and radiation only (e.g. no feedback from supernova taken into account) and that all the energy radiated by the stars is deposited into the ISM. Thus, the exact relation between the high-mass IMF slope and metallicity remains highly uncertain.
The purpose of this study is twofold. First, we aim to incorporate the interrelated initial binary parameter distributions and multiplicity statistics obtained by MD17 to determine their effects on the predicted rates and properties of CBM. Second, we investigate the importance of possible IMF variations for the merger rate calculations using the Marks et al. (2012) calibration of the IMF dependency on metallicity as an example of such a variation. To achieve this, we perform comparative population synthesis where we use the works of de Mink & Belczynski (2015b); Belczynski et al. (2016b) as references (hereafter dMB15 and B16, respectively). In Sect. 3.2 we describe the new initial conditions and compare these with the previously used distributions. In Sect. 5.2 we describe our computational method. In Sect. 7.3 we compare the distributions of the initial parameters of double compact merger progenitors in our simulations. In Sect. 3.5 we present the impact of the incorporated changes on the cosmological merger rates. In Sect. 7.5 we discuss the metallicity distribution of BH-BH mergers in our simulations and the significance of the top-heavy IMF in low-Z environments for the LIGO predictions. We conclude in Sect. 7.6.

## 3.2 INITIAL DISTRIBUTIONS

### 3.2.1 INTER-CORRELATED INITIAL BINARY PARAMETERS

In the present study, we account for intrinsic correlations between the initial binary star physical parameters. We used the distribution functions presented in section 9 of MD17. The correlations in the MS binary initial conditions are thoroughly discussed in that paper, but we summarize in this section the main results pertinent to the formation of compact objects mergers. dMB15 found that the majority of compact object mergers derive from MS binaries with initial orbital periods $\log P$ (days) = 2−4. Although for our simulations we generated companions across all orbital periods according to the distribution functions provided in MD17, in this section we focus the discussion on the companion star properties across intermediate periods $\log P$ (days) = 2−4.

**Binaries versus triples:** dMB15 and B16 assumed all companions to massive stars (M>10 $M_\odot$) were in binaries. In contrast, MD17 have modelled a companion star fraction and period distribution that includes true binaries as well as inner binaries and outer tertiaries in hierarchical triples. With increasing orbital period, the likelihood that a companion is an outer tertiary must increase. In fact, essentially all wide companions ($\log P > 5$) to massive stars are the outer tertiaries in hierarchical triples/quadruples (Sana et al. 2014; MD17). We model the probability that a companion is in the inner binary $\mathcal{P}_{\rm bin}(M_1, P)$ in a manner that reproduces the multiplicity statistics derived in MD17. Specifically, for $M_1 = 8\ M_\odot$, we find the probability decreases from $\mathcal{P}_{\rm bin} = 0.96$ for $\log P = 2$ to $\mathcal{P}_{\rm bin} = 0.60$ for $\log P = 4$. For $M_1 = 30\ M_\odot$, the triple/quadruple star fraction is larger, and so we adopt $\mathcal{P}_{\rm bin} = 0.93$ for $\log P = 2$ and $\mathcal{P}_{\rm bin} = 0.23$ for $\log P = 4$. We illustrate $\mathcal{P}_{\rm bin}(M_1, P)$ in Fig. 3.1.

**Companion star fraction:** dMB15 and B16 implemented a binary star fraction such that

$F_{logP=2-4;bin} \approx 28\%$ of massive primaries had binary star companions with periods log $P$ (days) = 2−4 and mass ratios $q$ = 0.1−1.0. The companion star fraction increases dramatically with primary mass (Abt et al., 1990; Raghavan et al., 2010; Sana et al., 2012; Chini et al., 2012; Duchêne & Kraus, 2013; Moe & Di Stefano, 2013, 2017). According to MD17, the intermediate-period companion star fraction increases from $F_{logP=2-4;comp}$ = 0.46 for $M_1$ = 8 $M_\odot$ to $F_{logP=2-4;comp}$ = 0.66 for $M_1$ = 30 $M_\odot$. Approximately two-thirds of O-type primaries have a companion with log $P$ (days) = 2−4 and $q > 0.1$. A significant fraction of these systems, especially those with longer periods log $P$ (days) = 3.5−4.0, are actually outer tertiaries in triples (see above and Fig. 3.1).

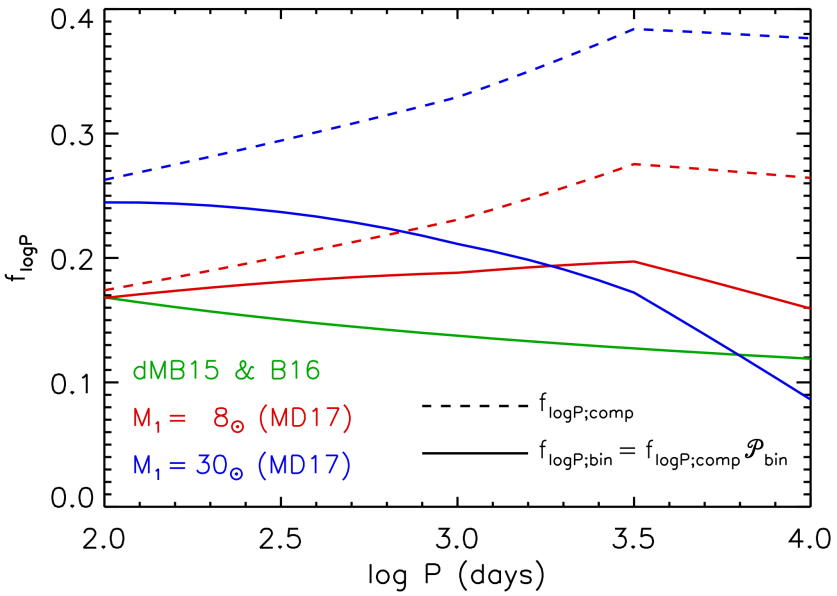


Figure 3.1: Frequency $f_{logP}$ of companions with $q > 0.1$ per decade of orbital period across log $P$ (days) = 2−4. We compare the distribution $f_{logP;comp}$ of all companions (binaries and tertiaries; dashed) to the distribution $f_{logP;bin} = f_{logP;bin} \times \mathcal{P}_{bin}$ of only the inner binaries (solid), where $\mathcal{P}_{bin}$ is the probability that the companion is a member of the inner binary. The overall binary fraction and binary period distribution across log $P$ (days) = 2−4 are similar between those adopted by dMB15 and B16 (green) and the values for $M_1$ = 8 $M_\odot$ (red) and $M_1$ = 30 $M_\odot$ (blue) primaries based on the multiplicity statistics presented in MD17.

**Period distribution:** dMB15 and B16 adopted a power-law binary period distribution $f_{logP;bin} \propto (\log P)^{-0.55}$ motivated by spectroscopic observations of massive binaries (Sana et al., 2012). These works normalize this period distribution such that integration $F_{logP=2-4;bin} = \int_2^4 f_{logP;bin} d(logP)$ = 0.28 reproduces the binary fraction across log $P$ (days) = 2−4. In the current study, we adopt a companion star period distribution $f_{logP;comp}(M_1, P)$ based on the analytic fits in MD17 that are shown in the lower panel of their Fig. 37. We then derive the inner binary period distribution $f_{logP;bin} = f_{logP;comp} \times \mathcal{P}_{bin}$. In Fig. 3.1, we show $f_{logP;bin}$ from dMB15 and B16, $f_{logP;comp}$ for $M_1$ = 8 $M_\odot$ and 30 $M_\odot$ taken directly from MD17, and $f_{logP;bin}$ for $M_1$ = 8 $M_\odot$ and 30 $M_\odot$ implemented in the current study. While companions in general are weighted towards longer periods, the inner

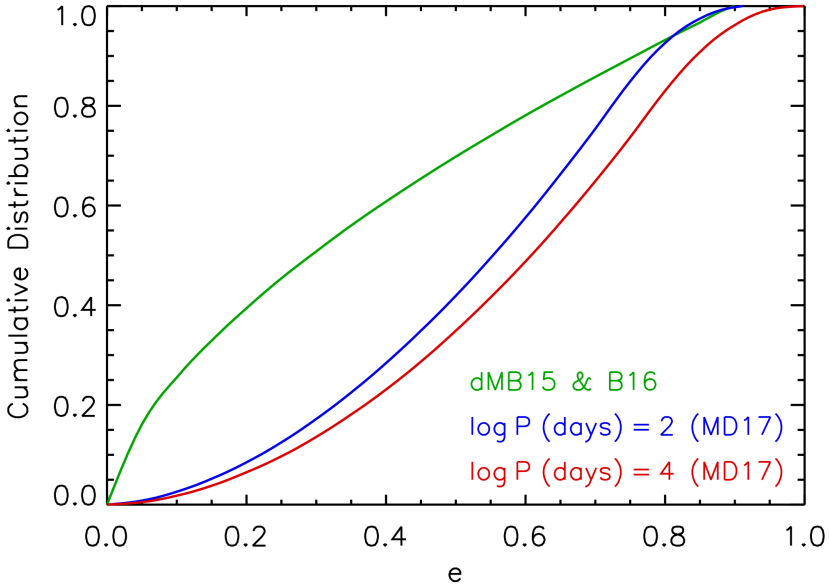


FIGURE 3.2: Cumulative distribution function of eccentricities. dMB15 and B16 adopted an eccentricity distribution $p_e \propto e^{-0.4}$ (green) based on a sample of massive spectroscopic binaries (Sana et al., 2012) that are dominated by short-period systems P < 20 days and therefore weighted towards lower eccentricities $< e > = 0.3$. MD17 (and references therein) found that massive binaries with intermediate (blue) and long (red) orbital periods are weighted towards higher eccentricities $< e > = 0.6$ and are sufficiently modelled by a power-law distribution $p_e \propto e^{0.8}$ with a turnover above $e > 0.8$.

binary period distribution is skewed towards shorter periods as implemented in dMB15 and B16 and found in Sana et al. (2012).

**Eccentricity distribution:** dMB15 and B16 incorporated a power-law eccentricity distribution $p_e \propto e^{\eta}$ with exponent $\eta = -0.4$ across the domain $e = 0.0$–$0.9$ , as motivated by Sana et al. (2012). However, the Sana et al. (2012) sample of spectroscopic binaries are dominated by systems with P < 20 days, therefore the power-law slope $\eta = -0.4$ is only appropriate for such short-period systems. MD17 have found that eccentricities become weighted towards higher values with increasing orbital period, which they model with two parameters. First, MD17 have defined the domain of the eccentricity distribution across the interval $e = 0.0$–$e_{\rm max}$, where $e_{\rm max}(P)$ is the maximum eccentricity possible without substantially filling the Roche lobes of the binary (Eqn. 3 in MD17). For P = 5 days, the binaries must have $e < e_{\rm max} \approx 0.5$ to be initially non-Roche-lobe filling. Meanwhile, binaries with log $P$ (days) = 2–4 can extend up to $e_{\rm max} \approx 0.95$. Second, MD17 have found the power-law slope $\eta$ also increases with increasing period. For massive binaries, they fit $\eta \approx 0.8$ for log $P$ (days) = 2–4. We adopt the power-law slopes $\eta(M_1, P)$ presented in MD17 across the domain $e = 0$–$0.8 e_{\rm max}$. At high eccentricities $e = (0.8$–$1.0) e_{\rm max}$, we assume the probability distribution function turns over according to a decreasing linear function such that $p_e(e = e_{\rm max}) = 0$. In Fig. 3.2, we compare the cumulative distribution function of the eccentricity distribution adopted in dMB15 and B16 to the updated distributions at log $P$ (days) = 2 and 4. As expected, the eccentricity distribution based on the Sana et al. (2012) sample is skewed towards lower values.

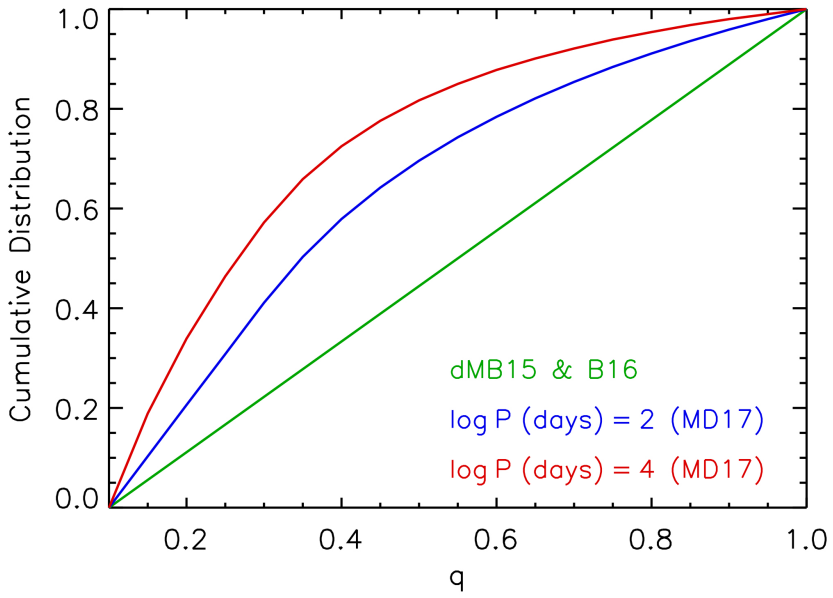


Figure 3.3: Cumulative distribution function of mass ratios. dMB15 and B16 adopted a uniform mass-ratio distribution $p_q \propto q^0$ (green) based on a sample of massive spectroscopic binaries (Sana et al., 2012) that are dominated by short-period systems P < 20 days. MD17 (and references therein) found that massive binaries with intermediate periods (blue and red) are weighted significantly towards smaller mass ratios.

**Mass ratio distribution:** dMB15 and B16 adopted a uniform mass-ratio distribution $f_q = q^0$. Again, this was based on a sample of massive spectroscopic binaries (Sana et al., 2012) that is dominated by short-period systems $P < 20$ days. Based on a series of observational evidence (long baseline interferometry, companions to Cepheids, eclipsing binaries, adaptive optics, Hubble imaging, etc.), MD17 have demonstrated that slightly wider massive binaries are weighted considerably towards smaller mass ratios. Across intermediate periods log $P$ (days) = 2−4, MD17 have found the mass-ratio distribution is accurately described by a two-component power-law $p_q \propto q^\gamma$ with slopes $\gamma_{\rm smallq}$ across small mass ratios $q$ = 0.1−0.3 and $\gamma_{\rm largeq}$ across large mass ratios $q$ = 0.3−1.0. For massive binaries and log $P$ (days) = 2, MD17 have fit $\gamma_{\rm smallq} = 0.0$ and $\gamma_{\rm largeq} = -1.4$, while for log $P$ (days) = 4, they have measured $\gamma_{\rm smallq} = -0.7$ and $\gamma_{\rm largeq} = -2.0$ (see their Fig. 35). In Fig. 3.3, we compare the cumulative mass-ratio distributions used by dMB15 and B16 to the updated distributions measured at log $P$ (days) = 2−4.

**Very massive binaries**: At present, there are no reliable observational measurements of the properties of very massive binaries with intermediate periods log $P$ (days) = 2−4 and primary masses $M_1 > 40\ M_\odot$. At these intermediate separations, the mass-ratio and eccentricity distributions do not significantly change across primary masses $8\ M_\odot < M_1 < 40\ M_\odot$. In addition, the inner binary fraction and inner binary period distribution across log $P$ (days) = 2−4 varies only slightly across the primary mass interval $8\ M_\odot < M_1 < 40\ M_\odot$ (see Fig. 3.1). We therefore assume that systems with $M_1 > 40\ M_\odot$ have the same period, eccentricity, mass-ratio distributions, and binary fractions as those systems with $M_1 = 40\ M_\odot$.

**Triple-star evolution:** We model the evolution of all inner binaries with StarTrack. For triples, we ignore the outer tertiaries except for the following case. If the inner binary initially has P < 5 days and q < 0.4, it most likely will undergo unstable Case A Roche lobe overflow (RLOF), merge on the MS, and effectively evolve as a single star. If the tertiary has log $P_{\rm outer}$ (days) $\lesssim 4$, then such a triple may lead to the formation of compact object merger. We model these triples with inner binaries $P_{\rm bin} < 5$ days and $q_{\rm bin} < 0.4$ as simple binaries, where the original inner binary merges to become the effective primary with combined mass $M_1 + M_2$ and the tertiary becomes the effective binary companion with mass $M_3$. For simplicity, we assume no rejuvenation of the merger product, i.e. evolve it as a star with the same age as its companion with mass $M_3$. About 10% of massive inner binaries with $P < 5$ days have outer tertiaries in tight, hierarchical configurations log $P_{\rm outer}$ (days) < 4 (MD17). This triple-star channel certainly does not dominate, but can contribute an additional ≈5–10% to the overall compact merger rate.

### 3.2.2 IMF AND ITS DEPENDENCE ON METALLICITY

We adopt the same IMF that was used by B16, as guided by the recent observations (Bastian et al., 2010),

$$dN/dM = \xi(M) \propto \begin{cases} M^{-1.3}, & \text{for } M/M_\odot \in [0.08, 0.5] \\ M^{-2.2}, & \text{for } M/M_\odot \in [0.5, 1.0] \\ M^{-\alpha_3}, & \text{for } M/M_\odot \in [1.0, 150.0] \end{cases}, \tag{3.1}$$

where for our standard model $\alpha_3 = 2.3$; we note that dMB15 adopt $\alpha_3 = 2.7$ but also investigate $\alpha_3$ = 2.2 and 3.2).

Additionally we calculate a model in which the IMF slope for massive stars depends on metallicity, as described below. In the following, we assume a conversion between [Fe/H] and Z given by Bertelli et al. (1994), appropriate for stars with solar-like fraction of iron among all the metal components.

Based on the observations of stellar clusters in the Milky Way and N-body simulations (Sect. 3.1) Marks et al. (2012) calibrated that $\alpha_{3;\rm Marks} = 2.63 + 0.66$[Fe/H] for [Fe/H] < −0.5, which corresponds to $Z \lesssim 0.0063$. We note that the above relation comes from a rather uncertain fit (see Fig. 4 of Marks et al., 2012) and is based on a model with several caveats (see discussion at the end of Sect. 3.1). Because the observations of OB associations and clusters in the Local Group do not support any significant deviations from $\alpha = 2.3$ for metallicities $Z \geq 0.004$ (Massey, 2003), we modify the relation for $\alpha_3$ proposed by Marks et al. (2012) such that the IMF dependence towards lower metallicity does not occur until Z < 0.004, and $\alpha_3 = 2.3$ for $Z \geq 0.004$. Marks et al. (2012) observational data extends down to about Z = 0.0001 ([Fe/H] ≈ −2.3, see their Fig. 4), and we decided to limit the further decrease of $\alpha_3$ for lower metallicities. Explicitly we adopt the

following formula:

$$\alpha_3(\mathrm{Z}) = \begin{cases} 2.3, & \text{for } Z \geq 0.004 \\ 2.3 + 0.76\,[\log \mathrm{Z} + 2.4], & \text{for } 0.0001 < Z < 0.004\,. \\ 1.1, & \text{for } Z < 0.0001 \end{cases} \tag{3.2}$$

For some example values of Z, this formula yields $\alpha_3(\mathrm{Z} = 0.1\ Z_\odot) = 2.07$ and $\alpha_3(\mathrm{Z} = 0.01\ Z_\odot) = 1.31$.

We note that we treat the IMF $\mathrm{d}N/\mathrm{d}M$ (all stars) and primary mass function $\mathrm{d}N/\mathrm{d}M_1$ (single stars and primaries in binaries) interchangeably. Across large masses $M > 1\ M_\odot$, both the IMF and primary mass function have the same slope $\alpha_3 = 2.3$ (Kroupa et al., 2013). The IMF and primary mass function only differ slightly across small masses $M < 1\ M_\odot$. Since $\alpha_3$ (and its dependence on metallicity) is the most important parameter for determining merger rates, the assumption that $\mathrm{d}N/\mathrm{d}M$ equals $\mathrm{d}N/\mathrm{d}M_1$ is justified.

## 3.3 Computational method

### 3.3.1 Physical assumptions – the StarTrack code

We utilized the StarTrack population synthesis code (Belczynski et al., 2002, 2008a; Dominik et al., 2012). StarTrack is developed based on analytical formulae for the evolution of a non-rotating star obtained by Hurley et al. (2000) from the fits to the grid of evolutionary tracks calculated by Pols et al. (1998). The original Hurley et al. (2000) models were updated with the prescriptions for the wind mass loss from O-B type stars (Vink et al., 2001), Wolf-Rayet stars (Hamann & Koesterke, 1998; Vink & de Koter, 2005), and enhanced mass loss rates for luminous blue variables (Belczynski et al., 2010a). For core-collapse supernovae we adopt the convection driven, neutrino enhanced "rapid" supernova engine from Fryer et al. (2012), which reproduces the observed mass gap between NSs and BHs (Belczynski et al., 2012b). The key parameter of this model, dependent on the mass of the CO core at the time of explosion, is the fraction of material ultimately falling back onto the proto compact object ($f_b$) and contributing to the final remnant mass. The supernova kick velocity is drawn from a Maxwellian distribution with $\sigma_{1D} = 265\,\mathrm{km\,s^{-1}}$ (Hobbs et al., 2005) and lowered proportionally to the amount of fallback, i.e. $V_{NK} = V_{NK;Hobbs}(1 - f_b)$. This effectively means that the most massive BHs in our simulations (up to $\sim 15\ M_\odot$ for $Z_\odot$ and $\sim 40\ M_\odot$ for $0.1\ Z_\odot$) are also typically those that receive a relatively small or zero natal kick (direct collapse).

We calculated the CE evolution in one step by applying the energy balance prescription of Webbink (1984). We adopt $\alpha_{\mathrm{CE}} = 1$ for the efficiency of energy transfer. The envelope binding parameter $\lambda$ is taken from the fits of Xu & Li (2010) and depends on the radius and the evolutionary state of the donor. There are large uncertainties concerning the stability of mass transfer initiated by a Hertzsprung gap (HG) donor star. Pavlovskii et al. (2017) recently reported that for a large range of donor radii and masses such mass transfer may actually be stable, rather than leading to a CE phase. While revised criteria for a range of different metallicities and other parameters are

still under preparation (Ivanova, private communication), we opted to not follow the evolution of systems with HG donors in which our standard criteria for the mass transfer stability (Eq. 49 of Belczynski et al., 2008a) indicate a dynamically unstable event.

Up until this point our physical assumptions are the same as in submodel B of dMB15 and standard model M1 of B16. The only recent update is the addition of mass loss due to pair-instability pulsations (model M10; Belczynski et al., 2016a). Such pulsations can affect stars with massive helium cores $M_{\rm He}$ between $\sim 40{-}45\ M_\odot$ and $\sim 60{-}65\ M_\odot$ and deplete them of a significant amount of mass ($M_{\rm ejecta} \sim 5{-}20\ M_\odot$; Heger & Woosley, 2002). We modelled this by assuming that stars with $M_{\rm He} = 45{-}65\ M_\odot$ are subject to pair-instability pulsations and lose all their mass above $45\ M_\odot$. We note that the inclusion of pair-instability mass loss does not affect our predictions for detections of double compact mergers with the LIGO O2 observational run sensitivity (Belczynski et al., 2016a), and is consistent with existing data (Fishbach & Holz, 2017a).

### 3.3.2 Cosmological calculations of the merger rates

We placed our simulated systems into a cosmological background by populating the Universe up to $z = 15$. We modelled binaries across 32 different metallicities covering the range from $0.005\ Z_\odot$ to $1.5\ Z_\odot$. In our standard model (I1) the IMF does not depend on metallicity, and so for each Z we use the same sample of $2 \times 10^6$ systems (single stars, binaries, triples) generated according to the multiplicity statistics described in Sect. 3.2 and a primary mass function $\xi(M_1) \propto M_1^{-\alpha_3}$ with $\alpha_3 = 2.3$ across $5\ M_\odot < M_1 < 150\ M_\odot$. We only evolve binaries ($\sim 72\%$ of systems with $M_1 > 5\ M_\odot$) and hierarchical triples ($\sim 3.6\%$), in which the inner binary is likely to merge during an early case A mass transfer (Sect. 3.2.1). For submodel I2 we assume the metallicity-dependent primary mass function according to Eqn. 3.2, and for each Z we generate a corresponding sample of $10^6$ initial systems.

We calculate the merger rate density as a function of redshift by integrating through the cosmic star formation rate (SFR) history as described in see Sect. 4 of Dominik et al. (2015) and Sect. 2.2 of Belczynski et al. (2016c). For each redshift bin $\Delta z = 0.1$ up to $z = 15$ we use the cosmic SFR

$$\mathrm{SFR}(z) = 0.015 \frac{(1+z)^{2.7}}{1 + [(1+z)/2.9]^{5.6}}\ \mathrm{M_\odot Mpc^{-3} yr^{-1}} \tag{3.3}$$

from Madau & Dickinson (2014) as implemented in B16. The contribution from each of the metallicities in our simulations at a given redshift of star formation $z_{\rm SF}$ is then calculated as a fraction of $\mathrm{SFR}(z_{\rm SF})$ according to the mean metallicity evolution model from Madau & Dickinson (2014), increased by 0.5 dex to better fit observational data (Vangioni et al., 2015), i.e.

$$\log(Z_{\rm mean}(z)) = 0.5 + \log\left(\frac{y\,(1-R)}{\rho_{\rm b}} \int_z^{20} \frac{97.8 \times 10^{10}\,\mathrm{SFR}(z')}{H_0\,E(z')\,(1+z')} dz'\right). \tag{3.4}$$

We adopt a return fraction $R = 0.27$ (fraction of stellar mass returned into the interstellar medium), a net metal yield of $y = 0.019$ (mass of metals ejected into the medium by stars per unit mass locked in stars), a baryon density $\rho_{\rm b} = 2.77 \times 10^{11}\,\Omega_{\rm b}\,h_0^2\ M_\odot\,\mathrm{Mpc^{-3}}$ with $\Omega_{\rm b} = 0.045$ and $h_0 = 0.7$,

a SFR from Eqn. 3.3, and $E(z) = \sqrt{\Omega_{\rm M}(1+z)^3 + \Omega_{\rm k}(1+z)^2 + \Omega_\Lambda}$ in a flat cosmology with $\Omega_\Lambda = 0.7$, $\Omega_{\rm M} = 0.3$, $\Omega_{\rm k} = 0$, and $H_0 = 70.0\,{\rm km\,s^{-1}\,Mpc^{-1}}$. We assume a log–normal distribution of metallicity with $\sigma = 0.5$ dex around the mean value at each redshift (Dvorkin et al., 2015).

Madau & Dickinson (2014) obtained their cosmic SFR based on the far-UV (FUV; 1500 ) and IR (8−1000 $\mu$m) luminosity functions. Both are regarded as good tracers of star formation as they are dominated by the contribution from short-lived massive stars: FUV directly and IR through re-radiation of dust-absorbed UV. Specifically, Madau & Dickinson (2014) converted strength of the 1500  line in the UV spectrum $L_\nu$(FUV) into a cosmic SFR by applying an adequate conversion factor $\mathcal{K}_{\rm FUV}$, such that SFR = $\mathcal{K}_{\rm FUV} \times L_\nu$(FUV) (their Eqn. 10). To calculate $\mathcal{K}_{\rm FUV}$ they assume a Salpeter IMF with slope $\alpha = 2.35$ across masses $M = 0.1{-}100\ M_\odot$ (Salpeter, 1955). It is therefore *inconsistent* to implement the above Eqn. 3.3 in combination with a more realistic Kroupa-like IMF that turns over below $M \lesssim 0.5\ M_\odot$. We introduce a conversion factor $\mathcal{K}_{\rm IMF}$ for a given IMF such that

$$\mathrm{SFR}_{\rm IMF}(z) = \mathcal{K}_{\rm IMF} \times \mathrm{SFR}_{\rm Salpeter}(z), \tag{3.5}$$

where $\mathrm{SFR}_{\rm Salpeter}(z)$ is given by Eqn. 3.3. In order to calculate $\mathcal{K}_{\rm IMF}$ for various IMFs we compute the corresponding UV spectra via Starburst99 code, designed to model spectrophotometric properties of star-forming galaxies (Leitherer et al., 1999; Vázquez & Leitherer, 2005; Leitherer et al., 2014). In other words, when changing the IMF, we normalize the SFR from Madau & Dickinson (2014) in such a way that the amount of UV observed at 1500 stays the same. Details are given in Appendix 3.A, together with a tabularized set of $\mathcal{K}_{\rm IMF}$ values at solar and subsolar metallicities for different Kroupa-like IMFs.

In the model with metallicity-dependent IMF at each redshift of star formation $z_{\rm SF}$ we use the mean metallicity of that redshift $Z_{\rm mean}(z_{\rm SF})$ to calculate a high-mass IMF slope (Eqn. 3.2). We then use an appropriate value of $\mathcal{K}_{\rm IMF}$ from Table 3.3 to correct the cosmic SFR (Eqn. 3.5). For example, the conversion to Kroupa-like IMF (Kroupa et al., 1993) with $\alpha_3 = 2.3$ (Bastian et al., 2010), the IMF which was assumed in a the recent studies Belczynski et al. (2016b,a), requires multiplying the cosmic SFR (Eqn. 3.3) by $\mathcal{K}_{{\rm IMF};\alpha_3=2.3} = 0.51$. [3]

The output of StarTrack and the cosmological calculations described above is in the form of CBM happening at different redshifts. Each event is assigned with a normalization factor calculated as a convolution of the cosmic SFR and the metallicity distribution at the redshift of the binary formation (Eqn. 7 of Belczynski et al. (2016c)). Based on that we compute the source frame merger rate density [$\mathrm{Gpc^{-3}\,yr^{-1}}$].

### 3.3.3 Calculations of predictions for the LIGO/Virgo detectors

Finally, we need to account for the detector sensitivity to produce predictions for the LIGO/Virgo observations. For each of our mergers we modelled the full inspiral-merger-ringdown waveform

[3] Such a correction is missing in all our previous studies, except for Chruslinska et al. (2018). However, its effect would be of secondary importance compared to uncertainties arising from evolutionary models (e.g. natal kicks), so their conclusions remain unchanged.

using the IMRPhenomD gravitational waveform templates (Khan et al., 2016; Husa et al., 2016). We adopt a fiducial O2 noise curve ("mid-high") from Abbott et al. (2016d). Following Belczynski et al. (2016b) we consider a merger to be detectable if the signal-to-noise ratio in a single detector is above a threshold value S/N = 8. We estimate detection rates as described in Belczynski et al. (2016c). This includes the calculation of detection probability $p_{\rm det}$, which takes into account the detector antenna pattern (LIGO samples a 'peanut-shaped' volume rather than an entire spherical volume enclosed by the horizon redshift; Chen et al., 2017). For increased accuracy with respect to Belczynski et al. (2016c), where we used an analytic fit to obtain $p_{\rm det}$ (Eqn. A2 of Dominik et al., 2015), in this work we interpolate the numerical data for the cumulative distribution function available on-line at `http://www.phy.olemiss.edu/~berti/research.html`. This improvement leads to a few per cent increase in detection rates.

### 3.3.4 DIFFERENCES WITH RESPECT TO BELCZYNSKI ET AL. (2016B) AND BELCZYNSKI ET AL. (2016A)

In terms of physical assumptions (Sect. 3.3.1), in the current study, we adopt exactly the model M10 from Belczynski et al. (2016a). Model M1 from B16 is also very similar, only differing by the lack of mass loss due to pair-instability pulsations.

There are, however, two differences between our current calculations and these two previous studies. We correct the assumed SFR (Eq. 3.3) derived from a Salpeter IMF for a more realistic Kroupa-like IMF (see Appendix 3.A), which lowers the predicted merger rates by a factor of ∼0.51 in the case of $\alpha_3 = 2.3$. In both Belczynski et al. (2016a) and B16 there was a mistake in the way the simulated systems were normalized to match the entire stellar population (i.e. the calculation of the simulated mass $M_{\rm sim}$). As a result, the calculated merger rates were about ∼1.82 smaller. The net effect of these two changes is a slight decrease of the merger rates (by a factor of 0.926). This is why the numbers we present for model M10 in the following sections are 0.926 times smaller than the corresponding values presented in Belczynski et al. (2016a). We note that in the most recent work, Belczynski et al. (2020b), the correction factor of 0.926 is already applied to all the models.

## 3.4 RESULTS

### 3.4.1 BIRTH PROPERTIES OF COMPACT BINARY MERGERS

Starting from the zero-age MS (ZAMS), we evolved $\sim 1.5 \times 10^6$ binaries with primaries of at least 5 $M_\odot$ drawn from the initial distributions of MD17. According to the assumed IMF and multiplicity statistics, our sample constitutes about 29% of the mass of all the stars forming at ZAMS, and so our simulations are normalized to a star-forming mass of $M_{\rm sim} = 1.687 \times 10^8\ M_\odot$. The formation efficiencies of CBM, depend significantly on metallicity, but are generally between $10^{-5}$ and $10^{-7}$ $[M_\odot^{-1}]$ (see Table 3.1); we define CMBs as the number of merging systems of a given type in our simulations per unit of star-forming mass, i.e. $X_{\rm CBM}\ (\ M_\odot^{-1}) = N_{\rm CBM}/M_{\rm sim}$.

Table 3.1: Comparison of the formation efficiencies per unit of star-forming mass of CBM: BH-BH, BH-NS, and NS-NS between the two models with different initial distributions: either Sana et al. (2012, , old) or MD17(new). The comparison is made at three different metallicities. No metallicity-dependence for the IMF is assumed here. We indicate in bold text the dominant metallicity (out of the three showed here) for the formation of each type of the double compact mergers.

| Metallicity merger type[b] | Formation efficiency $X_{\rm CBM}$ $(M_\odot^{-1})$[a] Sana+12 (model M10) | MD17 (model I1) | Relative MD17 / Sana |
|---|---|---|---|
| $Z = Z_\odot$ | | | |
| NS-NS | $\mathbf{8.3 \times 10^{-6}}$ | $\mathbf{3.8 \times 10^{-6}}$ | 0.46 |
| BH-NS[c] | $9.0 \times 10^{-8}$ | $1.1 \times 10^{-7}$ | 1.22 |
| BH-BH | $3.5 \times 10^{-7}$ | $1.5 \times 10^{-7}$ | 0.43 |
| $Z = 0.1\ Z_\odot$ | | | |
| NS-NS | $1.75 \times 10^{-6}$ | $1.0 \times 10^{-6}$ | 0.57 |
| BH-NS | $\mathbf{3.0 \times 10^{-6}}$ | $\mathbf{1.2 \times 10^{-6}}$ | 0.4 |
| BH-BH | $2.1 \times 10^{-5}$ | $8.4 \times 10^{-6}$ | 0.4 |
| $Z = 0.01\ Z_\odot$ | | | |
| NS-NS | $1.7 \times 10^{-6}$ | $1.2 \times 10^{-6}$ | 0.71 |
| BH-NS | $9.6 \times 10^{-7}$ | $3.6 \times 10^{-7}$ | 0.38 |
| BH-BH | $\mathbf{5.3 \times 10^{-5}}$ | $\mathbf{2.9 \times 10^{-5}}$ | 0.55 |

Notes:
[a] Compact binary merger formation efficiency per unit of star-forming mass: $X_{\rm CBM}$ $(M_\odot^{-1})$ = $N_{\rm CBM}/M_{\rm sim}$, where $M_{\rm sim;MD17} = 1.687 \times 10^8\ M_\odot$ and $M_{\rm sim;Sana} = 1.56 \times 10^8\ M_\odot$
[b] All the systems expected to merge within the Hubble time.
[c] Only a statistically insignificant (< 20) number of BH-NS mergers form at $Z = Z_\odot$ in our simulations.

We compare the birth properties of CBM progenitors between the two simulated samples: (1) one assuming the initial MS binary distributions of Sana et al. (2012) (old simulations from Belczynski et al., 2016a) andthe other adopting the recent results of MD17. We discuss the NS-NS mergers together with BH-BHs because these two merger types originate from systems with similar mass ratios and their distributions of initial pericentre separations and primary masses are clearly distinguishable. The BH-NS progenitors are presented separately.

#### 3.4.1.1 Progenitors of BH-BH and NS-NS mergers

In Fig. 3.4, we show the birth properties of systems that evolve to form BH-BH and NS-NS mergers. We only include double compact binaries that are expected to merge within the Hubble time. The histograms are normalized to unity for an easier comparison; see Table 3.1 for the relative formation efficiencies.

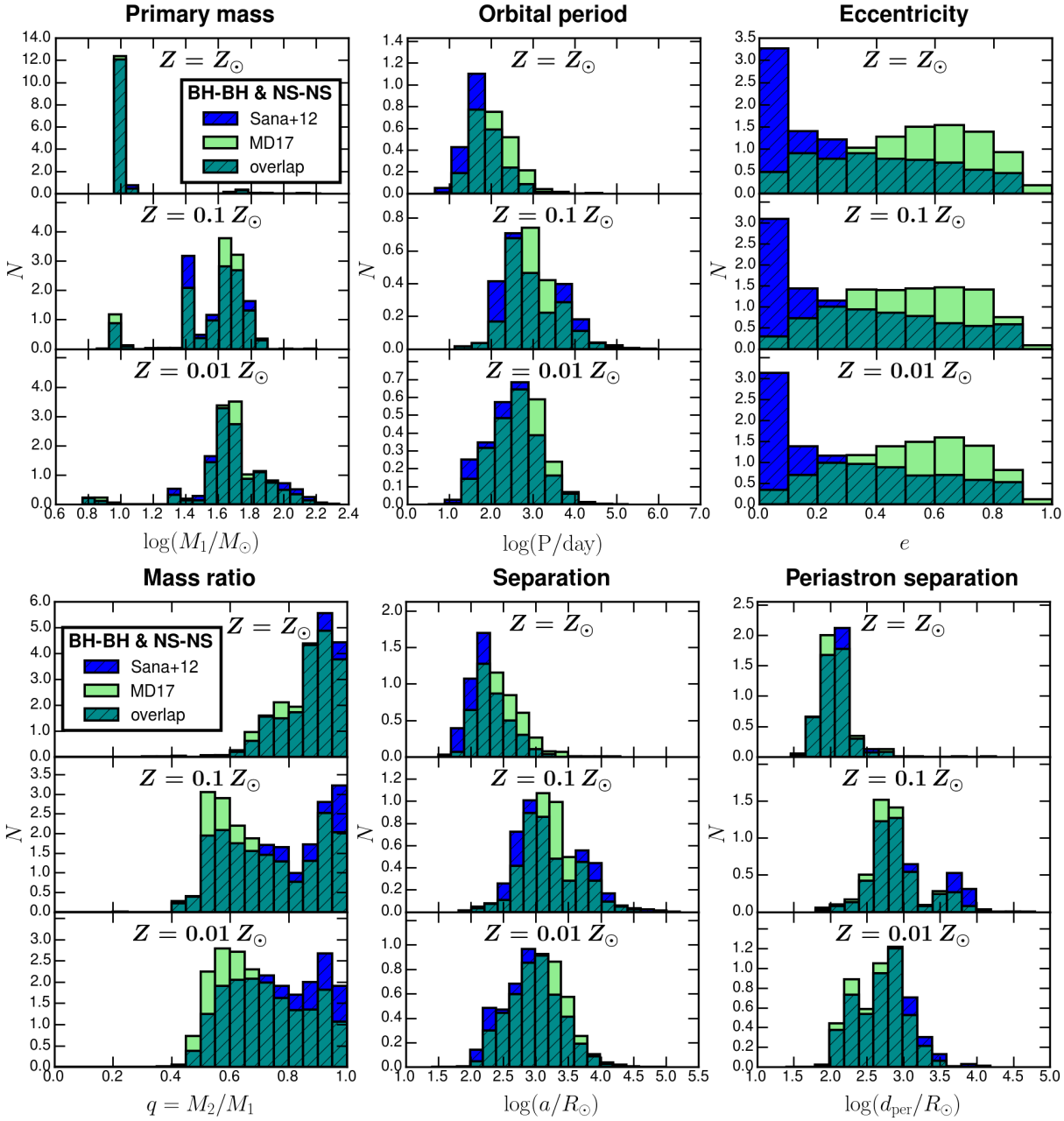


FIGURE 3.4: Birth distributions of initial ZAMS binary parameters of the progenitors of BH-BH and NS-NS mergers. The histograms are normalized to unity for an easier comparison. NS-NS mergers dominate at $Z = Z_\odot$ (upper panel) while BH-BH mergers dominate at $Z = 0.1\ Z_\odot$ and $Z = 0.01\ Z_\odot$ (lower panels).

**Primary masses**: The distributions of primary masses are noticeably different in different metallicities. The peak around 10 $M_\odot$ at $Z = 0.02$ corresponds to NS-NS progenitors, which are the dominant type of CBM at solar metallicity. At $Z = 0.002$ the formation of BH-BH begins to dominate and happens for primary masses $M_1 > 20\ M_\odot$, peaking around 25 and 45 $M_\odot$. This bimodal shape is a direct consequence of the bimodal distribution of CO core masses $M_{\mathrm{CO}}$ of supernova progenitors expected to undergo a direct BH formation. In the rapid supernova

engine we adopted (Fryer et al., 2012), BHs receive no natal kick on formation if $M_{\rm CO}$ is either between 6 and 7 $M_\odot$ or above 11 $M_\odot$ (see their Eqn. 16). At $Z = 0.01\ Z_\odot$ the higher mass peak corresponding to $M_{\rm CO} > 11\ M_\odot$ dominates.

The differences between the new and old initial distributions are very small. The NS-NS as well as lower mass BH-BH corresponding to $M_{\rm CO} = 6{-}7\ M_\odot$ are most preferably formed from systems with very high initial mass ratios $q > 0.8$, which is why there is relatively less of such systems in the simulations with MD17 initial conditions.

**Orbital periods, eccentricities, and periastron separations**: The new initial binary period distribution of MD17 is in general very similar in shape to that proposed by Sana et al. (2012) in the crucial range of $\log P$ (days) between 2 and 4 (especially for systems with massive primaries $\sim 30\ M_\odot$; see Fig. 3.1). However, there is a noticeable shift towards larger periods (and separations) among compact binary merger progenitors in the new simulations. This can be explained in connection with the eccentricity distribution of these systems. In the case of MD17 the eccentricity distribution is slightly skewed towards $e > 0.5$, which is very different from that of Sana et al. (2012) showing a strong preference for nearly circular orbits. As a result the periastron separation distributions in the new and old simulations are very similar. This showcases the fact that the pericentre separation $d_{\rm per}$ determines the evolutionary path of a binary with given component masses and decides whether or not it will form a compact binary merger. In the evolutionary channel involving a CE phase, only a fixed range of $d_{\rm per}$, that is independent of the choice of initial properties, results in the formation of CBM.

At $Z = Z_\odot$, where the formation of NS-NS dominates, the periastron separations are centred around $\sim 100\ R_\odot$. At $Z = 0.1\ Z_\odot$ BH-BH become dominant and shift the $d_{\rm per}$ distribution towards higher values of over $\sim 100\ R_\odot$. At this metallicity the distribution is clearly bimodal with peaks around $\sim 750\ R_\odot$ and $\sim 4000\ R_\odot$. This comes from the fact that at $Z \sim 0.1\ Z_\odot$ there are two relevant formation channels of merging BH-BH: the dominant channel (~70% of the systems), in which there is only one CE phase taking place after the first BH has already formed (the peak at $d_{\rm per} \sim 750\ R_\odot$); and another channel (~20% of the systems), in which there are two CE phases, one before each BH formation. The systems originating from the latter channel are those responsible for the second peak at $d_{\rm per} \sim 4000\ R_\odot$. These systems need to have larger initial $d_{\rm per}$ to prevent any RLOF during the HG evolutionary stage of the primary; we note that we do not allow for the CE phase from HG donors. Instead, the primary needs to initiate a RLOF and the CE phase later during the core helium burning phase. This channel becomes ineffective in our simulations for extremely low metallicities ($Z \lesssim 0.0005$), where stars do not increase their radii sufficiently after the HG stage. For that reason at $Z = 0.01\ Z_\odot$, the $d_{\rm per}$ distribution is no longer clearly bimodal. It is also slightly shifted towards smaller separations with respect to the distribution at $Z = 0.1\ Z_\odot$, again because of smaller sizes of the stars. Overall, the BH-BH formation channel involving two different CE phases is only relevant (i.e. at least 5% of all the BH-BH formed this way) at metallicity range $Z = 0.0005$ - $0.004$, contributing up to at most ~ 22% of the BH-BH formation at metallicity $Z \approx 0.0025$.

We note that the secondary peak in pericentre separations around $\sim 4000\ R_\odot$ at $Z = 0.1\ Z_\odot$ is

noticeably smaller in the simulations with the new initial distributions. This is because of the fact that, according to the multiplicity statistics of MD17, the number of inner binaries with massive primaries ($\gtrsim 30\ M_\odot$) having orbital periods of about $\log P\,(\mathrm{days}) \approx 3.5$ to 4.0 is smaller with respect to the old distributions of Sana et al. (2012); see Fig. 3.1.

**Mass ratios**: Merging NS-NS and BH-BH in our simulations originate almost exclusively from binaries with high mass ratios: $q_{\mathrm{NS-NS}} \gtrsim 0.6$ and $q_{\mathrm{BH-BH}} \gtrsim 0.5$, respectively (at $Z = 0.1\ Z_\odot$ the systems with initial $q < 0.5$ are all BH-NS). The initial mass ratio distribution of Sana et al. (2012) is flat in $q$. Meanwhile, the new results of MD17 include a distribution decreasing quickly with $q$ (see Fig. 3.3). This is reflected in the changes of the mass ratio distribution of CBM progenitors, which are slightly shifted towards $q \sim 0.5$ at $Z = 0.1\ Z_\odot$ and $Z = 0.01\ Z_\odot$ in the new simulations.

#### 3.4.1.2 PROGENITORS AND FORMATION OF BH-NS MERGERS

In Fig. 3.5, we show the birth properties of systems that evolve to form BH-NS mergers. This time, for simplicity, we focus only on the three most important parameters: primary mass, mass ratio, and periastron separation.

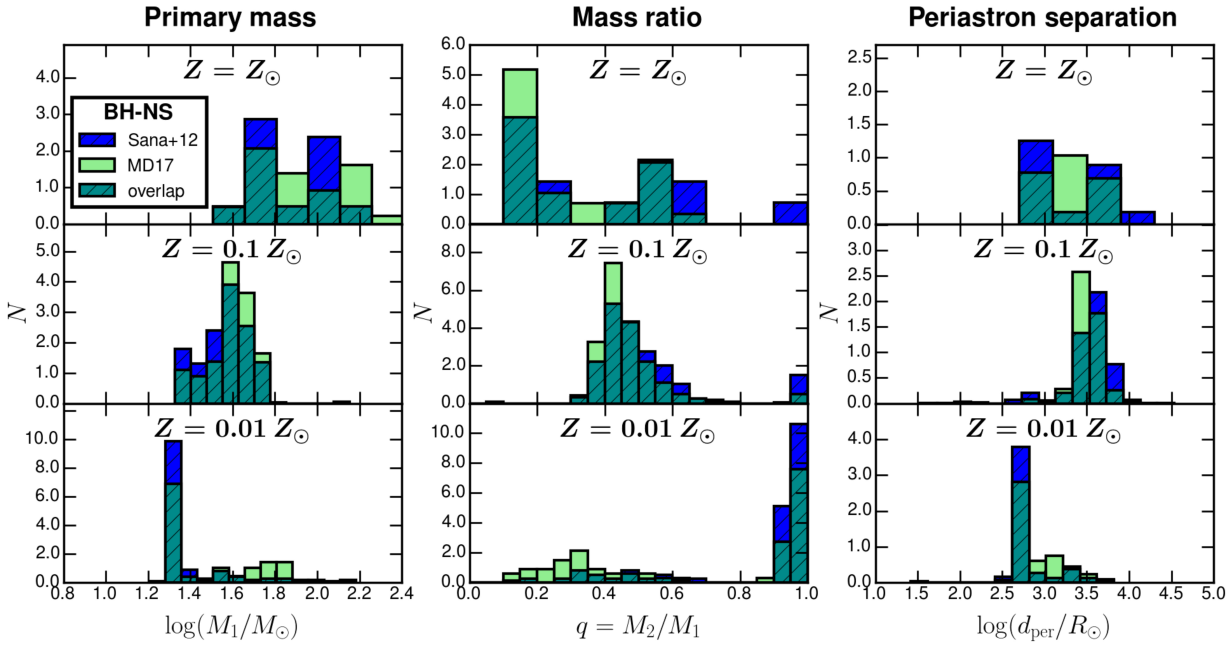


FIGURE 3.5: Birth distributions of initial ZAMS binary parameters of the progenitors of BH-NS mergers. The histograms are normalized to unity for an easier comparison. We note that the upper panels ($Z = Z_\odot$) are made based on a very small number of systems (< 20) that form in solar metallicity.

The formation of BH-NS mergers is very different in the three different metallicites shown: $Z_\odot$, 0.1 $Z_\odot$, and 0.01 $Z_\odot$. In the solar metallicity there are hardly any BH-NS systems formed. The histograms for $Z = Z_\odot$ are based on only around a dozen binaries, and, as a result, these histograms are not very meaningful. The reason why the BH-NS formation is so ineffective in

our simulations at solar metallicity is that the stars with $Z = Z_\odot$ already expand to their nearly maximum radius during the HG phase. This means that, in the majority of cases, the RLOF is initiated from the primary while it is a HG star. Because BH-NS systems typically originate from binaries with relatively small initial mass ratios of $q \lesssim 0.6$, then, according to the standard StarTrack criteria, such a mass transfer would most likely be flagged as unstable, leading to a CE phase from a HG donor. In this work, we decided to not follow the evolution of such systems (see Sect. 3.3.1 for more details).

At subsolar metallicity $Z = 0.1\ Z_\odot$ the formation of BH-NS mergers is much more effective, and the initial distributions are representative for the majority of BH-NS mergers formed across all of the 32 metallicites we compute. The primary expands much more after the HG phase than in the case of solar metallicity (Fig. 2 of Belczynski et al., 2010b) and, as a core-helium burning giant with a convective envelope, initiates an unstable RLOF and a CE phase. After the BH formation, the secondary eventually evolves off the MS, expands, and initiates a second CE episode. As a result, the binary is very close, the natal kick velocity gained by a newly formed NS does not disrupt the system and the binary merges within the Hubble time. We note that this is the exact same evolutionary route (i.e. two CE phases) that also operates in the case of BH-BH mergers in intermediate metallicites $Z = 0.0005$–$0.004$; see the paragraph on orbital periods in Section 3.4.1.1.

The distribution of primary masses at $Z = 0.1\ Z_\odot$ is slightly shifted towards lower values (peak at $\sim 40\ M_\odot$) with respect to the same distribution for BH-BH progenitors (peak at $\sim 50\ M_\odot$). The dominant range of mass ratios is between 0.3 and 0.6 (the contribution from $q > 0.95$ is described below). In the simulation with the updated initial distributions from MD17, the mass ratio distribution is slightly shifted towards smaller values. This, in turn, causes a small shift towards higher $M_1$ values, so that the secondary mass distribution (not explicitly shown here) stays roughly the same. The optimal periastron separation is about 3000 $R_\odot$ similar to the case of BH-BH mergers evolving through the same channel involving two CE phases; see the right peak in the periastron separation distribution for $Z = 0.1\ Z_\odot$ in Fig. 3.4. We note that in the case of new simulations with the initial conditions of MD17 there are fewer binaries with initial periods above $\log P$ (days) $\approx 3.5$ with respect to the old distributions of Sana et al. (2012), which is why the peak in the periastron separations is slightly shifted towards smaller values (also similarly to the BH-BH case at $Z = 0.1\ Z_\odot$).

In the case of very low metallicities (such as $Z = 0.01\ Z_\odot$) the main formation channel of BH-NS mergers described above is no longer efficient. This is because the lower the metallicity the more massive the BHs formed. For comparison, the least massive BHs in our simulations are of about 5.5 $M_\odot$ at $Z = 0.1\ Z_\odot$ and about 7.0 $M_\odot$ at metallicity $Z = 0.01\ Z_\odot$. As a result, at $Z = 0.01\ Z_\odot$, the mass ratio of the components at the point when the secondary expands and initiates a RLOF is not sufficiently high to cause an unstable mass transfer and a CE phase.

At $Z = 0.01\ Z_\odot$ another formation channel dominates, which is also present, yet not so important at higher metallicities. This channel involves binaries with a mass ratio close to unity ($q \gtrsim 0.9$), comprised of stars with masses that are close to the threshold between the NS and BH

formation ($M \sim 20\ M_{\odot}$). Because the binary components have similar masses, the secondary evolves transfer between the two core-helium burning stars, which reverses the mass ratio of the components. The primary eventually collapses to form a BH in a direct event with no mass eject and no natal kick. The 'Rapid' BH formation model of Fryer et al. (2012) predicts a 100% mass fallback for the least massive BH progenitors with CO core masses between 6 and 7 $M_{\odot}$; see their Eq. 16. The rejuvenated secondary continues to expand and initiates a second RLOF. This time the mass ratio is lower and the mass transfer becomes unstable, leading to a CE phase. The binary becomes close enough to survive the supernova and NS formation, and later becomes a BH-NS merger. This scenario requires a specific range of initial binary parameters and is much less effective than the more standard evolutionary route dominating the BH-NS formation at intermediate metallicities.

### 3.4.2 FORMATION OF COMPACT BINARY MERGERS ACROSS METALLICITY

In Fig. 3.6 we show the relation between the formation efficiency $X_{\rm CBM}$ ( $M_{\odot}^{-1}$) and metellicity for different types of CBM. We note that similar trends were obtained recently by Giacobbo & Mapelli (2018). It is evident that the formation of BH-BH mergers becomes most effective at low metallicities $Z \lesssim 0.1\ Z_{\odot}$. This is a well-known result (e.g. Belczynski et al., 2010b; Dominik et al., 2012; Eldridge & Stanway, 2016; Belczynski et al., 2016b; Mapelli et al., 2017; Giacobbo & Mapelli, 2018) for mainly two reasons: first, the fact that at lower metallicities the BH progenitors are relatively more massive and, therefore, more BHs are formed through direct collapse with zero natal kick, and second there is a higher chance for a CE event to be initiated by a core-helium burning donor, rather than by a HG donor, because of smaller radii of HG stars (Fig. 2 of Belczynski et al., 2010b).

According to stellar tracks from Hurley et al. (2000), at metallicities close to the solar $Z \simeq 0.02$, there is only a small range of separations at which a mass transfer from core-helium burning donors of $> 20\ M_{\odot}$ is initiated. Much more likely, the giant causes a RLOF earlier during its rapid HG evolution, in which case we choose to not allow for a CE evolution. Apart from strong stellar winds, this is what suppresses the formation of BH-BH and BH-NS compact binaries at metallicities close to the solar $Z \simeq 0.02$ in our simulations.

The formation efficiency of BH-NS mergers $X_{\rm BHNS}$ ( $M_{\odot}^{-1}$) does not increase in a similar fashion as $X_{\rm BHBH}$ ( $M_{\odot}^{-1}$) does at very low metallicities. There are two major factors at play. The main formation channel of BH-NS involving two CE phases becomes less effective in very low metallicities (Sect. 3.4.1.2). Additionally, natal kicks for NSs formed in core collapse are significant even at very low metallicities.

The formation of NS-NS mergers is much less metallicity-dependent, as was similarly found by Giacobbo & Mapelli (2018). It is slightly more efficient at metallicities similar to solar ($Z \simeq 0.02$) than it is at lower metallicities $Z \lesssim 0.005$. There is no one single reason for this behaviour, and it is most likely a combination of small effects such as different radii and different wind mass loss rates of stars with different metallicities. We thus consider this result to be much less robust than

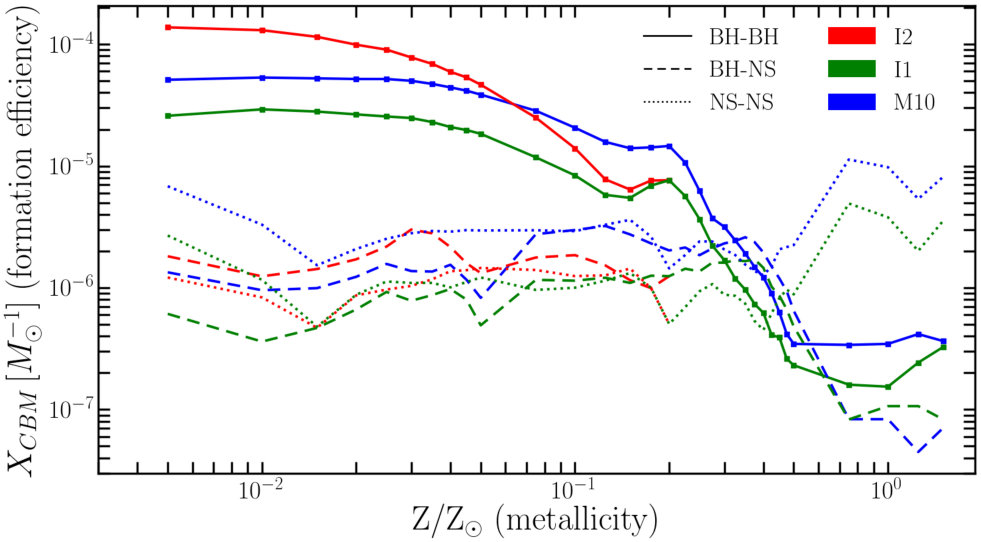


FIGURE 3.6: Formation efficiency (i.e. number of systems formed per unit of star-forming mass, $X_{\rm CBM}$ ( $M_\odot^{-1}$) = $N_{\rm CBM}/M_{\rm sim}$) of different types of CBM at different metallicities. We compute a grid of 32 different metallicities (indicated with filled squares at the BH-BH curves), ranging from 0.005 $Z_\odot$ to 1.5 $Z_\odot$. We indicate three different models: M10 in blue (initial distributions of Sana et al. 2012), I1 in green (initial distributions of MD17) and I2 in red (same as I1 but with a top-heavy IMF at low metallicities; see Eq. 3.2). We note that model I2 is only different from I1 at $Z < 0.004 = 0.2\ Z_\odot$.

the increasing formation efficiency of BH-BH mergers towards lower metallicity.

The updated initial binary distributions of MD17 (green lines, I1) result in smaller formation efficiencies of CBM across all the metallicities with respect to the previously adopted distributions of Sana et al. (2012, blue lines, M10). The only exception is the case of BH-NS mergers at $Z \approx Z_\odot$, where the formation efficiency $X_{\rm BHNS}$ ( $M_\odot^{-1}$) is at its lowest and there are few such systems in our simulations (fewer than 20). On the other hand, the inclusion of a top-heavy IMF for $Z < 0.004 = 0.2\ Z_\odot$ (red lines, I2) significantly increases the formation efficiency of BH-BH and BH-NS mergers by up to nearly an order of magnitude for the lowest $Z = 0.0001 = 0.005\ Z_\odot$ in the case of BH-BH. The NS-NS mergers originate from binaries with less massive primaries, which is why there is little change between models I1 and I2 in this case.

## 3.5 MERGER RATES AND LIGO/VIRGO PREDICTIONS

### 3.5.1 SOURCE-FRAME MERGER RATE DENSITY

In Fig. 3.7 we show the source frame BH-BH merger rate density (Gpc$^{-3}$ yr$^{-1}$) as a function of redshift for our three models. We note that the results for M10 are also corrected with respect to Belczynski et al. (2016a) for a typo in the calculation of simulation normalization, yielding a small net decrease of merger rates by a factor of 0.926 (Sect. 3.3.4).

The behaviour of the merger rate density relation with redshift (upper plot) closely resembles

the star formation history (Madau & Dickinson, 2014) and peaks around $z \approx 2$. This results from the fact that the distribution of merger delay times of close BH-BH binaries follows a power-law $\propto t_{\rm del}^{-1}$ (Dominik et al., 2012; Belczynski et al., 2016b), and most of the systems merge relatively shortly after their formation (a few hundred Myr). We note that the maximum of BH-BH merger rate density in model I2 is very slightly ($\Delta z \approx 0.2$) shifted towards smaller redshifts. This is because in this variation, at each redshift, we assume a different IMF based on the mean metallicity at that redshift, and consequently apply the adequate IMF-SFR correction factor (see Appendix 3.A for details). As a result, the location of the SFR maximum is slightly different.

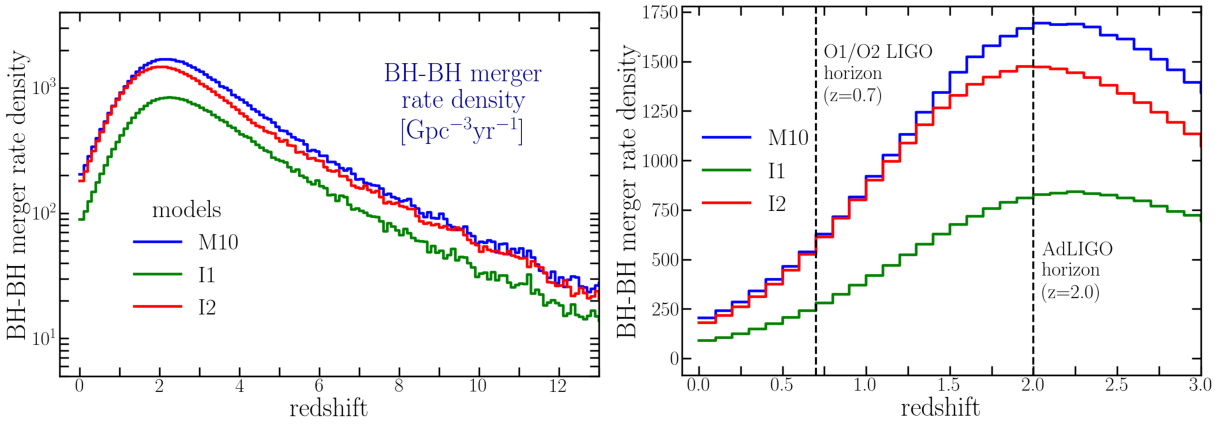


FIGURE 3.7: Source frame BH-BH merger rate density $Gpc^{-3}\ yr^{-1}$ as a function of redshift for our three models: M10 (binary distributions of Sana et al. (2012)), I1 (binary distributions of MD17) , and I2 (same as I1 but with a metallicity-dependent IMF). *Upper panel:* the peak around $z \approx 2$ in all the models corresponds to the maximum in the SFR (see text). *Lower panel:* the range of redshifts accessible with the current and future sensitivity of LIGO detectors. We indicate the horizon redshifts for observation of an optimally inclined BH-BH merger with a total mass of $\sim 80\ M_\odot$ (roughly the most massive systems in our simulations) for the sensitivities of O1 and O2 observing runs , and for the Advanced LIGO (AdLIGO). The detection distances for NS-NS mergers (Chen et al., 2017) were about $d_{\rm NSNS} = 70$ Mpc for O1 and O2 sensitivity (Abbott et al., 2018). The local BH-BH merger rate density (within $z < 0.02$) in our models are about 203 (M10), 89 (I1), and 181 Gpc$^{-3}$ yr$^{-1}$ (I2). The current limits imposed by the existing LIGO detections are 12–219 Gpc$^{-3}$ yr$^{-1}$ (Abbott et al., 2017b).

The lower panel shows the range of redshifts up to $z = 3.0$. We also indicate the horizon redshifts for observation of an optimally inclined BH-BH merger with a total mass of $\sim 80\ M_\odot$ (roughly the most massive systems in our simulations) for the sensitivities of O1 and O2 observing runs ($z_{\rm horizon} \approx 0.7$), and for the design sensitivity of Advanced LIGO ($z_{\rm horizon} \approx 2.0$; Abbott et al., 2018). For comparison, the detection distances for NS-NS mergers ($d_{\rm NSNS}$; i.e. the radius of a sphere with an equal volume to the peanut-shaped LIGO response function; see Chen et al., 2017) were about $d_{\rm NSNS} = 70$ Mpc for O1 and O2 sensitivity. The local BH-BH merger rate density (within $z < 0.02$) in our models are about 203 (M10), 89 (I1), and 181 Gpc$^{-3}$ yr$^{-1}$ (I2), which are all within the most up-to-date range determined by the existing LIGO detections (12–219 Gpc$^{-3}$ yr$^{-1}$ Abbott et al., 2017b).

TABLE 3.2: Merger rate densities and detection rates for the LIGO/Virgo O2 run sensitivity for three models: M10 (initial binary distributions from Sana et al. (2012)), I1 (updated distributions from MD17), and I2 (I1 plus top-heavy IMF for low metallicities from Marks et al. (2012)).

| Model merger type | Rate density[a] [Gpc$^{-3}$ yr$^{-1}$] | O2 rate[b] [yr$^{-1}$] | O2[c] [120 days] |
|---|---|---|---|
| M10 | | | |
| NS-NS | 68.2 | 0.09 | 0.03 |
| BH-NS | 26.7 | 0.42 | 0.22 |
| BH-BH | 203 | 111.6 | 36.7 |
| I1 | | | |
| NS-NS | 25.9 | 0.03 | 0.01 |
| BH-NS | 13.3 | 0.25 | 0.08 |
| BH-BH | 88.8 | 48.6 | 16 |
| I2 | | | |
| NS-NS | 24.4 | 0.03 | 0.01 |
| BH-NS | 16.5 | 0.38 | 0.13 |
| BH-BH | 181 | 122.7 | 40.3 |

NOTES:

[a] Local merger rate density within redshift $z < 0.1$.

[b] Detection rate for LIGO O2 observational run.

[c] Number of LIGO detections for effective observation time in O2.

### 3.5.2 LIGO/VIRGO DETECTION RATES

In Table 3.2, we summarize our predictions for the local (i.e. within $z < 0.02$) merger rate densities, detection rates ($R_{\rm det}\ yr^{-1}$) with the sensitivity of O1/O2 LIGO/Virgo observing runs, and corresponding numbers of detections assuming 120 days of coincident data acquisition. The inclusion of the updated initial MS binary distributions of MD17 (model I1) has led to a decrease in both the local BH-BH merger rate density and the detection rate during O2 by a factor of ~2.3 (with respect to model M10). The assumption of a metallicity-dependent IMF (model I2, see Eq. 3.2), on the other hand, causes an increase in the local BH-BH merger rate density by a factor of $\sim 2$, and an increase in the O2 detection rate by a larger factor of $\sim 2.5$ (with respect to model I1). The difference between these two factors arises from the fact that the top-heavy IMF for low metallicities assumed in I2 favours more massive BHs, which are easier to detect. We discuss the comparison of our results with LIGO/Virgo detection rates in Sect. 3.6.4.

### 3.5.3 METALLICITY DISTRIBUTION OF BH-BH PROGENITORS

In Fig. 3.8, we show the metallicity distributions of different types of CBM weighted by their detection rates with O1/O2 sensitivity. In the case of BH-BH mergers, the huge preference for very low metallicities ($Z \lesssim 0.001 = 0.05\ Z_\odot$) with respect to metallicities close to solar ($Z \gtrsim 0.01 = 0.5\ Z_\odot$) is already present when looking at the formation efficiencies across $Z$ alone (see Fig. 3.6). At that stage, which does not account for any cosmological calculations yet (i.e. SFR, cosmic metallicity distribution, BH-BH merger delay times), there are about 2 orders of magnitude more BH-BH mergers formed with low $Z \lesssim 0.001$ compared to $Z \sim Z_\odot$ (solely due to binary evolution effects). Notably, this difference grows much higher in the detector frame, with the values of $\mathrm{d}R_{\mathrm{det}}/\mathrm{d}Z$ being about 4 order of magnitude larger for $Z \lesssim 0.001$ than for $Z \sim Z_\odot$. This is a combination of two effects. First, at low metallicities BHs are born more massive and their mergers are easier to detect with the LIGO/Virgo sensitivity. Second, in our approach to population synthesis on cosmological scales (Sect. 3.3.2) the metallicity distribution of stars forming at redshifts around the maximum of the cosmic SFR at $z \approx 2$, from which most of the BH-BH merger progenitors originates (see Fig. 2 of B16), is centred at $Z < 0.1\ Z_\odot$ (see Fig. 6 of Extended Data of B16).

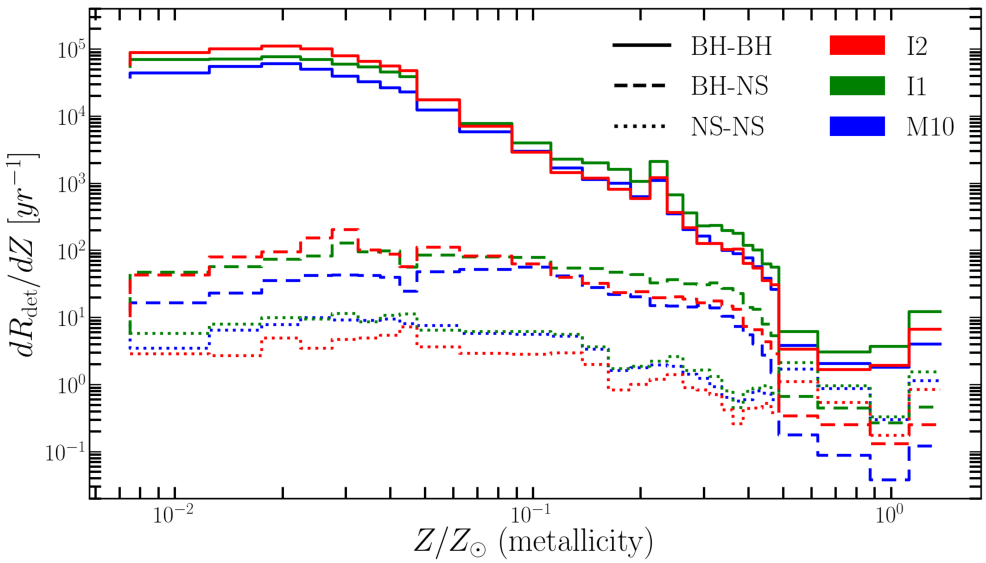


FIGURE 3.8: Detector-frame distribution of metallicities of BH-BH, BH-NS, and NS-NS merger progenitors. More than 90% of BH-BH merger detections in all our models are systems formed with metallicites lower than 10% of the solar metallicity, i.e. $Z < 0.1\ Z_\odot$. Such a strong dependence of compact binary merger formation with metallicity (see also Fig. 3.6), especially in the case of BH-BH systems, indicates the significance of SFRs at different metallicites across the Universe for the compact binary merger rates (see discussion in Sect. 3.6.3).

## 3.6 Discussion

### 3.6.1 Understanding the impact of the new initial distributions

Within the classical binary evolution scenario, our predictions for the merger rates of double compact objects based on the updated initial MS binary parameters from MD17 are $\sim 2-2.5$ times smaller than the results previously obtained by dMB15 and B16 from the distributions of Sana et al. (2012). This can be explained by looking at the differences between the two distributions within the areas of the parameter space that are most relevant for the formation of double compact object mergers. Let us first take a look at BH-BH and NS-NS progenitors.

(i) In agreement with dMB15, we find that the majority of BH-BH and NS-NS mergers originate from binaries with initial periods within $\log P$ (days) = 2−4. The fraction of primaries residing in such systems is about $F_{\log P=2-4;\mathrm{bin}} = 28\%$ in the case of Sana et al. (2012) distributions. Meanwhile, this value is higher by about $\sim 1.35$ in the case of statistics obtained by MD17 (Fig. 3.1): i.e. $F_{\log P=2-4;\mathrm{bin}} = 37\%$ for $M_1 = 8\ M_\odot$ primaries, and $F_{\log P=2-4;\mathrm{bin}} = 40\%$ for $M_1 = 30\ M_\odot$ primaries (regimes for NS-NS and BH-BH progenitors, respectively).

(ii) The eccentricity distribution based on the Sana et al. (2012) sample is skewed towards lower values with $<e> = 0.3$ compared to the statistics reported by MD17 with $<e> = 0.6$ in the case of massive binaries (Fig. 3.2). The progenitors of CBM derive from binaries with periastron separations $\log d_{\mathrm{per}}$ ( $R_\odot$) = 2−3.5, depending slightly on metallicity and the exact formation channel. By increasing the average initial eccentricity from $<e> = 0.3$ to 0.6, then the average orbital separation of the progenitors increases by a factor of (1−0.3)/(1−0.6) = 1.75. This corresponds to a shift in logarithmic orbital period of $\Delta \log P \approx 0.2$. Considering the progenitors derive from a broad parameter space of orbital periods $\log P$ (days) = 2−4, a slight shift of $\Delta \log P \approx 0.2$ due to the updated eccentricity distribution does not affect the predicted rates of compact object mergers.

(iii) Similar to dMB15, we find that nearly all BH-BH and NS-NS mergers derive from initial MS binaries with mass ratios $q = 0.5-1.0$. According to the old mass-ratio distribution from Sana et al. (2012), ≈55% of early-type binaries have mass ratios across this interval. According to the updated period-dependent mass-ratio distribution of MD17, however, only (17-28)% of massive binaries with $\log P$ (days) = 2−4 have mass ratios $q = 0.5-1.0$, which results in about ∼2.0−3.2 times fewer potential BH-BH and NS-NS merger progenitors.

Altogether, the new mass ratio distribution that is shifted towards smaller values with respect to the old distribution (iii) is the most significant update in the context of BH-BH and NS-NS mergers, and the differences between period distributions are of secondary importance (i). Based on the estimates presented above, we could expect that there should be roughly between 1.5 and 2.4 fewer BH-BH and NS-NS mergers in the updated simulations. This explains the results of our computations (see tables 3.1 and 3.2).

In the case of BH-NS mergers, the binary parameters of their progenitors depend strongly on metallicity (Fig. 3.5). Around solar metallicity, there are few to no BH-NS systems formed and our sample is not statistically significant. At subsolar metallicities of $\sim 0.1\ Z_\odot$, the main

formation channel involves two CE phases, and this channel dominates when summed across all metallicities. It requires the initial mass ratios between 0.3 and 0.6 (peaking around 0.4) and, more importantly, pericentre separations of $\log d_{\rm per}$ ( $R_\odot$) = 3.2−4, preferably over 3.5. The updated initial distributions predict fewer massive binaries this wide. Additionally, in most cases the NS is formed from a star with mass at the higher end of the mass range of NS progenitors ($15 \lesssim M_2/\ M_\odot \lesssim 22$), which helps to produce a high enough mass ratio at a BH-MS binary stage, so that a dynamically unstable mass transfer occurs and a CE phase is triggered. The shift towards smaller mass ratios in the updated distributions causes a corresponding shift towards slightly more massive primaries. This additionally decreases the BH-NS formation efficiency due to a declining slope of the IMF.

At very low $Z \sim 0.01\ Z_\odot$, the dominant formation channel involves binaries with components of initially similar masses that evolve into double-giant systems and experience a stable mass transfer instead of the first CE (Sect. 3.4.1.2). The requirement of $q > 0.9$ means that there are about three times fewer potential progenitors for this channel in the updated distributions. With all the metallicities combined, all the factors described above result in the merger rate of BH-NS systems being about two times smaller in the new simulations (Table 3.2).

### 3.6.2 SMALL IMPACT OF A TOP-HEAVY IMF

The uncertainty in the IMF is often considered to have a substantial impact on the compact binary merger rates, by a factor of a few (dMB15) up to an order of magnitude (see Fig. 20 of Kruckow et al., 2018). One could thus expect that the top-heavy IMF for low metallicities ($Z < 0.2\ Z_\odot$; see Eqn. 3.2) we implemented in model I2 would result in a significant increase of BH-BH merger rates. According to Fig. 3.8, the vast majority of BH-BH mergers detectable with LIGO/Virgo were formed in $Z < 0.1\ Z_\odot$ metallicity environments. In model I2, the IMF power-law exponent for massive stars is $\alpha_3 \approx 2.07$ for $Z = 0.1\ Z_\odot$ decreasing down to as low as $\alpha_3 \approx 1.31$ for $Z = 0.01\ Z_\odot$. For a fixed amount of stellar mass formed (i.e. fixed SFR) and with respect to the standard value $\alpha_3 = 2.3$ as in models M10 and I1, this would correspond to an increase in the number of primaries within $M_1 = 45{-}55\ M_\odot$ (highest bin in the primary mass distribution of BH-BH progenitors, Fig. 3.4) by a factor of about $\sim 2.2$ at $Z = 0.1\ Z_\odot$ and $\sim 5$ at $Z = 0.01\ Z_\odot$. Meanwhile, the merger rate density of BH-BH in model I2 (with a top-heavy IMF) is higher than in model I1 by only a factor of $\sim 2$.

This showcases the significance of keeping the consistency between an adopted cosmic SFR and an assumed IMF. Because the cosmic SFR is measured based on UV observations (Madau & Dickinson, 2014), we normalize our simulations in such a way that the total amount of UV light at 1500 stays roughly constant, irrespective of the assumed IMF (see Appendix 3.A). As most of the UV light is produced by massive stars, a top-heavy IMF is characterized by a higher UV luminosity per unit of stellar mass formed $\mathcal{U}$ ( $M_\odot^{-1}$) and must result in a rescaling of the SFR to a smaller value. A smaller SFR means fewer stars formed, which counteracts the fact that with a

top-heavy IMF a higher fraction of these stars are massive. A similar but inverted argument could be made for a top-light IMF (i.e. $\alpha_3 > 2.3$). Thus, the total number of massive stars formed stays roughly constant irrespective of the IMF variations, as it is constrained by the UV observations.

We show this quantitatively in Fig. 3.9, where, as a function of $\alpha_3$, we plot the relative number $\mathcal{R}(\alpha_3)$ of stars formed in a given mass bin $M_{\rm low}$-$M_{\rm high}$ (e.g. between 8 and 13 $M_\odot$, and so on) defined as

$$\mathcal{R}(\alpha_3) = \frac{M_{\rm total;1}(\alpha_3) \times \int_{M_{\rm low}}^{M_{\rm high}} \xi(\alpha_3, M) dM}{M_{\rm total;2}(\alpha_3 = 2.3) \times \int_{M_{\rm low}}^{M_{\rm high}} \xi(\alpha_3 = 2.3, M) dM}, \tag{3.6}$$

where $\xi(\alpha_3, M)$ is a Kroupa-like IMF in the form given by Eq. 3.1 for which we vary the high-mass slope $\alpha_3$, and $M_{\rm total;1}$ and $M_{\rm total;2}$ are the total amounts of stellar mass formed in models with different IMFs. The IMFs are normalized to unity, i.e. $\int_{0.08}^{150} \xi(\alpha_3, M) dM = 1.0$ for any slope $\alpha_3$. The upper panel represents simulations normalized to a fixed amount of stellar mass formed, irrespective of the IMF (the usually made assumption), so $M_{\rm total;1} = M_{\rm total;2}$. The lower panel, in turn, assumes a fixed UV luminosity of a star-forming population, so that $M_{\rm total;1} \times \mathcal{U}(\alpha_3) = M_{\rm total;2} \times \mathcal{U}(\alpha_3 = 2.3)$. The amount of UV light per unit of star-forming mass $\mathcal{U}$ ( $M_\odot^{-1}$) is inversely proportional to $\mathcal{K}$ coefficients in Eq. 3.7 and Table 3.3.

We note that although the relative number of primaries does not change by more than a factor of $\sim 2$ in any of the mass ranges and IMFs shown, the ratio of progenitors of massive BH-BH to NS-NS mergers changes more significantly. [4]

### 3.6.3 Population synthesis on cosmological scales

The discovery of GW150914 revealed the existence of stellar BHs with masses of $30-40\ M_\odot$ (Abbott et al., 2016c). Black holes this massive are only expected to form from low-metallicity stars $Z/\ Z_\odot \lesssim 0.3$ (Belczynski et al., 2010a), and this conclusion is strengthened by a recent update to Wolf-Rayet star winds (Vink, 2017). Additionally, Fig. 3.6 shows that the formation efficiency of BH-BH mergers is very strongly dependent on metallicity. For that reason, predictions for the rates of such events are sensitive to the applied distribution of metallicity of star formation throughout the Universe and they *cannot* be made by simply extrapolating results for a Milky Way-like galaxy, as still done by some authors.

We have adopted the mean metallicity-redshift relation from the chemical evolution model of Madau & Dickinson (2014, see Eqn. 3.4) with the level increased by 0.5 dex and with a Gaussian spread of $\sigma = 0.5$ dex, and used this relation to weight the contributions from different metallicities to the SFR at different redshifts. This cosmological information, combined with the LIGO/Virgo sensitivity, allowed us to transform our simulated CBM into detector-frame predictions.

[4]The simplified way we correct the SFR explains why the BH-BH merger rate increases by a factor 2 between models I1 and I2 while none of the curves in lower panel of Fig. 3.9 actually reaches the value of 2. In practice, at each redshift bin we assume that the amount of UV light per unit of star-forming mass is such as for the median metallicity (and IMF corresponding to it) at that redshift. However, given the uncertainty of the contributions from different metallicities to the cosmic SFR, this simplification has no meaningful impact on the results.

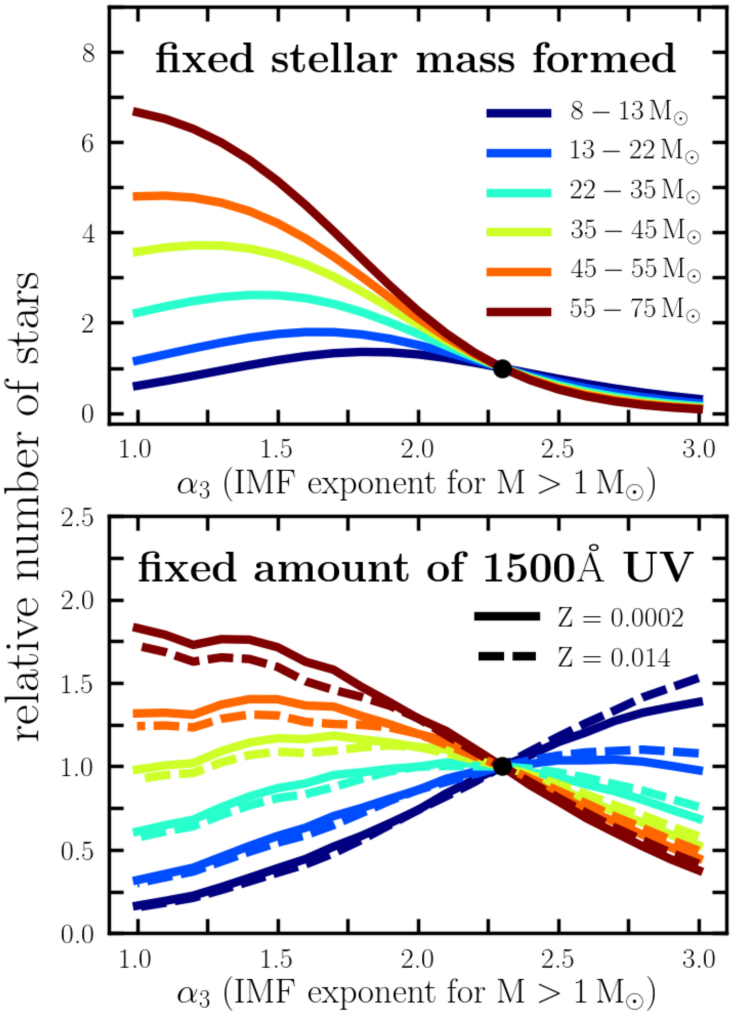


FIGURE 3.9: Relative numbers of massive stars $\mathcal{R}$ formed within multiple initial mass ranges as a function of power-law exponent $\alpha_3$ for the high-mass IMF component ($M > 1\,M_\odot$). See eq. 3.6 for the exact definition of $\mathcal{R}$. *Upper panel*: the same SFR, irrespective of the IMF changes. The number of stars is thus calculated with respect to a fixed stellar mass formed. *Lower panel*: SFR corrected for the IMF changes (see Eqn. 3.5). The number of stars is thus calculated with respect to a fixed amount of UV radiation at 1500 wavelength that is constrained by the observations (Madau & Dickinson, 2014).

However, the mean metallicity of the Universe (defined as the total mass of heavy elements ever produced per mass of baryons in the Universe) in general *does not* equal the mean metallicity of star formation at a given redshift. This simplification is a caveat of our model to keep in mind. The mean metallicity at which star formation takes place is likely higher, since the highest SFRs are revealed by massive galaxies (Lara-López et al., 2013), which are also relatively metal rich (e.g. Tremonti et al., 2004). Low-metallicity star formation in the local Universe, on the other hand, occurs mostly in low-mass dwarf galaxies (Andrews & Martini, 2013), which have relatively little star formation (Boogaard et al., 2018). For that reason, we are likely somewhat overestimating the current SFR of metal-poor massive stars. For example, according to our model, about 18% of massive stars that recently formed in the local Universe (z = 0) have $Z < 0.1\ Z_\odot$. Observations of nearby dwarf and spiral galaxies suggest only a few percent, perhaps at most 10%, of massive stars form locally at such low metallicity (see App. 3.B for a detailed calculation). While this signifies the existence of a problem, the issue is more complicated and requires a coherent and observationally based model of cosmic star formation at different metallicities and across different redshifts (Chruslinska et al. in prep.).

A different approach to population synthesis on a cosmological scale is to distribute simulated

systems over individual galaxies. This could be obtained in a semi-analytical manner by applying a galaxy mass function (Elbert et al., 2018) or fits to galaxy trees from cosmological simulations (Lamberts et al., 2016), and combining these with observationally inferred galaxy scaling relations for SFRs and metallicity distributions (eg. Behroozi et al., 2013). Alternatively, results from cosmological simulations could be applied directly to obtain similar information about star formation in individual galaxies (Schneider et al., 2017; Mapelli et al., 2017). Interestingly, Mapelli et al. (2017) predict that the distribution of metallicity of BH-BH merger progenitors peaks at around $\sim 0.1\ Z_{\odot}$ and declines towards lower $Z$, which conflicts with our Fig. 3.8. The most likely explanation of this discrepancy is that we are overestimating the contribution from very low metallicities at close redshifts of star formation. The majority of the low-metallicity content of the recent Universe is locked in dwarf galaxies with little star formation, for which our simplification that the mean metallicity of the Universe $\approx$ mean metallicity of star formation is likely less accurate. This interpretation also agrees with the fact that Mapelli et al. (2017) did not find the clearly bimodal distribution of massive BH-BH merger birth redshifts as shown in the case of our simulations in Fig. 2 of B16, but rather only the single maximum around the peak of cosmic star formation at $z \approx 2$. However, even if we were overpredicting the star formation in low metallicities $Z < 0.1\ Z_{\odot}$ at redshifts $z < 2$ to the point at which we would have to discard all our mergers formed in these conditions, this would still not affect our predictions for the merger rates by more than a factor of 2.

Although making predictions for CBM based on cosmological simulations as carried out by Schneider et al. (2017) or Mapelli et al. (2017) (or, in a simplified way, also by Belczynski et al. 2018) may be burdened with additional biases, this ultimately seems to be the superior approach that hopefully will allow us to confront models with various galactic properties in the case of mergers with identified hosts (such as GW170817, Abbott et al., 2017a).

Finally, we wish to highlight that the small impact of IMF variations on merger rates (3.6.2) is a general result that should also appear in the predictions based on cosmological simulations. Even though such simulations often provide SFR values as their output, changing the assumptions on the massive-star IMF without renormalizing the SFR make their results inconsistent with star formation tracers such as UV observations.

### 3.6.4 Comparison with LIGO/Virgo detection rates and other studies

We show the merger ($\mathrm{Gpc^{-3}yr^{-1}}$) and detection rates ($\mathrm{yr^{-1}}$) from our simulations in Table 3.3. While our models perform relatively well in retrieving the BH-BH merger rate as constrained by the LIGO/Virgo observations $R_{\mathrm{BHBH}}$ =12−213 $\mathrm{Gpc^{-3}\ yr^{-1}}$ (Abbott et al., 2017b), they underpredict the rate of NS-NS mergers that was inferred after the recent detection of GW170817: $R_{\mathrm{NSNS}} = 1540^{+3200}_{-1220}\ \mathrm{Gpc^{-3}\ yr^{-1}}$ (Abbott et al., 2017a) [5]. Recently, Chruslinska et al. (2018) analysed

[5]We note that because only one NS-NS merger has been detected so far, the lower limit on the inferred merger rate is rather poorly defined.

NS-NS merger rates within a large suite of STARTRACK models, varying multiple binary evolution assumptions, and found that it is, in fact, very difficult to obtain $\mathcal{R}_{\rm NSNS}$ consistent with the LIGO/Virgo constraints. The only three models marginally consistent with the reported NS-NS merger rates, which have $\mathcal{R}_{\rm NSNS}$ values of about 380, 450, and 630 Gpc$^{-3}$ yr$^{-1}$, overpredict the merger rate of double BHs, resulting in $\mathcal{R}_{\rm BHBH}$ of about 1070, 310, and 700 Gpc$^{-3}$ yr$^{-1}$, respectively. This discrepancy could perhaps be a hint that the stability criteria for mass transfer in Roche-lobe overflowing high-mass X-ray binaries were different in the cases of BH and NS accretors, resulting in a stable mass transfer (i.e. avoiding CE) for a large space of binary parameters in the case of BH accretors (see also Pavlovskii et al., 2017).

Similarly, using code C$_{\rm OM}$B$_{\rm IN}$E, Kruckow et al. (2018) obtained NS-NS merger rates of around 10 Gpc$^{-3}$yr$^{-1}$ in their default model; this is well below the LIGO/Virgo limits. Their most optimistic model yields a value of 159 Gpc$^{-3}$yr$^{-1}$, which could be increased further up to 400 Gpc$^{-3}$yr$^{-1}$ to be marginally consistent with the observational constraints if natal kick velocities were reduced by half. Contrary to Chruslinska et al. (2018), the optimistic model of Kruckow et al. (2018) does not overpredict the BH-BH merger rates. However, it was only calculated for a single metallicity value Z = 0.0088 = 0.44 $Z_\odot$ above the low-metallicity regime at which the BH-BH formation is the highest.

Interestingly, using code MOBSA combined with the results of Illustris simulations (Nelson et al., 2015), Mapelli & Giacobbo (2018) were able to obtain both NS-NS and BH-BH simultaneously consistent with the LIGO/Virgo constraints. It should be noted that they did have to assume both very low natal kicks ($\sigma \simeq 15$ km s$^{-1}$) for all of their core-collapse supernovae and a rather high efficiency of the CE ejection ($\alpha_{\rm CE} = 5$), which is a value that usually calls for some additional process aiding the CE ejection. The former assumption can to some extent be justified by the fact that NS progenitors in binary systems tend to get their envelopes stripped in mass transfer episodes, which leads to less-energetic supernovae and smaller mass ejections, and possibly natal kicks as small as $\sim 15$ km s$^{-1}$, although likely only in the case of ultra-stripped stars that also lose their helium envelope to a compact object accretor (Tauris et al., 2015). As not all NS progenitors in NS-NS systems are expected to be ultra-stripped (especially those that form the first NS), a single $\sigma \simeq 15$ km s$^{-1}$ value for all the core collapse supernovae may be an oversimplification (for comparison, see the model of Kruckow et al., 2018). Observationally, some Galactic close-orbit NS-NS systems show evidence of rather large natal kicks of over $> 100$ km s$^{-1}$, while others require small kick velocities $< 50$ km s$^{-1}$ (see Sect. 6.4 of Tauris et al., 2017).

## 3.7 SUMMARY

Observational studies have long hinted at probable correlations between the initial binary parameters primary mass ($M_1$), mass ratio ($q$), orbital period ($P$), and eccentricity ($e$) (Abt et al., 1990; Duchêne & Kraus, 2013), but hitherto the selection biases have been too large to accurately quantify the intrinsic relations. A recently published paper, Moe & Di Stefano (2017), analysed results from more than 20 massive star surveys and, for the first time, obtained a joint probability density

function $f(M_1, q, P, e)$ for the initial ZAMS binary parameters (Sect. 3.2). We implement this result and analyse its impact on the predictions of merger rates of double compact object detectable with the LIGO/Virgo interferometers that originate from the isolated evolution scenario involving a CE phase. Using the StarTrack rapid binary evolution code (Sect. 3.3.1, Belczynski et al., 2002, 2008a), we evolve a large population of massive MS binaries across a range of 32 metallicities from 0.005 $Z_\odot$ to 1.5 $Z_\odot$ with their initial parameters drawn from the interrelated distribution of Moe & Di Stefano (2017). We distribute our systems at cosmological scales according to an observationally inferred cosmic SFR and a mean metallicity-redshift relation obtained within a chemical evolution model by Madau & Dickinson (2014, see Sect. 3.3.2). We compare our results to those obtained by de Mink & Belczynski (2015b) and Belczynski et al. (2016b) who performed similar simulations but with the non-correlated initial binary distributions from Sana et al. (2012). Additionally, we discuss the level of uncertainty of compact binary merger rate predictions associated with possible variations of the massive star IMF. We make an in-depth study of one such variation, according to which the IMF becomes more top heavy (i.e. flatter power-law exponent for massive stars) the lower the metallicity of star formation (Marks et al., 2012, see Sects. 3.1 and 3.2.2). We make sure that along with the changes of the IMF, the amount of far-UV light at 1500 wavelength (based on which the cosmic SFR is measured Madau & Dickinson, 2014) stays the same.

We note that our merger rates are in good agreement with the LIGO/Virgo constraints in the case of BH-BH systems, but they are strikingly too small when it comes to NS-NS mergers (Sect. 3.5.2, see also Chruslinska et al., 2018). However, we predict that our results of the relative impact of initial distributions and IMF variations will hold in the general case of isolated evolution channels involving a CE phase, regardless of the absolute numbers of mergers obtained.

We arrive at the following conclusions:

(a) The introduction of the updated initial ZAMS binary distributions from MD17 (model I1) decreases the formation efficiency and, consequently, merger and detection rates of all types of CBM by a factor of about 2.1 - 2.6 with respect to the old simulations adopting Sana et al. (2012) distributions (model M10); see Sect. 3.5. This is a very small change in comparison to uncertainties associated with the binary evolution (e.g. Eldridge & Stanway, 2016; Mapelli et al., 2017; Stevenson et al., 2017b; Chruslinska et al., 2018; Kruckow et al., 2018).

In the case of BH-BH and NS-NS mergers, the major factor in play is the difference in the initial mass ratio distributions. Sana et al. (2012) obtaiedn their binary statistics based on the spectroscopic measurement of massive O-type stars. For that reason their sample is limited to $\log P$ (days) $< 3.5$ (spectroscopically detectable binaries) and dominated by very short-period orbits with P < 20 days, to which they fit a flat mass ratio distribution. However, MD17 have shown that wider binaries are weighted towards considerably smaller mass ratios (Fig. 3.3). According to their updated distributions, across intermediate periods $\log P$ (days) = 2 - 4, there are $\sim 2.5$ fewer systems with $q > 0.5$, which is the range of orbital periods and mass ratios at which BH-BH and NS-NS mergers are formed (see Fig. 3.4).

Of secondary importance is the difference between the orbital period distributions (up to 40%

more system in the orbital period range log $P$ (days) = 2 - 4, depending on metallicity), whereas the changes in the eccentricity statistics have negligible influence on merger rates even though an increase from <e>= 0.3 to <e>= 0.6 may seem significant at first.

(b) The introduction of a top-heavy IMF at low metallicities (Sect. 3.2.2, Marks et al., 2012) results in a small increase of BH-BH merger rates by only a factor of $\sim 2$, and even less significant differences in the case of BH-NS and NS-NS mergers (Table 3.2). This might seem surprising because for the values of power-law exponent $\alpha_3$ for the IMF of massive stars of $\alpha_3 \approx 1.8$ at $Z = 0.05\ Z_\odot$ and even $\alpha_3 \approx 1.3$ at $Z = 0.01\ Z_\odot$, we could expect an increase in the number of massive BH-BH progenitors (for a fixed stellar mass formed) by a factor of $\sim$4$-$5 with respect to the standard value $\alpha_3 = 2.3$. Interestingly, recent spectroscopic observations of 247 massive stars in the 30 Doradus star formation region reveal an IMF slope of $\alpha_3 = 1.90^{+0.37}_{-0.26}$ in the range $15 - 200\ M_\odot$ (Schneider et al., 2018). However, because the formation of CBM likely occurs at cosmological scales (e.g. Dominik et al., 2013; Mapelli et al., 2017), we argue that the simulations should be normalized to a fixed amount of UV light at wavelength 1500 (used as an SFR indicator) produced by a star-forming population. A more top-heavy IMF produces more UV light per unit of stellar mass, which forces a rescale of the cosmic SFR to a lower value and prevents the BH-BH merger rates from increasing by more than a factor of $\sim 2$. This is true even for very top-heavy IMFs with $\alpha_3$ value as low as 1.0 (Fig. 3.9). We conclude that the previously reported uncertainty by a factor of 6 up and down of the merger rate predictions due to possible variations in the IMF (de Mink & Belczynski, 2015b) is, in fact, not more significant than a factor of $\sim$2.

**ACKNOWLEDGEMENTS**

We thank the anonymous referee for very useful remarks. JK gratefully acknowledges comments and pointers from JJ Eldridge, Michela Mapelli, and Gijs Nelemans. KB acknowledges support from the Polish National Science Center (NCN) grants: Sonata Bis 2 DEC-2012/07/E/ST9/01360, Meastro 2015/18/A/ST9/00746, and Opus (2015/19/B/ST9/01099). MM acknowledges financial support from NASA's Einstein Postdoctoral Fellowship programme PF5-160139. DEH was partially supported by NSF grant PHY-1708081. They were also supported by the Kavli Institute for Cosmological Physics at the University of Chicago through an endowment from the Kavli Foundation.

## 3.A CONVERSION COEFFICIENTS BETWEEN SFR AND IMFS

As we describe in Sect. 3.3.2 , any cosmic SFR is associated with an assumed IMF and it is inconsistent to use it in combination with a different IMF. We therefore introduce a conversion factor $\mathcal{K}_{\rm IMF}$ to correct the cosmic SFR of Madau & Dickinson (2014) (Eqn. 3.3) obtained for the Salpeter IMF (Salpeter, 1955) for the purpose of combining it with a more realistic Kroupa-like IMF, i.e.

$$\mathrm{SFR}_{\rm IMF}(z) = \mathcal{K}_{\rm IMF} \times \mathrm{SFR}_{\rm Salpeter}(z) \tag{3.7}$$

where $\mathrm{SFR}_{\mathrm{Salpeter}}(z)$ is given by Eqn. 3.3. We calculate $\mathcal{K}_{\mathrm{IMF}}$ as a relative strength of the 1500 line in the UV spectrum of a star-forming region with SFR = 1.0 $M_\odot\, yr^{-1}$ and the Salpeter IMF with respect to the same SFR but with another given IMF.

In order to compute the UV spectra for different IMFs, we utilize the Starburst99 code, designed to model spectrophotometric properties of star-forming galaxies (Leitherer et al., 1999; Vázquez & Leitherer, 2005; Leitherer et al., 2014). We configurate Starburst99 to use the newest evolutionary tracks published by the Geneva group: for solar (Z = 0.014 Ekström et al., 2012) and subsolar metallicity (Z = 0.002 Georgy et al., 2013), which cover the mass range $M/\,M_\odot \in [0.8, 120]$. In this paper our population synthesis simulations covered a much larger grid of 32 different metallicities from Z = 0.0001 up to Z = 0.03. However, the differences in UV-to-SFR conversion factors for different metallicities are not very significant (see Fig. 3 of Madau & Dickinson, 2014). Thus, we apply $\mathcal{K}_{\mathrm{IMF}}$ calculated for Z = 0.014 Geneva stellar tracks in the case of the StarTrack models with Z ≥ 0.006, and apply $\mathcal{K}_{\mathrm{IMF}}$ calculated for Z = 0.002 to all the other StarTrack models for Z < 0.006. The upper mass limit 120 $M_\odot$ is a limitation of all the stellar tracks implemented in Starburst99. We calculate the UV spectra up to $10^8$ yr after the beginning of a constant star formation. By that time the 1500 line is expected to have reached its asymptotic strength already (see Fig. 2 of Madau & Dickinson, 2014).

In Table 3.3 we list the values of $\mathcal{K}_{\mathrm{IMF}}$ computed at solar and subsolar metallicity for multiple power-law exponents of the high-mass end of a Kroupa-like IMF. Even if the high-mass end of the IMF is significantly top heavy (e.g. $\alpha_3 = 1.0$), we find there are only ∼ 30% more stars with $M_1$=45 - 55 $M_\odot$ to match the same 1500 emission strength.

We wish to mention that the Starburst99 code does not incorporate the evolution of binaries. Interacting binaries, for instance, are expected to affect the emission properties of a star-forming population such as its ionizing flux or a UV luminosity (e.g. Stanway et al., 2016). Depending on metallicity and for a Kroupa-like IMF truncated at 100 $M_\odot$, Eldridge et al. (2017) have calculated that binary interactions increase the amount of radiation $\nu L_\nu$ at 1500 from a star-forming population by a factor of $\sim 1.2 - 1.25$ relative to a corresponding population of single stars (see their Table 4). We expect that the values of our conversion coefficients $\mathcal{K}$ in Table 3.3 could differ by a similar factor if the effect of binaries on spectral properties was taken into account.

## 3.B Local star formation rate at metallicities $Z < 0.1\ Z_\odot$

We use observational results to do a rough estimate of the local (i.e. z ∼ 0) SFR density at metallicities below 0.1 $Z_\odot$. At close redshifts, star formation at $Z < 0.1\ Z_\odot$ occurs in galaxies with mass < $10^7$ $M_\odot$ (Andrews & Martini, 2013). The local number density of star-forming galaxies with masses between $10^6$ and $10^7$ $M_\odot$ can be estimated as $10^{-0.8}$ $\mathrm{Mpc}^{-3}$ (from extrapolating the blue fit in Fig. 15 of Baldry et al., 2012), while their average SFR is measured to be around $10^{-2.5}$ $\mathrm{M_\odot\,yr^{-1}}$ (Boogaard et al., 2018). This implies a local SFR density at $Z < 0.1\ Z_\odot$ of $10^{-3.3}$ $\mathrm{M_\odot\,Mpc^{-3}\,yr^{-1}}$, which constitutes about ∼ 3% of the total SFR density at redshift z = 0 (from Eqn. 3.3). While the above estimate is highly uncertain, it seems unlikely that this fraction

TABLE 3.3: Conversion coefficients $\mathcal{K}_{\rm IMF}$ for a cosmic SFR between the Salpeter and different Kroupa-like IMFs. In the second column, we list metallicities corresponding to the IMF slopes $\alpha_3$ from the first column, assuming the IMF-metallicity relation given by Eq. 3.2 after Marks et al. (2012).

| IMF $\xi(M)$ | metallicity Z($\alpha_3$) inversed Eq.3.2 | $\mathcal{K}_{\rm IMF}$ Z = 0.014 | $\mathcal{K}_{\rm IMF}$ Z =0.002 | relative #stars 45 - 55 $M_\odot$ Z = 0.002 |
|---|---|---|---|---|
| Salpeter[a] | - | 1.0 | 1.0 | 1.25 |
| Kroupa[b] | | | | |
| $\alpha_3 = 3.0$ | - | 2.85 | 2.27 | 0.45 |
| $\alpha_3 = 2.9$ | - | 2.26 | 1.83 | 0.51 |
| $\alpha_3 = 2.8$ | - | 1.80 | 1.48 | 0.59 |
| $\alpha_3 = 2.7$ | - | 1.42 | 1.19 | 0.68 |
| $\alpha_3 = 2.6$ | - | 1.13 | 0.95 | 0.74 |
| $\alpha_3 = 2.5$ | - | 0.90 | 0.77 | 0.83 |
| $\alpha_3 = 2.4$ | - | 0.72 | 0.62 | 0.91 |
| $\alpha_3 = 2.3$ | $\geq 0.004$ | 0.58 | 0.51 | 1.0 |
| $\alpha_3 = 2.2$ | $\sim 0.0029$ | 0.47 | 0.42 | 1.08 |
| $\alpha_3 = 2.1$ | $\sim 0.0022$ | 0.39 | 0.35 | 1.15 |
| $\alpha_3 = 2.0$ | $\sim 0.0016$ | 0.33 | 0.29 | 1.20 |
| $\alpha_3 = 1.9$ | $\sim 0.0012$ | 0.28 | 0.25 | 1.25 |
| $\alpha_3 = 1.8$ | $\sim 0.0009$ | 0.24 | 0.22 | 1.3 |
| $\alpha_3 = 1.7$ | $\sim 0.0006$ | 0.21 | 0.20 | 1.36 |
| $\alpha_3 = 1.6$ | $\sim 0.0005$ | 0.19 | 0.18 | 1.37 |
| $\alpha_3 = 1.5$ | $\sim 0.0004$ | 0.18 | 0.17 | 1.41 |
| $\alpha_3 = 1.4$ | $\sim 0.0003$ | 0.17 | 0.16 | 1.41 |
| $\alpha_3 = 1.3$ | $\sim 0.0002$ | 0.16 | 0.15 | 1.37 |
| $\alpha_3 = 1.2$ | $\sim 0.00015$ | 0.15 | 0.14 | 1.31 |
| $\alpha_3 = 1.1$ | 0.0001 | 0.15 | 0.14 | 1.33 |
| $\alpha_3 = 1.0$ | <0.0001 | 0.15 | 0.14 | 1.32 |

NOTES:

[a] Single slope: $\xi(M) \propto M^{-2.35}$ for $M/\,M_\odot \in [0.1, 100]$, (Salpeter, 1955)

[b] Triple slope: $dN/dM = \xi(M) \propto \begin{cases} M^{-1.3}, & \text{for } M/M_\odot \in [0.08, 0.5] \\ M^{-2.2}, & \text{for } M/M_\odot \in [0.5, 1.0] \\ M^{-\alpha_3}, & \text{for } M/M_\odot \in [1.0, 150.0], \end{cases}$

where originally $\alpha_3 = 2.7$ in Kroupa et al. (1993).

could be higher than 10%.

Table 3.4: Number of mergers of respective types, BH-BH, BH-NS, or NS-NS, in our samples simulated for models I1 and I2 for each of the 32 metallicities we computed. Only systems expected to merge within the Hubble time are included.

| Metallicity | BH-BH model I1 (I2) | BH-NS model I1 (I2) | NS-NS model I1 (I2) |
|---|---|---|---|
| 0.0001 | 4364 (9856) | 103 (130) | 225 (42) |
| 0.0002 | 4924 (7982) | 61 (76) | 92 (25) |
| 0.0003 | 4724 (6375) | 79 (79) | 40 (13) |
| 0.0004 | 4480 (5387) | 112 (93) | 78 (29) |
| 0.0005 | 4310 (4762) | 156 (115) | 96 (20) |
| 0.0006 | 4184 (3988) | 132 (154) | 96 (29) |
| 0.0007 | 3878 (3700) | 147 (150) | 110 (33) |
| 0.0008 | 3532 (3087) | 165 (112) | 95 (43) |
| 0.0009 | 3333 (2685) | 135 (81) | 110 (36) |
| 0.001 | 3110 (2434) | 83 (71) | 114 (35) |
| 0.0015 | 2002 (1339) | 199 (96) | 94 (39) |
| 0.002 | 1424 (809) | 194 (107) | 103 (37) |
| 0.0025 | 987 (474) | 206 (96) | 116 (42) |
| 0.003 | 931 (407) | 188 (73) | 134 (50) |
| 0.0035 | 1176 (530) | 214 (69) | 99 (39) |
| 0.004 | 1296 (1296) | 212 (212) | 49 (49) |
| 0.0045 | 962 (962) | 244 (244) | 66 (66) |
| 0.005 | 622 (622) | 232 (232) | 92 (92) |
| 0.0055 | 376 (376) | 275 (275) | 100 (100) |
| 0.006 | 288 (288) | 274 (274) | 87 (87) |
| 0.0065 | 202 (202) | 285 (285) | 79 (79) |
| 0.007 | 164 (164) | 280 (280) | 79 (79) |
| 0.0075 | 126 (126) | 291 (291) | 50 (50) |
| 0.008 | 108 (108) | 247 (247) | 47 (47) |
| 0.0085 | 70 (70) | 172 (172) | 57 (57) |
| 0.009 | 67 (67) | 148 (148) | 76 (76) |
| 0.0095 | 45 (45) | 112 (112) | 81 (81) |
| 0.01 | 40 (40) | 83 (83) | 90 (90) |
| 0.015 | 27 (27) | 14 (14) | 642 (642) |
| 0.02 | 26 (26) | 18 (18) | 535 (535) |
| 0.025 | 41 (41) | 18 (18) | 274 (274) |
| 0.03 | 55 (55) | 14 (14) | 551 (551) |

# Chapter 4

# The evolutionary roads leading to low effective spins, high black hole masses, and O1/O2 rates of LIGO/Virgo binary black holes

K. Belczynski, J. Klencki, C.E. Fields, A. Olejak, E. Berti, G. Meynet, C.L. Fryer, D.E. Holz, R. O'Shaughnessy, D.A. Brown, T. Bulik, S.C. Leung, K. Nomoto, P. Madau, R. Hirschi, E. Kaiser, S. Jones, S. Mondal, M. Chruslinska, P. Drozda, D. Gerosa, Z. Doctor, M. Giersz, S. Ekstrom, C. Georgy, A. Askar, V. Baibhav, D. Wysocki, T. Natan, W.M. Farr, G. Wiktorowicz, M. Coleman Miller, B. Farr & J.-P. Lasota

*Astronomy & Astrophysics, volume 636, A104, (2020)*

**Abstract**

All ten LIGO/Virgo binary black hole (BH-BH) coalescences reported from the O1/O2 runs have near zero effective spins. There are only three potential explanations of this fact. If the BH spin magnitudes are large then *(i)* either both BH spin vectors must be nearly in the orbital plane or *(ii)* the spin angular momenta of the BHs must be oppositely directed and similar in magnitude. Or, *(iii)* the BH spin magnitudes are small. We test the third hypothesis within the framework of the classical isolated binary evolution scenario of the BH-BH merger formation. We test three models of angular momentum transport in massive stars: a mildly efficient transport by meridional currents (as employed in the Geneva code), an efficient transport by the Tayler-Spruit magnetic dynamo (as implemented in the MESA code), and a very-efficient transport (as proposed by Fuller et al.) to calculate natal BH spins. We allow for binary evolution to increase the BH spins through accretion and account for the potential spin-up of stars through tidal interactions. Additionally, we update the calculations of the stellar-origin BH masses, include revisions to the history of star formation and to the chemical evolution across cosmic time. We find that we can match simultaneously the observed BH-BH merger rate density, BH masses, and

effective spins. Models with efficient angular momentum transport are favored. The updated stellar-mass weighted gas-phase metallicity evolution now used in our models appears to be a key in better reproducing the LIGO/Virgo merger rate estimate. Mass losses during the pair-instability pulsation supernova phase are likely overestimated if the merger GW170729 hosts a BH more massive than 50 $M_\odot$. We also estimate rate of BH-NS mergers from recent LIGO/Virgo observations. If in fact angular momentum transport in massive stars is efficient, then any (electromagnetic or gravitational wave) observation of a rapidly spinning BH would indicate either a very effective tidal spin up–of the progenitor star (homogeneous evolution, high-mass X-ray binary formation through case A mass transfer, or a spin-up of a Wolf-Rayet star in a close binary by a close companion), or significant mass accretion by the hole, or a BH formation through the merger of two or more BHs (in a dense stellar cluster). Our updated models of BH-BH, BH-NS and NS-NS mergers are now publicly available at `www.syntheticuniverse.org` under the tab "StarTrack models vs. Gravitational Wave Observations".

## 4.1 INTRODUCTION

The LIGO/Virgo Collaboration has reported the detection of ten binary black hole (BH-BH) mergers during the O1/O2 observations: GW150914, GW151012, GW151226, GW170104, GW170608, GW170729, GW170809, GW170814, GW170818 and GW170823 (Abbott et al., 2019a,b). We list the basic properties of these mergers in Table 4.1.

In our analysis we use only the LIGO/Virgo–reported events but three additional BH-BH mergers, GW170121, GW170304, and GW170727, were detected at high confidence ($P_{\rm astro} > 0.98$[1]) by Venumadhav et al. (2019). They have low effective spins consistent with the triggers reported by the LIGO/Virgo collaboration. The three other events reported by Venumadhav et al. (2019) are most likely not of astrophysical origin. In particular GW170403, with a highly negative effective spin, was reported as the least secure event. Two more events were reported with high effective spins: one with $\chi_{\rm eff} = 0.7^{+0.2}_{-0.3}$ (Venumadhav et al., 2019) and the second with $\chi_{\rm eff} = 0.81^{+0.15}_{-0.21}$ (Zackay et al., 2019), however, these triggers have only a 56% and 71% chance of being of astrophysical origin, respectively.

The majority of the reported mergers contain "heavy" BHs with component masses > 20 $M_\odot$ and are consistent with being formed by isolated binary evolution of stars with metallicities $\lesssim 10\%\ Z_\odot$ and initial masses in the range 40–100 $M_\odot$, while lower mass BHs may have formed from lower mass stars or at higher metallicity (Belczynski et al., 2010b, 2016b). A typical evolution involves the interaction of stars in a binary through mass transfer and a common envelope phase (Tutukov & Yungelson, 1993; Lipunov et al., 1997; Belczynski et al., 2002; Voss & Tauris, 2003; Dominik et al., 2012; Eldridge & Stanway, 2016; Woosley, 2016; Stevenson et al., 2017a;

[1]LIGO/Virgo uses > 0.95 probability to report events of astrophysical origin

Kruckow et al., 2018; Hainich et al., 2018; Marchant et al., 2018; Spera et al., 2019) and its outcome was predicted to produce the first LIGO/Virgo sources (Belczynski et al., 2010a).

Table 4.1: LIGO/Virgo O1/O2 BH-BH mergers[a] .

| Event | $\chi_{\rm eff}$ | $M_{\rm tot}$ | $M_1$ | $M_2$ | $z$ |
|---|---|---|---|---|---|
| **GW150914** | -0.01 [-0.14,0.11] | 62.8 [59.9,65.9] | 35.6 [32.6,40.4] | 30.6 [26.2,33.6] | 0.09 [0.06,0.12] |
| **GW151012** | 0.04 [-0.15,0.32] | 36.3 [33.1,45.2] | 23.3 [17.8,37.3] | 13.6 [8.8,17.7] | 0.21 [0.12,0.30] |
| **GW151226** | 0.18 [0.06,0.38] | 20.6 [19.3,25.7] | 13.7 [10.5,22.5] | 7.7 [5.1,9.9] | 0.09 [0.05,0.13] |
| **GW170104** | -0.04 [-0.24,0.13] | 50.4 [46.7,55.0] | 31.0 [25.4,38.2] | 20.1 [15.6,25.0] | 0.19 [0.11,0.26] |
| **GW170608** | 0.03 [-0.04,0.22] | 17.7 [17.1,20.7] | 10.9 [9.2,16.2] | 7.6 [5.5,8.9] | 0.07 [0.05,0.09] |
| **GW170729** | 0.36 [0.11,0.57] | 86.3 [75.3,100] | 50.6 [40.4,67.2] | 34.3 [24.2,43.4] | 0.48 [0.28,0.67] |
| **GW170809** | 0.07 [-0.09,0.23] | 57.9 [54.3,63.2] | 35.2 [29.2,43.5] | 23.8 [18.7,29.0] | 0.20 [0.13,0.25] |
| **GW170814** | 0.07 [-0.04,0.19] | 54.1 [51.7,57.3] | 30.7 [27.7,36.4] | 25.3 [21.2,28.2] | 0.12 [0.08,0.15] |
| **GW170818** | -0.09 [-0.29,0.09] | 61.3 [57.7,65.8] | 35.5 [30.8,43.0] | 26.8 [21.6,31.1] | 0.20 v[0.13,0.27] |
| **GW170823** | 0.08 [-0.14,0.28] | 69.1 [62.3,78.4] | 39.6 [33.0,49.6] | 29.4 [22.3,28.6] | 0.34 [0.20,0.47] |

Notes:

[a] For all parameters average and 90% confidence limits are listed, $\chi_{\rm eff}$: effective spin parameter, $M_{\rm tot}$: total intrinsic BH-BH binary mass, $M_1$: primary BH intrinsic mass, $M_2$: secondary BH intrinsic mass, $z$: event redshift.

The dynamical formation scenario of BH-BH mergers is an evolutionary channel alternative to isolated binary evolution that could operate in globular clusters, nuclear clusters, or open/young clusters (Miller & Hamilton, 2002b,a; Portegies Zwart et al., 2004; Gültekin et al., 2004, 2006; O'Leary et al., 2007; Sadowski et al., 2008; Downing et al., 2010; Benacquista & Downing, 2013; Bae et al., 2014; Chatterjee et al., 2016; Mapelli, 2016; Hurley et al., 2016; Rodriguez et al., 2016b; VanLandingham et al., 2016; Askar et al., 2017; Arca-Sedda & Capuzzo-Dolcetta, 2017; Samsing, 2017; Morawski et al., 2018; Banerjee, 2018; Di Carlo et al., 2019; Zevin et al., 2019; Rodriguez et al., 2018a; Perna et al., 2019). The dynamical channel can also explain the range of BH masses observed by LIGO/Virgo.

However, these two basic scenarios, dynamical and isolated, predict different spin-orbit misalignment distributions, with dynamical formation generating nearly isotropic distributions (Mandel & O'Shaughnessy, 2010; Rodriguez et al., 2016c), while binary evolution favors distributions that show mostly small to moderate misalignments, with only a small fraction of mergers reaching high misalignments (Wysocki et al., 2018; Gerosa et al., 2018). A hybrid BH-BH merger formation channel that involves isolated triple (dynamically interacting) star systems (Antonini et al., 2017b) favors BH spin vectors that are located in the BH-BH orbital plane, with $\sim 90^\circ$ misalignment with respect to the orbital angular momentum if the tertiary dominates the angular momentum of the system (Antonini et al., 2017a).

The spin orientations of the BHs can therefore provide important information about their formation (Farr et al., 2017, 2018b; Vitale et al., 2017b). However, the effect of spin is sub-dominant in gravitational waveforms, so spins are more difficult to measure than masses. The waveform is most sensitive to the binary's effective spin

$$\chi_{\rm eff} \equiv \frac{M_{\rm BH1} a_{\rm spin1} \cos\Theta_1 + M_{\rm BH2} a_{\rm spin2} \cos\Theta_2}{M_{\rm BH1} + M_{\rm BH2}}, \tag{4.1}$$

with $a_{\rm spin1,2}$ being the BH spin magnitudes and $\Theta_{1,2}$ being the angles between the BH spins and the orbital angular momentum. The dimensionless BH spin magnitude is defined as

$$a_{\rm spin} \equiv \frac{c J_{\rm BH}}{G M_{\rm BH}^2}, \tag{4.2}$$

where $c$ is the speed of light, $G$ is the gravitational constant, and $M_{\rm BH}$ and $J_{\rm BH}$ are respectively the mass and angular momentum of the BH.

All ten of the BH-BH binaries observed by LIGO/Virgo are consistent with effective spins near zero. Indeed, within the 90% confidence levels reported by LIGO/Virgo all mergers are consistent with $-0.1 \lesssim \chi_{\rm eff} \lesssim 0.1$ (see Tab. 4.1). If the BH spin magnitudes are large, then either *(i)* both black hole spin vectors are close to the orbital plane, so that $\cos\Theta_{1,2} \approx 0$, or *(ii)* the black hole angular momenta are nearly equal in magnitude but close to oppositely directed. Alternatively, one can obtain small values of the effective spin parameter if *(iii)* BH spin magnitudes are small.

In this study we investigate the third possibility, i.e., that the spin magnitudes of BHs in BH-BH mergers detected by LIGO/Virgo are small. Our study is limited to the classical isolated binary evolution BH-BH formation scenario. We test several models of natal BH spins to predict the

effective spin parameters of BH-BH mergers in the local Universe and to compare them with LIGO/Virgo observations. Compared to Belczynski et al. (2016a,b,c), we incorporated updated mass loss by pair-instability pulsation supernovae, revised our model of accretion onto BHs in close binaries, allowed for effective tidal spin-up of Wolf-Rayet stars, and adopted a new model for the evolution of metallicity and the star formation rate across cosmic time.

To guide the reader through our article we will briefly summarize the most important ingredients and results of this study. Based on single stellar evolution calculations we introduce three BH natal spin models (see Sec. 4.2.1, and we argue that these models can be reasonably used in binary evolution as implemented in our calculations (see Sec. 4.4.2). We show that initial star rotation does not play a significant role, while angular momentum transport plays crucial role in setting the BH natal spin (see Sec. 4.4.1). In binary evolution, accretion/mass transfer (see Sec. 4.2.4) does not play significant role, while tidal interactions (see Sec. 4.2.5) may increase BH spins for about $20-30\%$ of the BH-BH mergers (see Sec. 4.3.4). Merger rates of NS-NS, BH-NS and BH-BH binaries are sensitive to assumptions on the common envelope and natal kicks, but also depend strongly on the assumed cosmic chemical evolution model while the change of merger rates with redshift depends mostly on the cosmic star-formation history (see Sec. 4.3.2).

## 4.2 MODEL

### 4.2.1 NATAL BLACK HOLE SPIN

Various rotating star models differ in terms of the physics of rotation, and in particular in the efficiency of angular momentum transport. Here we test three different models of angular momentum transport for massive stars. Moderate angular momentum transport is adopted along with Geneva stellar models (Eggenberger et al., 2008; Ekström et al., 2012) that are based on Zahn (1992) theory, in which angular momentum is mainly transported by meridional currents: the shellular model. Efficient angular momentum transport is adopted with standard MESA stellar models (calculated in this study), which use an efficient transport mechanism mediated by the action of the so-called "Tayler-Spruit magnetic dynamo" in the radiative zone (Spruit, 1999, 2002). Super-efficient angular momentum transport is based on the Tayler-Spruit dynamo modified to include stronger magnetic field generation that leads to more efficient angular momentum transport (Fuller et al., 2019; Ma & Fuller, 2019; Fuller & Ma, 2019).

To test the validity of each of these models through gravitational wave astrophysics, we compare their predictions with the LIGO/Virgo effective–spin estimates. For the Geneva (moderate) and MESA (efficient) angular momentum transport we use models for a wide range of metallicity: $Z = 0.014, 0.006, 0.002, 0.0004$ (see Appendix 4.A.1 and 4.A.2). We assume that stars on the zero age main sequence (ZAMS) have an equatorial velocity equal to 40% of the critical velocity,

defined as the velocity at which the centrifugal acceleration completely balances gravity.[2] To test the importance of the initial rotation rates we ran several models with different assumptions about this initial condition, see Section 4.4.1 and Figures 4.23 and 4.28. We find that the final core rotation rate is almost independent of the initial rotation rate but depends strongly on the angular momentum transport process included in the simulation (i.e. non-magnetic or magnetic). For the "Fuller" model (super efficient) of angular momentum transport we assume that the natal BH spin depends neither on initial stellar rotation nor on metallicity, since in each case almost all angular momentum is removed from the stellar core (Fuller et al., 2019; Ma & Fuller, 2019; Fuller & Ma, 2019).

The stellar models provide the angular momentum in each zone corresponding to a spherical shell in the star. We assume that angular momentum is conserved in the collapse phase, and calculate the angular momentum of the compact remnant by summing the angular momentum of the zones with enclosed mass lower than the compact remnant mass.

From the amount of angular momentum contained in the collapsing core, we calculate the dimensionless BH spin magnitude $a_{\rm spin}$. However, we limit the spin magnitude to 0.9: $a_{\rm spin} = \min(a_{\rm spin}, 0.9)$ to account for any potential processes that might remove some angular momentum during BH formation. We arbitrarily picked 0.9 as a maximum for the spin rate. The difficulty in predicting the fastest spin values is that they require high-angular momentum disk-forming infalls. There are several spurious mechanisms which can remove angular momentum from these accretion disks but for now we do not have means to perform predictive calculations of this effect. Disk winds are one example, however, the actual amount of material and angular momentum that is removed by such winds can vary dramatically (Vlahakis & Königl, 2001; Surman et al., 2006; Janiuk, 2017). Therefore, we have used $a_{\rm spin} = 0.9$ to denote any value between $0.9 - 1.0$, depending on these accretion loss mechanisms.

In Figures 4.1 and 4.2 we show the BH spins as a function of the progenitor's CO core mass for the Geneva and MESA models. We approximate the natal BH spin by simple fits. These rough fits are meant to reproduce the general trends in the data and are used in our population synthesis calculations. We list the actual data in Tables 4.5 and 4.6, so other fits can be attempted if desired.

For the Geneva models the natal BH spin may be approximated by:

$$a_{\rm spin} = \begin{cases} 0.85 & M_{\rm CO} \leq m_1 \\ aM_{\rm CO} + b & m_1 < M_{\rm CO} < m_2 \\ a_{\rm low} & M_{\rm CO} \geq m_2 \end{cases} \tag{4.3}$$

with $a = -0.088$ for all models; $b = 2.258$, $m_1 = 16.0\,M_\odot$, $m_2 = 24.2\,M_\odot$, $a_{\rm low} = 0.13$ for $Z = 0.014$; $b = 3.578$, $m_1 = 31.0\,M_\odot$, $m_2 = 37.8\,M_\odot$, $a_{\rm low} = 0.25$ for $Z = 0.006$; $b = 2.434$, $m_1 = 18.0\,M_\odot$, $m_2 = 27.7\,M_\odot$, $a_{\rm low} = 0.0$ for $Z = 0.002$; and $b = 3.666$, $m_1 = 32.0\,M_\odot$, $m_2 = 38.8\,M_\odot$, $a_{\rm low} = 0.25$ for $Z = 0.0004$. Note that progenitor stars with CO cores less massive

[2] `GENEC` and `MESA` use two slightly different definitions of the critical velocity. Maeder & Meynet (2000) discusses the two definitions. `MESA` models use their eq. (3.12), whereas `GENEC` models use the minimum between the values obtained from their eq. (3.14) and (3.19), respectively.

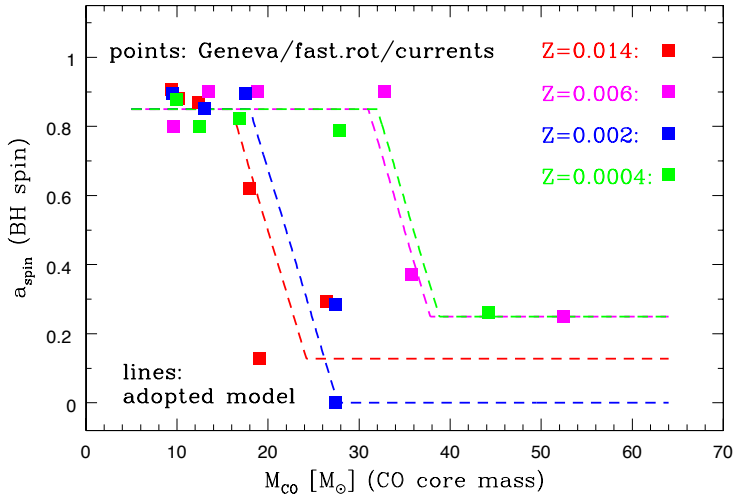


Figure 4.1: Magnitude of natal BH spin as a function of the CO core mass of the collapsing star for the `Geneva` stellar models with 40% critical initial velocity and mild angular momentum transport by meridional currents. Lines mark our adopted model for natal BH spins and its dependence on metallicity (see eq. 4.3). The star's CO core mass may be used as a proxy for the BH mass (see Appendix 4.A.3).

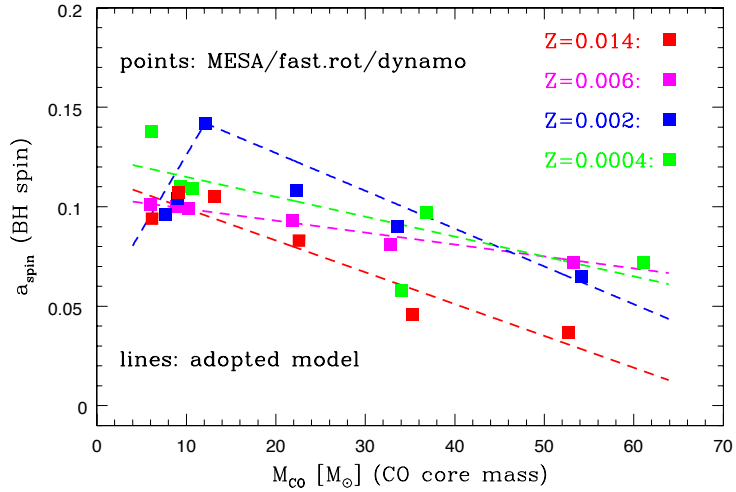


Figure 4.2: Magnitude of natal BH spin as a function of the CO core mass of the collapsing star for the `MESA` stellar models with 40% critical initial velocity and the Tayler-Spruit magnetic dynamo (efficient) angular momentum transport. Lines mark our adopted model for natal BH spins and its dependence on metallicity (see eq. 4.4).

than $\sim 20\ M_\odot$ (low- to intermediate-mass BHs) tend to produce high-spin BHs ($a_{\rm spin} \sim 0.8$–$0.9$), but higher mass stars (massive BHs) tend to produce low-spin BHs ($a_{\rm spin} \sim 0$–$0.3$). This general trend is easily understood. Stellar winds during the evolution of a massive star can carry away a considerable amount of angular momentum (Meynet et al., 2015). For the most massive stars, this mass loss is extensive, efficiently removing angular momentum and producing low-spin BHs. The data points also show a non-monotonic dependence on metallicity, which is the result of a complex and metallicity-dependent interplay between the strength of stellar winds, the extent of the H-burning shell, and the model for the efficiency of element diffusion within the meridional current (see Appendix 4.A.1).

For MESA models the natal BH spin may be approximated by:

$$a_{\rm spin} = \begin{cases} a_1 M_{\rm CO} + b_1 & M_{\rm CO} \leq m_1 \\ a_2 M_{\rm CO} + b_2 & M_{\rm CO} > m_1 \end{cases} \tag{4.4}$$

with $a_1 = -0.0016$, $b_1 = 0.115$, $m_1 = \infty$ for $Z = 0.014$; $a_1 = -0.0006$, $b_1 = 0.105$, $m_1 = \infty$ for $Z = 0.006$; $a_1 = 0.0076$, $b_1 = 0.050$, $a_2 = -0.0019$, $b_2 = 0.165$, $m_1 = 12.09\ M_\odot$ for $Z = 0.002$; and $a_1 = -0.0010$, $b_1 = 0.125$, $m_1 = \infty$ for $Z = 0.0004$. The MESA models include

the Tayler-Spruit magnetic dynamo and thus models of all masses and at all metallicities end up with low BH spin magnitudes in the range $0.05 \lesssim a \lesssim 0.15$. There is a mild tendency for lower metallicity and lower initial mass models to end up with slightly higher BH spin magnitudes but the dependence is much weaker than in the Geneva models, which do not include magnetic field related transport of angular momentum.

Finally, for the Fuller model that employs super-efficient angular momentum transport, we adopt a single value of BH natal spin for stars of all masses and all metallicities:

$$a_{\rm spin} = 0.01. \tag{4.5}$$

Note that single stellar models (of different mass and metallicity) presented by Fuller & Ma (2019) produce very low spins for BHs in range: $a = 0.003 - 0.035$ with a typical value of $a \sim 0.01$.

In our binary population synthesis calculations we employ the presented-above natal BH spin estimates obtained from single stellar evolution (see Sec. 4.2.7). The discussion of binary interactions that can change these natal BH spins (that are and are not taken into account) is given in Section 4.4.2.

### 4.2.2 BLACK HOLE SPIN MISALIGNMENT

To calculate the effective spin of BH-BH mergers we need to know the misalignment angles of the two BH spin vectors with respect to the orbital angular momentum vector: $\Theta_1$ and $\Theta_2$ (see eq. 4.1).

In our estimate of these angles we ignore the potential effects of tides and mass transfer/accretion: see Gerosa et al. (2013) and Wysocki et al. (2018) for alternatives and further discussion. However, in our calculations, we take into account the binary components spin precession. We assume that the two stars are born with spins that are fully aligned with the ZAMS binary orbital angular momentum ($\mathbf{L_0}$). At each BH formation, the natal kick may change the orbit and its orientation in space. After the first BH formation the new orbital angular momentum is $\mathbf{L_1}$, while after the second BH formation it is $\mathbf{L_2}$. After the first BH formation, if there was a natal kick, the binary component spins $\mathbf{S_1}$ and $\mathbf{S_2}$ are not aligned with the binary angular momentum vector. We assume that after the first BH formation both the BH spin and the companion star spin are small compared to the binary orbital angular momentum. With this assumption the total angular momentum of the binary is equal to the orbital angular momentum. Therefore, both the binary component spins precess around $\mathbf{L_1}$. The precession periods for the BH and the companion star spin are different. In this approximation the spin of the BH (or the star) can be described as a sum of two components $\mathbf{S_{1/2}} = \mathbf{S^{\parallel}_{1/2}} + \mathbf{S^{\perp}_{1/2}}$, where $\mathbf{S^{\parallel}_{1/2}}$ is the spin component parallel to the orbital angular momentum and $\mathbf{S^{\perp}_{1/2}}$ is the spin component perpendicular to the orbital angular momentum. During precession the former is constant and the latter has a constant value but rotates in the plane perpendicular to the direction of the angular orbital momentum. The precession period of each spin is different (Hamilton & Sarazin, 1982). Thus at the time of the second BH formation we choose random positions of each component vector on its precessing trajectory and they become $\mathbf{S'_1}$ and $\mathbf{S'_2}$ . The natal kick (if any) changes again the binary orbit orientation in space, which becomes now $\mathbf{L_2}$. We

follow all these changes to calculate the effective spin

$$\chi_{eff} = \frac{M_{\rm BH1}\mathbf{S'_1} + M_{\rm BH2}\mathbf{S'_2}}{M_{\rm BH1} + M_{\rm BH2}} \cdot \frac{\mathbf{L_2}}{|\mathbf{L_2}|} \tag{4.6}$$

Note that although (after the second BH formation) misaligned BH spins are subject to precession, the value of $\chi_{\rm eff}$ is expected to remain constant during the long inspiral towards the LIGO/Virgo band (Gerosa et al., 2015).

### 4.2.3 Black Hole Masses

In our calculation of BH masses we use formulas assuming both the rapid and delayed supernova engines (Fryer et al., 2012). The rapid development of the engine naturally creates a mass gap between NSs and BHs (dearth of compact objects in the range $2-5\ M_\odot$), while the delayed engine does produce compact objects in this range (Belczynski et al., 2012b). For single-star evolution, the delayed model minimum BH mass is $2.5\ M_\odot$, while it is $5\ M_\odot$ for the rapid model. Note that binary evolution may create light BHs ($\sim 2.5-5\ M_\odot$) by accretion induced collapse of a NS to a BH independent of supernova model (Belczynski & Taam, 2004).

The maximum mass of a BH is set by the maximum mass of a star and wind mass loss rates and depends sensitively on the potential explosive mass–loss during the final stages of the star's life. We adopt a rather conservative maximum initial mass for the stars: $M_{\rm ZAMS} < 150\ M_\odot$, although there seems to be evidence that stars with mass of $\sim 200-300\ M_\odot$ may exists even in the local Universe (Crowther et al., 2010). For stellar winds we adopt formulas based on theoretical predictions of radiation driven mass loss (Vink et al., 2001) with inclusion of Luminous Blue Variable mass loss (Belczynski et al., 2010b). These wind mass loss rates may be overestimated by as much as an order of magnitude (Oskinova et al., 2011; Ramachandran et al., 2019). Therefore we allow (conservatively) for the reduction of stellar wind mass loss rates to $f_{\rm wind} = 0.3$ of their currently adopted values.

We also allow for pair-instability supernovas (PSNs) to entirely disrupt massive stars (stars with He core mass in range $M_{\rm He} = 65-135\ M_\odot$) and leave no NS/BH remnant. For somewhat lower-mass stars (stars with He core mass in range $M_{\rm He} \approx 40-65\ M_\odot$) we allow for pair-instability pulsation supernovas (PPSNs). This process may remove the outer layers of a star, but does not lead to its disruption and allows for the BH formation in core collapse. We adopt three models for PPSN mass loss. In the first model we adopt strong PPSNs that are assumed to always remove the entire star mass above the inner $45.0\ M_\odot$ (Belczynski et al., 2016a) for stars with $M_{\rm He} = 45-65\ M_\odot$. Therefore, the post PPSN star mass is:

$$M_{\rm star}/\ M_\odot = 45.0 \quad 45.0 \le M_{\rm He} < 65.0\ M_\odot. \tag{4.7}$$

In the second model we adopt recent PPSN calculations that allow for as much as $51.2\ M_\odot$ of the star to remain bound after a PPSN (Leung et al., 2019). In this moderate PPSN model, the

explosive mass loss depends on the He core mass. The post PPSN star mass is:

$$M_{\rm star}/\,M_\odot = \begin{cases} 0.65M_{\rm He} + 12.2 & 40.0 \le M_{\rm He} < 60.0\ M_\odot \\ 51.2 & 60.0 \le M_{\rm He} < 62.5\ M_\odot \\ -14.3M_{\rm He} + 938.0 & 62.5 \le M_{\rm He} \le 65.0\ M_\odot. \end{cases} \tag{4.8}$$

Finally, we adopt a weak PPSN model that allows only for 50% of the mass loss calculated by Leung et al. (2019). In this scheme, the post PPSN star mass may reach 55.6 $M_\odot$, and we approximate the post PPSN star mass with:

$$M_{\rm star}/\,M_\odot = \begin{cases} 0.83M_{\rm He} + 6.0 & 40.0 \le M_{\rm He} < 60.0\ M_\odot \\ 55.6 & 60.0 \le M_{\rm He} < 62.5\ M_\odot \\ -14.3M_{\rm He} + 938.1 & 62.5 \le M_{\rm He} \le 65.0\ M_\odot. \end{cases} \tag{4.9}$$

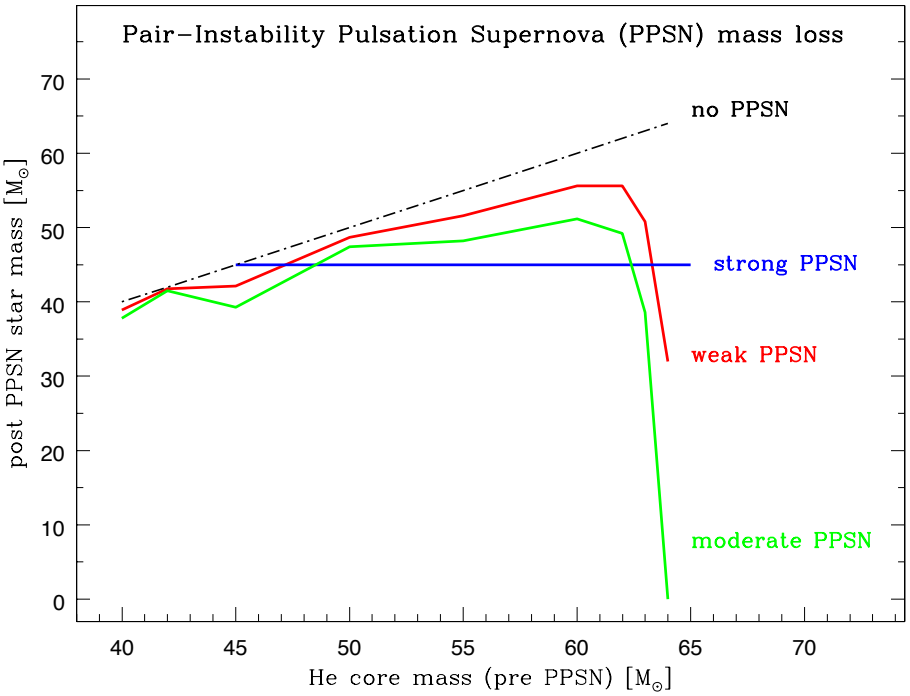


FIGURE 4.3: Adopted models for pair-instability pulsation supernova mass loss. For a given He core mass we show the mass of a star after PPSN mass loss. Moderate PPSN mass loss is adopted directly from Leung et al. (2019), while its modified (50% reduced mass loss) version is presented as weak PPSN model. Strong PPSN are adopted from Belczynski et al. (2016a).

All three models are shown in Figure 4.3. For the two models based on calculations from Leung et al. (2019) we note a steep decrease in post PPSN star mass for He core masses above $\sim 60\ M_\odot$. The masses of these He stars are very close to the boundary mass between the PPSN and the PSN. As the mass of the He star increases, the central temperature at the bounce increases and oxygen burning becomes more explosive and causes a larger amount of mass ejection. Eventually explosive oxygen burning in the $\sim 65\ M_\odot$ He star produces large enough nuclear energy to disrupt

the star completely with no BH remnant, i.e., induces PSN. The amount of mass ejection increases steeply as the He star mass increases from $\sim 60\ M_\odot$ to $\sim 65\ M_\odot$, because the oxygen burning rate is very sensitive to the temperature. Thus the remnant BH mass decreases steeply as the He star mass approaches $65\ M_\odot$.

In the PPSN mass regime massive BHs are formed, and according to our scheme (Fryer et al., 2012) these BHs form through collapse of the entire star into a BH (direct BH formation). However we allow for some mass loss in neutrinos. In the original formulas we have adopted a high neutrino fractional mass loss ($f_{\rm neu} = 0.1$; see e.g. Belczynski et al., 2016b), while here we also allow also for much smaller mass loss in some models ($f_{\rm neu} = 0.01$). The final BH mass, in case of the direct BH formation, is calculated from

$$M_{\rm BH} = (1 - f_{\rm neu}) M_{\rm star}, \tag{4.10}$$

where $M_{\rm star}$ denotes star's mass just prior the core collapse.

### 4.2.4 Black Hole Accretion Model

Mass accretion may increase the BH mass and spin after its formation. Here we test two models of accretion from a stable Roche lobe overflow (RLOF; not common envelope [CE]) mass-transfer or from stellar winds. The first model (efficient BH accretion) is based on the results of global, axisymmetric simulations of accretion disks with $\alpha P$ viscosity, disk winds and photon trapping performed by Ohsuga (2007). Belczynski et al. (2008b) obtained a fit to the results of Ohsuga (2007):

$$\log\left(\frac{\dot{M}_{\rm BH}}{\dot{M}_{\rm crit1}}\right) = \begin{cases} \log\left(\frac{|\dot{M}_{\rm don}|}{\dot{M}_{\rm crit1}}\right) & |\dot{M}_{\rm don}| \le \dot{M}_{\rm crit1} \\ 0.544 \log\left(\frac{|\dot{M}_{\rm don}|}{\dot{M}_{\rm crit1}}\right) & \dot{M}_{\rm crit1} < |\dot{M}_{\rm don}| \le 10 \times \dot{M}_{\rm crit1} \\ 0.934 \log\left(\frac{|\dot{M}_{\rm don}|}{\dot{M}_{\rm crit1}}\right) - 0.380 & |\dot{M}_{\rm don}| > 10 \times \dot{M}_{\rm crit1} \end{cases}, \tag{4.11}$$

where $\dot{M}_{\rm BH}$ is the mass accumulation rate onto the BH, $\dot{M}_{\rm crit1} = 2.6 \times 10^{-8} (M_{\rm BH}/10\ M_\odot)\ {\rm M}_\odot\ {\rm yr}^{-1}$ is the critical mass transfer rate (obtained from numerical simulations) above which the accretion onto the BH is not fully efficient, and $\dot{M}_{\rm don}$ is the mass transfer rate from the donor to the accretion disk around the BH. Note that above the critical mass transfer rate some mass transferred from the donor is lost/ejected from the system.

The second model (inefficient BH accretion) uses the analytical prescription of Shakura & Sunyaev (1973). In this model, disk winds play a significant role effectively limiting the mass accumulation for super-Eddington mass transfer rates by limiting the local accretion rate to its Eddington value. This model is supported by the numerical results of strong outflow from the super-critical accretion disk (Abolmasov et al., 2009; Sądowski et al., 2016), as well as by observations of many ultra luminous X-ray sources in centers of unusually large and bright emission nebulae which are powered by the accumulated kinetic energy of the outflow (Pakull & Mirioni,

2003; King, 2004), and also supported by the fact that the neutron star in Cygnus X-2 while being subject to high mass transfer rate ($\sim 10^{-5}$ $M_\odot$ $yr^{-1}$) has ejected most of the mass transferred from the donor star (King & Ritter, 1999).

In this model we assume that the mass accumulation rate onto the BH is given by

$$\dot{M}_{\rm BH} = f_1 f_2 \dot{M}_{\rm don}, \tag{4.12}$$

where $(1 - f_1)$ is the fraction of the mass transferred to the disk from the donor which is lost in wind from the outer part of the accretion disk. It is difficult to determine the wind mass loss rate from the outer part of the disk (see Sądowski et al., 2016), and we treat $f_1$ as a parameter in our model. For the current calculations we adopt $f_1 = 1$, i.e., no wind mass loss in the outer part of the disk, which maximizes accumulation of mass onto the BH. Similarly, $(1 - f_2)$ represents the fraction of mass which is lost from the inner part of the accretion disk. The value of $f_2$ depends on the mass transfer rate as:

$$f_2 = \begin{cases} 1, & \text{for } \dot{M}_{\rm don} \leq \dot{M}_{\rm crit2} \\ \frac{R_{\rm ISCO}}{R_{\rm sph}}, & \text{for } \dot{M}_{\rm don} > \dot{M}_{\rm crit2} \end{cases} \tag{4.13}$$

where the critical mass transfer rate is $\dot{M}_{\rm crit2} = \dot{M}_{\rm Edd} = 4.375\times10^{-8}(1+X)^{-1}(M_{\rm BH}/\ M_\odot)$ $M_\odot$ $yr^{-1}$, where hydrogen mass fraction $X$ is 0.7 for H-rich donor stars and 0.0 for H-deficient donor stars, $R_{\rm ISCO}$ is the innermost stable circular orbit radius, and $R_{\rm sph}$ is the spherisation radius, where the disk's height becomes comparable to the radius. $R_{\rm ISCO}$ depends on the spin value of the accreting BH and varies between $0.5R_{\rm S}$ (for a maximally prograde spinning BH) to $4.5R_{\rm S}$ (for a maximally retrograde spinning BH), where $R_{\rm S} = \frac{2GM_{\rm BH}}{c^2}$ is the Schwarzchild radius of a BH. $R_{\rm sph}$ is given by (Shakura & Sunyaev, 1973)

$$R_{\rm sph} = \frac{27}{4}\frac{\dot{M}_{\rm don}}{\dot{M}_{\rm Edd}}R_{\rm S}. \tag{4.14}$$

The above two equations are a simplified description of the change of the accretion mode onto compact objects. In particular, they lead to a jump in mass accretion rate onto a compact object when mass transfer from a donor star is equal to the critical mass transfer rate ($M_{\rm don} = \dot{M}_{\rm crit2}$). This simplification does not influence the results of our evolutionary calculations.

In our calculations we always assume a prograde BH spin, and the initial BH spin magnitude is adopted from a given stellar model (see Sec. 4.2.1) and then increased by accretion as detailed in Belczynski et al. (2008b). At sub-Eddington accretion rates ($\dot{M}_{\rm don} \leq \dot{M}_{\rm Edd}$), we assume that there is no mass loss from the inner part of the disk ($f_2 = 1$).

The mass accumulation onto a BH in the inefficient BH accretion model is always Eddington-limited ($\dot{M}_{\rm BH} < \dot{M}_{\rm Edd}$), whereas in the efficient BH accretion model it increases monotonically with the mass transfer rate and may significantly exceed $\dot{M}_{\rm Edd}$. These two models produce the same accumulation on a BH for mass transfer rates below $\dot{M}_{\rm crit1} = 0.06 \times \dot{M}_{\rm Edd}$ where both models give exactly the same prescription ($\dot{M}_{\rm BH} = |\dot{M}_{\rm don}|$, note that $\dot{M}_{\rm crit1} = 0.06\dot{M}_{\rm crit2}$).

As a result, the evolution of BH binaries which go through a phase of stable mass transfer with high (super-critical) mass transfer rate may be considerably different under different assumptions about the BH accumulation efficiency. However, the dominant formation channel for BH-BH

mergers (see Belczynski et al., 2016b, and also Fig. 4.8 and Fig. 4.9) contains no such phase. Along the way to formation of most BH-BH mergers in our models, accretion of matter by a BH takes place only during a short-lived CE event or as result of capturing a fraction of a stellar wind from the companion. Accretion during CE can be best related to the Bondi-Hoyle accretion and has been found to be rather insignificant (less than $\sim 1\ M_\odot$ for a typical $30\ M_\odot$ BH, see Sec. 4.A.7 for a detailed discussion of recent calculations of accretion during CE). The wind-fed accretion during the subsequent phase of a compact BH – Wolf-Rayet (BH-WR) binary evolution is even less significant, partially due to small wind-mass loss rates from low metallicity systems (which are the progenitors of most BH-BH mergers).

Having said that, the BH accretion models presented in this section can play an important role in certain sub-dominant channels for the BH-BH merger formation. In Fig. 4.4 we showcase the time evolution of the mass transfer and accretion rates as well as the BH spin and mass in a system in which the BH accretion is particularly significant. The system began its evolution as two ZAMS stars with masses of 84.6 $M_\odot$ and 48 $M_\odot$ formed at a very low metallicity $Z = 0.0002$ in a binary with separation of about 1900 $R_\odot$. At the age of 3.8 Myr the primary, now a 66 $M_\odot$ helium-core burning star with a radius of 800 $R_\odot$, goes into RLOF and initiates a CE phase. As a result, the primary becomes a 36 $M_\odot$ WR star and the binary separation decreases down to 30 $R_\odot$. With the orbit already being quite compact, the companion MS star ($\sim 47\ M_\odot$) initiates another RLOF and starts stable mass transfer back onto the WR primary. The WR star grows to about 39 $M_\odot$, before collapsing directly into a 35.54 $M_\odot$ BH at the age of 4 Myr (with no natal kick, 10% of mass being lost in neutrinos, and the natal spin of $a_{\rm init} = 0.832$ adopted from Geneva BH natal spin model). Soon thereafter, the companion MS initiates a RLOF again and the first phase of stable, super-critical mass transfer onto the newly-formed BH begins ($\dot{M}_{\rm don} \sim$ a few $\times\ 10^{-5}$ M$_\odot$ yr$^{-1}$). At that moment the system may be potentially observable as an ultraluminous X-ray source (see e.g., Wiktorowicz et al., 2019, for the recent analysis of these objects). The mass transfer continues up until about $t = 4.8$ Myr (Fig. 4.4), at which point the donor is at the very end of its MS evolution and contracts a bit, causing a temporary detachment. The mass transfer starts again when the companion begins to expand on its HG at the age of about $t = 5.9$ Myr having mass of 28 $M_\odot$. The rate is high ($\sim 10^{-3}$ M$_\odot$ yr$^{-1}$), but the phase is short-lived (7.7 kyr). Finally, the last phase of mass transfer occurs when the companion is a slowly expanding core helium burning star and terminates at about 5.25 Myr.

The net result of the subsequent stable mass transfer phases shown in Fig. 4.4 is an increase of the binary separation, which at the point of the final detachment is about 160 $R_\odot$ (similar in both accretion models). At that point the donor star has been stripped almost down to its helium core and has a remaining mass of only about 10 $M_\odot$.

Since accumulation of mass onto the BH (dashed lines in the top panel of Fig. 4.4) is different in the two models for super-critical mass transfer rates, the final BH mass is also different: 42.08 $M_\odot$ for the efficient BH accretion model and 35.66 $M_\odot$ for the inefficient BH accretion model (Fig. 4.4, middle panel). We also note that the BH spin, was increased to 0.948 for the efficient model and to 0.835 for the inefficient model.

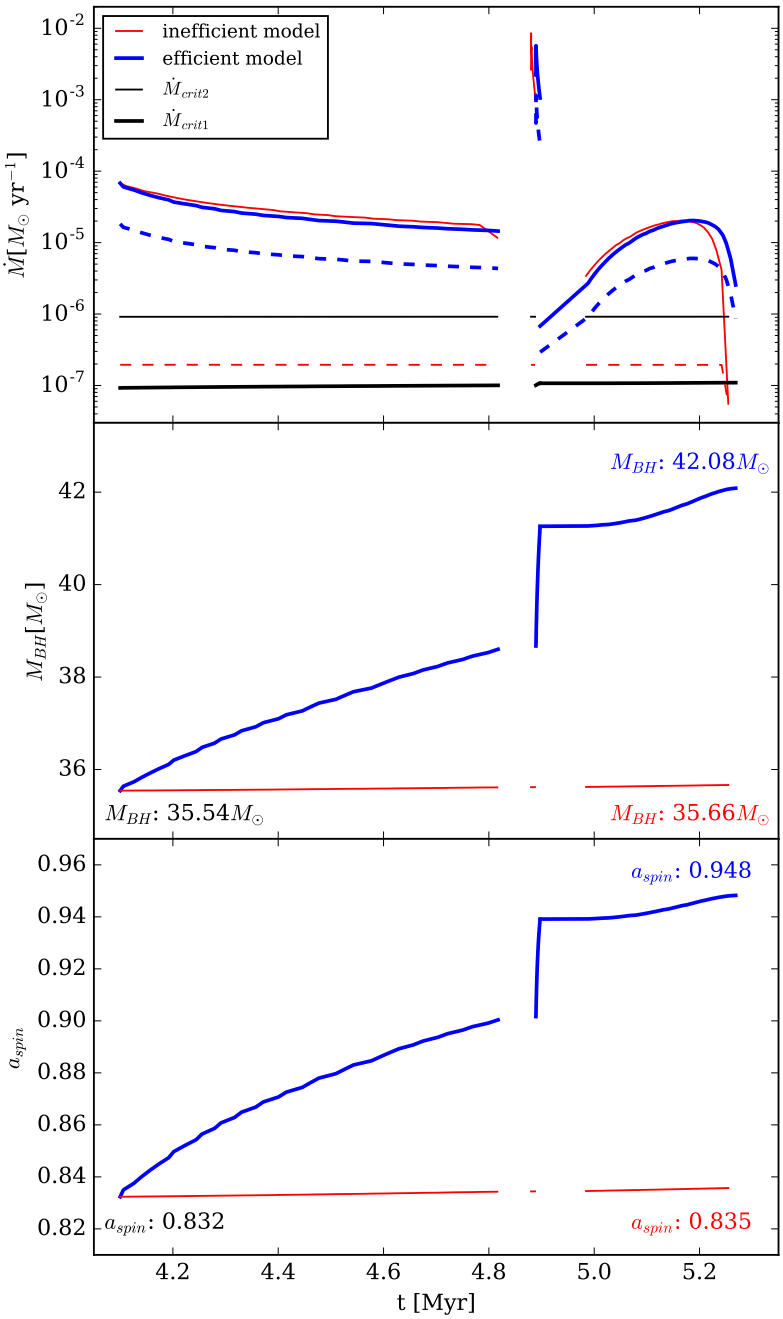


FIGURE 4.4: The figure shows the comparison of the two black hole accretion models employed in the `StarTrack` code. Presented are the evolution of the mass transfer rate from a donor star ($\dot{M}_{\rm don}$; top panel, solid lines), BH mass accumulation rate ($\dot{M}_{\rm BH}$; top panel, dashed lines), the BH mass ($M_{\rm BH}$; middle panel), and the BH spin ($a_{\rm spin}$; bottom panel) during the RLOF stable mass transfer phases. Critical mass transfer rates (above which mass ejection from a system is expected) are provided for reference. During the first part of the RLOF ($t \approx 4 - 4.8$ Myr) the donor is a MS star, during the short-duration peak it is a HG star ($t \approx 4.9$ Myr), and for the remaining RLOF it is a helium-core burning star. See Sec. 4.2.4 for a description of the full evolutionary path and both accretion models.

This particular binary ends its evolution at $t \approx 5.6$ Myr forming a BH-BH with masses of 35.7 $M_\odot$ and 6.2 $M_\odot$ for the inefficient model, or 42.1 $M_\odot$ and 6.0 $M_\odot$ for the efficient model. The delay time to merger is about 3 Myr. The second BH is formed through a supernova explosion with a natal kick. As the separation before the supernova explosion was relatively large in both accretion models ($\sim 160\ R_\odot$), the formation of a binary that could merge within the Hubble time was only possible thanks to the preferentially oriented natal kick, which decreased the separation down to $\sim 90\ R_\odot$ and, more importantly, induced a high eccentricity of $e > 0.988$ (from a $e = 0.0$ pre-supernova value). Such an influence of a natal kick on the binary orbit is very rare (Andrews & Zezas, 2019), so the above example is an extreme example of a BH-BH merger formation. In

the vast majority of systems, the impact of the accretion model on the BH-BH formation is much smaller.

### 4.2.5 Tidal Interactions

In this section, we discuss the efficiency of tidal spin-up in close binaries. Our standard implementation of tides follows from Hurley et al. (2002) and is based on the standard Zahn (1977, 1989) theory as updated by more recent calibrations (Claret, 2007). These prescriptions, which are laid out in Belczynski et al. (2008a), result in rather weak tidal interactions between stars in binary systems. This is particularly true for very massive stars (e.g., progenitors of BHs) that evolve so fast that the tides do not affect significantly their rotation.

In our classical BH-BH formation scenario (Belczynski et al., 2016b), the only evolutionary phase at which tides could spin-up either of the BH progenitors happens after the CE phase when the initially wide binary ($a \gtrsim 1000\ R_\odot$) is reduced to a rather tight orbit ($a \lesssim 100\ R_\odot$). Such a configuration will consist of at least one stripped stellar core (WR star): BH-WR, WR-BH or WR-WR binaries.

Recently Kushnir et al. (2016); Zaldarriaga et al. (2017); Kushnir et al. (2017); Hotokezaka & Piran (2017c); Qin et al. (2018) investigated the strength and treatment of tides and they argued that WR stars may potentially be significantly spun up if placed in very close binaries with massive companions (e.g., immediate progenitors of BH-BH mergers).

To determine the upper limit to the spins produced by tidal locking, we ignore the orbital evolution and assume that the entire star is tidally locked to the orbit (see the discussion below), i.e., rigidly rotating. The orbital period then provides the spin period of the WR star and implementing these spin periods into our stellar models, we can calculate the angular momentum in the star and use this angular momentum to obtain the spin period of the collapsed star, assumed to be the BH spin. Figure 4.5 shows the resultant black-hole spin magnitudes for our $Z = 0.014$ and $Z = 0.0004$ MESA models. For most of the models with orbital periods in the range $P_{\rm orb} = 0.1 - 1.3$ d, the resultant BH spin magnitude can be fit by an exponential:

$$a_{\rm spin} = e^{-0.1(P_{\rm orb}/P_0 - 1)^{1.1}} + 0.125, \tag{4.15}$$

where $P_{\rm orb}$ is the orbital period in seconds and $P_0 = 4000$ s. For systems with orbital periods below 0.1 d, the resultant BH spin is maximal. For systems with orbital periods longer than $\sim 1.3$ d, tidal locking takes longer than the duration of the relevant evolutionary phase and there is no significant spin-up (in which case the tidal spin-up is ignored). The fit with eq. 4.15 is shown as the black curve in Figure 4.5.

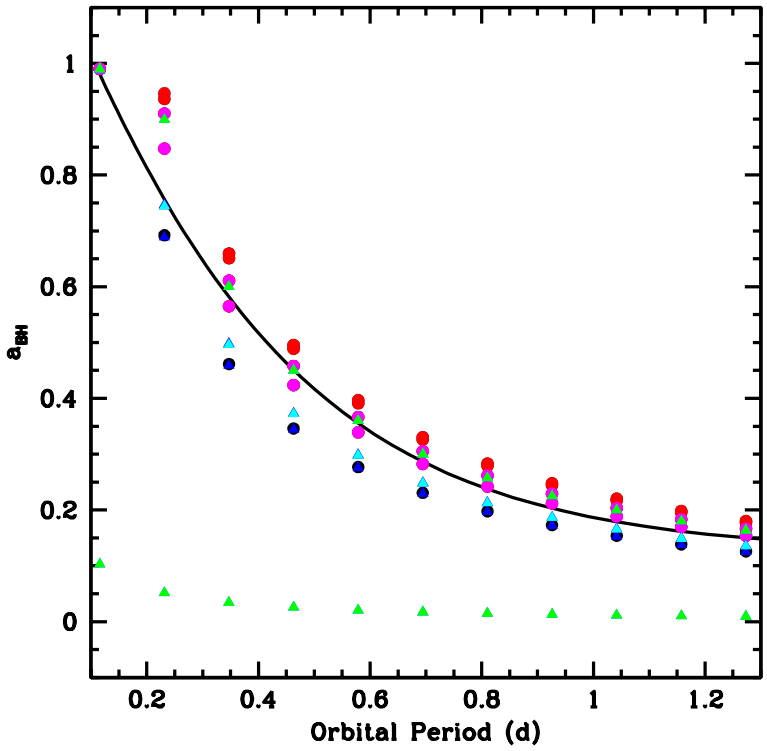


FIGURE 4.5: Black hole spin magnitudes as a function of the orbital period for our $Z = 0.014$ (circles) and $Z = 0.0004$ (triangles) MESA models. The color coding corresponds to the black hole remnants with masses: $M_{\rm BH} < 15\,M_\odot$ (black/blue), $15\,M_\odot < M_{\rm BH} < 30\,M_\odot$ (cyan/red), $M_{\rm BH} > 30\,M_\odot$ (green/magenta). Binary systems with short orbital periods: $0.1 - 1.3$d and WR stars will produce BHs with broad range of spin magnitudes: $0.15 - 1$. Systems with orbital periods below 0.1d form black holes from tidally locked WR stars, and the BH spins are maximal. Binaries with an orbital period above 1.3d produce BHs with spins below 0.2 and typically are not tidally locked at all. A set of the most massive, lowest-metallicity stars have such dense cores that tidal spin-up does not dramatically increase their angular momentum and these stars require orbital periods of less than 0.1d to have spin values above 0.1 (lower set of green triangles). However, we ignore this fact, and let these cores to be spun-up to estimate the maximal effect of tidal interactions in our models (higher set of green triangles). The black curve shows our fit to the BH spin magnitude as a function of orbital period.

Note that the proposal by Kushnir et al. (2016); Zaldarriaga et al. (2017); Kushnir et al. (2017); Hotokezaka & Piran (2017c) according to which every BH formed from a WR star subject to tidal interactions is spun-up to maximum ($a_{\rm spin} = 1$) is subject to three caveats. First, for systems that are undergoing tidal synchronization it is assumed that the BH is formed with a maximal spin without close scrutiny of the WR star structure and its evolution under strong tidal interactions. Second, the scheme ignores the fact that WR wind mass–loss (depending on metallicity of the WR star) may widen the system pushing it into a regime where synchronization is not maintained. Third, the tidal locking of the WR star pumps orbital energy into the WR star spin and thus causes the orbit to decay. This may lead to a merger of a WR star with its companion barring the formation of a

BH-BH binary. A detailed analysis of this complex interplay of stellar structure, stellar winds, and tidal interactions in the context of long Gamma Ray Bursts and BH-BH formation was presented by Detmers et al. (2008) and by Qin et al. (2018). In particular, Detmers et al. (2008) found that the majority of close BH-WR systems that are subject to strong tidal interactions either evolve to long periods (for high metallicity) or undergo a component merger before the BH-BH formation (for low metallicity). On the other hand, Qin et al. (2018) found that most close BH-WR systems will increase their periods resulting in a wide range of secondary BH spins ($a_{\rm spin} = 0 - 1$). In the light of these detailed calculations, our adopted simple model (see eq. 4.15) resembles the Qin et al. (2018) scheme and allows for a broad range of BH spin magnitudes if the WR star forming a BH is a subject to strong tidal interactions. We should stress that we use this model only as an alternative to our standard assumption according to which the effect of tidal spin-up in close binaries on the BH natal spin magnitude is ignored (as we use single stellar models to estimate natal BH spins; see Sec. 4.2.1).

Recently, Bavera et al. (2020) updated some of the Qin et al. (2018) calculations. One should note that these studies follow the angular momentum transport in stars only during the WR stage that will form the second-born BH in BH-BH merger. Additionally, it is assumed that the first BH is born with zero spin ($a = 0$) and that the WR star that will form the second BH is also born spinless. Such simplifying assumptions allow to match LIGO/Virgo BH-BH effective spins which are mostly consistent with zero. However, it was only tested for initially non-spinning WR stars, and therefore did not take into account the fact that for inefficient angular momentum transport and high initial stellar rotation, WR stars can be born with high spins. Then for high-spinning WR stars and for inefficient angular momentum transport a significant fraction of the second-born BHs would have high spins independent of tidal interactions. This is demonstrated by our models that employ inefficient (Geneva) angular momentum transport, in which BHs (both first-born and second-born) may have high spins (see Fig. 4.1 and Fig. 4.18).

### 4.2.6 Cosmic Star Formation History and Metallicity Evolution

Starting from 2016 (e.g., Belczynski et al. (2016b)) we have been using the cosmic star formation density (SFRD) determinations from Madau & Dickinson (2014), which are based on a number of deep UV and infrared galaxy surveys. We refer to this SFRD as the “old SFRD" formula. Here, we adopt two best-fitting comoving SFRDs from Madau & Fragos (2017), which update the previous formula by better reproducing a number of recent $4 < z < 10$ results:

$$sfr(z) = \mathcal{K}_{\rm IMF} 0.015 \frac{(1.0+z)^{2.6}}{1.0 + ((1.0+z)/3.2)^{6.2}}\ {\rm M}_\odot\ {\rm Mpc}^{-3}\ {\rm yr}^{-1}. \tag{4.16}$$

The correction factor $\mathcal{K}_{\rm IMF}$ adjusts the SFRD for the assumed IMF to the Salpeter IMF (i.e. $\mathcal{K}_{\rm IMF;Salpeter} = 1.0$). In this work we adopt a three component broken power-law Kroupa IMF with $\alpha_3 = -2.35$ (see App. 4.A.7 for details), for which the correction factor is $\mathcal{K}_{\rm IMF;Kroupa} \approx 0.66$ (Madau & Fragos, 2017).

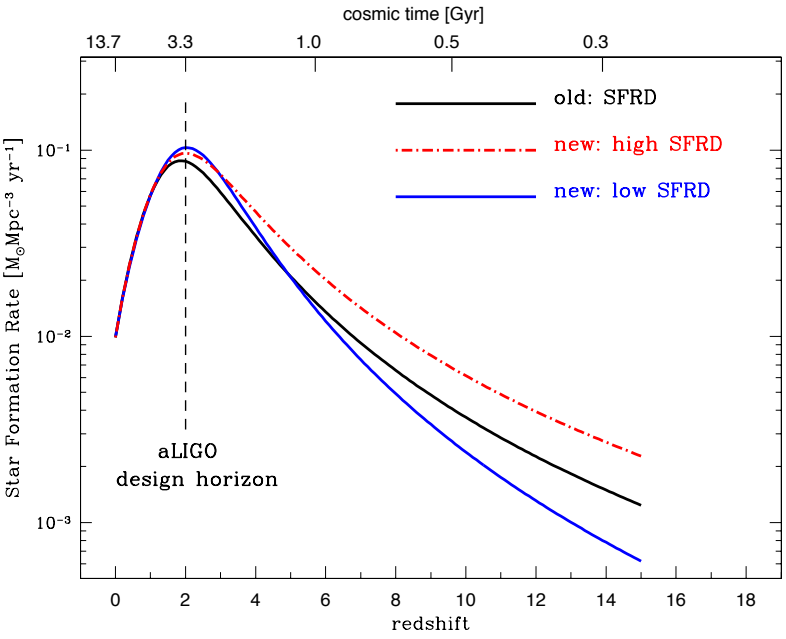


FIGURE 4.6: The cosmic star formation histories adopted in our modeling (see Sec. 4.2.6 for details). Note how the different SFRDs agree at low redshifts ($z \lesssim 2$), while they disagree by as much as a factor of three at earlier epochs.

We refer to the SFRD given by Eqn. 4.16 as to the "low SFRD", since it is based on a conversion from luminosity density to SFRD in which all published galaxy luminosity functions (LFs) have been conservatively integrated down to the same limiting luminosity of $0.03\,L_*$, where $L_*$ is the characteristic luminosity of a Schechter function. For completeness, in the following we shall also provide results for a "high" model in which the comoving SFRD is increased at high redshifts to account for a steep faint end of the LF:

$$sfr(z) = \mathcal{K}_{\rm IMF} 0.015 \frac{(1.0+z)^{2.7}}{1.0 + ((1.0+z)/3.0)^{5.35}}\ {\rm M}_\odot\ {\rm Mpc}^{-3}\ {\rm yr}^{-1}. \tag{4.17}$$

We will refer to this formula as the "high SFRD". These expressions bracket uncertainties in the contribution to the early SFRD by galaxies fainter than −16 mag, but agree at $z < 2$. Our adopted SFRDs are shown in Figure 4.6.

Our modeling of the metallicity of the star-forming gas has also been updated as follows. In previous calculations, we used the evolving mean cosmic metallicity $Z(z)$ from Madau & Dickinson (2014), which is the ratio between the total mass density of heavy elements produced over cosmic time and the cosmic baryon density. This quantity had to be increased by 0.5 dex to better account for various supernovae and GRB observations (Belczynski et al., 2016b). At each redshift $z = 0 - 15$ we further assumed that the distribution of $\log(Z/\,Z_\odot)$ was a Gaussian centered at the average metallicity and with a dispersion of $\sigma = 0.5$ dex. Stellar populations (Population I/II stars) with various metallicities were subsequently evolved, to check whether they produce NS-NS, BH-NS or BH-BH mergers detectable by LIGO/Virgo for a given instruments' sensitivity (see Sec. 4.A.8).

This approach does not properly describe the metallicity evolution of the star-forming gas within galaxies, as only a small fraction of the baryons in the Universe are polluted with heavy elements and take part in the baryon cycle of galaxy evolution (e.g. Chruslinska & Nelemans, 2019a). Our

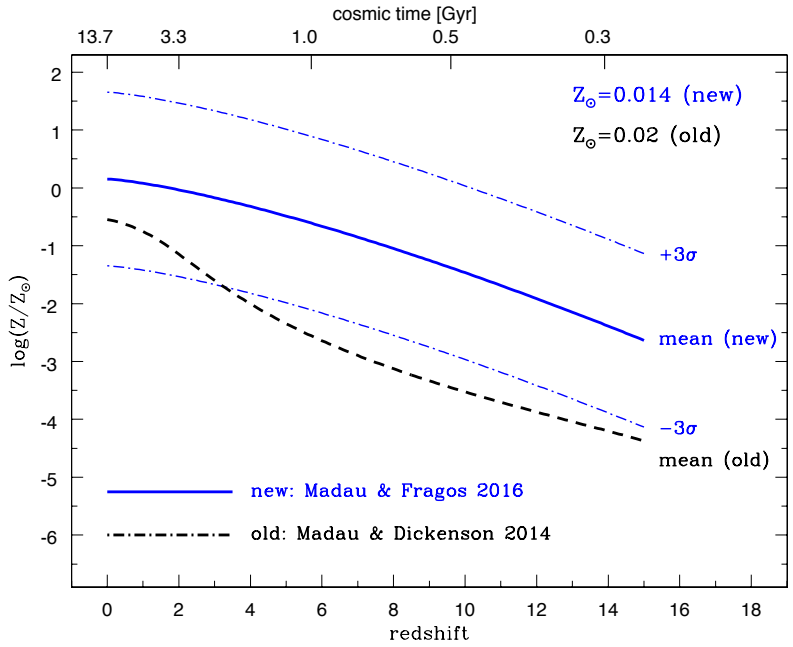


FIGURE 4.7: Stellar mass-weighted gas-phase metallicity versus redshift, $Z(z)$. At every epoch, we adopted a Gaussian distribution of $\log(Z/\,Z_\odot)$, centered at the mean metallicity and with dispersion $\sigma = 0.5$ dex. Note that the new metallicity for the star forming gas is noticeably higher than the mean cosmic metallicity adopted in the past (see Sec. 4.2.6).

improved calculations follow Madau & Fragos (2017). The gas-phase oxygen abundance is known to correlate strongly with the total stellar mass of star-forming galaxies: this "mass-metallicity relation" (MZR) has been shown to extend down to low-luminosity galaxies with stellar masses $\sim 10^6\ M_\odot$ (Berg et al., 2012) and out to redshift 3.5 (Maiolino et al., 2008). Numerical modeling by Zahid et al. (2014) suggests that the MZR originates from a more fundamental, universal relationship between the metallicity and the stellar-to-gas mass ratio that is followed by all galaxies as they evolve. We have assumed that the Zahid et al. (2014) MZR holds at all redshifts, and integrated this relation over the evolving galaxy stellar mass function at $0 < z < 7$ to compute a mean stellar mass-weighted gas-phase metallicity (see Madau & Fragos 2017 for details and references) as:

$$\log(Z/\,Z_\odot) = 0.153 - 0.074 z^{1.34}. \tag{4.18}$$

As before, we assume the same distribution of $\log(Z/Z_\odot)$, but centered around this new average. Note that this is a simplification and this distribution may not be symmetric (Chruslinska & Nelemans, 2019a). Recently, Chruslinska & Nelemans (2019b) provided an observation-based distribution of the star formation rate density over metallicities and redshifts and discussed the uncertainty of this distribution. We note that the metallicity distribution used in our paper peaks at similar metallicities as the high-metallicity extreme reported by those authors at $z \lesssim 3$ and at noticeably higher metallicities at $z > 3$. However, at those high redshifts the distribution is poorly constrained by current observations.

There is no consensus on the value of solar metallicity, and no value within range $Z_\odot = 0.012 - 0.02$ can be rejected at the moment (Vagnozzi, 2017). In our models we use either $Z_\odot = 0.014$ or $Z_\odot = 0.02$. A comparison between the adopted old and new mean gas-phase metallicities versus redshift is shown in Figure 4.7.

### 4.2.7 CALCULATIONS

Our binary evolution calculations were performed with the upgraded population synthesis code `StarTrack` (Belczynski et al., 2002, 2008a). Improvements to the code include updates to the treatment of the common envelope (CE) evolution, compact object mass calculations including the effect of pair-instability pulsation supernovae and pair-instability supernovae, and new BH natal spin prescriptions (Sec. 4.2.1), among other upgrades (see Appendix 4.A.7).

We consider fourteen different realizations (models) of our classical isolated binary evolution to test whether it is possible to form LIGO/Virgo BH-BH mergers with the observed rates, masses and effective spins. The first two models correspond to our previous calculations with fallback-decreased, BH mass-dependent (M10) and high, mass-independent (M13) BH natal kicks with input physics listed in Table 4.2 and detailed in (Belczynski et al., 2016b,a).

The next four models include different input physics on mass transfer, BH accretion in the CE phase, and the approximation of effects of stellar rotation on the BH mass (see Appendix 4.A.7). These models include natal kicks which are fallback-decreased, BH mass-dependent (M20); small, BH mass-independent (M26; $\sigma = 70$ km s$^{-1}$); intermediate, BH mass-independent (M25; $\sigma = 130$ km s$^{-1}$); and high, BH mass-independent (M23; $\sigma = 265$ km s$^{-1}$).

The above six models employ BH natal spins adopted from the Geneva model with mild angular momentum transport in massive stars (eq. 4.3), SFRD and average metallicity evolution with redshift from Madau & Dickinson (2014), and high value of solar metallicity $Z = 0.02$. The next eight models represent our current update (2019) and tests of input physics.

M30 employs the rapid supernova engine model for NS/BH mass from Fryer et al. (2012) supplemented with weak PPSN (eq. 4.9), 1% neutrino mass loss at the BH formation and 10% neutrino mass loss at the NS formation (eq. 4.10), fallback-decreased, BH/NS mass-dependent, natal kicks (1D $\sigma = 265$ km s$^{-1}$), 50% non-conservative RLOF, 5% Bondi-Hoyle accretion during CE, inefficient accretion onto BH/NS during stable mass transfer and capture from stellar winds (Sec. 4.2.4), BH natal spins from MESA (eq. 4.4), SFRD and average metallicity evolution from Madau & Fragos (2017) (eqs. 4.16 and 4.18), and we adopt a low value for the solar metallicity $Z = 0.014$. In this model we do not take into account additional effects of rotation as is done in model M20, we use the standard stellar winds from Vink et al. (2001) with addition of LBV winds from Belczynski et al. (2010b), and we employ the initial binary parameters from Sana et al. (2012) as discussed in de Mink & Belczynski (2015a).

Models M33 and M35 are the same as model M30, but mass independent NS/BH natal kicks (not affected by fallback) are employed: high natal kicks with 1D $\sigma = 265$ km s$^{-1}$ (M33) and intermediate natal kicks with 1D $\sigma = 130$ km s$^{-1}$ (M35).

Model M40 is the same as model M30, but employs a different model for BH spins: Fuller model (eq. 4.5). Model M43 is the same as model M40, but it employs mass independent NS/BH natal kicks with 1D $\sigma = 265$ km s$^{-1}$.

Model M50 is the same as model M30, but employs mass loss rates reduced to 30% for all the stars (see Sec. 4.A.7 for a justification).

Model M60 is the same as model M30, but employs strong PPSN (eq. 4.7) with 10% neutrino mass loss for both BH and NS.

Model M70 is the same as model M30, but employs moderate PPSN (eq. 4.8).

Models that allow CE with HG donors will be marked as submodels MXX.A, while models that do not allow CE with HG donors will be marked as as MXX.B (Belczynski et al., 2007).

In all models we assume BH natal kicks to be randomly oriented, thus generating BH spin misalignments with respect to the orbital angular momentum. Note that our models are by no means exhaustive in terms of probing the evolutionary uncertainties. However, they allow us to test the key parameters that set BH spin magnitudes and misalignments, and thus the effective spin: angular momentum transport in massive stars, accretion onto the BH and its progenitor, tidal interactions and BH natal kicks. Table 4.2 gives an overview of the models, and in Appendix 4.A.7 we describe the details of our binary population synthesis calculations.

Table 4.2: Binary evolution models

| Model | Main features |
|---|---|
| **M10** | 2016 standard input physics:<br>– rapid SNa BH masses Fryer et al. (2012)<br>– with strong PPSN and with PSN<br>– 10% neutrino mass loss at BH/NS formation<br>– low-to-no BH natal kicks (set by fallback)<br>– high NS kicks: $\sigma$ = 265 km s$^{-1}$ with fallback<br>– 50% non-conservative RLOF<br>– 10% Bondi-Hoyle accretion onto NS/BH in CE<br>– efficient accretion onto BH in stable MT/winds<br>– no effects of rotation on stellar evolution[a]<br>– initial binary parameters: Sana et al. (2012)<br>– massive star winds: Vink et al. (2001) + LBV[b]<br>– BH spins: Geneva models (eq. 4.3)<br>– SFRD($z$) and $Z(z)$: Madau & Dickinson (2014)<br>– solar metallicity: $Z_\odot$ = 0.02 |
| **M13** | as in M10, but with:<br>– high BH/NS natal kicks: $\sigma$ = 265 km s$^{-1}$ |
| **M20** | modified input physics, as in M10, but with:<br>– 80% non-conservative RLOF (Sec. 4.A.7)<br>– 5% Bondi-Hoyle accretion onto NS/BH in CE<br>– rotation increases CO core mass (by 20%) |
| **M26** | as in M20, but with:<br>– small BH/NS natal kicks: $\sigma$ = 70 km s$^{-1}$ |
| **M25** | as in M20, but with:<br>– intermediate BH/NS natal kicks: $\sigma$ = 130 km s$^{-1}$ |

TABLE 4.2: Binary evolution models

| Model | Main features |
|---|---|
| **M23** | as in M20, but with:<br>– high BH/NS natal kicks: $\sigma$ = 265 km s$^{-1}$ |
| **M30** | 2019 standard input physics:<br>– rapid SNa BH masses Fryer et al. (2012)<br>– with weak PPSN and with PSN<br>– 1% neutrino mass loss at BH formation<br>– 10% neutrino mass loss at NS formation<br>– low-to-no BH natal kicks (set by fallback)<br>– high NS kicks: $\sigma$ = 265 km s$^{-1}$ with fallback<br>– 50% non-conservative RLOF<br>– 5% Bondi-Hoyle accretion onto NS/BH in CE<br>– inefficient accretion onto BH in stable MT/winds<br>– no effects of rotation on stellar evolution[a]<br>– initial binary parameters: Sana et al. (2012)<br>– massive star winds: Vink et al. (2001) + LBV[b]<br>– BH spins: MESA models (eq. 4.4)<br>– SFRD($z$) and $Z(z)$: Madau & Fragos (2017)<br>– solar metallicity: $Z_\odot$ = 0.014 |
| **M33** | as in M30, but with:<br>– high BH/NS natal kicks: $\sigma$ = 265 km s$^{-1}$ |
| **M35** | as in M30, but with:<br>– intermediate BH/NS natal kicks: $\sigma$ = 130 km s$^{-1}$ |
| **M40** | as in M30, but with:<br>– BH spins: Fuller model (eq. 4.5) |
| **M43** | as in M40, but with:<br>– high BH/NS natal kicks: $\sigma$ = 265 km s$^{-1}$ |
| **M50** | as in M30, but with:<br>– 30% of wind mass loss rates for all stars |
| **M60** | as in M30, but with:<br>– strong PPSN, 10% neutrino mass loss for BH/NS |
| **M70** | as in M30, but with:<br>– moderate PPSN |

NOTES:

[a] Stellar spins are followed (tides, magnetic braking, change of inertia), but rotation does not alter the star properties (He/CO core mass).

[b] Luminous Blue Variable winds: $1.5 \times 10^{-4}$ M$_\odot$ yr$^{-1}$.

The StarTrack population synthesis code is used to generate populations of BH-BH/BH-NS/NS-NS systems. The star's initial properties (mass and metallicity) are used to calculate stellar evolution. Binary interactions (mass gain/loss in RLOF and CE events) are taken into account through rejuvenation/de-rejuvenation in estimating the final stellar properties (mass and CO core mass) at the time of core-collapse, which are then used to obtain the NS/BH natal mass (see Appendix 4.A.3). In binary calculations we use non-rotating stellar models (Hurley et al., 2000). We record whether any of the binary components accreted significant amounts of mass ($\gtrsim 10\%$ of its own mass). If accretion occurred during main sequence, and if the accreting star was of low metallicity ($Z < 0.002$), we assume in models M20, M23, M25 and M26 that the star will produce a more massive CO core (by 20%), and thus a more massive NS/BH, to mimic the effects of increased mixing due to rapid rotation induced by accretion (see Appendix 4.A.7).

At BH formation we use single stellar models to estimate the BH natal spin magnitude through the CO-core mass-spin relations proposed in Section 4.2.1. In these estimates we assume that a star with a given CO core mass (as estimated from a binary evolution) forms a BH with spin given by single stellar models. This scheme ignores the effects of mass accretion on the stellar spin of the BH progenitor that may increase the BH's natal spin. Obviously this is far from perfect, and stellar rotation models will need to be fully integrated into binary population synthesis in the future. However, this is impossible at the moment due to the lack of stellar models with consistent input physics that would appropriately sample mass, metallicity and rotation for massive stars and naked stellar cores (as stellar cores are much more often exposed in binary evolution than is single star evolution).

Note also that we use moderately high initial stellar spins that assume 40% of break-up velocity in single stellar models. Depending on a mass and stellar structure of a model, this gives a range of $250 - 450$ km s$^{-1}$ initial rotation speeds at the equator (see Tab. 4.5 and 4.6). For comparison, the observed spins of massive stars show a bimodal distribution (Ramírez-Agudelo et al., 2013), with one large peak at $\sim 100$ km s$^{-1}$ and another small peak at $\sim 400$ km s$^{-1}$.

A first-born BH can accrete mass from its unevolved companion either during the RLOF/CE stages or from the companion's winds. These effects are included in our calculations, and the BH spin is increased accordingly. The second-born BH preserves its natal spin as it does not accrete mass. However, note that we allow for the possibility of the tidal spin up of BH progenitors and allow for significant increase of the BH spin as compared to BH spins that result from single stellar models (Sec. 4.2.5).

In all cases, we assume that the stellar spins are initially aligned ($\Theta_1 = \Theta_2 = 0$) with the orbital angular momentum of the main–sequence star binary. At BH formation we estimate the spin vector misalignment due to natal kicks. We allow for BH spin realignment neither during the mass transfer phases, nor by tidal interaction between the stars in a binary. Note that with this approach we may be overestimating the BH spin misalignment, but only for models with high to moderate BH natal kicks (see Sec. 4.2.2 for details).

## 4.3 RESULTS

We have estimated the double compact object merger rate densities, merger detection rates, merger masses, and BH-BH effective spins using the methods presented in Belczynski et al. (2016c,b) along with updates and revisions presented in the present study (see Sec. 4.2). In the following sections we will discuss some particular properties of our models. In our study, we do not exhaust the information that can be extracted from our models. Focusing on BH-BH mergers, we instead show some particular examples of what can be obtained with population synthesis modeling in context of the LIGO/Virgo sources. For now, we compare our models to the LIGO/Virgo observations showing that some models fit the data better than other, but only in terms of the observed allowed ranges of rates, masses and effective spins. Note that we do not yet attempt to match particular distributions' shapes (for BH masses and effective spins) or the rate of increase of merger rates with redshift. However, anyone interested in such comparisons can easily perform them on our models as we make them publicly accessible through our website `www.syntheticuniverse.org`.

### 4.3.1 BINARY EVOLUTION OF BH-BH MERGERS

In this section we present several examples of binary evolution leading to the formation of BH-BH mergers. In the framework of the Geneva model of angular momentum transport, it is challenging to explain mergers with very low effective spin parameters as lots of BHs are formed with high or moderate spin magnitudes (see Fig. 4.1). Yet, it is not impossible. Therefore, we show examples of evolution that can lead to the formation of merger resembling GW170104, which has one of the lowest measured effective spin parameters: $-0.24 < \chi_{\rm eff} < 0.13$ (90% confidence limits). In the framework of MESA angular momentum transport, it is challenging to explain mergers with moderate and high effective spin parameters as lots of BHs are formed with low spin magnitudes (see Fig. 4.2). Yet, we show that we can form mergers that are consistent even with GW170729, which is the merger that has the highest effective spin yet measured: $0.11 < \chi_{\rm eff} < 0.57$ (90% confidence limits).

#### 4.3.1.1 THE CASE OF GW170104

Here we present a proof-of-principle scenario demonstrating that isolated binary evolution with the Geneva model of angular momentum transport can form a BH-BH merger with BH masses and effective spin compatible with LIGO's observation of GW170104, in particular, its very low effective spin.

Within our models with the Geneva angular momentum transport (M10, M13, M20, M23, M25, M26) we search for systems with BH masses and effective spins within LIGO's 90% credible limits: $25.4 < M_{\rm BH1} < 38.2\ M_{\odot}$, $15.6 < M_{\rm BH2} < 25.0\ M_{\odot}$, $-0.24 < \chi_{\rm eff} < 0.13$. The upper bound on $\chi_{\rm eff}$ may actually be as high as $\chi_{\rm eff} \approx 0.2$ (Appendix 4.A.5). For example, within model M20 it is indeed possible to form a BH-BH merger resembling GW170104: $M_{\rm BH1} = 33.3\ M_{\odot}$, $M_{\rm BH2} = 24.7\ M_{\odot}$, $\chi_{\rm eff} = 0.09$. The evolutionary history of such a merger is presented in Figure 4.8.

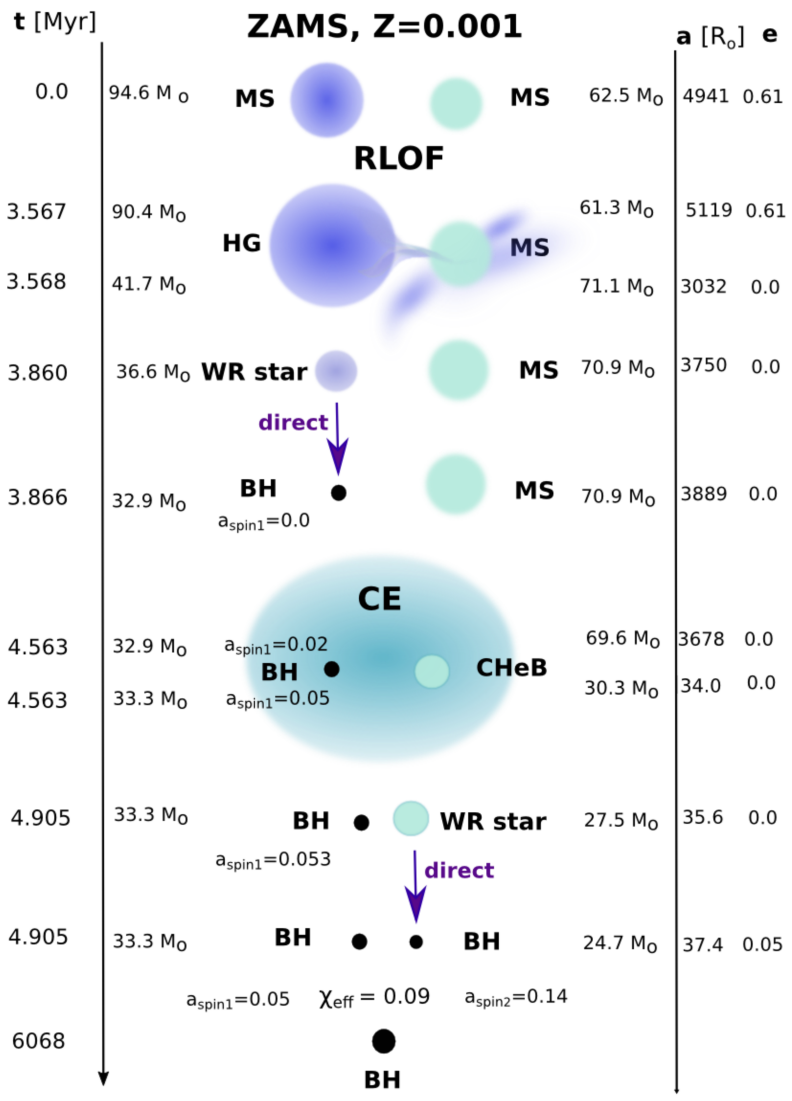


FIGURE 4.8: Example of a possible route leading to the formation of a BH-BH merger similar to GW170104. This example follows the classical isolated binary evolution channel. In this model (M20.B) we employ the Geneva BH natal spins, assume that massive BHs do not receive natal kicks and that their spins are aligned with the binary angular momentum ($\Theta_1 = \Theta_2 = 0°$), producing an upper limit on the effective spin parameter ($\chi_{\rm eff}$). Yet, this system has $\chi_{\rm eff} = 0.09$, within LIGO's 90% credible limits for GW170104 [−0.24:0.13]. Both BH masses are also within the limits: $M_{\rm BH1} = 31.0\,M_\odot$ [25.4:38.2] and $M_{\rm BH2} = 20.1\,M_\odot$ [15.6:25.0].

Note that model M20 is rather conservative regarding assumptions on natal kicks, which are strongly suppressed by the fallback material. Massive BH spins are mostly aligned with the binary angular momentum ($\cos\Theta_1 = \cos\Theta_2 = 1$), thus maximizing the value of the effective spin. For all the other models (with the exception of M10) the BH spins will tend to be misaligned, decreasing the value of the effective spin and making it even easier to produce systems with low effective spin values (as observed in GW170104).

Although the BH spin can be modified by accretion from a binary companion, the amount of matter accreted in our calculations is very modest, and the accretion-induced spin-up of BHs is not significant. In the example shown in Figure 4.8, the first-born massive BH forms with no spin ($a_{\rm spin1} = 0$), then it accretes very little mass from its MS companion wind increasing its spin only to $a_{\rm spin1} = 0.02$. Most of the accretion occurs during the CE phase ($0.4\,M_\odot$) and the BH increases its spin to $a_{\rm spin1} = 0.05$. Finally, the BH accretes very little mass from its Wolf-Rayet star companion wind, increasing its spin to its final value of $a_{\rm spin1} = 0.053$. The second-born BH

forms with a natal spin of $a_{\rm spin1} = 0.14$ and it is not spun up, as it does not accrete any material. In other words we predict that LIGO/Virgo observations of BH-BH mergers will probe the natal BH spin distribution, up to evolutionary effects of order 0.05 in dimensionless spin.

Note also that this particular system is not subject to a potential WR-star tidal spin-up in a BH-WR binary (the last evolutionary stage before the BH-BH formation). The system separation at this stage ($a \approx 35\ R_\odot$) is too large for the tides to effectively spin-up WR star ($P_{\rm orb} > 1.3$d, see Sec. 4.2.5). The full details of this evolutionary example are given in Appendix 4.A.4.

#### 4.3.1.2 THE CASE OF GW170729

In a subset of our binary evolution models M30.A/B, M33.A/B, M35.A/B, M50.A/B, M60.A/B, and M70.A/B the natal BH spins are obtained from stellar models calculated with the MESA code under the assumption of efficient angular momentum transport in the stellar interiors (see Sect. 4.2.1 and Fig. 4.2). In this framework, the initial BH spins are always small ($a_{\rm spin} \lesssim 0.15$), mostly independent of the progenitor mass and metallicity. Small natal BH spin values can in principle be increased during further evolution as result of mass accretion. However, in the isolated binary evolution channel for BH-BH mergers, the first formed BH can only accrete mass during the CE inspiral and through accretion of the wind from its stellar companion. We find that, in our simulations, neither of those two processes leads to a significant increase of the BH spin which is primarily the consequence of: *(i)* inefficient (5-10%) Bondi-Hoyle accretion rate onto BH in the short-lived CE phase (e.g., MacLeod et al., 2017) and *(ii)* small wind mass loss rates from low metallicity stars (Vink et al., 2001). This means that the small natal BH spins in the framework of efficient angular momentum transport in stellar interiors do result in small effective spin values of BH-BH mergers (typically $\chi_{\rm eff} \lesssim 0.25$).

Here we present a proof-of-principle scenario demonstrating that even the BH-BH merger event with the largest effective spin value reported to date (GW170729, $\chi_{\rm eff} = 0.36^{+0.21}_{-0.25}$) can be reconstructed in the isolated–binary evolution channel with small natal BH spin values given by eq. 4.4. Within our models with efficient (MESA) angular momentum transport we search for systems with BH masses and effective spin within LIGO's 90% credible limits for GW170729: $40.4 < M_{\rm BH1} < 67.2\ M_\odot$, $24.2 < M_{\rm BH2} < 43.4\ M_\odot$, $0.11 < \chi_{\rm eff} < 0.57$. For example, within the model M30.B it is indeed possible to form a BH-BH merger resembling GW170729: $M_{\rm BH1} = 55.0\ M_\odot$, $M_{\rm BH2} = 32.8\ M_\odot$, $\chi_{\rm eff} = 0.137$. The evolutionary history of such a merger is presented in Figure 4.9. Both the BHs where formed in direct collapse with small but non-zero natal spins ($a_{\rm spin1} = 0.093$ and $a_{\rm spin2} = 0.073$). For reasons discussed above, the BH formed first accreted only a very modest amount of mass during binary evolution ($< 1.0\ M_\odot$), which led to an increase of its spin to $a_{\rm spin1} = 0.176$. The final effective spin of the merging BH-BH system is $\chi_{\rm eff} = 0.137$, and thus it is in (marginal) agreement with the 90% credible limits for GW170729.

It should be noted that the spin value for the secondary BH presented in the above example (Fig. 4.9; $a_{\rm spin2} = 0.073$) is most likely underestimated because this example neglects the potential tidal spin-up of the secondary WR star (direct progenitor of the second BH) during the BH-WR stage (see Sec. 4.2.5). Since the orbital separation during the BH-WR phase is very small

($a \approx 7\ R_\odot$), tidal interactions are expected to be efficient in spinning-up the WR star. In fact, in the case of this system the timescale of WR tidal synchronization as approximated by Zaldarriaga et al. (2017, see our Eq. 4.15) is only $t_{\rm sync} \approx 11$ yr, which is a few orders of magnitude shorter than the duration of BH-WR stage ($\sim 2 \times 10^5$ yr). Thus, the secondary WR star has most likely become fully synchronized with the orbit by the time it collapsed to form the second BH. If we assume that such a rapidly rotating WR star collapses into an also rapidly spinning BH ($a_{\rm spin2} = 1.0$) then the effective spin of the BH-BH merger in Fig. 4.9 would become $\chi_{\rm eff} = 0.484$, still well within the 90% credible limits for GW170729. The large range of $\chi_{\rm eff}$ values that spans from 0.137 to 0.484 encloses all the possible results of the uncertain process of tidal spin-up in BH-WR binaries and its effect on the secondary BH spin.

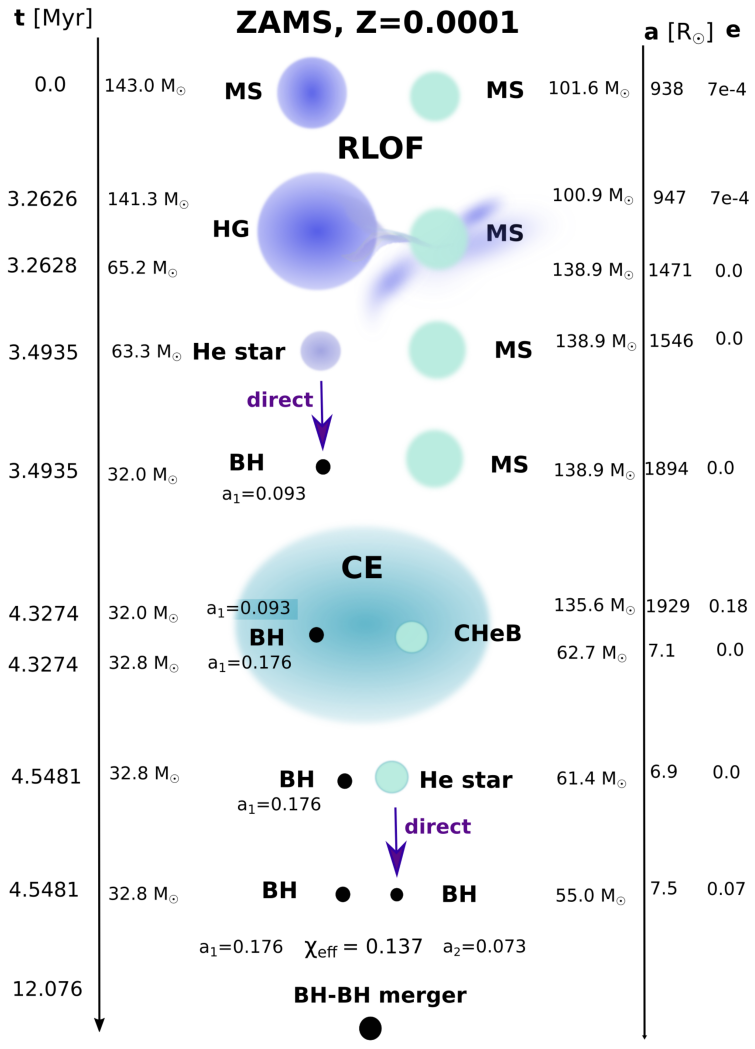


FIGURE 4.9: Example of a possible route leading to the formation of a BH-BH merger similar to GW170729. This example follows the classical isolated binary evolution channel. In this model (M30.B) we employ the MESA BH natal spins, assume that massive BHs do not receive natal kicks and that their spins are aligned with the binary angular momentum ($\Theta_1 = \Theta_2 = 0°$), producing an upper limit on the effective spin parameter ($\chi_{\rm eff}$). Note that given the small binary separation at the BH-WR stage ($a \approx 7\ R_\odot$), the WR star is most likely going to become tidally synchronized (see Sec. 4.2.5). If we assume that the rapidly rotating WR star collapses into rapidly spinning BH ($a_{\rm spin2} = 1$) then the effective spin of the presented system would increase from $\chi_{\rm eff} = 0.137$ (no tidal spin-up; presented on the Figure) to $\chi_{\rm eff} = 0.484$ (full tidal spin-up). Both values are within the LIGO/Virgo 90% credible limits for GW170729 [0.11:0.57]. Both BH masses are also within the limits: $M_{\rm BH1} = 50.6\ M_\odot$ [40.4:67.2] and $M_{\rm BH2} = 34.3\ M_\odot$ [24.2:43.4].

We caution that the simple fact that a particular BH-BH system can be reproduced in a given binary evolution channel does not in itself guarantee consistency between population synthesis results and observations. Such consistency can only be tested by comparing the entire populations. We discuss the distributions of BH-BH mergers parameters obtained in our simulation in the following sections.

### 4.3.2 MERGER RATE DENSITY AND DETECTION RATE

Tables 4.3 and 4.4 summarize our predictions for the local (redshift $z \sim 0$) merger rate density, the detection rate for LIGO/Virgo's mid-high sensitivity curve (that may be taken as an approximation of O3 observing run) along with the maximum horizon redshift for the best located/oriented source in a given merger type category: NS-NS, BH-NS, BH-BH.

The predicted BH-BH merger rate densities vary between 1.24 and 1368 $\mathrm{Gpc^{-3}\ yr^{-1}}$ across our models. A number of models (M13.A, M23.A/B, M25.B, M26.B, M30.B, M33.A, M40.B, M43.A, M50.B, M60.B, M70.B) produce rates within the allowable range determined by the first 10 LIGO/Virgo detections (9.7–101 $\mathrm{Gpc^{-3}\ yr^{-1}}$: Abbott et al. (2019b)). The predicted NS-NS merger rate densities vary between 49.3 and 524 $\mathrm{Gpc^{-3}\ yr^{-1}}$ for the tested models. A number of models (M10.A,M13.A, M20.A, M23.A, M25.A, M26.A, M30.A/B, M33.A, M35.A/B, M40.A/B, M43.A, M50.A, M60.A/B, M70.A/B) produce rates within allowable range determined by the first LIGO/Virgo detection (110–3840 $\mathrm{Gpc^{-3}\ yr^{-1}}$: Abbott et al. (2019b)). The predicted BH-NS merger rate densities vary between 0.48 and 297 $\mathrm{Gpc^{-3}\ yr^{-1}}$ for the tested models. So far all the models produce rates within an upper limit determined by the non-detection in the O1/O2 LIGO/Virgo runs ($< 610\ \mathrm{Gpc^{-3}\ yr^{-1}}$: Abbott et al. (2019b)).

Figure 4.10 shows the intrinsic BH-BH merger rate density (not weighted by LIGO/Virgo detection probability) evolution with redshift for models M10.B and M30.B that employ different star formation rate and cosmic evolution of metallicity. We note that model M10.B which employs $Z(z)$ measured from stars generates higher (by factor of $\sim 5$ at low redshifts $z < 2$) rates than the model M30.B that employs $Z(z)$ as measured by the metallicity of star forming gas at any given redshift. The choice of $Z(z)$ is one of the most important factors affecting local (low $z$) merger rate densities for BH-BH mergers. This is because with decreasing metallicity we expect *(i)* an increase of the BH mass (Belczynski et al., 2010b) and *(ii)* an increase of the BH-BH merger formation efficiency per unit mass (Belczynski et al., 2010a). Therefore, models with lower $Z(z)$ result in higher BH-BH merger rates.

Note that the difference in SFRD($z$) between the two models does not affect significantly the rates as the differences in star formation are relatively small (see Fig. 4.6). Note also that for the two updated (new) models of the SFRD($z$), there is virtually no difference in the BH-BH merger rates at low redshifts ($z < 2$), while differences ($\sim$ factor of a few) begin to appear only at higher redshifts. For our updated models we use a SFRD($z$) with low star formation at high redshifts. This particular choice does not affect any of our conclusions for LIGO/Virgo as these instruments are not expected to probe sources at high redshifts ($z > 2$).

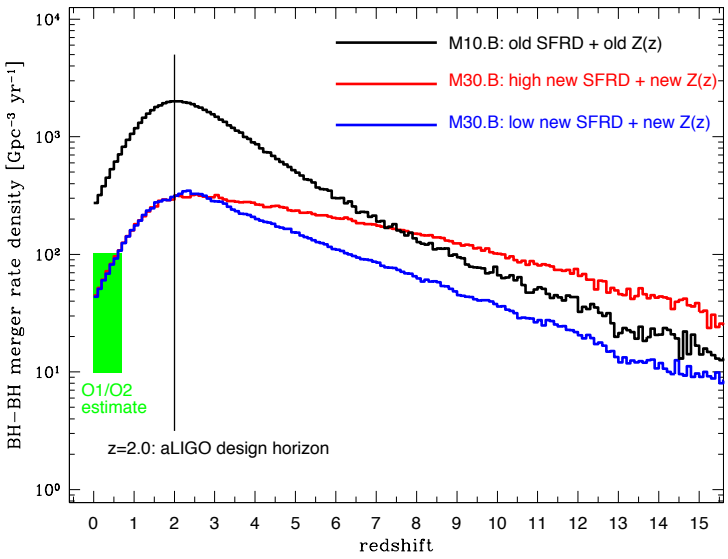


FIGURE 4.10: Merger rate density of BH-BH mergers from Population I/II stars. We employ models M10.B and M30.B to illustrate the effects of our assumptions on the star formation rate and cosmic metallicity evolution on the BH-BH mergers. LIGO/Virgo O1/O2 constraint on the BH-BH merger rate in local Universe is also shown. Note that the decrease of the BH-BH merger rate density at low-redshift (from old to new models) is due to the average metallicity of stars at any given redshift in old models, being much lower than the average metallicity of stars in new models (see Sec. 4.3.2 for details).

There are different PPSN models employed in models M10.B (strong PPSN; low maximum BH mass) and M30.B (weak PPSN; high maximum BH mass). However, this does not affect significantly the intrinsic merger rate density in a given volume that is presented in Figure 4.10. This is because the number of BH-BH binaries is about the same in each of the PPSN models. However, the differences in BH masses affect notably the detection rates. For example, compare the detection rate of BH-BH mergers in models M30.A/B and M60.A/B that differ only by PPSN input physics (see Tables 4.3 and 4.4).

Figure 4.11 demonstrates the effects of the CE phase and natal kicks on the intrinsic BH-BH merger rate density. We use a sequence of four models with exactly the same input physics that differ only in various assumptions about the CE phase and natal kicks. With the optimistic approach to the CE and natal kicks (that allows for survival of the CE phase with HG donors and very low or zero BH natal kicks; model M30.A) the local ($z = 0$) merger rate density is relatively high: $\mathcal{R}_{\rm BHBH} = 641$ Gpc$^{-3}$ yr$^{-1}$. When we apply a more restrictive approach to the CE phase, but keep the same natal kicks as above (CE survival not allowed for HG donors; model M30.B) then we note a significant decrease in the rate: $\mathcal{R}_{\rm BHBH} = 43.7$ Gpc$^{-3}$ yr$^{-1}$. Adding to the above moderate natal kicks and keeping the restrictive CE-phase approach (model M35.B) decreases the rate further: $\mathcal{R}_{\rm BHBH} = 4.69$ Gpc$^{-3}$ yr$^{-1}$. An additional increase of natal kicks (model M33.B) with the same restrictive CE-phase approach, brings the rate to a very low value: $\mathcal{R}_{\rm BHBH} = 1.37$ Gpc$^{-3}$ yr$^{-1}$. Comparison with the LIGO/Virgo rate estimate shows that models M30.A, M35.B, M33.B are excluded. It means, that within our limited sample of evolutionary models, some combinations of CE-phase approach and natal kicks can be excluded as not likely. For example, moderate to high natal kicks and a restrictive CE-phase treatment are an unlikely combination. Note, however, that we cannot draw conclusions about the rates based solely on the natal kicks or solely on the

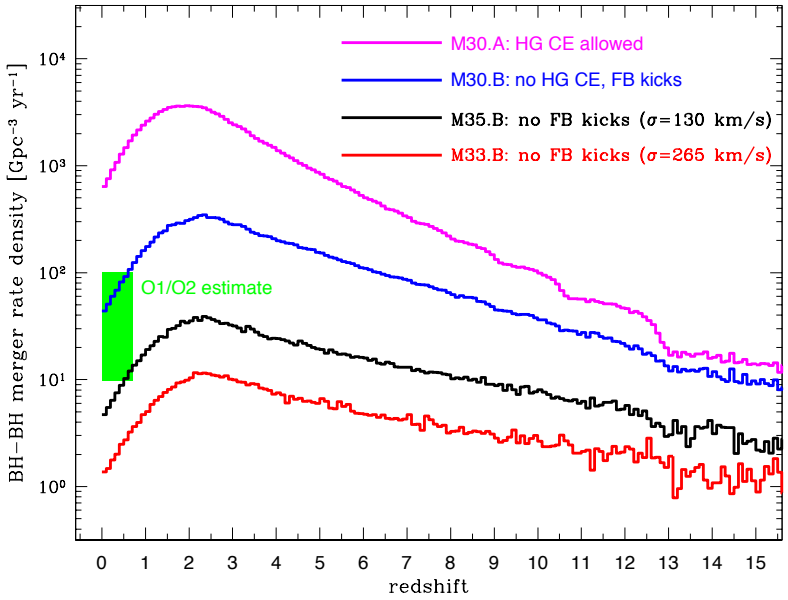


FIGURE 4.11: Merger rate density of BH-BH mergers for various assumptions about the common envelope and BH natal kicks. The possibility of development and survival of the CE phase with a Hertzsprung gap donor, increases the low-redshift BH-BH merger rate density by $\sim$ 1 order of magnitude: compare models M30.A and M30.B (a similar effect is found for other models). Natal kicks tend to decrease the BH-BH merger rate density by $\sim$ 1.5 order of magnitude: from fall-back attenuated natal kicks (almost no BH natal kicks: model M30.B) to full scale BH natal kicks (as high as observed for Galactic single pulsars: model M33.B). Note the degeneracy between the tested input physics; by applying high natal kicks we can bring model M30.A down to agree with the LIGO/Virgo estimate, or by allowing for HG CE we can bring models M35.B and M33.B up to also match the LIGO/Virgo constraint.

CE-phase approach, because the results are degenerate with respect to these two major factors. For example, if we apply the optimistic CE-phase approach to models with moderate to high natal kicks then both these models fit within (or very close to) the LIGO/Virgo rate estimate. In particular, we find $\mathcal{R}_{\rm BHBH} = 109$ Gpc$^{-3}$ yr$^{-1}$ for model M35.A (moderate natal kicks and optimistic CE=phase) and $\mathcal{R}_{\rm BHBH} = 19.5$ Gpc$^{-3}$ yr$^{-1}$ for model M33.A (high natal kicks and optimistic CE-phase).

Figure 4.12 shows the intrinsic merger rate density for all types of mergers: NS-NS, BH-NS and BH-BH. As an example we use model M30.A/B. As discussed above, the local BH-BH intrinsic merger rate density for model M30.B ($\mathcal{R}_{\rm BHBH} = 43.7$ Gpc$^{-3}$ yr$^{-1}$) is within the LIGO/Virgo estimate. The predicted local BH-NS intrinsic merger rate density for model M30.B ($\mathcal{R}_{\rm BHNS} = 11.1$ Gpc$^{-3}$ yr$^{-1}$) is within the LIGO/Virgo upper limit. The local intrinsic merger rate density for NS-NS systems is only just above LIGO/Virgo 90% level lower limit for model M30.B ($\mathcal{R}_{\rm NSNS} = 122$ Gpc$^{-3}$ yr$^{-1}$), while it is well within the LIGO/Virgo estimate for model M30.A ($\mathcal{R}_{\rm NSNS} = 426$ Gpc$^{-3}$ yr$^{-1}$).

Detection rates (Tables 4.3 and 4.4) are based on each source merger redshift, its mass (we use mass dependent waveforms for each merger) and take into account the LIGO detector

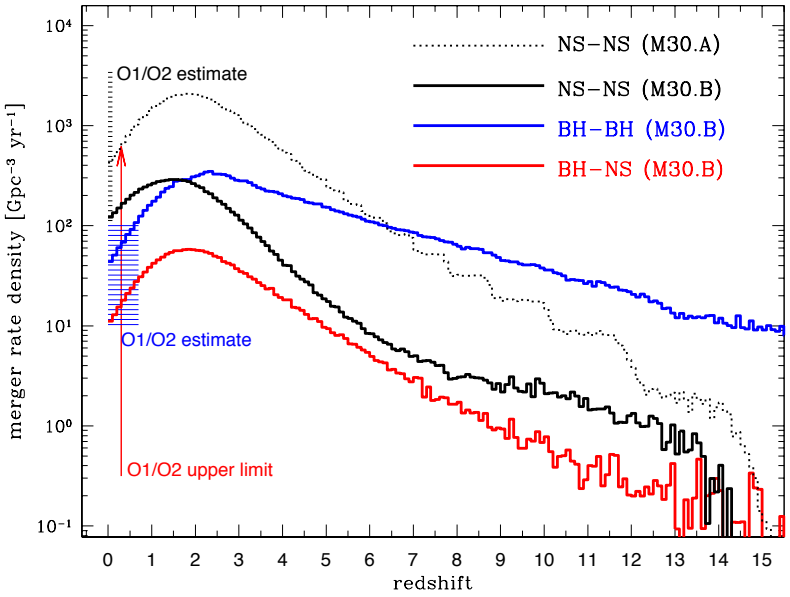


FIGURE 4.12: Merger rate density of NS-NS, BH-NS and BH-BH mergers for model M30. For comparison, we show LIGO/Virgo O1/O2 constraints on merger rate densities. While actual estimates are available for the BH-BH and NS-NS mergers, only an upper limit is available for the BH-NS mergers from O1/O2 data (but see Sec. 4.A.9). Note that the presented merger rate densities are consistent with the LIGO/Virgo estimates.

antenna (peanut-shaped) pattern. For this particular estimate we employ LIGO sensitivity labeled "mid-high" that approximately corresponds to the current (O3) LIGO sensitivity (for details see Appendix 4.A.8). The detection rate is then a convolution of the merger rate density (and its change with redshift within the LIGO horizon for a given source type) and the mass distribution of given source type (NS-NS, BH-NS, BH-BH). For clarity, we list the horizon redshift for the best located/oriented (directly overhead source with an orbital plane perpendicular to the line of sight) source within each merger type. This naturally corresponds to the furthest detectable redshift (distance) of the most massive source within each merger type found in our simulations.

TABLE 4.3: Local merger rate densities and LIGO/Virgo detection rates.

| Model | Merger | Rate density[a] [Gpc$^{-3}$ yr$^{-1}$] | detection rate[b] [yr$^{-1}$] | $z_{\rm hor}$[c] |
|---|---|---|---|---|
| **M10.B** | NS-NS | 65.2 | 0.289 | 0.081 |
| | BH-NS | 28.8 | 2.419 | 0.404 |
| | **BH-BH** | **274** | 536.2 | 0.961 |
| **M13.B** | NS-NS | 49.3 | 0.226 | 0.082 |
| | BH-NS | 2.43 | 0.246 | 0.397 |
| | **BH-BH** | **8.63** | 16.60 | 1.031 |
| **M20.B** | NS-NS | 84.3 | 0.358 | 0.081 |
| | BH-NS | 96.6 | 6.525 | 0.405 |
| | **BH-BH** | **469** | 783.7 | 0.955 |
| **M26.B** | NS-NS | 107 | 0.453 | 0.082 |
| | BH-NS | 42.4 | 2.880 | 0.401 |
| | **BH-BH** | **132** | 192.8 | 0.958 |
| **M25.B** | NS-NS | 105 | 0.447 | 0.081 |

TABLE 4.3: Local merger rate densities and LIGO/Virgo detection rates.

| Model | Merger | Rate density[a] [Gpc$^{-3}$ yr$^{-1}$] | detection rate[b] [yr$^{-1}$] | $z_{\rm hor}$[c] |
|---|---|---|---|---|
| | BH-NS | 17.2 | 1.486 | 0.426 |
| | **BH-BH** | **62.8** | 105.4 | 0.953 |
| **M23.B** | NS-NS | 53.0 | 0.225 | 0.080 |
| | BH-NS | 4.17 | 0.337 | 0.397 |
| | **BH-BH** | **16.6** | 26.29 | 1.024 |
| **M30.B** | NS-NS | 122 | 0.514 | 0.081 |
| | BH-NS | 11.1 | 0.800 | 0.433 |
| | **BH-BH** | **43.7** | 50.95 | 1.152 |
| **M35.B** | NS-NS | 143 | 0.608 | 0.081 |
| | BH-NS | 3.10 | 0.206 | 0.444 |
| | **BH-BH** | **4.69** | 6.627 | 1.152 |
| **M33.B** | NS-NS | 79.6 | 0.333 | 0.080 |
| | BH-NS | 0.48 | 0.031 | 0.392 |
| | **BH-BH** | **1.37** | 1.714 | 1.147 |
| **M40.B** | NS-NS | 122 | 0.508 | 0.081 |
| | BH-NS | 10.2 | 0.752 | 0.391 |
| | **BH-BH** | **39.2** | 42.98 | 1.152 |
| **M43.B** | NS-NS | 76.7 | 0.319 | 0.080 |
| | BH-NS | 0.61 | 0.044 | 0.381 |
| | **BH-BH** | **1.24** | 1.578 | 1.150 |
| **M50.B** | NS-NS | 93.2 | 0.395 | 0.081 |
| | BH-NS | 8.54 | 0.702 | 0.489 |
| | **BH-BH** | **64.2** | 133.4 | 1.153 |
| **M60.B** | NS-NS | 118 | 0.499 | 0.080 |
| | BH-NS | 12.1 | 0.817 | 0.363 |
| | **BH-BH** | **46.2** | 41.88 | 0.949 |
| **M70.B** | NS-NS | 120 | 0.505 | 0.081 |
| | BH-NS | 10.7 | 0.765 | 0.396 |
| | **BH-BH** | **43.9** | 51.37 | 1.107 |

NOTES:

[a] Local merger rate density at redshift $z = 0$ (note rate increase with $z$).

[b] Detection rate for LIGO/Virgo mid-high range (O3 proxy).

[c] Redshift for the most distant source detectable (best located/oriented).

Table 4.4: Local merger rate densities and LIGO/Virgo detection rates.

| Model | Merger | Rate density[a] [Gpc$^{-3}$ yr$^{-1}$] | detection rate[b] [yr$^{-1}$] | $z_{\rm hor}$[c] |
|---|---|---|---|---|
| **M10.A** | NS-NS | 230 | 1.022 | 0.083 |
| | BH-NS | 99.6 | 6.289 | 0.404 |
| | **BH-BH** | **1368** | 3464 | 0.973 |
| **M13.A** | NS-NS | 193 | 0.858 | 0.083 |
| | BH-NS | 23.3 | 1.179 | 0.396 |
| | **BH-BH** | **52.6** | 77.19 | 1.031 |
| **M20.A** | NS-NS | 260 | 1.094 | 0.082 |
| | BH-NS | 272 | 15.85 | 0.405 |
| | **BH-BH** | **1285** | 2765 | 0.973 |
| **M26.A** | NS-NS | 374 | 1.604 | 0.082 |
| | BH-NS | 297 | 15.78 | 0.402 |
| | **BH-BH** | **531** | 706.6 | 0.958 |
| **M25.A** | NS-NS | 310 | 1.333 | 0.082 |
| | BH-NS | 152 | 8.272 | 0.426 |
| | **BH-BH** | **226** | 292.0 | 0.953 |
| **M23.A** | NS-NS | 204 | 0.858 | 0.082 |
| | BH-NS | 45.4 | 2.280 | 0.397 |
| | **BH-BH** | **50.8** | 63.02 | 1.024 |
| **M30.A** | NS-NS | 426 | 1.789 | 0.083 |
| | BH-NS | 113 | 6.451 | 0.433 |
| | **BH-BH** | **641** | 1023 | 1.152 |
| **M35.A** | NS-NS | 524 | 2.237 | 0.082 |
| | BH-NS | 73.3 | 3.526 | 0.444 |
| | **BH-BH** | **109** | 108.2 | 1.152 |
| **M33.A** | NS-NS | 321 | 1.329 | 0.082 |
| | BH-NS | 21.1 | 0.935 | 0.392 |
| | **BH-BH** | **19.5** | 19.41 | 1.149 |
| **M40.A** | NS-NS | 434 | 1.822 | 0.082 |
| | BH-NS | 114 | 6.531 | 0.422 |
| | **BH-BH** | **627** | 947.3 | 1.152 |
| **M43.A** | NS-NS | 323 | 1.346 | 0.082 |
| | BH-NS | 21.5 | 0.944 | 0.381 |
| | **BH-BH** | **19.5** | 20.07 | 1.151 |
| **M50.A** | NS-NS | 408 | 1.691 | 0.082 |
| | BH-NS | 101 | 5.595 | 0.489 |
| | **BH-BH** | **1114** | 2843 | 1.153 |

TABLE 4.4: Local merger rate densities and LIGO/Virgo detection rates.

| Model | Merger | Rate density[a] [Gpc$^{-3}$ yr$^{-1}$] | detection rate[b] [yr$^{-1}$] | $z_{\rm hor}$[c] |
|---|---|---|---|---|
| **M60.A** | NS-NS | 429 | 1.805 | 0.082 |
| | BH-NS | 108 | 5.727 | 0.363 |
| | **BH-BH** | **640** | 837.0 | 0.949 |
| **M70.A** | NS-NS | 428 | 1.805 | 0.082 |
| | BH-NS | 108 | 6.107 | 0.408 |
| | **BH-BH** | **637** | 1017 | 1.107 |

NOTES:

[a] Local merger rate density at redshift $z = 0$ (note rate increase with $z$).

[b] Detection rate for LIGO/Virgo mid-high range (O3 proxy).

[c] Redshift for the most distant source detectable (best located/oriented).

### 4.3.3 BH MASSES

In this section we discuss the masses of BHs in BH-BH mergers, focusing on either the individual component masses, $M_{\rm BH1}$ (more massive component) and $M_{\rm BH2}$ (less massive component), or the total merger mass, $M_{\rm tot} = M_{\rm BH1} + M_{\rm BH2}$.

Figure 4.13 shows the intrinsic (source frame) distributions of the individual BH masses ($M_{\rm BH1}$ and $M_{\rm BH2}$ shown together in one distribution) and the total BH-BH merger masses for our three models of PPSN: M30.B (weak PPSN), M70.B (moderate PPSN), and M60.B (strong PPSN). These distributions are weighted by the intrinsic merger rate density for all BH-BH mergers (independent of mass) within a given redshift ($z < 2$). As clearly seen, the different PPSN treatments in the models shown here impact the maximum BH mass generated. In our calculations, the individual BH masses in merging binaries extend to $M_{\rm BH,max} \sim 40\ M_\odot$ in M60.B, $M_{\rm BH,max} \sim 50\ M_\odot$ in M70.B, and $M_{\rm BH,max} \sim 55\ M_\odot$ in M30.B. For comparison, among all the candidates reported by LIGO/Virgo (see Tab. 4.1), the largest mean mass for any individual BH is 50.6 $M_\odot$ (for GW170729); even most optimistically (within the 90% credible limits), the largest BH reported in a binary is only 67.2 $M_\odot$ (again for GW170729). The total BH-BH merger mass reaches $M_{\rm BH,max} \sim 80\ M_\odot$ in M60.B, $M_{\rm BH,max} \sim 100\ M_\odot$ in M70.B, and $M_{\rm BH,max} \sim 110\ M_\odot$ in M30.B. For comparison, LIGO/Virgo total mean BH-BH mass estimates reach 86.3 $M_\odot$, while the 90% confidence level on the most massive BH-BH merger is as high as 100 $M_\odot$. The distributions approximately resemble steep power-laws: $\sim M^{-3.6}$ for individual BH mass, and $\sim M^{-4.0}$ for total BH-BH mass. [Unless otherwise noted, all exponents refer to a power law fit to all merging binaries, covering the full mass range.] The power law index depends weakly on the PPSN model.

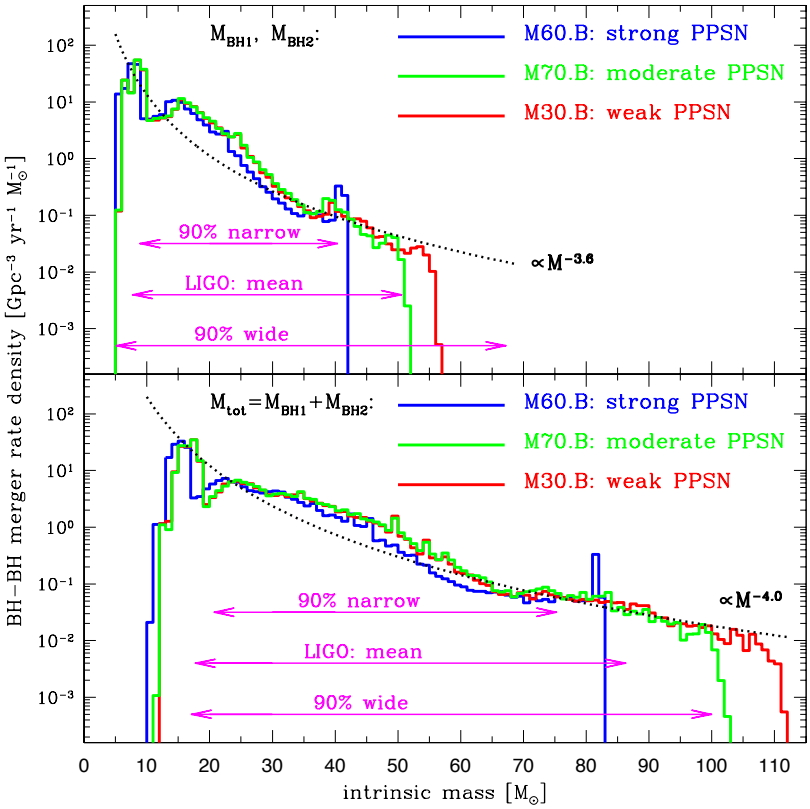


FIGURE 4.13: BH masses in BH-BH mergers within the design advanced–LIGO horizon ($z < 2$) for models M60.B (strong pair-instability pulsation supernovae), M70.B (moderate PPSN), and M30.B (weak PPSN). The top panel shows the distribution of individual BH masses, while the bottom panel shows the total BH-BH system mass. All distributions are intrinsic (neither redshifted nor weighted by detection probability). For comparison, we also indicate the range of LIGO/Virgo O1/O2 mean mass estimates and their most narrow and the widest allowed range within 90% confidence limits. Individual BH masses may reach $\sim 40\ M_\odot$ (M60.B) and $\sim 55\ M_\odot$ (M30.B), while the total BH-BH mass may reach $\sim 80\ M_\odot$ (M60.B) and $\sim 110\ M_\odot$ (M30.B). Note that these distributions only very approximately resemble power-laws: $\sim M^{-3.6}$ (for individual BH masses) and $\sim M^{-4.0}$ (for total BH-BH mass). Power-law fits (dashed black lines) were performed for model M30.B in the log-log space.

Figure 4.14 illustrates the effect of different $Z(z)$ assumptions on source frame BH mass distributions. We choose models M10.B and M60.B that utilize the same strong PPSN model, but employ slow $Z(z)$ evolution based on an older estimate and faster $Z(z)$ evolution based on a more recent estimate, respectively. For both models the range of BH masses (whether individual BH masses or total BH-BH merger masses) is very similar. The same PPSN model leads to a similar cutoff BH mass at the high mass end. However, we note the change in steepness of the power-laws which approximate these distributions. For individual BH masses the slope changes from $\sim M^{-2.9}$ for model M10.B to $\sim M^{-3.3}$ for model M60.B. For total BH-BH masses the slope changes from $\sim M^{-1.7}$ for model M10.B to $\sim M^{-2.9}$ for model M60.B. This comes from the fact that in models with high numbers of low metallicity stars (e.g., M10.B) BH masses are (on average) higher and therefore the distributions are flatter than in models with small number of low metallicity stars

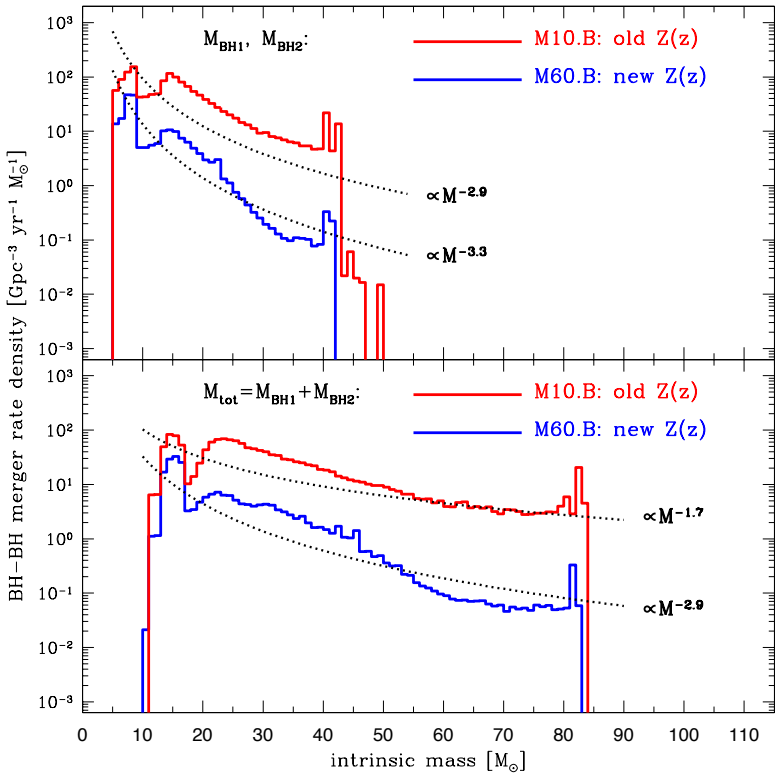


FIGURE 4.14: BH masses in BH-BH mergers within design advanced–LIGO sensitivity ($z < 2$) for models M10.B (that employs old average metallicity cosmic evolution) and M60.B (new average metallicity evolution). BH masses are calculated with the same formulas in both models. Top panel shows distribution of individual BH masses, while the bottom panel shows the total BH-BH system mass. All distributions are intrinsic (not redshifted nor weighted by detection probability). Note that application of new metallicity evolution with redshift (less low-Z stars: less high mass BHs) results in somewhat steeper BH mass distributions as contrasted with application of old metallicity evolution (more low-Z stars: more high mass BHs). Power-law fits (dashed black lines) were performed for both models in the log-log space.

(e.g., M60.B).

In Figure 4.15 we show the intrinsic (source frame) distributions of the more massive BH mass ($M_{\rm BH1}$) weighted by the intrinsic merger rate density for all BH-BH mergers (independent of mass) within a given redshift ($z < 2$). We present two groups of models. In one, we alter the amount of PPSN mass-loss: M60.B (strong mass-loss), M70.B (moderate mass-loss) and M30.B (weak mass-loss). All these models tend to have similar and rather steep power-law distribution of larger BH mass ($\propto M^{-3.6}$). In the second group we show models that tend to produce shallower power-law distributions ($\propto M^{-2.4}$): M10.B (old $Z(z)$ relation with standard stellar winds and restrictive CE treatment), M50.A (new $Z(z)$ relation with 30% reduced stellar winds and optimistic CE), and M50.B (new $Z(z)$ relation with 30% reduced stellar winds and restrictive CE). Clearly models that tend to produce more low metallicity stars (e.g., M10) and models with reduced stellar winds (e.g., M50) generate more massive BHs and produce shallower distributions. However, our

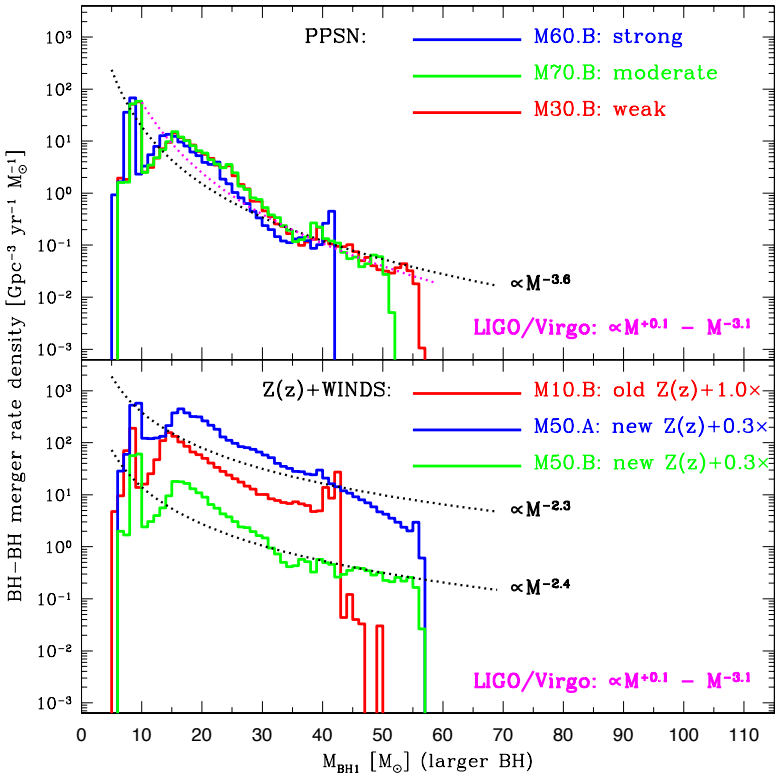


FIGURE 4.15: The larger (more massive) BH mass distributions in BH-BH mergers within design advanced–LIGO sensitivity ($z < 2$) for models M60.B, M70.B, M30.B, M10.B, M50.A, M50.B. Power-law fits (dashed black lines) were performed for model M30.B in the top panel ($\propto M^{-3.6}$), and for models M50.A ($\propto M^{-2.3}$) and M50.B ($\propto M^{-2.4}$) in the bottom panel in the log-log space. These distributions can be compared with other theoretical predictions (e.g., Fig. 1 of Mapelli et al. (2019), or Fig. 4 of Stevenson et al. (2019) that seem to be close to $\propto M^{-2} - M^{-3}$; note that power-laws shown in the latter work are not correct) or with the LIGO/Virgo observational estimate of $\propto M^{-1.6}$ with large uncertainty on the power-law index: $\propto M^{+0.1} - M^{-3.1}$ (Fig. 1 in Abbott et al. (2019a)). Some of our models (e.g., top panel) show somewhat steeper relations, while other models (bottom panel) are in agreement with LIGO/Virgo estimate.

mass distributions are not perfect power laws, particularly at low mass. For example, a power law approximation to our simulation data restricted to the mass range of reported LIGO/Virgo observations will recover a steeper power law exponent. For comparison, LIGO/Virgo infers a phenomenological pure power law distribution of $\propto M^{+0.1} - M^{-3.1}$ (Abbott et al. (2019a) based on observations spanning $M_{\rm BH1}$; see their Fig.1). When comparing our calculations to LIGO/Virgo observations in this way, the estimated power law exponent depends sensitively on the choice of the low-mass cutoff $M_{\rm BH1}$, where our models predict a substantial structure in the mass distribution.

Figure 4.16 shows the total BH-BH merger mass distributions weighted by the LIGO detection probability (dependent on mass). We show models with different assumptions on PPSN (M30.B, M60.B, M70.B) and contrast them with LIGO/Virgo observations. These distributions are flatter than the intrinsic mass distributions as more massive mergers are detected in larger volumes (and

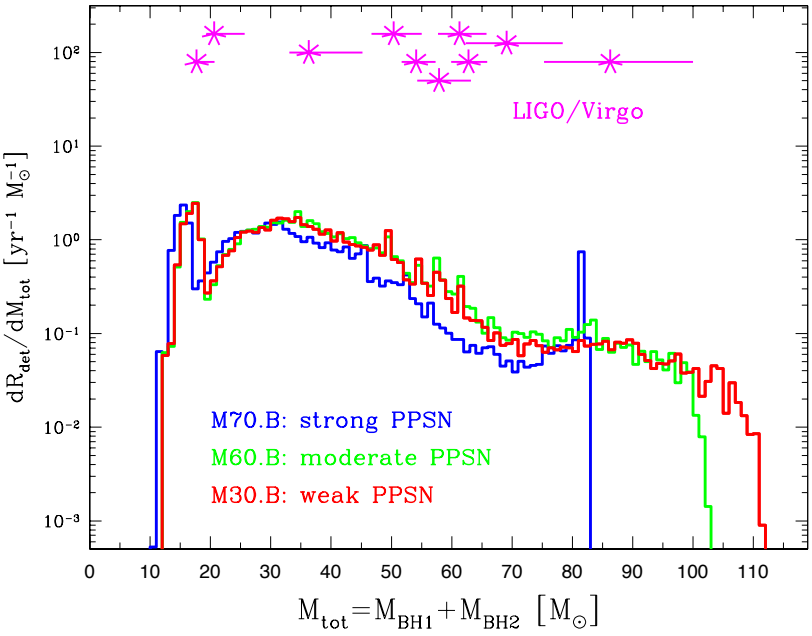


FIGURE 4.16: Detection weighted BH-BH merger total intrinsic (not redshifted) mass for models with different assumptions on the pair-instability pulsation supernovae: M70.B (strong PPSN), M60.B (moderate PPSN), M30.B (weak PPSN). For comparison, we also show LIGO/Virgo O1/O2 mean total mass estimates and their 90% confidence limits.

thus in larger numbers) than lower mass mergers. Naturally, the maximum BH-BH mass cut-offs are the same as for the intrinsic distributions. Note that within observational uncertainties, all these three models can reproduce the range of the detected BH-BH total masses. However, a closer inspection of the distribution of observational points shows an overabundance of points near $M_{\rm tot} \sim 50$–$70\ M_\odot$ with respect to the models. At this point we do not attempt to match this apparent peak in the observed distribution (this can wait for LIGO/Virgo to publish another set of detections), but we have just tested one potential change to the input physics (see below) that may affect the shape of the total mass distribution for massive BH-BH mergers.

In Figure 4.17 we re–plot the model M30.B (with weak PPSN and restrictive CE-phase treatment) employing the standard theoretical estimates of wind mass-loss rates (rather high wind mass-loss rates; Vink et al. (2001)). Additionally, we show the distributions for models M50.A and M50.B for which we reduce all stellar wind mass loss to 30% of the values used in all other models, but the rest of the input physics is exactly the same as in model M30.A/B. We note the appearance of a very prominent peak in the total BH-BH mass distribution at $M_{\rm tot} \sim 80$–$100\ M_\odot$ in model M50.B (weak PPSN and restrictive CE-phase treatment) as compared to the model M30.B distribution. That peak disappears in model M50.A (weak PPSN and optimistic CE-phase treatment), but the distribution becomes much flatter than for model M30.B. These models seem to better reproduce the distribution of observational points. In Sec. 4.4.4 we present a brief discussion comparing synthetic `StarTrack` data with LIGO/Virgo data on BH masses.

### 4.3.4 BH-BH EFFECTIVE SPINS

In this section we present our predictions for the effective spins of BH-BH mergers. Having shown that we can reproduce the effective spins (whether low or high) with some of our adopted BH spin models (Geneva or MESA), we wish to see whether we can also reproduce the effective spin

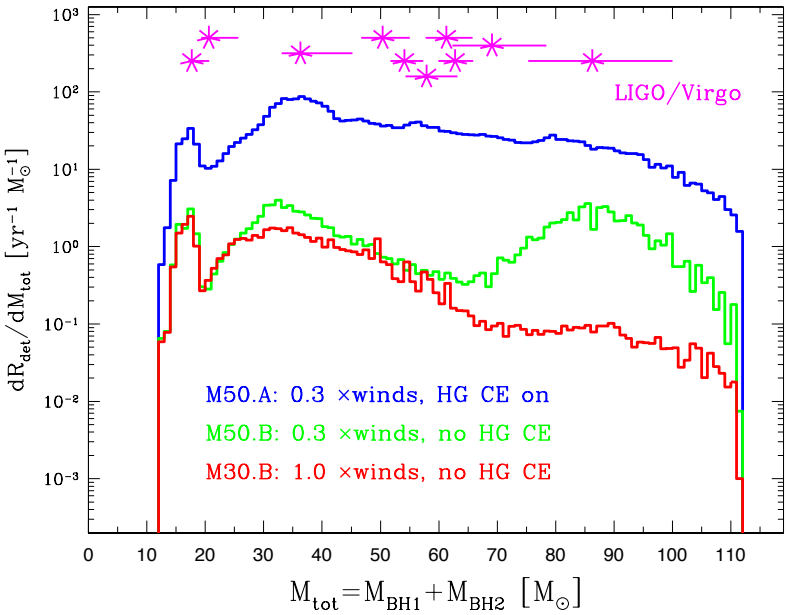


FIGURE 4.17: Detection weighted BH-BH merger total intrinsic (not redshifted) mass for models with different assumptions on wind mass loss and common envelope development: M50.B (weak stellar winds and optimistic CE), M50.B (weak stellar winds and pessimistic CE), M30.B (strong stellar winds and pessimistic CE). For comparison, we also show LIGO/Virgo O1/O2 mean total mass estimates and their 90% confidence limits. Note that although no model seems to reproduce the observed LIGO/Virgo BH-BH total mass distribution, one can expect that some interplay of several parameters (winds, CE, PPSN, Z(z)) may possibly in future reproduce the shape of the observed distribution. For example, stronger PPSN and higher Z(z) (not shown here) will tend to shift the highest BH masses to lower values. This calls for further parameter study calculations.

distribution (or rather range of observed values) of *all* the reported LIGO/Virgo BH-BH mergers.

In Figure 4.18 we show the measurements of the effective spins in the LIGO/Virgo BH-BH merger observations, superimposed with the $\chi_{\rm eff}$ predictions calculated using the BH natal spins from the Geneva evolutionary calculations. All of the LIGO/Virgo observations cluster around zero ($\chi_{\rm eff} \sim 0$). For the comparison we use two models: model M20.B, with fallback-decreased BH natal kicks (effectively no kicks for massive BHs, and small kicks for low mass BHs) and the model M23.B, with high BH kicks that are independent of the BH mass (with 1-dimensional $\sigma = 265$ km s$^{-1}$). Our model distributions peak at high values ($\chi_{\rm eff} \sim 0.9$) and then quickly fall off toward small values (note logarithmic scale on Fig. 4.18).

Mergers with high values of the effective spin host BHs with high spins. In the Geneva model, these BHs can form with either low or high masses, depending on the chemical composition of the progenitor stars (Fig. 4.1). Mergers with low effective spins originate predominantly from systems with high-mass BHs. Strong natal kicks (as in model M23.B) produce higher misalignment of the BH spins with respect to the binary's angular momentum vector during the BH formation, and this decreases the value of the effective spin. Note that although both distributions are similar and peak at high values, natal kicks decrease the effective spin parameter (average $\chi_{\rm eff} = 0.3$; M23.B) as

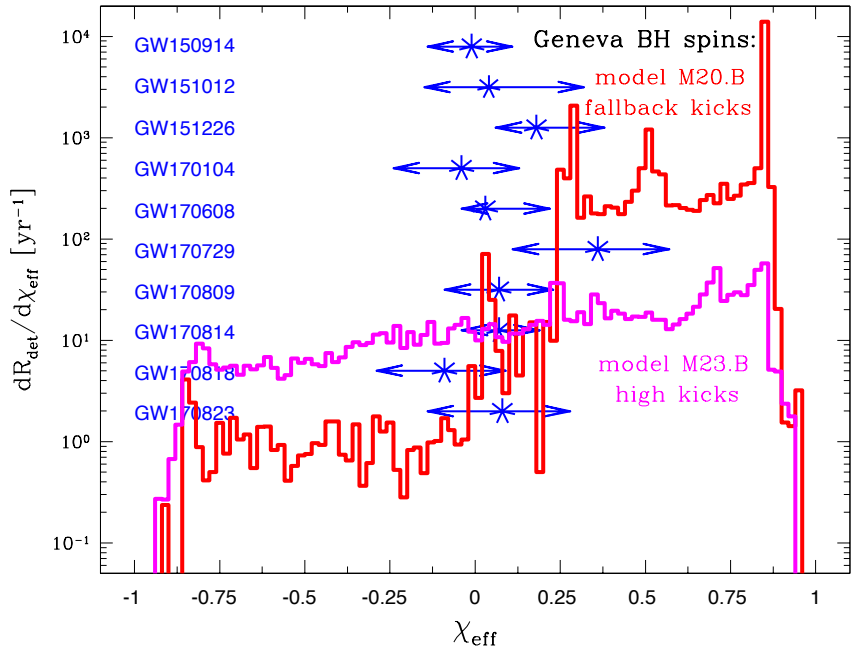


FIGURE 4.18: Detection weighted distribution of effective spin parameter of BH-BH mergers for model M20.B (fallback decreased BH kicks; no BH kicks for massive BHs) and M23.B (high BH natal kicks with $1D\ \sigma = 265$ km s$^{-1}$ for all BHs) with Geneva mildly efficient angular momentum transport. Note that both distributions peak at high values ($\chi_{\rm eff} \sim 0.9$). Natal kicks decrease the effective spin parameter (average $\chi_{\rm eff} = 0.3$; M23.B) as compared to model with almost no BH kicks (average $\chi_{\rm eff} = 0.7$; M20.B). For comparison we show the 90% credible limits (blue arrows) and the most likely values (blue stars) of the effective spin parameter for ten LIGO/Virgo BH-BH mergers. Although we can recover all the reported values, the predicted peak of $\chi_{\rm eff}$ distribution is not coincident with the current LIGO/Virgo data. It indicates that BHs have typically lower spins than resulting from the Geneva model for BH natal spins, or that the detected BH-BH mergers are not formed in the classical isolated binary evolution.

compared to model with almost no BH kicks ($\chi_{\rm eff} = 0.7$; M20.B). The fraction of BH-BH mergers with negative $\chi_{\rm eff}$ is sizeable in model M23.B (27.4%), while it is negligible in model M20.B ($\sim 0.3$%).

We can recover all the reported values within both models (more easily with model M23.B than with M20.B), but our predicted $\chi_{\rm eff}$ distributions using Geneva spins as inputs are not consistent with the current LIGO/Virgo data. For example, for each of our models and for $N$ observations, we can ask whether we would expect at least one measurement with a maximum value of $\chi_{\rm eff}$ above what has been observed thus far; i.e., $1 - P(< \chi_{\rm eff})^N$, where $P(< \chi_{\rm eff})$ is the cumulative distribution implied by the detection-weighted $\chi_{\rm eff}$ distribution reported in Figure 4.18. Even considering only subsets of events, such as the high-mass or low-mass events, we find a small ($1.1 \times 10^{-4}$ for M23.B) to infinitesimal ($6.7 \times 10^{-10}$ for M20.B) probability that the predicted spin distribution is compatible with observations reported to date.

Note that to reach this conclusion we have used two extreme natal kick models. In particular,

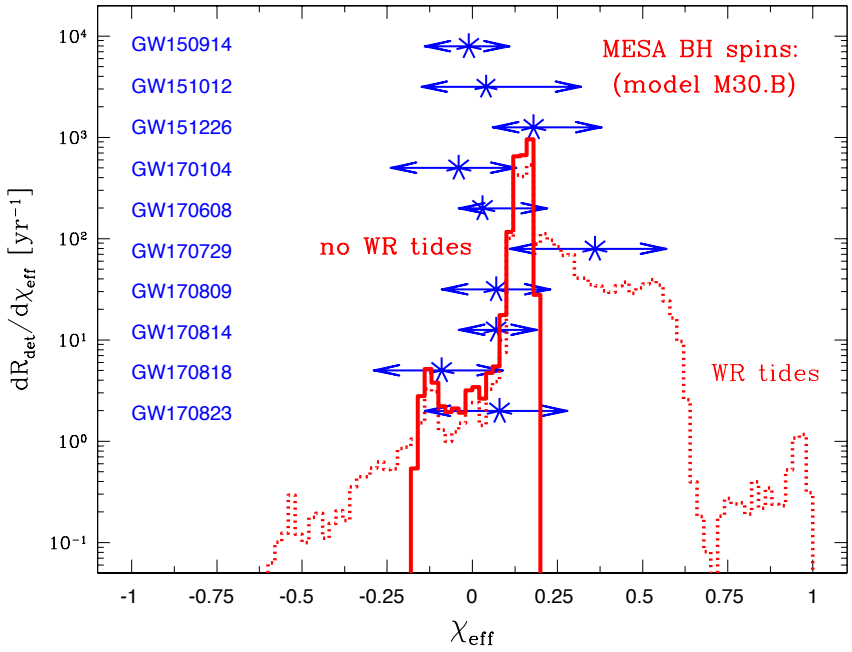


FIGURE 4.19: Detection weighted distribution of the effective spin parameter of BH-BH mergers for model M30.B with MESA efficient angular momentum transport and fallback decreased BH kicks (no BH kicks for massive BHs). We either do not allow for efficient tidal spin-up of WR stars that are the most common immediate progenitors of BHs in our models (natal BH spin is calculated directly from MESA stellar models), or we take it into account (natal BH spin is then calculated as described in Sec. 4.2.5 if the WR star progenitor was subject to an efficient tidal spin-up). For the "no WR tides" approach we find a rather narrow distribution of effective spins ($-0.2 \lesssim \chi_{eff} \lesssim 0.2$) that is peaked at positive values (average $\chi_{\rm eff} = 0.15$). For efficient "WR tides" the distribution is broad ($-0.5 \lesssim \chi_{eff} \lesssim 1.0$) with a peak at $\chi_{eff} \sim 0.15$ ($\sim 73\%$) and a tail with $\chi_{eff} \gtrsim 0.25$ (27%). For comparison we show the 90% credible limits (blue arrows) and the most likely values (blue stars) of the effective spin parameter for ten LIGO/Virgo BH-BH mergers.

we have tested a model with high BH natal kicks, that tends to maximize the BH spin-orbit misalignment and therefore decrease our predicted effective spins. Although BH natal kicks as high as those adopted in model M23.B (with average 3-dimensional velocity of $\sim 400$ km s$^{-1}$) cannot yet be observationally excluded (Belczynski et al., 2016c), it is unlikely for BHs to receive larger natal kicks than adopted in this model (Mandel, 2016; Repetto et al., 2017). Note that in these models, we allow neither for any processes that could realign the BH spins, nor for an effective tidal spin-up of stars in the binary progenitors of BH-BH mergers. These processes might increase the effective spin parameter for some BH-BH progenitors, thus shifting our results for Geneva model of BH natal spins even further away from the LIGO/Virgo observations.

In Figure 4.19 we present the effective spin distribution for the model M30.B that employs the MESA BH natal spins. We show two versions of this model: one in which we do not allow and one that allows for efficient tidal interactions in close binaries (that host WR stars; see Sec. 4.2.5). The version with no efficient tides shows a narrow distribution of effective spins: $-0.2 \lesssim \chi_{eff} \lesssim 0.2$

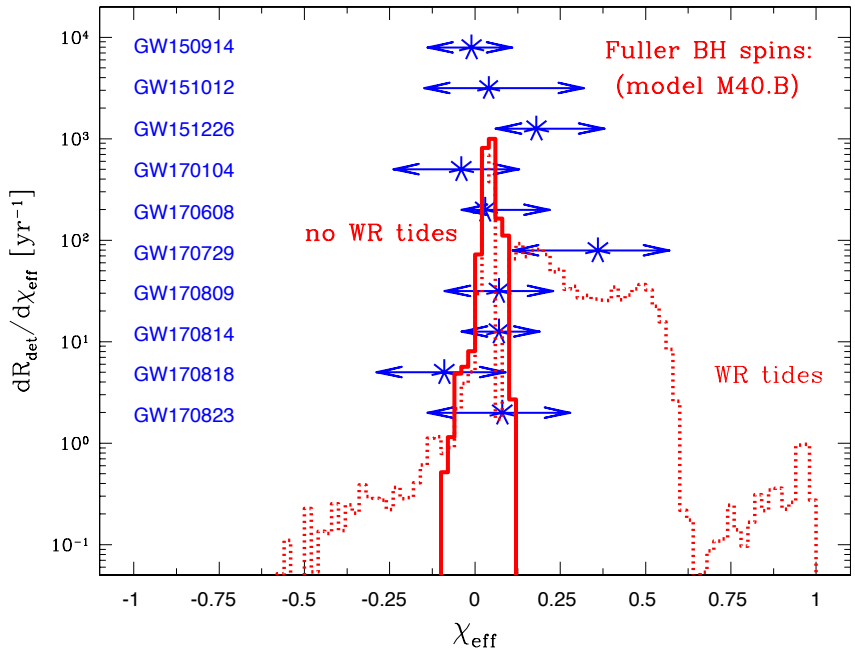


FIGURE 4.20: Detection weighted distribution of the effective spin parameter of BH-BH mergers for model M40.B with Fuller super-efficient angular momentum transport and fallback decreased BH kicks (no BH kicks for massive BHs). We either do not allow for the efficient tidal spin-up of WR stars that are the most common immediate progenitors of BHs in our models (natal BH spin is calculated directly from MESA stellar models), or we take it into account (natal BH spin is then calculated as described in Sec. 4.2.5 if the WR star progenitor was subject to an efficient tidal spin-up). For the "no WR tides" approach we find very narrow distribution of effective spins ($-0.1 \lesssim \chi_{eff} \lesssim 0.1$) that is peaked at positive values (average $\chi_{\rm eff} = 0.05$). For efficient "WR tides" the distribution is broad ($-0.5 \lesssim \chi_{eff} \lesssim 1.0$) with a peak at $\chi_{eff} \sim 0.05$ ($\sim 78\%$) and a tail with $\chi_{eff} \gtrsim 0.25$ (22%). For comparison we show 90% credible limits (blue arrows) and the most likely values (blue stars) of effective spin parameter for ten LIGO/Virgo BH-BH mergers.

that is peaked at positive values: average $\chi_{\rm eff} = 0.15$). This limited range of effective spins follows directly from the underlying BH natal spin model that allows only for narrow range of BH spin magnitudes $a_{\rm spin} \sim 0.05$-$0.15$ (see Fig. 4.2). The BH spins are, at most, moderately increased by accretion from the binary companion (see Figs. 4.8 and 4.9) and this tends to slightly extend the distribution to higher positive values. The distribution is only moderately affected by small-to-no BH natal kicks (fall-back decreased kicks are employed in this model) producing a small population of BH-BH mergers with negative effective spins. On the other hand the variation with the efficient WR tides generates a rather broad effective spin distribution: $-0.5 \lesssim \chi_{eff} \lesssim 1.0$ with a peak at: $\chi_{eff} \sim 0.15$ ($\sim 80\%$) and a tail with $\chi_{eff} \gtrsim 0.25$ (27%). This is because in this variation about $1/3$ of systems are subject to significant tidal spin-up of at least one binary component and they produce large BH spins. The tail shows a significant drop beyond $\chi_{eff} \gtrsim 0.6$. Systems with $0.25 \lesssim \chi_{eff} \lesssim 0.6$ are these in which only one binary component was subject to tidal spin-up, while systems with $\chi_{eff} \gtrsim 0.6$ are those with both binary components being subject

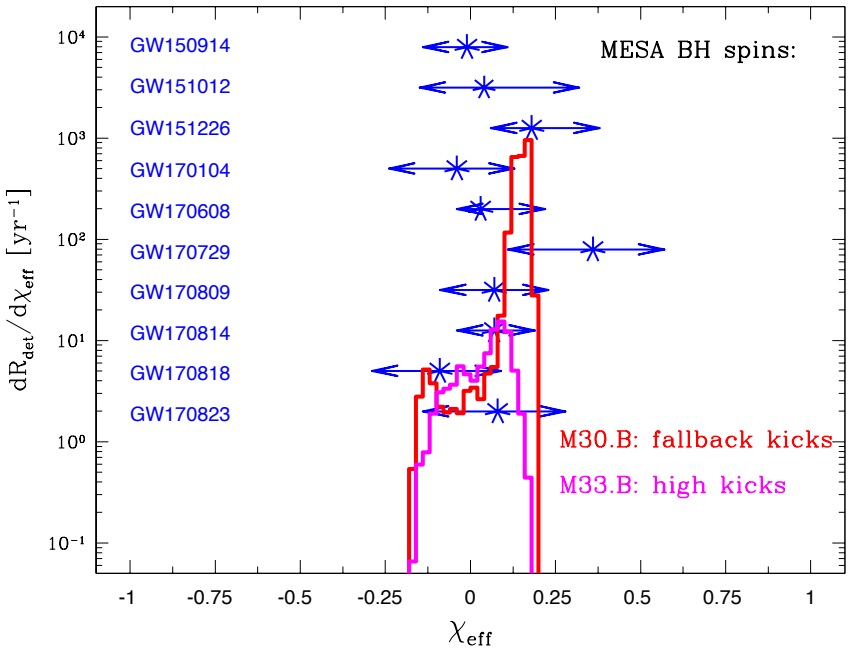


FIGURE 4.21: Detection weighted distribution of the effective spin parameter of BH-BH mergers for model M30.B with fallback decreased natal kicks (low natal BH kicks for low-mass BHs, and no natal kicks for high-mass BHs) and for model M33.B with high natal kicks (all BHs, independent of mass, are subject to natal kicks drawn from a 1D Maxwellian distribution with $\sigma$ = 265 km s$^{-1}$). Note that the average effective spin decreases from model M30.B ($\chi_{\rm eff}$ = 0.15) to model M33.B ($\chi_{\rm eff}$ = 0.04) as an effect of natal kicks that tend to misalign BH spins and lower the effective spin (see eq. 4.1). For comparison we show the 90% credible limits (blue arrows) and the most likely values (blue stars) of the effective spin parameter for ten LIGO/Virgo BH-BH mergers.

to tidal spin-up in close WR-WR binaries.

In Figure 4.20 we present the effective spin distribution for model M40.B that employs Fuller BH natal spins. We also show two versions of this model: one without efficient WR tides and one with the tides. The distribution is very narrow: $-0.1 \lesssim \chi_{eff} \lesssim 0.1$ and is peaked at positive values: average $\chi_{\rm eff}$ = 0.05. This comes directly from the assumption of very low natal BH spins: $a_{\rm spin}$ = 0.01 (see eq. 4.5). For such a low value of natal BH spins, the effective spin of BH-BH mergers is $\chi_{\rm eff} \sim 0$. Binary accretion onto the second-born BH spreads effective spins to $\chi_{\rm eff} \sim 0.1$, while small natal kicks applied to some (low-mass) BHs in this model create a tail extending to low negative values $\chi_{\rm eff} \sim -0.1$. For efficient "WR tides" the distribution is broad: $-0.5 \lesssim \chi_{eff} \lesssim 1.0$ with a peak at $\chi_{eff} \sim 0.05$ ($\sim$ 78%) and a tail with $\chi_{eff} \gtrsim 0.25$ (22%).

In Figures 4.21 and 4.22 we present the effect of high BH natal kicks on the effective spin distributions in models that employ MESA and Fuller BH natal spins. For MESA BH natal kicks we use two models: M30.B (fallback-decreased natal kicks: low-to-no BH kicks), and M33.B (high natal kicks, independent of BH mass, drawn from a 1D Maxwellian distribution with $\sigma$ = 265 km s$^{-1}$). Note that the average effective spin decreases from model M30.B: $\chi_{\rm eff}$ = 0.15 to model M33.B: $\chi_{\rm eff}$ = 0.04. This is an effect of the natal kicks that tend to misalign BH spins and

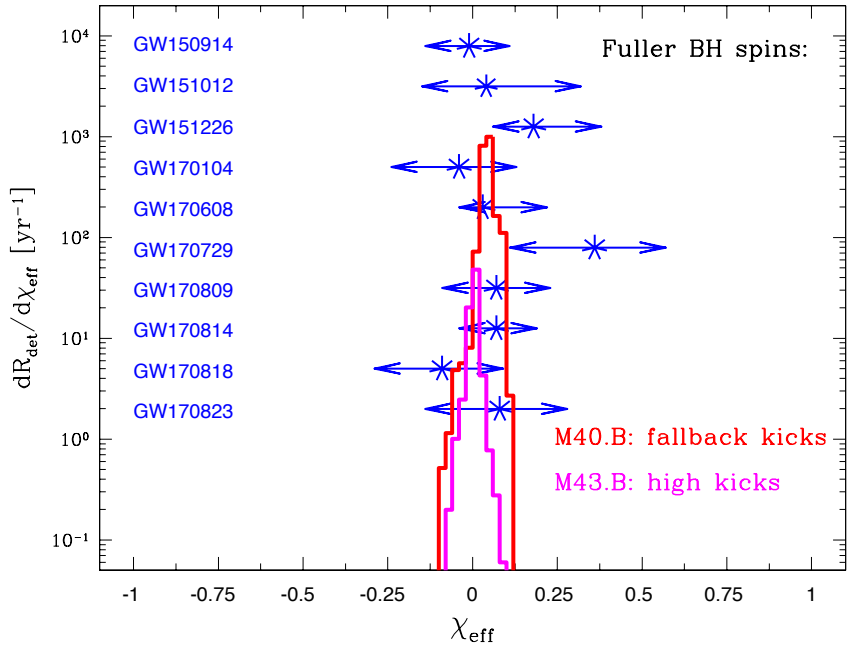


FIGURE 4.22: Detection weighted distribution of the effective spin parameter of BH-BH mergers for model M40.B with fallback decreased natal kicks (low natal BH kicks for low-mass BHs, and no natal kicks for high-mass BHs) and for model M43.B with high natal kicks (all BHs, independent of mass, are subject to natal kicks drawn from a 1D Maxwellian distribution with $\sigma = 265$ km s$^{-1}$). Note that the average effective spin decreases from model M40.B ($\chi_{\rm eff} = 0.05$) to model M43.B ($\chi_{\rm eff} = 0.004$) as an effect of the natal kicks that tend to misalign BH spins and lower the effective spin (see eq. 4.1). For comparison we show the 90% credible limits (blue arrows) and the most likely values (blue stars) of the effective spin parameter for ten LIGO/Virgo BH-BH mergers.

lower the effective spin. For Fuller BH natal kicks we use two models: M40.B (fallback-decreased natal kicks), and M43.B (high natal kicks). We also note that the average effective spin decreases with increasing natal kicks: from model M40.B: $\chi_{\rm eff} = 0.05$ to model M43.B: $\chi_{\rm eff} = 0.004$.

## 4.4 DISCUSSION

### 4.4.1 ANGULAR MOMENTUM TRANSPORT IN MASSIVE STARS

In this section we discuss the dependence of the final angular momentum of the star at core collapse on angular momentum transport prescriptions and initial (ZAMS) rotation rate.

In order to evaluate the dependence of the final angular momentum on angular momentum transport prescriptions and initial rotation rate, we ran three additional 32 $M_\odot$ models at a metallicity of $Z = 0.002$: a slow initial rotation ($V_{\rm ini} = 100$ km s$^{-1}$) non-magnetic ("noTS", where TS stands for the Tayler-Spruit dynamo) model with both the Geneva and MESA code as well as a slow initial rotation ($V_{\rm ini} = 100$ km s$^{-1}$) magnetic ("TS") model with the MESA code. The specific angular momentum profile of these models at the end of core He-burning are shown in

Figure 4.23. The helium core, which will form the bulk of the black hole, extends from the center to about 12 $M_\odot$ in all the models plotted. For comparison, we also show the specific angular momentum profiles for our two fast initial rotation models ($V_{\rm ini}/V_{\rm crit}$ = 40% : $V_{\rm ini} \approx 340$ km s$^{-1}$) for 32 $M_\odot$ star with $Z = 0.002$ calculated with MESA-TS and Geneva no-TS assumptions. Note that these two fast models are used to calculate BH spin magnitudes employed in our population synthesis calculations (and that are referred to as MESA BH spins and Geneva BH spins).

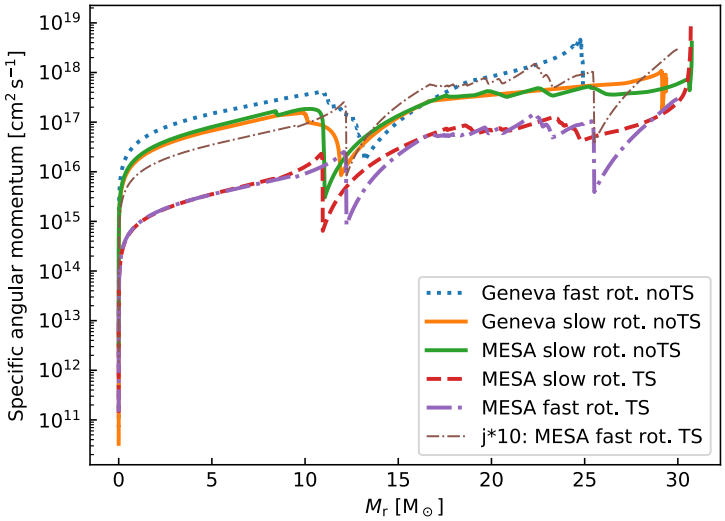


Figure 4.23: Specific angular momentum profile at the end of core He-burning for the 32 $M_\odot$ models at $Z = 0.002$ calculated with a range of physical ingredients and initial rotation rates: the Geneva fast rotation model (model listed in Table 4.5 with $V_{\rm ini}/V_{\rm crit}$ = 40%, $V_{\rm ini}$ = 341.9 km s$^{-1}$, dotted blue line), the Geneva slow rotation model ($V_{\rm ini}$ = 100 km s$^{-1}$, solid orange line). Both these Geneva models do not include the Tayler-Spruit magnetic dynamo ("noTS"). We also show: the MESA slow rotation non-magnetic ("noTS") model ($V_{\rm ini}$ = 100 km s$^{-1}$, solid green line), the MESA slow rotation magnetic ("TS") model ($V_{\rm ini}$ = 100 km s$^{-1}$, dashed red line), the MESA fast rotation magnetic ("TS") model (model listed in Table 4.6, dot-dashed purple line). The brown thin dot-dashed line corresponds to the specific angular momentum of the MESA fast rotation model multiplied by a factor of 10 to facilitate comparisons.

Comparing various models, we see the following dependencies:

1. Comparing the magnetic slow and fast rotation MESA models (dashed red and purple lines, respectively), we see that they end with a very similar final angular momentum ($a_{\rm spin}$ = 0.084 and $a_{\rm spin}$ = 0.087 for the slow and fast rotation models, respectively[3]). There is thus very little dependence on the initial velocity in magnetic models. This is due to a weaker magnetic instability (and thus less efficient angular momentum transport) in slower rotation models. We would thus expect slower rotation magnetic models to have a very similar final angular momentum content as the fast models listed in Table 4.6.

[3]The values of dimensionless spun parameter, correspond to a specific angular momentum of Fig. 4.23 $\sim 4.54\times10^{15}$ cm$^2$/s; see Eq. (4.2).

2. Comparing the magnetic (MESA slow and fast rotation; dashed red and purple lines) and non-magnetic models (MESA and GENEVA no-TS slow rotation and GENEVA fast rotation no-TS models; blue, green and orange lines), we see that the non-magnetic models have final angular momenta that are more than a factor of 10 higher than the magnetic models (the angular momentum profile of the MESA fast rotation TS model multiplied by a factor of 10 is shown to facilitate the comparison; brown line). This means that for the "lower" end of the massive star range, non-magnetic models predict BHs rotating near or above critical rotation ($a_{\rm spin} \gtrsim 0.9$).

3. Comparing the slow rotation, *non-magnetic*, Geneva and MESA models (solid orange and green lines, respectively), the final angular momentum is very similar. The small differences in angular momentum profiles arise from small differences of the core sizes between the two codes (a result of the different treatment of the convective boundary mixing). We thus see that the two codes give consistent results when using a similar treatment of the angular momentum transport (without magnetic fields).

The correlations of the angular momentum content listed above apply directly to black hole spins. We thus expect (slow and fast) rotating magnetic models to end up in low BH spin ($a_{\rm spin} \sim 0.1$) and non-magnetic (slow and fast) rotating models to result in BH with large spins ($a_{\rm spin} \gtrsim 0.8$). The change of the initial stellar rotation from fast ($\sim 340$ km s$^{-1}$; 40% critical) to slow ($\sim 100$ km s$^{-1}$) does not significantly affect our estimates of the BH natal spin. In Sec. 4.A.2 we present more detailed information and show that even when we increase rotation to $\sim 680$ km s$^{-1}$ (80% critical) our conclusions remain unchanged (see also Fig. 4.28). Note that the observed distribution of massive star spins is rather broad ($0 - 600$ km s$^{-1}$), with two distinctive peaks: one (dominant) at $\sim 100$ km s$^{-1}$ and one (small) at $\sim 400$ km s$^{-1}$ (Ramírez-Agudelo et al., 2013). These correlations were studied for a single mass ($32\,M_\odot$: the lower end of the massive star range) at one metallicity ($Z = 0.002$) and with two models of angular momentum transport (the Tayler-Spruit theory for the magnetic dynamo and meridional currents which dominate angular momentum transport while TS dynamo is switched off). More in-depth studies, especially for higher masses are needed to confirm these correlations.

Our models also make predictions for the birth spin periods of neutron stars and it is worthwhile comparing these predictions with the estimates of these spin periods from observations. Stars with zero-age main sequence masses lying between $\sim 8 - 20\,M_\odot$ (Fryer et al., 1999, 2012) and more massive stars whose mass loss is sufficiently extreme to dramatically alter the CO core mass will collapse to form neutron stars (through normal supernovae). If the CO cores are rotating and the magnetic fields are sufficiently strong, these neutron stars will emit as pulsars. By studying the distribution of spins in these pulsars, we can place constraints on the rotation period of the stars prior to collapse. This spin distribution also could provide some indication of the role angular momentum can play in normal "core-collapse" supernovae. However, in section 4.A.6 in the Appendix we study this problem and arrive to the conclusion that NS spins cannot be directly used

to test angular momentum transport in massive stars as various (highly uncertain) mechanisms may spin down or spin up NS after its formation.

### 4.4.2 Using Single Stellar Models in Binary Simulations

Although to estimate the BH natal spins we use single stellar models (see Sec. 4.2.1), we use binary evolution models to estimate the BH-BH merger effective spins (see Sec. 4.2.6). This is not fully consistent as our approach does not take into account an important effect in binary evolution that may influence the natal BH spin, that is the spin-up of stars (progenitors of BHs) during the RLOF phases. This process typically affects the secondary star of the BH-BH progenitors (Figs. 4.8 and 4.9: see the second evolutionary stage in both cases). Depending on the donor mass and our assumption on how much mass is accreted during the RLOF (in most models we allow for 50% of mass lost by the donor to be accreted by its companion; but see models M20.A/B–M26.A/B) the main sequence secondary accretes anywhere from several to several tens of solar masses. This is most likely enough to significantly spin-up even a massive star (Packet, 1981). However, there is a good chance that at least some of this extra angular momentum is later removed from the secondary star.

When the accretion and spin-up end, the secondary star is still on the main sequence. It will be therefore subject to angular momentum transport and losses (through winds) during a significant fraction of its subsequent lifetime. Obviously, there is less time in our binary evolution sequences for secondaries to lose extra angular momentum as compared with single stellar models initiated at ZAMS. On the other hand, there are binary interactions that help the secondary stars to get rid of extra angular momentum after the RLOF/accretion phase.

This happens when the secondary star expands significantly after the RLOF and leaving the main sequence and is subject to tidal spin-down as this occurs on a very wide orbit (Figs. 4.8 and 4.9: see the third and fourth evolutionary stage in both cases). Then the expansion leads to a CE phase, and the entire secondary's H-rich envelope (with all its angular momentum content) is removed from the binary (Figs. 4.8 and 4.9: see the fifth evolutionary stage in both cases). Any extra angular momentum from accretion during the main sequence that is left in the He-core of the secondary can contribute to an extra spin of the BH with respect to single stellar models but this would not change our conclusions significantly. If we increased the spin magnitudes of the secondary BHs, then the distributions of BH-BH effective spin parameters would become somewhat wider, and the effective spins would mostly shift to larger positive values. This would be qualitatively similar to the effect of efficient WR tides on secondary stars (see Figs. 4.19 and 4.20) for models with the effective angular momentum transport (MESA and Fuller models). For the model with inefficient angular momentum transport (Geneva model) the BH spins (on average) are already high so increasing stellar spin may only shift this model (in terms of effective spin parameter) even further away from LIGO/Virgo observations.

Also the scenario in which the star is stripped of its envelope does not generally affect the trend in rotation rates discussed in Sec. 4.4.1. Indeed, the effective angular momentum transport

through a magnetic dynamo only operates when there is a shear allowing the development of a magnetohydrodynamic instability. Hence, different rotation rates between the core and the envelope are crucial since they create the shear. In models including magnetic fields, the transport of most of the angular momentum occurs during the short phase between core hydrogen depletion and core helium ignition (during this short phase, the core contracts and spins up whereas the envelope expands and slows down, thus, creating a strong shear). Therefore, any stripping through binary interaction during core helium burning or afterwards does not affect significantly the slowdown of the cores. Stripping during the MS, however, is more complicated. There are two opposite effects. The first is that mass loss removes also angular momentum. The second is that if the entire hydrogen-rich layer is removed, then there is no envelope left to expand at the end of the MS and the spin-down of the core by internal angular momentum transport (core-envelope coupling) is reduced. In non-magnetic models, spin-down of the core is weak anyway and models still end up with relatively large spin values, $a_{\rm spin}$ : 0.25 to maximum spin (see Tab. 4.5). In magnetic models, removal of the hydrogen-rich outer layer significantly reduces the spin-down of the core in the contraction phase after the MS and the core may keep its fast rotation rate (see also Fuller & Ma (2019)).

The majority of binaries that produce NS-NS/BH-NS/BH-BH mergers in our models have large initial orbital separations ($\gtrsim$ 1000 $R_\odot$; de Mink & Belczynski (2015a)). Therefore, binary interactions (CE or stable RLOF; see Fig. 4.8 and 4.9) that remove H-rich stellar envelopes happen either at the end of HG or during CHeB so that values of the natal compact body spin are not significantly affected.

Therefore one may safely conclude that neither accretion spin-up of stars nor increasing the initial stellar rotation rate (see Sec. 4.4.1) can significantly modify our conclusions about the natal spins of merging binary compact objects resulting from isolated evolution. However,we do not include quasi-homogeneous evolution scenarios discussed by Chrimes et al. (2020).

Note that other processes that can affect BH spin in binary evolution are taken into account in our calculations. Besides tidal interactions that we probe with recent models presented in literature (see Sec. 4.2.5), we also account for accretion onto BH that may lead to BH spin-up. The spin-up is calculated using the formalism presented by Belczynski et al. (2008b). There are two potential phases of accretion onto the first-formed BH in our major evolutionary scenario: during the CE phase from the H-rich envelope of the secondary and after the CE phase from the He-rich wind of the WR secondary (Figs. 4.8 and 4.9: see the fifth and sixth evolutionary stage in both cases). Since accretion leads to (usually very small or only modest) increase of the first BH spin magnitude, it tends to slightly broaden the effective spin parameter distribution.

### 4.4.3 BH-BH/BH-NS/NS-NS MERGER RATE DENSITIES

The predicted merger rate density of coalescing double compact object binaries depends on the particular formation scenario which is assumed. In the following two sections we discuss our merger rates obtained for isolated binary evolution and contrast them with BH-BH merger rates

obtained from dynamical evolution in globular clusters. In summary, the typical globular cluster rates (5 $\mathrm{Gpc}^{-3}\ \mathrm{yr}^{-1}$) can explain about 10% of the LIGO/Virgo BH-BH mergers (the empirical rate peaks at $\sim 50\ \mathrm{Gpc}^{-3}\ \mathrm{yr}^{-1}$) while the remaining 90% of the observed rate can be easily explained by isolated binary BH-BH formation (see Tab. 4.3 and 4.4).

#### 4.4.3.1 Isolated Binary Evolution

We have presented a range of models and their rate densities. The rate density in each case is the result of several assumptions: starting from the cosmic star formation, metallicity evolution, going on through the initial binary parameters and the binary evolution model to the implied delay time (between the birth of a binary and the final merger of two compact objects) distribution. For each model we have calculated the local merger rate density ($z = 0$) as well as the predicted LIGO/Virgo detection rate in O3, see Tables 4.3 and 4.4. The local rate densities of BH-BH and NS-NS mergers that we have obtained are directly comparable with the rate limits inferred by LIGO/Virgo at the conclusion of the O1/O2 observing runs, see Figure 4.24. Additionally, based on the recent LIGO/Virgo candidate (S190814bv) for a very likely ($\sim 99\%$ in the reported mass-based source classification) BH-NS merger from August 14 (LVC, 2019a,b), we estimate the BH-NS merger rate density of $\mathcal{R} = 1.6 - 60\ \mathrm{Gpc}^{-3}\ \mathrm{yr}^{-1}$ (see Appendix 4.A.9 for explanation), which can also be confronted with our models.

In addition to the overall rate of events, the relative rates of the three generic categories of events (BH-BH, BH-NS, NS-NS) provide particularly valuable constraints. With this in mind, in Figures 4.24 and 4.25 we show the rates of all three source categories. The horizontal and vertical bands represent the allowed rates consistent with current LIGO/Virgo data. Superimposed on the LIGO/Virgo bands are the rate predictions from a range of our models, with the red diamonds from submodel A (the optimistic approach to common envelope, in which CE events with Hertzsprung gap donors are allowed to survive), and the blue diamonds from submodel B (the pessimistic approach to common envelope, in which CE events with Hertzsprung gap donors are not allowed to survive). We note that in both figures there are many models that fall in the central sweet spot of the figure.

Looking at Figure 4.24, we see that the existing O1/O2 run bounds on the NS-NS and BH-BH merger rate densities already allow excluding some of the models. In the standard model group with the 2016 assumptions the only model consistent with the data is M13.A, which requires high BH/NS natal kicks. If we allow some modified physics we can also add model M23.A. From the group of models with updated physics of 2019, we can select two: M30.B ad M33.A, that are consistent with observations. Allowing for models with some modifications we can also include the models M40.B and M43.A as well as M60.B and M70.B. Thus we can see that the 2016 standard model is consistent with the merger rate density O1/O2 runs data provided that the natal kicks are large. This may be in contradiction to some observations of BH in binaries that indicate small BH natal kicks, however, such a conclusion requires more detailed studies. The updated model of 2019 is consistent with the data. It also allows for certain modifications such as probing the origin of BH spins or the inclusion of various models of PPSNs.

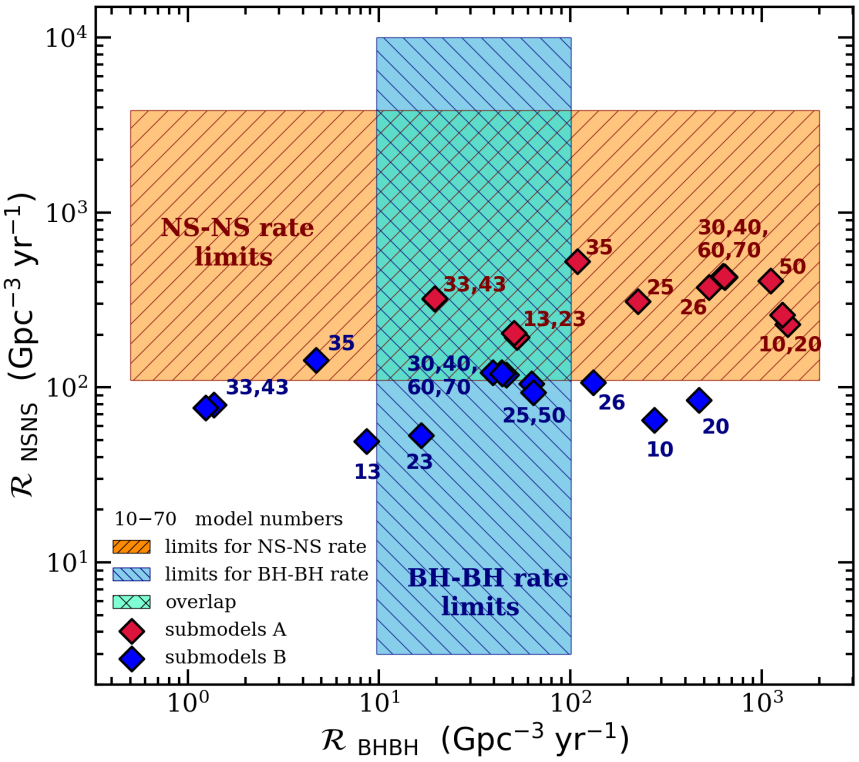


FIGURE 4.24: Comparison of the local merger rate densities of BH-BH and NS-NS mergers from all our models (see Tables 4.3 and 4.4) with the current limits inferred from the O1/O2 LIGO/Virgo observational runs: 9.7–101 Gpc$^{-3}$ yr$^{-1}$ for the BH-BH mergers and 110–3840 Gpc$^{-3}$ yr$^{-1}$ for the NS-NS events (Abbott et al., 2019b). Models consistent with the observational limits are: M13.A, M23.A, M33.A, M43.A, M30.B, M40.B, M60.B, M70.B. Note that while some of the models are consistent with the observational constraints and others are not, it is not straightforward to draw conclusions about the physical ingredients of the models at this stage due to degeneracies in the impact of various assumptions on the theoretical merger rates (see Sect. 4.4.3.1).

The inclusion of the BH-NS merger rate estimate (based on the O1/O2 runs and ongoing O3 run[4] (see Appendix 4.A.9) in Figure 4.25 offers additional insights. Of particular interest are models which fall in the central overlap region of *both* Figures 4.24 and 4.25. For example, M13.A, M23.A, M33.A, M43.A, M30.B, M40.B, M60.B and M70.B fall within the observed range for all three rates. A number of trends are evident from looking at both figures together. For example, we note that the B class of submodels, without the inclusion of HG donors in the CE evolution, brings many of the models into the center of the BH-BH/BH-NS plot. However, this same change brings some of the models into tension or only into marginal agreement with the data on the BH-BH/NS-NS plot. In other words, submodel A is almost entirely excluded in Figure 4.25, while submodel B is almost entirely excluded in Figure 4.24. This might be a preliminary indication that the NS-NS systems do allow for CE with HG donors, while BH-NS systems do not. However, there are other factors that are relevant for the relative merger rates of

[4]Under assumption that the reported gravitational-wave signal from S190814bv is in fact BH-NS merger and not BH-BH merger, both options being allowed.

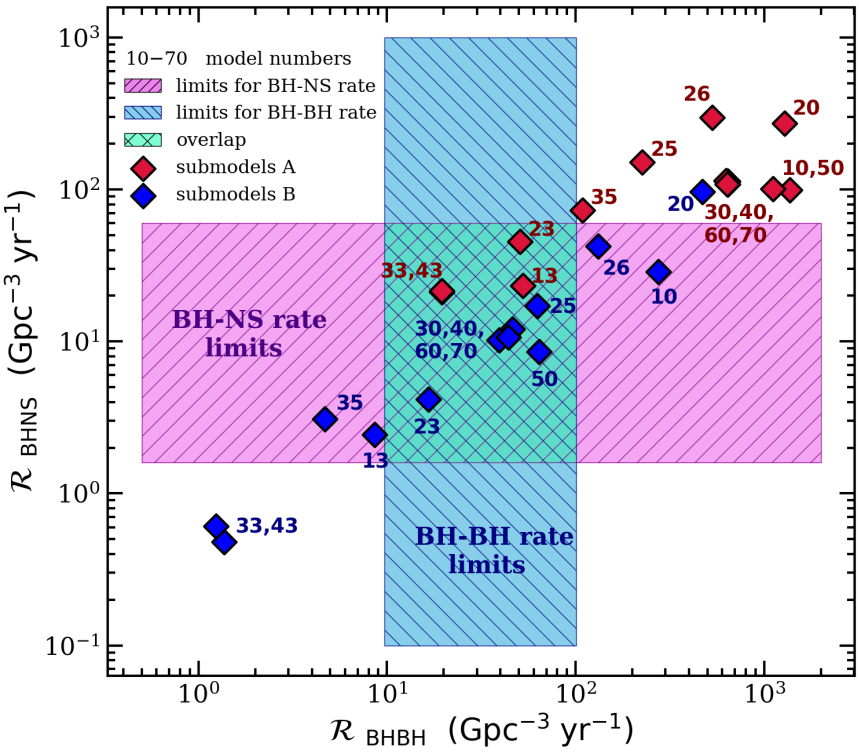


Figure 4.25: Comparison of the local merger rate densities of BH-BH and BH-NS mergers from all our models (see Tables 4.3 and 4.4) with the current limits: 9.7–101 Gpc$^{-3}$ yr$^{-1}$ for the BH-BH mergers (LIGO/Virgo O1/O2) and 1.6–60 Gpc$^{-3}$ yr$^{-1}$ for the BH-NS events (based on the LIGO/Virgo O3 candidate of the first BH-NS system, S190814bv (LVC, 2019a,b); see Sec. 4.A.9 for details). Models consistent with the observational limits are: M13.A, M23.A, M33.A, M43.A, M23.B, M25.B, M30.B, M40.B, M50.B, M60.B, M70.B. Note also that the BH-NS merger rates from our models span the range between 0.48 and 297 Gpc$^{-3}$ yr$^{-1}$, which is consistent with the upper limit determined by their non-detection in O1/O2 LIGO/Virgo runs ($< 610$ Gpc$^{-3}$ yr$^{-1}$, Abbott et al. (2019b)).

different source types. For example, improving the metallicity evolution (which shifts the net star formation across the cosmic history towards higher metallicities) appears to shift down the BH-BH merger rates while leaving the NS-NS merger rates relatively unchanged (see also Chruslinska & Nelemans (2019a)).

In all cases that we consider the merger rate density increases with increasing redshift, peaks at about $z \approx 2$ and then decreases. A rough approximation of the scaling of the merger rate density with redshift in the range $z \lesssim 2$ can be approximated as $\propto (1+z)^{1.5}$, however, the exponent is not well constrained. It is quite interesting to note that the assumed shape of the star formation rate history within the allowed bounds does not strongly influence the shape of the dependence of the merger rate density on redshift within $z \lesssim 2$, see Figure 4.10.

We expect that most of the remaining ambiguities should be resolved with the release of analysis of the O3 data. Assuming that these observations will yield about a hundred detections, we expect the bounds on the rates to narrow by a factor of three. This should allow us to strongly constrain the models presented in this paper based on the event rates alone. It should be stressed, however, that

even then it will not be straightforward to constrain the underlying physics. Variations in different ingredients of a model can have a degenerate effect on the resulting merger rates. For instance, the inclusion of HG donors in the CE evolution (going from submodels B to A) leads to an increase in the merger rates, but so does the lowering of BH/NS natal kicks (see Sect. 4.3.2 and Fig. 4.11 for details). The CE treatment and the natal kicks are only two of the many ingredients of our models, each of those ingredients being to some extent uncertain. This introduces a degeneracy that cannot easily be resolved at the moment. In the future, we can hope that the higher number of detected mergers allow us to combine all the inferred observables (e.g., rates, masses, spins, redshifts, host galaxies) in order to break the degeneracies and put better constraints on the model's input physics.

This being said, submodels A: M13.A, M33.A, M43.A appear to be consistent with all rate estimates (although on the high end of the BH-NS limits). This shows the effect of the high natal kicks that reduce high BH-BH merger rates typically found in the submodels A. At the same time these high natal kicks do no affect the NS-NS merger rates significantly, as in our standard approach (fallback decreased kicks) NS natal kicks are already high. Submodels B: M30.B, M40.B, M60.B and M70.B, that appear consistent with all rate estimates, indicate that high average cosmic metallicity in unison with exclusion of CE events with HG donors may reduce high BH-BH merger rates in comparison with older models and with submodels A. Note that these models include our current standard approach to input physics, with the two efficient angular momentum transport mechanism (MESA and Fuller models), and with the three prescriptions for PPSN (weak, moderate and strong) mass loss. Note that some models are very close to be consistent with all rate constraints. Model M50.B is one such example. In this model we have reduced stellar winds to 30% of their standard values. Typically, BHs will form with higher mass in this model. Additionally, with such low wind mass-loss rates for massive stars it is possible to form $\sim 60\ M_\odot$ BHs in a solar metallicity environment ($Z = 0.02$) while still avoiding PPSN mass loss (see Belczynski et al. (2020a) for discussion). At such mass-loss rates single stars (or stars in wide non-interacting binaries) may form $\sim 40\ M_\odot$ He cores with $\sim 20 - 30\ M_\odot$ H-rich envelopes leading to massive BH formation even at high metallicity. Such massive BHs would be found either as single BHs through microlensing surveys (e.g., Wyrzykowski & Mandel (2020)) or in wide binaries through radial velocity surveys (motion of the companion star). Note that such massive BHs would not necessarily add to either LIGO/Virgo or X-ray binary populations that form (at least in classical isolated binary evolution) from interacting binaries in which stars lose their H-rich envelopes (e.g., this study, Wiktorowicz et al. (2014)). There is, of course, a complicated interdependence of the various aspects of these models, and this subset of models does not fully cover the parameter space. Nonetheless, these general trends may provide important clues about the underlying stellar and binary physics.

#### 4.4.3.2 DYNAMICAL EVOLUTION IN GLOBULAR CLUSTERS

In dense stellar environments, even binaries that are initially too wide to inspiral via gravitational radiation in a Hubble time can be hardened and induced to merge by binary-single and binary-binary interactions. Moreover, single BHs can segregate to the cluster center due to dynamical friction

and form close binary systems that can merge due to gravitational radiation. Thus dense stellar systems such as globular clusters can be highly efficient per stellar mass at producing BH-BH mergers. However, only a small fraction of stars are in globular clusters or similarly dense systems ($\sim 10^{-4} - 10^{-3}$, depending on the type of galaxy). This turns out to mean that the plausible rate density of mergers in dense stellar systems is low. A strong upper bound can be obtained (see Mandel & Farmer (2018)) by noting that there is roughly one globular cluster per $\mathrm{Mpc}^3$ in the local Universe. If each globular has $\sim 10^6$ stars (the actual average is a few times lower than this), $\sim 10^{-3}$ of stars become black holes, and all black holes pair up and merge in a Hubble time of $\sim 10^{10}$ years, then at most the rate will be $\sim 10^6 \times 10^{-3}/(10^{10}\ \mathrm{yr} \times 1\ \mathrm{Mpc}^3)$, or $\sim 100\ \mathrm{Gpc}^{-3}\ \mathrm{yr}^{-1}$. In reality, the expected rate from clusters is 10 to 100 times lower, for a discussion see Mandel & Farmer (2018).

It does seem likely that globular cluster masses at formation were a few times larger than they are today. For example, it has been estimated that $\sim 60\% - 70\%$ of cluster mass is lost in a Hubble time due to dynamical evolution and interactions with the host galaxy (Chatterjee et al., 2010; Giersz et al., 2013; Webb & Leigh, 2015). However, recent realistic estimates of BH-BH merger rate densities from globular clusters are typically few $\mathrm{Gpc}^{-3}\ \mathrm{yr}^{-1}$ (Rodriguez et al., 2016a; Askar et al., 2017; Park et al., 2017; Hong et al., 2018; Choksi et al., 2019). Recoil during binary-single and binary-binary interactions can be sufficient to eject a binary from its host globular, with the result that the majority of such mergers are expected to occur outside the globular (Portegies Zwart & McMillan (2000) and many subsequent papers).

### 4.4.4 BH Masses

An important test of population synthesis models is the direct comparison of their predictions of the mass distribution of binary black holes with the observed distribution from gravitational-wave detections. The masses of black holes are among the best measured quantities of the LIGO/Virgo sources. In particular, the chirp mass is often measured to high accuracy ($O(5\%)$ or better) for lower–mass mergers with a significant number of inspiral cycles detected in the LIGO/Virgo sensitivity band. For the higher mass systems, the total mass can be measured with reasonable accuracy. The individual component masses are often more poorly measured, and equivalently, the mass ratio is often relatively poorly constrained. For this discussion we focus on the shape of the mass distribution.

As LIGO/Virgo continues to add to the sample of binary black holes, the inferred underlying mass distributions become increasingly well constrained. Some preliminary limits are already presented in Abbott et al. (2019a). In particular, that paper employs a number of different fits to the mass distribution of the more massive components of the detected binaries. For the purpose of comparison we use the Model B from this paper, which consists of a power-law in $M_{\mathrm{BH1}}$ with upper and lower mass cutoffs and a power-law in the binary mass ratio. The mass cutoff accounts for the dearth of high-mass black holes (Fishbach & Holz, 2017a), as would be expected from PSN and PPSN (Belczynski et al., 2016a). LIGO/Virgo finds a power law index in range $\alpha = -3.1$

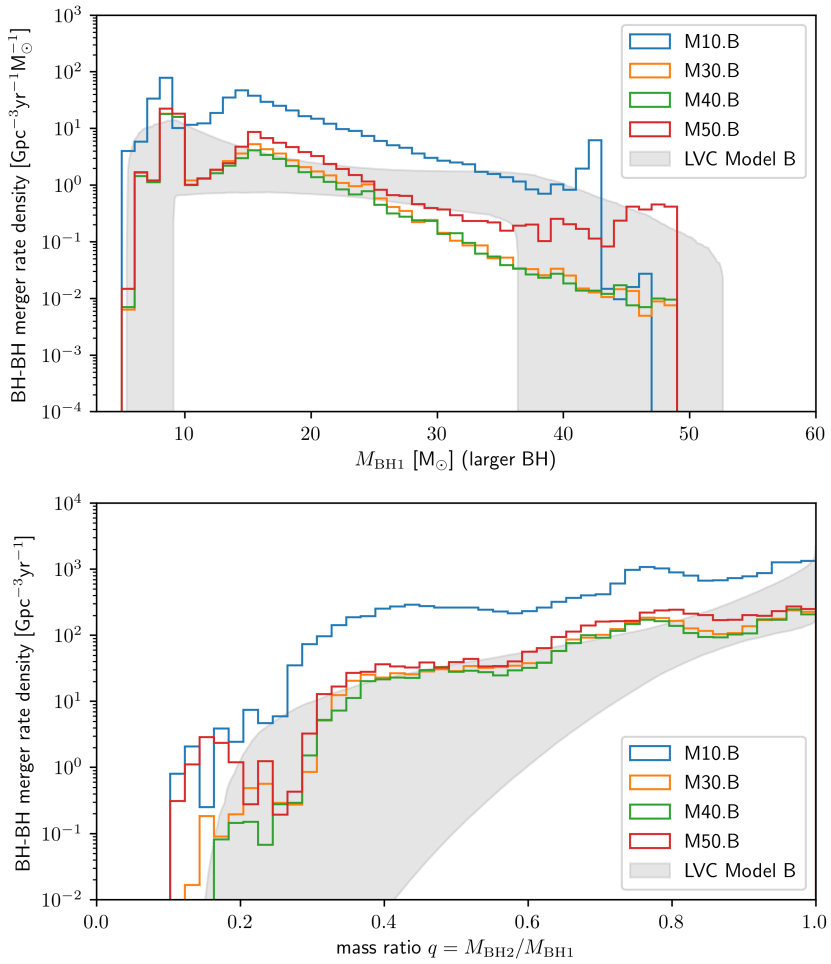


FIGURE 4.26: The intrinsic merger rate distribution as a function of primary black hole mass $M_{\rm BH1}$ (*top*) and binary mass ratio $M_{\rm BH2}/M_{\rm BH1}$ of BH-BH mergers (*bottom*) for different `StarTrack` model choices. The gray bands show the 90% confidence limits on the populations inferred in Abbott et al. (2019a) using the phenomenological Model B.

to $\alpha = 0.1$ with peak probability at $\alpha = -1.6$ [5], and with an upper mass cutoff between 36.3 $M_\odot$ and 57 $M_\odot$.

In Fig. 4.26, we show the intrinsic rate density of mergers averaged out to $z = 0.5$ versus the mass of the more massive BHs in BH-BH mergers ($M_{\rm BH1}$; upper figure) and the mass ratio $q = M_{\rm BH2}/M_{\rm BH1}$ (lower figure) for several of our models and compare them with the fits to Model B from Abbott et al. (2019a). Although Model B does not have the freedom to capture some of the features of the population synthesis distributions, the overall rate densities of the mass distribution found in the LIGO/Virgo collaboration analysis (shown in gray) are quite similar to those obtained, for example, in models M30.B, M40.B, and M50.B. We emphasize that the shapes of the primary mass distributions we obtain in these `StarTrack` models are better fit to exponentials than to power-laws and that there are some interesting features in the mass distributions at low BH mass. Nevertheless, compared to our theoretical models, the LIGO/Virgo Model B fits to the 10 O1/O2 BH-BHs exhibit a similar falloff of the primary mass distribution towards higher masses, lower and upper mass cutoffs, and a falloff of the mass ratio distribution at more unequal masses.

At this point we do not attempt any more elaborate fits to the O1/O2 data than the comparison

[5]Note that the LIGO/Virgo power law index is defined with a minus sign in front (see eq. 2 of Abbott et al. (2019a).

to the LIGO/Virgo phenomenological models, as these can wait till more LIGO/Virgo data points become available. For anyone interested in such fits, all our data is available online. With $O(100)$ BH-BH mergers expected for the entirety of O3, we will be able to test the existence of some of the finer features seen in our mass distributions as well as the goodness-of-fit of exponentials versus power-laws to the primary masses.

### 4.4.5 BH-BH Effective Spins

The rate of BH-BH mergers with different effective spins provides several reliable features that we can use to corroborate and constrain our models with present and future GW observations.

First and foremost, as has been discussed in our and other previous work, our binary evolution models only rarely if ever produce binaries with $\chi_{\rm eff}$ significantly below zero (see Figs. 4.18, 4.19, 4.20, 4.21). This void provides an opportunity to identify the unique contribution from alternative formation channels, as our models cannot produce a preponderance of events with negative effective spins.

Second, our predicted effective spin distributions have sharp cutoff-like features in each of the one (or sometimes two) subpopulations that dominate the detection rate versus effective spin. For example, the black hole spin distribution drops sharply for $\chi_{\rm eff} \gtrsim 0.9$ in the inefficient Geneva angular momentum transport mechanism (Fig. 4.18), above 0.2 for the binary black holes not spun up by tides in the MESA models; above 0.6 for the subpopulation of BH-BH with a tidally-spun-up WR progenitor in the MESA models (Fig. 4.19); and near 0.1 for the Fuller models (Fig. 4.20). Sharp cutoffs like these are rapidly identified empirically, allowing future gravitational-wave observations to constrain the BH natal spin distribution, and the physics of tidal spinup.

Third, for models with WR tides (e.g., M30.B and M40.B shown in Figs 4.19 and 4.20), our effective spin distribution has two well-separated subpopulations (a peak and a tail), associated with the principal channel and the WR-spinup channel. In other words, the gravitational-wave population may allow us to reliably associate specific binary physics to specific binary black hole mergers, and thus to measure the relative proportions (and properties) of BH-BH systems forming through each channel.

While our binary evolution models have many parameters, because of the limited role of accretion on the BH spin, very few parameters have more impact on the $\chi_{\rm eff}$ distribution than the physics we have described above. For example, we have shown with Figure 4.22 that BH kicks have a relatively modest effect on the shape of the $\chi_{\rm eff}$ distribution. Strong BH kicks can for example make the $\chi_{\rm eff}$ distribution more symmetric and isotropic, effectively by disrupting binaries which would otherwise dominate the sharp cutoffs at the largest values of $\chi_{\rm eff}$. In other words, these kicks make the $\chi_{\rm eff}$ merger rate smaller and with a less prominent (and therefore more difficult to identify) cutoff. Though this poorly constrained physics of natal kicks can reduce the rate at which $\chi_{\rm eff}$ measurements can inform about the binary evolution and diminish the contrast of the features we have described above, they cannot erase them, particularly features such as the second population of WR tidally spun-up stars or the low probability of mergers with large negative $\chi_{\rm eff}$.

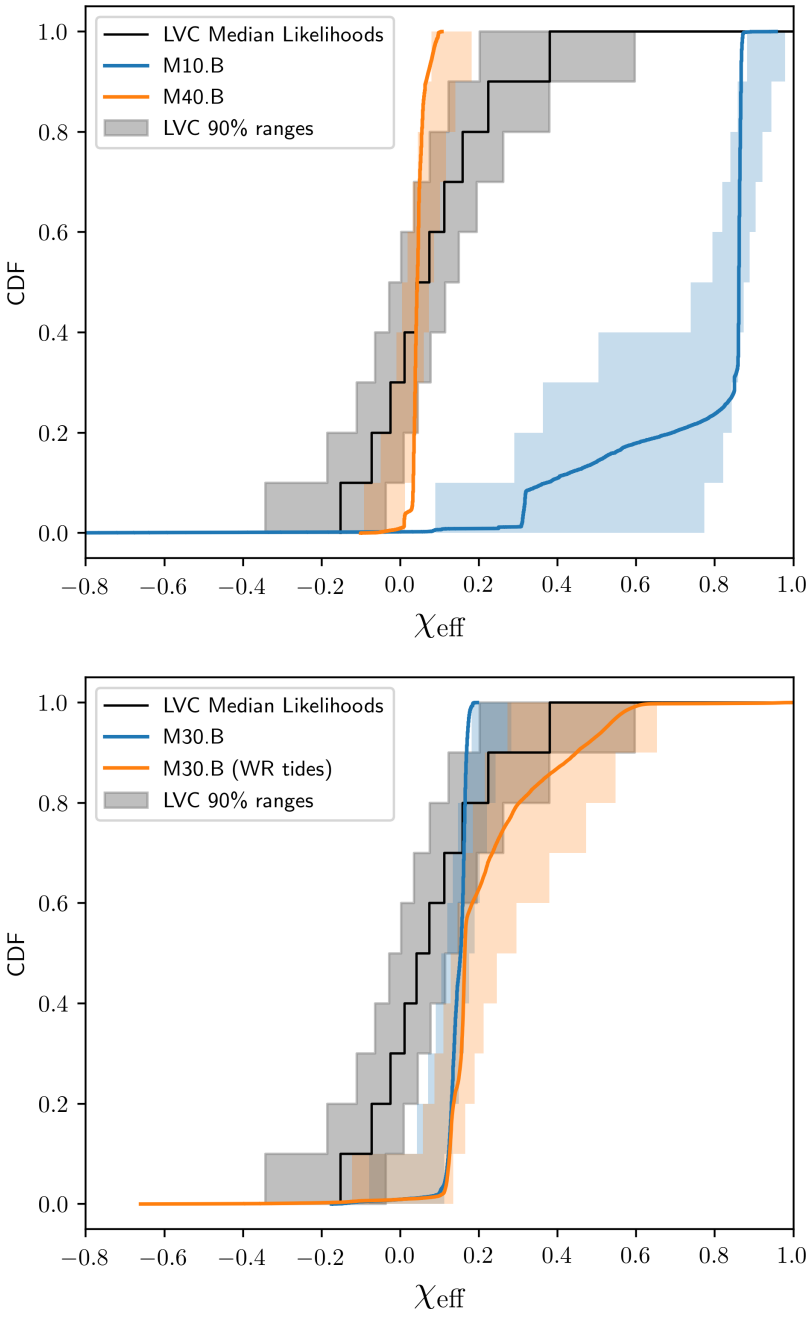


FIGURE 4.27: The cumulative density functions (CDFs) of four `StarTrack` models versus effective spins $\chi_{\rm eff}$. Solid color lines correspond to $\chi_{\rm eff}$ CDF of detectable events for each model. The black line shows the $\chi_{\rm eff}$ CDF of median likelihoods of the O1/O2 LVC events, and the gray region bounds CDFs of the 5th and 95th percentiles of the likelihoods from LVC parameter estimation. In the corresponding colored shaded regions, we show the 90% range of 5000 mock observed CDFs under each model. To generate a mock observed CDF, we draw 10 $\chi_{\rm eff}$ values from the detected population under a given model and add random Gaussian noise with $\sigma = 0.05$, which is approximately the uncertainty in $\chi_{\rm eff}$ likelihoods from the events of GWTC-1 (we resample any samples with $|\chi_{\rm eff}| > 1$ after adding noise).

In Fig. 4.27, we show the cumulative density functions (CDFs) of the effective spin $\chi_{\rm eff}$ for a select set of our models and compare them to the $\chi_{\rm eff}$ measured for the 10 O1/O2 BH-BH mergers. For each model we show the $\chi_{\rm eff}$ CDF of detectable events as a color solid line. In the corresponding colored shaded regions, we show the 90% range of 5000 mock observed CDFs under each model. To generate a mock observed CDF, we draw 10 $\chi_{\rm eff}$ values from the detected population under a given model and add random Gaussian noise with $\sigma = 0.05$, which is approximately the uncertainty in $\chi_{\rm eff}$ likelihoods from the events of GWTC-1 (we resample any samples with $|\chi_{\rm eff}| > 1$ after adding noise). The black line shows the $\chi_{\rm eff}$ CDF of median likelihoods of the O1/O2 LVC events, and the gray region bounds CDFs of the 5th and 95th

percentiles of the likelihoods from LVC parameter estimation. Notably, these effective spins are clustered around zero effective spin, indicating that model M10.B's predicted spins are disfavored by the data. Models M30.B (no WR tides), M30.B (WR tides), and M40.B are much more consistent with these observations, and with the LIGO/Virgo collaboration analysis in Abbott et al. (2019a), which finds a preference for most effective spins to be very close to zero (see Fig. 12 in Abbott et al. (2019a)). That analysis finds that only a few tens of percent of the observed BH-BH mergers have $|\chi_{\rm eff}| > 0.05$, and of those with $|\chi_{\rm eff}| > 0.05$, almost all are likely to have positive $\chi_{\rm eff}$. For the moment the observed $\chi_{\rm eff}$ distribution does not allow to test the importance of WR star tides during the evolution towards a BH even if it seems to slightly favor the no-tide path. Overall, the limited BH-BH sample from O1/O2 does not strongly constrain the BH spins other than to the conclusion that the effective spins tend to be near zero. However, it suggests that O3 should provide data that will allow selecting evolutionary path that lead to BH-BH mergers.

#### 4.4.5.1 Dichotomy of LIGO/Virgo BHs and HMXB BHs

LIGO/Virgo BHs are mostly massive (see Tab. 4.1) and it seems that the spins of these BHs are small. Unfortunately, the spin magnitudes of massive BHs with $M_{\rm BH} > 15\ M_\odot$ are not constrained by other observational means. For example, the three most massive BHs in wind-fed high mass X-ray binaries (HMXB) for which we have spin estimates are at roughly $1/3$ or $1/2$ the mass of the larger-mass LIGO/Virgo BHs. The estimated masses and spins of these BHs can be found online at `https://universeathome.pl/universe/blackholes.php`: LMC X-1, $M_{\rm BH} = 10.9 \pm 1.6\ M_\odot$ ($a_{\rm spin} = 0.92$); Cyg X-1, $M_{\rm BH} = 14.8 \pm 0.1\ M_\odot$ ($a_{\rm spin} > 0.983$); M33 X-7, $M_{\rm BH} = 15.7 \pm 1.5\ M_\odot$ ($a_{\rm spin} = 0.84$). Note that BH spins can be measured by two methods: disk reflection and disk continuum. For LMC-1 and Cyg X-1 BH spins from both methods are consistent, while for M33 X-7 BH spin was estimated only through disk continuum (Miller & Miller, 2015). There is an apparent tension between the spin estimates of LIGO/Virgo BHs and BHs in these HMXBs. However, this tension can be possibly avoided if HMXBs and LIGO/Virgo systems form through different evolutionary scenarios.

First, none of these three HMXBs is expected to produce a BH-BH merger. Future evolution of these systems was studied and it was shown that none of these systems will form a BH-BH merger. They will either end up as single objects (in which BH merges with its massive companion star), or at best they may form BH-NS systems (Belczynski et al., 2012a). Note that this conclusion was reached in the framework of the classical binary evolution that does not take into account homogeneous evolution of rapidly rotating stars that allows for the formation of BH-BH mergers in alternative ways (Marchant et al., 2016; Mandel & de Mink, 2016; de Mink & Mandel, 2016).

Second, it was argued that HMXBs and LIGO/Virgo systems may form through different evolutionary scenarios. As explained in the past, the classical isolated binary evolution channel forms BH-BH mergers from (initially) very wide binaries ($a \gtrsim 1000\ R_\odot$; see Fig. 4.8 or 4.9 or de Mink & Belczynski (2015a); Belczynski et al. (2016b)). Therefore, if the tidal spin-up operates, it only acts at the very end of the evolution during the BH-WR stage (potentially) spinning up some fraction of the second-born BHs in BH-BH mergers (see Sec. 4.2.5 and 4.3.4). This makes the

majority of BHs in BH-BH mergers to have low spins if efficient angular momentum transport is adopted for massive stars (as in our MESA or Fuller models). On the other hand, HMXBs were proposed to form from initially very close binaries ($a \sim 100\ R_{\odot}$, e.g., Valsecchi et al. (2010); Qin et al. (2019)). In such scenario a system with a massive main sequence primary is tidally locked so, through its evolution, its spin is kept high at the expense of the orbital angular momentum. At such small orbital separations the binary undergoes case A mass transfer and/or homogeneous evolution that keeps reducing H-rich envelope of the donor primary and keeps it from expanding. After main sequence evolution, the primary is a compact WR star that quickly collapses to a BH. The BH is found in the near proximity of its companion star (if natal kick is small), naturally producing a (wind-fed) HMXB. Possibly, tidal interactions can keep the primary spin high until the end of its nuclear evolution which would lead to the formation of a rapidly spinning BH. However, the detailed evolutionary calculations have shown that if efficient (Tayler-Spruit dynamo) angular momentum transport is assumed for the primary star, then properties of the three HMXBs considered here can not be reproduced (Qin et al., 2019).

Therefore, the tension still exists, albeit it seems like HMXBs and LIGO/Virgo BH-BH mergers originate from different initial populations of binaries (close versus wide), but specific details of evolution leading to the formation of HMXBs need to be worked out.

Note that formation scenarios that require rapidly spinning stars (whether they lead to formation of BH-BH mergers or BH HMXBs) are not available in our study. Rapid rotation induces efficient mixing and reduces radial expansion of stars in homogeneous or semi-homogeneous evolution. Our calculations can only be applied to slow- or moderately-rotating stars in classical binary evolution. Both binary channels (homogeneous and classical) do not exclude but rather complement each other.

Finally one should stress that estimates of BH spins through properties of their accretion disks, are not *direct* spin measurements but are model–dependent, so there is still a possibility that the tension is only apparent.

### 4.4.6 ORIGIN OF LIGO/VIRGO BHS

At the moment (only O1/O2: data available) it seems that the classical isolated binary evolution formation channel can explain all the basic properties of the LIGO/Virgo BH-BH mergers. This does not mean than other channels do not contribute to LIGO/Virgo detections. For example, if we compare the average rate estimates of the isolated binary channels (see Tab. 4.3 and 4.4) and the dynamical formation channels in globular clusters (see Sec. 4.4.3.2) it appears that 1 in 10 BH-BH mergers might come from a globular cluster. There may be yet another dynamical contribution from young open clusters to BH-BH formations (Ziosi et al., 2014; Di Carlo et al., 2019). Even the homogeneous isolated binary channel is not excluded by the observed LIGO/Virgo low BH-BH effective spins, as apparently BHs with a broad range of spins ($a_{\rm spin} \sim 0.2 - 1$) can be produced also in this scenario (Ph. Podsiadlowski, private communication). In the published models with rather sparse metallicity sampling and conservative evolutionary assumptions (e.g.,

no pair-instability pulsation supernova mass loss[6]) BH spins are found in somewhat narrower range: $a_{\rm spin} \sim 0.4 - 1$ for $M_{\rm BH} \lesssim 60\ M_\odot$ (e.g., see Fig.9 of Marchant et al. (2016)).

If a BH-BH merger is discovered with either of the binary components in the mass range $70/80 \lesssim M_{\rm BH} \lesssim 135\ M_\odot$ with high spin $a_{\rm spin} \approx 0.7$, this would strongly suggest a dynamical formation scenario. The lower-mass limit corresponds to the pair-instability pulsation supernova effects on the presupernova star and on the remnant BH mass (Woosley, 2017; Limongi & Chieffi, 2018; Belczynski et al., 2020a), while the upper mass limit corresponds to the end of the pair-instability supernova process, that is believed to disrupt the entire star without BH formation (Fryer & Kalogera, 2001; Heger & Woosley, 2002). The lack of BHs in this mass range is referred to as the "second mass gap" (Belczynski et al., 2014; Spera et al., 2015; Marchant et al., 2016; Fishbach & Holz, 2017b). It seems unlikely that isolated binaries can fill this gap, but repeated BH-BH mergers in dense environments could produce such heavy BHs, and it is expected that they would have moderately high spins $a_{\rm spin} \approx 0.7$ (Gerosa & Berti, 2017; Fishbach et al., 2017). However, it cannot be excluded that a BH with high mass and low spin is formed by a merger of two BHs (Belczynski & Banerjee, 2020). Alternatively, the detection of a low-spin BH with mass within the second mass gap may point to either *(i)* inconsistencies in pair-instability supernova theory, or *(ii)* a primordial BH origin (Green, 2017). There is also an issue of the second mass gap width. The lower bound may be as high as $70 - 80\ M_\odot$ depending on details of input physics in stellar models (Limongi & Chieffi, 2018; Belczynski et al., 2020a). The upper bound may change if fusion reaction rates of heavy elements that are involved in pair-instability supernovae change. Note that the reaction rates are uncertain (Fields et al., 2018). Possibly, the second mass gap is narrower than currently believed.

In the classical isolated binary evolution channel we have shown that, if LIGO/Virgo observations of BH-BH mergers remain consistent with small effective spins $\chi_{\rm eff} \simeq 0$, this would indicate that low natal spins are common in BHs. In this case, our work shows that stellar models with mild rotational coupling between the stellar interior (core) and the outer zones (envelope) would be disfavored. Our main finding is that angular momentum transport in massive stars (so far unconstrained by the electromagnetic observations) is more efficient than predicted by the Geneva shellular model. This demonstrates how LIGO/Virgo observations can be used to make clear astrophysical inferences and guide stellar evolution astrophysics. Our conclusion is not subject to the main known population synthesis uncertainties, since we have explored a large range of the key parameters: BH natal kicks, initial star rotation, tides, spin-up by accretion onto BHs.

Note that adjusting the angular momentum transport to produce low spinning BHs in BH-BH mergers, to fit LIGO/Virgo observations, leads to several astrophysical inferences and constraints on massive binary evolution. (i) RLOF between two massive stars (see second evolutionary stage in BH-BH formation; Fig. 4.8 or 4.9) cannot effectively spin up the core of the accreting MS star (since this would produce a BH with large spin). This can be avoided if the RLOF is highly non-conservative and not much mass is accreted onto MS star (this is not excluded by any EM

[6]Note that pair-instability pulsation supernova mass loss, if taken into account, can reduce spin by about 30% (Marchant et al., 2018).

observations). Note that we have assumed that 50 – 80% of the mass is lost in RLOF, but in our models this fraction can be easily increased. Alternatively, if accretion is significant and if the entire star is spun-up; then we obtain an additional constraint on the angular momentum transport. It needs to be effective enough to remove most of the angular momentum from the highly spinning core to the envelope in about 1 Myr (time between RLOF and CE which expels the envelope from the binary). *(ii)* Spin-up of the first-formed BH by accretion in the CE phase must be negligible as predicted by recent studies (MacLeod et al., 2017; Murguia-Berthier et al., 2017a; Holgado et al., 2017, see the fifth evolutionary stage in BH-BH formation; Fig. 4.8 and 4.9). *(iii)* Tidal torques are not effective in BH-WR binaries that form BH-BH mergers, as the WR star spin-up would lead to the formation of a highly spinning BH (see the sixth evolutionary stage in BH-BH formation; Fig. 4.8 and 4.9). In our evolution a small, but significant fraction ($\sim 20-30\%$; see Figs. 4.19 and 4.20) of the BH-WR/WR-BH/WR-WR binaries are found on orbits smaller than $\sim 10-20\ R_{\odot}$ (orbital periods $P_{\rm orb} < 1.3$ d) for which the tides are expected to be effective for WR stars (Kushnir et al., 2016; Zaldarriaga et al., 2017; Qin et al., 2018). Therefore if there are no detections of highly spinning BHs in LIGO/Virgo observations it will imply that tides are not as effective as argued by recent work, or that BH-BH mergers are not produced by the isolated classical binary evolution (Hotokezaka & Piran, 2017c). Note, however, that already one event (GW170729) may have an effective spin as high as $\chi_{\rm eff} = 0.57$ (90% credible limits; see Tab. 4.1). On the other hand, in ten events one can expect one outlier within the 90% credible limits. Therefore at the moment the comparison of models with observations remains inconclusive in respect to tides. Yet, the comparison of models predicting tidally spun-up stars, producing highly spinning BHs, with the number of LIGO/Virgo high effective spin BH-BH mergers may help to constrain the strength of tides in near future.

Finally, note that our main conclusion that angular momentum transport needs to be more effective than predicted by shellular model for massive stars adds support to the similar conclusion that was reached for low-mass stars from Kepler asteroseismology data (Cantiello et al., 2014).

## 4.5 CONCLUSIONS

We have updated our method of population synthesis calculations with revised and extended input physics that is important for the formation of double compact object mergers: BH-BH, BH-NS and NS-NS. New models of pair-instability pulsation supernovae that are crucial in mass estimates of heavy black holes have been introduced. We have employed the recent estimates of star–formation rate density and cosmic metallicity evolution in our calculations. These two factors play an important role in setting the double compact object merger rates (Belczynski et al., 2010a; Dominik et al., 2013; Chruslinska & Nelemans, 2019a; Neijssel et al., 2019). We have introduced new models for BH natal spin that allow for a direct comparison with LIGO/Virgo estimates of the effective spin parameter of BH-BH mergers. These models connect gravitational-wave observations with detailed stellar evolution calculations of angular momentum transport in massive stars that is otherwise hidden from electromagnetic observations. We have also allowed for

significantly decreased stellar winds with respect to the standard wind prescriptions (Vink et al., 2001) used in modeling. Winds are an important factor that sets the shape of black hole mass distribution. Finally, updated prescriptions of accretion onto compact objects in stable Roche-lobe overflow, common envelope, and from stellar winds have been used in our calculations.

In the following we summarize our main findings.

1. Our study is the first to employ detailed single stellar evolutionary calculations in binary population synthesis to compare LIGO/Virgo BH-BH effective spins with those resulting from several angular momentum transport mechanisms. If LIGO/Virgo BH-BH mergers originate from the classical isolated binary evolution channel, then their low effective spins inform about the effective angular momentum transport in massive stars and most likely disfavor effective tidal interactions in close binaries with WR stars. According to our evolutionary framework the Tayler-Spruit magnetic dynamo (as implemented in the MESA or in the Fuller model) reproduces the effective spin measurements very well, while meridional currents (as implemented in the Geneva model) are inconsistent with the current LIGO/Virgo data.

2. For some of our models the predicted merger rate densities of BH-BH, BH-NS and NS-NS systems are within the LIGO/Virgo empirical estimates. The rates depend strongly on the cosmic metallicity evolution, the choice of NS/BH natal kicks and the treatment of the common envelope phase. Due to the similar effects of these factors on the rates, it is still not possible to derive strong conclusions about any of these pieces of input physics separately. However, some combinations of parameters may be already excluded. Inter-parameter degeneracies are an important factor that cannot be overlooked in deriving astrophysical conclusions from gravitational-wave observations.

3. The range of the observed BH masses appears to be in agreement with all three of our adopted PPSN models: from strong PPSN with maximum BH mass of $M_{\rm BH,max} \sim 40\ M_\odot$, to moderate PPSN with $M_{\rm BH,max} \sim 50\ M_\odot$, and to weak PPSN with $M_{\rm BH,max} \sim 55\ M_\odot$. If heavier BHs are observed it will indicate that, either the pair-instability pulsation supernovae and the pair-instability supernovae do not work as predicted, or that BHs with very heavy mass originate from other formation channels. The values of BH spins may distinguish these two possibilities. If a massive BH ($\sim 100\ M_\odot$) is observed with low spin it will indicate a classical isolated binary evolution formation channel, but such an observation will cast shadow on PPSN/PSN predictions. If, however, such a BH is found to have a large spin as expected from consecutive BH mergers, then its presence will point to formation in a dense stellar environment (e.g., globular cluster).

4. If, based on our limited set of models and the initial ten O1/O2 detections, we were to make statements about the physics of massive binaries, we could venture to say that with our revised cosmic metallicity evolution it seems that to reproduce simultaneously the observed BH-BH, BH-NS, and NS-NS merger rates one should use submodels B (no CE allowed with

HG donors) if BH kicks are low, but if these kicks are high, submodels A (CE allowed with HG donors) should be preferred. If individual BH masses are in fact as high as LIGO/Virgo reports for the most likely values from O1/O2 run (e.g., 50.6 $M_{\odot}$ for GW170729) then we can already exclude strong mass ejection during the PPSN.

Note that similar conclusions were reached by Bavera et al. (2020) and Neijssel et al. (2019), although somewhat different approach to detailed stellar evolution models and a different population synthesis code was used.

**ACKNOWLEDGEMENTS**

We have benefited from comments from Selma de Mink, Enrico Ramirez-Ruiz, Ilya Mandel, Thomas Janka, Serena Repetto, Simon Stevenson, Sambaran Banerjee, Tom Maccarone, Craig Heinke, Phil Charles, Doron Kushnir, Tsvi Piran, Miguel Holgado, Antonio Claret, Tassos Fragos, Philipp Podsiadlowski, and Matt Benacquista. We would like to thank thousands of `Universe@home` users that have provided their personal computers and phones for our simulations, and in particular to Krzysztof Piszczek (program IT managers). KB acknowledges support from the Polish National Science Center (NCN) grant Maestro (2018/30/A/ST9/00050) and KB, SM and JPL from the NCN grant OPUS (2015/19/B/ST9/01099). JK and MC acknowledge support from the Netherlands Organisation for Scientific Research (NWO). C.E.F. acknowledges support from a Pre-doctoral Fellowship administered by the National Academies of Sciences, Engineering, and Medicine on behalf of the Ford Foundation, an Edward J Petry Graduate Fellowship from Michigan State University, and the National Science Foundation Graduate Research Fellowship Program under grant number DGE1424871. MG ans AA were partially supported by the National Science Centre, Poland, through the grant UMO-2016/23/B/ST9/02732. This work has been supported by the EU COST Action CA16117 (ChETEC). RH, KN, KB acknowledge support from the World Premier International Research Centre Initiative (WPI Initiative), MEXT, Japan. D.G. is supported by Leverhulme Trust Grant No. RPG-2019-350 and by NASA through Einstein Postdoctoral Fellowship Grant No. PF6-170152 awarded by the Chandra X-ray Center, which is operated by the Smithsonian Astrophysical Observatory for NASA under contract NAS8-03060. TB acknowledges support from the Polish National Science Center (NCN) Grant No. UMO-2014/14/M/ST9/00707. EB is supported by NSF Grants No. PHY-1607130, AST-1716715, and by FCT contract IF/00797/2014/CP1214/CT0012 under the IF2014 Programme. C.G., G.M., and S.E. acknowledge support from the Swiss National Science Foundation (project number 200020-160119). ROS is supported by NSF AST-1412449, PHY-1505629, and PHY- 1607520. DAB acknowledges support from National Science Foundation Grant No. PHY-1404395. G.W. is partly supported by the President's International Fellowship Initiative (PIFI) of the Chinese Academy of Sciences under grant no.2018PM0017 and by the Strategic Priority Research Program of the Chinese Academy of Science Multi-waveband Gravitational Wave Universe (Grant No. XDB23040000). AA is supported by the Carl Tryggers Foundation for Scientific Research through the grant CTS 17:113. MCM acknowledges support by NASA grant 80NSSC18K0527. This research was supported in part by the National Science Foundation under Grant No. NSF

PHY-1748958 to KITP UC Santa Barbara. Several authors (KB, EB, CLF, DAB, DEH, RO, KN, MCM, GM, JPL) were supported by KITP UC Santa Barbara to work on this project. JPL was supported by a grant from the French Space Agency CNES. S.C.L acknowledges support by the funding HST-AR-15021.001-A. DEH was partially supported by NSF grant PHY-1708081, and also by the Kavli Institute for Cosmological Physics at the University of Chicago through an endowment from the Kavli Foundation. He also gratefully acknowledges support from a Marion and Stuart Rice Award. We thank the Niels Bohr Institute for its hospitality while part of this work was completed, and acknowledge the Kavli Foundation and the DNRF for supporting the 2017 Kavli Summer Program.

# 4.A Appendix

Data availability: data generated during this project with population synthesis code `StarTrack` is available online: `www.syntheticuniverse.org` under the tab "StarTrack models vs. Gravitational Wave Observations". Code availability: the `StarTrack` code is not an open source code and is not publicly available. New models will be calculated upon requests to the first author: chrisbelczynski@gmail.com.

## 4.A.1 Geneva Stellar Models

The physics included in the employed `Geneva` rotating models is described in detail in Eggenberger et al. (2008); Ekström et al. (2012). The models have been computed with a modest core-overshooting during the core H- and He-burning phase (the core has been extended beyond the Schwarzschild limit by a length given by 10% of the local pressure scale height). Mass loss rates by stellar winds are accounted for (see the above references for the details). The effects of rotation are included according to the theory by Zahn (1992). In these models, the transport of the angular momentum and the mixing of the chemical species in the radiative zones are due to shear instabilities and meridional currents. In contrast with many stellar models in which the effects of meridional currents are accounted for by a diffusion equation, in the present models the angular momentum transport is accounted for by solving an advective equation. In essence, transport by meridional currents is an advective process. Diffusion treatments can lead not only to wrong estimates of the amplitude, but also to wrong signs (a diffusive process always tends to flatten any gradient, while an advective process can increase gradients in some circumstances). Note also that shear instabilities are the main drivers for the transport of the chemical species, while angular momentum is mainly transported by meridional currents. The angular momentum transport by meridional currents mildly couples the core rotation with that of the envelope. In the convective zones, the transport of angular momentum and chemical species is assumed to be extremely efficient: convective zones are assumed to rotate as a solid body, and the chemical composition is homogenized.

In Table 4.5 we present a suite of Geneva evolutionary models (Ekström et al., 2012; Georgy et al., 2013; Groh et al., 2019) and Eggenberger et al. (in preparation) with $M_{\rm zams} = 9$–$120\ M_\odot$ for a wide range of chemical compositions: $Z = 0.014$–$0.0004$. Specifically, we are listing CO core mass for each evolutionary model along with our estimate of the associated BH spin magnitude (see Fig. 4.1 for a plot of the relation between the two).

The spin magnitude is very sensitive to the BH mass ($\propto 1/M_{\rm BH}^2$; see eq. 4.2). The CO core mass may be taken as a proxy for BH mass (cf. Appendix 4.A.3 and Figure 4.29). Below we present the behavior of the CO core mass within the Geneva models. This discussion explains the non-monotonic dependence of BH spin on metallicity.

As naturally expected, the CO core mass increases with the initial stellar mass within models of the same metallicity. This intuitive trend is reversed only at the highest metallicity considered here ($Z = 0.014$), at which stellar winds are most efficient in mass removal. In particular, this is true for very massive stars ($M_{\rm zams} \gtrsim 100\ M_\odot$).

Another intuitive expectation is not supported by these stellar models. For a given initial stellar mass, one may naively expect that the CO core mass would increase with decreasing metallicity, as winds are getting weaker and star remains more massive. However, for example for $M_{\rm zams} = 85\ M_\odot$ we find $M_{\rm CO,2} = 26.4,\ 35.8,\ 27.4,\ 44.2\ M_\odot$ for $Z = 0.014,\ 0.006,\ 0.002,\ 0.0004$, respectively. In the following, we explain this non-monotonic behavior in terms of our adopted stellar model.

Stellar winds are weaker at low metallicity thus this leads to increase of the CO core mass with decreasing metallicity. This general trend is mitigated by two other physical processes. Decreasing metallicity leads to the formation of extended convective H-burning shells that tend to slow down the growth of the He core (and subsequently the CO core) mass. At high $Z$ massive stars lose most of their envelopes, so there is no vertical structure available for extended convective H-burning shell. The H-burning shell is compact and moves outwards (once H is totally depleted) through the envelope, adding mass to the underlying He core. At low $Z$, massive stars not only retain their envelopes longer, but they are also more compact, and increased density helps to form extended convective zones. Within the extended convective shell reaching far above H-burning (which occurs only at the shell base), intensive mixing keeps bringing new fuel to the H-burning zone (keeping it in the same position), and keeps redistributing newly formed He across this large shell. Instead of adding He to the core, the newly formed He is redistributed through the material of the extended convective shell. Another process that leads to CO core mass decrease with metallicity is connected to the diffusion of elements due to the action of meridional currents and turbulence. With decreasing metallicity stars are more compact and the vertical scale of diffusion decreases, leading to less effective mixing of fresh fuel into burning zones. This, in turn, lowers the CO core mass.

For the particular set of assumptions used in the Geneva code, the non-monotonic behavior of the CO core mass is the effect of the complex and metallicity-dependent interplay of strength of stellar winds, the H-burning shell extent, and the model for the efficiency of element diffusion within the meridional current. This explains the non-monotonic metallicity dependence of our BH natal spin model (see Fig. 4.1).

Table 4.5: Geneva stellar models[a] .

| Z | $M_{\rm ZAMS}$ [ $M_\odot$] | $V_{\rm rot,i}$ [km s$^{-1}$] | $M_{\rm He}$ [ $M_\odot$] | $M_{\rm CO,1}$ [ $M_\odot$] | $M_{\rm CO,2}$ [ $M_\odot$] | $P_{NS}$, $a_{\rm spin}$ [ms,] | $M_{\rm NS/BH}$ [ $M_\odot$] | $M_{\rm star,g}$ [ $M_\odot$] | $M_{\rm star,st1}$ [ $M_\odot$] | $M_{\rm star,st2}$ [ $M_\odot$] |
|---|---|---|---|---|---|---|---|---|---|---|
| **Z=0.014** | 9 | 248 | 2.9 | 1.61 | 2.40 | 0.6 | 1.18 | 8.5 | 8.5 | 8.9 |
| | 12 | 262 | 3.8 | 2.26 | 3.40 | 0.6 | 1.19 | 10.2 | 11.0 | 11.7 |
| | 15 | 271 | 5.1 | 3.07 | 4.59 | 0.5 | 1.35 | 11.1 | 11.3 | 13.9 |
| | 20 | 274 | 7.1 | 4.50 | 6.86 | 0.5 | 1.76 | 7.2 | 12.3 | 17.6 |
| | 25 | 295 | 9.7 | 6.69 | 9.38 | 0.90 | 9.66 | 9.7 | 9.2 | 20.4 |
| | 32 | 306 | 10.1 | 7.45 | 10.1 | 0.88 | 6.24 | 10.1 | 10.5 | 23.4 |
| | 40 | 314 | 12.3 | 9.29 | 12.3 | 0.87 | 7.88 | 12.3 | 11.6 | 22.1 |
| | 60 | 346 | 18.0 | 14.2 | 18.0 | 0.62 | 14.2 | 18.0 | 13.5 | 36.0 |
| | 85 | 368 | 26.4 | 21.6 | 26.4 | 0.29 | 21.6 | 26.4 | 18.1 | 52.6 |
| | 120 | 389 | 19.0 | 15.2 | 19.0 | 0.13 | 15.2 | 19.0 | 20.7 | 66.9 |
| **Z=0.006** | 15 | 271 | 5.1 | 2.87 | 4.71 | 0.5 | 1.30 | 14.0 | 13.5 | 14.5 |
| | 20 | 292 | 7.2 | 4.41 | 7.02 | 0.5 | 1.72 | 13.9 | 16.7 | 19.0 |
| | 25 | 301 | 9.6 | 6.50 | 9.55 | 0.80 | 9.62 | 10.5 | 17.8 | 22.8 |
| | 32 | 334 | 13.5 | 9.98 | 13.4 | 0.90 | 11.6 | 13.6 | 17.5 | 27.5 |
| | 40 | 334 | 18.9 | 14.9 | 18.7 | 0.90 | 18.9 | 18.9 | 14.8 | 21.3 |
| | 60 | 378 | 32.8 | 28.3 | 32.8 | 0.90 | 28.2 | 32.8 | 18.9 | 38.6 |
| | 85 | 410 | 35.8 | 30.2 | 35.8 | 0.37 | 30.1 | 35.8 | 28.8 | 61.5 |
| | 120 | 435 | 52.5 | 45.1 | 52.4 | 0.25 | 42.3 | 52.5 | 31.4 | 77.9 |
| **Z=0.002** | 9 | 255 | 2.8 | 1.55 | 1.59 | 0.5 | 1.20 | 8.9 | 8.4 | 8.9 |
| | 12 | 271 | 3.9 | 2.01 | 3.17 | 0.5 | 1.20 | 11.8 | 9.4 | 11.3 |
| | 15 | 303 | 5.0 | 2.76 | 4.65 | 0.5 | 1.26 | 14.7 | 12.8 | 14.6 |
| | 20 | 305 | 7.2 | 4.36 | 7.04 | 0.5 | 1.73 | 18.7 | 17.8 | 19.3 |
| | 25 | 319 | 9.6 | 6.29 | 9.42 | 0.90 | 9.56 | 21.8 | 19.8 | 23.4 |
| | 32 | 338 | 13.1 | 9.32 | 13.0 | 0.85 | 10.2 | 24.1 | 18.9 | 28.0 |

TABLE 4.5: Geneva stellar models[a] .

| Z | $M_{\rm ZAMS}$ [ $M_\odot$] | $V_{\rm rot,i}$ [km s$^{-1}$] | $M_{\rm He}$ [ $M_\odot$] | $M_{\rm CO,1}$ [ $M_\odot$] | $M_{\rm CO,2}$ [ $M_\odot$] | $P_{NS}$, $a_{\rm spin}$ [ms,] | $M_{\rm NS/BH}$ [ $M_\odot$] | $M_{\rm star,g}$ [ $M_\odot$] | $M_{\rm star,st1}$ [ $M_\odot$] | $M_{\rm star,st2}$ [ $M_\odot$] |
|---|---|---|---|---|---|---|---|---|---|---|
| | 40 | 358 | 17.6 | 13.3 | 17.5 | 0.90 | 17.6 | 27.4 | 14.5 | 17.1 |
| | 60 | 400 | 31.6 | 26.7 | 27.4 | 0.001 | 31.6 | 39.1 | 22.8 | 39.3 |
| | 85 | 435 | 45.3 | 26.7 | 27.4 | 0.28 | 43.0 | 74.8 | 35.7 | 66.6 |
| | 120 | 438 | 85.6 | 76.4 | 83.2 | PSN | 0.0 | 85.6 | 46.6 | 91.6 |
| **Z=0.0004** | 9 | 270 | 1.6 | 1.54 | 1.59 | 0.6 | 1.20 | 8.90 | 8.9 | 9.0 |
| | 12 | 285 | 3.9 | 2.02 | 3.28 | 0.6 | 1.19 | 11.9 | 11.8 | 11.9 |
| | 15 | 319 | 5.0 | 2.87 | 4.81 | 0.5 | 1.28 | 14.9 | 14.8 | 14.9 |
| | 20 | 314 | 7.8 | 4.84 | 7.35 | 0.4 | 1.86 | 19.4 | 19.7 | 19.9 |
| | 25 | 343 | 10.0 | 6.60 | 9.81 | 0.88 | 10.0 | 24.0 | 24.4 | 24.8 |
| | 32 | 366 | 12.6 | 8.71 | 12.5 | 0.80 | 8.86 | 30.5 | 30.0 | 31.4 |
| | 40 | 393 | 16.9 | 12.5 | 16.9 | 0.82 | 12.5 | 34.6 | 15.6 | 23.4 |
| | 60 | 435 | 28.4 | 28.4 | 27.8 | 0.79 | 28.4 | 49.9 | 24.9 | 41.7 |
| | 85 | 469 | 47.0 | 40.1 | 44.2 | 0.26 | 44.6 | 57.8 | 37.9 | 68.5 |
| | 120 | 463 | 70.2 | 62.1 | 65.3 | PSN | 0.0 | 92.5 | 66.6 | 104 |

NOTES:

[a] For all models we list: $Z$: metallicity, $M_{\rm ZAMS}$: initial star mass, $V_{\rm rot,i}$: initial rotation at equator, $M_{\rm He}$: He core mass, $M_{\rm CO,1}$: CO core mass defined by $< 1\%$ He (used in MESA), $M_{\rm CO,2}$: CO core mass defined by $> 20\%$ CO (adopted in our study), $P_{\rm NS}$, $a_{\rm spin}$: for NSs, the NS spin period in milliseconds, for BHs, the dimensionless spin magnitude, $M_{\rm NS/BH}$: remnant mass, $M_{\rm star,g}$: final mass of a star in Geneva code, $M_{\rm star,st1}$: final mass of a star in `StarTrack` with standard winds, $M_{\rm star,st2}$: final mass of a star in `StarTrack` with reduced (30%) winds.

### 4.A.2 MESA Stellar Models

The MESA stellar models were evolved using MESA revision 10398 (Paxton et al., 2011, 2013, 2015, 2018, 2019). The models are evolved from the pre-main sequence to core He-depletion. We use temporal and spatial parameters similar to those used in Farmer et al. (2016) and Fields et al. (2018) that provide convergence to the $\approx 10\%$ level. The MESA models use the mesa-49.net network that follows 49 isotopes from $^{1}$H to $^{34}$S. We include mass loss using the 'Dutch' wind scheme with an efficiency value of 0.8 (Nieuwenhuijzen & de Jager, 1990a; Nugis & Lamers, 2000a; Vink et al., 2001; Glebbeek et al., 2009). We use the Ledoux criterion for convection with mixing length $\alpha_{\rm MLT} = 1.6$, and the mlt++ approximation for convection (Paxton et al., 2013).

Additional mixing processes due to convective boundary mixing are included using the exponentially decaying diffusion coefficient framework of Herwig (2000) based on hydrodynamic simulations of Freytag et al. (1996). The following values of $f$ were used: $f = 0.014$ above H- and He-burning regions, $f = 0.001$ below H- and He-burning regions, $f = 0$ elsewhere. Note that the additional parameter, $f_0 = 0.001$ was used, where $f_0 H_P$ is the distance from the boundary inside the convective zone where the exponential decay starts. Jones et al. (2015) compare GENEC models to MESA models and find that using $f = 0.022$ on top of convective core H and He burning in MESA matches GENEC models with a penetrative overshoot, $\alpha_{\rm ov} = 0.2 H_P$. Given that the GENEC models used in this paper use $\alpha_{\rm ov} = 0.1 H_P$, using $f = 0.014$ in MESA yields similar core masses and lifetimes.

In MESA, rotation is implemented using the shellular approximation (Zahn, 1992; Meynet & Maeder, 1997). In our models, we initialize solid body, uniform rotation at the zero age main-sequence as a fraction of the Keplerian critical rotation rate, in most of our models this value is 40%. We use the suggested values from (Heger et al., 2000) for the diffusion coefficients for the transport of angular momentum and material due to various instabilities. Of the most influential of these mechanisms included in the MESA models is the Tayler-Spruit dynamo. The modeling of this dynamo in the stellar models increases the efficiency in angular momentum transport and can lead to a significantly different angular momentum profiles and core rotation rates (Heger et al., 2005, see also Sec. 4.4.1).

We find that, at the essence, the Taylor-Spruit dynamo dominates the transport of angular momentum in our MESA models and is very efficient at transporting the angular momentum from the core to the upper layers, from which it is lost in winds. As a result, all our models end with a very similar (small) amount of angular momentum and thus small spin parameter $a < 0.15$ , see Figure 4.2 and also Table. 4.6. Given that stronger stellar winds lead to a more efficient loss of angular momentum, one would expect a dependence of the final spin on mass and metallicity. We find a hint of such a dependence in our models: the more massive as well as the higher metallicity models tend to end with systematically lower final spins (Fig. 4.2). However, this is not very clear in our models, and the impact of mass and metallicity is sub-dominant to the fact that the efficient transport of angular momentum through the Taylor-Spruit dynamo leads to small spins.

A star might spin up during its main-sequence evolution due to mass accretion from a companion or be born as a very fast rotator. We mimic this scenario with a single, very fast rotating MESA

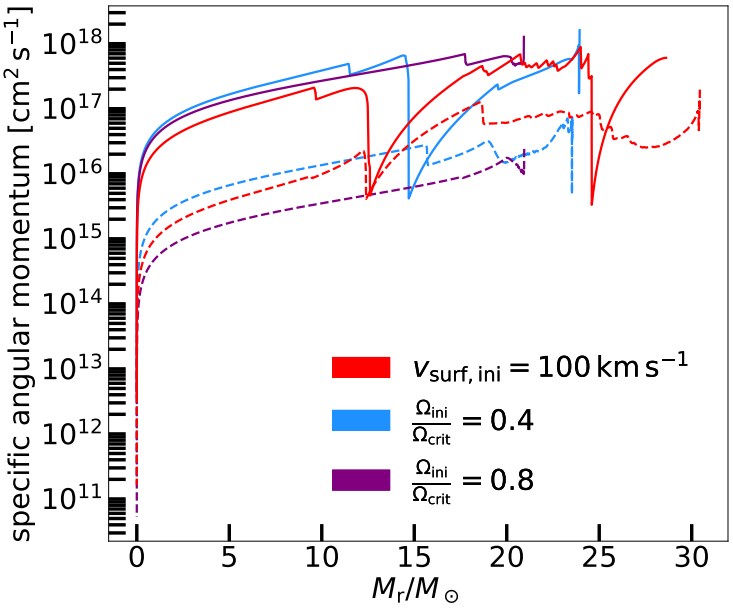


FIGURE 4.28: Specific angular momentum profile at the end of core helium burning for the 32 $M_\odot$ MESA models at $Z = 0.002$. The models were calculated with different initial rotation rates; slow (100 km s$^{-1}$, red), fast (40% of critical rotation, blue) and very fast (80% of critical rotation, purple). Magnetic (dashed line) and non-magnetic models (solid line) are considered. Large dips in the curve indicate the base of a convective region, where angular momentum transport is very efficient. The maximal extent of the curves to the right indicate the mass of the star. We can see from these curves that the faster rotating models lose more mass in winds due to rotation-enhanced mass loss.

model and compare it to the slow and fast rotating 32 $M_\odot$ MESA models plotted in Figure 4.23 for both, magnetic and non-magnetic angular momentum transport. The specific angular momentum profile at core helium depletion of the very fast rotating models is presented in Figure 4.28. It clearly shows, as already pointed out earlier, that the rotation rate at core helium depletion depends mainly on the angular momentum transport mechanism (the difference between the models using the Taylor-Spruit dynamo will be further reduced during the advanced phases of stellar evolution) and not the initial rotation rate. This is a result of the evolution after the main-sequence where the Taylor-Spruit dynamo extracts most of the angular momentum from the core. The core contracts due to the missing energy generation and the envelope expands as a consequence of the virial theorem and energy conservation. The contracting core spins up faster in the models with faster initial rotation, creating a stronger shear between core and envelope. The stronger shear leads to a stronger angular momentum transport of the magnetic dynamo ($\nu_{\rm ST} \sim -(\frac{d\ln\Omega}{d\ln r})^2$) in a region where stratification is dominated by the chemical composition gradient (Spruit, 2002), which is the case for the region above the helium core where the shear develops after the MS evolution in a massive star), resulting in similar specific angular momentum profiles. Therefore, a star that is either spun up by a binary companion or is born fast will still end its life with a slow spinning core when an efficient angular momentum transport mechanism is active.

In the non-magnetic models presented in Figure 4.28, most of the angular momentum is transported in the short phase between core hydrogen and helium burning (as in the magnetic models) but the transport is much less efficient. Therefore, the core of models excluding magnetic fields will not be able to slow down and will have a high final rotation rate.

Table 4.6: MESA stellar models with 40% critical initial rotation[a] .

| Z | $M_{\rm ZAMS}$ [ $M_\odot$] | $V_{\rm rot,i}$ [km s$^{-1}$] | $M_{\rm He}$ [ $M_\odot$] | $M_{\rm CO,1}$ [ $M_\odot$] | $M_{\rm CO,2}$ [ $M_\odot$] | $P_{NS}$, $a_{\rm spin}$ [ms,] | $M_{\rm NS/BH}$ [ $M_\odot$] | $M_{\rm star,m}$ [ $M_\odot$] | $M_{\rm star,st1}$ [ $M_\odot$] | $M_{\rm star,st2}$ [ $M_\odot$] |
|---|---|---|---|---|---|---|---|---|---|---|
| **Z=0.014** | 10 | 257 | 2.9 | 1.2 | 1.5 | 8.0 | 1.20 | 3.4 | 9.4 | 9.8 |
| | 15 | 270 | 4.5 | 2.2 | 2.7 | 6.4 | 1.27 | 5.7 | 11.3 | 13.9 |
| | 20 | 274 | 6.7 | 3.6 | 4.6 | 4.4 | 1.79 | 10.8 | 12.3 | 17.6 |
| | 25 | 276 | 7.8 | 4.2 | 6.2 | 0.094 | 6.16 | 19.9 | 9.2 | 20.4 |
| | 32 | 272 | 12.0 | 7.9 | 9.1 | 0.107 | 9.23 | 25.3 | 10.5 | 23.4 |
| | 40 | 267 | 16.6 | 11.8 | 13.2 | 0.105 | 16.8 | 27.8 | 11.6 | 22.1 |
| | 60 | 254 | 27.6 | 21.1 | 22.6 | 0.083 | 28.0 | 46.5 | 13.5 | 36.0 |
| | 85 | 239 | 41.6 | 33.4 | 35.2 | 0.046 | 42.6 | 56.2 | 18.1 | 52.6 |
| | 120 | 220 | 60.8 | 49.9 | 52.8 | 0.037 | 55.0 | 80.0 | 20.7 | 66.9 |
| **Z=0.006** | 10 | 268 | 2.9 | 1.0 | 1.6 | 6.7 | 1.20 | 3.9 | 9.6 | 9.9 |
| | 15 | 279 | 4.7 | 2.2 | 2.9 | 5.9 | 1.32 | 10.0 | 13.5 | 14.5 |
| | 20 | 293 | 6.8 | 3.8 | 4.6 | 9.7 | 1.79 | 18.3 | 16.7 | 19.0 |
| | 25 | 296 | 8.6 | 5.1 | 6.0 | 0.101 | 8.67 | 23.0 | 17.8 | 22.8 |
| | 32 | 295 | 11.8 | 7.9 | 8.9 | 0.100 | 8.87 | 29.3 | 17.5 | 27.5 |
| | 40 | 289 | 14.4 | 8.9 | 10.3 | 0.099 | 16.1 | 31.3 | 14.8 | 21.3 |
| | 60 | 277 | 26.6 | 20.3 | 21.9 | 0.093 | 26.8 | 52.4 | 18.9 | 38.6 |
| | 85 | 266 | 39.9 | 31.2 | 32.9 | 0.081 | 47.1 | 69.0 | 28.8 | 61.5 |
| | 120 | 251 | 61.8 | 50.6 | 53.3 | 0.072 | 55.0 | 91.7 | 31.4 | 77.9 |
| **Z=0.002** | 10 | 285 | 3.0 | 1.1 | 1.6 | 7.1 | 1.20 | 6.5 | 8.4 | 9.6 |
| | 15 | 298 | 4.9 | 2.5 | 3.0 | 7.7 | 1.35 | 14.7 | 12.8 | 14.6 |
| | 20 | 305 | 6.6 | 3.7 | 4.3 | 7.6 | 1.72 | 19.5 | 17.8 | 19.3 |
| | 25 | 310 | 8.2 | 4.9 | 7.7 | 0.096 | 8.29 | 23.9 | 19.8 | 23.4 |
| | 32 | 312 | 12.0 | 8.1 | 9.0 | 0.104 | 9.11 | 30.4 | 18.9 | 28.0 |
| | 40 | 313 | 15.4 | 10.9 | 12.1 | 0.142 | 15.4 | 37.3 | 14.5 | 17.1 |

TABLE 4.6: MESA stellar models with 40% critical initial rotation[a] .

| Z | $M_{\rm ZAMS}$ [ $M_\odot$] | $V_{\rm rot,i}$ [km s$^{-1}$] | $M_{\rm He}$ [ $M_\odot$] | $M_{\rm CO,1}$ [ $M_\odot$] | $M_{\rm CO,2}$ [ $M_\odot$] | $P_{NS}$, $a_{\rm spin}$ [ms,] | $M_{\rm NS/BH}$ [ $M_\odot$] | $M_{\rm star,m}$ [ $M_\odot$] | $M_{\rm star,st1}$ [ $M_\odot$] | $M_{\rm star,st2}$ [ $M_\odot$] |
|---|---|---|---|---|---|---|---|---|---|---|
| | 60 | 304 | 26.9 | 20.8 | 22.4 | 0.108 | 27.0 | 55.1 | 22.8 | 39.3 |
| | 85 | 286 | 39.5 | 31.6 | 33.6 | 0.090 | 39.7 | 76.9 | 35.7 | 66.6 |
| | 120 | 268 | 60.9 | 50.1 | 54.1 | 0.065 | 55.0 | 105 | 46.6 | 91.6 |
| **Z=0.0004** | 10 | 302 | 3.1 | 1.4 | 1.7 | 7.1 | 1.20 | 9.8 | 9.9 | 10.0 |
| | 15 | 315 | 4.9 | 2.5 | 3.1 | 8.5 | 1.36 | 14.9 | 14.8 | 14.9 |
| | 20 | 323 | 6.8 | 3.9 | 4.6 | 5.2 | 1.79 | 19.7 | 19.7 | 19.9 |
| | 25 | 329 | 8.7 | 5.4 | 6.2 | 0.138 | 8.81 | 24.5 | 24.4 | 24.8 |
| | 32 | 335 | 12.4 | 8.3 | 9.3 | 0.110 | 9.83 | 31.0 | 30.0 | 31.4 |
| | 40 | 338 | 14.3 | 9.7 | 10.7 | 0.109 | 13.7 | 38.3 | 15.6 | 23.4 |
| | 60 | 341 | 40.0 | 32.3 | 34.1 | 0.058 | 43.1 | 55.7 | 24.9 | 41.7 |
| | 85 | 340 | 43.3 | 34.7 | 36.9 | 0.097 | 41.7 | 79.9 | 37.9 | 68.5 |
| | 120 | 334 | 63.1 | 47.3 | 61.1 | 0.072 | 28.4 | 112 | 66.6 | 104 |

NOTES:

[a] For all models we list: $Z$: metallicity, $M_{\rm ZAMS}$: initial star mass, $V_{\rm rot,i}$: initial rotation at equator, $M_{\rm He}$: He core mass, $M_{\rm CO,1}$: CO core mass defined by $< 1\%$ He (used in MESA), $M_{\rm CO,2}$: CO core mass defined by $> 20\%$ CO (adopted in our study), $P_{\rm NS}$, $a_{\rm spin}$: for NSs, the NS spin period in milliseconds, for BHs, the dimensionless spin magnitude, $M_{\rm NS/BH}$: remnant mass, $M_{\rm star,m}$: final mass of a star in MESA, $M_{\rm star,st1}$: final mass of a star in `StarTrack` with standard winds, $M_{\rm star,st2}$: final mass of a star in `StarTrack` with reduced (30%) winds.

There are dips in the angular momentum profiles in Figure 4.28, One of the red curves (slowest rotation) has two dips, because when helium is exhausted in the core there is a convective hydrogen zone (starting at 12 $M_\odot$) and the surface convective zone (starting at 25 $M_\odot$) present. This is not the case in the other models because *(i)* they evolve more to the blue (to higher temperature), *(ii)* faster rotating models tend to smooth temperature and chemical composition, leading to a shorter time with convective hydrogen core and *(iii)* some models lose nearly their entire envelope, hence, there is no surface nor hydrogen convective zone. Models with high rotation end evolution with lower total mass as visible in Figure 4.28. Rotation enhances mass loss in general in several ways: directly by reducing the effective gravity, indirectly by rotation-induced mixing leading to increased luminosities and sometimes leading to quicker evolution to the red supergiant or WR phases. For the very fast rotating models evolving quasi-chemically homogeneously, the dominant effects are rotation-induced mixing leading to increased luminosities, which in turn enhances the wind mass loss and reaching the WR phase earlier in the evolution.

We note that apart from the spin values, there are also differences between the final CO core masses between `GENEC` and `MESA` models (Table 4.5 and 4.6). Some level of discrepancy is not unexpected solely due to the fact that those sets of models were run with slight differences in the efficiency of chemical mixing, criteria for convection, and treatment of convective boundary regions. More importantly, even though both sets of modes were computed using similar prescriptions for mass loss, differences in evolution in the HR diagram alone can lead to significant differences in the total amount of mass lost in winds and therefore the final CO core masses. This can be most clearly seen when comparing the most massive Solar metallicity models ($Z = 0.014$, initial masses 60, 85, and 125 $M_\odot$), in which case the `MESA` models end their evolution with noticeably higher CO core masses. We caution that in the case of such massive stars and especially at higher metallicity, the difficulties in numerical treatment of radiation-dominated, super-adiabatic envelope layers can lead to significant differences in the HR diagram evolution between different codes (Paxton et al., 2013). Given that such envelopes are likely dynamically unstable and highly turbulent, any 1D models of late evolution of massive stars should be consider highly uncertain.

All `MESA` inlists used to produce these models are publicly available at mesastar.org.

### 4.A.3 CO Core Mass versus BH Mass

The relation between the BH mass at formation and the final CO core mass of its progenitor in our simulations is set by formulae based on supernova modeling (the 'Rapid' engine of Fryer et al., 2012), together with the pre-supernova mass of the star that is set by stellar and binary evolution. In Figure 4.29 we show the $M_{\rm CO}$–$M_{\rm BH}$ relation for BH-BH mergers detectable in the O1/O2 LIGO runs within models M30, M50, M60, and M70. The presented models are different in ways that affect the BH formation masses, i.e. the PPSN/PSN prescription (see Sec. 4.2.3) as well as the assumed fraction of mass lost in neutrinos during a BH formation (1% in M30, M50, M70 and 10% in M60). Note that even though we plot $M_{\rm BH}$ at the moment of BH formation, it is very similar to the final BH mass. We note that the CO core masses presented in Figure 4.29

are the final CO core masses (just before the BH formation), which in some cases have already been reduced due to PPSN mass loss. Those are the $M_{\rm CO}$ masses that we use in order to assign the newly formed BHs with natal spins (see Sec. 4.2.1).

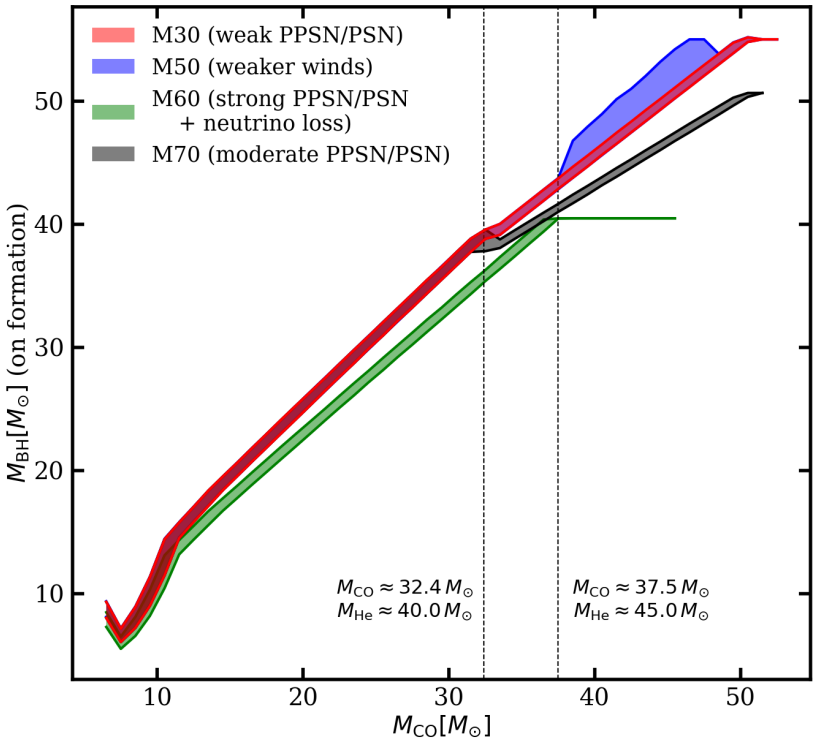


FIGURE 4.29: Final CO core masses of BH progenitors and their corresponding BH formation masses for the components (both primary and secondary) of detectable merging BH-BH systems in four of our models: M30, M50, M60, and M70 (see Table. 4.2 for an overview of all the model ingredients). For readability, the filled areas encapsulate 96% of all the BHs, excluding few outliers and showcasing the $M_{\rm CO}$ to $M_{\rm BH}$ relation for the representative majority. The presented models are different in ways that affect the BH formation masses, i.e. the PPSN/PSN prescription (see Sec. 4.2.3) as well as the assumed fraction of mass lost in neutrinos during a BH formation (1% in M30, M50, M70 and 10% in M60). Notice that model M70 only differs from M30 and M50 for $M_{\rm CO} \gtrsim 32.4\ M_\odot$, whereas model M50 only differs from M30 for $M_{\rm CO} > 37.5\ M_\odot$. Those threshold core masses correspond to the threshold helium core masses $M_{\rm He}$ in different models PPSN/PSN prescriptions.

In general, the $M_{\rm CO}$ to $M_{\rm BH}$ relation is quite similar between our models and, for the most part, almost linear. The initial decrease in $M_{\rm BH}$ (for $M_{\rm CO} < 7.5\ M_\odot$), and the subsequence increase followed by a change in slope at around $M_{\rm CO} = 11\ M_\odot$ are the results of changes in the fraction of material $f_{\rm fb}$ that falls back onto the proto-NS in the 'Rapid' supernovae engine (see Eq. 16 in Fryer et al., 2012). The maximum fall-back ($f_{\rm fb} = 1.0$, a direct collapse formation of a BH) is expected for the CO core masses $M_{\rm CO}$ either in range between 6 and 7 $M_\odot$ or for $M_{\rm CO} > 11\ M_\odot$. Partial fall-back and the ejection of some of the pre-SN mass for progenitors with $M_{\rm CO}$ within 7 and 11 $M_\odot$ is what is responsible for the dip in $M_{\rm BH}$ in Figure 4.29 at the lower $M_{\rm CO}$ end.

The fact that BH masses are systematically smaller in model M60 compared to other models is a direct consequence of a higher mass fraction being lost in neutrinos during a BH formation (10% in M60 compared to 1% in other models).

The influence of PPSN/PSN kicks in above $M_{\rm CO} \approx 32.4\ M_\odot$ for models M30, M50, M70 (which corresponds to $M_{\rm He} \approx 40\ M_\odot$) and above $M_{\rm CO} \approx 37.5\ M_\odot$ in the case of M60 ($M_{\rm He} \approx 45\ M_\odot$). Above this core mass, PPSN removes outer part of the envelope and therefore reduces the final pre-SN mass with respect to evolution without PPSN (see Fig. 4.3). This leads to a smaller mass of the BH formed in direct collapse of the remaining post-PPSN star. As expected, Figure 4.29 reveals that the more mass is lost in PPSN (depending on the model) the smaller the final BH mass. Finally, in the case of most massive stars ($M_{\rm He} > 65\ M_\odot$) all the models assume that a PSN disrupts the entire star and that no remnant remains.

The impact of weaker stellar winds in model M50 (30% of mass loss in winds at any evolutionary stage compared to other models) on the $M_{\rm CO}$ to $M_{\rm BH}$ relation is relatively small, only differentiating models M30 and M50 in any way for $M_{\rm CO} > 40\ M_\odot$. This is because, in most cases of the BH-BH merger formation, both and primary and secondary are going to lose their entire envelope prior to core collapse anyway, due to RLOF. In fact, as many as 90% of all the BH formed from $M_{\rm CO} > 40\ M_\odot$ progenitors in model M50 fall into the same area in Figure 4.29 as BHs in model M30.

### 4.A.4 Making GW170104

Figure 4.8 shows the formation and evolution of a binary which results in a BH-BH merger with properties similar to GW170104. This particular system was evolved within our model M20 (see Sec. 4.2.7 for an overview of our models and Sec. 4.A.7 for an overview of our binary evolution calculations) under the assumptions of Geneva-based BH natal spins (Fig. 4.1) and no WR spin-up during the BH-WR stage (Sec. 4.2.5. The progenitor binary was formed in a low-metallicity environment $Z = 0.001$ (5% $Z_\odot$) as a pair of MS stars with masses of 94.6 $M_\odot$ and 62.5 $M_\odot$ on a wide orbit, with pericenter distance of $\sim 2000\ R_\odot$. As the primary ends its MS evolution and rapidly expands as a HG star, it initiates a stable case-B mass transfer. In model M20 we assume that 20% of the mass is accreted by the MS companion, while the other 80% is lost from the system. During mass transfer the primary is stripped of almost all of the H-rich envelope, and it becomes a naked helium WR star with mass of 41.7 $M_\odot$. Only 0.3 Myr later it finishes its nuclear evolution and forms a BH ($M_{\rm BH1} = 32.9\ M_\odot$) in a direct collapse event (no natal kick), losing 10% of its mass in neutrino emission. The mass of the CO core of the BH progenitor is $M_{\rm CO} = 29.6\ M_\odot$, which means that the first BH is formed with zero natal spin ($a_{\rm spin1} = 0.0$, see Fig. 4.1 for $Z = 0.002$ (used as representative for $Z = 0.001$).

The companion, on the other hand, has increased its mass during the mass transfer to 71.1 $M_\odot$. It has also been rejuvenated (which we model according to eq. 58 of Belczynski et al. (2008a)) and spun up. At the offset of mass transfer, it is about 80% of its way through the MS phase. During the HG stage it expands to 1330 $R_\odot$, which is, however, not enough to cause a Roche lobe overflow

(RLOF). It further increases its radius to 1650 $R_\odot$ as a core-He-burning (CHeB) supergiant, at which point it initiates a dynamically unstable mass transfer and the common envelope (CE) phase. As a result, the wide binary orbit ($a = 3678\ R_\odot$) decays to $a = 34\ R_\odot$, and the secondary is left without any envelope as a naked WR star. We assume a 5% Bondi-Hoyle accretion rate onto a compact object during CE, which leads the first BH to only a slight increase in mass (by 0.6 $M_\odot$) and spin ($a_{\rm spin1} = 0.05$). Shortly after (0.3 Myr after the CE) the secondary forms a BH with mass $M_{\rm BH2} = 24.7\ M_\odot$ in a direct collapse with no natal kick and only 10% neutrino mass loss. Because the secondary accretes a significant fraction of its mass ($\sim 20\%$) while still on the MS, we assume that its increased rotation leads to a $\sim 20\%$ increase of the CO core mass with respect to the non-rotating stellar models (see Sec. 4.A.7). With the increased CO core mass of $M_{\rm CO} = 26.0\ M_\odot$, the second BH is assigned an initial spin of $a_{\rm spin2} = 0.14$.

The BH-BH is formed after 4.9 Myr of binary evolution on a close ($a = 37.4\ R_\odot$), almost circular ($e = 0.05$) orbit. The time to coalescence via gravitational wave emission is 6.1 Gyr. For this particular evolution/model we assume no natal kicks at the formation of the massive BHs, so the BH spin vectors are aligned with the binary angular momentum ($\Theta_1 = \Theta_2 = 0°$). This produces an upper limit on the effective spin parameter (see eq. 4.1). For these particular BH masses, spins and spin tilts, we obtain a rather low effective spin $\chi_{\rm eff} = 0.09$. The progenitor binary forms at $z = 1.2$, so $\sim 5$ Gyr after the Big Bang (close to a peak in star formation: $z \approx 2$ means 3.2 Gyr after the Big Bang), and the BH-BH merger takes place at $z = 0.2$ ($\sim 11$ Gyr after the Big Bang). The gravitational waves from the BH-BH merger propagate for $\sim 2.5$ Gyr to reach the LIGO detectors at the present time. All of the system properties are within 90% of the credible limits of GW170104 (Abbott et al., 2017, see also Sec. 4.A.5 for a revised limits on $\chi_{\rm eff}$).

### 4.A.5 THE EFFECTIVE SPIN PARAMETER: $\chi_{\rm eff}$

The Bayesian analysis of GW170104 reported in Abbott et al. (2017) adopts prior assumptions about the relative likelihood of different spin magnitudes (uniform) and directions (isotropic). These assumptions are not suitable for comparison to the binary evolution model we adopt, which requires both individual spins to be initially aligned and then only mildly (if at all) misaligned by natal kicks. Recent detailed analysis addressing the impact of prior assumptions showed that they can indeed impact the inferred parameters (Vitale et al., 2017a; Williamson et al., 2017).

We therefore reassess the reported limit, concluding that $\chi_{\rm eff} < 0.2$ at approximately 90% confidence in the context of our model. We can justify this reanalysis using only the reported LIGO result on $\chi_{\rm eff}$, restricted to $\chi_{\rm eff} > 0$. Approximating the LIGO distribution as nearly normal with mean $\mu = -0.21$ and width $\sigma_\chi \simeq 0.155$, we construct a truncated normal distribution $\propto \theta(\chi) \exp -(\chi + \mu)^2/2\sigma^2$, which has a 90% upper limit at $x \simeq 0.2$.

We arrive at a similar result by reanalyzing the underlying LIGO data using the same model and techniques (including the prior), then restricting to configurations with positive individual spins $\chi_{1,z}, \chi_{2,z} > 0$. Our revised upper limit is consistent with the range of plausible $\chi_{\rm eff}$, as reported by Abbott et al. (2017) (see Fig. 5 of the supplementary material), corresponding to

approximately a 98–99% confidence limit within the strong assumptions of their original analysis.

## 4.A.6 NS Spins

### 4.A.6.1 Observed Pulsar Spin Period Distribution

Although astronomers have amassed a large sample of pulsar spin-period measurements, extrapolating from observed periods to birth periods is an open area of research (for a review, see Miller & Miller, 2015). Because pulsar emission spins down the neutron star with time, any estimate of the birth period requires an estimate of the pulsar age, and an understanding of the rate of spin-down from pulsar emission (including an understanding of magnetic field evolution in neutron stars). The age of a pulsar ($t_{\rm pulsar}$) can be estimated assuming the angular momentum is lost through electromagnetic radiation from a pulsar with dipole magnetic fields (Manchester & Taylor, 1977):

$$t_{\rm pulsar} = \frac{P}{(n-1)\dot{P}}(1-(P_0/P)^{n-1}), \tag{4.19}$$

where $n$ is the pulsar braking index ($n = 3$ for magnetic dipole radiation), $P_0$, $P$ are respectively the initial and current pulsar spin periods. If the age of the pulsar is known by other means (e.g., the supernova remnant age), measurements of the spin period along with constraints on the braking index provide an estimate of the birth spin period. Clearly the pulsar age depends on the choice of $n$. In addition, other sources of angular momentum loss exist: e.g. nonsphericities of the neutron star can cause gravitational wave emission, lowering the spin period.

Despite these uncertainties, astronomers have estimated the neutron star birth spin period distribution. The fastest pulsars could be born spinning less than 10 ms (the Crab pulsar is believed to have been born spinning at 17 ms). Popov & Turolla (2012) found that a Gaussian with an average spin period of 100 ms (with a $1-\sigma$ deviation of 100 ms) fits the observations. Faucher-Giguère & Kaspi (2006) found a slightly higher average, 300 ms ($1\sigma$ deviation of 150 ms). Igoshev & Popov (2013) argue that the differences between these two studies could be explained by the choice of magnetic field evolution and either distribution could be made consistent with the data. Noutsos et al. (2013) also obtained a distribution of periods peaking below 125 ms, but found an additional set of long-period birth spins ($> 0.5$ s). They found that poor age estimates limit determinations of the birth pulsar spin distribution and described methods to estimate pulsar ages kinematically.

With these uncertainties in mind, we can now compare stellar models to the observed spin distribution. As with the stars forming black holes, we can estimate the birth spins of of neutron stars from their massive star progenitors by assuming that the angular momentum of the collapsing core is accreted onto the proto-neutron star along with its mass. We limit the accreted angular momentum ($j_{\rm acc}$) to the centrifugally supported value:

$$j_{\rm acc} = min(j_{\rm shell}, \sqrt{r_{\rm NS} G M_{\rm encl}}) \tag{4.20}$$

where $j_{\rm shell}$ is the angular momentum of the accreting shell, $r_{\rm NS}$ is the neutron star radius, $G$ is the gravitational constant and $M_{\rm encl}$ is the mass enclosed in the shell. For the neutron star radius, we

assume a 10 km. We consider only compact remnants with masses below 2.5 $M_\odot$ as this is our adopted maximum NS mass. By summing up the angular momentum from the accreted material, we obtain the total angular momentum of the compact remnant. The moment of inertia of a neutron star ($I_{\rm NS}$) depends upon the equation of state (Worley et al., 2008) and can vary by roughly 50% with the choice of the equation of state but it is roughly linear with neutron star mass. For our calculations, we assume

$$I_{\rm NS} = 1.5 \times 10^{45} (M_{\rm NS}/M_\odot)\ {\rm g\,cm^2} \tag{4.21}$$

where $M_{\rm NS}$ is the neutron star mass. With the total angular momentum and moment of inertia, we can determine the birth spin period of the neutron stars from our progenitors (Figure 4.30). The spins from these models assume stars born rotating at 40% breakup velocity, producing core spins near the maximum allowed by a given angular momentum transport mechanism. We have not included any angular momentum loss mechanisms, but there are several possibilities of extracting rotational energy from the protoneutron star. For example, if the rotational energy is tapped to help driving the explosion (e.g., by interaction with a disk or when forming a magnetar), the total angular momentum of the system will be reduced. Therefore the rotation rates produced in our models are only upper limits on the real spin rates.

The results of Figure 4.30 demonstrate that some magnetic braking is needed to reduce the angular momentum of the core, confirming decades-old arguments for magnetic breaking (Heger et al., 2000; Fryer & Heger, 2000). The Geneva models with the original distribution of angular momentum through a star produce only sub-ms pulsars. While the spins from these models without magnetic coupling have too much angular momentum, they are ideally suited to determine the amount of coupling needed to produce the correct spin periods. We assume the angular momentum is distributed with a constant angular velocity (solid body rotation) across the mass of different cores. If we assume the angular momentum to be conserved, we can calculate the angular velocity of the core and recalculate the spin of the pulsar produced. For example, if we sum up the angular momentum of the CO core and divide it by its moment of inertia, we get an average angular velocity. If we use this constant angular velocity to redistribute the angular momentum in the CO core, we revise our estimate of the spin of the compact remnant. For this redistribution, the spin periods remain below a ms (magenta triangles). To truly slow down the birth spin periods of neutron star, we must couple the angular momentum through the helium core (meaning that one assumes a constant angular velocity from star center to the outer boundary of the helium core). Figure 4.30 shows the resultant spins if we assume coupling through the helium core with a helium core definition of $X_{\rm He} > 0.4$, $X_{\rm H} < 0.01$ (blue squares), and $X_{\rm He} > 0.5$ (red empty circles). This produces maximum birth spin periods of between $\sim 10 - 1000$ ms. Further coupling, the H-rich layers, would produce spin periods (solid green circles) that are too slow to match the observed pulsar distribution. Given that these spins are maximum spin values (recall that we are using fast rotating progenitors and assuming no angular momentum loss in the explosion mechanism), our pulsar spin observations argue against angular-momentum coupling beyond the helium core.

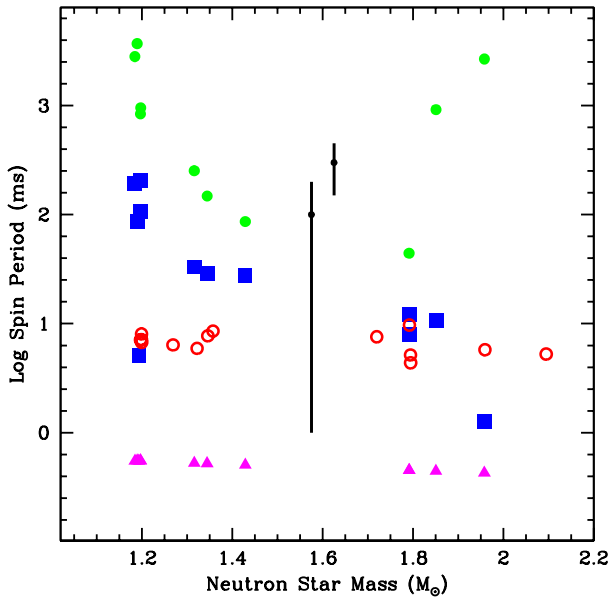


Figure 4.30: Neutron star spins from our progenitors as a function of neutron star mass. We assume any remnant from our suite of models with a mass below 2.5 $M_\odot$ is a neutron star and consider only these remnants. With the Geneva models, we have studied the angular momentum coupling of different burning layers and their effect on the neutron star spin. The Geneva models with the original mild coupling produce spin periods shorter than 1 ms (not shown here, but very close to magenta triangles; see below). Some angular momentum loss in the supernova engine (e.g. magnetic coupling such as a magnetar engine) would be required to slow neutron stars down for such models to match the data. The spins are nearly the same if the coupling extends through the CO core (magenta triangles). Coupling through the helium layer (blue squares and empty red circles; different helium core definitions) and hydrogen layer (green solid circles) produces slower neutron stars. The helium-coupled models match the data (but realize that we are using rapidly rotating progenitors with no angular momentum loss during NS formation). The MESA models (not shown here) with the Tayler-Spruit dynamo produce $\sim 10$ ms pulsars; generating spins that match fastest-spinning pulsars with rapidly spinning progenitor stars, an indication that the MESA models produce reasonable coupling results. The Fuller models (not shown here) do not produce rotating neutron stars, requiring spin-up mechanisms in the supernova engine to match the data. For comparison we also mark (with black lines) the range of two observational estimates. More details on models and observations are given in Sec. 4.A.6.1.

If we compare the spin periods produced using our MESA models using a prescription similar to Heger et al. (2000), we find spin periods of roughly $\sim 6-10$ ms, matching the fastest-spinning non-recycled pulsars and the results of Heger et al. (2000); Fryer & Heger (2000). These periods are produced using rapidly spinning progenitors, so we would expect their periods to match the fastest-spinning systems and this result is a relatively good match to the observed pulsar distribution. For the Fuller models, the birth spin period would be too slow to match the data, arguing for some mechanism to spin-up the neutron star. Simulations of the asymmetries in the engine do show spin-up in the core. The amount of spin-up, and whether it is sufficient to solely explain the pulsar spin periods, remains a matter of debate (Blondin & Mezzacappa, 2007; Fryer & Young, 2007;

Foglizzo et al., 2009; Rantsiou et al., 2011; Kazeroni et al., 2016).

#### 4.A.6.2 ROTATIONAL EXPLOSION PROPERTIES

It has been argued that fast spinning magnetars can drive a subset of supernova explosions. Here we determine the role spins can play in the supernova explosion itself. With strong (magnetar-strength: $\sim 10^{15}$ Gauss) magnetic fields, a pulsar can quickly release the rotational energy of a newly formed neutron star. To calculate the energy available for such a model, we need to estimate the rotational energy of the neutron star:

$$E_{\rm rot} = 1/2 I_{\rm NS} \omega^2 = 5 \times 10^{50} (\omega/1000 Hz)^2 \,{\rm erg} \tag{4.22}$$

where $\omega$ is the angular velocity. If the neutron star is spinning with a ms period (e.g., original Geneva models), it can produce a $10^{51}$ erg explosion if it can tap 10% of the rotational energy to drive a jet. With the $6-10$ ms periods (e.g., MESA models with rapidly rotating stars) we find that, even if all of the rotational energy is tapped to drive an explosion, rotation is unable to produce a normal-energy supernova. If the strong magnetic fields are formed quickly, a spin-powered magnetar engine will deposit its energy in the slowly-moving ejecta, accelerating this innermost material (and adding additional heating) but not contributing significantly to the total energy budget of the explosion.

Similarly, because the angular momentum is lowest in the cores of these stars, such models are unable to form a disk around the neutron star. Hence, engines that invoke jets produced by magnetic fields generated in a disk will not work. Note, however, that a disk can form after the formation of a 3 $M_\odot$ remnant (presumably a black hole) as then more angular momentum is trapped in the remnant. It is likely that any model with Tayler-Spruit efficient angular momentum transport (e.g., MESA or Fuller models) invoking these engines will have to rely upon some means to spin up the star prior to collapse (see review by Fryer et al., 1999). Note that this statement does not depend on the initial stellar spin of models as independent of adopted initial spin, both MESA and Fuller models end up with very small angular momentum in the core (see Fig. 4.23). Such rare spin-up events would be able to explain rare outbursts such as gamma-ray bursts but, if these spins are correct, it is unlikely that magnetars or disks play a big role in explaining supernovae (for a review, see Fryer et al., 2019).

### 4.A.7 BINARY EVOLUTION CALCULATIONS

We employ the `StarTrack` population synthesis code (Belczynski et al., 2002, 2008a). The existing improvements relevant for massive star evolution include updates to the treatment of CE evolution (Dominik et al., 2012), the compact object masses produced by core collapse/supernovae (Fryer et al., 2012; Belczynski et al., 2012b) including the effect of pair-instability pulsation supernovae and pair-instability supernovae (Belczynski et al., 2016a), stellar binary initial conditions set by observations (de Mink & Belczynski, 2015a), and observationally constrained star formation rate and metallicity evolution over cosmic time (Madau & Dickinson, 2014; Belczynski et al.,

2016b). The code adopts by default the fallback-decreased natal kick prescription (see below). Additionally, we explore three different models for the BH natal spins proposed in the current upgrade (Sec. 4.2.1) as well as three different models for PPSN/PSN (Sec. 4.2.3).

In our population synthesis calculations we evolve stars on a finite grid of metallicity: $Z = 0.0001, 0.0002, 0.0003, 0.0004, 0.0005, 0.0006, 0.0007, 0.0008, 0.009, 0.001, 0.0015, 0.002, 0.0025, 0.003, 0.0035, 0.004, 0.0045, 0.05, 0.006, 0.0065, 0.007, 0.0075, 0.008, 0.0085, 0.009, 0.0095, 0.01, 0.015, 0.02, 0.025, 0.03$. If in our population synthesis model the metallicity is $Z < 0.00089$ we adopt the BH spin model corresponding to $Z = 0.0004$; if $0.00089 \leq Z < 0.00346$ we adopt the BH spin model corresponding to $Z = 0.002$; if $0.00346 \leq Z < 0.00916$ we adopt the BH spin model corresponding to $Z = 0.006$; and if $Z \geq 0.00916$ we adopt the BH spin model corresponding to $Z = 0.014$. The limits are half points in decimal logarithm between the four metallicities of the BH natal spin model ($Z = 0.014,\ 0.006,\ 0.002,\ 0.0004$).

For the initial orbital period distribution of massive binaries we use $f_p(\log p/\mathrm{day}) \propto (\log p/\mathrm{day})^{-0.5}$ in range $[0.15, 5.5]$ (Sana et al., 2012). For the initial eccentricity distribution we use $f_e(e) \propto e^{-0.42}$ in the range $[0.0, 0.9]$. The initial mass of the primary star is taken from a broken power law IMF: $\propto M^{-1.3}$ for $0.08 \leq M < 0.5\ M_\odot$, $\propto M^{-2.2}$ for $0.5 \leq M < 1.0\ M_\odot$, and $\propto M^{-2.3}$ for $1.0 \leq M \leq 150\ M_\odot$ (Kroupa, 2001; Bastian et al., 2010; Duchêne & Kraus, 2013). The initial secondary mass is taken from a uniform mass ratio distribution $f_q(q) \propto q^0$ in the range $q \in [0.1, 1]$.

We adopt maximum binary fraction: $f_{\rm bi} = 1.0$ for stars of any mass and any metallicity. This is a sound assumption for massive stars of non-negligible metallicity (Raghavan et al., 2010; Chini et al., 2012; Moe & Di Stefano, 2013, 2017). However, the binarity may be smaller for low mass stars, e.g., $f_{\rm bi} = 0.5$ (2/3 of stars in binaries). For each metallicity we evolve $N = 2 \times 10^6$ massive binaries (primary mass $> 5\ M_\odot$, secondary mass $> 3\ M_\odot$) and this corresponds to the total simulation stellar mass of $M_{\rm sim} = 1.9 \times 10^8\ M_\odot$ (all stars over entire IMF) for $f_{\rm bi} = 1.0$. Note that had we assumed $f_{\rm bi} = 0.5$ for all stars then $M_{\rm sim} = 2.8 \times 10^8\ M_\odot$. Therefore, such a change would decrease of all our rate predictions for double compact objects by $\sim 30\%$ (see eq.7 of Belczynski et al. (2016c)).

The initial distributions described above assume that all the binary parameters are independent from each other. However, various correlations between those parameters have long been hinted by the observations (eg. Abt et al., 1990; Duchêne & Kraus, 2013). It was only recently that Moe & Di Stefano (2017), using results from more than 20 surveys of massive binary stars, were able to fit analytic functions to the correlated distributions and obtain a join probability density function $f(M_1, q, P, e) \neq f(M_1)f(q)f(P)f(e)$. In some pockets of the entire parameter space they found differences larger than an order of magnitude with respect to the typically used method of combining several independent distributions. Similarly, even though a conclusive evidence for significant IMF variations with environmental conditions is still lacking, there is an increasing amount of results suggesting such departures from the IMF universality (Bastian et al., 2010; Kroupa et al., 2013). Notably, both theoretical arguments (see Klencki et al., 2018, for an overview) and observations of some GCs in the Milky Way (Marks & Kroupa, 2012; Marks et al.,

2012) seem to point towards a top-heavy IMF[7] in low-metallicity galaxies, which are likely an important formation site of massive BH-BH mergers. Recently, Klencki et al. (2018) analyzed the significance of the inter-correlations in initial distributions quantified by Moe & Di Stefano (2017) as well as of the possible variations in the IMF slope for the massive stars on the formation rate and properties of compact binary mergers. They found that the effect of those factors is very small compared to other uncertainties (eg. rates affected by less than a factor of 2). Their result holds even for very significant changes in the IMF slope due to the coupling of the IMF and the cosmic SFRD. This justifies the simplified assumptions of the universal IMF and non-correlated initial binary parameter distributions used in this study.

For old models (M10 and M13) we have redone the calculations with the same input physics, but with the addition of the new distribution of natal BH spins. Additionally, we have updated the calibration for all models (decreasing rates by a factor of 0.926) to account for small inconsistencies in our previous estimates (Klencki et al., 2018). Below we comment on factors introduced in our new models (M20, M23, M25, M26).

The fraction of mass retained in the binary ($f_a$) during stable RLOF is not well established, and could be fully conservative ($f_a = 1$), fully non-conservative ($f_a = 0$), or anywhere in between (e.g., Meurs & van den Heuvel (1989)). Donor stars are typically the more massive components, as they are the ones that evolve (and typically expand) more quickly. Consequently, more massive donors often have a much shorter thermal timescale than their companions. For that reason, in the case of a thermal-timescale mass transfer when the mass transfer rate is related to the thermal-timescale of the donor star, the less massive companions will not have enough time to thermally readjust in order to accommodate all of the transferred mass. This likely leads to a large fraction of the transferred mass being ejected from the system. Even in the case of a slower, nuclear-timescale mass transfer, accretion is typically expected to be small because the accretor quickly becomes spun up to its critical surface rotation velocity. We note that the picture is possibly more complicated due to the uncertain efficiency of stellar winds in carrying away the angular momentum from the accretor surface (eg. Vanbeveren et al., 2018).

Nonetheless, we decided to revise and test our assumption on the accretion efficiency. In the previous work (as well as the remaining models in this study) we adopted $f_a = 0.5$. Recent estimates of mass transferring BH-BH progenitors resulted (typically) in $f_a < 0.5$ (Stevenson et al., 2017a), so in models M20-M26 we adopt $f_a = 0.2$. As a consequence, the secondary stars (accretors) remain less massive than in our previous models, and this generates a wider BH-BH binary mass ratio distribution than reported in our earlier studies. The efficiency of accretion in the first episode of mass transfer was noted to have possible impact on the BH-NS formation (Kruckow et al., 2018). Note that Stevenson et al. (2017a) used not a single value for $f_a$, but estimated the accretion efficiency from the relative thermal timescales of the donor and accretor for a given binary.

Even a small amount of accretion during RLOF (~ few percent of the accretor's mass) may effectively spin up accreting stars (Packet, 1981). With our adopted RLOF retention fraction of

[7]With respect to the IMF assumed in this study.

$f_a = 0.2$, accretors in BH-BH progenitor binaries typically gain about 10 $M_\odot$, which is enough to spin up even very massive stars. This accretion usually happens around the middle (or shortly thereafter) of the accretor's main sequence life, and therefore it allows for effective rotational mixing and the formation of more massive He and CO cores. `Geneva` stellar evolution models indicate that the CO core masses in rotating stars (40% critical velocity) are 20% more massive than in non-rotating models. So far all CO core masses calculated in our binary evolution models were obtained from non-rotating models (Hurley et al., 2000). Here we increase CO core mass of accreting low-metallicity ($Z < 0.002$) MS stars by 20%. For high-metallicity stars, the effects of rotation on the CO core mass are suppressed due to angular momentum loss through stellar winds (Georgy et al., 2012). This change may increase the mass of the second BH, and also lower its spin magnitude. In all models we assume that material is lost from a binary in RLOF with specific angular momentum $dJ/dt = j_{\rm loss}[J_{\rm orb}/(M_{\rm don} + M_{\rm acc})](1 - f_a)dM_{\rm RLOF}/dt$, with $j_{\rm loss} = 1.0$ (Podsiadlowski et al., 1992).

Our criteria for the mass transfer stability and the occurrence of CE are described in detail in Sec.5 of Belczynski et al. (2008a). To treat CE evolution we assume energy balance with fully effective conversion of orbital energy into envelope ejection ($\alpha = 1.0$), while the envelope binding energy for massive stars is calibrated using a parameter $\lambda$ that depends on stellar radius, mass, and metallicity for all models. For massive stars we assume $\lambda \approx 0.1$ Xu & Li (2010). Additionally, we either allow or do not allow (submodels A and B) for HG stars to initiate and survive CE evolution Belczynski et al. (2007); Pavlovskii et al. (2017). In submodels A only stars with well developed core-envelope boundary (beyond HG) can successfully initiate and survive CE, depending on the energy balance. In submodels B we also allow for HG stars to initiate and survive CE. Recent calculations show that the accretion rates onto compact objects in CE inspiral can be reduced even by a factor of $10^{-2}$ with respect to the rates resulting from the Bondi-Hoyle approximation when the structure of the envelope (in particular, the density gradients around the inspiraling object) are taken into account (Ricker & Taam, 2008; MacLeod et al., 2017; Murguia-Berthier et al., 2017a; Holgado et al., 2017). MacLeod & Ramirez-Ruiz (2015a) argue that accretion structures forming around compact objects embedded in the CE may span a large fraction of the envelope radius, and so traverse substantial density gradients. Introducing gradients in the CE structure leads to net non-zero angular momentum of the flow around an accreting object (which is not the case in the standard Hoyle formalism), and by doing so limits accretion: steeper density gradients correspond to smaller accretion. The typical values of the density gradients found by these authors introduce a considerable perturbation to the flow. For most density gradients considered by MacLeod et al. (2017), the accretion rate is well below 10% of Bondi-Hoyle accretion rate. Based on these findings, we adopt $f_{\rm bond} = 5\%$ of the Bondi-Hoyle accretion rate onto a BH in CE in our current simulations. Therefore massive BHs ($M_{\rm BH} \sim 30\ M_\odot$) accrete $\sim 0.5\ M_\odot$ in a typical CE event, as opposed to $\sim 1.0\ M_\odot$ in our earlier calculations ($f_{\rm bond} = 10\%$). To assess the Bondi-Hoyle accretion rate we follow the approach presented in Belczynski et al. (2002).

Spectroscopic analysis of OB stars in the Local Group (MW, SMC, LMC, eg. Oskinova et al., 2013; Hainich et al., 2018; Ramachandran et al., 2019) as well as other low-metallicity

dwarf galaxies (eg. Bouret et al., 2015) has shown a systematic offset in the wind mass loss rates between theoretical predictions (Vink et al., 2001, assumed in most our models) and the empirical $\log\dot{M}-\log L$ relation. Namely, the theoretical models seem to overestimate the actual wind mass loss rates of hot stars by at least a factor of a few. The most likely cause for this discrepancy is clumping of the wind, which is not accounted for in the standard models of radiatively driven smooth winds. For that reason, in model M50 we reduce all the wind mass loss rates down to 30% of the usually assumed values.

Compact remnants formed in supernovae can receive proper motions via two classes of engine-driven natal kicks: asymmetric matter ejecta or asymmetric neutrino emission. For BHs, asymmetric matter ejection mechanisms only work when matter is ejected, as opposed to prompt collapse or complete recapture of all ejected material ("fallback"). In our calculations, we expect that only a small fraction of systems eject a substantial amount of matter, enabling a substantial BH natal recoil kick. In contrast, asymmetric neutrino emission mechanisms operate even without any mass ejection, and thus they can affect any model of BH formation. Although neutrino mechanisms have been invoked to explain recoil velocities of pulsars and X-ray binaries (Lai & Qian, 1998; Repetto & Nelemans, 2015), the proposed kick models all require strong magnetic fields. Models without strong magnetic fields are unable to produce significant neutrino kicks (Tamborra et al., 2014).

The sterile neutrino oscillation model (Kusenko & Segrè, 1996; Fryer & Kusenko, 2006) argued that neutrinos produced in the core could oscillate to sterile neutrinos and escape the core. Large magnetic fields align the ions and electrons, forcing both the neutrino scattering and absorption cross sections to be anisotropic. To ensure asymmetric neutrino emission, these strong magnetic fields must be at the last scattering surface for the neutrinos. If the magnetic field in the core is high enough to align the ions and electrons, the neutrinos in the core will be anisotropic. If these neutrinos oscillate into sterile neutrinos, they can escape, retaining their anisotropies and generating large natal kicks.

Alternatively, the neutrino bubble instability (Socrates et al., 2005) argues that magnetic-acoustic instabilities develop, transporting neutrino radiation to the photosphere. These instabilities carry neutrinos, and the luminosity escaping the neutrinosphere will be enhanced at these "bubbles". If the magnetic-acoustic bubbles are globally asymmetric, the neutrino emission will also be asymmetric, producing a neutrino-driven kick. Current supernova calculations have several limitations: (i) they do not model high magnetic fields, (ii) they do not sufficiently resolve the hydrodynamics, and (iii) they do not include the neutrino oscillation physics necessary to produce these kicks. So high, neutrino-driven BH natal kicks cannot be ruled out.

In models M10 and M20 we test asymmetric mass ejection kicks, as we employ fallback-decreased natal kicks Fryer et al. (2012). To mimic asymmetric neutrino emission mechanisms, we explore an alternative phenomenological prescription for BH natal kicks in models M13, M23, M25, M26, M33, M35, and M43 where we impart kicks which are random in direction, with magnitude drawn from a Maxwellian with a given 1-dimensional $\sigma$, independent of the BH mass or its progenitor history (see Tab. 4.2).

### 4.A.8 Detectabilty of Mergers in Gravitational Waves

All the compact object mergers are redistributed according to star formation history across cosmic time ($z \approx 0$–$15$ for Population I and II stars; e.g., Madau & Dickinson (2014)), taking into account the time delay between binary formation at Zero Age Main Sequence and the merger.

For each merger at redshift $z$ we use phenomenological inspiral–merger–ringdown waveforms (IMRPhenomD; Khan et al. (2016)) to calculate the signal-to-noise ratio in the O1/O2 LIGO runs. A given merger is considered detectable (depending on its random sky location and orbital orientation with respect to the detectors) if the signal-to-noise ratio in a single detector is greater than 8. Only detectable mergers are used in our comparisons with O1/O2 data (e.g., rates in Tables 4.3, 4.4, or effective spins in Sec. 4.3.4).

With this method we obtain a self-consistent redshift distribution of mergers in the local Universe, and we also account for LIGO/Virgo detectability of our synthetic mergers (in particular, more massive mergers can be detected at larger redshifts). A more detailed description of detectability criteria can be found in Belczynski et al. (2016c,b,a).

### 4.A.9 BH-NS merger rate limits from the ongoing O3 run

Here, we analyze the constraint on the rate density of BH-NS mergers that the recent LIGO/Virgo candidate (LVC, 2019a,b, S190814bv)[8] entails.

We do not know the mass of the object but we assume that the mass of the NS $M_{\rm NS}$ must be in the range from 1.3 to 3 $M_\odot$, while the BH mass $M_{\rm BH}$ is in the range from 5 to 50 $M_\odot$. We denote the chirp mass of the system as $\mathcal{M}$. The O3 has lasted for about 4.5 months with the 80% uptime which given the effective observation time $t_{\rm obs}$ of 150 days, or 0.41 years for O1/O2 and $t_{\rm obs}$ of 3.6 months, or 0.30 years. For the range of the search we assume that the sensitivity to NS-NS mergers was $r_{\rm NSNS} = 80\,{\rm Mpc}$ (O1/O2) and $r_{\rm NSNS} = 135\,{\rm Mpc}$ (O3). We can estimate the range to the BH-NS merges from

$$r_{\rm BHNS} = r_{\rm NSNS} \times (\mathcal{M}/1.2\ M_\odot)^{5/6}, \tag{4.23}$$

where we assumed that the fiducial chirp mass of a NS-NS system is 1.2 $M_\odot$. The observed volume is then $V_{\rm BHNS} = (4/3)\pi r^3_{\rm BHNS}$. The rate density of BH-NS mergers, estimated from this one event, can be estimated as

$$\mathcal{R} = \frac{1}{(t_{\rm obs} V_{\rm BHNS})_{\rm O1/O2} + (t_{\rm obs} V_{\rm BHNS})_{\rm O3}} = 1.6 - 60\ {\rm Gpc^{-3}\ yr^{-1}}, \tag{4.24}$$

and the range corresponds to the limits in which we have allowed NS and BH mass to vary. This estimate will go down by approximately a factor of two if no similar objects will be detected in the remainder of O3 (0.7 yr). On the other hand, the range will become narrower once we know the mass estimates of NS and BH. Note however, that including the effect of Poisson distribution width will broaden the result again. Thus we are confident that the above estimate is approximately accurate under the assumption that the detected system was in fact BH-NS merger and not BH-BH

[8] see https://gracedb.ligo.org/superevents/S190814bv/

merger with a very light secondary BH. We confront the merger rate limit estimated above with the results from our models in Figure 4.25.

# Chapter 5

# Massive donors in interacting binaries: effect of metallicity

J. Klencki, G. Nelemans, A.G. Istrate & O. Pols

*Astronomy & Astrophysics, volume 638, A55, (2020)*

**Abstract**

Metallicity is known to significantly affect the radial expansion of a massive star: the lower the metallicity, the more compact the star, especially during its post-main sequence evolution. Our goal is to study this effect in the context of binary evolution.

Using the stellar-evolution code MESA, we computed evolutionary tracks of massive stars at six different metallicities between 1.0 $Z_\odot$ and 0.01 $Z_\odot$. We explored variations of factors known to affect the radial expansion of massive stars (e.g., semiconvection, overshooting, or rotation). Using observational constraints, we find support for an evolution in which already at a metallicity $Z \approx 0.2\, Z_\odot$ massive stars remain relatively compact ($\sim 100\, R_\odot$) during the Hertzprung-gap (HG) phase and most of their expansion occurs during core-helium burning (CHeB).

Consequently, we show that metallicity has a strong influence on the type of mass transfer evolution in binary systems. At solar metallicity, a case-B mass transfer is initiated shortly after the end of the main sequence, and a giant donor is almost always a rapidly expanding HG star. However, at lower metallicity, the parameter space for mass transfer from a more evolved, slowly expanding CHeB star increases dramatically. This means that envelope stripping and formation of helium stars in low-metallicity environments occurs later in the evolution of the donor, implying a shorter duration of the Wolf-Rayet phase (even by an order of magnitude) and higher final core masses. This metallicity effect is independent of the effect of metallicity-dependent stellar winds.

At metallicities $Z \leq 0.04\ Z_{\odot}$ , a significant fraction of massive stars in binaries with periods longer than 100 days engages in the first episode of mass transfer very late into their evolution, when they already have a well-developed CO core. The remaining lifetime ($\lesssim 10^4$ yr) is unlikely to be long enough to strip the entire H-rich envelope. Cases of unstable mass transfer leading to a merger would produce CO cores that spin fast at the moment of collapse.

We find that the parameter space for mass transfer from massive donors ($> 40\ M_{\odot}$) with outer convective envelopes is extremely small or even nonexistent. We briefly discuss this finding in the context of the formation of binary black hole mergers.

## 5.1 INTRODUCTION

Massive stars ($> 8\ M_{\odot}$) play a vital role in the evolution of the Universe and various branches of astronomy. They provide feedback and chemical enrichment in star-forming galaxies and stellar clusters, they are responsible for supernovae and nucleosynthesis of heavy elements, and they lead to the formation of neutron stars and black holes (e.g., Langer, 2012). One key factor that significantly affects the evolution and fate of massive stars is wind mass-loss (Smith, 2014). In particular, the strength of line-driven winds of hot massive stars is metallicity dependent, as is indicated by observations and predicted theoretically (Puls et al., 1996; Vink et al., 2001; Puls et al., 2008). This introduces a relation between metallicity and the evolution of massive stars. As a result, it is believed that certain stellar-origin phenomena are predominantly or even exclusively associated with low-metallicity environments, for instance, massive stellar black holes (BHs, Zampieri & Roberts, 2009; Mapelli et al., 2009; Belczynski et al., 2010b; Spera et al., 2015), single stellar origin long gamma ray bursts (GRBs, Yoon et al., 2006), chemically homogeneous stars and binaries (de Mink et al., 2009a; de Mink & Mandel, 2016; Marchant et al., 2017), or pair-instability supernovae (Heger & Woosley, 2002; Heger et al., 2003; Farmer et al., 2019). Metallicity is likely to play a role in the formation efficiency of compact binary mergers and gravitational-wave sources (e.g., Klencki et al., 2018; Giacobbo et al., 2018; Chruslinska & Nelemans, 2019a)

Metallicity also influences stellar radii. On the main sequence (MS), stars at low metallicity remain more compact than their higher metallicity counterparts (the difference can be especially large for stars with masses $\gtrsim 50\ M_{\odot}$; Sanyal et al., 2017). The sizes of more evolved post-MS massive stars can be influenced by their metallicity even more significantly (Brunish & Truran, 1982; Baraffe & El Eid, 1991). When stellar evolution tracks are compared across different metallicities, increasingly more massive-star models remain relatively compact during the phase of rapid Hertzprung-Gap (HG) expansion as the metallicity ($Z$) decreases, see for example, Brott et al. (2011a, models at $Z = 0.0088$, 0.0047, and 0.0021), Georgy et al. (2013, $Z = 0.002$), Groh et al. (2019, $Z = 0.0004$), Schootemeijer et al. (2019, $Z = 0.0034$), or Marigo et al. (2001, $Z = 0$, Pop-III ). Such stars regain thermal equilibrium and start the core-helium burning phase (CHeB) as B- or A-type blue supergiants (BSGs, $R \sim 100\ R_{\odot}$) and typically reach the sizes of red supergiants

(RSGs, $R \sim 1000\ R_\odot$) only at the final stages of CHeB or during even more advanced evolutionary phases.

The way in which a star changes its radius during its evolution is especially important when it is a member of a binary system: any Roche-lobe overflow (RLOF) and mass-transfer phase is usually associated with a phase of expansion of the donor star. The vast majority of massive stars are formed in binary and higher-order systems (Sana et al., 2012; Duchêne & Kraus, 2013), in which, more often than not, they will at some point engage in RLOF (Sana et al., 2013). For this reason, it is essential to place the evolution of single massive stars into the binary perspective and to analyze the models from the point of view of such stars becoming donors in mass transfer episodes. Because of the effect of metallicity on the radial evolution of stars, two binary systems at different metallicities with otherwise identical initial parameters can enter mass transfer at very different ages, with the donor stars being at different evolutionary stages and leading to different fates. For instance, de Mink et al. (2008) pointed out that the small sizes of HG stars at very low metallicity ($Z = 0.00001$) can allow for many more cases of case C mass transfer when the donor stars have well-developed carbon-oxygen (CO) cores. This evolutionary route may be required in some binary formation scenarios of long GRBs (see the discussion in Wolf & Podsiadlowski, 2007, and Sec. 5.5.5). Klencki & Nelemans (2019, and in much more detail in Klencki et al. in prep.) suggested that mass transfer from a slowly expanding CHeB donor (typical for subsolar metallicity) can relax to a nuclear-timescale evolution instead of stripping the entire envelope of the giant donor on a much shorter thermal timescale, as is the case of HG donors (typical for solar metallicity, Kippenhahn & Weigert, 1967).

In this paper we argue that because of the effect it has on the stellar radii, metallicity can have significant implications for the evolution of massive binaries at various orbital periods and deserves a detailed study. To this end, we employ the MESA stellar evolution code (Paxton et al., 2011, 2013, 2015) to compute stellar tracks of massive stars between 10 and 80 $M_\odot$ for six metallicities between $Z = 0.017 = Z_\odot$ and $Z = 0.00017 = 0.01\ Z_\odot$. We investigate several variations in the input physical parameters that are known to affect the radial expansion of massive stars (e.g., semiconvection, overshooting, and rotation) and constrain the models by observations of supergiants in the Small Magellanic Cloud (SMC) and in the Milky Way.

The paper is organized as follows. In Section 2 we describe our computational method and physical assumptions. In Section 3 we present our results: stellar evolutionary tracks, and the inferred binary parameter ranges for different cases of mass transfer. In Section 4 we compare our reference model and its variations to the observational constraints. In Section 5 we discuss the robustness of our results as well as the implications of our findings. We conclude in Section 6. A detailed study of the actual mass transfer phases is presented in a separate paper (Klencki et al. in prep.).

## 5.2 STELLAR MODELS: PHYSICAL INGREDIENTS

We employed the MESA stellar evolution code of Paxton et al. (2011, 2015, 2019)[1]. We modeled convection using the mixing-length theory (Böhm-Vitense, 1958) with a mixing-length parameter $\alpha = 1.5$, and we adopted the Ledoux criterion for convection. We accounted for semiconvection following Langer et al. (1983) with a relatively high efficiency parameter $\alpha_{\rm SC} = 100.0$, as guided by the recent results of Schootemeijer et al. (2019). While the value of $\alpha_{\rm SC}$ has been shown to have limited effect on the MS evolution, its effect on the post-MS expansion in radius can be substantial (see Sec. 5.5.1 and App. 5.B). In Sec. 5.3.3 we also explore variations with $\alpha_{\rm SC} = 1.0$ and 10.0.

We accounted for convective overshooting above the hydrogen-burning core by applying the step overshooting formalism with an overshooting length $\sigma_{\rm ov}$ of 0.345 pressure scale heights based on the calibration of Brott et al. (2011a) for a $16\,M_\odot$ star. This also agrees with the best fits to the SMC supergiant population obtained by Schootemeijer et al. (2019) for $\sigma_{\rm ov}$ of 0.33. While there is increasing evidence for a relation between $\sigma_{\rm ov}$ and the stellar mass (e.g., Claret & Torres, 2018, also Grin et al., private communication), a quantitative calibration for the massive stars is still lacking. We assumed the same amount of overshooting above the helium-burning core. For consistency with Schootemeijer et al. (2019), we assumed no overshooting associated with burning shells and convective zones in stellar envelopes. In Sec. 5.3.3 we also explore variations with the lower convective overshooting efficiency calibrated by Choi et al. (2016).

We modeled stellar winds following Brott et al. (2011a). For hot ($T_{\rm eff} > 25\,kK$) and hydrogen-rich ($X_{\rm S} > 0.7$) stars, we adopted the mass-loss rates from Vink et al. (2000, 2001). For hydrogen-poor stars ($X_{\rm S} < 0.4$), we applied the wind mass-loss as calculated by Hamann et al. (1995), divided by 10 (Yoon et al., 2006). For stars with intermediate hydrogen abundances ($0.4 < X_{\rm S} < 0.7$), we linearly interpolated between the two. For cooler stars ($T_{\rm eff} < 25\,kK$), we took the maximum of the two wind mass-loss rates as calculated from the methods of Vink et al. (2001) and Nieuwenhuijzen & de Jager (1990b). All these mass-loss rates for hydrogen-rich and hydrogen-poor stars include a metallicity dependence of $\dot{M} \propto (Z/\,Z_\odot)^{0.85}$ (Vink et al., 2001; Vink & de Koter, 2005).

For the value of solar metallicity, we assumed $Z_\odot = 0.017$ (Grevesse & Sauval, 1998). Given a metallicity $Z$, we calculated the initial helium abundance as $Y$ as $Y = Y_{\rm proto} + (Y_\odot - Y_{\rm proto})Z/\,Z_\odot$, where $Y_\odot = 0.28$ Grevesse et al. (1996) and $Y_{\rm proto} = 0.249$ (Planck Collaboration et al., 2016). The hydrogen abundance follows as $X = 1 - Y - Z$. Relative abundances of other elements were assumed to be same as in Grevesse et al. (1996).

We avoided using the MLT++ option in MESA (Paxton et al., 2013) in our reference model. While MLT++ typically helps with many numerical problems in evolving a massive star until the Wolf-Rayet (WR) stage, it also artificially reduces the stellar radii during the giant phase and therefore affects the predictions for mass transfer evolution. We consider a variation with MLT++ in Sec. 5.3.3 (and also App. 5.A). We used nuclear reaction networks provided with MESA: `basic.net` for H and He burning, and `co_burn.net` for C and O burning.

[1] MESA version r11554, `http://mesa.sourceforge.net/`.

We computed models in the mass range between 10 and 80 $M_\odot$ in steps of 2 $M_\odot$ (below 20 $M_\odot$) or 2.5 $M_\odot$ (above 20 $M_\odot$) at six different metallicities: $Z$ = 0.017, 0.0068, 0.0034, 0.0017, 0.00068, and 0.00017 (which correspond to 1.0 $Z_\odot$, 0.4 $Z_\odot$, 0.2 $Z_\odot$, 0.1 $Z_\odot$, 0.04 $Z_\odot$, and 0.01 $Z_\odot$). Most of our models are nonrotating, but we also explored rotating models with the initial rotation rate set to 40% of the critical value ($\Omega/\Omega_{\rm crit}$ = 0.4). In these models we included the effects of Eddington-Sweet circulation, secular shear instabilities, and the Goldreich-Schubert-Fricke instability, with an efficiency factor $f_c = 1/30$ (see the calibration to nitrogen enrichment in rotating stars and the references in Heger et al., 2000; Brott et al., 2011a).

There is no one common termination condition for all our models. Because the goal is to study single stellar tracks in the context of binary evolution and massive interacting binaries, we are interested in the evolution of single stars roughly until they have reached their largest radius. By that point, if they were members of binary systems, they would usually have gone into RLOF. In some cases, typically at low metallicity or for the low-mass end of our grid, stars continue to expand even during the late evolutionary stages of advanced burning and reach their maximum sizes near the very end of their lives. In these cases we evolved our models until the onset of oxygen burning. At this stage, a massive star is only about a year away from core collapse (depending on the mass), and there is no time left for any significant change in its size. In the remaining cases, the expansion of stars is quenched earlier through strong stellar winds. When a significant fraction of the envelope mass has been lost, the evolution in the Hertzprung-Russel (HR) diagram turns around toward higher effective temperatures. From that point onward, as increasingly more mass is lost from the envelope, the star continues to decrease in radius to eventually become a WR star. This part of the evolution is not relevant in the case of interacting binaries: either a RLOF would have occurred earlier, or it is not going to occur at all. In these cases we only evolved the models until the final turnaround in the HR diagram has been reached (taking into account the possibility of blue loops). The resulting mass transfer and post-mass transfer evolution is discussed in Klencki et al. (in prep.).

The MESA inlists (input files) used in this work are available at `http://cococubed.asu.edu/mesa_market/inlists.html`. All the output files, in particular stellar tracks, can be found at `https://zenodo.org/communities/mesa`.

## 5.3 Results

### 5.3.1 Stellar tracks and radius evolution of massive stars

In Figure 5.1 we show HR diagrams with evolutionary tracks of single stars with masses between 10 and 80 $M_\odot$ computed for solar ($Z = Z_\odot = 0.017$), subsolar (SMC-like, $Z = 0.2\ Z_\odot = 0.0034$), and very low metallicity ($Z = 0.01\ Z_\odot = 0.00017$). In the appendix (Fig. 5.11) we provide additional plots for intermediate metallicity values (0.4 $Z_\odot$, 0.1 $Z_\odot$, and 0.04 $Z_\odot$). Only the evolution until the maximum radial expansion and the subsequent decrease in radius by $\sim 20\%$ is shown (i.e., excluding the final leftward evolution toward WR stars in the case of high-mass

and high-metallicity models). Circles in Fig. 5.1 mark the position of a star during its post-MS evolution taken every 50,000 years. Thus, a clustering of circles corresponds to the relatively long-lived phase of core-helium burning (CHeB). It also indicates which part of the HR diagram is most likely to be occupied by a population of observed single stars (excluding MS stars), as predicted by our models. A lack of circles corresponds to the MS evolution and to phases of rapid expansion: the HG (between the end of MS and the onset of CHeB) and the helium HG (HeHG, between the end of CHeB and the onset of carbon burning). The track colors correspond to the central helium abundance.

When the location and evolution of CHeB stars in the HR diagram across different metallicities (i.e. the clustering of the circles) are compared, a metallicity trend in the post-MS radius evolution of massive stars is evident. The lower the metallicity, the smaller (and hotter) the massive stars at the end of the rapid HG expansion and during the subsequent CHeB phase. At solar metallicity (top panel), models below $\sim 65\ M_\odot$ expand all the way to the red giant branch (RGB, $\log T_{\rm eff} \lesssim 3.7$) during the short-lived HG phase, and almost their maximum radii at that stage ($R_{\rm HG;max} \sim 300 - 2000\ R_\odot$, depending on the mass). At this point, the models with masses $\lesssim 40\ M_\odot$ begin the slower core-helium burning evolution, whereas the more massive models quickly turn around toward the left in the HR diagram because of extensive mass loss. In the case of even more massive models ($M > 65\ M_\odot$), strong winds quench expansion at smaller sizes (up to $\sim 100\ R_\odot$). At SMC-like metallicity (middle panel, $Z = 0.2\ Z_\odot$), the post-MS radius evolution of models between $\sim 16$ and $\sim 40\,\mathrm{M}_\odot$ is significantly different to their solar metallicity counterparts. Instead of expanding all the way to the RGB during the HG phase, these models regain thermal equilibrium at much smaller radii ($\sim 100\ R_\odot$) as slowly evolving CHeB stars. At very low metallicity (bottom panel, $Z = 0.01\ Z_\odot$), the onset of the CHeB phase is located at even higher effective temperature (and smaller radius) for the entire mass range 10-80 $M_\odot$.

The position of the terminal-age MS (TAMS) changes with metallicity as well: the lower the metallicity, the hotter and smaller the MS stars (with the exception of the most massive models at solar metallicity). The largest differences between metallicities appear at the high-mass end of our grid ($\gtrsim 40\ M_\odot$). Notably, around the $40 - 50\ M_\odot$ range at solar metallicity (top panel) and above $\sim 60\ M_\odot$ at SMC-like metallicity (middle panel), models expand up to $\sim 1000\ R_\odot$ at the end of the MS. This is a signature of inflated envelopes, and this phenomenon was previously described by Kato (1985) for very massive MS stars and by Petrovic et al. (2006) for WR stars. In such stars, the Eddington limit is locally exceeded sufficiently close to the top of their envelopes (in this case, at the iron opacity peak). To prevent $L_{\rm rad}$ from exceeding $L_{\rm Edd}$, the layers above expand substantially and the envelope becomes extremely diluted and extended in radius (i.e., inflated), with a density inversion formed at the top (see Gräfener et al., 2012; Sanyal et al., 2015, for details). The differences in position of the TAMS at the high-mass end between different metallicities are primarily associated with the relative strength of stellar winds and the metallicity dependence of the envelope inflation in massive stars (Sanyal et al., 2017). The small sizes of our $M > 65\ M_\odot$ models at solar metallicity are in general agreement with the models by Sanyal et al. (2015), whose models never reach an effective temperature of $T_{\rm eff} \approx 15kK$ ($\sim 4.2$ in log) above a certain mass.

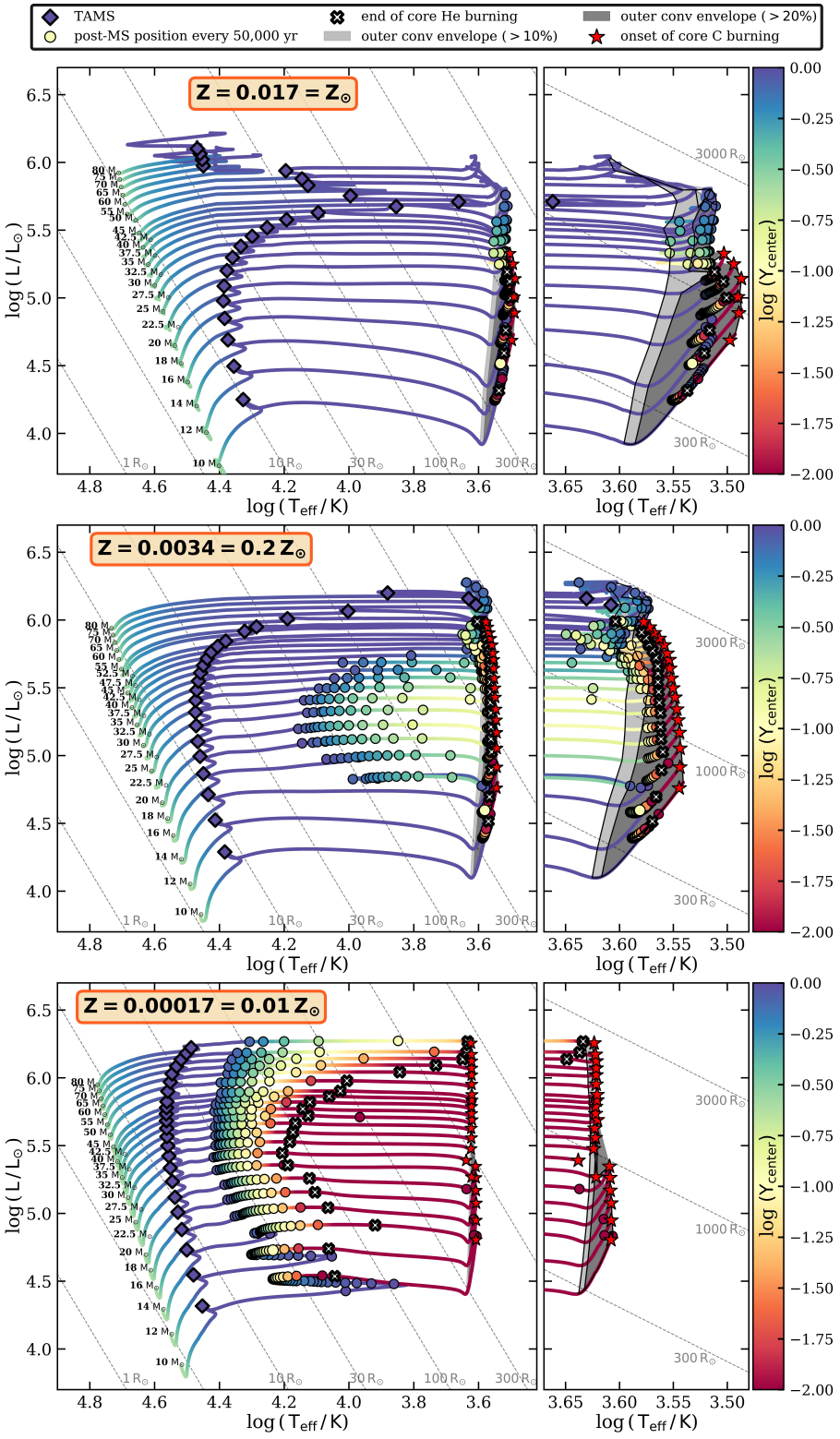


FIGURE 5.1: Evolutionary tracks of single stars of masses between 10 and 80 $M_\odot$ computed at three different metallicities: solar (top), SMC-like (middle), and very low metallicity $Z = 0.01\,Z_\odot$ (bottom). See Fig. 5.11 for tracks at three additional metallicities. Filled circles mark the position of a star during its post-MS evolution taken every 50,000 years. Color indicates the central helium abundance ($Y_C$, in logarithmic scale). With a cross we mark the end of core-helium burning ($Y_C < 10^{-3}$), and with a red star we mark the onset of core-carbon burning ($X_C^{\text{carbon}} < 0.95\,X_{C;\text{max}}^{\text{carbon}}$). Shaded regions mark stars with outer convective envelope layers of at least 10% (or 20%) of the mass of the entire star. For tracks that turn around towards the hotter part of the HR diagram (and the WR regime) because of extensive mass loss, we only show the evolution until shortly after the maximum radius has been reached.

In the case of very low metallicity (bottom panel, $Z = 0.01\ Z_\odot$), most of the models reach the end of CHeB while still in the blue part of the HR diagram ( $\log(T_{\rm eff}/{\rm K}) \sim 4.1$). These models expand significantly during the subsequent contraction of the CO core and the HeHG phase and reach the RGB by the very end of their evolution, sometimes shortly ($\sim$ 1000 yr) before the final core collapse. This is also the case for $Z = 0.04\ Z_\odot$ models in Fig. 5.11, but to a lesser extent.

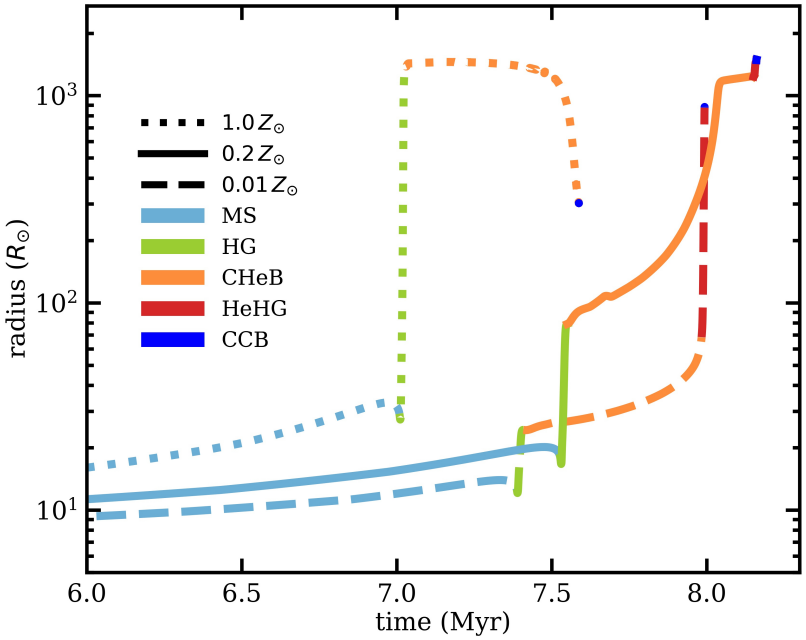


FIGURE 5.2: Radius evolution of a 25 $M_\odot$ single star model at solar ($Z = 0.017 = Z_\odot$), SMC-like ($Z = 0.0034 = 0.2\,Z_\odot$), and very low metallicity ($Z = 0.00017 = 0.01\ Z_\odot$). The lines are color-coded according to different evolutionary stages.

In summary, depending on the metallicity, a substantial expansion in radius can occur at a completely different evolutionary stage of a massive star. We illustrate this in Fig. 5.2, where we show the time evolution of the radius of a 25 $M_\odot$ model for three different metallicities. At solar metallicity, most of the expansion occurs during the HG phase, when the star expands rapidly on a thermal timescale. At subsolar SMC-like metallicity ($Z = 0.2\ Z_\odot$), most of the expansion takes place during CHeB, when the star is in thermal equilibrium and the radius changes slowly on a nuclear timescale. Very low metallicity stars expand significantly only after the end of CHeB during another phase of rapid out-of-equilibrium expansion: the HeHG phase. What follows is the core-carbon burning stage (CCB).

### 5.3.2 BINARY PARAMETER RANGES FOR DIFFERENT DONOR TYPES

In this section we take a binary perspective: we use the stellar tracks presented in the previous section to determine the evolutionary state of a donor star at the onset of mass transfer depending on the binary orbital period and metallicity. In order to do so, we assume that our single stellar models represent the evolution of the more massive component in a binary system until the eventual RLOF. We assume that the companion has half the mass of the primary star (mass ratio $q = 0.5$) and that its mass loss in winds is negligible compared to that of the primary. For simplicity, we assume that the amount of mass accreted by the companion from the wind is negligible and that its

mass is constant. We then compute the effect of the wind mass loss of the primary on the binary orbit by assuming that all the mass that the primary loses carries specific angular momentum equal to the specific orbital angular momentum of the primary.

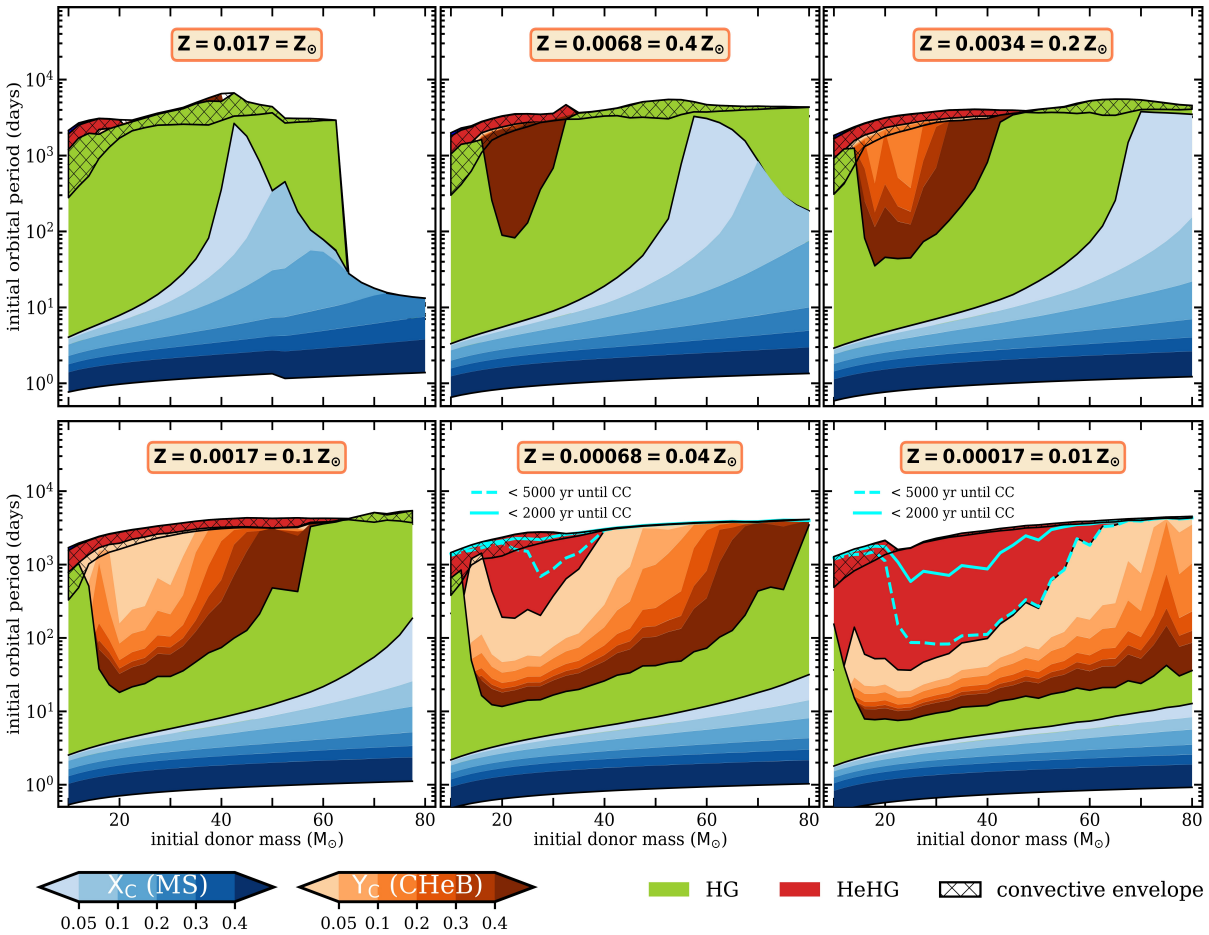


FIGURE 5.3: Evolutionary state of a donor star at the point of RLOF in massive interacting binaries as a function of initial donor mass (at the ZAMS) and initial orbital period, estimated based on the single stellar tracks presented in Sec. 5.3.1. The companion is assumed to be twice less massive (initial mass ratio $q = 0.5$), and it can be viewed as either a less massive star or under additional assumptions about the previous evolution (see text) as a stellar BH. Different shades of blue (orange) correspond to different central abundances of hydrogen (helium), indicating how advanced the MS (CHeB) evolution is. Hatched regions indicate donors with outer convective envelopes (at least 10% in mass coordinate). Cyan lines mark the threshold above which the donors are only 2000 or 5000 years away from the core-collapse (only shown for the two lowest metallicities for clarity).

The less massive companion can be considered to be either a less massive MS star or a stellar black hole (BH). The latter case would mean that the now more massive stellar component is what used to be the secondary star in a zero-age binary, and that the star that used to be the actual primary has already collapsed into a BH. Before BH formation, the binary has most likely gone through a phase of mass transfer. In this case, the now more massive stellar component of the BH binary has previously been an accretor.

With these assumptions, we plot in Fig. 7.1 in different colors the evolutionary state of the massive donor star at the point of RLOF as a function of the initial donor mass (i.e., at the zero-age main sequence, ZAMS, not at RLOF) and initial orbital period for different metallicities. When the companion is assumed to be a stellar BH, the initial period roughly corresponds to the orbital period at the moment of the BH formation. We neglect the effect of spin-orbit coupling by tidal interactions, which would shrink the pre-RLOF orbits by a small factor (see, e.g., Hurley et al., 2002) and shift the boundaries in Fig. 7.1 to somewhat higher initial orbital period values.

Several trends with metallicity are present in Fig. 7.1. We describe them below.

1. The lower the metallicity, the more evolved the donor stars at the point of RLOF. In particular, at $Z = Z_\odot$ and $0.4\ Z_\odot$ , almost all cases of mass transfer from an evolved (post-MS) donor involve a rapidly expanding HG star (green). As the metallicity decreases, however, the parameter space for RLOF initiated by a slowly expanding CHeB supergiant increases (orange) and also includes increaslingly more massive donors. This is a natural consequence of the fact that low-metallicity stars expand less strongly during the immediate post-MS expansion (HG phase) and can regain thermal equilibrium as much smaller CHeB stars ($\sim 100\ R_\odot$) than their higher metallicity counterparts ($\sim 1000\ R_\odot$), see Sect. 5.3.1. We discuss the implications of this trend for the binary formation channel of stripped helium stars in Sec. 5.5.3. The difference in post-MS radius expansion between low- and high -metallicity stars may also have significant consequences for the mass transfer evolution itself, see discussion in Sec. 5.5.4.

2. The lower the metallicity, the smaller the parameter space for RLOF from convective donors (marked with the hatched area in Fig. 7.1). The parameter space for convective donors disappears almost completely in the case of the more massive ($M > 40\ M_\odot$) models at very low metallicity ($Z = 0.04\ Z_\odot$ and $Z = 0.01\ Z_\odot$). It is also quenched in the case of the most massive models ($M > 65\ M_\odot$) at solar metallicity because these models only attain relatively small sizes. Only a small fraction of massive BH binaries evolve through mass transfer initiated by a convective envelope donor. This fact may have important consequences for the common-envelope (CE) formation channel of double BH binary mergers (see also Sec. 5.3.4 and the discussion in Sec. 5.5.5).

3. The lower the metallicity, the larger the parameter space for a late RLOF, that is, RLOF from a star that is only several thousand years away from core collapse. For a metallicity between 0.017 ( $Z_\odot$) and 0.0017 ($0.1\ Z_\odot$) , the parameter space for such a late RLOF is very small (even smaller than for convective donors) and limited to $M \lesssim 40\ M_\odot$. However, for very low metallicities, that is, $Z = 0.04\ Z_\odot$ and $0.01\ Z_\odot$, the probability of a late RLOF grows significantly, as highlighted by the cyan threshold lines. See Sec. 5.5.5 for a further discussion.

4. The lower the metallicity, the smaller the parameter space for mass transfer from MS donors. This is to a large extent a consequence of the formation of inflated envelopes in massive MS

stars that evolve near the Eddington limit (Sanyal et al., 2015). The sets of tracks at higher metallicities (1.0, 0.4, and 0.2 $Z_\odot$) all include a mass range in which the models become inflated and expand up to $\sim 1000\ R_\odot$ at the end of the MS (which corresponds to initial orbital periods for RLOF of $\gtrsim 1000$ days in Fig. 7.1). As the metallicity decreases, this mass range shifts toward higher masses (see also Sanyal et al., 2017). As a result, for $Z \leq 0.1\ Z_\odot$ the envelopes of MS stars do not become inflated within the mass limits of our grid (up to 80 $M_\odot$). It should be noted that normal not inflated MS stars at lower metallicity are also smaller than their higher metallicity counterparts.

### 5.3.3 Model variations

In order to illustrate the uncertainty in binary parameter ranges for the different evolutionary states of donor stars presented in Fig. 7.1, we explore in Fig. 5.4 several variations in the input parameters for one particular metallicity: $Z = 0.0017 = 0.1\ Z_\odot$ (see Fig. 5.12 in the Appendix for additional figures at different metallicities). Fig. 5.4a corresponds to the reference set of stellar tracks presented in the previous sections, computed using the assumptions described in Sec. 5.2. In particular, our reference model assumes step overshooting with $\sigma_{\rm ov;step} = 0.345$ (Brott et al., 2011a), high efficiency of semiconvective mixing ($\alpha_{\rm sc} = 100.0$), no MLT++ approach, and nonrotating models.

The model Fig. 5.4b assumes a different parameterization of convective overshooting (see Sec. 3.6.2 of Choi et al., 2016), one calibrated to reproduce the shape of the MS turnoff in the open cluster M67 (Magic et al., 2010). It is expressed according to the exponential formulation of overshooting (Herwig, 2000) with the characteristic length $\sigma_{\rm ov;exp} = 0.016$ for the core overshooting. This value is roughly equivalent to $\sigma_{\rm ov;step} = 0.2$ in the step overshooting description. Additionally, we tested that the calibration of overshooting carried out by Brott et al. (2011a) (based on the value of $\log(g)$ at the Henyey hook of $\sim 16\ M_\odot$ stars in the LMC clusters NGC 2004 and N11) can be best fit in the exponential overshooting description with $\sigma_{\rm ov;exp} \approx 0.03$. Thus, the Choi exponential parameterization effectively results in smaller overshooting than the step overshooting parameterization employed in Brott et al. (2011a) and in our reference model.

The model in Fig. 5.4c assumes somewhat less efficient semiconvection ($\alpha_{\rm sc} = 10$) than in the reference model ($\alpha_{\rm sc} = 100$). Both values appear to be consistent with the tentative observational constraints (Schootemeijer et al., 2019, see also Sec. 5.4). In Fig. 5.4d we show a model with even less efficient semiconvection, $\alpha_{\rm sc} = 1$. This model is disfavored based on the above-mentioned observations, see also Sec.5.4.1.

The model in Fig. 5.4e includes the MLT++ approach in MESA, which was developed to model convection in radiation-dominated superadiabatic envelope layers (Paxton et al., 2013). In short, the MLT++ option enforces a reduction in the temperature gradient in radiation-dominated convective zones, which effectively reduces superadiabacity and prevents the formation of density inversions. A more detailed explanation is provided in Appendix 5.A, where we also briefly discuss a link between density inversions in envelopes of massive stars and enhanced mass-loss rates

beyond the Humphreys-Davidson limit. Crucially, MLT++ also increases the effective temperature of the model and thus reduces the radius expansion of massive models, which in turn reduces the parameter space for mass transfer in massive wide systems. This is shown the bottom left panel of Fig. 5.4 and in the comparison of two HR diagrams of stellar tracks computed with and without MLT++ in Fig. 5.5. Other methods of preventing density inversions (e.g., using the density scale height or increasing the mass-loss rate) have a similar effect of increasing the effective temperatures of massive supergiants (e.g., Maeder, 1987).

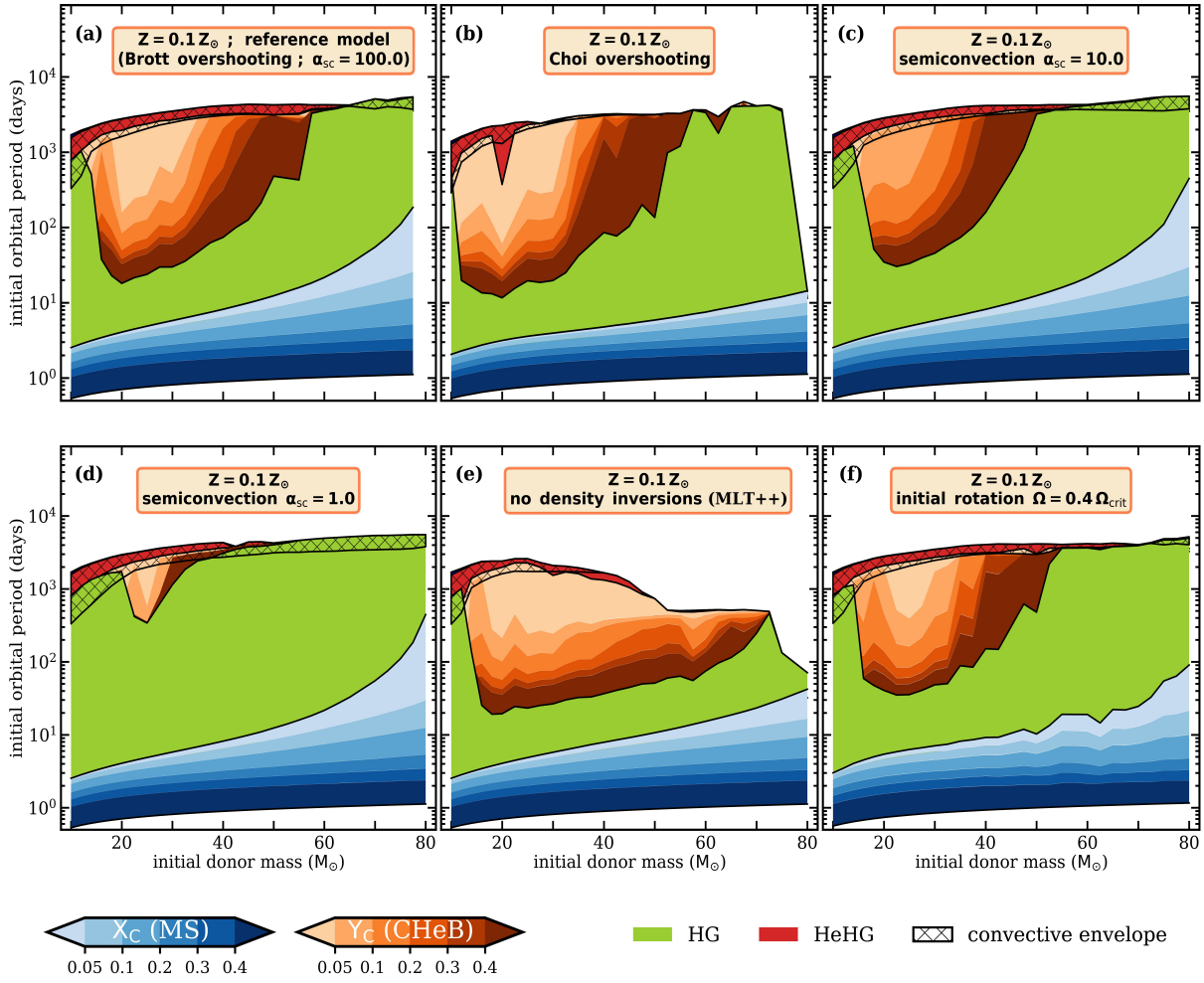


FIGURE 5.4: Same as Fig. 7.1, but computed for one particular metallicity ($Z = 0.0017 = 0.1\ Z_{\odot}$) and exploring several variations in the input parameters to the model with respect to the reference model presented in the previous sections (and in the top left panel): different overshooting parameterization (Choi et al., 2016), lower efficiency of semiconvective mixing ($\alpha_{\rm sc} = 10$ or $\alpha_{\rm sc} = 1$), application of MLT++ treatment of convection in radiation-dominated superadiabatic envelope layers (Paxton et al., 2013), and initial rotation velocity $\Omega = 0.4\Omega_{\rm crit}$. In the case of $Z = 0.2\ Z_{\odot}$, for which observation of evolved supergiants SMC can be used to constrain the models, none of the model variations presented above can be excluded, except for the one with $\alpha_{\rm sc} = 1$; see Sec. 5.4.

Finally, in Fig. 5.4f we show a model with evolution tracks of rotating stars with an initial

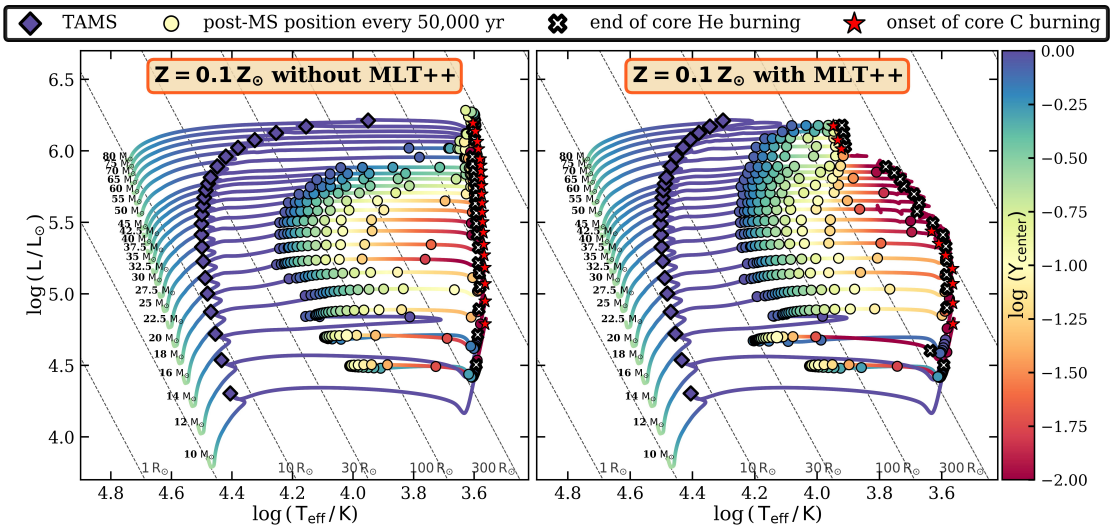


Figure 5.5: Effect of MLT++ on the evolution of massive stars in the HR diagram. The various scatter points have the same meaning and color scale as in Fig. 5.1 and 5.11. In the most massive stars, in which the density in regions with $L_{\rm rad}$ / $L_{\rm Edd} > 1$ is so small that it limits the efficiency of convection, a temperature gradient becomes superadiabatic and a density inversion develops in order to stabilize the structure (see App. 5.A). The MLT++ approach gradually smooths the temperature gradient and reduces superadiabaticy, also removing density inversions and the $L_{\rm rad}$ / $L_{\rm Edd}$ excess in the most massive stars. A direct consequence of the MLT++ treatment of convection is that the effective temperature becomes higher, as illustrated by the above figure.

angular velocity $\Omega/\Omega_{\rm crit} = 0.4$. This value was chosen to allow for a comparison with the GENEVA tracks (e.g., Georgy et al., 2013; Groh et al., 2019). Similarly to Schootemeijer et al. (2019), we find that such moderate rotation does not have a significant effect on the post-MS radius evolution. However, we note that for a more rapid initial rotation rate $\Omega/\Omega_{\rm crit} \approx 0.6$, the most massive models in our grid at $Z = 0.1\ Z_\odot$ ($\gtrsim 65\ M_\odot$) would enter the chemically homogeneous evolution regime.

Similar figures to Fig. 5.4 for another four metallicities ($Z = 0.4\ Z_\odot$, $0.2\ Z_\odot$, $0.04\ Z_\odot$, and $0.01\ Z_\odot$) can be found in the Appendix in Fig. 5.12. In Sec. 5.4 we show that for $Z = 0.2\ Z_\odot$ none of the model variations discussed above, except for the model with $\alpha_{\rm sc} = 1$, can be confidently excluded based on the observed samples of supergiants in the SMC ($Z_{\rm SMC} \approx 0.2\ Z_\odot$). At even lower metallicities, the model uncertainties are all the more unconstrained.

### 5.3.4 Convective envelope donors

Whether or not a donor star has an outer convective envelope is particularly important for the question of mass transfer stability (e.g., Hjellming & Webbink, 1987; Soberman et al., 1997). In short, convective stars respond to mass loss by adiabatically expanding[2] , whereas stars with radiative envelopes respond by adiabatically contracting. For this reason, mass transfer from stars

[2]This may no longer be true in stars with a sufficiently well-developed superadiabatic layer in the outer envelope (Woods & Ivanova, 2011; Pavlovskii & Ivanova, 2015).

with outer convective envelopes is more likely to become dynamically unstable, possibly leading to a CE evolution (Webbink, 1984; Hjellming & Webbink, 1987; Ivanova et al., 2013b; Ge et al., 2015; Pavlovskii & Ivanova, 2015). To take this into account, population synthesis codes need to assume different stability criteria depending on whether the donor has a radiative or convective envelope. Analytical fits to evolutionary tracks that many of such codes are based on (e.g., the SSE/BSE method Hurley et al., 2000, 2002) do not usually include an explicit information about the type of the stellar envelope. For this reason, stability criteria are sometimes based on the evolutionary type of the star alone (e.g., Belczynski et al., 2008a; Vigna-Gómez et al., 2018). This can lead to large errors: as Fig. 7.1 shows, the occurrence of outer convective envelopes cannot be unambiguously linked to any particular evolutionary phase. In particular, the mass transfer instability (and CE evolution) may be substantially overpredicted in this calculation if CHeB donors are assumed to respond to mass loss as convective stars.

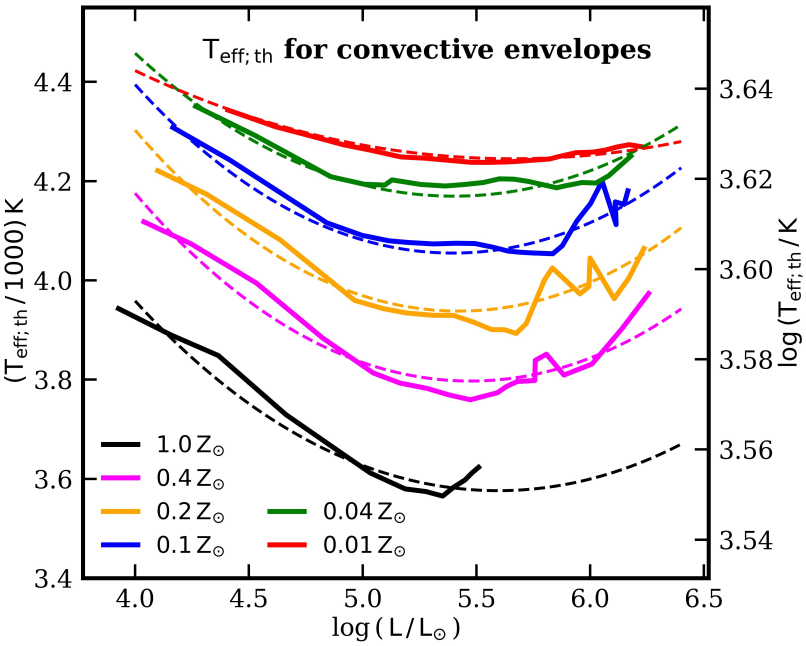


FIGURE 5.6: Threshold effective temperature $T_{\rm eff;th}$ below which at least 10% of the outer mass in a star is convective. Solid lines correspond to our stellar models, and the dashes lines show the numerical fit described with Eqs. 5.1 and 5.2.

Instead, mass transfer stability criteria should include a relation to the effective temperature of the donor star, which is the primary factor that determines the occurrence of a convective envelope. In Fig. 5.6 we plot as a function of luminosity and for various metallicities the threshold effective temperature $T_{\rm eff;th}$ below which at least 10% of the outer mass of the star is convective. Solid lines correspond to the stellar tracks computed in this work (see Fig. 5.1 and 5.11 for HR diagrams). Dashed lines are the result of a numerical fit described by the following relation:

$$\log(T_{\rm eff;th}/{\rm K}) = a_1 \log(L/L_\odot)^2 + a_2 \log(L/L_\odot) + a_3, \tag{5.1}$$

where the coefficients $a_i$ for $i$ in $\{1, 2, 3\}$ are given as a function of metallicity,

$$a_i = b_{1i} \log(Z/Z_\odot)^2 + b_{2i} \log(Z/Z_\odot) + b_{3i}. \tag{5.2}$$

The values of the nine $b_{ij}$ coefficients are given in Table 5.1. Notably, $T_{\rm eff;th}$ in Fig. 5.6 depends on $Z$: the lower the metallicity, the higher the threshold temperature for convective envelopes. The reason

Table 5.1: Values of $b_{ij}$ coefficients in Eq. 5.2.

| $b_{ij}$ | $i = 1$ | $i = 2$ | $i = 3$ |
|---|---|---|---|
| $j = 1$ | −0.0060 | −0.0066 | 0.0173 |
| $j = 2$ | 0.0596 | 0.0587 | −0.1940 |
| $j = 3$ | −0.1637 | −0.1967 | 4.0962 |

is that the Hayashi line depends on metallicity for a given value of the mixing-length parameter, where fully convective stars of high $Z$ have larger radii (and lower effective temperatures) than their lower metallicity counterparts. It should be noted, however, that the debate on whether the effective temperatures of RSGs (an indication for the Hayashi line) do indeed depend on their metallicity is still ongoing. Based on effective temperatures derived from spectral energy distribution fits, Davies et al. (2015) and Patrick et al. (2015) did not find any significant trend between $Z$ and $T_{\rm eff}$ of RSGs of various metallicities from several different host galaxies (although this conclusion may depend on the method for determining $T_{\rm eff}$, see Sec. 4.5 of Chun et al. 2018). Britavskiy et al. (2019) performed a similar analysis on a sample of RSGs from dwarf irregular galaxies from the Local Group, arguing in favor of a trend in which the minimum effective temperature increases toward lower metallicities. Another piece of the puzzle has recently been added by Chun et al. (2018), who found that the inferred effective temperatures of RSGs in various local galaxies could be better matched by stellar models in which the mixing length increases with metallicity (see also Tayar et al., 2017). With all these results in mind, we stress that our fits in Fig. 5.6 are primarily meant to serve as a simple and approximate method for determining the transition from radiative to convective-envelope giants in population synthesis. We especially urge caution when a connection is made between the metallicity trend in Fig. 5.6 and expected effective temperatures of RSGs or maximum stellar radii of stars at different metallicities.

## 5.4 Comparison with observations: clues for post-MS expansion

The question of the post-MS expansion and blue-to-red evolution of massive stars is a long-standing problem in stellar astrophysics, with models being very sensitive to the adopted assumptions (see e.g., Langer, 1991; Eldridge et al., 2008; Meynet et al., 2013). Most notably, it was shown that the degree of the HG expansion crucially depends on the efficiency of overshooting and semiconvective mixing (Langer et al., 1989; Stothers & Chin, 1992; Langer & Maeder, 1995), with rotational mixing also playing a role, see Georgy et al. (2013). The observable BSG-to-RSG ratio can be used as a diagnostic tool in an attempt to calibrate the models (e.g., Eldridge et al., 2008; Georgy et al., 2013; Choi et al., 2016). Traditionally, the BSG group comprises O, B, and A stellar types ($\log T_{\rm eff} \gtrsim 3.9$) and the RSG group is composed of K and M supergiants ($\log T_{\rm eff} \lesssim 3.7$, e.g., Eggenberger et al., 2002; Massey, 2003). In this way, the BSG group includes MS stars (O-type stars) and is dominated by them in terms of numbers. This limits the accuracy of the method in

constraining specifically the post-MS phase of evolution.

A slightly modified approach has recently been carried out by Schootemeijer et al. (2019), who constructed a sample of BSGs from the SMC by combining only the B- and A-type stars ($3.85 \gtrsim \log T_{\rm eff} \lesssim 4.4$). In this way, they were able to probe predominantly the post-MS phase of evolution at the SMC metallicity (see Fig. 5.1). Notably, Schootemeijer et al. (2019) showed that models that assume the Schwarzschild criterion for convection (an assumption that is often made in previous calculations of massive-star models), which is equivalent to extremely efficient semiconvection, tend to underestimate the degree of the post-MS expansion and underpredict the number of RSGs. The disagreement of such models with observations has been pointed out by previous authors (e.g., Georgy et al., 2013).

### 5.4.1 SMC-LIKE METALLICITY ($Z = 0.2\ Z_\odot$)

We took an approach similar to that of Schootemeijer et al. (2019) and compared our $Z = 0.2\ Z_\odot$ models with the observed population of luminous ($\log(L/L_\odot) \geq 4.7$) supergiants in the SMC with effective temperatures $\log(T_{\rm eff}/{\rm K}) \lesssim 4.35$. Following Drout et al. (2009), we defined RSGs as supergiants cooler than a threshold effective temperature $\log(T_{\rm eff;thresh}/{\rm K}) = 3.68$. We aim to compare the number of RSGs to the number of hotter supergiants from the effective temperature range between $\log(T_{\rm eff}/{\rm K}) = 3.68$ and 4.35. In this way, we constrain the post-MS expansion of our models, which either expand all the way to the red giant branch during the HG phase and spend most of the CHeB lifetime as RSGs, or they complete the HG expansion as hotter stars and spend a significant fraction of the CHeB lifetime with $\log(T_{\rm eff}/{\rm K})$ between 3.68 and 4.35. We note that in our $Z = 0.2\ Z_\odot$ tracks the convective RSG branch is located at slightly lower temperatures (at $\log(T_{\rm eff}/{\rm K}) \lesssim 3.6$, depending on luminosity, see Fig. 5.1) than the assumed threshold temperature $\log(T_{\rm eff;thresh}/{\rm K}) = 3.68$ and than the measured effective temperatures of most of the RSGs in the SMC (e.g., obtained through spectral energy distrigution fitting Davies et al., 2018). This is a likely sign that our assumed mixing length parameter $\alpha = 1.5$ is somewhat too small. For example, Chun et al. (2018) reported that models with $\alpha \approx 2$ agree better with temperatures of cool supergiants from the SMC. However, this discrepancy in temperatures of RSGs does not significantly affect the prediction for the number of RSGs from our models because for the majority of the models, the time that stars spend with $\log(T_{\rm eff}/{\rm K})$ between 3.6 and 3.68 is far shorter than the CHeB lifetime. We point out that other factors such as the effect of binary interactions or the shortcomings of the mixing-length theory in massive convective-envelope giants (see App. 5.A) are likely to be a higher-order source of uncertainty.

For the sample of RSGs, we relied on the most recent investigation of the population of cool supergiants in the SMC by Davies et al. (2018). The authors combined a number of input catalogs in order to construct a highly complete sample of cool luminous SMC stars with effective temperatures $\log(T_{\rm eff}/{\rm K}) \lesssim 3.74$ (based on the effective temperature scale of Tabernero et al., 2018). Out of 151 stars with $\log(L/L_\odot) \geq 4.7$ in their sample, 147 meet our RSG criteria ($\log(T_{\rm eff}/{\rm K}) < 3.68$).

As explained above, we mean to compare the number of RSGs with stars in the temperature range $3.68 < \log(T_{\rm eff}/{\rm K}) < 4.35$. This includes both yellow supergiants (YSGs) ($3.68 \geq \log(T_{\rm eff}/{\rm K}) \leq 3.88$ Drout et al., 2009) and BSGs with $\log(T_{\rm eff}/{\rm K})$ between 3.88 and 4.35. To construct a combined sample of YSGs and BSGs, we relied on several different studies. In the temperature range $3.68 < \log(T_{\rm eff}/{\rm K}) < 3.74$, four YSGs were reported by Davies et al. (2018). A survey by Neugent et al. (2010), targeting YSGs and cool BSGs and identifying their SMC membership based on their radial velocities, found 40 stars in the temperature range $3.74 < \log(T_{\rm eff}/{\rm K}) < 4.1$ (eight of which were YSGs at $\log(T_{\rm eff}/{\rm K}) < 3.88$). The authors estimated the completeness of their sample to be high and that only a few rather than tens of objects were missing, especially at the higher luminosity end that we are interested here (i.e., $\log(L/L_{\odot}) > 4.7$). Finally, 42 BSGs in the SMC with temperatures within $4.1 < \log(T_{\rm eff}/{\rm K}) < 4.35$ have recently been reported by Kalari et al. (2018) with luminosities that meet our criteria. In total, the authors provided physical parameters of 69 BSGs, which were selected from the OGLE-II I-band imagining survey based on availability of multi-epoch photometry. Notably, a total of 110 BSGs were identified in the OGLE-II I-band data, which in turn is a fraction of 179 SMC BSGs reported in the catalog of massive SMC stars by Bonanos et al. (2010).

The combined number of BSGs and YSGs in our sample is thus 86, and the ratio of BSGs plus YSGs to RSGs is equal to $86/147 \approx 0.59$. As described above, the number of luminous BSGs in our sample is likely underestimated in the temperature range $4.1 < \log(T_{\rm eff}/{\rm K}) < 4.35$, possibly by a factor of a few. Nonetheless, we consider the samples of RSGs and BSGs plus YSGs constructed in this way to be representative of the underlying population and sufficiently complete to compare with our models.

In Fig. 5.7 we plot luminosity distributions of RSGs and BSGs plus YSGs (top and middle panels, respectively), and the number ratio of BSGs plus YSGs to RSGs (bottom panel). Diamond points correspond to the observational samples described above, with Poissonian uncertainties marked as well (90% confidence level). Solid-line histograms correspond to several different sets of stellar tracks at $Z = 0.0034 = 0.2\,Z_{\odot}$ (see Sec. 5.3.3 for a description of various models). To construct the histograms, we assumed a constant star formation rate and the Salpeter initial mass function slope for massive stars ($dN/dM \propto M^{-2.35}$ Salpeter, 1955). We normalized the histograms to the total number of 233 supergiants in the observed sample. We stress that the comparison in Fig. 5.7 is rather tentative because it attempts to compare single stellar tracks with a population of stars that are likely affected by binary evolution (most massive stars are born in binaries; Sana et al., 2012; Moe & Di Stefano, 2017). Additionally, the BSG, YSG, and RSG samples are not constructed in an unbiased and homogeneous way.

In the low-luminosity range ($\log(L/L_{\odot}) \lesssim 5.2$), most of the models agree reasonably well with observations, up to a factor of a few in BSG plus YSG and RSG counts. Because the character of the comparison is tentative, we deem these discrepancies insufficient to confidently reject the models. The possible exception is the model with Choi overshooting, for which the ratio of BSGs plus YSGs to RSGs appears to be significantly too high in all three low luminosity bins ($\log(L/L_{\odot}) < 5.4$). It seems challenging to explain this discrepancy by the unaccounted-for

binary effects because binary interactions would likely further reduce the theoretically expected number of RSGs (e.g., stars that lose mass in mass transfer become bluer). Unless the observed sample is missing most of the SMC BSGs or YSGs and the real ratio of BSGs plus YSGs to RSGs is a few times higher, the model with Choi overshooting is most likely disfavored.

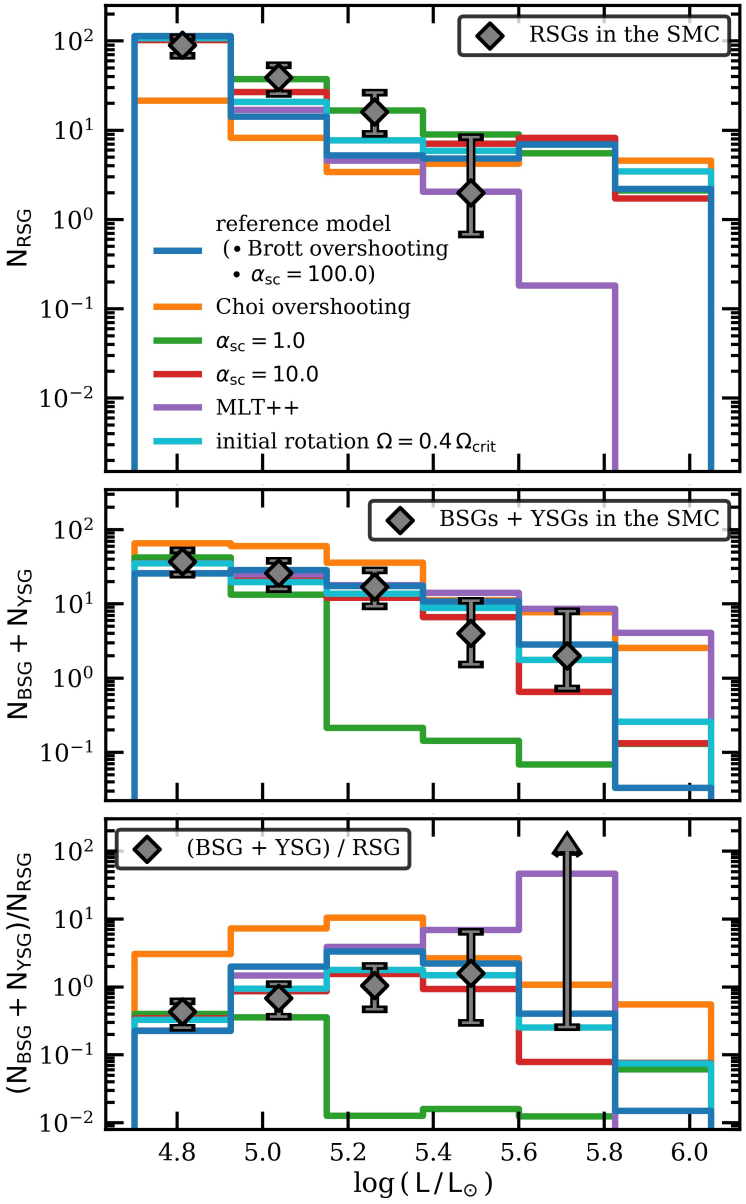


FIGURE 5.7: Distributions of RSG and BSG plus YSG number counts (top and middle panels, respectively), as well as the number ratio of BSGs plus YSGs to RSGs (bottom panel) in logarithmic luminosity bins between 4.7 and 6.05 in $\log(L/L_\odot)$. Diamond scatter points correspond to observational samples of 147 RSGs (with $\log(T_{\rm eff}/{\rm K}) < 3.68$) and 86 BSGs plus YSGs (with $\log(T_{\rm eff}/{\rm K})$ between 3.68 and 4.35). Uncertainties correspond to 90% confidence limits assuming a Poissonian distribution for the number of supergiants in each bin. Only a lower limit is available for the ratio of BSGs plus YSGs to RSGs in the luminosity bin $5.6 \lesssim \log(L/L_\odot) \lesssim 5.8$. Solid-line histograms, normalized to 233 stars in total, correspond to several different sets of stellar tracks at $Z = 0.0034 = 0.2\,Z_\odot$ metallicity.

In the high-luminosity range the discrepancies between models and observations become larger. In particular, no RSGs are observed in the SMC with luminosities above $\log(L/L_\odot) \approx 5.6$ (the highest luminosity reported by Davies et al. 2018 is $\log(L/L_\odot) = 5.55 \pm 0.01$), while all models but one predict at least a few of them in every 233 SMC supergiants. At the same time, several BSGs are observed with luminosities between 5.6 and 5.8 in $\log(L/L_\odot)$. This may indicate that stars with masses $\gtrsim 40\,M_\odot$ at $Z = 0.2\,Z_\odot$ either do not expand to become RSGs at all or that the RSG phase is extremely short in this case. This might simply be due to rotation. For instance,

Schootemeijer et al. (2019) found fewer RSGs in the upper part of the HR diagram in their models with rotation than in the nonrotating tracks (initial velocity of 300 km s$^{-1}$, see their Fig. 11). A short-lived (and therefore difficult to observe) RSG phase of $M \gtrsim 40\ M_\odot$ stars might be a result of increased mass-loss rates due to dust-driven winds (Chieffi & Limongi, 2013) or proximity to the Eddington limit (Chen et al., 2015).

Alternatively, the lack of RSGs above $\log(L/L_\odot) \approx 5.6$ may suggest that density inversions that would form in envelopes of such stars (in 1D models at least) either do not form at all because of an additional energy transport mechanism that prevents superadiabacity, or that such inversions are prone to instabilities and extensive mass loss (possibly the luminous blue variables phenomenon). For this reason, the model in which the formation of density inversions is prevented (the MLT++ approach) does not have solutions in the upper right corner of the HR diagram (see Fig. 5.5) and is statistically consistent with the lack of RSGs above $\log(L/L_\odot) = 5.6$ in Fig. 5.7. On the other hand, the MLT++ model predicts about 15 BSGs above $\log(L/L_\odot) = 5.6$, while only 2 such stars are present in the observed samples. Finally, the lack of RSGs from $M \gtrsim 40\ M_\odot$ stars might arise because binary interactions dominate the evolution of massive stars and prevent them from becoming as large as $\gtrsim 2000\ R_\odot$. Regardless of the reason, it seems unlikely that it has much to do with the tendency of some of the low-metallicity stars to begin the CHeB phase already as BSGs. We note that there appears to be a general lack of very massive (luminous; $\log(L/L_\odot) > 5.8$) stars in the observed samples compared to our theoretical predictions. This might be an indication that very massive stars ($M \gtrsim 60\ M_\odot$) are rare in the SMC for reasons that are yet to be understood.

The middle panel of Fig. 5.7 shows that most of the models agree reasonably well with observations. The only exception are tracks that are computed with the lowest efficiency of semiconvective mixing, that is, $\alpha_{\rm sc} = 1$. In this case, the model predicts no BSGs or YSGs with luminosities $\log(L/L_\odot) > 5.2$ in the observed sample, while in reality, there are 23 such stars. Consequently, the ratio of BSGs plus YSGs to RSGs at $\log(L/L_\odot) > 5.2$ in the model with $\alpha_{\rm sc} = 1$ is strongly inconsistent with the observations (see the bottom panel).

One possible explanation for this discrepancy that should be considered is the effect of mass transfer evolution in binary systems. As we show in our upcoming paper, Klencki et al. (in prep), donor stars in stable mass transfer events are unlikely to help alleviate the issue because in the case of the $\alpha_{\rm sc} = 1$ model, they would quickly become too hot to qualify for our BSG or YSG categories. On the other hand, sufficiently rejuvenated accretor stars or products of stellar mergers from early case B (or very late case A) mass transfer might produce CHeB supergiants that evolve as BSGs or YSGs with luminosities $\log(L/L_\odot) > 5.2$ (Justham et al., 2014). Because the parameter space for this type of evolution is limited, however, it is not clear whether such mass gainers or stellar mergers can fully account for the underabundance of BSGs plus YSGs from single stellar evolution in the model with $\alpha_{\rm sc} = 1$ (although mass gainers in general may be quite common among apparently single stars; de Mink et al., 2014). With this caveat in mind, we consider the model with $\alpha_{\rm sc} = 1$ (and similar models in which most of the CHeB evolution at $Z = 0.2\ Z_\odot$ takes place during the RSG stage) to be disfavored by the observations.

### 5.4.2 SOLAR METALLICITY

In the solar metallicity case, it is not feasible to use the ratio of BSGs plus YSGs to RSGs to constrain the post-MS radius evolution because of the larger (and more mass-dependent) sizes of MS stars. This makes it difficult to probe the post-MS phase of evolution alone. Additionally, it is more challenging to obtain a reasonably complete sample of supergiants in the Milky Way. Instead, we take a different approach to compare our $Z = Z_\odot$ tracks with observations. Recently, Castro et al. (2014) compiled a Galactic sample of massive stars in the spectroscopic HR diagram (sHR, Langer & Kudritzki, 2014) and compared them to single stellar tracks from Brott et al. (2011a) and Ekström et al. (2012).

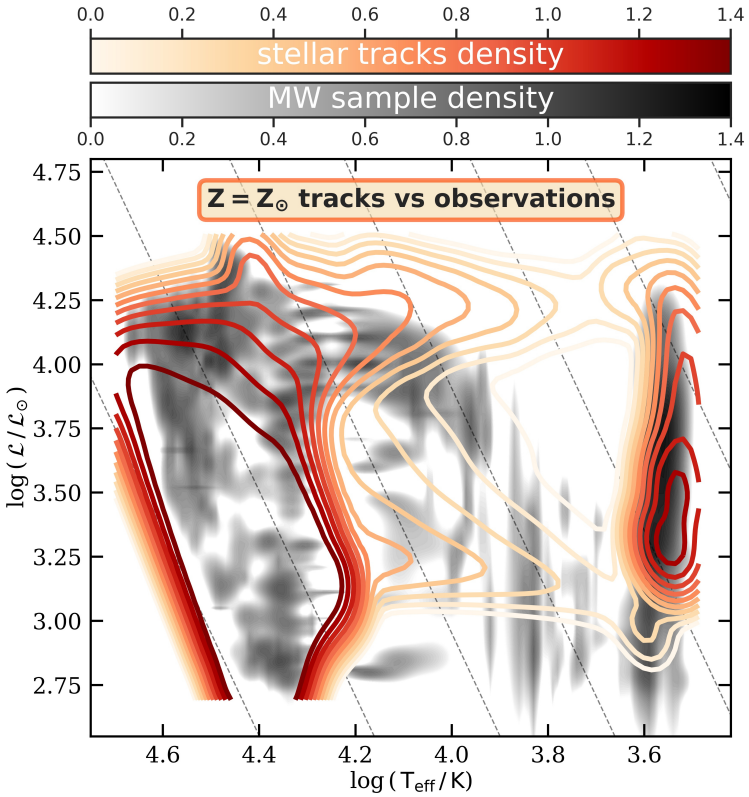


FIGURE 5.8: Comparison of our stellar tracks computed at solar metallicity with the observed sample of Galactic massive stars collected by Castro et al. (2014). The observations are plotted as a density map in a logarithmic grayscale. We overplot contours of the theoretical distribution of stars obtained from our reference model at $Z = Z_\odot$ in color (also in a logarithmic scaling). The lack of observed stars in the parameter range of $3.7 \lesssim \log(T_{\rm eff}/K) \lesssim 3.9$ and $3.5 \lesssim \log(\mathcal{L}/\mathcal{L}_\odot) \lesssim 4.0$ is a tentative piece of evidence that solar metallicity massive stars (mass range of about 16 to 40 $M_\odot$) expand until the red giant branch during the HG phase.

Their sample is not complete; it was collected from various surveys that often had different scientific goals, therefore it is biased in several ways. This leads to an overpopulation of stars in certain regions such as the instability strip or the O- and early B-type temperature ranges.

Nonetheless, certain sharp features of stellar tracks, such as the position of the TAMS or the red-giant branch, can be constrained.

In Fig. 5.8 we compare the sample collected by Castro et al. (2014) with our reference model in the sHR diagram (where $\mathcal{L} = T_{\rm eff}^4/g$). The observations are plotted in the background as a grayscale density map (reproduced after Castro et al. 2014 with permission from the authors). We overplot contours of the theoretical distribution of stars obtained from our single stellar tracks at $Z = Z_\odot$ in color. The theoretical prediction was obtained under the assumption of the Salpeter initial mass function for $M \geq 10\ M_\odot$ (Salpeter, 1955). We also assumed that all such massive stars are formed in binary systems (e.g., Duchêne & Kraus, 2013; Moe & Di Stefano, 2017) and that their evolution can be approximated with our single tracks only until the eventual RLOF. For the initial orbital period distribution, we assumed $dN/d(\log \mathrm{P}) \propto (\log \mathrm{P})^{-0.55}$ for $\log \mathrm{P}$ in range $[0.15, 4.0]$ (Sana et al., 2012), and for simplicity, we assumed a fixed initial mass ratio of 0.5 and circular orbits. We assumed that when a star initiates RLOF and starts losing mass from its envelope, then it immediately becomes a hot helium star that does not fit into the $T_{\rm eff}$ range in Fig. 5.8, and we did not include it in the theoretical distribution of stars in the figure. In our upcoming paper with binary models (Klencki et al. in prep.), we find that this is a good assumption in the case of stellar models in which the rapid HG expansion continues until the red giant branch (e.g., in the $Z = Z_\odot$ case), but not in the case of models with much smaller HG stars (e.g., the $Z = 0.2\ Z_\odot$ case). The 2D probability density function of stars in the sHR diagram was estimated from discrete stellar tracks computed in this study through a kernel-density estimation using Gaussian kernels (method `stats.gaussian_kde` from the SciPy package Virtanen et al., 2019).

The agreement of our theoretical distribution with observations is not perfect, although it is certainly not worse than in the case of the tracks by Brott et al. (2011a) or Ekström et al. (2012), see Castro et al. (2014). Perhaps the most significant discrepancy is that we predict many more RSGs ( $\log(T_{\rm eff}/\mathrm{K}) \lesssim 3.68$) and B-type stars ( $\log(T_{\rm eff}/\mathrm{K})$ between 4 and 4.2) in the high-$\mathcal{L}$ region above 4.25 than what is observed. This might be an indication that the line-driven wind mass-loss prescriptions used in our models overestimate the mass-loss rates at solar metallicity (when a star loses mass from its envelope, it tends to move upward in the sHR diagram because $\mathcal{L} \propto L/M$). In the case of B-type massive stars, this is supported by some empirical evidence (e.g., Oskinova et al., 2011; Hainich et al., 2018).

From the point of view of the post-MS expansion and blue to red evolution, the interesting region of the sHR diagram is the parameter range of about $3.7 \lesssim \log(T_{\rm eff}/K) \lesssim 3.9$ and $3.5 \lesssim \log(\mathcal{L}/\mathcal{L}_\odot) \lesssim 4.0$. This corresponds to the YSG position of massive stars in the range of about 16 to 40 $M_\odot$. If, similarly to the subsolar metallicity case, these stars were to slow down their HG expansion and continue with the CHeB evolution as BSGs at first and later as YSGs, then we would expect them to populate this region in the sHR diagram. The lack of observed stars in this parameter range in the sample compiled by Castro et al. (2014) (which notably includes stars in the same $T_{\rm eff}$ range, but at lower $\mathcal{L}$) is a tentative piece of evidence that solar metallicity massive stars expand to the red giant branch during the HG phase.

## 5.5 DISCUSSION

The stellar tracks computed in this work show a gradual metallicity trend in the post-MS radius expansion of stars: the lower the metallicity, the stronger the tendency of massive stars to limit the rapid HG expansion and regain thermal equilibrium as helium-burning supergiants already in the blue part of the HR diagram, as much more compact stars than RSGs. In other words, the maximum size of massive HG stars decreases with metallicity. This trend has previously been described by Brunish & Truran (1982) and Baraffe & El Eid (1991) and also appears in some of the more recent single stellar tracks computed by other authors (e.g., Marigo et al., 2001; de Mink et al., 2008; Ekström et al., 2012; Georgy et al., 2013; Tang et al., 2014; Choi et al., 2016; Groh et al., 2019). In the following sections we discuss the origin and the robustness of this result, as well as some of its implications in the context of massive binary evolution.

### 5.5.1 WHY DOES THE SIZE OF MASSIVE HG STARS DECREASE WITH METALLICITY?

Some low-metallicity models begin the CHeB phase as more compact stars than their higher metallicity counterparts because of the complicated interplay between at least two metallicity-dependent factors: higher central temperatures and central densities at TAMS of low-$Z$ stars (resulting in a less pronounced mirror effect during the HG phase) and lower opacities in their envelopes (enabling smaller radius solutions) (see Brunish & Truran (1982); Baraffe & El Eid (1991); Langer (1991); Groh et al. (2019)). The wind mass-loss rate also plays a role. In general, a giant star with stronger winds has a more extended envelope than an otherwise very similar model with weaker winds, resulting in an increased rate of redward evolution (Brunish & Truran, 1982). A notable exception are the models of MS and WR stars with inflated envelopes, for which the inflated envelope solution was found to disappear for mass-loss rates above a certain critical value (Petrovic et al., 2006).

However, the way in which a star of a given mass and metallicity expands after the end of MS is not a robust result of evolutionary computations. In some cases, it depends sensitively on rather uncertain input parameters. For example, even at a metallicity as low as $Z = 0.0017$, it is possible to have stellar tracks in which the most massive stars reach the RSG stage during the short-lived HG phase, similarly to solar metallicity models (see the model with $\alpha_{\rm sc} = 1$ in Fig. 5.4).

The key factor that essentially determines the post-MS radius expansion in cases sensitive to model assumptions is the H/He abundance profile in the layer just above the helium core. Depending on the efficiency of mixing, it can vary from a shallow linear slope (i.e., left at the end of the MS by the retreating convective core) to an extremely steep H/He gradient, almost a step function (e.g., Schootemeijer & Langer, 2018). The abundance profile is important because it determines the location and strength of hydrogen-shell burning, which in turn determines the size of HG stars (see Kippenhahn & Weigert 1990 and also Georgy et al. 2013). In Appendix 5.B we show in detail how different efficiencies of semiconvective mixing ($\alpha_{\rm sc} = 1$ or 100) result in

different H/He abundance profiles above the helium cores of our 25 $M_\odot$ models, leading to vastly different degrees of HG radius expansion (see also Schootemeijer et al., 2019).

In addition to semiconvection, other uncertain mixing processes affect the H/He abundance in the layer above the helium core. For example, convective core overshooting (Langer et al., 1985; Stothers & Chin, 1992; Langer & Maeder, 1995), rotational mixing and instabilities (Georgy et al., 2013), and most likely, shell overshooting. Purely numerical aspects such as the determination of convective boundaries in stellar evolution codes also play a role (see, e.g., the convective pre-mixing approach in Paxton et al., 2018, 2019). The effect of all these factors on the abundance profile above the helium core is uncertain and most likely degenerate (Meynet et al., 2013).

### 5.5.2 How robust is the trend with the metallicity?

Because of the uncertainties in modeling the radial expansion of post-MS massive stars, it is vital to turn toward observations. The relative numbers of blue and yellow supergiants compared to red supergiants in the SMC indicate that already at $Z = Z_{\rm SMC} \approx 0.2\ Z_\odot$ , some massive stars (roughly between 15 and 40 $M_\odot$) spend most of their CHeB lifetimes as BSGs or YSGs, see Sec. 5.4.1. The same conclusion has been reached previously by Schootemeijer et al. (2019). This allows us to reject models with relatively inefficient mixing in the zone above the helium core, for instance, the model with $\alpha_{\rm sc} = 1.0$. On the other hand, the lack of YSGs with spectroscopic luminosities $\mathcal{L}/\mathcal{L}_\odot \gtrsim 3.6$ in the spectroscopic HR diagram of massive Galactic stars (Castro et al., 2014) indicates that stars of the same mass but higher metallicity (e.g., $Z \sim Z_\odot$) burn helium predominantly as RSGs, see Sec. 5.4.2.

These two pieces of evidence increase the credibility of our reference set of stellar tracks in terms of predicting the radius evolution of massive stars. Notably, the metallicity trend in the degree of post-MS expansion is present in all our models with variations in the input physical parameters as well as in the stellar tracks with rotation (see Sec. 5.3.3 and Fig. 5.12 in the appendix). While the exact boundaries between evolutionary stages of the donor stars in interacting binaries in Fig. 7.1 should be considered rather uncertain, it appears that the trend with metallicity and its implications are a robust prediction of stellar models.

### 5.5.3 WR stars formed through binary interactions

As we illustrated in Sec. 5.3.2, the lower the metallicity, the more evolved are massive stars in binary systems at the point when they initiate mass transfer through RLOF. At $Z = Z_\odot$ and $0.4\ Z_\odot$, a giant donor is almost always a star that has just completed its MS evolution and is rapidly expanding during the HG phase. During mass transfer, such a star very quickly ($\lesssim 10^4$ yr, i.e., on a thermal timescale) loses almost its entire envelope and reveals its helium core (Kippenhahn & Weigert, 1967). In this way, a WR star can be formed by means of binary interactions (e.g., Maeder & Meynet, 1994; Bartzakos et al., 2001). The lack of a hydrogen envelope means that the helium core cannot grow in mass because of hydrogen-shell burning. Instead, the naked core loses mass in strong WR winds during the subsequent evolution. Recently, Woosley (2019) quantified

these two effects on the final core masses and other core properties with respect to single stellar evolution. They did so by computing models of single naked helium stars, starting from the onset of helium burning. This choice of the starting point assumes that binary interactions strip the hydrogen envelope during the HG evolution (i.e., immediately before the onset of CHeB), which is a well-justified assumption only in the high-metallicity case.

However, low-metallicity massive stars tend to remain more compact during the HG phase. As a result, at $Z \leq 0.2\ Z_{\odot}$, the scenario in which the hydrogen envelope is lost during the HG evolution is no longer the dominating case. Instead, in somewhat wider systems (orbital periods $> 10 - 50$ days, depending on metallicity), the RLOF mass transfer is initiated only after a significant fraction of the helium-burning lifetime, see Fig. 7.1. In such cases, the hydrogen envelope is preserved for longer and the helium core of the donor star has already grown in mass since the end of the MS as a result of hydrogen-shell burning. The remaining lifetime of such a donor after the start of RLOF is shorter than in the case of a HG donor star (in some cases, by more than an order of magnitude). This means that WR stars originating from intermediate- to long-period interacting binaries at low metallicity have much shorter lifetimes than stars in higher-metallicity environments, which likely plays a role in the WR demographics in different host galaxies. Additionally, this shorter duration of the WR stage (after the RLOF) and the longer-lasting hydrogen-shell burning (before the RLOF and the resulting loss of the H-rich envelope) both work in favor of higher final core masses compared to stars that lose their hydrogen envelopes at the onset of CHeB (as assumed in Woosley, 2019).

Interestingly, the time interval between the end of the MS and the onset of mass transfer through RLOF may affect the H/He abundance gradient at the surface of the resulting WR star. The longer the envelope is preserved, the more time there is for internal mixing (mainly semiconvection) to steepen the H/He gradient at the boundary of the helium core (see Appendix 5.B and also Schootemeijer & Langer, 2018). These layers then become the surface layers of the WR star after the envelope is stripped. The surface H/He abundance gradients of WR stars might be indirectly inferred from observations and used to constrain the evolution of their progenitors (Schootemeijer & Langer, 2018).

### 5.5.4 MASS TRANSFER EVOLUTION AND SLOW ENVELOPE STRIPPING

As the metallicity decreases, increasingly more cases of mass transfer are initiated by slowly expanding CHeB giants (Fig. 7.1). Such donors do not necessarily become stripped of their entire envelopes on a short thermal timescale as is traditionally predicted for evolved giant donors (Kippenhahn & Weigert, 1967) and implemented in population-synthesis codes (e.g., Kruckow et al., 2018). Klencki & Nelemans (2019) showed an example of a detailed model of an interacting binary system comprising a 25 $M_{\odot}$ donor star (a CHeB giant) and a 10 $M_{\odot}$ BH accretor at subsolar metallicity $Z = 0.2\ Z_{\odot}$, in which mass transfer continues on a nuclear timescale of helium burning until the end of the CHeB phase. Throughout the entire mass transfer phase, the donor star maintains several solar masses of the hydrogen-rich envelope ($\sim 2\ M_{\odot}$ at the point of core-helium

depletion). We discuss this type of mass transfer evolution in much more detail in Klencki et al. (in prep.).

When we assume that mass transfer from relatively compact CHeB stars could last for significantly longer than mass transfer from rapidly expanding HG donors (i.e., a nuclear timescale instead of a thermal timescale), then according to Fig. 7.1 we expect to find significantly more mass-transferring systems per unit of star formation rate in a low-metallicity galaxy compared to a high-metallicity one. This might be particularly interesting in the case of binaries with compact accretors, such as high-mass X-ray binaries. Observationally, X-ray binaries are indeed significantly more common in low-metallicity galaxies (e.g., by a factor of $\sim 10$ in blue compact dwarf galaxies; Brorby et al., 2014).

### 5.5.5 Late cases of RLOF: progenitors of type II supernovae, long GRBs, and binary BH mergers?

An interesting case is formed by systems in which the first RLOF takes place already very late into the evolution of the donor star, after most (or all) of the helium has been burned, for example, $Y_C < 0.05$. Such a case of mass transfer is sometimes referred to as case C mass transfer and corresponds to donors at the final stages of CHeB and to HeHG and SHeB donors in Figs. 7.1 and 5.4. We find that the parameter space for late case C mass transfer is a strong function of metallicity. At $Z \gtrsim 0.2\ Z_\odot$ , such systems are very rare compared to all the other cases. At metallicities $Z \leq 0.1\ Z_\odot$ , the probability of late RLOF becomes significantly higher, up to $\sim 40\%$ of all systems at $Z = 0.01\ Z_\odot$, see Fig. 7.1.

In many systems that evolve through such a case of late mass transfer, only several thousand years are left from the point of RLOF to the collapse of the donor's core. This is not enough time to fully strip the hydrogen-rich envelope of a giant star, even if mass transfer is proceeding on a thermal timescale. Thus, a supernova from such a star would most likely appear as a hydrogen-rich type II supernova with a blue or yellow supergiant progenitor. In higher metallicity environments, a similar star would have been stripped of its hydrogen-rich envelope because mass transfer would have occurred far earlier during its evolution, and would explode as a type Ib or Ic supernova. Notably, any mass lost from a binary as a result of such a late case C mass transfer (stable or unstable) is expected to still be present in the proximity of the system at the time of supernova ($\sim 0.1$ pc for material ejected with velocity of $\sim 100$ km s$^{-1}$ traveling for $\sim 1000$ yr, see, e.g., Sun et al., 2020).

Systems in which late case C mass transfer becomes unstable and leads to a merger are among the promising candidates for the origin of long GRBs (Fryer & Young, 2007). Because of the short remaining lifetime of the merger product, its CO core maintains rapid rotation until the collapse without losing much of the angular momentum in winds, as is required in the collapsar model (Woosley, 1993). Notably, long GRBs are typically found in low-metallicity hosts (Fruchter et al., 2006; Wolf & Podsiadlowski, 2007).

Evolution through unstable mass transfer and successful CE ejection is one of the most

promising formation channels for compact binary mergers. Importantly, mass transfer is more prone to become unstable and to lead to CE evolution if the donor has a convective (rather than radiative) outer envelope (see Sec. 5.3.4 and references therein). Additionally, in the case of BH accretors, convective-envelope donors are more likely to satisfy the energy budget for the CE ejection (i.e., avoiding a merger within the CE; Kruckow et al., 2016). Here, we find that the parameter space for mass transfer from convective-envelope donors is very small at all metallicities, and that it disappears completely for $M \gtrsim 40\ M_\odot$ donors at $Z \leq 0.04\ Z_\odot$ metallicity. In reality, this parameter space may be even smaller than predicted in our models: the observational lack of RSGs above $\log(L/L_\odot) \approx 5.6$ in the nearby galaxies (Davies et al., 2018; Chun et al., 2018, , see also Sec. 5.4.1) may indicate that also in the higher metallicity environments ($Z \geq 0.2\ Z_\odot$) stars with masses above $\sim 40\ M_\odot$ never develop outer convective envelopes. For the CE evolution scenario to explain the observed population of binary BH mergers, we either need this channel to work also when the mass transfer is initiated by a radiative envelope donor, or the parameters of progenitor binaries need to be fine-tuned to the small parameter space for mass transfer from convective envelope donors.

Notably, we find that almost all cases of mass transfer from convective envelope donors with masses $\lesssim 60\ M_\odot$ and metallicities $\leq 0.2\ Z_\odot$ are associated with the late case of RLOF from a core-helium depleted star, that is, a HeHG donor (see Fig. 7.1). The remaining lifetime of the donor star (up to $10^4$ years) is an upper limit for the duration of the subsequent BH-WR stage. This is at least an order of magnitude shorter than the full duration of the CHeB phase, that is, the lifetime of a WR star, if the envelope is stripped shortly after the end of the MS. The duration of the BH-WR stage is relevant for the degree of tidal spin-up of the WR star, which may be of importance for the spin of the second formed BH (e.g., Kushnir et al., 2016; Hotokezaka & Piran, 2017b; Zaldarriaga et al., 2018).

## 5.6 CONCLUSIONS

We showed that metallicity has a strong influence on the type of mass transfer evolution that is expected in massive binaries. To do so, we computed a set of evolutionary tracks of stars between 10 and 80 $M_\odot$ for six different metallicities ranging from $Z = 0.017 = Z_\odot$ to $Z = 0.00017 = 0.01\ Z_\odot$ (both nonrotating and rotating models with $\Omega_{\rm init}/\Omega_{\rm crit} = 0.4$). We explored several variations of factors known to affect the radial expansion of massive stars (e.g., semiconvection and overshooting) and compared our models with observations. Our conclusions are summarized below.

- The lower the metallicity, the stronger the tendency of massive stars to remain relatively compact during the phase of rapid HG expansion ($\sim 100\ R_\odot$) and only reach the red giant branch towards the end of helium burning (CHeB phase) or later, during contraction of the CO core (HeHG phase). At solar metallicity, no models behave in this way, and a post-MS donor in an interacting binary is almost exclusively a rapidly expanding HG star. At $Z = 0.1\ Z_\odot$ , stars in the mass range between $\sim 16$ and $50\ M_\odot$ remain relatively compact

before the onset of CHeB, and a slowly expanding CHeB star is the typical donor in binaries with periods above $\sim$ 40 days. At $Z = 0.01\ Z_\odot$ , stars of all masses in our grid remain compact during the HG expansion. As a result, CHeB or HeHG stars are the most likely post-MS donors at very low metallicity.

- This metallicity trend is a relatively robust prediction of stellar models that is supported by the observations of blue and red supergiants in the Milky Way and in the SMC. The exact mass range for the compact HG evolution at any given metallicity is considered highly uncertain. Models that predict the HG expansion to reach the red giant branch for all masses at $Z = 0.2\ Z_\odot$ are ruled out by the observations (e.g., the model with a relatively inefficient semiconvection $\alpha_{\rm SC} = 1.0$).

- At low metallicities ($\leq 0.2\ Z_\odot$), most massive stars can become stripped of their envelopes to form helium stars only after a substantial fraction of their helium-burning lifetime, as opposed to losing their envelopes shortly after the end of MS (as is often assumed, e.g., Woosley, 2019). This implies a shorter duration of the WR phase and a more massive final core.

- As the metallicity decreases, increasingly more massive stars engage in their first mass transfer episode only very late in their evolution, after the core is almost completely depleted of helium ($Y_{\rm C} < 0.05$) and less then $10^4$ yr remains until the collapse of the core. The short remaining lifetime is unlikely to be long enough to strip the giant star of its entire hydrogen-rich envelope before the possible supernova.

- The binary parameter space for RLOF from convective envelope donors is very small, and it decreases with metallicity. For example, in the $0.1\ Z_\odot$ metallicity case, it is only about 0.2 dex wide in $\log(P/\mathrm{day})$, see Fig. 7.1. At metallicities $Z \leq 0.04\ Z_\odot$ , we find no mass transfer from convective envelope donors with masses above $\sim 40\ M_\odot$ in our models. The lack of red supergiants with luminosities above $\log(L/L_\odot) \approx 5.6$ in local galaxies may indicate that the same is true for higher metallicities $Z \geq 0.2\ Z_\odot$.

- No particular evolutionary stage can be used as a proxy for determining whether a star has a convective or a radiative envelope in population synthesis calculations. Instead, we provide fits for the threshold effective temperature below which stars develop outer convective envelopes (of at least 10% in mass), see Eqn. 5.1 and Fig. 5.6.

**Acknowledgements**

The authors would like to thank the referee for suggestions and comments that helped to improve the paper. We would also like to thank Selma de Mink, Stephen Justham, Abel Schootemeijer, Rob Farmer, Ylva Götberg, Martyna Chruslinska, Eva Laplace, and Manos Zapartas for valuable discussions and suggestions. We are grateful to Norberto Castro for sharing the density map of the sample of Galactic massive stars in the spectroscopic HR diagram. The authors acknowledge support from the Netherlands Organization for Scientific Research (NWO).

## 5.A DENSITY INVERSIONS, MLT++, AND THE HD LIMIT

In massive stars, subsurface convective zones can develop as a consequence of iron and helium opacity peaks (Cantiello et al., 2009). At the same time, the low density and temperature in the outermost envelope layers of extended supergiants makes the convective energy transport ineffective. This leads to superadiabatic temperature gradients and requires most of the energy to be transported through radiation (e.g., Pavlovskii & Ivanova, 2015). In the case of stars that evolve near their Eddington limit, the subsurface opacity peaks and inefficient convection lead to a situation in which the radiative luminosity locally exceeds the Eddington limit in the envelope. The structure can become stabilized by a density inversion (Gräfener et al., 2012). In this way, the formation of density inversions in 1D stellar models is a natural consequence of sufficiently high luminosities in massive stars, with the metallicity and opacities playing an important role (see also Paxton et al., 2013).

On the one hand, density inversions and inefficient superadiabatic convection pose a numerical challenge that can lead to prohibitively short time steps. At the same time, many authors have considered such inversions unphysical in the first place and applied ad hoc solutions in order to remove them from stellar models, for example, by substituting pressure scale height with density scale height (e.g., Stothers & Chin, 1973; Ekström et al., 2012; Yusof et al., 2013) or by capping the temperature gradient at an imposed upper limit (e.g., Bressan et al., 1993; Fagotto et al., 1994). Others would argue in favor of stability of density inversions (Glatzel & Kiriakidis, 1993; Sanyal et al., 2015, 2017) with the caveat that this inversion might be suppressed by extremely strong winds (Asplund, 1998). In any case, the fact that in superadiabatic layers the convective velocity approaches the speed of sound indicates that the standard mixing-length theory is beyond its domain of applicability, and that most likely 3D hydrodynamical simulations are required in order to advance the ongoing debate. Similarly to other ad hoc solutions mentioned above, MLT++ is a stellar engineering solution to prevent the formation of density inversions in MESA. It gradually reduces the temperature gradient and thus the superadiabaticy in some radiation-dominated convective zones (see Paxton et al., 2013), which not only eliminates density inversions, but also alleviates many numerical difficulties. Crucially, MLT++ also increases the effective temperature of the model, similarly to other methods of preventing density inversions (e.g., using the density scale height or increasing the mass-loss rate Maeder, 1987). The increase in effective temperature, even though somewhat artificial in the ad hoc methods such as MLT++, mimics an effect that an increased mass-loss rate would have on stars in the upper right corner of the HR diagram. It has been proposed that exceeding the Eddington limit in subsurface layers, the associated density inversions, and hydrodynamical turbulence and shocks in superadiabatic convective zones might be responsible for extreme mass loss of luminous supergiants and the luminous blue variable phenomenon (e.g., Owocki et al., 2004; van Marle et al., 2008; Quataert et al., 2016). This finds support in the fact that the location of the Eddington limit in the HR diagram coincides with the empirical HD limit (Humphreys & Davidson, 1979, 1994; Ulmer & Fitzpatrick, 1998), a line in the upper right side of the HR diagram beyond which almost no stars are observed in the Milky Way

and in the Large Magellanic Cloud. Moreover, the Eddington factor $\Gamma$ has been identified as the key parameter determining the mass-loss rates of massive WR stars (Vink et al., 2011; Gräfener et al., 2011). Chen et al. (2015) assumed that the same $\Gamma$ dependence of the mass-loss rates applies to all stars (together with the metallicity scaling proposed by Gräfener & Hamann 2008), and obtained stellar tracks that agree reasonably well with the HD limit at solar and LMC metallicities. A similar effect could be achieved through the use of MLT++ or the density scale height in place of the pressure scale height in superadiabatic zones. In this sense, stellar tracks computed with MLT++ might be more accurate in estimating the binary parameter space for mass transfer from the most massive and largest stars in our grid ($\gtrsim 50\ M_\odot$). On the other hand, it is currently unknown whether the empirical HD limit also appears in low-metallicity environments ($Z \lesssim 0.2\ Z_\odot$). In the case of solar metallicity, for which the HD limit is best evidenced, our non-MLT++ tracks also reproduce the lack of stars in the upper right corner of the HR diagram. Additionally, Chun et al. (2018) found a better agreement with the Galactic sample of luminous RSGs when MLT++ was not used. It remains certain that any numerical results for the maximum radii of massive stars ($\gtrsim 50\ M_\odot$) based on 1D stellar evolution computations should be considered highly uncertain.

## 5.B Internal mixing during the Hertzprung gap phase

During the MS evolution of a massive star, the shrinking convective core leaves a region with a composition gradient behind. The corresponding gradient of mean-molecular weight stabilizes this region against convection, and at least initially, the composition is primarily being mixed by a slower process: semiconvection (Langer et al., 1985). The semiconvective zone becomes most extended immediately after the end of the MS when the star rapidly expands during the HG phase and hydrogen-shell burning becomes important. The mixing that occurs during this short-lived phase ($\sim 10^4$ yr) has a key effect on the stellar radius at the onset of helium burning and the blue to red evolution in the HR diagram (e.g., Langer, 1991).

In Fig. 5.9 we show Kippenhahn diagrams of three models of a single 25 $M_\odot$ star: at 0.2 $Z_\odot$ with efficient semiconvection, at 0.2 $Z_\odot$ but with less efficient semiconvection, and at 1.0 $Z_\odot$ with efficient semiconvection. The diagrams are centered around the short-lived phase between the end of MS and the onset of helium burning, see also Fig. 5 of Schootemeijer et al. (2019). If semiconvection is efficient and quick to sufficiently flatten the composition gradient for convective mixing to fully kick in, then a single extended convective zone is eventually formed at the top of the hydrogen shell (the top and bottom panels). In the case of less efficient semiconvection, multiple separate convective zones are formed instead, with semiconvective regions in between them (see, e.g., Fig. 5 of Langer et al., 1985). This can be understood in the following way: with less efficient semiconvection, the composition gradient is not flatenned quickly enough for an extended convective zone to form during the short-lived HG phase. However, when any small zone becomes locally unstable to convection, its composition is mixed very quickly. This eliminates any composition gradient within that region, which helps to maintain convective mixing. At the same time, the gradient at the edges of the small convective region becomes steeper, which

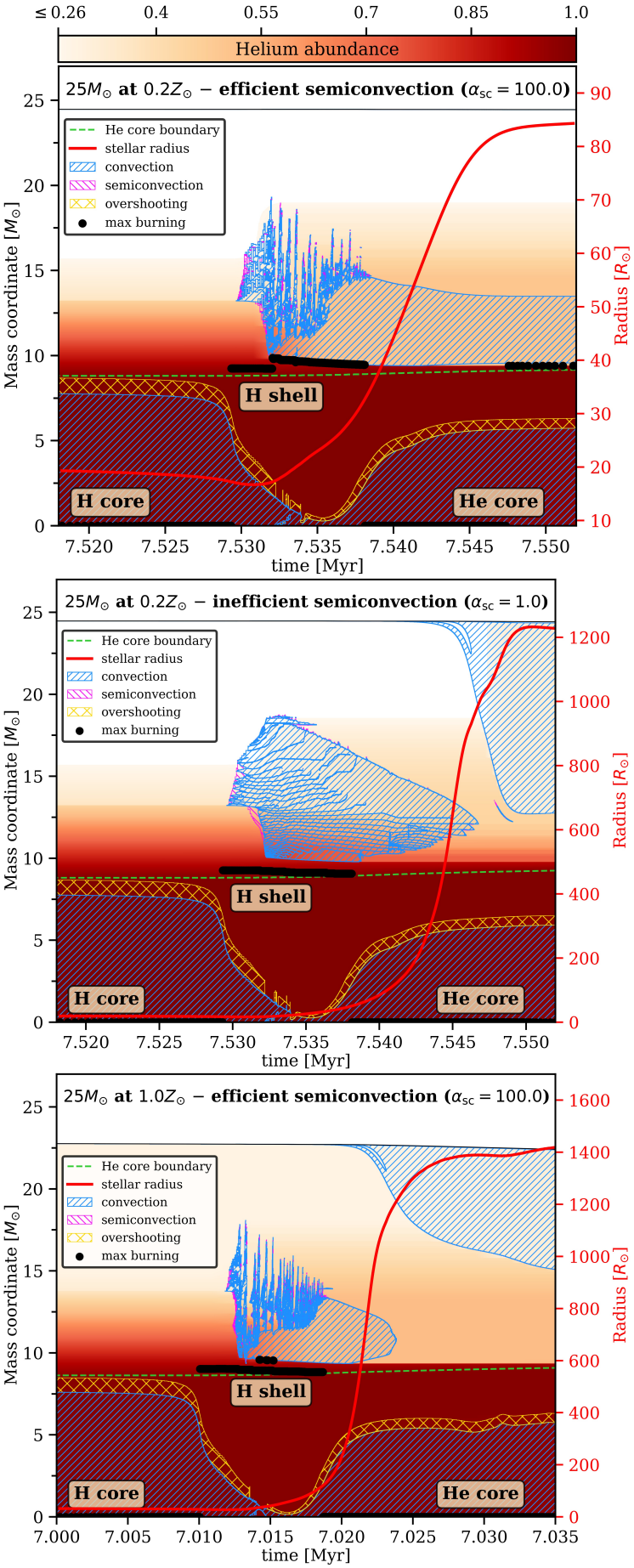


FIGURE 5.9: Kippenhahn diagrams of three models of a single 25 $M_\odot$ star: at 0.2 $Z_\odot$ with efficient semiconvection ($\alpha_{sc}$ = 100, top panel), at 0.2 $Z_\odot$ but with inefficient semiconvection ($\alpha_{sc}$ = 1, middle panel), and at 1.0 $Z_\odot$ with efficient semiconvection ($\alpha_{sc}$ = 100, bottom panel). We also mark the stellar radius (red solid line, labeled on the right-hand side) to show the influence of mixing on the evolution in the HR diagram. In the solar metallicity case, even if the mixing is efficient, the model expands to $R > 1000\ R_\odot$ during the HG phase. The resulting helium abundance profiles are shown in Fig. 5.10.

increases the stability of neighboring zones against convection, and they can only be mixed further by semiconvection. If semiconvection in such neighboring zones is not efficient, then the small convective zone becomes isolated and cannot merge with other similar small convective regions. An onion-like structure with multiple convective and semiconvective zones emerges, as in the middle panel of Fig. 5.9.

The interplay between semiconvective and convective mixing ultimately determines the abundance profile in the region above the hydrogen shell. In Fig. 5.10 we show helium abundance profiles taken at the end of MS (before the mixing) and after the convective helium core develops (after the mixing) for the three models shown in Fig. 5.9. Efficient mixing ($\alpha_{\rm sc} = 100$) results in a plateau of helium abundance at the bottom of the envelope, much different from the step-like profile that forms in the case of less efficient mixing ($\alpha_{\rm sc} = 1$). This plateau is a common feature of all our post-MS donor stars in binary models as well. See also Schootemeijer & Langer (2018) for a discussion of how the resulting H/He gradient is connected to surface abundances of WR stars. In the efficient mixing case, the envelope has become more enriched in helium, and at the same time, a larger amount of hydrogen has been brought down as fuel for the shell burning. In the solar metallicity case, even if the mixing is efficient, the model expands to $R > 1000\ R_\odot$ during the HG phase.

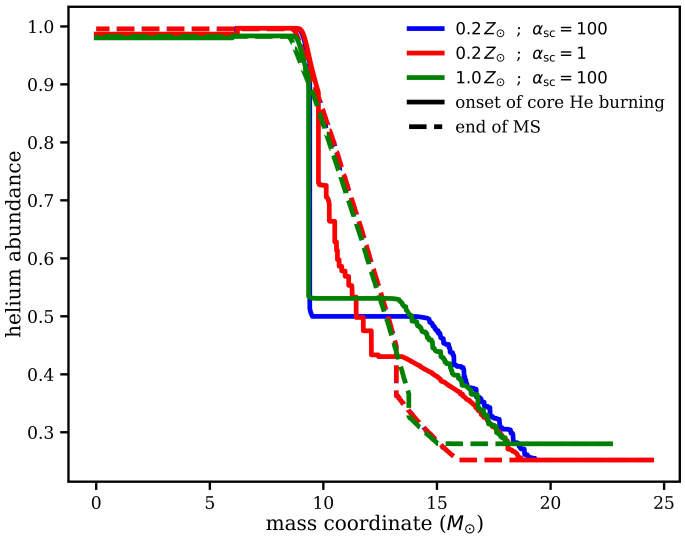


FIGURE 5.10: Helium abundance profiles of models shown in Fig. 5.9, taken from the point at the end of the MS and before the mixing (dashed lines) and after a convective helium burning core fully develops (solid lines).

We comment that the forest-like structure of short-lived extended convective zones that form in models with efficient semiconvection has been found in MESA models by other author as well (e.g., Farmer et al., 2016; Schootemeijer & Langer, 2018). Its exact behavior appears very chaotic and is subject to numerical settings and resolution. This mixing affects the composition in the region above the single convective zone: it creates a step-like decrease in $Y$ between mass coordinates $\sim 15$ and $20\ M_\odot$ in Fig. 5.10, the details of which are considered highly uncertain. Notably, we have found that models running with convective premixing (Paxton et al., 2019) without any limits on the velocity of a convective boundary advance (CONV_PREMIX_TIME_FACTOR = 0.0 in the MESA jargon) are effective in forming a single extended convective zone even with $\alpha_{\rm sc} = 1$.

## 5.C ADDITIONAL HR DIAGRAMS

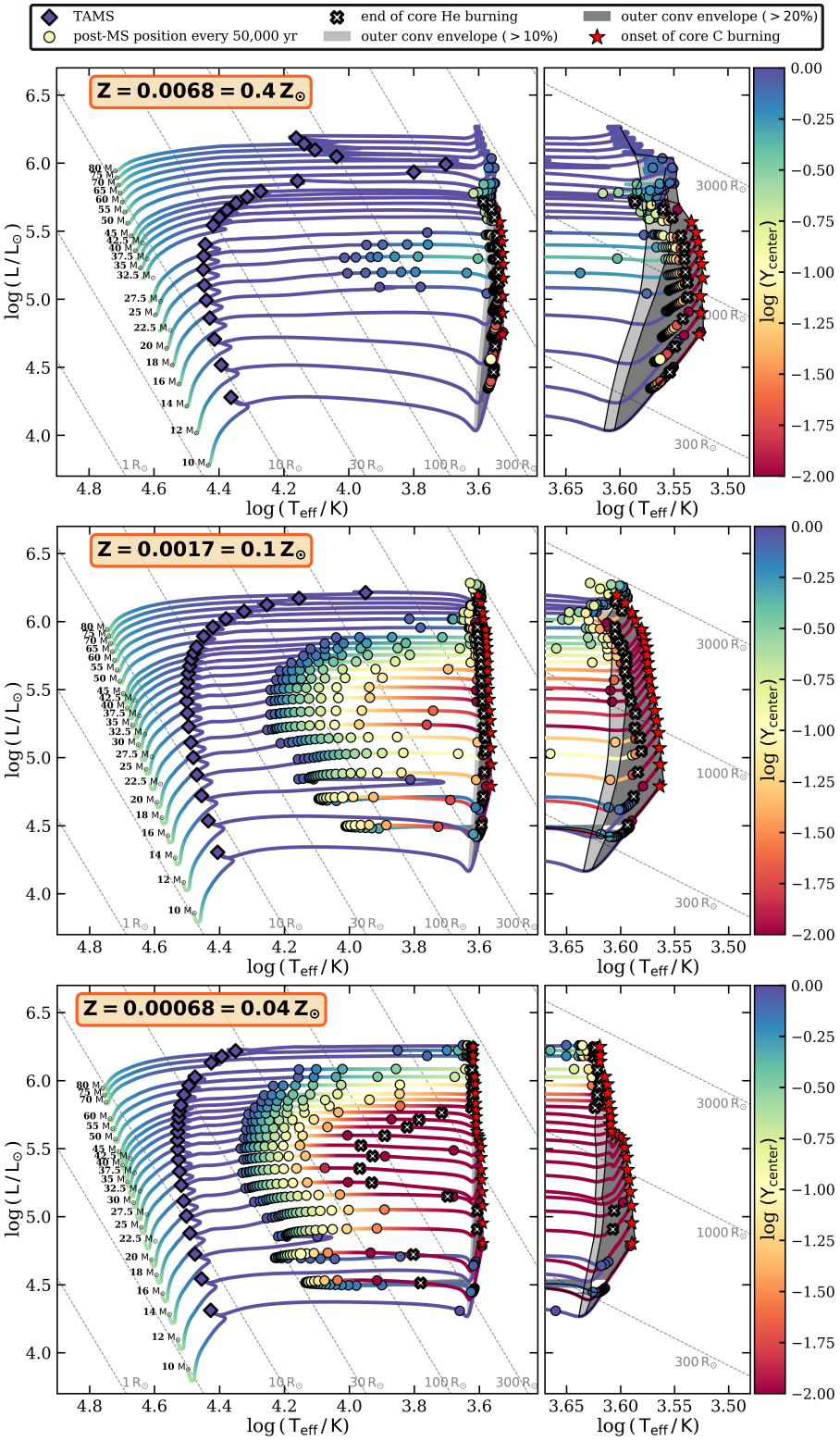


FIGURE 5.11: Same as Fig. 5.1 but for 3 additional metallicities.

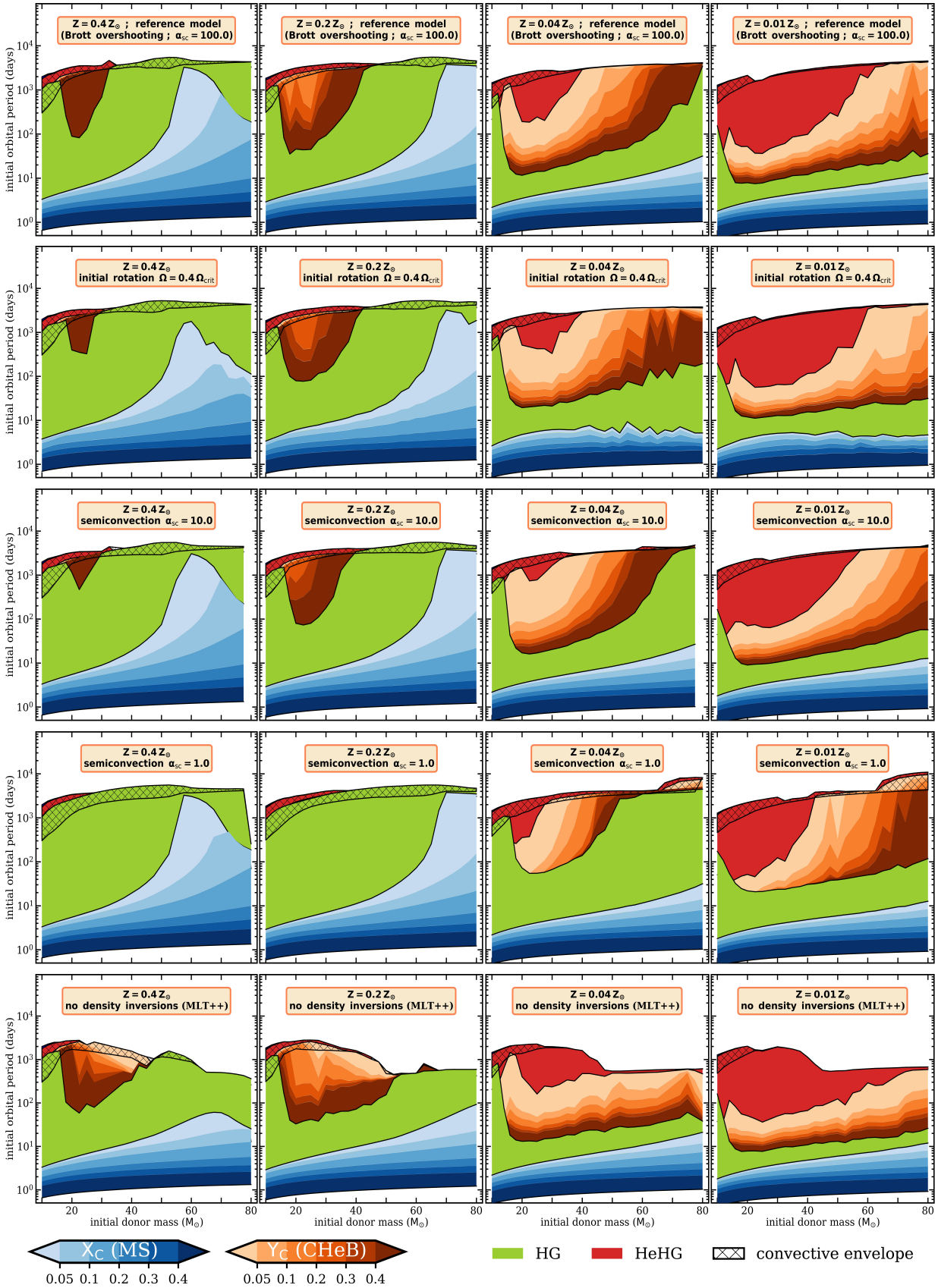


Figure 5.12: Same as Fig. 5.4, but for other metallicities.

# Chapter 6

# It has to be cool: supergiant progenitors of binary black hole mergers from common-envelope evolution

J. Klencki, G. Nelemans, A.G. Istrate & M. Chruslinska

*Astronomy & Astrophysics, volume 645, A54, (2021)*

**Abstract**

Common-envelope (CE) evolution in massive binary systems is thought to be one of the most promising channels for the formation of compact binary mergers. In the case of merging binary black holes (BBHs), the essential CE phase takes place at a stage when the first BH is already formed and the companion star expands as a supergiant. We aim to decipher the kinds of BH binaries with supergiant companions that could potentially evolve through and survive a CE phase. To this end, we compute envelope binding energies from detailed massive stellar models at different evolutionary stages and metallicities. We make multiple physically extreme choices of assumptions that favor easier CE ejection as well as account for recent advancements in mass-transfer stability criteria.

We find that even with the most optimistic assumptions, a successful CE ejection in BH binaries is only possible if the donor is a massive convective-envelope giant, namely a red supergiant (RSG). The same is true for neutron-star binaries with massive companions. In other words, pre-CE progenitors of BBH mergers are BH binaries with RSG companions. We find that because of its influence on the radial expansion of massive giants, metallicity has an indirect but a very strong effect on the chemical profile, density structure, and the binding energies of RSG envelopes. Our results suggest that merger rates from population-synthesis models could be severely overestimated, especially at low metallicity. Additionally, the lack of observed

RSGs with luminosities above $\log(L/L_\odot) \approx 5.6{-}5.8$, corresponding to stars with $M \gtrsim 40\ M_\odot$, puts into question the viability of the CE channel for the formation of the most massive BBH mergers. Either such RSGs elude detection due to very short lifetimes, or they do not exist and the CE channel can only produce BBH systems with total mass $\lesssim 50\ M_\odot$. Finally, we discuss an alternative CE scenario in which a partial envelope ejection is followed by a phase of possibly long and stable mass transfer.

## 6.1 INTRODUCTION

Since the discovery of the first gravitational wave (GW) signal from a binary black hole (BBH) coalescence by the Advanced LIGO Interferometer in September 2015 (GW150914, Abbott et al., 2016b), the LIGO/Virgo Collaboration has reported the detection of nine further BBH mergers by the end of its second observing run O2 (Abbott et al., 2019b). The third observing run O3 has been concluded and a large number of publicly issued alerts is an indication that a few tens of additional detections of BBH mergers will soon be announced, including the recently published discoveries of GW190412 (The LIGO Scientific Collaboration et al., 2020a), GW190814 (being either a BBH or a BH-neutron star(NS) merger; Abbott et al., 2020b), and GW190521 (The LIGO Scientific Collaboration et al., 2020b). With the growing population of BBHs, the discussion of possible formation scenarios of compact binary mergers is as lively as ever. A large number of channels have been put forward, especially in the case of BBHs. These include but are not limited to the formation from isolated binaries through common-envelope (CE) evolution (Dominik et al., 2012; Mennekens & Vanbeveren, 2014; Belczynski et al., 2016c; Eldridge & Stanway, 2016; Klencki et al., 2018; Mapelli & Giacobbo, 2018; Kruckow et al., 2018; Breivik et al., 2020) or in a chemically homogeneous evolution regime (Mandel & de Mink, 2016; de Mink & Mandel, 2016; Marchant et al., 2016), dynamical formation in globular clusters (Rodriguez et al., 2016b; Askar et al., 2017; Samsing, 2017), in nuclear clusters (Arca-Sedda & Gualandris, 2018; Fragione & Kocsis, 2019), or in disks of active galactic nuclei (AGNs; Antonini & Rasio, 2016; Stone et al., 2017; McKernan et al., 2018), as well as formation channels involving triple (Antonini et al., 2017b) or quadruple stellar systems (Fragione et al., 2019). So far, it has not been possible to distinguish between various channels based on the gravitational wave information alone. In particular, the promising method of distinguishing between dynamical and isolated binary formation based on the BBH spin-orbit misalignment distribution (Farr et al., 2017, 2018a) is hindered by our lack of knowledge of the natal black hole (BH) spins and, to a lesser extend, the possibility of BH natal kicks changing the spin orientation (O'Shaughnessy et al., 2017b; Gerosa et al., 2018; Belczynski et al., 2020b; Bavera et al., 2020). As a result, the contribution of various channels to the entire population of BBH mergers is usually estimated on theoretical grounds (Abadie et al., 2010; Barack et al., 2019). The CE evolution channel is sometimes considered to be especially promising thanks to its potential to produce a relatively high merger rate of BBHs compared to other channels, although any rate prediction from theoretical population models are highly uncertain.

The essential stage in the CE evolution channel is a dynamically unstable phase of mass transfer

that leads to rapid spiraling in of the companion object inside the shared envelope originating from the giant donor star (Paczynski, 1976; Webbink, 1984; Iben & Livio, 1993; Podsiadlowski, 2001; Ivanova et al., 2013b). The drag force is thought to cause a dramatic shrinkage of the binary separation, and the dissipated orbital energy to lead to an ejection of the CE (under the right circumstances) or a merger otherwise. The huge range in both timescales and length scales involved in this complex process makes hydrodynamic simulations challenging (e.g., Ricker & Taam, 2012; Passy et al., 2012; Nandez & Ivanova, 2016; MacLeod et al., 2017; Fragos et al., 2019). As a result, the exact outcome of the CE phase is difficult to predict. However, there is a substantial amount of evidence for significant orbital shrinkage in progenitors of various short-period systems such as cataclysmic variables (e.g., Paczynski, 1976; Meyer & Meyer-Hofmeister, 1979), binary white dwarfs (e.g. Han, 1998; Nelemans et al., 2000, 2001), or binary neutron stars (BNSs; e.g., van den Heuvel, 1994; Tauris & van den Heuvel, 2006; Chruslinska et al., 2018; Vigna-Gómez et al., 2020), which cannot be explained without invoking a mechanism such as the CE phase.

In the case of more massive stars, which are the progenitors of stellar BHs ($\gtrsim 20\ M_\odot$), such observational support is more difficult to find and comes mainly from the population of short-period ($< 1$ day) X-ray binaries with stellar BH accretors and low-mass ($\lesssim 1\ M_\odot$) donors (BH-LMXBs; Casares & Jonker, 2014), which are believed to have formed through CE evolution (Portegies Zwart et al., 1997; Kalogera, 1999). High-mass X-ray binaries hosting stellar BHs and Wolf-Rayet (WR) companions in short-period orbits of a few hours up to two days, such as Cygnus X-3, IC10 X-1, and NGC300X-1, may also be products of the CE evolution (Lommen et al., 2005; Carpano et al., 2007), although whether or not they could originate from stable mass transfer evolution instead is debated(van den Heuvel et al., 2017). Notably, such systems could be the immediate progenitors of merging BBH or BH–NS systems (Bulik et al., 2011; Belczynski et al., 2013). On top of that, hydrodynamic simulations of the CE phase are particularly challenging in the case of massive stars (see Ricker et al., 2019, for details) and most of the hitherto results have been limited to low-mass giants, which are WD progenitors.

Motivated by the LIGO discoveries of the BBH mergers GW150914 and GW151226, Kruckow et al. (2016) analyzed the prospect of successful CE evolution in binaries of stellar BHs and massive companions (i.e., potential BBH progenitors) by considering the energy balance between the envelope binding energy and the available energy sources (van den Heuvel, 1976; Webbink, 1984; Ivanova et al., 2013b). They concluded that for the right binary parameters, the CE evolution channel may indeed operate for massive stars in a similar way to low- and intermediate-mass donors, and that it may produce BBH systems with individual BH masses all the way up to the lower edge of the pair-instability supernova (PISN) BH mass gap (at $\sim 45 - 55\ M_\odot$, e.g., Heger et al. 2003; Woosley 2017; Leung et al. 2019; Renzo et al. 2020, although the limit could perhaps be moved to higher masses within the uncertainty of the $^{12}\mathrm{C}(\alpha, \gamma)^{16}\mathrm{O}$ reaction rate, Farmer et al. 2019).

Here, we extend the analysis of Kruckow et al. (2016) by additionally accounting for conditions necessary for the mass transfer to become dynamically unstable (i.e., for the occurrence of CE evolution). Such conditions can usually be formulated in the form of a threshold mass ratio, such

that for mass ratios $q = M_{\rm donor}/M_{\rm accretor}$ above a critical value $q_{\rm crit}$ the mass transfer becomes unstable, whereas for $q < q_{\rm crit}$ the CE evolution is avoided. Importantly, the mass ratio $q$ plays a significant role in considerations of the CE energy budget: the lower the $q$ (i.e., a more equal-mass system) the larger the energy input from orbital shrinkage, which makes it more likely to unbind the envelope and survive the CE phase (e.g., Fig. 6 of Kruckow et al., 2016). Recent studies of mass transfer stability from massive giants reveal that the mass transfer remains stable for a larger parameter space than previously thought, thus avoiding a CE evolution in the majority of cases (Woods & Ivanova, 2011; Pavlovskii et al., 2017). It is therefore essential to consider realistic $q_{\rm crit}$ values when addressing the question of CE ejectability in BBH progenitors.

In Sect. 6.2 we describe the ingredients of our model: (a) detailed stellar models of massive giants for six metallicities between $Z = 0.017 = Z_\odot$ and $Z = 0.00017 = 0.01\ Z_\odot$, (b) conditions for mass-transfer instability and the occurrence of CE evolution, and (c) the assumed contribution of various energy sources and sinks to the overall energy budget of the CE evolution. In Sect. 7.3 we present our calculated envelope binding energies, highlighting the substantial impact of outer convective envelopes. Furthermore, we compute the parameter space for successful CE ejections and explore the impact of various assumptions. Finally, we explore the predicted population of CE survivors in the Hertzprung-Russell (HR) diagram. We discuss various aspects of our findings in Sect. 7.5 and conclude in Sect. 6.5.

## 6.2 THE MODEL

### 6.2.1 STELLAR MODELS OF MASSIVE GIANTS

We use rotating single stellar models from Klencki et al. (2020) computed with the MESA stellar evolution code (Paxton et al., 2011, 2013, 2015, 2018, 2019). The use of single models unperturbed by previous binary interactions is a simplification because in most realistic scenarios the stellar companion in a BH binary is a mass gainer from a mass transfer phase that was initiated by the BH progenitor (also in the case of BBH merger progenitors, e.g., Belczynski et al., 2016b). While this has become common practice, there is an important caveat to mention. We discuss this topic further in connection to those results that are likely the most sensitive to the assumption of single stellar models (see Sects. 6.3.4 and 6.4.1).

The tracks from Klencki et al. (2020) cover a range of masses from 10 to 80 $M_\odot$ and six metallicity values, $Z = 0.017$, 0.0068, 0.0034, 0.0017, 0.00068, and 0.00017 (or in fractions of the solar metallicity: 1.0, 0.4, 0.2, 0.1, 0.04, and 0.01 $Z_\odot$, where we assume $Z_\odot = 0.017$ after Grevesse et al. 1996), with the initial rotation rate set to 40% of the critical value ($\Omega/\Omega_{\rm crit} = 0.4$). We note that for higher initial rotation rates, massive stars of $M \gtrsim 50\ M_\odot$ at very low metallicities were shown to evolve in a chemically homogeneous way (e.g., Marchant et al., 2017). Convection was modeled using the mixing-length theory (Böhm-Vitense, 1958) with a mixing length of $\alpha_{\rm ML} = 1.5$ and following the Ledoux criteria for convection with a high efficiency of semiconvective mixing $\alpha_{\rm SC} = 100$. The models assume step overshooting above the hydrogen and helium burning

cores with an overshooting length of 0.345 pressure scale heights (Brott et al., 2011a). The wind mass-loss was modeled, following (Brott et al., 2011a), as a combination of mass-loss recipes from Nieuwenhuijzen & de Jager (1990b), Hamann et al. (1995), and Vink et al. (2001). Notably, the models from Klencki et al. (2020) were computed under a set of assumptions that maximizes the potential of massive stars to reach the sizes of red-supergiants and to develop deep outer convective envelopes: with no luminous blue variable (LBV) mass-loss above the Humphreys-Davidson limit and without preventing the formation of density inversions by the use of MLT++ in MESA (see Appendix A in Klencki et al. 2020). Such an approach allows us to explore the maximum potential parameter space for binary interactions in wide binaries and consequently the maximum parameter space for CE evolution. In the case of convective-envelope stars with initial masses $\gtrsim 40\ M_\odot$ the true parameter space might be significantly smaller, as discussed in Sect. 6.4.2. We refer to Klencki et al. (2020) for a description of other physical ingredients of the models and `https://zenodo.org/record/3740578#.X1s2cnVfguw` for the MESA input files. In Appendix 6.B we demonstrate the models are numerically robust for the purposes of this work.

### 6.2.2 Conditions for mass-transfer instability

Mass transfer in a binary can become dynamically unstable when either the donor or the accretor (or both) expands too much in size with respect to its Roche-lobe. It was shown that if the timescale of mass transfer is short compared to the thermal timescale of the mass gainer then the accreting star could be driven out of thermal equilibrium and expand significantly (e.g., Benson, 1970; Neo et al., 1977), filling its Roche-lobe and leading to the formation of a contact binary (Pols, 1994; Wellstein et al., 2001) and potentially a CE evolution (de Mink et al., 2007; Marchant et al., 2016). Details of this process remain largely uncertain, partly because of the complicated gas dynamics in semi-detached binaries (Lubow & Shu, 1975), poorly constrained specific entropy of the accreted material (Shu & Lubow, 1981), and unknown efficiency of accretion by stars rotating near their breakup limit (Popham & Narayan 1991, see also discussion by de Mink et al. 2013).

However, the focus of this study is mass transfer in the case of compact-object accretors: stellar BHs or NSs.[1] Based on X-ray binaries such as Cyg X-2 (King & Ritter, 1999) and SS433 (Fabrika, 2004), it is believed that unlike a stellar accretor, a BH or a NS can deal with very high mass transfer rates via jets and disk outflows which prevent the nonaccreted matter from piling up and eventually overflowing their Roche-lobes. For that reason, for the remainder of this section we discuss mass transfer instability due to an increasing Roche-lobe overflow by the donor star. As explained above, in the case of stellar accretors the mass transfer could be unstable in many more cases.

Donor stars with outer radiative envelopes (the case that dominates the parameter space) respond to mass loss by contraction on the adiabatic timescale (Hjellming & Webbink, 1987; Soberman et al., 1997). In other words, they are characterized by a positive value of $\zeta_{\rm ad} = (\partial \log R/\partial \log M)_{\rm ad}$.

[1] We note that double-core CE evolution, when both the donor and the accretor are evolved giants, could also lead to the formation of compact binary mergers, although this channel requires both stars to be of very similar mass (e.g., Bethe & Brown, 1998; Dewi et al., 2006).

In such a case, the mass transfer can become unstable on the adiabatic timescale only when the size of the Roche-lobe is shrinking more quickly than the size of the radiative donor, which is possible if the mass ratio $q = M_{\rm donor}/M_{\rm accretor}$ is higher than some critical value $q_{\rm crit;rad}$. Traditionally, radiative-envelope post-main sequence(MS) giants were assumed to be described by $\zeta_{\rm ad} \approx 6.5$, which corresponds to $q_{\rm crit} \approx 3.5 - 4$ (Tout et al., 1997; Hurley et al., 2002): a value that is often assumed (e.g., Schneider et al., 2015; van den Heuvel et al., 2017; Vigna-Gómez et al., 2018). Detailed models of mass transfer from intermediate-mass radiative-envelope donors ($\sim 1$ to 6 $M_\odot$) also found stability for mass ratios of up to about four (e.g., Tauris et al., 2000; Chen & Han, 2002; Ivanova & Taam, 2004). Observationally, the well-studied SS433 system, which consists of a Roche-lobe-filling A-type supergiant ($\sim 12.3\ M_\odot$) and a stellar BH ($\sim 4.3\ M_\odot$) in a 13.1 day period orbit (Hillwig & Gies, 2008), is a likely case of stable mass transfer evolution that has already been ongoing for $\sim 10^5$ yr (with the likely initial value of $q \approx 3 - 4$ King et al., 2000; Begelman et al., 2006; van den Heuvel et al., 2017). Notably, mass transfer from MS donors was found to be less stable with typical $q_{\rm crit;MS} \approx 1.5$ (de Mink et al., 2007).

A single value of $\zeta_{\rm ad}$ across the entire mass and radius spectrum of post-MS stars is a serious simplification. Ge et al. (2015) computed adiabatic responses for a large grid of models (donor masses between 0.1 and 100 $M_\odot$), also taking into account the possibility of a delayed dynamical instability (Ge et al., 2010). The authors found that the value of $\zeta_{\rm ad} = 6.5$ and the critical mass ratio $q_{\rm crit;rad}$ between 3 and 5 could be a good approximation in the case of stars below 10 $M_\odot$. However, for more massive post-MS stars these latter authors find a higher $q_{\rm crit;rad}$ of at least 5, and even $q_{\rm crit;rad} > 10$ for $R > 300\ R_\odot$ (going up to extreme $q_{\rm crit;rad} > 20$ for $R > 1000\ R_\odot$).

Donor stars with outer convective envelopes on the other hand are expected to respond to mass loss by expanding on the adiabatic timescale. This makes the mass transfer from convective donors much more prone to dynamical instability than from radiative donors. Many authors have relied on condensed polytrope models of Hjellming & Webbink (1987) to obtain the value of $\zeta_{\rm ad}$ for convective-envelope donors, which typically leads to critical mass ratios $q_{\rm crit;conv}$ of about 0.8.

It is important to take into account the caveats associated to the numbers cited above. The value of $\zeta_{\rm ad}$ derived in the adiabatic approximation (e.g., Hjellming & Webbink, 1987; Tout et al., 1997; Ge et al., 2015) is only valid for predicting the donor behavior if the outer envelope thermal timescale is much longer than the adiabatic timescale (i.e., the entropy profile can be considered constant). This is not necessarily the case for outer envelopes of massive stars with large radii. Woods & Ivanova (2011) showed that in the case of convective donors the thermal timescale in the outermost superadiabatic layer of the envelope (which forms on top of the convective zone) can become even smaller than the dynamical timescale. These latter authors found that thermal relaxation of such outer layers can effectively increase the stability of mass transfer (by up to a factor of $\sim 1.7$ in $q_{\rm crit;conv}$ in the limited number of cases investigated by the authors).[2] In the case

[2]Another issue with applying condensed polytropes to compute $\zeta_{\rm ad}$ of convective donors as in Hjellming & Webbink (1987) is that in massive stars the superadiabatic layer is large enough to have to be taken into account and consequently the n = 3/2 polytrope is no longer a valid approximation of the entropy profile (Woods & Ivanova, 2011; Pavlovskii & Ivanova, 2015).

of massive radiative donors, a qualitatively opposite effect of decreased stability is expected (see Sect. 4.1 of Ge et al., 2015), which is why the values of $q_{\rm crit;rad} > 10$ are most likely overestimated.

The fact that thermal relaxations needs to be taken into account means that mass transfer stability from massive giants cannot be reliably predicted without detailed evolutionary calculations. Some such results are already available. Using 1D stellar codes with hydrodynamic terms to probe the rapid donor response, both Passy et al. (2012) and Pavlovskii & Ivanova (2015) found that the initial reaction of convective-envelope stars to mass loss is a slight contraction, contrary to what the adiabatic models predict. This increases the stability, in line with the conclusions of Woods & Ivanova (2011). Taking overflow through the outer Langrangian point as instability criteria, Pavlovskii & Ivanova (2015) obtained revised critical mass ratios for convective donors $q_{\rm crit;conv} = 1.5 - 2.2$, computed for models of up to 50 $M_\odot$ in which the outer convective envelope is well developed ($M_{\rm conv} \gtrsim 0.3 M_{\rm donor}$). For donors with less developed convective envelopes Pavlovskii & Ivanova (2015) obtain stability up to the highest mass ratio in their grid, $q = 3.5$, though they do not specify the exact $M_{\rm conv}$ value. In a recent work focused on intermediate-mass donors ($M_{\rm donor}$ between 1 and 8 $M_\odot$) Misra et al. (2020) found stable mass transfer evolution from convective-envelope donors for mass ratios up to $q \sim 2$.

In the case of massive radiative-envelope donors with $M_{\rm donor}$ between 20 and 80 $M_\odot$ (or donors with shallow outer convective envelopes), Pavlovskii et al. (2017) found that the previously accepted stability criteria should also be revised. By computing detailed models of mass transfer in binary systems with BH accretors, they consistently obtained stable mass transfer for mass ratios as high as $6 - 8$ from $M_{\rm donor} \geq 40$ $M_\odot$ donors.[3] This further supports the trend that $q_{\rm crit;rad}$ is typically larger for more massive stars ($M > 10$ $M_\odot$) than the $3.5 - 4$ critical mass ratios for intermediate mass giants. In an upcoming paper (Klencki et al. in prep.) with detailed binary models, we obtain stable mass transfer from massive radiative donors for mass ratios up to $q \approx 5$.

It is clear that the problem of mass transfer stability from massive giants is far from being fully understood. In particular, detailed 1D mass transfer simulations have to rely on approximate methods for computing the mass transfer rate through the $L_1$ nozzle (e.g., Kolb & Ritter, 1990). One obstacle going forward is that long-term 3D mass-transfer simulations (i.e., not just the initial donor response) are unlikely to be possible in the near future. However, at the same time there is a growing number of results indicating that mass transfer from massive radiative-envelope donors might be stable for mass ratios at least as high as approximately five.

### 6.2.3 Energy budget criterion for a successful CE ejection

We estimate the fate of the CE phase based on the energy formalism (van den Heuvel 1976; Tutukov & Yungelson 1979; Iben & Tutukov 1984; Webbink 1984; Livio & Soker 1988, see also De Marco et al. 2011; Ivanova et al. 2013b for more recent reviews of this formalism), in which the difference in orbital energies between the initial and the final state, $\Delta E_{\rm orb}$, multiplied by an efficiency parameter $\alpha_{\rm CE}$ is equated to the energy needed to unbind the envelope $E_{\rm bind}$:

[3] In the case of $M_{\rm donor} < 40$ $M_\odot$, Pavlovskii et al. (2017) only tested mass ratios up to 4.

$E_{\rm bind} \approx \alpha_{\rm CE}\Delta E_{\rm orb}$. We extend this energy budget by including an additional term of energy feedback from accretion of matter by the spiraling-in BH: $\Delta E_{\rm acc}$. The full equation takes the following form.

$$\begin{aligned} E_{\rm bind} &= \Delta E_{\rm acc} + \alpha_{\rm CE}\Delta E_{\rm orb} \\ &= \Delta E_{\rm acc} + \alpha_{\rm CE}\left( - \frac{GM_{\rm donor}M_{\rm BH}}{2a_{\rm i}} + \frac{GM_{\rm core}M_{\rm BH}}{2a_{\rm f}}\right). \end{aligned} \tag{6.1}$$

Here, $M_{\rm donor}$ is the mass of the giant donor that initiates the CE phase, $M_{\rm core}$ is the mass of its core that becomes the remnant after a successful envelope ejection, $M_{\rm BH}$ is the mass of the BH accretor, and $a_{\rm i}$ and $a_{\rm f}$ is the separation at the onset and at the end of the CE phase, respectively. The $\alpha_{\rm CE}$ parameter accounts for the fact that not all the orbital energy can be deposited into the envelope without any losses and as such takes a value of between 0 and 1. Notably, $\alpha_{\rm CE} = 1.0$ is quite extreme as it assumes no energy loss in any form from the system. For comparison, in their 3D hydrodynamic simulations of the dynamical phase of CE evolution from low-mass giants (typically spanning several years), Nandez et al. (2015); Nandez & Ivanova (2016) found that usually about 30%−40% of the orbital energy leaves the system as residual (mainly kinetic) energy of the unbound ejecta. In 1D synthetic models of the potentially longer lasting (10−1000 years) self-regulated phase, during which most of the input heat is radiated away, Clayton et al. (2017) found $\alpha_{\rm CE}$ values in the range 0.046−0.25. At the same time, $\alpha_{\rm CE} \approx 2$ was inferred from 1D simulations by Fragos et al. (2019) in the case of NS accretors and $\alpha_{\rm CE}$ as large as 5 (or even larger) is often used in population synthesis, especially that of compact binary mergers (e.g., Mapelli & Giacobbo, 2018). In Sect. 6.4.1 we further discuss the uncertainties on the value of $\alpha_{\rm CE}$ together with possibilites of $\alpha_{\rm CE} > 1$ considered in the literature.

Following Voss & Tauris (2003) and Kruckow et al. (2016), we estimate the energy feedback from accretion as the Eddington luminosity of the BH ($\dot{L}_{\rm Edd}$) multiplied by the CE duration $\tau_{\rm CE}$:

$$\Delta E_{\rm acc} = \dot{L}_{\rm Edd}\tau_{\rm CE} \approx 1.6 \times 10^{48}{\rm erg}\left(\frac{M_{\rm BH}}{M_\odot}\right)\left(\frac{\tau_{\rm CE}}{1000{\rm yr}}\right). \tag{6.2}$$

We discuss this approach in view of hydrodynamic models of accretion during CE in Sect. 6.4.1.

To compute the energy needed to unbind the envelope $E_{\rm bind}$ we take three terms into account: the energy needed to overcome the gravitational potential of the envelope $-E_{\rm grav}$, lowered by the thermal energy stored in the envelope $U_{\rm th}$ (kinetic energy of particles and the energy stored in radiation, Han et al., 1994) as well as the recombination energy $E_{\rm rec}$ available if all the ions recombine into atoms and atoms associate into molecules (the latter is mostly relevant for $H_2$, Ivanova, 2015). Therefore, $E_{\rm bind}$ is calculated as:

$$\begin{aligned} E_{\rm bind} &= -E_{\rm grav} - U_{\rm th} - E_{\rm rec} \\ &= -\int_{core}^{surface}\left(-\frac{GM(r)}{r} + u\right){\rm d}m, \end{aligned} \tag{6.3}$$

where $u$ is the internal energy (both thermal and recombination energy) per unit mass. In MESA the value of $u$ in each layer is taken from the tabulated equation of state (Sect. 4.2 of Paxton et al.,

2011). We note that it might be more physically accurate to treat the energy from recombination as a separate energy source rather than to include it in the envelope binding energy because this energy is not available immediately, and its release must be triggered at a later stage of the CE phase (Ivanova, 2015). It is also not clear how much of this energy can in practice be used to help eject the envelope (Nandez et al., 2015). However, similarly to Wang et al. (2016), we opt to include $E_{\rm rec}$ in $E_{\rm bind}$ so that the binding energy computed this way combines all the terms derived from the structure of the giant donor. We note that the contribution of the recombination energy to the total internal energy of massive giant envelopes is relatively small ($< 10\%$, see Kruckow et al., 2016).

An important choice that has to be made when computing $E_{\rm bind}$ is that of the boundary between the core (which will become the remnant of the giant donor) and the ejected envelope, the so called bifurcation point. Tauris & Dewi (2001) showed that because most of the binding energy is located in deep envelope layers close to the helium core, the exact choice of the bifurcation point can have a substantial impact on the calculated binding energy. A number of criteria for the core-envelope boundary during the CE ejection have been proposed in the literature (see Sect. 4 of Ivanova et al., 2013b). In particular, Ivanova (2011b) suggested that the bifurcation point location can be associated with the point of maximum compression $M_{\rm cp}$ within the H-burning shell, which is where the value of $P/\rho$ has a local maximum. They argued that for masses $M > M_{\rm cp}$ the remnant would re-expand on a thermal timescale after the CE ejection or possibly still during the CE phase itself, either causing another phase of mass transfer or prolonging the CE evolution, ultimately leaving behind a remnant with $M \approx M_{\rm cp}$.[4] Kruckow et al. (2016) found that in most giants the location of the maximum-compression point can be approximated by the mass coordinate where $X_{\rm H} = 0.1$ and used that as their criterion for the bifurcation point. Here we follow this latter approach; see Sect. 6.4.6 for further discussion on this topic.

Having computed $E_{\rm bind}$ from stellar models and assumed the value for $\alpha_{\rm CE}$, we can use Eq. 6.1 to calculate the post-CE separation $a_{\rm f}$ of a binary with a given BH mass. A successful CE ejection takes place if the remnant core of the giant donor is smaller than its Roche lobe in the post-CE binary. We estimate the size of the remnant $R_{\rm remnant}$ to be equal to the outer radial coordinate of the core in the pre-CE model of the giant donor multiplied by a factor of two, as guided by Ivanova (2011b), to account for the fact that the compressed core expands in radius during the CE phase itself.

Finally, for practical purposes, the envelope binding energy is often written as (de Kool, 1990)

$$E_{\rm bind} = \frac{G M_{\rm donor} M_{\rm env}}{\lambda_{\rm CE} R_{\rm donor}}, \tag{6.4}$$

where $R_{\rm donor}$ is the radius of the giant donor, $M_{\rm env}$ is the mass of its envelope ($M_{\rm env} = M_{\rm donor} - M_{\rm core}$), and $\lambda_{\rm CE}$ is a parameter that depends on the detailed envelope structure. In Appendix 6.A we

[4] It is worth pointing out that Ivanova (2011b) emulated the CE evolution by studying adiabatic mass-loss sequences, thus preventing any thermal relaxation of the donor star. If, however, a CE phase is characterized by the thermal-timescale then the maximum compression point could move during the CE event with respect to its pre-CE location.

provide fits to $\lambda_{\rm CE}$ values computed in this work, with application to population synthesis.

### 6.2.4 MODEL SUMMARY: THE "OPTIMISTIC" CHOICE OF ASSUMPTIONS

Our goal is to find the extend to which BH binaries with massive stellar companions can evolve through and survive a CE phase. Therefore, whenever possible, we make choices of assumptions that would facilitate an easier CE ejection. For clarity, these choices are summarized below (see Sect. 6.2.2 and Sect. 6.2.3 for details). We refer to Sect. 6.4.1 for a discussion of different assumptions and other caveats of the method.

– For a binary with a giant donor of a given mass and a BH accretor that undergoes a CE evolution, the final separation will be larger (and therefore the CE survival more likely) for larger BH masses, as can be deduced from Eq. 6.1. Therefore, we assume optimistically low values for the critical (minimum) mass ratios $q_{\rm crit} = M_{\rm donor}/M_{\rm BH}$ that are required for the CE evolution to occur: $q_{\rm crit;conv} = 1.5$ for convective-envelope donors and $q_{\rm crit;rad} = 3.5$ for post-MS radiative-envelope donors. Additionally, we classify a giant star as already convective when the outermost 10% of the envelope (in mass) is convective (disregarding the sometimes-present insignificantly small surface radiative layers).

– We compute envelope binding energies $E_{\rm bind}$ under assumptions that all the internal energy as well as the entire energy released during recombination can be used to help unbind the envelope (Eq. 6.3).

– We assume that orbital energy from the binary orbit shrinking within the CE can be transferred to the envelope without any losses, that is, $\alpha_{\rm CE} = 1.0$ in Eq. 6.1.

– We assume that the envelope acceleration is perfectly fine-tuned to reach exactly the local escape velocity, that is, there is no term for residual kinetic energy at infinity in Eq. 6.1.

– We include energy feedback from accretion $\Delta E_{\rm acc} = L_{\rm Edd}\tau_{\rm CE}$ and assume a relatively long duration of the CE phase, namely $\tau_{\rm CE} = 1000$ yr (Ivanova et al., 2013b). For instance, for a 1.4 $M_\odot$ NS this yields $\Delta E_{\rm acc} \approx 2\times10^{48}$erg, whereas for a 20 $M_\odot$ BH this yields about $\Delta E_{\rm acc} \approx 3\times10^{49}$erg. The relevance of these values compared to the envelope binding energy can be seen in the following section.

## 6.3 RESULTS

### 6.3.1 THE ENVELOPE BINDING ENERGY: IMPACT OF THE OUTER CONVECTIVE LAYER

In Figure 6.1 we plot the envelope binding energy $E_{\rm bind}$ of massive giants (i.e., the post-MS part of the evolution) of several chosen masses at each of the six studied metallicities. Colors in Fig. 6.1 indicate what fraction $f_{\rm conv}$ of the envelope mass is in the outer convective zone, that is, $f_{\rm conv} = M_{\rm env;conv}/M_{\rm env}$, where $M_{\rm env;conv}$ is the mass of the outer convective zone and $M_{\rm env}$ is the envelope mass. In particular, $f_{\rm conv} = 0.0$ indicates a giant with a radiative outer envelope. The

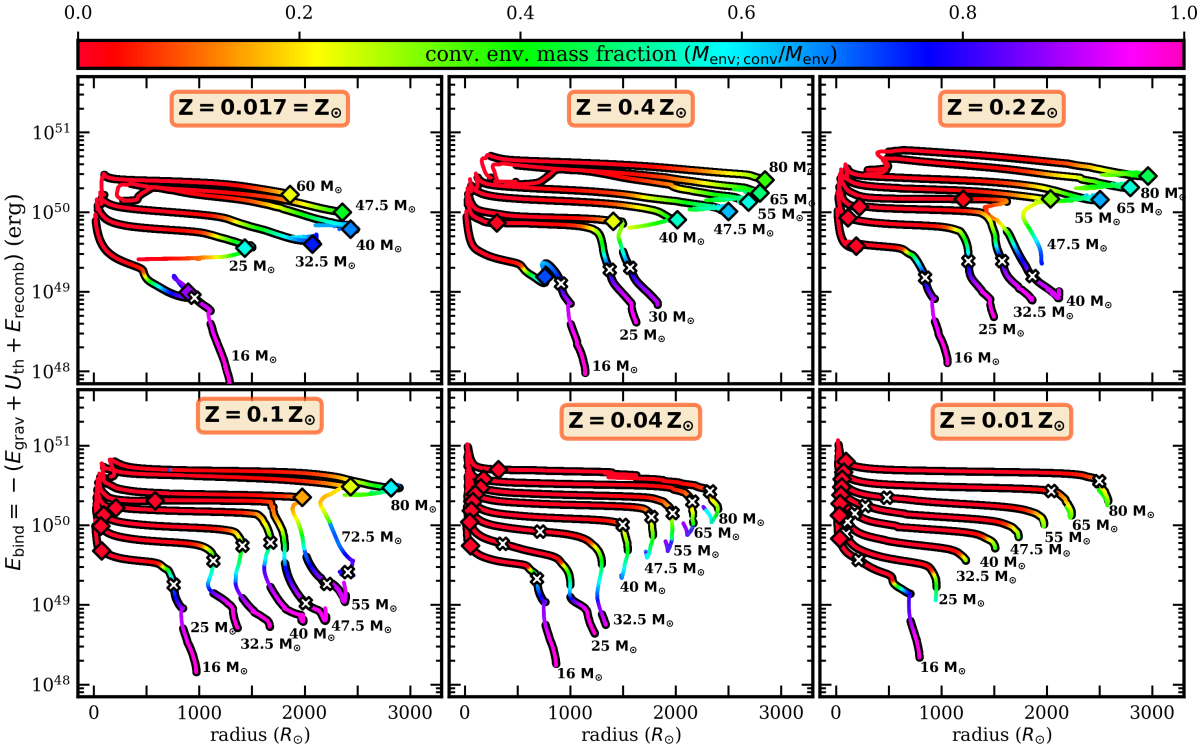


FIGURE 6.1: Envelope binding energies $E_{\rm bind}$ of massive giants (i.e., the post-MS part of the evolution) as a function of their radius for six different metallicities (selected models from Klencki et al. 2020). See Fig. 6.16 for a figure including all the masses in the grid and Fig. 6.17 for a figure showing all the corresponding $\lambda_{\rm CE}$ values. $E_{\rm bind}$ combines the gravitational potential energy as well as the internal energy (including the recombination terms); see Eq. 6.3. Only post-MS evolution is shown. Colors indicate what fraction of the envelope mass is in the outer convective zone (i.e., $M_{\rm env;conv}/M_{\rm env}$). Diamonds (same coloring) and white crosses mark the onset and end of core-helium burning, respectively. Part of the evolution when the radius is increasing beyond the previously largest radius that has been reached, i.e., the part relevant for RLOF and mass transfer, is shaded in black. Development of a deep outer convective envelope layer can lead to a very significant decrease in the binding energy, unless the giant is a HG star (i.e., before the core-helium ignition); see Sect. 6.3.4 for details.

binding energies were computed from stellar models described in Sect. 6.2.1 under the assumption that all of the thermal energy as well as the recombination energy can be used to help eject the envelope during a CE phase (see Sect. 6.2.3 for details).

Diamonds in Fig. 6.1 mark the onset of core-helium burning (defined as the point when central helium abundance $Y_{\rm C}$ drops below 0.975), meaning that all of the previous evolution is the Hertzprung-Gap (HG) phase. White crosses correspond to the central helium depletion ($Y_{\rm C} < 10^{-3}$). At solar metallicity (top-left panel), most of the radial expansion of a giant happens already during the HG phase for all the masses considered here. As the metallicity decreases, more and more massive stars remain relatively compact during their HG evolution and most of the expansion in their case takes place during core-helium burning. Massive models at the lowest metallicity in our grid ($Z = 0.01\ Z_\odot$, the lower right panel) remain compact for even longer and

only expand significantly after the central helium depletion. This is a well-known relationship between metallicity and the degree of post-MS expansion of massive giants, details of which are sensitive to a number of poorly constrained ingredients of stellar models such as convective boundary mixing, semiconvection, or rotational mixing (e.g., Georgy et al., 2013; Schootemeijer et al., 2019; Higgins & Vink, 2019; Klencki et al., 2020; Kaiser et al., 2020). We note that some of the most massive models in Fig. 6.1 for metallicities $Z \geq 0.1\ Z_\odot$ were not evolved all the way until the central helium depletion but only to the point when strong stellar winds started to cause significant shedding of the giant's envelope, causing it to decrease in radius and begin a blueward evolution in the HR diagram towards the WR stage.

The overall behavior of $E_{\rm bind}$ as a function of radius in Fig. 6.1 is similar to what was found in previous studies (Dewi & Tauris, 2000; Podsiadlowski et al., 2003; Loveridge et al., 2011; Wang et al., 2016). Notably, some of the models reveal a significant decrease in the envelope binding energy when approaching their largest radii, in some cases by more than an order of magnitude. The sudden drop in $E_{\rm bind}$ coincides with the point when the outer envelope of the giant becomes convective. This is because the entire outer convective zone of an envelope is located at relatively large radial coordinates and as a result its density is small and is very loosely bound to the star (see Fig. 2 of Podsiadlowski, 2001).

However, development of a deep outer convective layer does not always lead to a significant decrease in the binding energy. The most massive giants at metallicities $Z = 1.0\ Z_\odot$, $0.4\ Z_\odot$, $0.2\ Z_\odot$, and $0.1\ Z_\odot$ in Fig. 6.1 expand enough to become convective (up to $f_{\rm conv} \approx 0.6$), yet their $E_{\rm bind}$ barely decreases as a result of that. Those are the models in which the outer layers already become convective during the HG phase, that is, before the onset of core-helium burning, as indicated by the diamonds in Fig. 6.1. As a result, because of its impact on the radial expansion of massive giants, metallicity has an indirect but very strong effect on the binding energy of a convective-envelope giant. The reason why the binding energy does not significantly decrease when the envelope becomes convective in HG giants requires a detailed explanation; see Sect. 6.3.4.

### 6.3.2 COMMON-ENVELOPE EJECTABILITY IN BBH MERGER PROGENITORS

Here we study the possibility of ejecting envelopes with $E_{\rm bind}$ computed in the previous section during the CE evolution (i.e., the CE ejectability) in binaries with stellar BH companions, potential progenitors of BBH mergers. Our goal is to find the maximum parameter space in which the CE ejection is feasible according to energy budget considerations introduced in detail in Sect. 6.2.3. To this end, we make a number of optimistic assumptions summarized in Sect. 6.2.4, each of them increasing the energy sources relative to energy sinks and thus making a CE ejection more likely.

For each evolutionary track of a massive giant analyzed in this work, we compute what would be the outcome separation of a CE phase initiated by that star at any given point during its post-MS evolution assuming a circular binary in which the companion is a BH with mass $M_{\rm BH} = M_{\rm donor}/q_{\rm crit}$ (we note that $M_{\rm donor} < M_{\rm ZAMS}$ due to wind mass loss, where ZAMS stands for zero-age main sequence). Survival of the CE evolution is then determined based on the size of the remnant core

of the CE donor $R_{\rm remnant}$ (estimated as twice the radial coordinate of the outer core boundary in the pre-CE structure of the donor; see Sect. 6.2.3) compared to the size of its Roche lobe in the post-CE binary $R_{\rm RL;post-CE}$. Values $R_{\rm remnant}/R_{\rm RL;post-CE} > 1$ indicate a merger during the CE phase, whereas $R_{\rm remnant}/R_{\rm RL;post-CE} \leq 1$ indicates a successful CE ejection.

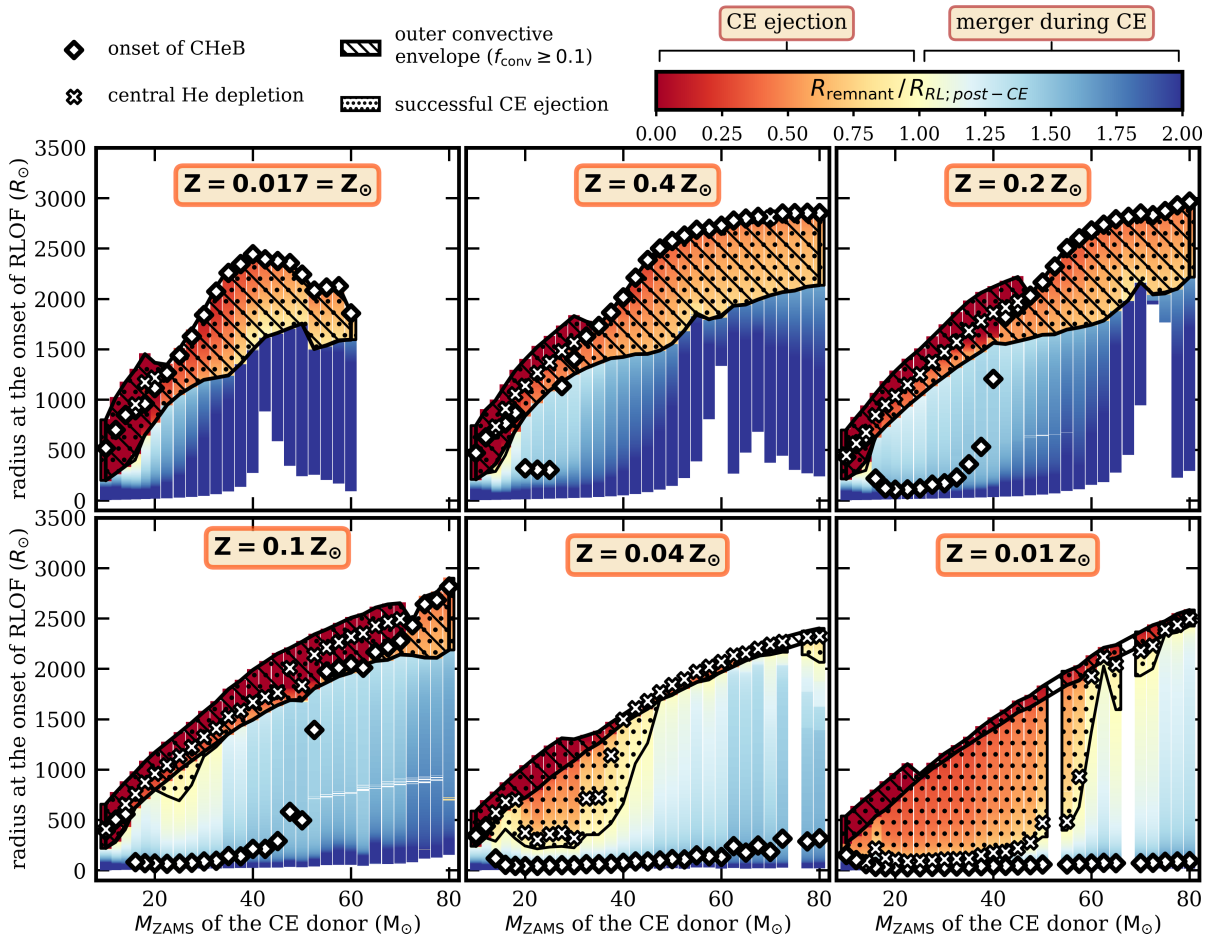


FIGURE 6.2: Common-envelope ejectability in binaries with massive giant donor stars and BH companions. For each evolutionary track of a massive giant with $M_{\rm ZAMS}$ between 10 and 80 $M_\odot$, we compute what would be the outcome of a CE phase initiated by that star at any given point during its post-MS evolution in a circular binary with a BH companion with mass $M_{\rm BH} = M_{\rm donor}/q_{\rm crit}$ (see text for detailed assumptions). The resulting ratio of the size of the remnant core of the CE donor $R_{\rm remnant}$ and the size of its Roche lobe $R_{\rm RL;post-CE}$ is color-coded in the figure as a function of $M_{\rm ZAMS}$ and the radius of the giant at the onset of the CE phase. Radii above the white diamonds (crosses) indicate giants that are past the onset (end) of core-helium burning in their evolution. The hatched region marks the parameter space where the giant donor has an outer convective envelope with $f_{\rm conv} = M_{\rm conv}/M_{\rm env} \geq 0.1$. The dotted region marks the parameter space where the CE ejection is possible (i.e., $R_{\rm remnant}/R_{\rm RL;post-CE} < 1.0$).

The result is showed in Fig. 6.2 where, as a function of $M_{\rm ZAMS}$ and the radius of the giant at the onset of the CE phase, we color-code what would be the resulting ratio $R_{\rm remnant}/R_{\rm RL;post-CE}$ in a post-CE binary. We note that at solar metallicity (top left panel), stars above 60 $M_\odot$ do not expand

in their post-MS evolution because of strong mass-loss in winds, and this is the reason they do not show in Fig. 6.2 (this result depends on the assumed mass-loss recipe and could to some extent be affected by the numerical accuracy of MS models with inflated envelopes; see Appendix 6.B). Missing masses (one at $Z = 0.04\ Z_\odot$ and two at $Z = 0.01\ Z_\odot$) are nonconverging MESA models.

The most striking finding is that the parameter space for successful CE ejections (marked as the dotted area) is almost exclusively limited to cases in which the CE evolution is initiated by a giant donor with an outer convective envelope (marked by the hatched area). The only exception are some of the radiative-envelope donors with $M_{\rm ZAMS} \lesssim 40\ M_\odot$ at $Z = 0.04\ Z_\odot$ and $M_{\rm ZAMS} \lesssim 60\ M_\odot$ at $Z = 0.01\ Z_\odot$. This is the result of convective-envelope giants having smaller envelope binding energies compared to radiative-envelope stars (see Fig. 6.1 and the associated text), combined with the fact that $q_{\rm crit;conv} < q_{\rm crit;rad}$, which means that BH accretors can be more massive in CE events initiated by convective-envelope donors.

We can also see in Fig. 6.2 that among the potential CE survivors, the $R_{\rm remnant}/R_{\rm RL;post-CE}$ ratio is either only slightly smaller than 1.0 (yellow to orange colors) or significantly smaller than 1.0 (dark red colors). Generally, the first group corresponds to convective giants that are still at the HG phase (below diamonds in Fig. 6.2) and their $E_{\rm bind}$ did not decrease as significantly with the increasing convective-envelope mass fraction $f_{\rm conv}$ (even for $f_{\rm conv} \gtrsim 0.6$), as also seen in Fig. 6.1. Given a number of optimistic assumptions in our model, it is uncertain whether or not models from the first group, with the relatively high binding energies, can survive the CE phase (see also Fig. 6.5 below). The second group are cases in which the CE evolution is initiated by a much more evolved star, with a helium-depleted core (above the crosses in Fig. 6.2) and a deep outer-convective envelope $f_{\rm conv} > 0.5$. The envelopes of such giants are very loosely bound (see Sect. 6.3.1) and not much orbital shrinkage is needed to provide energy for their ejection. As a result, the energy budget method predicts $R_{\rm remnant}/R_{\rm RL;post-CE}$ ratios that are below 0.1. In reality, it seems unlikely that the remnant of the donor would fill such a small fraction of its Roche lobe in the post-CE system because in that case the companion would never be at the bottom layers of the donor's envelope, and would therefore be unable to help in their ejection. As such, very small $R_{\rm remnant}/R_{\rm RL;post-CE}$ ratios in Fig. 6.2 should rather be interpreted as cases in which the CE ejection can be easily achieved in terms of the energy budget, not as a reliable prediction of the post-CE binary separation.

The above distinction between the two types of convective-envelope donors also shows that the evolutionary stage of the donor can have a significant impact on the outcome of the CE phase. We illustrate the differences between envelope structures of giants that become convective during the rapid HG expansion and those that reach the convective-envelope stage later during their evolution in Sect. 6.3.4. Notably, whether a star becomes convective during the HG expansion or only later during its evolution is an uncertain outcome of detailed stellar models but its relation to metallicity appears robust (e.g., Schootemeijer et al., 2019; Klencki et al., 2020).

Even though BH binaries are the main focus of this study, we also consider CE ejectability in systems in which the accretor is a NS with $M_{\rm NS} = 2\ M_\odot$ (with all the other assumptions being the same). The result is plotted in Fig. 6.18 in the Appendix. Because of the lower accretor mass,

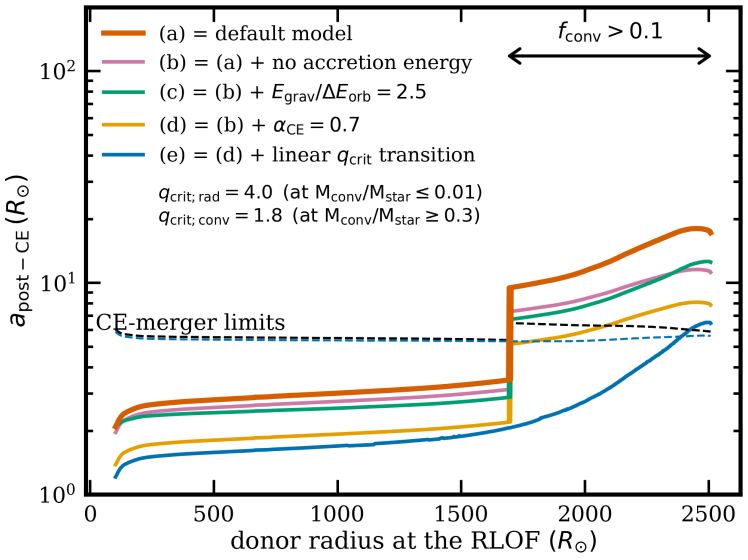


FIGURE 6.3: Exploring CE ejectability for a BH binary with a $M = 55\ M_\odot$ giant donor at $Z = 0.2\ Z_\odot$ metallicity as a function of the giant's radius at the onset of a CE phase. See text for the explanation of different models (a)-(e). Cases where the post-CE separation $a_{post-CE}$ is greater than the minimum separation required to avoid a merger (marked as a black dashed line for models (a)-(d) and a dashed purple line for model (e)) survive the CE phase.

the parameter space for CE ejection in NS binaries is smaller than in the case of BH binaries. Interestingly, it is limited to cases in which the donor is already a core-helium depleted star. In such systems there might be no additional case BB mass transfer phase after a successful CE ejection, in contrast to what has been advocated in the classical picture of the double NS binary formation (for a recent review see Tauris et al., 2017). We leave further discussion of this finding to future studies.

In Fig. 6.3, similar to Fig. 6 of Kruckow et al. (2016), we explore how several variations in the assumptions of the default model would affect the separation of the post-CE binary $a_{post-CE}$ and the CE ejectability. We examine the case of a giant CE donor with $M_{ZAMS} = 55\ M_\odot$ at $Z = 0.2\ Z_\odot$ metallicity, showing $a_{post-CE}$ as a function of its radius at the moment of Roche-lobe overflow (RLOF). The default "optimistic" model is plotted in blue as model (a); see Sect. 6.2.4 for the summary of its assumptions. Cases where $a_{post-CE}$ is greater than the minimum separation required to avoid a merger (marked as a black dashed line) is the parameter space for CE ejectability. We note that this is limited to convective-envelope donor cases ($f_{conv} > 0.1$). Slow changes in the dashed line are related to the evolution of the core radius (contraction) as well as to a transition from the radiative to the convective envelope stage at around $R_{donor} \approx 1700\ R_\odot$, at which point the assumed binary mass ratio decreases from $q_{crit;rad} = 3.5$ to $q_{crit;conv} = 1.5$.

Model (b), plotted in green in Fig. 3, is different from the default model in that it does not include the $\Delta E_{acc}$ term in Eq. 6.1. It corresponds to a situation where the energetic feedback from accretion is significantly smaller than the Eddington luminosity or where the duration of the CE phase is much shorter than the assumed 1000 yr. Excluding $E_{acc}$ from the energy budget affects the post-CE separation by less than a factor of two for the 55 $M_\odot$ donor in Fig. 6.3. The effect is larger for lower mass stars (see for example a 30 $M_\odot$ donor case in Fig. 6.4) because of their lower binding energies. We note that $\Delta E_{acc} \propto M_{accretor}$ (Eq. 6.2), and so for a given mass ratio $M_{donor}/M_{accretor} = q_{crit}$ the energy from accretion scales linearly with the donor mass. We discuss super-Eddington accretion during a CE phase in Sect. 6.4.1.

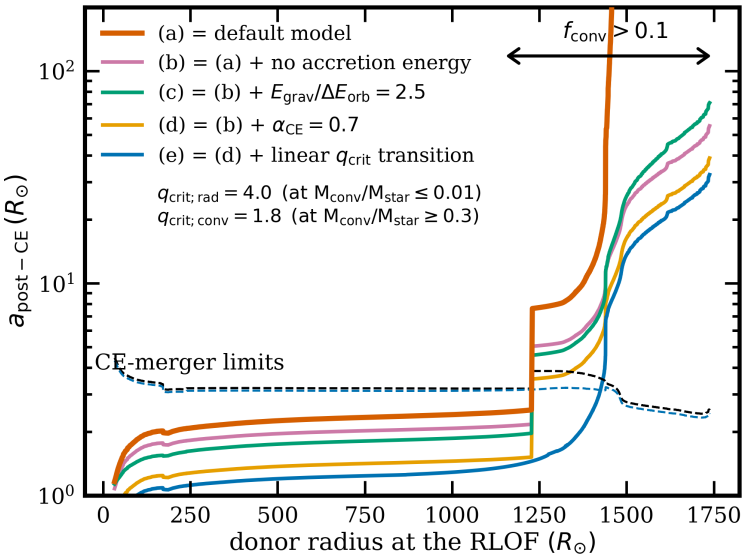


FIGURE 6.4: Same as Fig. 6.3 but for a 30 $M_\odot$ model at 0.2 $Z_\odot$ metallicity. For the donor radii $R \gtrsim 1400\ R_\odot$ the outer envelope becomes deeply convective during a core-helium burning stage, which causes a significant decrease in the binding energy of the model (Fig. 6.1) and an increase in the post-CE separation $a_{\rm post-CE}$.

Instead of relating the change in orbital energy $\Delta E_{\rm orb}$ to the envelope binding energy $E_{\rm bind}$ via the $\alpha_{\rm CE}$ parameter, one can relate $\Delta E_{\rm orb}$ to just the gravitational potential component of the binding energy: $\Delta E_{\rm grav}/\Delta E_{\rm orb} = \alpha_{\rm grav}$. In 1D hydrodynamic simulations of an inwardly spiralling CE inside the envelope of a 12 $M_\odot$ red supergiant, Fragos et al. (2019) find $\alpha_{\rm grav} \approx 2.7$. Three-dimensional models of the CE phase from low-mass giants by Passy et al. (2012) and Ohlmann et al. (2016) find similar values of $\alpha_{\rm grav} \approx 2.0$ and $\approx 2.5$, respectively. Model (c) in Fig. 6.3 (in red) assumes $\alpha_{\rm grav} = 2.5$ and is in fact very similar to the same model but with $\alpha_{\rm CE} = 1.0$ (in green). This can be expected based on the typical ratio of thermal internal energy $U_{\rm th}$ and the gravitational potential energy $E_{\rm grav}$ in a giant's envelope; see section 3.2 in Fragos et al. (2019).

Importantly, the assumption of $\alpha_{\rm CE} = 1.0$ does not only imply perfect energy transfer (e.g., no radiative losses), but also perfect fine-tuning when the ejected envelope becomes accelerated to gain precisely the local escape velocity. In reality, this is unlikely to be the case. Nandez et al. (2015); Nandez & Ivanova (2016) carried out 3D hydrodynamic simulations of CE events with low-mass giants and found that typically about 30%−40% of the orbital energy leaves the system as residual (mainly kinetic) energy of the unbound ejecta. This corresponds to model (d) in Fig. 6.3, with $\alpha_{\rm CE} = 0.7$. We note that in this model, only half of the convective-envelope donor cases survive the inward spiralling of the CE (the orange line rises above the black dashed threshold in the middle of the $f_{\rm conv} > 0.1$ region).

Finally, in model (e) plotted in purple we also apply a smooth transition of the critical mass ratio from $q_{\rm crit} = 4.0$ for radiative donors with $M_{\rm conv}/M_{\rm star} \leq 0.01$ up to $q_{\rm crit} = 1.8$ for convective-envelope giants with $M_{\rm conv}/M_{\rm star} \geq 0.3$ as a linear function of $M_{\rm conv}/M_{\rm star}$. This makes this model consistent with the results of Pavlovskii & Ivanova (2015), who find $q_{\rm crit;conv}$ between 1.5 and 2.2 for giants with deep convective envelopes of $M_{\rm conv}/M_{\rm star} \geq 0.3$ and $q_{\rm crit} > 3.5$ for less convective giants. Our default classification criteria for convective-envelope donors ($f_{\rm conv} = M_{\rm conv}/M_{\rm env} \geq 0.1$) also includes the in-between cases of mostly radiative-envelope donors

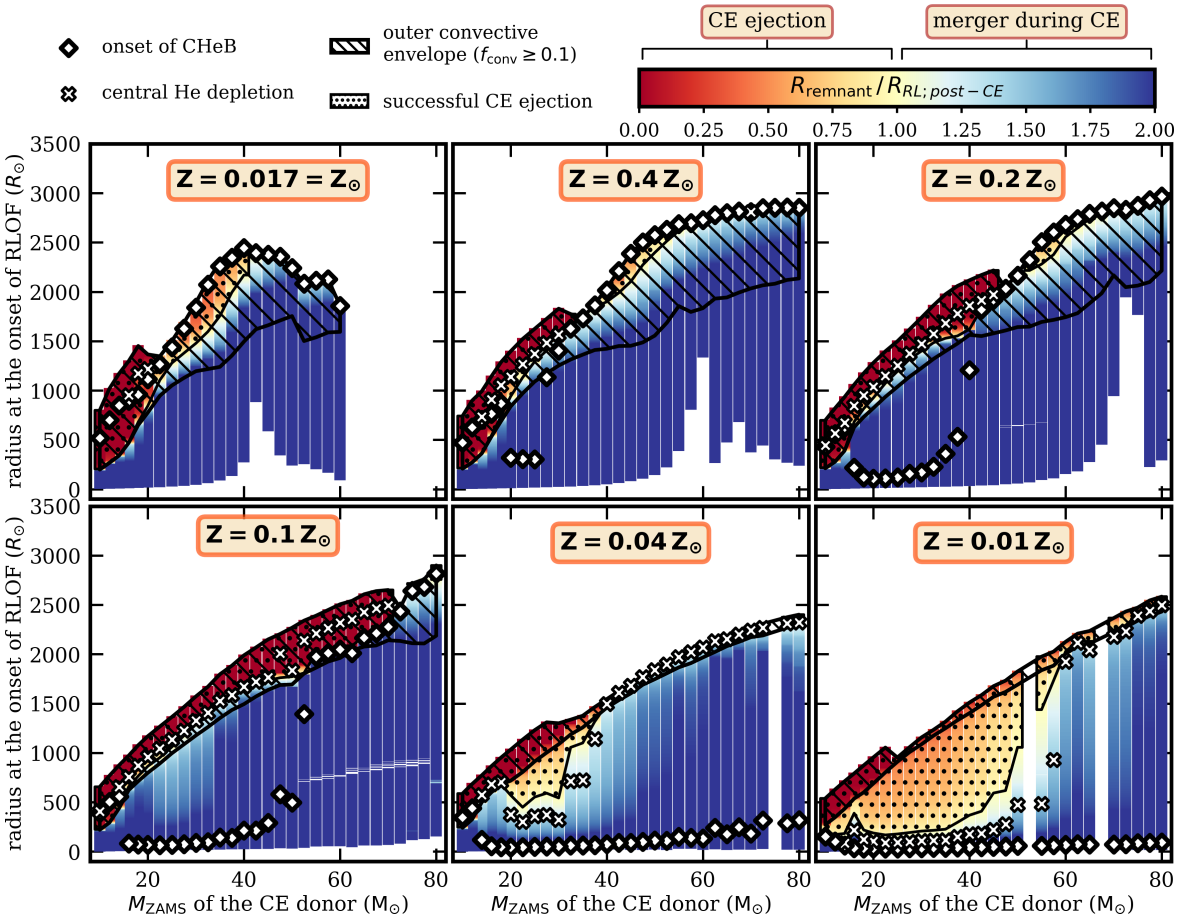


FIGURE 6.5: Same as Fig. 6.2 but assuming a more realistic energy budget and the mass transfer stability criteria: $\alpha_{CE} = 0.7$ instead of $\alpha_{CE} = 1.0$ and a smooth transition of $q_{crit}$ from $q_{crit} = 4.0$ for radiative donors with $M_{conv}/M_{star} \leq 0.01$ up to $q_{crit} = 1.8$ for convective-envelope giants with $M_{conv}/M_{star} \geq 0.3$ as a linear function of $M_{conv}/M_{star}$. We note that $f_{conv} = M_{conv}/M_{env}$, and $f_{conv} > 0.1$ region is hatched in the figure.

with relatively shallow convective envelopes, for which the mass transfer is more stable than for giants with deep convective envelopes. The CE ejection in model (e) is only possible in a small number of cases when the 55 $M_\odot$ giant is close to its maximum size and its outer convective envelope is the most extended.

In Fig. 6.4 we plot the same model variations as in Fig.6.3 but for a lower mass, namely 30 $M_\odot$, giant (also at $Z = 0.2\ Z_\odot$ metallicity). The main difference is that for donor radii above $\sim 1450\ R_\odot$ all explored variations result in a successful CE ejection. This is because at that point the 30 $M_\odot$ model develops a deeply convective envelope at late stages of core-helium burning, which leads to a significant decrease in its binding energy for $R \gtrsim 1400\ R_\odot$ (see Fig. 6.1). In fact, at those stages the envelope is so loosely bound that the accretion term $\Delta E_{acc}$ alone is larger than $E_{bind}$. Figure 6.4 illustrates that in models with loosely bound deep convective envelopes the estimated post-CE separation is often significantly larger than the CE-merger limit. In those cases (appearing in dark red in Fig. 6.2) the CE ejectability does not significantly depend on the particular choice of

assumptions for the energy budget.

Models (b)-(e) in Fig. 6.3 show that our reference model (a) yields a reasonable but very optimistic result in terms of CE ejectability shown in Fig. 6.2. For comparison, in Fig. 6.5 we make less optimistic but probably more realistic assumptions of $\alpha_{\rm CE} = 0.7$ and a smooth linear transition of $q_{\rm crit}$ between radiative and convective envelope donors as in model (e) above. The result is a significantly reduced parameter space for CE survival, mostly limited to the cases of loosely bound convective envelopes in core-helium burning or more evolved giants.

### 6.3.3 IT HAS TO BE COOL: TIGHT LINK BETWEEN THE CE DONORS AND RED SUPERGIANTS

In the previous section we show that unstable mass transfer evolution followed by a CE phase and a successful CE ejection in binaries with BH or NS accretors is only energetically feasible (even under optimistic assumptions) if the donor star is a massive supergiant with an outer convective envelope; see Fig. 6.2 and Fig. 6.18. Observationally, such stars appear as red supergiants (RGSs) with effective temperatures of about $\log(T_{\rm eff}/{\rm K}) \lesssim 3.7$ (depending on the exact position of the Hayashi line at a given metallicity).

We illustrate this in an HR diagram for the SMC-like metallicity ($Z \approx 0.2\ Z_\odot$ Venn, 1999) in Fig. 6.6, in which the estimated region of CE ejectability is marked in green (this corresponds to the dotted area in the top-right panel of Fig. 6.2). The part of that parameter space marked in violet are cases in which the CE ejection is also possible with NS accretors.

For comparison, we mark the positions of known RSGs in the SMC from the samples of Davies et al. (2018, with effective temperatures based on spectral-energy density fits) and Levesque et al. (2006, with effective temperatures from atmospheric model fits).

For reference, the light-blue line around $\log(T_{\rm eff}/{\rm K}) \approx 3.65$ marks the threshold temperature $T_{\rm eff;th}$ below which at least 10% of the mass of the star is in the outer-convective envelope (from Sect. 3.4 of Klencki et al., 2020). The fact that many of the RSGs in the sample collected by Davies et al. (2018) are hotter than $T_{\rm eff;th}$ and fall outside of the predicted temperature range of RSGs in the green area in Fig. 6.6 is a likely indication that the value of the mixing-length parameter $\alpha_{\rm ML} = 1.5$ in the models from Klencki et al. (2020) is somewhat too small.[5]

The brightest RSG in the SMC has a luminosity of $\log(L/L_\odot) = 5.55 \pm 0.1$ (Davies et al., 2018). A similar empirical upper luminosity limit for RSGs of $\log(L/L_\odot)_{\rm RSG;max} \approx 5.6 - 5.8$ has been found also for other local galaxies of different types and compositions: the Milky Way ($Z = 0.02$ Levesque et al., 2006), M31 ($Z = 0.04$ Neugent et al., 2020), the Large Magellanic Cloud ($Z = 0.007$ Davies et al., 2018), and several dwarf irregular galaxies ([Fe/H] between $-1.0$ and $-0.4$, Britavskiy et al. 2019). This limit is marked in Fig. 6.6 at an approximate luminosity $\log(L/L_\odot)_{\rm RSG;max} = 5.7$, which corresponds to stars with initial masses $M_{\rm ZAMS} \approx 40\ M_\odot$. The existence of the empirical upper luminosity limit $\log(L/L_\odot)_{\rm RSG;max}$ could be an indication that

[5] A mixing length of around 2 would probably result in better agreement with the observed RSG samples (Chun et al., 2018).

more massive stars never expand to reach the RSG stage during their evolution, because of for example extensive mass loss at the uncertain luminous blue variable stage. In view of our findings, this would likely prevent donors with $M_{\rm ZAMS} \gtrsim 40\ M_\odot$ from forming BBH mergers in the CE evolution channel.

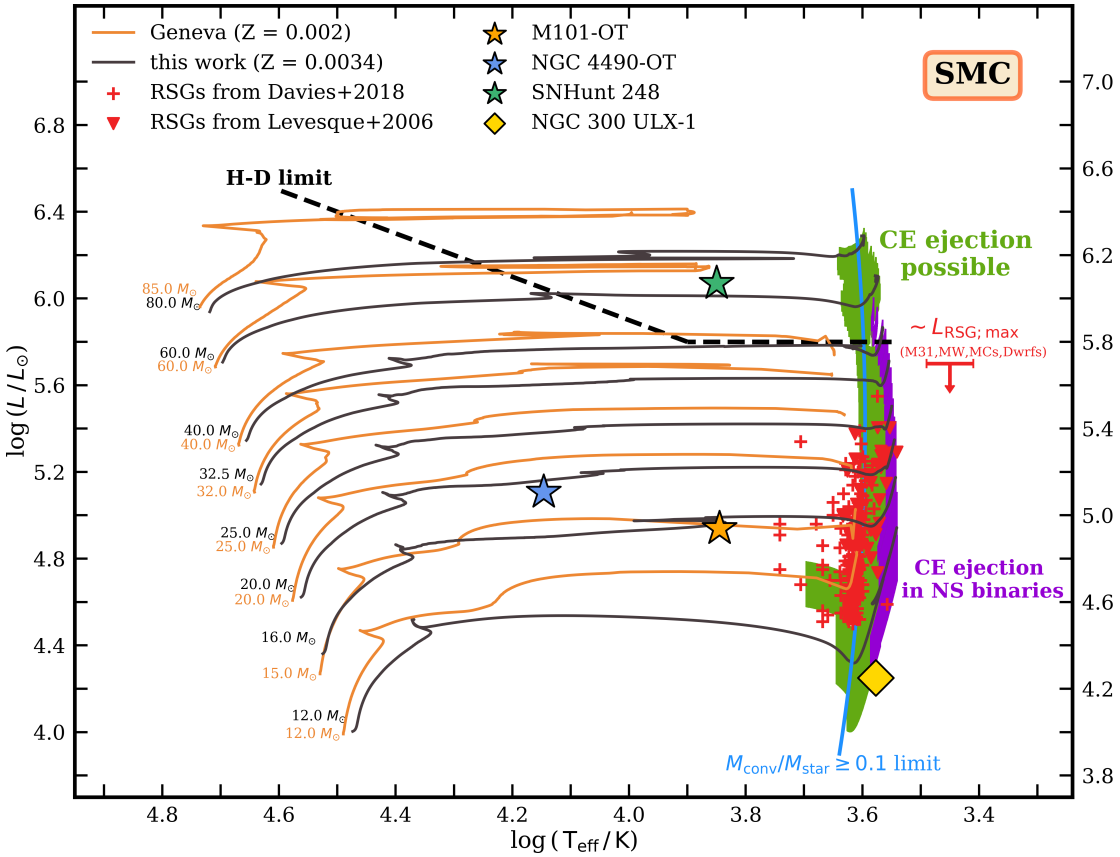


Figure 6.6: HR diagram for the SMC-like metallicity ($Z \approx 0.2\ Z_\odot$ Venn, 1999) in which the green area marks the position of donor stars at the onset of RLOF for which a CE evolution with a successful CE ejection in BH binaries is possible. A smaller violet area marks the subset of donors for which CE ejection is also possible in the case of NS accretors ($M_{\rm NS} = 2\ M_\odot$). A definitive association of donors to successful CE evolution events with cool (red) supergiants ( $\log(T_{\rm eff}/{\rm K}) \lesssim 3.7$) is clear. Two sets of selected stellar tracks are plotted: models from Klencki et al. (2020), which are the main focus of this paper, and models from (Georgy et al., 2013) computed with the GENEVA code. Physical parameters of RSGs observed in the SMC are taken from Levesque et al. (2006) and Davies et al. (2018). The black dashed line marks the empirical Humphreys-Davidson (H-D) limit, beyond which almost no stars in the Milky Way or in the LMC are observed (Humphreys & Davidson, 1979, 1994; Ulmer & Fitzpatrick, 1998). The light-blue line shows the threshold effective temperature below which at least 10% of the mass of models from Klencki et al. (2020) is in the outer-convective envelope. Colored stars mark the inferred physical parameters of three different massive star progenitors of luminous-red novae (LRNe; Smith et al., 2016; Blagorodnova et al., 2017; Mauerhan et al., 2018). The yellow diamond shows the RSG donor in a pulsating ultra-luminous X-ray (ULX) source NGC 300 ULX-1 (Heida et al., 2019).

Lack of RSGs above a certain luminosity limit has been purposefully recovered in various

stellar tracks of massive stars. As an example, in Fig. 6.6 we plot several rotating stellar tracks computed with the GENEVA code for $Z = 0.002$ (Georgy et al., 2013). For reference, we also show a few corresponding tracks from (Klencki et al., 2020) that were used to compute envelope binding energies in this work.[6] The lack of most luminous RSGs in the GENEVA tracks is most likely a result of increasing mass-loss rates in stars with super-Eddington layers (Ekström et al., 2012) as well as of suppressing density inversions in radiation-dominated stars by using a mixing length taken on the density rather than on the pressure scale height (Appendix A of Klencki et al., 2020). We discuss the empirical $\log(L/L_{\odot})_{\rm RSG;max}$ limit in the context of CE evolution and the formation of BBH mergers in Sect. 6.4.2.

It is worth noting that CE evolution in a binary with a BH or a NS accretor is preceded by a phase of essentially stable mass transfer that takes place between the moment of RLOF and the onset of the CE phase (MacLeod et al., 2018b,a; MacLeod & Loeb, 2020b). During this stage the mass transfer rate gradually increases at a rate which is primarily dictated by the thermal timescale of the envelope of the donor (also in the case of convective-envelope donors; see Woods & Ivanova, 2011; Pavlovskii & Ivanova, 2015). In the case of massive donors, this indicates a duration of the order of $\sim 10^4$ yr, and a loss of even $\sim 30\%$ mass from the envelope of the donor (MacLeod & Loeb, 2020a, also Ivanova, private communication).[7] Observationally, a system at this stage would likely appear as a bright X-ray binary: a ULX. In the case of potential CE survivors among BH and NS binaries, this corresponds to ULXs with RSG donor stars. Several such systems with donor stars spectroscopically confirmed to be RSGs are known to date (Heida et al., 2015, 2016; Lau et al., 2019; Heida et al., 2019). In the case of one of the sources, a pulsating ULX dubbed NGC 300 ULX-1, Heida et al. (2019) were able to model the spectrum of the optical counterpart as a sum of three components: a blue excess (likely due to X-ray irradiation), a red excess (likely due to dust), and a stellar atmosphere model of an RSG with $T_{\rm eff} = 3650$ - $3900$ K and $\log(L/L_{\odot}) = 4.25 \pm 0.1$ (marked in Fig. 6.6). López et al. (2020) completed a systematic search for near-infrared candidate counterparts to nearby ULXs and concluded that ULXs with RSG donors constitute about $\sim 4\%$ of the observed ULX population, which is about four times more than predicted by population-synthesis models (Wiktorowicz et al., 2017). One reason for this discrepancy could be that rapid binary evolution codes assume that the moment of RLOF is also the onset of CE evolution, without modelling the intermediate mass transfer phase.

One observational signature of the CE phase itself are LRNe, red transients characterized by a rapid rise in luminosity followed by a lengthy plateau (Soker & Tylenda, 2003; Kulkarni et al., 2007; Tylenda et al., 2011; Ivanova et al., 2013a; Kochanek, 2014; Howitt et al., 2020). In several cases, archival multiband observations from before the LRN have revealed the progenitors to be consistent with massive giants: notably a $\sim 18\ M_{\odot}$ progenitor to M101-OT (Blagorodnova et al.,

[6]The fact that GENEVA models are hotter and more luminous during the MS is most likely a result of a higher efficiency of rotational mixing in GENEVA models compared to models computed by Klencki et al. (2020).

[7]An exception are systems that become unstable on a shorter timescales due to Darwin instability (Darwin, 1879; Eggleton & Kiseleva-Eggleton, 2001), which could predominantly occur in cases of extreme mass ratios ($q \gtrsim 10$ Rasio, 1995).

2017) and a $\sim 60\ M_\odot$ progenitor to SNHunt 248 (Mauerhan et al., 2018), as well as a putative single-band detection of an LBV-like progenitor to NGC 4490-OT (Smith et al., 2016). In none of these cases was the progenitor consistent with a RSG; see Fig. 6.6. According to our findings, this might be an indication that these CE events finished in mergers, although our results may not be directly applicable to CE cases with stellar accretors. As a final remark, it was recently shown by Ginat et al. (2020) that inward spiralling of compact accretors during the final stages of CE evolution could produce a GW signature which might be detectable by the next-generation GW detectors such as Laser Interferometer Space Antenna (LISA).

### 6.3.4 A DETAILED LOOK AT THE STRUCTURE AND THE BINDING ENERGY OF CONVECTIVE-ENVELOPE GIANTS

In Sect. 6.3.1 we found that the envelope of a massive giant can become significantly less bound when it transitions from a radiative to a convective state, with $E_{\rm bind}$ decreasing by an order of magnitude or more. An exception to this rule are giants that become convective already during the HG phase, for which the decrease in the binding energy is much less significant. In this section we explain the origin of this behavior.

In Fig. 6.7 we illustrate this transition for a model with $M_{\rm ZAMS} = 47.5\ M_\odot$ and $Z = 0.1\ Z_\odot$, which develops a deep outer convective envelope during late stages of core-helium burning and is an example of a model for which the associated decrease in $E_{\rm bind}$ is very significant. Panel 6.7a shows the Kippenhahn diagram of the model (excluding the initial part of the MS when $X_{\rm H;C} > 0.55$) with stellar radius plotted in red. In panel 6.7b, one can see that the binding energy $E_{\rm bind}$ slowly decreases during the core-helium burning phase and then decreases significantly as the envelope becomes deeply convective (and $f_{\rm conv}$ increases).

The next three panels of Fig. 7 show a more detailed view of the internal structure of the star at several selected moments during its evolution. Panel 6.7c shows the internal mass-radius profiles, with the outer convective zone being marked in thicker lines. The bifurcation point of each profile, which is the point that divides between the ejected envelope and the remaining remnant of the donor in a CE event, is marked with a solid vertical line located at $X_{\rm H} = 0.1$. With time (i.e., profile colors changing from blue to red) the inner part of the star contracts as a result of continuous burning in the core. On the other hand, as the envelope becomes increasingly convective, the outer layers in the star move to larger radial coordinates. The point in between the contracting and the expanding layers of the star, located at the mass coordinate of about $\sim 23\ M_\odot$ in panel 6.7c, is an important divergence point. The helium abundance profiles in panel 6.7d reveal that the divergence point coincides with a steep composition jump at the boundary between the helium core (where $X_{\rm He} \approx 1$ in the helium shell) and the H-rich envelope. Importantly, it also closely coincides with the assumed location of the bifurcation point, marked with dashed vertical lines. In other words, the part of the giant above the bifurcation point, which would need to be ejected in a successful CE phase, is also the part that expands to larger radii coordinates as the outer envelope becomes increasingly convective. As a result, the entire envelope becomes less gravitationally

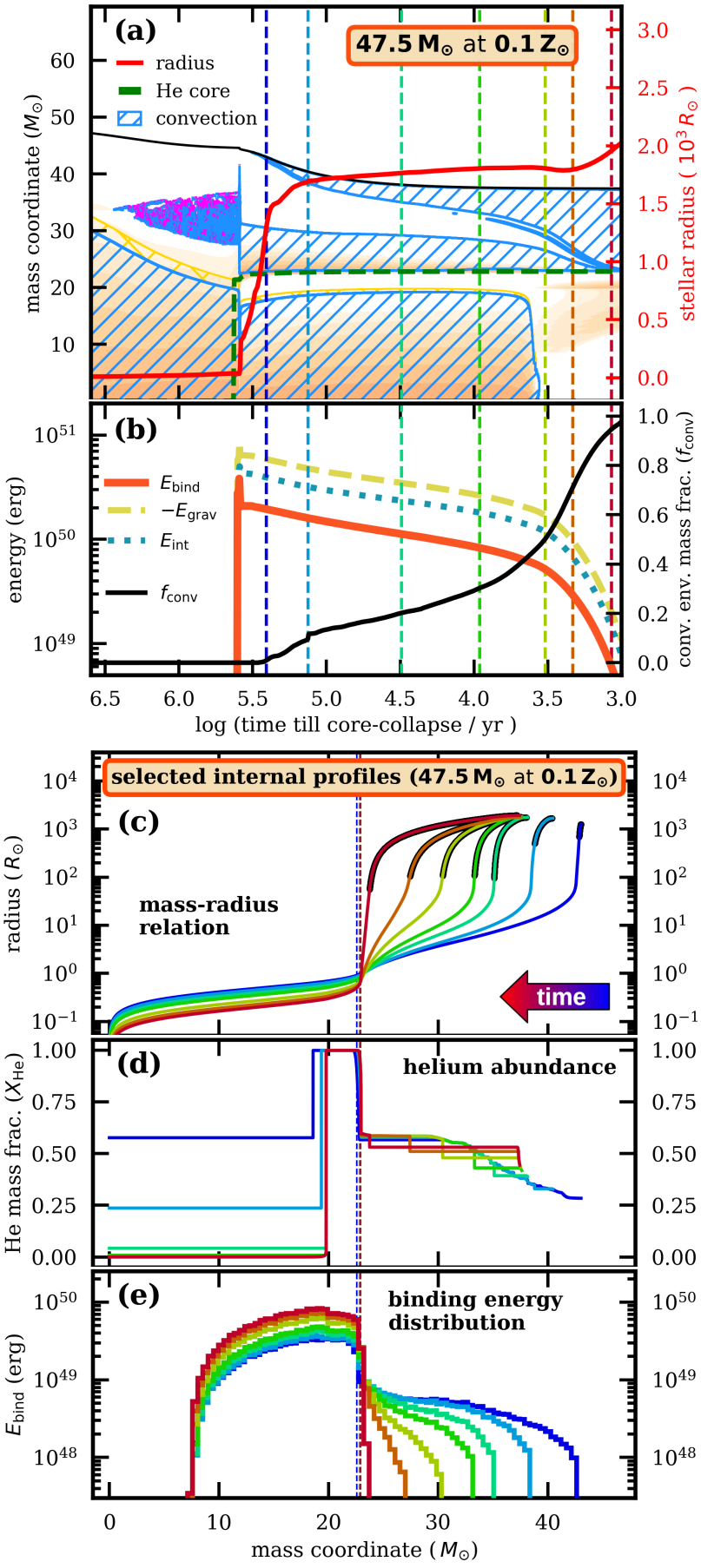


FIGURE 6.7: Detailed look at the evolution of a $M_{\rm ZAMS} = 47.5\,M_\odot$ model at $Z = 0.1\,Z_\odot$ metallicity. Panel (a) shows the Kippenhahn diagram with stellar radius over-plotted in red. We note that the purple color shows regions of semiconvective mixing. Panel (b) shows the time evolution of the binding energy $E_{\rm bind}$ and its components: $E_{\rm grav}$ and $E_{\rm int} = U_{\rm th} + E_{\rm rec}$ (see Eq. 6.3) together with the convective envelope mass fraction $f_{\rm conv}$. Panels (c), (d), and (e) show several internal profiles of the model, the position of which are marked in panels (a) and (b) with dashed vertical lines in corresponding colors. The outer convective zone is marked in bold in panel (c). Solid vertical lines in panels (c), (d), and (e) mark the core-envelope boundary for the CE evolution (i.e., the bifurcation point at $X_{\rm H} = 0.1$).

bound (see panel 6.7e) and $E_{\rm bind}$ steeply decreases when $f_{\rm conv}$ increases.

As pointed out above, giants that expand to develop a deep outer convective envelope already during the HG phase do not see their envelope binding energies decrease in a significant way as a result of that. In Fig. 6.8 we illustrate an example of such a case, a model with $M_{\rm ZAMS} = 47.5\ M_\odot$ and $Z = 0.4\ Z_\odot$; in panels (a)-(e) we plot the same quantities as in the corresponding panels in Fig. 6.7. We note that the two upper panels, 6.8a and 6.8b, have a different scaling on the x-axis (linear) than panels 6.7a and 6.7b (logarithmic) as they only focus on the part of the evolution during which the radius substantially increases (the part relevant for mass transfer interactions). The decrease in $E_{\rm bind}$ at around 4.54 Myr in panel 6.8b is initiated by a contraction of the inner parts of the star after the end of MS and the associated expansion of the outer layers (before the outer envelope becomes convective), as also seen at the very beginning of $E_{\rm bind}$ evolution in panel 6.7b for the $Z = 0.1\ Z_\odot$ giant. During the development of an outer convective envelope ($f_{\rm conv} \approx 0.6$) the binding energy decreases by less than a factor of two.

The bottom three panels in Fig. 6.8 illustrate the essential difference in the structure of a convective HG star compared to a more evolved convective giant from Fig. 6.7. As the outer convective zone extends deeper and deeper inside the envelope (panel 6.8c), the outer layers of the star expand to larger radial coordinates, while the inner part of the star slightly contracts. This is a similar behavior to that seen in panel 6.7c. However, in the case of the HG giant in panel 6.8c, the divergence point between the contracting and the expanding part of the star is no longer located very close to the helium-core boundary at a mass coordinate $\approx 23\ M_\odot$ (where $X_{\rm He} \approx 1$) but appears higher up inside the star at $\approx 26\ M_\odot$. We find that such a different location of the divergence point in HG giants is associated with a distinctively different internal abundance profile; see panel 6.8d. In regards to the composition jump near the helium core where $X_{\rm He} \approx 1$ is smaller than that in panel 6.7d, the helium abundance only drops down to $X_{\rm He} \approx 0.75$, forms a plateau, and then starts to gradually decrease again at a mass coordinate of about $26\ M_\odot$. One can see that the divergence point is roughly associated with the secondary drop when $X_{\rm He}$ decreases below $\sim 0.75$. The consequences of the structural change on the binding energy distribution within the envelope can be seen in panel 6.8e. The $\sim 2-3\ M_\odot$ of helium-dominated material ($X_{\rm He} \approx 0.75$) at the bottom of the envelope move slightly inward inside the star and their binding energy increases, which counteracts the decreasing binding energy of the outer convective layers. As a result, the overall binding energy of the envelope remains roughly unaffected.

We find that the example in Fig. 6.8 is representative for models of giants that reach the convective-envelope stage during HG expansion. The reason for the crucial difference in helium abundance profiles between panels 6.7d and 6.8d has to do with the size of an intermediate convective zone (ICZ)[8] that develops in a star on top of the hydrogen-burning shell right after the end of the MS, that is, during the phase of rapid HG expansion when the star is out of thermal equilibrium (e.g., Langer et al., 1985; Schootemeijer et al., 2019; Kaiser et al., 2020).

[8]We note that the term intermediate convective zone sometimes also refers to a region of semiconvective and convective mixing that can take place above the H-burning core already during the MS; see for instance Farmer et al. (2016). Here, we follow a slightly different nomenclature (e.g., Langer et al., 1985; Kaiser et al., 2020).

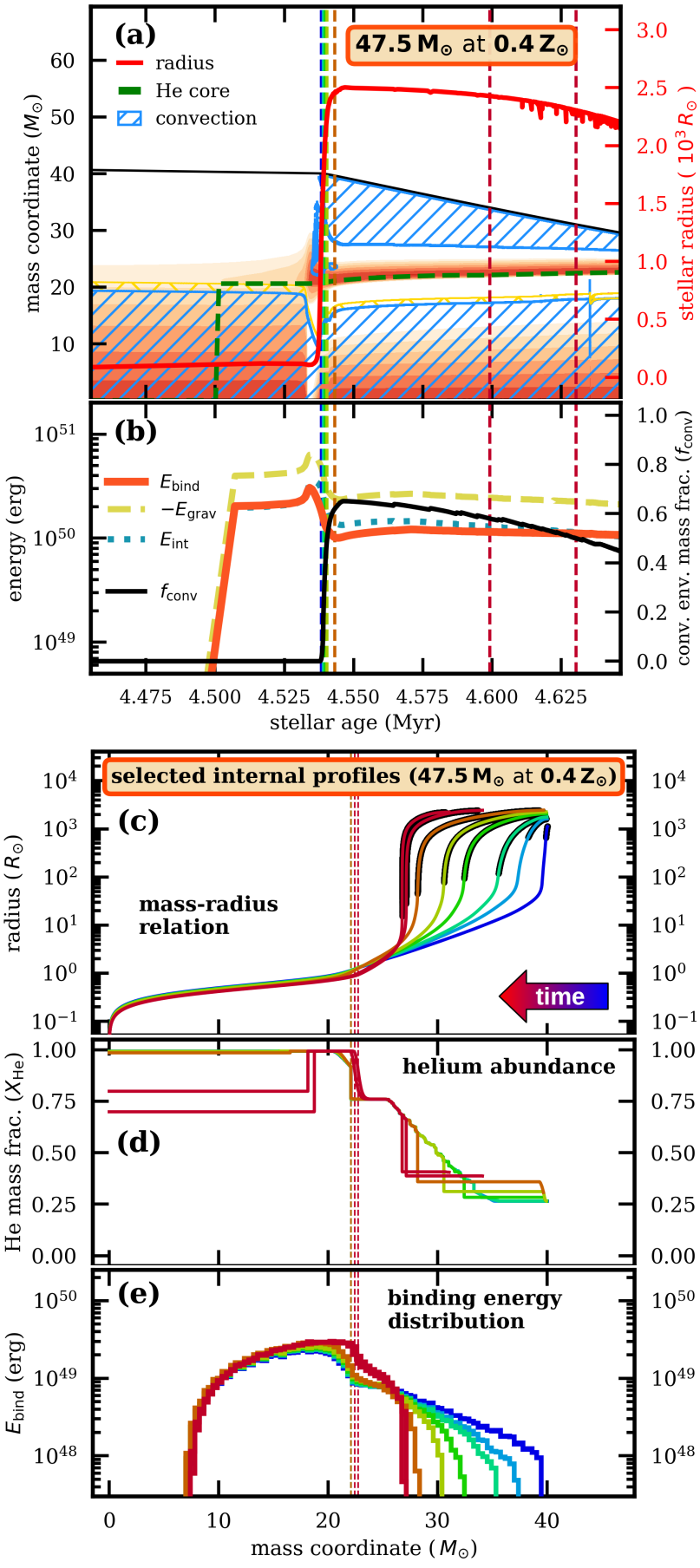


FIGURE 6.8: Similar to Fig. 6.7 but for a model with $M_{\rm ZAMS}$ = 47.5 $M_\odot$ at $Z$ = 0.4 $Z_\odot$ metallicity. Panels (a) and (b) The two upper panels (a) and (b) are centered on the evolutionary phase during which the radius substantially increases, which is mainly the phase of rapid HG expansion. The different structural response of the envelope to the outer convective zone in panel (c), associated with differences in the abundance profile in panel (d), leads to a much smaller impact of the increasing $f_{\rm conv}$ on the envelope binding energy $E_{\rm bind}$ (see text for details).

In models that by this stage have already expanded all the way to the red-giant branch and developed an outer convective envelope, the ICZ tends to quickly disappear, as in the model in Fig. 6.8 and as also found by previous authors (e.g., Langer et al., 1985; Schootemeijer et al., 2019; Davies & Dessart, 2019; Kaiser et al., 2020). In contrast, in models where the star expands less during the HG stage and stably burns helium as a blue or yellow supergiant, the ICZ does not disappear quite as quickly and becomes more extended (in mass coordinate), as in the model in Fig. 6.7. A more extended ICZ means that more hydrogen is mixed from the H-rich envelope into the He-rich layers above the helium core, and as a result the composition jump at the core-envelope boundary is larger and the helium abundance at the bottom of the envelope is smaller, as can be seen by comparing Fig. 6.7d with Fig. 6.8d. Another difference between the models in Fig. 6.7 and Fig. 6.8 is that in the 0.1 $Z_\odot$ case the H-burning shell remains convective throughout the core-helium burning while in the 0.4 $Z_\odot$ case the ICZ disappears and the H-burning shell becomes radiative. Compared to the role played by the ICZ, which is present in both cases, the nature of the H-burning shell does not appear to be an important factor for the abundance profiles shown in Fig. 6.7d and Fig. 6.8d; these abundance patters are already determined by the ICZ.

The reasoning presented above explains the relation between the degree of expansion during the HG phase, the size of the ICZ, and the abundance profile of deep envelope layers. However, the precise extent of the ICZ in a given model has to be considered as highly uncertain; it is sensitive to the assumed efficiency of semiconvective mixing (Schootemeijer et al., 2019), convective overshooting (Kaiser et al., 2020), numerical accuracy of stellar models (see Appendix 6.B and Farmer et al., 2016), and treatment of convective boundaries in regions with steep composition changes (see e.g., the `convective premixing` scheme introduced in MESA Paxton et al. (2019)). However, perhaps most importantly, the extent of the ICZ likely depends on the abundance profile above the H-burning shell left behind by the previous evolution. It is therefore sensitive to rotational mixing (Georgy et al., 2013) and to (semi)convective mixing above the H-burning core already during the MS (Farmer et al., 2016). Additionally, in the case of a past accretor from previous mass transfer phases (which is most definitely relevant for the case of companions in BH binaries studied here), the abundance profile above the H-burning shell can be significantly different compared to an unperturbed single stellar model due to rejuvenation and growth of the H-burning core of the mass gainer (Hellings, 1983, 1984; Braun & Langer, 1995; Wellstein et al., 2001; Dray & Tout, 2007).

It is also worth mentioning that the relation between the degree of HG expansion and the degree of mixing in the ICZ operates both ways: if the mixing is not very efficient, then a certain model may expand to the RSG stage, whereas the same model but with efficient mixing (e.g., by semiconvection or rotationally induced mixing) will in some cases expand much less and burn helium as a blue supergiant (see Appendix B of Klencki et al., 2020). This provides a possibility to calibrate models using the observed ratio of blue to red supergiants. For example, the post-MS expansion of the models used in this study was calibrated to match the ratio observed in the SMC.

In summary, the internal structure and chemical profiles presented here suffer from uncertainties in various internal mixing processes and numerical challenges associated with the ICZ, and are

likely affected by a previous accretion phase. Nevertheless, it seems reasonable to expect some systematic differences in the envelope structure (and the binding energy) between stars that become convective during the HG phase and those that only become convective much later during there evolution. The examples shown in Fig. 6.7 and Fig. 6.8 offer some guidance as to what these differences could look like.

It is interesting to speculate about the consequences of different envelope structures of giants seen in Figs. 6.7 and 6.8 for the CE evolution itself, in particular given that the location of the divergence point in the $Z = 0.4\ Z_{\odot}$ model is substantially different from that of the bifurcation point (under usual assumptions). We discuss this further in Sect. 6.4.6. The examples given in Figs. 6.7 and 6.8 show that the internal envelope structure of a convective-envelope supergiant can depend significantly on the evolutionary stage of the star.

## 6.4 DISCUSSION

### 6.4.1 HOW ROBUST IS THE PREDICTION THAT CE EVOLUTION IN BH BINARIES REQUIRES RSG DONORS?

In Sect. 6.3.2 we show that the parameter space for CE ejectability in binaries with BH or NS accretors is limited to donors with outer convective envelopes, that is, cool supergiants (RSGs, see Fig. 6.6). This conclusion was reached by pursuing a very optimistic case of the energy budget of CE evolution (Sec. 6.2.4). In particular, we assumed that the entire energy input from orbital shrinkage, the internal energy of the envelope, recombination energy, and the energy input from accretion can be transferred into kinetic energy and used to help unbind the envelope. We also assumed no energy loss in any form (i.e., $\alpha_{\rm CE} = 1.0$), neglecting energy sinks such as radiation from the surface or excess kinetic energy in outflows. These assumptions are clearly extreme. For instance, in view of hydrodynamic simulations, a more realistic assumption would be $\alpha_{\rm CE} \lesssim 0.7$ or even $\alpha_{\rm CE} \sim 0.1$ during the possibly reached self-regulated phase of the CE evolution (see Sect. 6.2.3 for details). These results suggest that the parameter space for a successful CE ejection in Figs. 6.2 and 6.6 is most likely an upper limit on the true (realistic) CE ejectability; see for example Fig. 6.5.

From the observational side, various attempts have been made in the past to constrain the CE ejection efficiency $\alpha_{\rm CE}$ by linking post-CE systems to their reconstructed pre-CE progenitors (e.g., Nelemans et al., 2000; Zorotovic et al., 2010, 2011; De Marco et al., 2011; Davis et al., 2012; Portegies Zwart, 2013). While most of these results suffer from uncertainties in the reconstruction technique of pre-CE parameters and the $\alpha_{\rm CE}$ values they yield are degenerated with the binding energy parameter $\lambda_{\rm CE}$, for the majority of the post-CE systems the inferred values of $\alpha_{\rm CE}$ are clearly below 1.0, although in some cases only when the internal envelope energy is included (see e.g., De Marco et al., 2011, for a discussion of the impact of thermal energy on the inferred $\alpha_{\rm CE}$ values). However, it is worth pointing out that the formation of three double helium white dwarfs analyzed by Nelemans et al. (2000) as well as one of the post-CE systems analyzed by De Marco

et al. (2011) seemingly cannot be reconstructed without $\alpha_{\rm CE} > 1$. This might be a signal of the limitations of the energy budget formalism, some of which we discuss below. This might also be an indication that CE evolution does not always take place when we expect it to. Another type of system for which values of $\alpha_{\rm CE} > 1.0$ were advocated, and perhaps more relevant in the context of massive stars and BBH merger progenitors, are BH low-mass X-ray binaries (BH-LMXBs, e.g., Kalogera, 1999; Podsiadlowski et al., 2003). In Sect. 6.4.5 we analyze their case in more detail and argue that $\alpha_{\rm CE} \leq 1.0$ could potentially be sufficient.

There are two caveats of our method: the possible contribution of other energy sources in CE ejection (unaccounted for in our energy budget) and lower envelope binding energies. Apart from the energy terms considered in this work, other energy sources have been discussed in the literature. One possible addition is the energy from nuclear burning (e.g., Ivanova & Podsiadlowski, 2003). However, as pointed out by Ivanova et al. (2013b), when the donor's envelope is lifted from the core, the nuclear energy input is most likely going to decrease with respect to radiative losses from an expanding emitting area.[9]

Another addition to the energy budget that has been proposed is an enthalpy term $P/\rho$ (Ivanova & Chaichenets, 2011). While enthalpy is primarily responsible for energy redistribution (rather than being a new energy source Ivanova et al., 2013b), it leads to solutions with quasi-steady outflows from envelopes even before their total energy becomes positive. However, this requires the CE ejection to happen on a long thermal timescale (e.g., after a self-regulated spiral-in phase), at which point radiative losses increase significantly and our assumptions with $\alpha_{\rm CE} = 1.0$ are extremely optimistic (e.g., Clayton et al. 2017 find $\alpha_{\rm CE}$ between 0.046 and 0.25).

Here, we considered energy input from accretion $\Delta E_{\rm acc}$ estimated as Eddington luminosity of the compact accretor multiplied by 1000 yr, similarly to Voss & Tauris (2003) and Kruckow et al. (2016). It should be noted that the accretion rate does not need to be Eddington limited due to neutrino cooling and photon trapping inside the accretion flow inside the CE (e.g., Houck & Chevalier, 1991; Edgar, 2004; MacLeod & Ramirez-Ruiz, 2015a). Furthermore, in rare instances super-Eddington accretion during a CE phase could produce BHs with masses in the PISN mass gap (van Son et al., 2020). While the luminosity that is radiated away and absorbed by the surrounding envelope is still likely of the order of the Eddington luminosity, the total accretion luminosity estimated as $\eta \dot{M} c^2$ (with $\eta \sim 0.1$) could be in some cases much higher (MacLeod & Ramirez-Ruiz, 2015b; MacLeod et al., 2017; De et al., 2020). If the accretion is taking place through an accretion disk then polar outflows or jets could serve as a way of transferring this super-Eddington power to the envelope, thus helping in its ejection (Armitage & Livio, 2000; Soker, 2015). However, among other uncertainties related to this process, it is unclear whether a persistent accretion disk forms around an embedded compact object. Hydrodynamic simulations by Murguia-Berthier et al. (2017b) suggest that accretion through a disk is a rare and transitory phase, which may occur when a BH or a NS passes through zones of partial ionization in the outer envelope layers.

Apart from the uncertainties of the CE energy budget discussed above, there are caveats associated with calculations of envelope binding energies $E_{\rm bind}$ of massive giant donors. First,

[9] An exception could be nondegenerate accretors, e.g., low-mass MS stars (Podsiadlowski et al., 2010).

the value of $E_{\rm bind}$ can be very sensitive to the location of the bifurcation point, that is, the lower limit in the integral in Eq. 6.3. We discuss this further as a partial envelope ejection scenario in Sect. 6.4.6. Second, we used single stellar models to infer binding energies of stars which have most likely been mass gainers in a mass transfer phase in the past. While this is common practice, the envelope structure of a rejuvenated star could be quite different from that of a single unperturbed star of the same mass (Braun & Langer, 1995; Wellstein et al., 2001; Dray & Tout, 2007). Third, $E_{\rm bind}$ values computed from single stellar models represent the binding energy at the point of RLOF rather than at the onset of the CE phase. In reality, before the mass transfer rate increases sufficiently and the system becomes dynamically unstable, a giant donor is likely going to lose a sizable part of its envelope as a result of pre-CE mass transfer (MacLeod & Loeb, 2020a). This could mean that $E_{\rm bind}$ values relevant for the CE evolution are smaller than those calculated in Sect. 6.3.1. On the other hand, because most of the binding energy is located in deep envelope layers (those close to the helium core), a loss of even 30% of the mass from the outermost layers of a giant star does not necessarily have any significant impact on the total binding energy (Klencki et al., in prep.). Additionally, a pre-CE mass transfer from a donor that is more massive than the accretor is going to shrink the orbital separation even before the onset of the CE phase.

In summary, unless jets play a crucial role in driving CE ejection (e.g., Soker, 2015; Shiber et al., 2019), our model for the CE outcome and binary survival is optimistic with respect to more realistic assumptions. As such, the expectation that CE ejection in binaries with BH or NS accretors requires RSG donors currently appears quite robust. A possible alternative scenario of a partial envelope ejection followed by an immediate phase of stable mass transfer is suggested in Sect. 6.4.6.

### 6.4.2 UPPER LUMINOSITY LIMIT OF RSGS: INDICATION OF A MAXIMUM MASS BEYOND WHICH THE CE CHANNEL DOES NOT OPERATE?

We have shown that according to the current understanding of the CE evolution and based on unperturbed single star models of the donor star, a CE ejection in a BH binary is only possible if the CE phase was initiated by a convective-envelope donor. Observationally, such donors are cool supergiants (RSGs); see Fig. 6.6. Interestingly, there appears to be an upper RSG luminosity limit of $\log(L/L_\odot)_{\rm RSG;max} \approx 5.8$, which corresponds to $M_{\rm ZAMS} \approx 40\ M_\odot$, above which no RSGs are observed in the Milky Way or several other local galaxies of different types and compositions (see Sect. 6.3.3 and references therein). This leads to the question of whether stars with $M_{\rm ZAMS} \gtrsim 40\ M_\odot$ ever expand to become RSGs with significant outer convective envelopes, or whether the apparent limit $\log(L/L_\odot)_{\rm RSG;max}$ indicates a maximum donor mass of about $\sim 40\ M_\odot$ beyond which the CE channel does not operate. Such a limit would correspond to an upper limit on the secondary BH mass at about $\sim 20\ M_\odot$ (mass of the helium core of a $40\ M_\odot$ giant) as well as imply an upper limit on the primary BH mass at $M_{\rm BH;max} = M_{\rm RSG;max}/q_{\rm crit;conv} \approx$ 25-30 $M_\odot$ for $M_{\rm RSG;max} = 40\ M_\odot$ and $q_{\rm crit;conv} = 1.5$. This is in tension with observations as about half of the BBH merger detections reported to date are consistent with total binary masses beyond $50\ M_\odot$

(Abbott et al., 2019b). We note that this concern was first raised by Mennekens & Vanbeveren (2014) who argued that because stars with masses above 40 $M_\odot$ do not become RSGs, the formation of the most massive BBH mergers from isolated binary evolution is rather unlikely.

On one hand, it is possible that radial expansion of the most massive stars is quenched due to extensive mass loss before they reach the RSG stage (e.g., Vanbeveren, 1991; Vanbeveren et al., 1998; Smith, 2014). This is in line with the fact that the empirical HD limit in the upper right corner of the HR diagram (Humphreys & Davidson, 1979; Ulmer & Fitzpatrick, 1998), beyond which almost no stars are observed in the Milky Way or in the LMC, coincides with a significant increase in stellar winds and the occurrence of the luminous blue variable phenomenon (Humphreys & Davidson, 1994; Smith et al., 2011; Gräfener et al., 2012; Jiang et al., 2015, 2018). Alternatively, the upper right corner of the HR diagram might be unpopulated because of a currently unknown process that would prevent the formation of extended superadiabatic layers and density inversions in radiation-dominated envelopes of massive giants that evolve close to the Eddington limit; see Appendix A of Klencki et al. (2020). Stellar engineering solutions which effectively mimic such a process in 1D stellar codes (motivated to some extent by numerical difficulties that occur otherwise) produce evolutionary tracks with no RSGs above a certain luminosity limit. In the case of stars that were mass transfer accretors in the past (which is likely the case for stellar companions in BH binaries), they were shown to avoid the RSG stage in the non-rejuvenated cases, which could be relevant for stars that accreted during late MS stages or during their post-MS evolution (e.g., Braun & Langer, 1995), similarly to products of case B stellar mergers (Vanbeveren et al., 2013; Justham et al., 2014).

On the other hand, it is also possible that stars with $M_{\rm ZAMS} \gtrsim 40\ M_\odot$ do expand to the RSG stage but their RSG lifetime is very short (e.g., several hundred years), which is why they are not observed. This could be due to high mass-loss rates from loosely bound and turbulent convective envelopes of RSGs and a blueward evolution once most of the envelope is lost, as could be obtained in stellar tracks (e.g., Chen et al., 2015). It is also possible, especially at low metallicity (e.g., Klencki et al., 2020), that the RSG stage is reached very late into the evolution of a massive star, once most or all of the helium has been burnt in the core, resulting in a short RSG lifetime (Higgins & Vink, 2020).

At present, it remains unclear whether or not stars above $M_{\rm ZAMS} \approx 40\ M_\odot$ expand to the RSG stage during their evolution, especially in very low-metallicity environments for which observations are sparse. Therefore, the CE evolution channel could in principle produce BBH mergers with both component masses all the way up to the PISN mass gap. However, the lack of observations of RSGs above a certain luminosity limit is a warning sign which ultimately needs to be addressed in detail. Alternatively, if it is shown beyond doubt that most of the BBH merger population originates from the CE evolution channel, then their rate might be an indication that at least some of the stars more massive than 40 $M_\odot$ do reach the RSG stage but have so far eluded observation.

### 6.4.3 IMPLICATIONS FOR POPULATION SYNTHESIS AND MERGER RATES OF COMPACT BINARIES

Here we discuss the implications of our findings for the formation rate of compact binary mergers through the CE evolution channel. Given that the parameter space for mass transfer from convective-envelope donors is very small and limited to a narrow range in orbital periods (see Fig. 3 in Klencki et al. 2020), one may wonder whether it is possible for the CE evolution channel alone to explain the BBH merger rate inferred from observations, as reported by many authors in population synthesis calculations. At face value, this is not necessarily a problem because only a small fraction of all massive binaries need to finish their evolution as merging BBH systems in order to explain the local merger rate (roughly 1 every 100 systems, e.g., Chruslinska & Nelemans, 2019a; Neijssel et al., 2019; Giacobbo & Mapelli, 2020). In practice, however compact binary mergers in population-synthesis models originate from a much larger binary parameter space, with many systems evolving through a CE phase initiated by a nonconvective donor (de Mink & Belczynski, 2015a; Klencki et al., 2018). For instance, in a recent state-of-the-art population-synthesis model by Vigna-Gómez et al. (2020) only $\sim 20\%$ of CE episodes leading to the formation of a BNS merger were initiated by a cool supergiant with an outer convective envelope (in their dominant channel for the BNS formation).

There are two main reasons why, according to our findings, population-synthesis models tend to overpredict the number of systems that evolve through and survive a CE phase. First, following the BSE code (Hurley et al., 2002), it is customary for its successors to rely on evolutionary type of the donor (as defined in Hurley et al., 2000), rather than the type of its envelope, in order to choose the appropriate critical mass ratio or the value of $\zeta_{\rm ad}$ to determine mass transfer stability. In some cases this has led to erroneously applying stability criteria for convective-envelope donors (i.e., more prone to evolve through a CE phase) to all stars of the core-helium burning CHeB type: notably in the StarTrack population synthesis code (Belczynski et al., 2008a; Dominik et al., 2012; Belczynski et al., 2016b) as well as in the COMPAS code (Stevenson et al., 2017a; Vigna-Gómez et al., 2018). Donors of the CHeB type are especially common at subsolar metallicity environments, but most of them have outer radiative envelopes and only those that have expanded to the red-giant branch can be treated as convective-envelope donors (see Fig. 3 and Sect. 3.4 of Klencki et al., 2020). This mistake has led to an artificially increased number of CE evolution cases from CHeB donors in population synthesis, especially at low metallicity and in the mass regime of BH progenitors. Besides having an impact on the merger rates, it could be partly responsible for the significant preference for low metallicity in the formation of BBH mergers predicted by Belczynski et al. (2010b) as well as more recent population-synthesis models.[10]

Secondly, the envelope binding energies of massive radiative-envelope giants could be underestimated in some population-synthesis calculations, which tend to assume $\lambda_{\rm CE} = 0.05$ (e.g., Dominik et al., 2012; Belczynski et al., 2016b; Stevenson et al., 2017a; Neijssel et al., 2019) or

[10]The low metallicity is likely favored regardless because of weaker stellar winds, but possibly to a lesser extent than in most population-synthesis models.

0.1 (Mapelli et al., 2017; Giacobbo et al., 2018), while lower values of the order of $\sim 0.01$ would be more appropriate for stars with $M_{\rm ZAMS} \gtrsim 30\ M_\odot$ at the giant stage before an outer convective envelope is formed (see Fig. 6.17 as well as Podsiadlowski et al., 2003; Loveridge et al., 2011; Wang et al., 2016; Kruckow et al., 2016). [11] The assumption of $\lambda_{\rm CE} = 0.05 - 0.1$ is usually justified by the fits obtained by Xu & Li (2010). However, these latter authors only computed models with masses up to $M_{\rm ZAMS} = 20\ M_\odot$. In a later paper from the same group, Wang et al. (2016) extended the fits to higher masses and showed a further decrease in $\lambda_{\rm CE}$ down to $\sim 0.01$ for more massive and larger radiative-envelope giants, similar to other studies as well as in line with the results presented here in Sect. 6.3.1. In the case of convective-envelope giants, that is, also those with $M > 20\ M_\odot$, the binding energies can be much smaller (reaching $\lambda_{\rm CE}$ values as large as $\sim 0.2 - 0.3$), although that could strongly depend on the evolutionary stage of the star (see Sect. 6.3.4).

It should be noted that for the lowest metallicity studied here ($Z = 0.01\ Z_\odot$), we find a significant parameter space for CE ejectability also in the case of nonconvective donors, although only those with masses $M_{\rm ZAMS} < 50\ M_\odot$ (see Fig. 6.2 and Fig. 6.5). Whether that could be enough to reproduce the BBH merger rate is debatable. While in the current population-synthesis models the formation of BBH mergers is indeed most efficient at very low metallicity $Z \approx 0.01\ Z_\odot$ (e.g., Klencki et al., 2018; Neijssel et al., 2019; Graziani et al., 2020), its contribution has to be weighted by the corresponding fraction of the star formation rate (SFR) at $Z \approx 0.01\ Z_\odot$. Chruslinska & Nelemans (2019b) shows that this fraction is negligible in the local Universe and that it is still small within redshifts $z < 3$ (see their Fig. 8 and C.1). As a result, metallicity of the BBH merger population may actually peak at $Z > 0.01\ Z_\odot$ (Broekgaarden et al. in prep).

In summary, if our approach accurately predicts the upper limits on CE ejectability in binaries with BH or NS accretors and the CE survival is indeed only possible in the case of convective-envelope donors (see Sect. 6.4.1 for caveats), then the formation of compact binary mergers could be significantly overestimated in some population-synthesis models (i.e., by a factor of a few or more), especially at low metallicity. Additionally, whether or not massive stars ($\gtrsim 40\ M_\odot$) ever expand to become RSGs with outer convective envelopes during their evolution remains an open question (Sect. 6.4.2). If the answer is negative then that would further reduce the BBH merger population that could originate from the CE evolution channel, and indicate an upper limit on the primary BH mass at $\sim$ 25-30 $M_\odot$ and on the total BBH merger mass at about $\sim 50\ M_\odot$, in tension with the most massive BBH mergers detected to date (see Sect. 6.4.2 for details and also Mennekens & Vanbeveren, 2014). It is worth noting that in most population-synthesis models stellar tracks for $M_{\rm ZAMS} > 40\ M_\odot$ do expand to reach the RSG stage, with RSG luminosities above the observational upper limit at $\log(L/L_\odot)_{\rm RSG;max} \approx 5.8$.

[11] Whether $\lambda_{\rm CE}$ increases again once the outer convective envelope develops may depend on the evolutionary stage (see Sect. 6.3.4), with convective giants above a certain metallicity-dependent mass possibly maintaining $\lambda_{\rm CE} \approx 0.01$.

### 6.4.4 TIDAL SPIN-UP IN CLOSE BH-WR BINARIES

In the previous sections we discussed how the formation of BBH mergers through the CE evolution channel is most likely only possible if the CE phase is initiated by a massive convective-envelope donor, that is, a cool supergiant. Interestingly, low metallicity models of massive stars ($Z \lesssim 0.2\ Z_{\odot}$) often expand to the convective-envelope stage very late in their evolution, during advanced burning stages after core-helium depletion, just several thousand years away from the core-collapse (see Fig. 6.2 as well as Fig. 3 in Klencki et al., 2020).

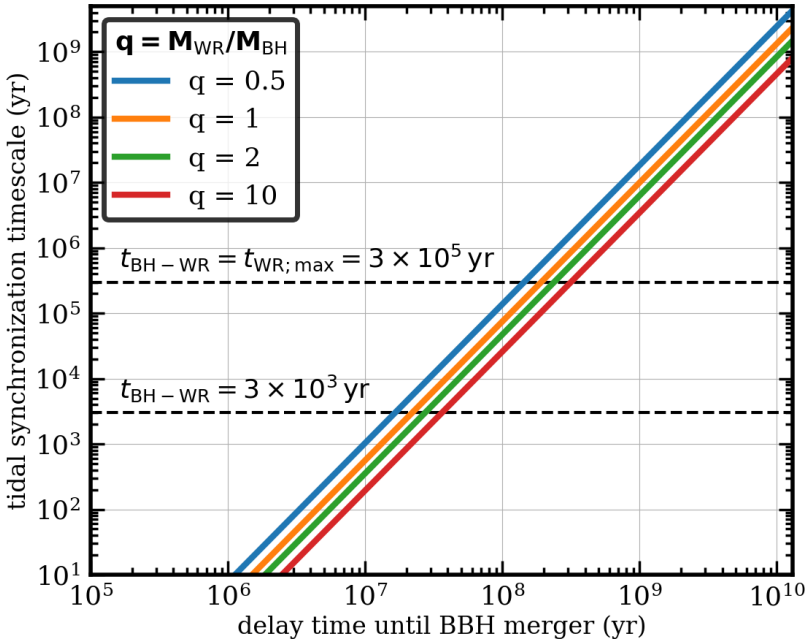


FIGURE 6.9: Relation between the tidal synchronization timescale in a BH-WR binary and the delay time (between the formation and the merger) of the corresponding BBH system plotted for several different mass ratios $q = M_{\rm WR}/M_{\rm BH}$, using Eq. 14 from Kushnir et al. (2016). Tidal interactions can efficiently spin-up the WR star only if the synchronization timescale is shorter than the BH-WR binary lifetime $t_{\rm BH-WR}$. The two dashed horizontal lines mark two different values of $t_{\rm BH-WR}$: roughly the maximum WR lifetime $\sim 3 \times 10^5$ yr, assumed by several authors (e.g., Kushnir et al., 2016; Hotokezaka & Piran, 2017b; Piran & Hotokezaka, 2018), and a significantly smaller value $t_{\rm BH-WR} = 3 \times 10^3$ yr which is more realistic in the case of the CE channel at low metallicity.

The remaining lifetime of the donor star is a strict upper limit on the duration of the subsequent BH–WR stage, which is a stage that likely follows right after the CE is ejected. Close BH–WR binaries are speculated to be the most immediate progenitors of BBH systems that merge within the Hubble time. In fact, several examples of such systems are known and observable as bright X-ray sources (e.g., Carpano et al., 2007; Bulik et al., 2011; Belczynski et al., 2013; Liu et al., 2013). It was proposed that the interplay between tidal interactions (spin-up) and the wind mass-loss (spin-down of the WR star) during the BH-WR stage is crucial for the final WR spin value and that in systems with a sufficiently small separation the WR star should always be critically spinning at core collapse (Kushnir et al., 2016). Several authors predict that if some of the BBH

LIGO/Virgo sources were formed by binary evolution then tidal spin-up during the BH-WR stage would have to be responsible for a subpopulation of BBH mergers in which the secondary BH is formed with the maximum spin ($a = 1$) and the effective spin $\chi_{\rm eff}$ is positive (Hotokezaka & Piran, 2017b,a; Zaldarriaga et al., 2018; Piran & Hotokezaka, 2018). The recently announced discovery of GW190412 (The LIGO Scientific Collaboration et al., 2020a), a BBH merger with $\chi_{\rm eff} = 0.17 - 0.59$ or $\chi_{\rm eff} = 0.64 - 0.99$, depending on the choice of the priors (Mandel & Fragos, 2020), might be the first representative of this subpopulation.

However, if the duration of the BH-WR stage $t_{\rm BH-WR}$ at low metallicity is typically very short (several thousand years), as suggested by the considerations above, then the BH-WR binary needs to be extremely compact for any significant spin-up of the WR star. Binary separation at the BH–WR stage can be related to the separation of the descendant BBH system, which in turn is the main factor determining the delay time until the BBH merges due to GW emission. Kushnir et al. (2016) derived an approximate relation between the tidal synchronization timescale of a BH–WR binary and the delay time of a corresponding BBH system $t_{\rm delay}$ (see their Eq. 14). In Fig. 6.9, we plot this relation for several different mass ratios. We also mark two values of $t_{\rm BH-WR}$: the approximate CHeB duration of massive stars, which is the maximum lifetime of a WR star, $\sim 3 \times 10^5$ yr, as assumed by several authors (e.g.. Kushnir et al., 2016; Hotokezaka & Piran, 2017b; Piran & Hotokezaka, 2018), and a significantly smaller value $t_{\rm BH-WR} = 3 \times 10^3$ yr which is more realistic in the case of CE evolution at low metallicity. Figure 6.9 shows that for short BH–WR lifetimes of several thousand years, only BBH mergers with very short delay times ($\lesssim 30$ Myr) can have the spin of the secondary BH affected by tidal spin-up. It is currently unknown whether BBH mergers with such short delay times can form in the CE evolution channel. If such systems are nonexistent or very rare then our results indicate that tidal spin-up during the BH-WR stage is unlikely to have any significant effect on the $\chi_{\rm eff}$ distribution of local BBH mergers, especially these formed at low metallicity.

### 6.4.5 Common-envelope ejection in BH-LMXB progenitors

Most of the known Galactic BHs reside in BH-LMXBs in which the companion is typically a MS star with $M \lesssim 1\ M_\odot$ and the orbital period is very short (usually $< 1$ day) (Casares & Jonker, 2014; Tetarenko et al., 2016b). The formation of such systems is a long-standing puzzle. Given the extreme mass ratio and small separation of BH-LMXBs, their progenitors have most likely evolved through a CE phase. However, it was argued by several authors on the basis of energy budget considerations that a secondary of only $\lesssim 1.5\ M_\odot$ would not be able to provide enough energy to unbind the envelope of a massive BH progenitor (Portegies Zwart et al. 1997; Kalogera 1999; Podsiadlowski et al. 2003; Justham et al. 2006; Yungelson & Lasota 2008, although see Yungelson et al. 2006). This led to the suggestion of an extremely high CE efficiency, that is, a possibility of $\alpha_{\rm CE}$ larger than 1 (even as high as a few tens in the case of BH-LMXBs). This apparent violation of energy conservation could be interpreted as some unknown mechanism that is unaccounted for in the standard energy budget (e.g., Podsiadlowski et al., 2010). The assumption of $\alpha_{\rm CE}$ larger than

1 has also made its way to population-synthesis models of compact binary mergers (e.g., Giacobbo & Mapelli, 2018; Evans et al., 2020).

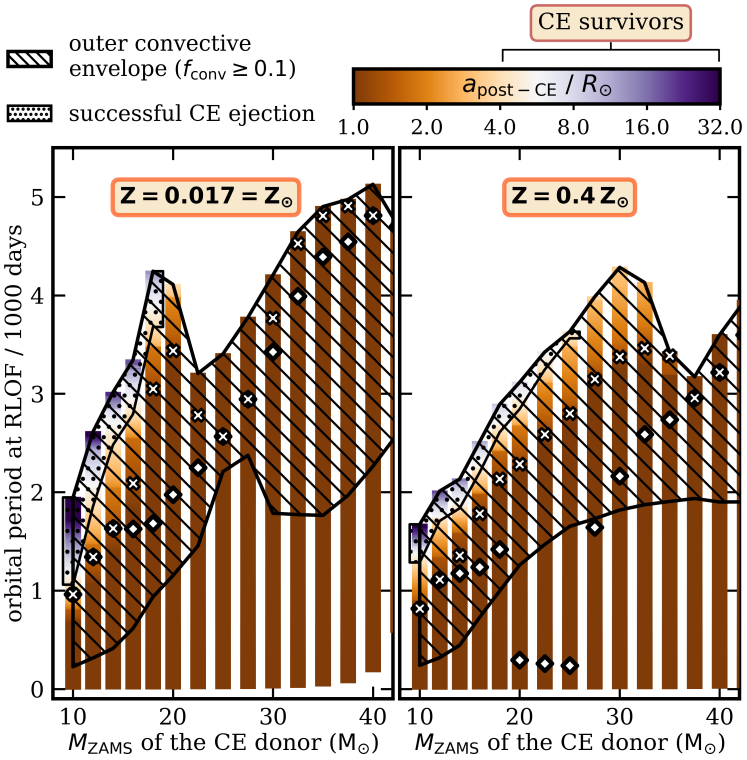


FIGURE 6.10: Common-envelope ejectability in binaries with a massive donor ($M_{ZAMS} = 10 - 40\ M_\odot$) and a low-mass secondary of 1.0 $M_\odot$, shown for two metallicites that are the most relevant for the Milky Way. Notation is the same as in Fig. 6.2, except that the Y-axis shows orbital period instead of the donor radius and the color indicates the post-CE orbital separation $a_{post-CE}$ estimated from the energy budget (Sect. 6.2.3) without the accretion term $\Delta E_{acc}$. Separations $a_{post-CE} \approx 4 - 10\ R_\odot$ are in line with the formation of the observed population of short-period BH-LMXBs (Kalogera, 1999; Repetto & Nelemans, 2015).

Interestingly, the binding energies of convective-envelope supergiants at advanced evolutionary stages (Fig. 6.1) described in detail in Sect. 6.3.4 are low enough to allow for a CE ejection even in the case of low-mass secondaries, without the need for $\alpha_{CE} > 1$. Figure 6.10, which is similar to Fig. 6.2, shows CE ejectability in binaries with massive CE donors ($M_{ZAMS} = 10 - 40\ M_\odot$) in which the companion is a 1.0 $M_\odot$ star, that is, potential BH-LMXB progenitors (depending on the minimum mass required for the formation of a BH). Post-CE separations $a_{post-CE}$, color-coded in the figure, follow from the energy budget described in Sect. 6.2.3 without the energy term from accretion (due to the stellar nature of the secondary). Separations within $a_{post-CE} \approx 4 - 10\ R_\odot$ agree well with the estimated separations of short-period BH-LMXB progenitors at the moment of the BH formation (Kalogera, 1999; Repetto & Nelemans, 2015). We note that at solar metallicity (the left panel) the decrease in envelope binding energy of convective-envelope giants is quenched for masses $M_{ZAMS} \gtrsim 20\ M_\odot$ due to mass loss in our models (see also Podsiadlowski et al., 2003, and Fig. 6.1). If $M_{ZAMS} \approx 20\ M_\odot$ is the minimum mass required for the formation of a BH then none of the survivors in the left panel of Fig. 6.10 could be progenitors of BH-LMXBs. However, at the lower metallicity of $Z = 0.4\ Z_\odot = 0.0068$ the range of survivors extends to $M_{ZAMS} = 25\ M_\odot$ (the right panel). Given that the average metallicity of the Milky Way stars is subsolar (e.g., $Z = 0.0088$ with the assumptions taken by Brott et al., 2011a), Fig. 6.10 suggests that at least some of the Galactic BH-LMXBs could be formed through CE evolution without $\alpha_{CE}$ exceeding 1. Moreover, as pointed out by Yungelson et al. (2006), because mass-loss rates from massive

stars are uncertain, it is possible that for a different set of mass-loss assumptions the range of CE survivors at the solar metallicity would extend to $M_{\rm ZAMS} > 20\ M_\odot$ as well (Smith, 2014; Renzo et al., 2017). Finally, there might be islands of nonexplodability in the lower ZAMS mass range where some progenitors with $M_{\rm ZAMS} < 20\ M_\odot$ end their lives in failed explosions and produce BHs as well (O'Connor & Ott, 2011; Ugliano et al., 2012; Ertl et al., 2016, 2020; Couch et al., 2020; Patton & Sukhbold, 2020).

A separate question is whether the parameter space for CE ejection in Fig. 6.10 is large enough to produce the entire Galactic population of BH-LMXBs, something that population-synthesis models have been struggling with (e.g., Wiktorowicz et al., 2014). Notably, other formation channels for BH-LMXBs have also been suggested, for example intermediate-mass X-ray binaries with magnetic donors (Justham et al., 2006), formation in hierarchical triplets (Naoz et al., 2016), or dynamical formation through tidal capture in the field (Michaely & Perets, 2016; Klencki et al., 2017).

### 6.4.6 Alternative scenario: partial envelope ejection followed by stable mass transfer

It is well known that the binding energy of a giant star is very sensitive to the exact location of the core-envelope boundary for CE ejection, that is, the bifurcation point (Dewi & Tauris, 2000; Tauris & Dewi, 2001; Ivanova, 2011a; De Marco et al., 2011; Kruckow et al., 2016). This is because most of the binding energy is stored is deep envelope layers close to the helium core (see Fig. 6.7e and Fig. 6.8e as well as Fig. 3 in Kruckow et al. 2016). As a result, moving the bifurcation point upwards by even a few percent of the total mass of a giant may reduce the envelope binding energy by an order of magnitude or even more. Here, following Ivanova (2011a), the bifurcation point is assumed to be the maximum compression point $M_{\rm cp}$ within the H-burning shell (i.e., a local maximum of $P/\rho$), which in massive evolved stars corresponds very well to the point of steep composition gradient at the hydrogen abundance $X_{\rm H} \sim 0.05 - 0.15$. This is a standard assumption made across the recent literature (Xu & Li, 2010; Loveridge et al., 2011; Wang et al., 2016; Kruckow et al., 2016).

Interestingly, in the envelope structure of a $\sim 35\ M_\odot$ convective giant at $Z = 0.4\ Z_\odot$ in Fig. 6.8 (originally $M_{\rm ZAMS} = 47.5\ M_\odot$), the layers above the bifurcation point, located at $M_{\rm cp} \approx 23\ M_\odot$, are still compressed at very compact radial coordinates $R < 5\ R_\odot$; see Fig. 6.8c. These layers are helium rich ($X_{\rm He} \approx 0.75$) and extend out to mass coordinate $M \approx 26\ M_\odot$ at which point a steep density and composition gradient separates them from the loosely bound outer convective zone. As the model evolves from yellow to red profiles in Fig. 6.8c, when a significant amount of mass ($\sim 10\ M_\odot$) is being lost in winds and the envelope becomes increasingly convective, the entire inner part of the star out to $M \approx 26\ M_\odot$ contracts slightly while the layers above are expanding. We find that such an envelope structure is characteristic of massive giants that become convective as a result of a rapid expansion during the HG phase. It is distinctively different from the structure of low-mass red giants or massive giants that develop outer convective zones at a more advanced

evolutionary stage (e.g., Fig. 6.7), in which the convective zone can extend deep down close to the helium core and the maximum compression point is also a clear divergence point between the expanding and contracting parts of the star.

Given the compact size of layers above the helium core in the model from Fig. 6.8, it is possible to imagine a partial envelope ejection in which only the extended and loosely bound outer part of the envelop is ejected during the CE phase (at mass coordinates $> 26\ M_\odot$). This would imply a bifurcation point located at $\sim 3\ M_\odot$ above the standard core-envelope boundary and a much lower envelope binding energy. For such a partial envelope ejection during inward spiralling of a CE to be possible, the helium-rich layers at the bottom of the envelope are likely required to remain compact during mass loss from the outer envelope layers taking place on the short CE timescale. Whether or not this is likely to happen needs to be confirmed with detailed stellar models. The first step has recently been carried out by Fragos et al. (2019), who, in their hydrodynamic 1D model of an inwardly spiralling NS inside the envelope of a $12\ M_\odot$ giant, found evidence for a CE ejection at a point when some of the envelope layers ($\sim 0.3 - 0.5\ M_\odot$ with $X_{\rm He} \approx 0.7$ ) still remain on top of the helium core.

A separate but important question is what would happen with the system right after such a CE phase. One possibility is that the partially stripped donor star would re-expand again on the thermal timescale ($\sim 100 - 1000$ yr) leading to RLOF and another phase of mass transfer, as also discussed by Kruckow et al. (2016). Such behavior was found by Ivanova (2011a) in models of stripped giants with remaining masses above the maximum compression point. Interestingly, Quast et al. (2019) recently showed that mass transfer from a massive giant that has been stripped down to its deep helium-enriched layers could be stable for significantly unequal mass ratios and proceed on a long nuclear timescale of core-helium burning ($\sim 10^5$ yr) with a super-Eddington mass transfer rate. Taken together, these results support the idea of an alternative scenario to the classical evolution through a CE phase: a scenario in which a partial envelope ejection during the CE phase is followed by a long-lasting phase of stable mass transfer from a helium-enriched star, likely a blue supergiant, during which the system appears as a ULX.

It should be noted that the high mass-transfer stability in models by Quast et al. (2019) was obtained only if the giant was to lose most but not all of its envelope during the CE phase ($\gtrsim 90\%$ in mass), at which point the helium-rich layers close to the helium core would be brought to the surface. At a first glance, this suggests that a certain level of fine-tuning is required. On the other hand, Quast et al. (2019) only explored synthetic models with simple internal abundance profiles. In real supergiants, depending on the size of the ICZ above the H-burning shell during the previous evolution, helium-rich layers ($X_{\rm He} \sim 0.5 - 0.7$) might extend to layers located significantly higher up inside the envelope (e.g., Figs 6.7d and 6.8d). This could also be the case for accretors from a past mass transfer phase, especially if a significant amount of He-rich material was accreted. Such a structure could possibly support stable mass transfer evolution also when a different, smaller part of the H-rich envelope is ejected in the CE phase, especially at lower metallicity where stripped stars are more compact (Götberg et al., 2017, 2018; Klencki & Nelemans, 2019; Laplace et al., 2020).

The final separation of a binary system once both a partial envelope ejection and a further mass transfer phase are concluded depends on the mass of the compact accretor, how conservative the second stable mass transfer is, and how much angular momentum is carried away in the nonaccreted matter. For instance, Fragos et al. (2019) estimated that a potential post-CE mass transfer phase would further decrease the separation in their binary of a 1.4 $M_\odot$ NS and a 3.2 $M_\odot$ stripped donor by a factor of $\sim$ 1.5. This, combined with the orbital shrinkage during the CE phase, can be translated into a single effective $\alpha_{\rm CE}$ value. In the case of the system computed by Fragos et al. (2019), the authors estimated an effective ratio $\Delta E_{\rm grav}/\Delta E_{\rm orb} = \alpha_{\rm grav} \approx 5$, which roughly translates to $\alpha_{\rm CE} \approx 2$, essentially indicating a more likely CE ejection and binary survival compared to the classical picture of CE evolution in which the entire envelope is ejected immediately. [12] In the case of more massive accretors, such as for example typical stellar BHs, the orbital separation would likely decrease less or even increase as a result of a more equal mass ratio during the stable mass transfer phase, thus producing intermediate- rather than short-period systems. The fact that some of the recently ejected matter from the CE phase would likely still remain in the proximity of the system (e.g., as a circumbinary disk) makes predictions for the evolution of orbital parameters rather uncertain. The alleged noninteracting BH binary system with orbital period of $\sim$ 83 days and a companion $\sim$ 3 $M_\odot$ star discovered by Thompson et al. (2019), although see van den Heuvel & Tauris (2020) and Thompson et al. (2020), might be a product of such an evolution if a CE phase was initiated by the BH massive progenitor.

In summary, a different location of the bifurcation point in supergiant donors would result in lower envelope binding energies and could in principle allow for CE ejections even in the case of nonconvective donors. It would also lead to another phase of mass transfer after the end of the CE phase. It seems unlikely that close (merging) BBH systems could be the final product of such an evolution but if they were then the corresponding BBH merger rate could possibly be linked to the number density of observed ULX sources (Inoue et al., 2016; Finke & Razzaque, 2017; Klencki & Nelemans, 2019; Mondal et al., 2020).

## 6.5 Conclusions

We studied envelope binding energies in detailed massive stellar models at different evolutionary stages and metallicities in order to decipher the kinds of binaries with BH or NS accretors and supergiant donors that could realistically be expected to evolve through and survive a CE phase, thus making them potential progenitors of compact binary mergers. In pursuit of the most optimistic case, we assumed an extreme version of the CE energy budget, in which all the energy sources are fully efficient (orbital shrinkage, internal energy, recombination energy, energy from accretion), energy sinks are neglected (e.g., no energy loss in radiation), and the envelope acceleration is perfectly fine-tuned to the local escape velocity. We computed envelope binding energies from detailed stellar models of massive stars ($M_{\rm ZAMS}$ between 10 and 80 $M_\odot$) at six different

[12] We note that $\alpha_{\rm CE}$ from the notation of Fragos et al. (2019) is the same as $\alpha_{\rm grav}$ in ours.

metallicities from $Z = 0.017$ to 0.00017 and taking $X_{\rm H} = 0.1$ criteria for the bifurcation point. We assumed that the CE evolution occurs in binaries with BH or NS accretors with mass ratios $q = M_{\rm donor}/M_{\rm accretor}$ larger than $q_{\rm crit;rad} = 3.5$ for radiative-envelope donors and $q_{\rm crit;conv} = 1.5$ for convective-envelope donors. This choice might be optimistic in view of the recently found increased stability of mass transfer from massive giant donors (Ge et al., 2015; Pavlovskii et al., 2017). Our findings are summarized below.

– Envelope binding energy of a supergiant depends very strongly on not only the envelope type (convective vs. radiative) but also the evolutionary stage, which in turn is related to metallicity. The binding energy can decrease very significantly (by more than an order of magnitude) when the envelope becomes convective during core-helium burning or at a later evolutionary stage. However, a transition from a radiative to a convective state in an envelope of a rapidly expanding HG giant does not affect the binding energy nearly as significantly. As a result, through its impact on the radial expansion of massive giants, metallicity could have an indirect but very strong effect on the binding energies of convective-envelope giants and may be a crucial factor determining the fraction of systems surviving the CE phase. This conclusion depends on the presence of the ICZ during the HG phase. In Appendix 6.A we provide fits to $\lambda_{\rm CE}$ values which can be used in population-synthesis calculations.

– Survival of the CE phase in binaries with BH or NS accretors is strongly limited to cases in which the donor star is a convective-envelope red supergiant. This is the case even under several optimistic assumptions working in favor of an easier CE ejection. Ultra-luminous X-ray sources with RSG donors might be the immediate progenitors of such CE events and subsequent compact binary mergers.

– If stars above $\sim 40\ M_\odot$ never expand to the RSG stage, as suggested by the empirical upper luminosity limit of RSGs at $\log(L/L_\odot)_{\rm RSG;max} \approx 5.7$, then our result indicates an upper limit on the total BBH merger mass at about $\sim 50\ M_\odot$ and the primary BH mass at $\sim$ 25-30 $M_\odot$. This would be in tension with the CE channel being the origin of about half of the BBH mergers detected to date.

– Merger rates of compact binaries formed through the CE evolution might be severely overestimated in some of the recent population-synthesis models due to (a) extrapolation of $\lambda_{\rm CE}$ values fitted to $M_{\rm ZAMS} \leq 20\ M_\odot$ models to obtain binding energies of much more massive stars (with $M_{\rm ZAMS}$ as high as $100 - 150\ M_\odot$) and (b) a practice of treating all core-helium burning stars as convective-envelope giants. The latter issue is likely partially responsible for the significantly higher formation rate of BBH mergers at low metallicity in these models.

– Lifetimes of close BH-WR systems (i.e., CE survivors) formed at low metallicity are typically very short (several thousand years), especially at $Z \leq 0.1\ Z_\odot$. Only those with the smallest orbital separations, producing BBH mergers with short delay times ($\lesssim 30$ Myr), are likely to experience any significant tidal spin-up of the WR star.

– Models at $M_{\rm ZAMS} \lesssim 20{-}40\ M_\odot$ (depending on $Z$) remain RSGs at advanced evolutionary stages after the end of core-helium burning. Their envelopes can become deeply convective, leading to exceptionally small binding energies ($\lambda_{\rm CE} \sim 1.0$). For such donors, CE ejections appears

energetically possible even for low-mass (1 $M_\odot$) MS accretors, making them potential progenitors of BH-LMXBs without the need for $\alpha_{\rm CE} > 1.0$.

– Envelopes of more massive stars ($M_{\rm ZAMS} \gtrsim 40\ M_\odot$), even if they reach the RSG stage, never become fully convective as their $M_{\rm conv}/M_{\rm env}$ ratio does not exceed $\sim 0.7$. In some models, layers above the helium core remain very compact ($< 5\ R_\odot$) all the way up to a steep density gradient near the bottom of the convective envelope, which revives the question of the exact location of the core-envelope boundary in CE evolution. Eventual partial envelope ejection during the CE phase would likely lead to another, possibly stable and long-lasting phase of mass transfer.

– Because of its influence on the radial expansion of massive giants, metallicity affects the degree of internal mixing in deep envelope layers of supergiants. As a result, two RSGs similar in terms of mass, radius, and luminosity but of differing metallicity can have very different chemical profiles, density structures, and envelope binding energies. This might need to be taken into account when constructing RSG models for an input to hydrodynamic simulations of the CE phase.

**Acknowledgements**

We would like to thank the anonymous referee for a very thorough review and multiple useful comments and suggestions that helped to improve this work. The authors acknowledge support from the Netherlands Organisation for Scientific Research (NWO). It is a pleasure to acknowledge valuable discussions and suggestions from Alejandro Vigna-Góomez, Natasha Ivanova, Nadia Blagorodnova, Morgan MacLeod, Onno Pols, Kristhell López, Marianne Heida, Karel Temmink, Glenn-Michael Oomen, Raphael Hirschi, Stephen Justham, Selma de Mink, and Ilya Mandel.

## 6.A Common-envelope binding energy parameter fits

To facilitate the use of our results for instance in population-synthesis studies, we provide fits to the $\lambda$ parameter, which is commonly used to describe the binding energy of the envelope and relate it to the properties of the donor star in CE phase (see Eq. 6.4). We fit $\log_{10}(\lambda)$ as a function of the radius of the giant donor star $\log_{10}(\mathrm{R})$ with a third-order polynomial:

$$\log_{10}(\lambda) = \mathrm{a_i}\log_{10}(\mathrm{R}/\mathrm{R}_\odot)^3 + \mathrm{b_i}\log_{10}(\mathrm{R}/\mathrm{R}_\odot)^2 + \mathrm{c_i}\log_{10}(\mathrm{R}/\mathrm{R}_\odot) + \mathrm{d_i}. \tag{6.5}$$

The fit is divided in three ranges in R: coefficients with i=1 are applicable for $\mathrm{R} < \mathrm{R}_{12}$, those with i=2 describe $\lambda$ between $\mathrm{R}_{12} < \mathrm{R} < \mathrm{R}_{23}$ , and those with i=3 describe $\lambda$ between $\mathrm{R}_{23} < \mathrm{R} < \mathrm{R}_{\rm max}$. The fitted coefficients and ranges depend on the stellar mass and metallicity and are given for each of the stellar models considered in this study under the following url: `https://ftp.science.ru.nl/astro/jklencki/`. The example fit for 10, 20, and 40 $M_\odot$ models at Z=0.2 $Z_\odot$ is shown in Fig. 6.11. Below $R_{12}$ (cyan diamond in Fig. 6.11), $\lambda$ decreases monotonically as a function of radius. The relation starts to bend around $R_{12}$, when the mass fraction in the convective envelope increases (except for the highest stellar masses $\gtrsim 50\ M_\odot$ at the highest metallicities considered in this study, see Sect. 6.3.1). In our fits, $R_{12}$ corresponds to the radius at which the effective temperature reaches the value below which at least 10% of the outer mass in a star becomes convective (see Fig.

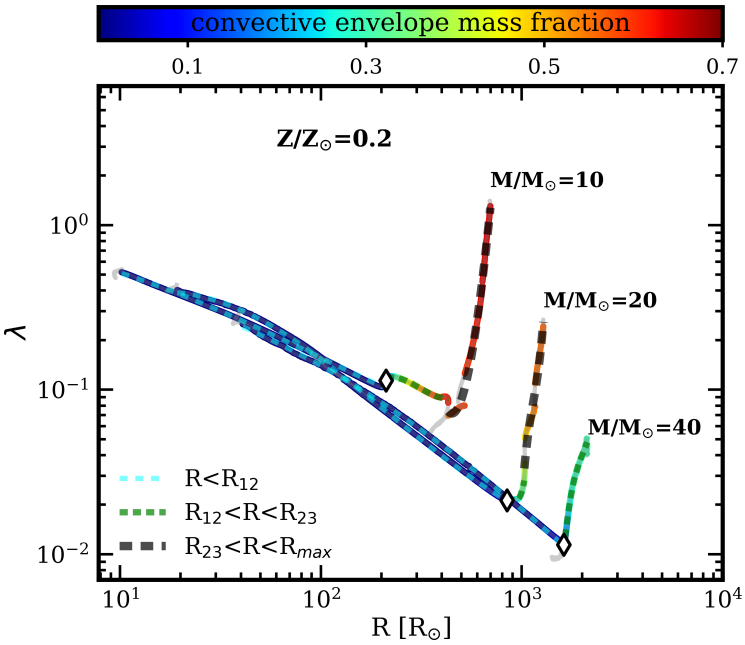


FIGURE 6.11: Polynomial fits to CE binding energy parameter ($\lambda$) as a function of radius shown for three example stellar models. The dashed lines in different colors indicate different ranges in which the fits have been made. The cyan diamond indicates the radius at which at least 10% of the mass of the envelope becomes convective, separating the first and the second fitted ranges. The background lines are colored according to the convective envelope mass fraction. The gray parts, where the radius was smaller than the maximum radius reached during the previous evolution, were not included in the fit.

6 in Klencki et al. 2020). The third range $R_{23}$ <R< $R_{max}$ was introduced to improve the quality of the fit at the highest radii, where $\lambda$ rapidly increases. For the most massive donors, the third range is not necessary (in those cases $R_{23} = R_{max}$). Only the parts where the radius of the star increases beyond the largest radius reached during its previous evolution (relevant for the onset of the mass transfer and common envelope) are included in the fit.

## 6.B NUMERICAL ROBUSTNESS OF MODELS

### 6.B.1 THE SETUP

In this section, we explore the numerical robustness of models from Klencki et al. (2020) (analyzed in this work) with respect to variations in spacial and temporal resolution. For an example of what an extended analysis of this kind could look like, we refer the reader to Farmer et al. (2016). Here, we mainly emphasize the model properties that are the most relevant in the context of CE evolution: the internal envelope structure and the envelope binding energy. MESA offers various controls to specify the mass (spacial) resolution of a model. One such parameter is `mesh_delta_coeff` which controls the global factor limiting the allowed change in stellar structure quantities between two adjacent cells. Lowering the value of `mesh_delta_coeff` leads to a higher number of cells (roughly by the same factor). The default value in MESA is `mesh_delta_coeff` = 1.0, whereas the default value for the models used in this work is `mesh_delta_coeff` = 0.8. Here, we also test `mesh_delta_coeff` = 0.6 (variation a). Another parameter controlling mass resolution is `max_dq`, which sets the maximum cell mass in units of the mass of the star. The default MESA

value is max_dq = $10^{-2}$, whereas the value used by Klencki et al. (2020) is max_dq = $10^{-3}$. Here, we also test max_dq = $3.3\times10^{-4}$ (variation b). Apart from the two mesh controls mentioned above, models from Klencki et al. (2020) were computed with increased spacial resolution in regions with high H/He abundance gradients; see https://zenodo.org/record/3740578#.X1s21nVfguw for all the input MESA files.

As in the case of spacial resolution, MESA offers a large variety of parameters to control the time-step. One such parameter is varcontrol_target, which controls the maximum allowed relative change in stellar structure quantities between two subsequent time-steps (if the change is greater, then the time-steps needs to be reduced). The default value in MESA as well as in the models used in this work is varcontrol_target = $10^{-4}$. Here, we also explore a variation with varcontrol_target = $3.3\times10^{-5}$ (variation c). Another relevant parameter is delta_HR_limit, which limits the change in position in the HR diagram between two subsequent time-steps. This is particularly important during the phase of evolution right after the end of MS when a star is rapidly expanding on a short thermal timescale, the core is contracting, and a convective zone is typically forming above the hydrogen burning shell (e.g., Langer et al., 1985; Schootemeijer et al., 2019; Klencki et al., 2020). In default MESA, this control is disabled, whereas the models used in this work take delta_HR_limit = $10^{-3}$. Here, we also test the value delta_HR_limit = $3.3\times10^{-4}$ (variation d).

To get a better idea of the numerical robustness of our models, we computed four variations (a-d) described above, two with increased spacial resolution and two with increased temporal resolution. For each variation we computed stellar models at ten different masses: 12, 16, 20, 25, 32.5, 40, 47.5, 55, 65, and 80 $M_\odot$. We explored four different metallicities: 0.4, 0.2, 0.1, and 0.04 $Z_\odot$ (with $Z_\odot = 0.017$).

### 6.B.2 NUMERICAL ROBUSTNESS: ENVELOPE BINDING ENERGIES

In Fig. 6.12, similarly to Fig. 6.1, we compare the envelope binding energies (plotted as a function of the stellar radius) in four numerical variations with the default models used throughout this study. We plot selected models at ten different masses and four different metallicities as listed above. Diamonds mark the onset of core-helium burning ($Y_C$ drops below 0.975), crosses indicate central helium depletion ($Y_C < 0.001$). Shaded regions mark the area of uncertainty span by model variations, with interchanging colors to increase readability. We note that only the post-MS evolution is included in the figure. For simplicity, the end of MS is determined based on the helium core mass becoming nonzero in MESA but it coincides quite well with a condition $X_C < 10^{-6}$ (i.e. core-hydrogen depletion).

There are three ways in which the numerically varied models are different from the default ones. First, there are clear discrepancies in the evolution of the most massive models right after the end of the MS (except for the lowest metallicity 0.04 $Z_\odot$). We find that these models are numerically not robust (not converged) in terms of their stellar radii at terminal-age MS (TAMS) and also during the final MS stages. For instance, numerical variations in the three most massive models at 0.4 $Z_\odot$

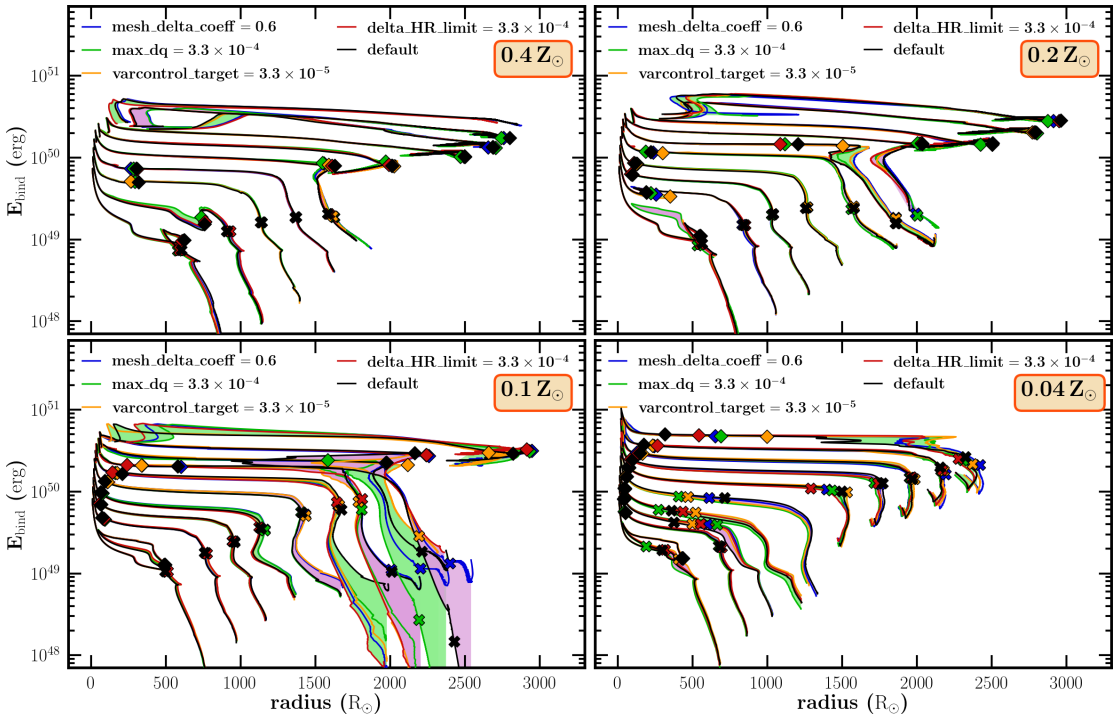


FIGURE 6.12: Comparison between the envelope binding energies $E_{\rm bind}$ of selected stellar models computed with the default assumptions (black line) and in four model variations with increased spacial or temporal resolution (see text for details), plotted as a function of the stellar radius. Selected stellar masses are 12, 16, 20, 25, 32.5, 40, 47.5, 55, 65, and 80 $M_\odot$. Each panel shows a different metallicity. Diamonds mark the onset of core-helium burning, crosses indicate central helium depletion. Shaded regions mark the area of uncertainty span by model variations, with interchanging colors to increase readability. We note that only the post-MS evolution is included in the figure. Differences between the models are likely mainly due to envelope inflation and density inversions in the outer envelopes; see text for details. None of the numerical difficulties affect the conclusions of this study.

(55 $M_\odot$, 65 $M_\odot$, and 80 $M_\odot$) show changes in the TAMS radius as large as 100 – 200 $R_\odot$. Even larger is the numerical noise in the TAMS radius of the 80 $M_\odot$ models at 0.1 $Z_\odot$ (spread from $\sim$ 130 to 550 $R_\odot$) and, especially, the 80 $M_\odot$ models at 0.2 $Z_\odot$ metallicity ($\sim$ 1000 – 1200 $R_\odot$ for models with increased spacial resolution, $\sim$ 550 $R_\odot$ otherwise). The problems arise due to envelope inflation which occurs in these models during late stages of MS (e.g., Gräfener et al., 2012; Sanyal et al., 2015, 2017) and poses a well-known numerical challenge for 1D stellar codes of computing extremely diluted radiation-dominated envelopes with a density inversion (see Sect. 7 in Paxton et al. 2013 and Appendix A in Klencki et al. 2020). Notably, it was shown that in 3D simulations the envelopes do not become as inflated as in 1D stellar models (i.e., the radius is smaller Jiang et al., 2018), which shows the limitations of 1D codes in computing the radii of very massive MS stars. In the context of the present study and CE ejectability, uncertainty in the final MS radii leads to uncertainty in the exact size and shape of the excluded MS area in Fig. 6.2.

Second, Fig. 6.12 shows significant differences between the stellar radii of some of the models at the RSG stage (typically the more massive ones), when the star is already expanded to its almost

largest radius and the outer convective zone is growing. Once again, during this part of the evolution a density inversion is particularly large, which leads to numerical difficulties. This is also when the superadiabatic layer, where the convection becomes supersonic and the mixing-length theory is outside its region of applicability, is the most extended. As such, paraphrasing Paxton et al. (2013), stellar radii of massive RSGs from any 1D stellar evolution calculation should be considered highly uncertain. Notably, much of the radius uncertainty is associated with the period of temporary contraction in models that reach the RSG stage before the onset of core-helium burning. In the context of binary evolution and a possibility of RLOF, this phase is not very relevant and does not affect out results. The more important is the uncertainty in the maximum radius reached during the phase of rapid HG expansion, which is just before the above-mentioned occasional contraction. In this case the numerical noise is less consequential: the typical radius variations are smaller than 5% with an exception of the 55 $M_\odot$ models at 0.1 $Z_\odot$ ($\sim$ 10% uncertainty).

Apart from discrepancies in the stellar radius, some of the models at $Z = 0.1\ Z_\odot$ show large numerical noise in the envelope binding energy $E_{\rm bind}$ during late evolutionary stages, when the envelope becomes deeply convective and the value of $E_{\rm bind}$ decreases significantly. This is due to variations in the exact location of the bifurcation point between these models (i.e., the boundary between the ejected envelope and the remaining remnant of the donor star during a CE phase), as we demonstrate below. This means that while the prediction of much lower binding energies of deeply convective RSGs at advanced stages of core-helium burning appears robust (and so does the prediction that CE ejection is possible for these donors), the exact values of $E_{\rm bind}$ for the loosely bound envelopes of these stars should be considered highly uncertain in our models.

Third, as indicated by different locations of diamonds and crosses between some of the model variations in Fig. 6.12, stellar radius of a model during a transitory phase (onset or end of core-helium burning) is in some cases not numerically robust in our models. This likely has to do with the fact that stellar radii of blue supergiants are very sensitive to the exact abundance profile in the bottom envelope layers surrounding the hydrogen burning shell (e.g., Georgy et al., 2013; Klencki et al., 2020; Kaiser et al., 2020). The abundance pattern in this part of the star is a result of internal mixing which takes place shortly after the end of the MS and is notoriously difficult to compute in stellar models due to a abundance discontinuities (a step-like profile) left by semiconvection (Farmer et al., 2016).

It is important to stress that while the models used in this work are in some aspects not numerically robust, as revealed by Fig. 6.12, the overall behavior of the binding energy as a function of radius (and therefore the convective-envelope mass fraction $f_{\rm conv}$) is robust. In particular, numerical variations in the value of $E_{\rm bind}$ for radiative-envelope donors are never larger than 15% and typically below 10%, which is rather insignificant in view of various physical uncertainties in the energy-budget formalism for CE evolution (see Sect. 6.4.1). The numerical uncertainty of our models does not affect any of the results presented in Sect. 6.3.1 and Sect. 6.3.2 (at least within the scope explored above).

### 6.B.3 NUMERICAL ROBUSTNESS: DETAILED INTERNAL STRUCTURE

In Fig. 6.14 and Fig. 6.13 we take a look at numerical robustness of the internal structure of the two $M_{\rm ZAMS} = 47.5\ M_\odot$ models studied in detail in Sect. 6.3.4. Similarly to Fig. 6.7 and Fig. 6.8, with different colors we plot internal profiles selected based on their increasing depth of the outer convective zone $f_{\rm conv}$ (going from blue to red). We compare the default model (solid line) with numerical variations, investigating the helium abundance and the mass–radius profile. Vertical lines mark the bifurcation point for CE evolution.

None of the numerical variations in Fig. 6.13 show any significant change with respect to our standard model. The largest variation in the bifurcation point location between models with different resolution is about 1.4% in mass and about 2% in radius.

The lower metallicity model $Z = 0.1\ Z_\odot$ in Fig. 6.14 on the other hand reveals two uncertainties. First, because of the uncertain radius of a core-helium burning blue/yellow supergiant for a given central helium abundance as discussed at the end of Sect. 6.B.2, different models in Fig. 6.14 reach the same outer convective zone depth at slightly different times. This is the most evident with the light-blue profiles, for which the total stellar mass is clearly different between model variations. The overall shape of each profile is unaffected.

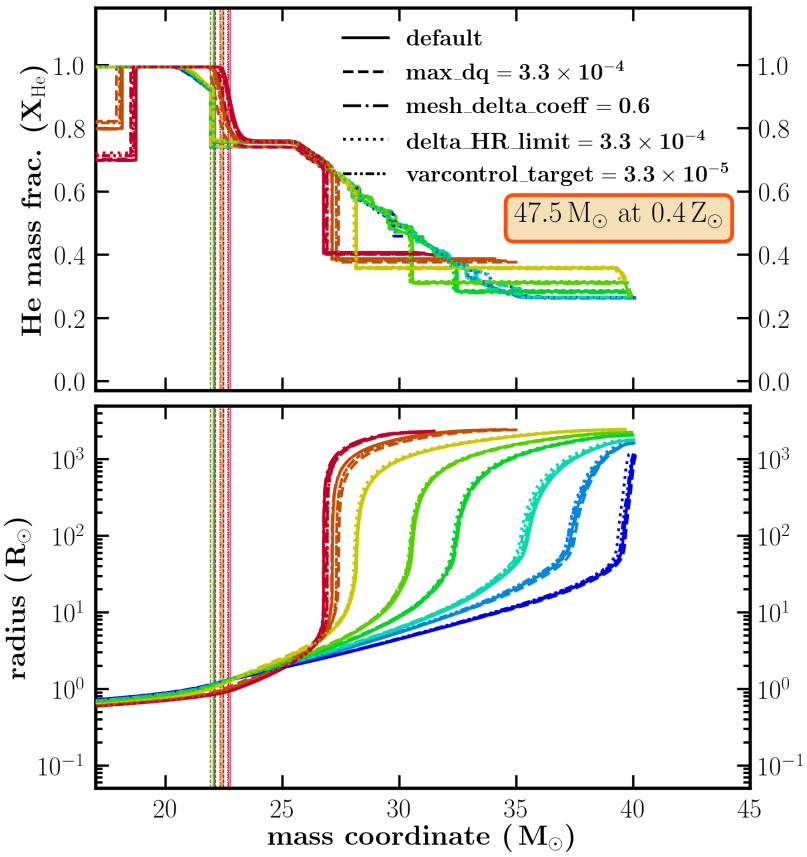


FIGURE 6.13: Comparison of the internal helium abundance and mass-radius profiles between the standard model (solid lines) and numerical variations with increased resolution (other lines), plotted for the case with $M_{\rm ZAMS} = 47.5\ M_\odot$ and $0.4\ Z_\odot$ analyzed in Sect. 6.3.4. As in Fig. 6.8, different colors correspond to different internal profiles of a model selected based on the depth of the outer convective zone (increasing as the color changes from blue to red). Vertical lines show the location of the bifurcation point for CE evolution.

Second, in the case of internal profiles of very deeply convective envelopes (the orange and red lines), there are some differences in the slope of the mass–radius profile near the bifurcation point (especially the model with `varcontrol_target` $= 3.3 \times 10^{-5}$ compared to all the others). While

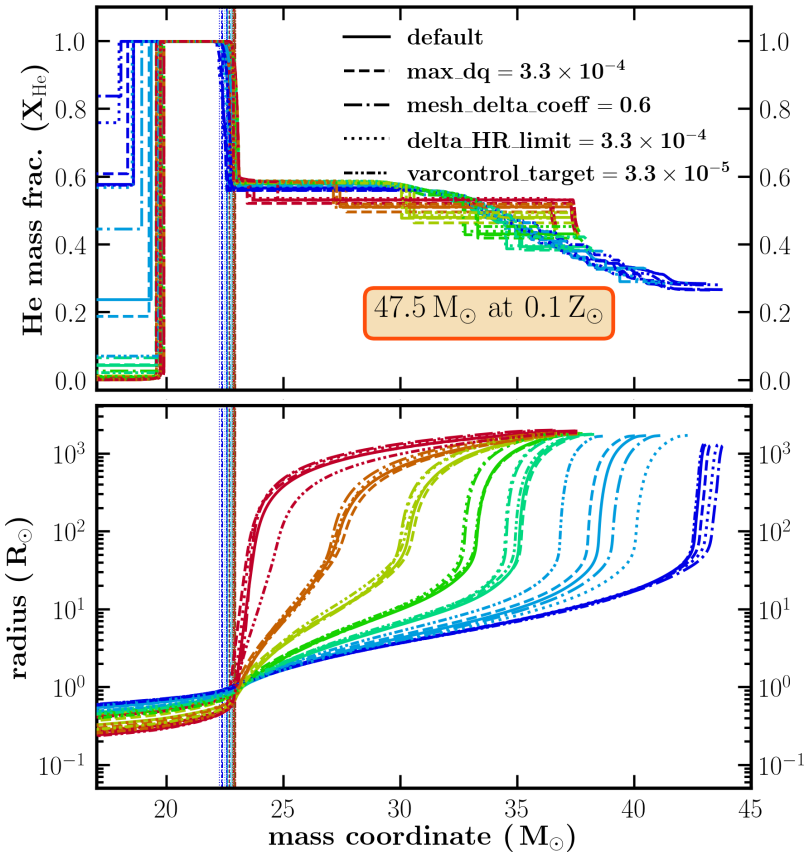


FIGURE 6.14: Same as Fig. 6.13 but for a model at $Z = 0.1\ Z_\odot$ metallicity (see also Fig. 6.7 in the main text).

these variations do not lead to any significant uncertainty in the mass coordinate of the bifurcation point (which does not vary by more than 1.5%) they do result in the radial coordinate being up to $\sim 30\%$ larger in the variation with `max_dq` $= 3.3 \times 10^{-4}$ (0.9 $R_\odot$ instead of 0.7 $R_\odot$, roughly). This propagates to very noticeable differences in the late envelope binding energy evolution of some of the $Z = 0.1\ Z_\odot$ models (see Fig. 6.12) when their envelopes become the most expanded, the most deeply convective, and the least gravitationally bound.

Most importantly, the overall shape of internal profiles in Fig. 6.14 and Fig. 6.13 is unaffected by an increase in resolution, and the results presented in Sect. 6.3.4 are numerically robust.

### 6.B.4 NUMERICAL ROBUSTNESS: HR DIAGRAM AT $Z = 0.2\ Z_\odot$

In Fig. 6.15, similarly to Fig. 6.6, we plot an HR diagram with selected models at $0.2\ Z_\odot$ metallicity (SMC-like). We compare models computed with increased resolution (various colors) to the standard models used in this work (in black). See the figure caption for a description of the symbols. None of the numerical variations show very significant discrepancies with respect to the default model. One noticeable difference is in the location of the core-helium burning phase in the HR diagram (marked with circular dots). In particular, the 12 $M_\odot$ model experiences a blue loop in a variation with `max_dq` $= 3.3 \times 10^{-4}$ (increased minimal cell size). These differences do not affect the envelope binding energies or the results on CE ejectability. As discussed in Sect. 6.B.2, numerical tests reveal that the sizes of MS stars with inflated envelopes are not a robust prediction

of our models, showing variations for the most massive models in metallicities $Z \geq 0.1\ Z_{\odot}$. This can also be seen in Fig. 6.15 in the form of a chaotic behavior of the 80 $M_{\odot}$ model in the final stages of the MS.

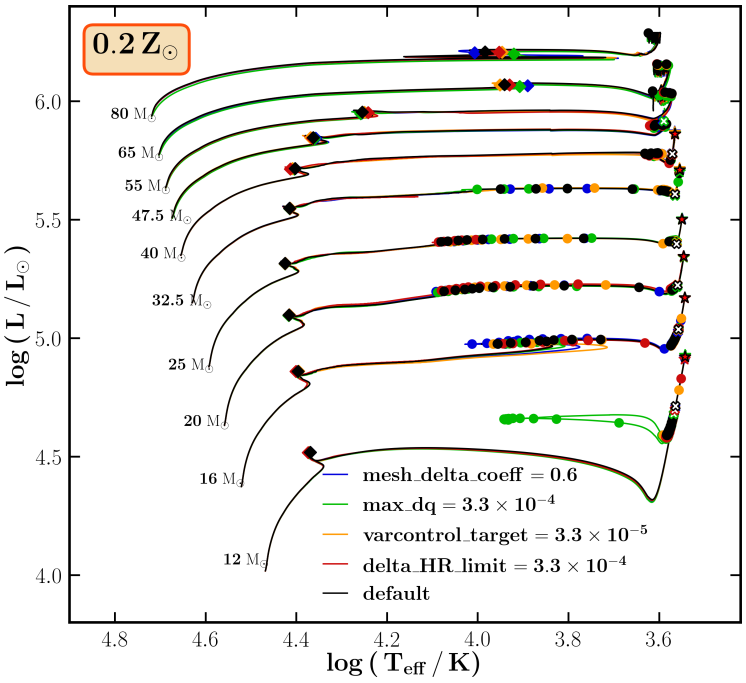


FIGURE 6.15: HR diagram with selected models at 0.2 $Z_{\odot}$ metallicity (SMC-like). We compare models computed with increased resolution (various colors) to the standard models used in this work (in black). Diamonds mark the terminal-age MS, dots mark the position of the star taken every 50,000 years during its post-MS evolution, white crosses mark the end of core-helium burning, whereas red stars mark the end of central carbon burning.

## 6.C ADDITIONAL FIGURES

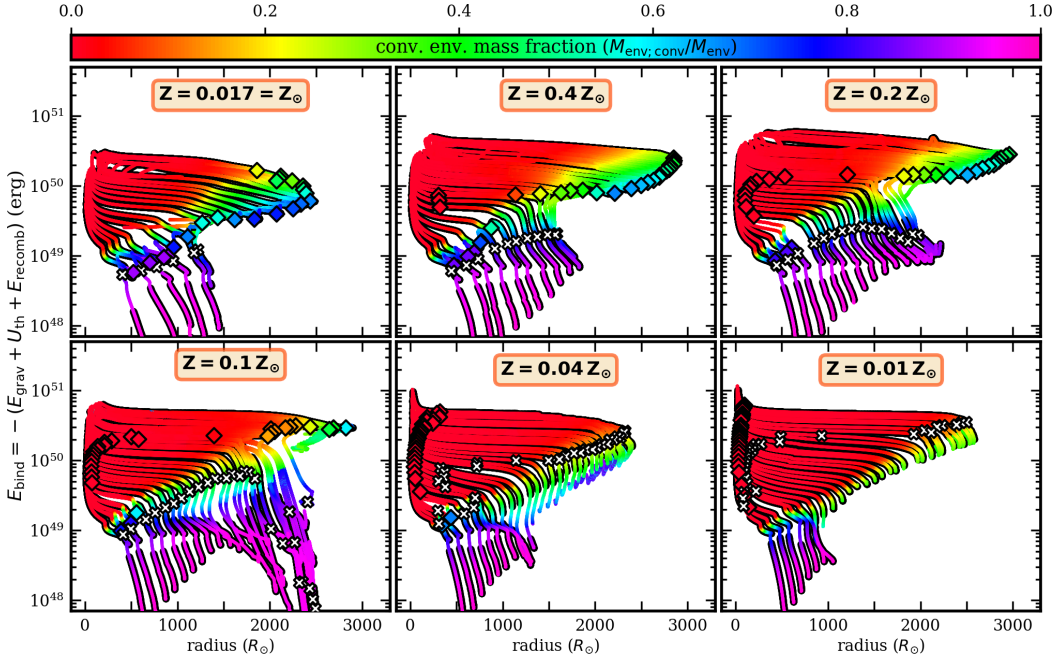


FIGURE 6.16: Same as Fig. 6.1 but with all the masses in our grid (30 models between 10 and 80 $M_{\odot}$ for each metallicity).

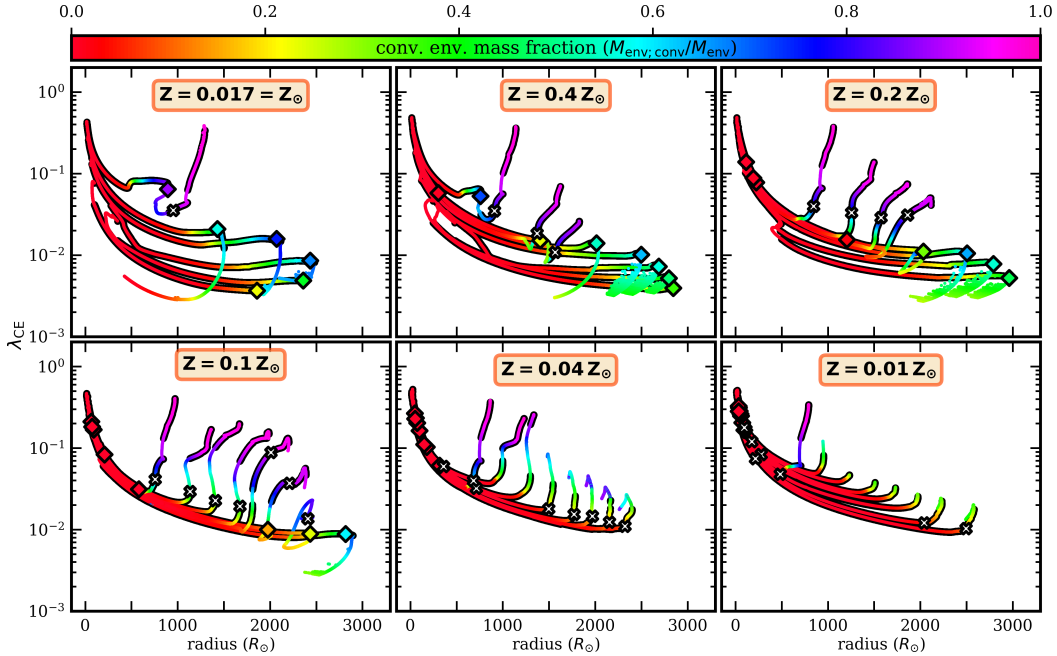


FIGURE 6.17: Same as Fig. 6.1, but showing the evolution of $\lambda_{CE}$ parameter instead of the envelope binding energy. Diamonds indicate the onset of core-helium burning, crosses indicate the end of core-helium burning.

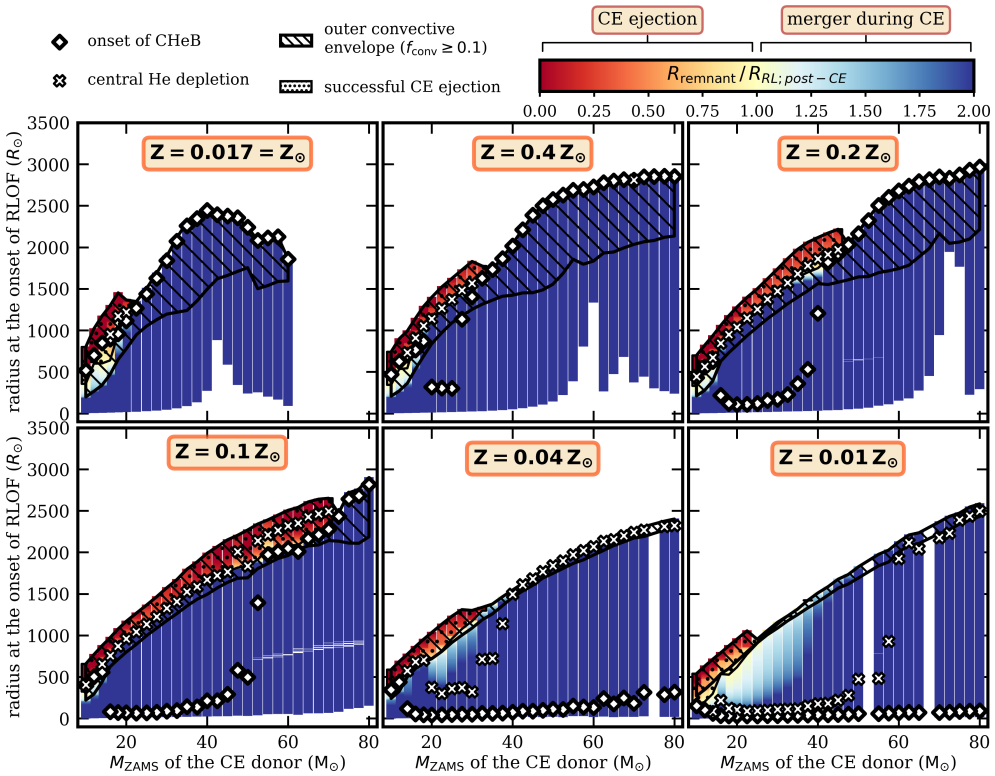


FIGURE 6.18: Same as Fig. 6.2 with the companion being a 2 $M_\odot$ NS. The parameter space for CE ejections is limited to cases in which the envelope binding energies have decreased significantly due to the donor becoming a convective-envelope giant at an advanced evolutionary stage.

# Chapter 7

# Partial envelope stripping and nuclear-timescale mass transfer from evolved supergiants at low metallicity

J. Klencki, A.G. Istrate, G. Nelemans & O. Pols

*to be submitted*

**Abstract**

Stable mass transfer from a massive post-main sequence (post-MS) donor is thought to be a short-lived event of thermal-timescale mass transfer ($\sim 10^{-3}\,\mathrm{M_\odot\,yr^{-1}}$) which within $\lesssim 10^4$ yr strips the donor star of nearly its entire H-rich envelope, producing a hot, compact helium star. This long-standing picture is based on stellar models with rapidly-expanding Hertzprung Gap (HG) donor stars. Motivated by a finding that in low-metallicity binaries, post-MS mass transfer may instead be initiated by donors already at the core-helium burning (CHeB) stage, we use the MESA stellar-evolution code to compute grids of detailed massive binary models at three metallicities: those of the Sun, the Large Magellanic Cloud (LMC, $Z_{\mathrm{Fe;LMC}}/Z_{\mathrm{Fe;\odot}} \approx 0.36$), and the Small Magellanic Cloud (SMC, $Z_{\mathrm{Fe;SMC}}/Z_{\mathrm{Fe;\odot}} \approx 0.2$). Our grids span a wide range in orbital periods ($\sim$ 3 to 5000 days) and initial primary masses (10 $M_\odot$ to 36-53 $M_\odot$, depending on metallicity).

We find that metallicity strongly influences the course and outcome of mass-transfer evolution. At LMC and SMC compositions, the majority of binary models with donor masses $\geq 17\ M_\odot$ evolve through one of the two novel types of post-MS mass transfer: (a) mass exchange on the long nuclear timescale ($\Delta T_{\mathrm{MT}} \gtrsim 10^5$ yr, $\dot{M} \sim 10^{-5}\,\mathrm{M_\odot\,yr^{-1}}$) that continues until the end of the CHeB phase, or (b) rapid mass transfer leading to detached binaries with mass-losers that are only partially stripped of their envelopes. In neither (a) or (b) does the donor become a fully stripped helium star by the end of

CHeB. Boundaries between the different types of post-MS mass transfer evolution are associated with the degree of rapid post-MS expansion of massive stars and, for a given metallicity, are sensitive to the assumptions about internal mixing.

At low metallicity, due to partial envelope stripping, we predict fewer hot, fully stripped stars formed through binary interactions as well as higher compactness of the pre-supernova core structures of mass losers. Nuclear-timescale post-MS mass transfer gives rise to a population of interacting binaries with blue and yellow supergiant donors. It also suggests a strong preference for metal-poor galaxies of ultra-luminous X-ray sources with black-hole (BH) accretors and massive donors, some of which might be the immediate progenitors of binary BH mergers. Partially-stripped stars could potentially explain the puzzling nitrogen-enriched slowly-rotating (super)giants in the LMC.

## 7.1 INTRODUCTION

Massive stars do not live alone. The majority are formed in close binary or higher-order systems in which they are destined to strongly interact with their companions by transferring mass and angular momentum (Sana et al., 2012; Moe & Di Stefano, 2017). Mass transfer has significant consequences for basic properties and final fates of both stars. Many mass losers become helium-rich stripped stars, from hot subdwarfs to Wolf-Rayet (WR) stars, (depending on the mass; Paczyński, 1967; van den Heuvel, 1975; Vanbeveren, 1991; Podsiadlowski et al., 1992; De Loore & De Greve, 1992; Petrovic et al., 2005; Eldridge et al., 2008; Götberg et al., 2017; Laplace et al., 2020), and a UV-bright prominent source of ionizing photons (Götberg et al., 2018, 2020). Mass gainers and stellar mergers, on the other hand, are the likely explanation for the existence of blue stragglers (McCrea, 1964; Pols, 1994; Braun & Langer, 1995; Glebbeek et al., 2013; Schneider et al., 2015), may dominate the population of rapidly rotating stars (de Mink et al., 2013) in particular Be stars (Pols et al., 1991; Shao & Li, 2014), lead to formation of magnetic fields in stars (Ferrario et al., 2009; Schneider et al., 2019), and a peculiar class of supernovae from blue-supergiant progenitors (including the most recent naked-eye supernova SN 1987A, see Podsiadlowski et al., 1990; Justham et al., 2014). Prior mass transfer interactions have been shown to leave clear signatures in the properties of stellar cores at core collapse, affect lightcurves and yields of the resulting supernovae, and play an important role in deciding whether the final remnant will be a neutron star (NS) or a black hole (BH, Morris & Podsiadlowski, 2007; Justham et al., 2014; Woosley, 2019; Schneider et al., 2021; Laplace et al., 2021; Vartanyan et al., 2021). Through mass transfer, binaries enrich the interstellar medium with processed material (de Mink et al., 2009b), shine as X-ray binaries (van den Heuvel & De Loore, 1973; van den Heuvel, 1975; Verbunt, 1993), and bring two BHs or neutron stars NSs close together, driving them to merge and blaze in gravitational waves (GW; Tutukov & Yungelson, 1993; Portegies Zwart & Yungelson, 1998; Belczynski et al., 2002; Voss & Tauris, 2003) in the most energetic spectacles observed to date (Abbott et al., 2016b).

In most massive binary systems, a phase of mass transfer is initiated when one of the stars evolves off the main sequence (MS) and expands significantly leading to the so-called case B Roche-lobe overflow (RLOF, Kippenhahn & Weigert, 1967; Paczyński, 1971). [1] The textbook view of case B mass transfer is that the donor star looses nearly its entire H-rich envelope in a short-lived phase of thermal-timescale mass exchange ($\lesssim 10^4$ yr Kippenhahn & Weigert, 1967; Paczyński, 1971; van den Heuvel, 1975; Podsiadlowski et al., 1992; Vanbeveren et al., 1998). This is because the donor is thought to usually be a rapidly-expanding H-shell burning giant, a Hertzprung gap (HG) star. It is out of thermal-equilibrium even before any RLOF occurs and would need to expand all the way to the red giant branch in order to regain a stable thermal structure. In a close binary, this continuous rapid expansion of the donor star is what causes the mass transfer to proceed on the thermal timescale until only a thin envelope layer remains. By the time the binary detaches, the donor becomes a stripped star, composed predominantly of helium.

This paradigm may no longer be true for massive binaries in low-metallicity (low-Z) environments. As pointed out by de Mink et al. (2008) and recently shown in much detail by Klencki et al. (2020), metallicity has a strong effect on what is the typical evolutionary state of donors when they initiate a case B mass transfer phase in a population of massive binaries. While at high (Solar-like) metallicity a post-MS interaction nearly always occurs when the donor is expanding as a HG star, it has been shown that at low metallicity the parameter space for RLOF from core-He burning donors becomes very significant (and possibly dominant above a certain mass, see Klencki et al., 2020). In contrast to HG donors, stars that are already at the core-He burning stage are in thermal equilibrium and slowly expanding on the nuclear timescale of $\sim 10^6$ yr. Mass transfer from such donors has never been studied with detailed binary evolution models and its understanding is still lacking.

At the same time, various observational clues suggest that metallicity has a strong influence on the evolution of massive stars and binaries. Long gamma-ray bursts (Graham & Fruchter, 2013), superluminous supernovae (Gal-Yam, 2012), and ultra-lumionous X-ray (ULX) sources (Kovlakas et al., 2020) all preferentially occur in low-Z galaxies. Similarly, Type Ic supernovae with broad lines in the spectra are typically found in metal-poor hosts, whereas normal Type Ic supernovae avoid dwarf galaxies (Modjaz et al., 2011). It has been suggested that BHs with masses above $\sim 30\ M_\odot$, frequently found in binary BH mergers detected in GW by LIGO/Virgo (Abbott et al., 2020a), may originate from metal-poor environments, where the reduced strength of line-driven winds allows for the formation of more massive BHs (e.g. Belczynski et al., 2010a; Vink et al., 2021). Thanks to their close proximity to the Milky Way, the Small and the Large Magellanic Cloud (SMC and LMC, respectively) serve as excellent test-beds of massive star evolution at low metallicity. Large-scale spectroscopic surveys of the Magellanic Clouds have revealed populations of stars that cannot be explained by current models, in particular the slowly-rotating nitrogen-enriched (super)giants (Evans et al., 2006; Hunter et al., 2008; McEvoy et al., 2015; Grin et al., 2017). The

[1] There is some ambiguity in the literature as to whether the term case B mass transfer refers to only the cases initiated before the onset of core-He burning or also during that phase of evolution. Throughout this paper, we will adapt the latter naming convention.

population of high-mass X-ray binaries (HMXBs) also appears to be metallicity-dependent, with a surprisingly large number of Be HMXBs found in the Magellanic Clouds (Dray, 2006).

Motivated by the importance of low metallicity on the evolution of massive stars, evidenced on both theoretical and observational grounds, in this work we follow up on Klencki et al. (2020) and explore mass-transfer evolution in massive binaries of different metallicities.

The paper is organized as follows. In Section 7.2 we describe our computational method and physical assumptions as well as the parameter space explored with our models. In Section 7.3 we present the results from our binary evolution sequences, focusing on the mass-transfer evolution from post-MS donors. In Section 7.4 we take an in-depth look at the origin of different types of mass-transfer evolution found in Sec. 7.3. In Section 7.5 we discuss the caveats of our models as well as various implications of the findings. We conclude in Section 7.6.

## 7.2 METHOD: BINARY STELLAR EVOLUTION MODELS

### 7.2.1 PHYSICAL INGREDIENTS: SINGLE AND BINARY EVOLUTION

We employ the MESA stellar evolution code (Paxton et al., 2011, 2013, 2015, 2018, 2019) [2]. Convection is modeled using the mixing-length theory (Böhm-Vitense, 1958) with the mixing length of $\alpha = 1.5$. We employ the Ledoux criterion for convection and account for semiconvective mixing with an efficiency of $\alpha_{\rm SC} = 33$. We account for convective core-overshooting by applying step overshooting with an overshooting length $\sigma_{\rm ov} = 0.33$ (Brott et al., 2011a). Such choices of overshooting and semiconvection efficiency were shown to be in good agreement with the observed ratio of blue and red supergiants in the SMC (Schootemeijer et al., 2019; Klencki et al., 2020).

Models are computed at three different initial chemical compositions: either at Solar metallicity with $Z = 0.017$ and abundance ratios from Grevesse et al. (1996) or with non-Solar abundance ratios of the Magellanic Clouds following Brott et al. (2011a). In the case of the LMC that yields $Z_{\rm LMC} \approx 0.0048$ and the relative iron abundance $Z_{\rm Fe;LMC}/Z_{\rm Fe;\odot} \approx 0.36$, whereas in the case of SMC: $Z_{\rm SMC} \approx 0.0022$ and the relative iron abundance $Z_{\rm Fe;SMC}/Z_{\rm Fe;\odot} \approx 0.2$. Similarly to Langer et al. (2020), we use custom-made OPAL opacity tables (Iglesias & Rogers, 1996) corresponding to the adopted initial abundances of the SMC or the LMC.

The winds of stars on the cool side of the bi-stability jump with $T_{\rm eff} < 0.95\ T_{\rm eff;jump} \approx 25$ kK (see Eqn. 15 in Vink et al. 2001) are modeled as the larger of the mass-loss rates from Vink et al. (2001) and Nieuwenhuijzen & de Jager (1990b). The winds of stars on the hot side of the bi-stability jump (with $T_{\rm eff} > 1.05\ T_{\rm eff;jump}$) are modeled as a combination of several different prescriptions, depending on the surface hydrogen abundance $X$. For stars with $X > 0.45$, we follow Vink et al. (2001). For stars with $0.1 < X < 0.35$, we apply the empirical mass-loss rates from Nugis & Lamers (2000b). For (nearly) hydrogen-free stars with $X < 0.05$, we follow Yoon (2017), whose prescriptions for WNE stars are based on the results from (Hainich et al., 2014) and for WC/WO stars were derived by (Tramper et al., 2016). In the intermediate $X$ regimes, as well

[2]MESA version r11554, `http://mesa.sourceforge.net/`

as in the temperature range around the bi-stability jump $0.95 < T_{\rm eff}/T_{\rm eff;jump} < 1.05$, we linearly interpolate between the above prescriptions to provide smooth transitions.

In addition, when using the Vink et al. (2001) prescription at $T_{\rm eff} > T_{\rm eff;jump}$ (optically thin winds of OB supergiants), we account for the possible transition to the optically thick WR-type mass loss. Both theoretical (Gräfener & Hamann, 2008; Vink et al., 2011; Sander et al., 2020) and empirical studies (Gräfener et al., 2011; Bestenlehner et al., 2014) suggest that this transition takes place when the Eddington factor $\Gamma_{\rm e} = 10^{-4.813}(1 + X)(L/L_{\odot})(M/M_{\odot})^{-1}$ becomes sufficiently large, which typically happens when a substantial amount of mass has already been lost (either in winds or as a result of mass transfer). Here, we follow Gräfener & Hamann (2008) and assume that this threshold is at $\Gamma_{\rm e} \approx 0.1 + \Gamma_0$ where $\Gamma_0$ is metallicity (iron) dependent and equals to 0.326, 0.468, and 0.514 for our Solar, LMC, and SMC iron abundances, respectively (Eqn. 6 of Gräfener & Hamann 2008). We maintain the Vink et al. (2001) mass-loss rate for $\Gamma_{\rm e} - \Gamma_0 < 0.08$, whereas for $\Gamma_{\rm e} - \Gamma_0 > 0.12$ we apply the theoretical recipe for optically thick winds from Gräfener & Hamann (2008). For intermediate Eddington factors, we linearly interpolate between the two mass-loss rates.

We include rotationally-induced mixing of elements due to Eddington-Sweet circulation, secular shear instabilities, and the Goldreich-Schubert-Fricke instability, with an efficiency factor $f_c = 1/30$ (Heger et al., 2000; Brott et al., 2011a). We model rotationally-enhanced mass loss as in Langer (1998), see implementation in Paxton et al. (2013). In most of our models, we avoid using the MLT++ option in MESA (Paxton et al., 2013) as it was shown to artificially reduce the stellar radii during the giant phases of evolution and therefore could affect the behavior of stars during mass transfer. In the few cases of the most massive donors in our grid (36 $M_{\odot}$, 44 $M_{\odot}$, and 53 $M_{\odot}$ at Solar, LMC, and SMC compositions, respectively) we resort to a limited use of MLT++ by gradually reducing superadiabacity in outer layers ($T < 10^6$ K) of donors once they have reached the mass-transfer rate of $\log(\dot{M}) = -2.5$. These models would have not converged otherwise due to numerical difficulties arising at the bottom of a subsurface convective zone located at the iron opacity peak.

We follow the formalism of Kolb & Ritter (1990) to calculate the mass-transfer rate through the L1 Lagrangian point. This includes both the optically-thin regime of mass transfer when $R_{\rm don}$ is still slightly smaller than $R_{\rm RL}$, where $R_{\rm don}$ is the radius of the donor star and $R_{\rm RL}$ is the size of its Roche lobe, as well as the main phase of mass transfer when $R_{\rm don} > R_{\rm RL}$. The mass transfer is assumed to remain stable for as long as the binary model computes, i.e. unstable cases are when the mass transfer rate clearly diverges to infinity and the simulation stops.

The main focus of the paper is to study the behavior of the donor star during a phase of mass transfer and to understand how the halted post-MS expansion of low-metallicity massive stars influences their evolution as donors in interacting binaries. Therefore, for simplicity, in our binary models we only evolve the primary (donor) star and treat the companion as a point mass. We also assume that the accretion efficiency is Eddington-limited, which in practice will mean nearly fully non-conservative mass transfer. We further assume that the specific angular momentum of the mass ejected from the system is that of the accretor on its binary orbit (i.e. the isotropic

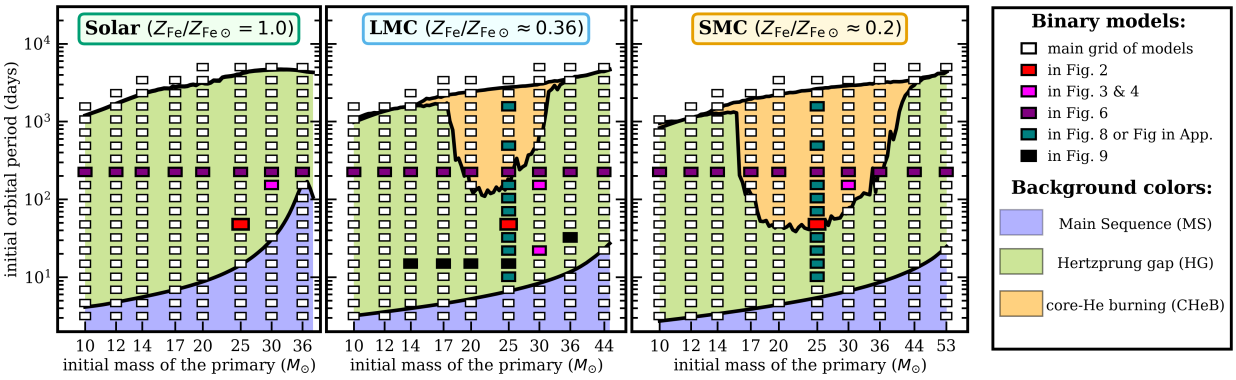


FIGURE 7.1: Distribution of the main grid of binary models at each metallicity over the parameter space of initial orbital periods and primary masses. Background color indicates the evolutionary stage of the primary star at the onset of mass transfer through RLOF. We differentiate between core-H burning donors (shades of blue), H-shell burning donors (i.e. donors that experience the Hertzprung-gap phase of rapid expansion; green), as well as core-He burning donors (shades of orange). The initial mass ratio is $q = M_2/M_1 = 0.6$. Colored rectangles indicate which models from the grid are showed in figures throughout the paper (see legend).

re-emission mode). These assumptions make our models well suited to represent systems with compact-object accretors (specifically BHs, given that our accretors are always more massive than 6 $M_\odot$). However, as we argue in Sec. 7.5.2, all our main findings and conclusions also hold in the case of systems with stellar accretors. Throughout the paper we will thus not assume anything about the nature of the companion unless explicitly stated otherwise.

We model the spin-up of the primary due to tidal interactions following the synchronization timescale for radiative envelopes from Hurley et al. (2002). In MESA the angular momentum from tides is being deposited in such a way that each layer is being synchronized on the same timescale. We include the effect of isotropic wind mass-loss on the evolution of orbital parameters as well as the spin of the mass-losing star.

### 7.2.2 INITIAL PARAMETER SPACE AND STOPPING CONDITIONS

We compute three main grids of binary models: at Solar, LMC, and SMC composition. Each grid spans 20 different initial orbital periods $P_{\rm ini}$ ranging from $\approx 3.16$ to 5012 days, spaced in equal logarithmic steps. The SMC grid spans 10 different initial primary masses $M_1$: 10, 12, 14, 17, 20, 25, 30, 36, 44, and 53 $M_\odot$. The LMC grid ends at 44 $M_\odot$ whereas at Solar metallicity we compute models until 36 $M_\odot$. The default initial mass ratio $q = M_2/M_1$ is $q = 0.6$ for our main grids. For the case of $M_1 = 25$ $M_\odot$ and $P_{\rm ini} \approx 47$ days we compute additional models with the mass ratio $q$ varying from 0.1 to 1.5 (15 models). We do this by preserving the structure of the donor at RLOF taken from the standard binary model with $q = 0.6$ and manually adjusting the mass ratio and orbital separation in such a way that at the moment of RLOF the donor has the same radius for any $q$. This approximation is justified because the tidal spin-up of the donor star, which would have been different in the evolution prior to RLOF for different mass ratios, is insignificant for binaries

this wide. The primaries are initialized with a small initial rotational velocity of 30 km/s. All the binaries are circular.

Figure 7.1 illustrates how our grids of binary models cover the parameter space for a mass transfer interaction initiated by donors at different evolutionary stages, similarly to figures in Klencki et al. (2020). At each composition, the grid covers the entire range of periods for a post-MS mass transfer interaction and fully encloses the range of masses at which donors begin the core-He burning stage as blue supergiants (at LMC and SMC compositions). In addition, each grid includes a small number of binaries that evolved through a case-A mass-transfer phase (i.e. initiated by a MS star). These models are beyond the main scope of the paper and will not be discussed in detail.

All the binary sequences terminate at central helium depletion ($Y_{\rm center} < 10^{-6}$). The remaining lifetimes of massive stars from that point on until the final core-collapse are short compared to hydrogen- and helium-burning lifetimes ($< 10^5$ yr or even $< 10^4$ yr for the more massive among our primaries).

## 7.3 Results

### 7.3.1 Nuclear-timescale mass transfer and partial envelope stripping

We begin describing the results by taking a close look at binary evolution models from the middle of our grids: systems with initial primary masses of $M_1 = 25\ M_\odot$ and orbital periods $P_{\rm ini} \approx 47$ days. For this selected case of $M_1$ and $P_{\rm ini}$, apart from the default initial mass ratio between the binary components $q = M_2/M_1 = 0.6$, we computed additional mass transfer sequences with varying mass ratios $q$ from 0.1 to 1.5, as described in Sec. 7.2.2. In each case, the size of the primary (donor) star at the moment of RLOF was about $R_{\rm RLOF} \approx 90\ R_\odot$. At both Solar and LMC compositions, the primary star of that radius was still a rapidly-expanding HG giant, whereas at SMC composition the donor was already at the core-He burning stage. For the selected $M_1 = 25\ M_\odot$ case, in Fig. 7.2 we plot the time evolution of the mass transfer rate (upper panels) and envelope masses (lower panels) for three metallicities and various mass ratios $q$.

We find a remarkable difference in the mass-transfer evolution between the Solar case and the low-Z models of the LMC and SMC compositions. At Solar Z, irrespective of the mass ratio, the mass transfer interaction is a short-lived and violent event. Over the course of only several thousand years the donor star is stripped of its nearly entire H-rich envelope. This is a phase of thermal-timescale mass transfer with the rate reaching $\log(\dot{M}) \sim 10^{-2}\,{\rm M}_\odot\,{\rm yr}^{-1}$. The thin remaining envelope layer ($\sim 1\ M_\odot$) is further quickly lost in winds and the primary becomes a fully stripped helium star. This type of evolution is the canonical picture of how a case-B mass transfer interaction can lead to the envelope loss and formation of stripped stars of various kinds, from subdwarfs to WR stars (see Sec. 7.1 and the references therein).

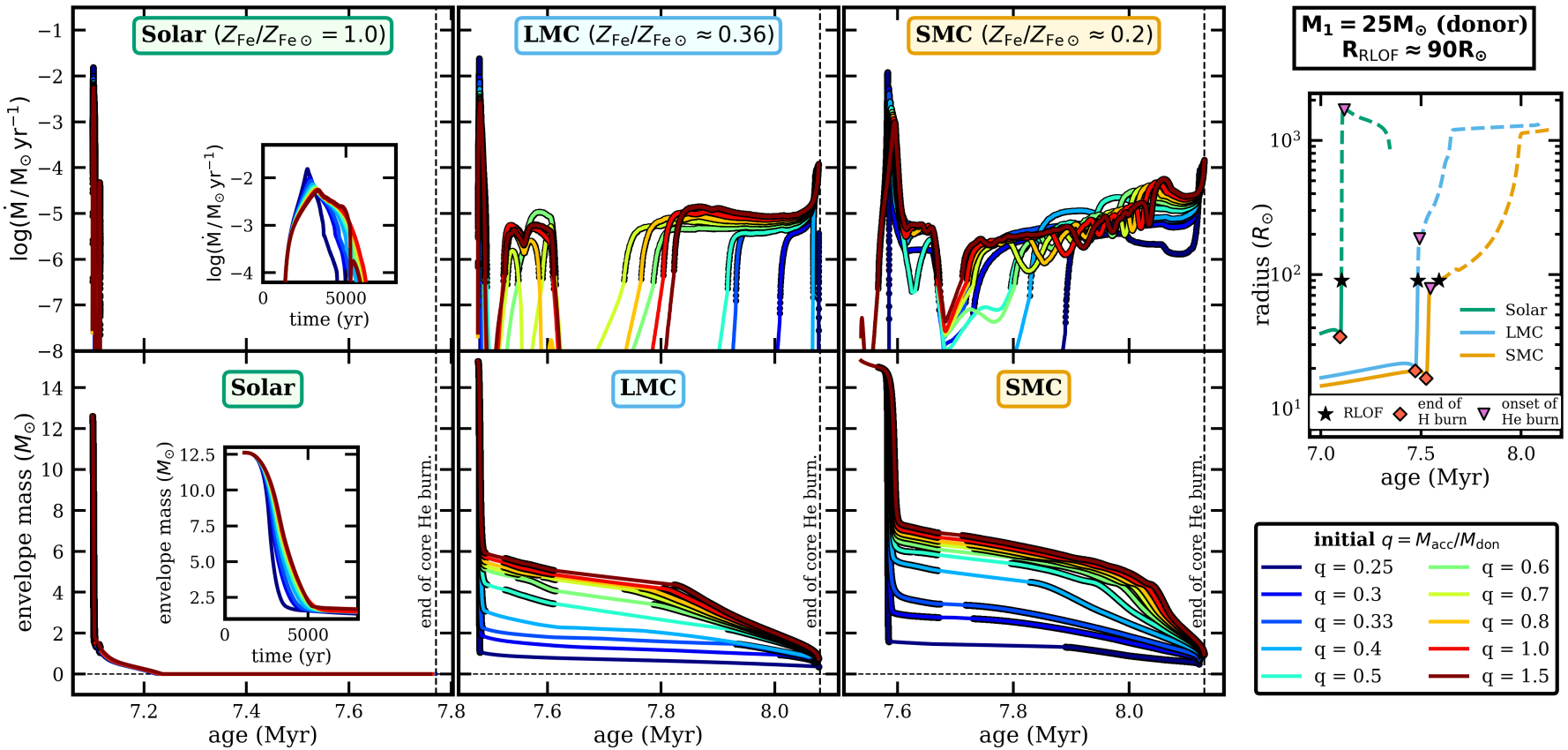


FIGURE 7.2: Mass transfer evolution in binaries with a 25 $M_\odot$ primary (initial mass) compared between the three different metallicities. Top panels show the mass-transfer rate, bottom panels show the mass of the hydrogen-rich envelope ($X_H > 10^{-3}$). Different colors correspond to different mass ratios between the binary components $q = M_2/M_1$, varying from 0.1 and 1.5 (the donor stays the same). In each case the primary overflows its Roche lobe at radius of around $R_{RLOF} \approx 90\ R_\odot$, see the radius-age diagram on the right-hand side. In models with $q \leq 0.225$ (not shown in the figure) the mass transfer became dynamically unstable. Models terminate at the end of core-He burning.

However, the evolution of LMC and SMC models in Fig. 7.2 turns out to be substantially different. In these low-Z cases the initial rapid (thermal) phase of mass transfer slows down or terminates while a significant part of the envelope is still retained ($M_{\rm env;left}$ from $\sim 1$ up to even 7 $M_\odot$, depending on the mass ratio and metallicity). In models with $M_{\rm env;left} \gtrsim 2.5\ M_\odot$, the partially-stripped donor continues its evolution as a core He-burning star and its slow expansion leads to a long phase of nuclear-timescale mass transfer (a few times $10^5$ yr, $\log(\dot{M}) \sim 10^{-6} - 10^{-5}\,{\rm M_\odot\,yr^{-1}}$). The slow mass transfer dominates the rest of the evolution: it persists at least until the end of core-He burning, at which point we terminate our models (the remaining lifetime is relatively short, $< 0.1$ Myr). Occasionally the mass exchange may be interrupted by temporary detachments, in particular around the age of 7.6 (7.7) Myr of the LMC (SMC) models. These are caused by (typically subtle) contractions of the donor star in response to changes of the hydrogen abundance in the moving location of the H-burning shell. A similar transition in the H shell was previously found to trigger a blue-loop evolution in 15 $M_\odot$ stellar models by Langer et al. (1985). Oscillations in the mass transfer rate during the nuclear-timescale phase are associated with changes in the helium abundance of the outer donor layers as it is being stripped deeper into layers that used to be convective during MS (see Sec.7.4).

The few models with the lowest envelope masses $M_{\rm env;left} \lesssim 2.5\ M_\odot$ left after the initial rapid mass transfer, i.e. models with $q \lesssim 0.4$ at LMC and $q = 0.25$ at SMC composition, show a somewhat different type of evolution. These binaries remain detached for most of their He-burning lifetime, with possibly only a relatively brief episode of nuclear-timescale mass transfer close to the end of this phase. Notably, in none of the LMC or SMC models is the envelope fully lost in winds or mass transfer (by the end of core-He burning), which is partly due to weaker winds at low Z. In fact, at no point does the primary become a hot ( $\log(T_{\rm eff}/{\rm K}) \gtrsim 4.6$) stripped helium star, in sharp contrast to the Solar metallicity case.

Besides the mass ratio, another factor that affects $M_{\rm env;left}$ is the initial orbital period $P_{\rm ini}$. In Fig. 7.3, we illustrate this for the case of models with $M_1 = 25\ M_\odot$ primary at the SMC metallicity (see Fig. 7.16 for the LMC case). The shorter the orbital period, the less massive is the envelope that remains after the initial rapid mass transfer phase. We notice that $M_{\rm env;left}$ is especially sensitive to $P_{\rm ini}$ and $q$ for the shortest periods and the most extreme mass ratio, i.e. in the regime that leads to the lowest (although non-zero) $M_{\rm env;left}$ values and evolution with long detachment phases. On the other hand, above a certain mass ratio and orbital period, the donors tend to slow down the mass transfer rate at similar $M_{\rm env;left}$ values and then continue to transfer mass on the nuclear timescale. We discuss those findings in view of the donor envelope structure in Sec. 7.4. We note that although not explored in the current study, the degree of envelope stripping is expected to also depend on the assumptions about the accretion efficiency and angular momentum of the non-accreted matter, i.e. all the factors that influence the evolution of the Roche lobe size of the donor star.

As previously mentioned and illustrated in the donor radius panel of Fig. 7.3, temporary detachments happening at $\sim 7.7$ Myr are caused by relatively modest contractions of donors during the core-He burning phase (by $10 - 20\%$ in this particular case). We find that this behavior is

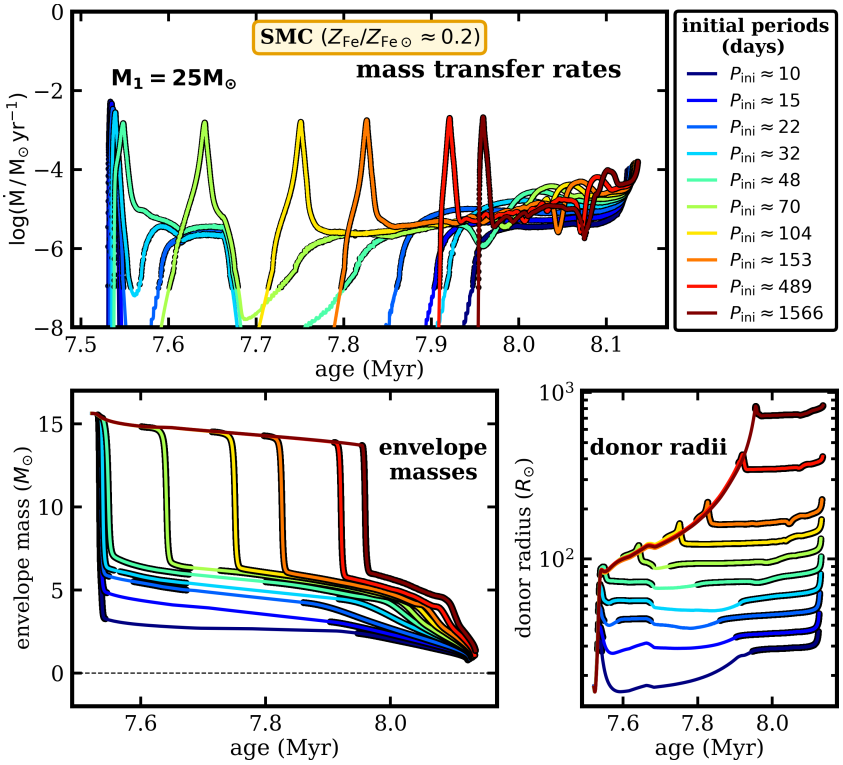


FIGURE 7.3: Mass transfer evolution in binaries with a 25 $M_\odot$ primary (initial mass), SMC composition, and various initial orbital periods $P_{ini}$. The shorter the orbital period, the lower the envelope mass $M_{env;left}$ that remains after the initial phase of rapid (thermal) mass transfer.

distinctively different from detachments observed in the few models with the most extreme mass ratios and tightest orbits (and therefore lowest $M_{env;left}$, e.g. the $P_{ini} \approx 10$ and 15 days models in Fig. 7.3), as in those cases the donor contracts much more significantly with respect to its Roche lobe. In Fig. 7.4 and Fig. 7.5 we will better characterize this type of evolution and refer to it as mass transfer events leading to long-lived partially-stripped stars in detached binaries.

The reason why the mass transfer evolution is so different between the Solar and low-Z cases in Fig. 7.2 is related to radial expansion of mass-losing stars and the size that a partially-stripped donor of a given metallicity would need to have in order to regain thermal equilibrium. We discuss this is detail in Sec. 7.4 and Fig. 7.12. In summary, we find that a partially-stripped donor of Solar $Z$ would need to expand to a size of a red supergiant to regain equilibrium, $\sim 1800\ R_\odot$, which is much larger than a size of its Roche lobe. As a result, the donor keeps rapidly expanding and the thermal-timescale mass transfer continues until it strips nearly entire envelope, at which point the donor finally contracts to become a hot stripped star. In contrast, the donors of LMC and SMC compositions ($M_1 = 25\ M_\odot$) that are partially-stripped in the initial phase of rapid mass transfer can be in thermal equilibrium at a much smaller size $\sim 50\ R_\odot$, which is similar to that of their Roche lobes. As a result, they can regain equilibrium and slow down the mass transfer interaction or even detach. In a similar way, single massive low-Z stars may remain relatively compact before the onset of the core-He burning, avoiding a rapid HG expansion until the red giant branch (in particular the 25 $M_\odot$ models, see the radius-age diagram on the right-hand side of Fig. 7.2). In fact, as we will show in Sec. 7.3.2, we find nuclear-timescale mass transfer evolution in models with donor masses roughly from the mass range in which the halted HG expansion happens.

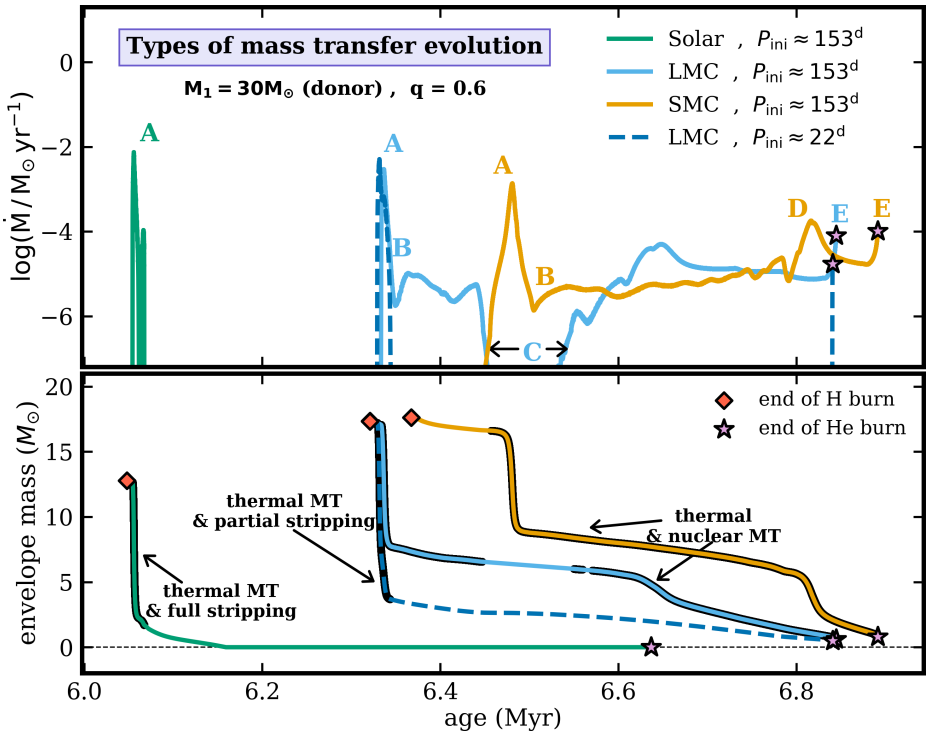


FIGURE 7.4: Three different types of mass-transfer evolution found across our binary models, illustrated with cases with $M_1 = 30\ M_\odot$ primaries and different compositions (metallicities). Top panels show the mass-transfer rate, bottom panels show mass of the envelope. Letters mark distinctive events that may occur during the evolution as following. A: a phase of rapid thermal-timescale mass transfer, B: a point when the donor regains thermal equilibrium and the mass transfer transitions to the nuclear timescale, C: phases of detachment, D: temporary mass-transfer rate increase when the donor becomes stripped down to layers that used to be in the intermediate convective zone, and E: mass transfer peak associated with the end of core-He burning and re-expansion of the donor.

Throughout our binary grid, we find three qualitatively different types of mass-transfer evolution, which we illustrate in Fig. 7.4 (using the $M_1 = 30\ M_\odot$ case as an example). In Fig. 7.5, we plot the corresponding donor tracks in the HR diagram, with the phase of RLOF shown in bold and crosses indicating where the donor spends most of its core-He burning lifetime (spaced every 50,000 yr).

The Solar metallicity donor transfers nearly its entire envelope ($M_{\rm env;left} \approx 1.7\ M_\odot$) during a phase of thermal-timescale mass transfer (labeled 'A'). After detachment it rapidly contracts and moves leftwards in the HR diagram to spend most of its He-burning lifetime ($\sim 85\%\Delta t_{\rm He;burn}$) as a hot UV-bright stripped star with $\log(T_{\rm eff}/{\rm K}) \approx 5.1$ (labeled 'C') before central He exhaustion (labeled 'E').

The LMC donor in a binary with $P_{\rm ini} \approx 22$ days (dashed line) also experiences only a brief phase of thermal-timescale mass exchange (labeled 'A'). In contrast to the Solar case, it retains a bigger envelope ($M_{\rm env;left} \approx 3.7\ M_\odot$) that is never fully lost in winds. The donor burns He as a partially stripped star in a detached binary (labeled 'C'). It is much cooler and bigger than a stripped star: $\log(T_{\rm eff}/{\rm K}) \approx 4.4$ and $R \approx 30\ R_\odot$. In fact, its locus in the HR diagram is similar to that of a single $30\ M_\odot$ star at the end stages of MS or early stages of post-MS evolution. The

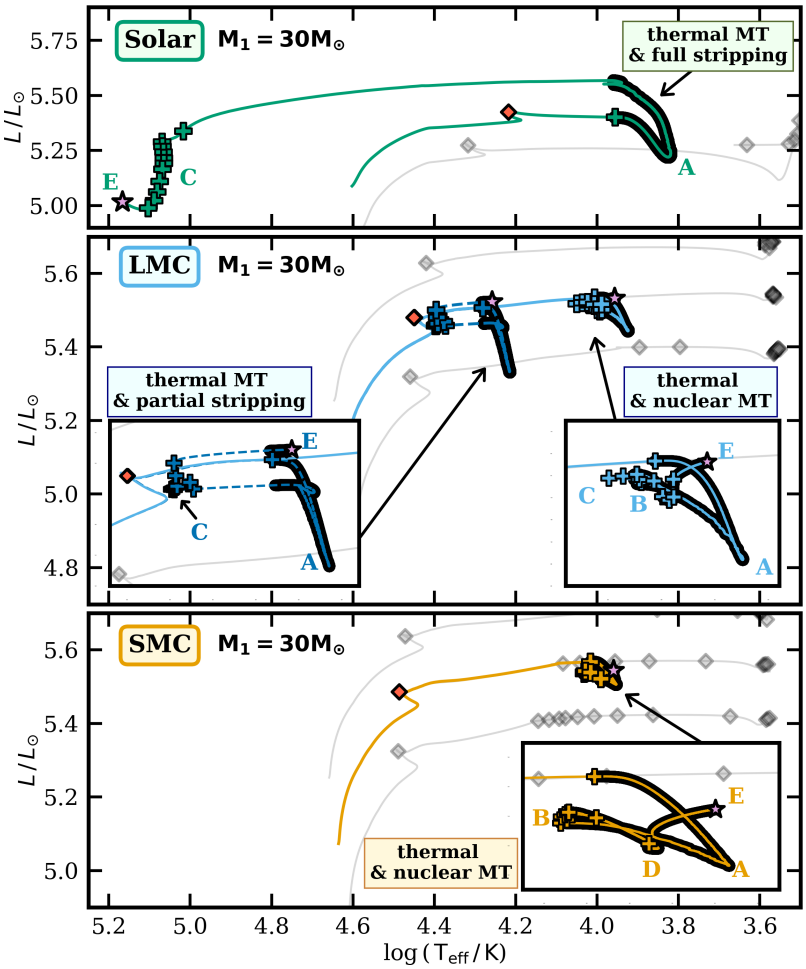


FIGURE 7.5: Evolution of primaries (donors) from models shown in Fig. 7.4 in the HR diagram. Letters correspond to the same events in the mass transfer evolution as before (see caption of Fig. 7.4 or text). These models illustrate the three main types of stable post-MS mass transfer evolution: thermal-timescale mass transfer producing hot (fully) stripped stars (top panel), thermal-timescale mass transfer producing much cooler, partially stripped stars (middle panel, case on the left-hand side), as well as binaries that evolve through phases of nuclear-timescale mass transfer (the remaining two models).

post-interaction nature of a partially-stripped donor may be revealed through measurements of increased helium and nitrogen abundances as well as its low spectroscopic mass, see Sec. 7.3.3 for a further discussion. At the very end of core-He burning, the donor expands again leading to another phase of mass transfer (the so-called case BB RLOF). The outcome of this phase and the final evolutionary stages before the core-collapse of the donor are outside the scope of this work.

The evolution of the LMC model with $P_{\rm ini} \approx 153$ days as well as the SMC model is dominated by long phases of nuclear-timescale mass transfer. After the initial rapid mass-transfer (labeled 'A'), these donors regain thermal-equilibrium and the mass-transfer rate decreases (labeled 'B'). During the subsequent phase of slow and long-lived mass transfer, their position in the HR diagram hardly changes at all. Note that the temporary detachment in the LMC model (labeled 'C') is associated with only a slight contraction of the donor star and therefore no significant displacement in the HR diagram. We find that binaries evolving through a nuclear-timescale mass transfer often experience a secondary ('delayed') peak of mass transfer rate which we label with 'D' in Fig. 7.4 and Fig. 7.5. This peak in $\dot{M}$ is associated with the donor being stripped down to a helium abundance plateau left by layers that used to be fully convective as part of the so-called intermediate convective zone. We discuss this in more detail in Sec. 7.4. Once again, at the final stages of He-burning the donor stars expand leading to a phase of thermal-timescale mass transfer at the point of central-He

exhaustion (labeled 'E').

In the following sections we discuss the parameter space for the different types of mass transfer evolution illustrated above.

### 7.3.2 PARAMETER SPACE FOR NUCLEAR-TIMESCALE MASS TRANSFER

In the previous section we demonstrated that a post-MS mass transfer in massive low-Z binaries can be long and slow, proceeding on a nuclear-timescale and leading to only partial envelope stripping. In this section we analyze the parameter space for this type of evolution. Fig. 7.6 includes results from our entire grid of binary models (initial mass ratio $q = 0.6$). Each model is represented by a rectangle that is colored according to the integrated duration of RLOF mass transfer in that model, on a logarithmic scale from $10^4$ to $10^6$ yr. White rectangles with an empty star represent non-interacting models (the widest model in each column). Hatched rectangles with a red star are non-converged models (due to numerical issues). In addition, similarly to Fig. 7.1, in the background of Fig. 7.6 we color-code the parameter ranges for RLOF corresponding to different evolutionary stages of the donor star: MS donors (purple), rapidly-expanding HG donors (green), and core-He burning donors (orange). Note that each mass includes at least one case-A mass transfer model, i.e. with a donor star that is still on MS. In what follows we focus only on wider binaries: those that interact during the post-MS evolution of the donor.

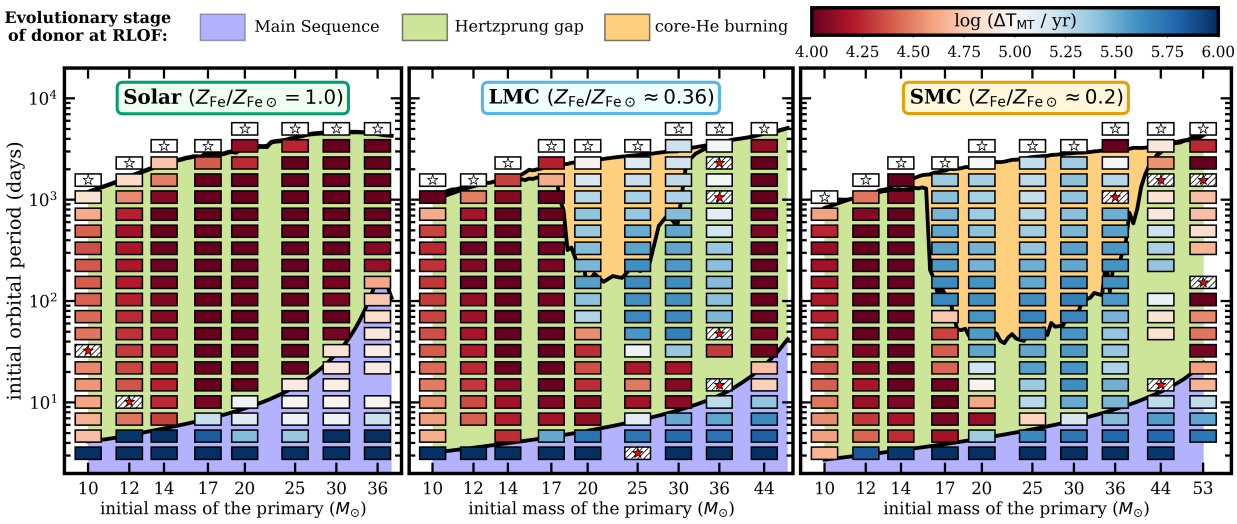


FIGURE 7.6: Integrated duration of mass transfer through RLOF ($\Delta T_{MT}$) in all the binary models computed across different primary masses $M_1$, orbital periods $P_{ini}$, and metallicities. Each binary evolution model is represented by a rectangle colored according to its corresponding $\log(\Delta T_{MT}/yr)$ value. The binary models are mapped onto the parameter space of varying $M_1$ and $P_{ini}$, with the background colors indicating the evolutionary state of the donor star at the moment of the initial RLOF (similar to Fig. 7.1): the MS donors (blue-ish), rapidly expanding HG donors (green), and core-He burning donors (orange). Rectangles colored in various shades of blue correspond to models that evolve through a phase of nuclear-timescale mass transfer.

Rectangles colored in various shades of blue in Fig. 7.6 correspond to models that evolve through a phase of nuclear-timescale mass transfer (with duration $\log(\Delta T_{MT}/\mathrm{yr}) > 5$). In a similar Fig. 7.8, which maps the major types of mass transfer evolution found across the grid of models, we distinguish the nuclear-timescale cases in magenta. We find that the parameter space for this type of evolution is related to the parameter space for RLOF from core-He burning donors, but not identical. This is the mass range of primaries with a low degree of rapid post-MS expansion (the HG phase), in which stars can burn He as blue/yellow supergiants. Intuitively, it makes sense that those are the donors that can regain thermal equilibrium while only partially stripped and transfer mass on the nuclear timescale of core-He burning. Somewhat surprisingly though, we find nuclear-timescale evolution not only in models in which such donors were already at the core-he burning stage at the moment of RLOF but also in tighter systems, in which the donors are rapidly-expanding HG stars (e.g. models with $P_{\mathrm{ini}} \approx 10 - 30$ days and $M_1 = 20 - 36\ M_\odot$ in the SMC grid). This is because in those cases the donor star has started the core-He burning phase soon after the onset of mass transfer and can then regain thermal equilibrium. We also find models with long interaction phases for primary masses slightly above the bulk mass range in which the HG expansion is halted, i.e. $M_1 = 36\ M_\odot$ and $M_1 = 44\ M_\odot$ in the LMC and SMC cases, respectively. It turns out that the parameter space for nuclear-timescale mass transfer is much larger than simply the parameter space for mass transfer initiated at the He burning stage.

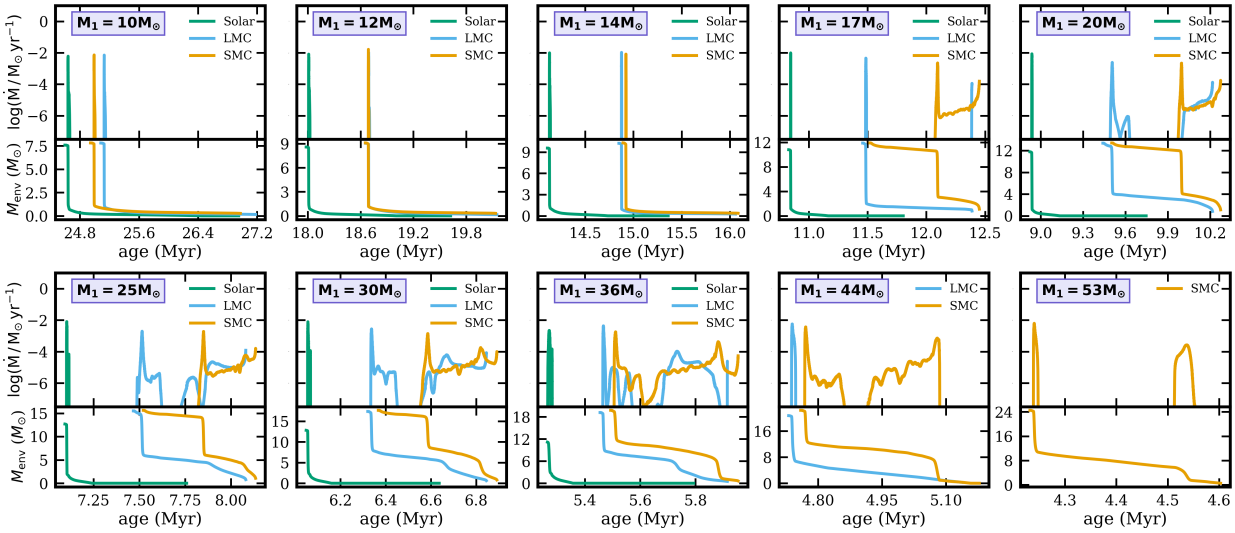


FIGURE 7.7: Mass-transfer rate and the envelope mass as a function of time in binary models evolving through a case B mass-transfer phase. Different panels correspond to different initial masses of the donor ($M_1$) and colors indicate the three different initial compositions considered. All the models shown were computed with initial orbital period $P \approx 225$ days and initial mass ratio $q = 0.6$. At Solar metallicity, the case B mass transfer is always a short-lived phase ($< 10^4$ yr) that strips the (nearly) entire hydrogen envelope leaving behind a stripped helium core. However, at subsolar metallicities of the LMC and SMC above a certain donor mass, a significant part of the envelope may be stripped on a much longer nuclear timescale of core He burning. Such donors remain only partially stripped stars for the duration of core-He burning.

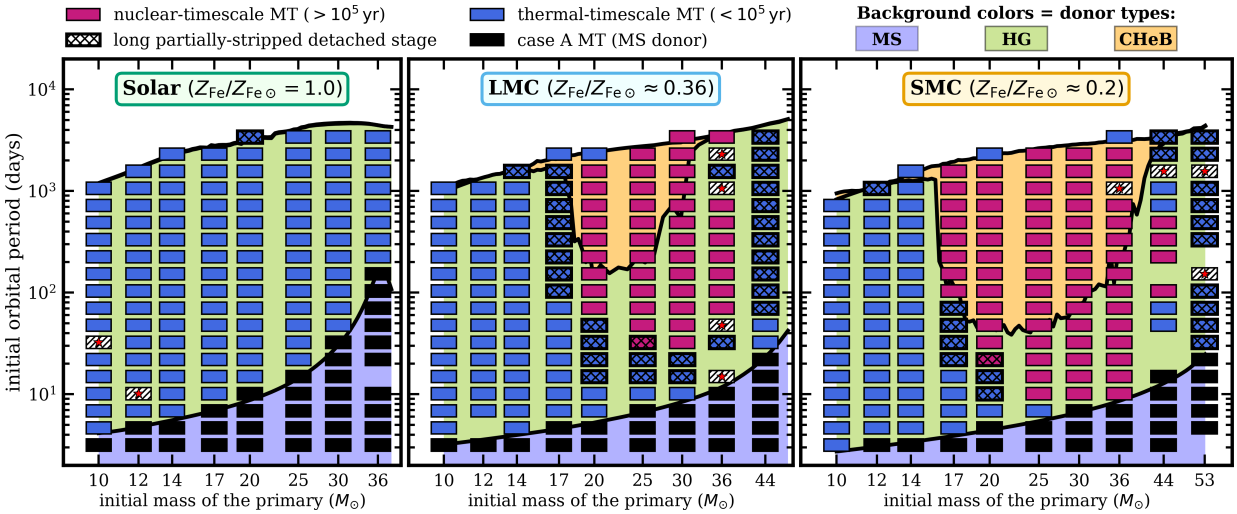


FIGURE 7.8: Major types of mass transfer evolution found across the grid of binary models. Similarly to Fig. 7.6, each binary model is represented by a rectangle and the background colors indicate the evolutionary state of the donor at the moment of the initial RLOF (Main Sequence, Hertzprung gap, or core-He burning). Missing rectangles are non-converged models. Black rectangles correspond to models in which the mass transfer takes place already during the MS. Among binaries with a post-MS interaction, we differentiate between those that evolve through phase(s) of nuclear-timescale mass transfer ($\Delta T_{MT} > 10^5$ yr, in magenta) and those in which the interaction happens on a short thermal timescale ($\Delta T_{MT} < 10^5$ yr, typically $< 10^4$ yr, in blue). In addition, in hatch are models in which the post-interaction donor phase with $T_{eff} < T_{eff;ZAMS}$ is long ($> 0.75$ the core-He burning lifetime), i.e. models leading to partially-stripped rather than hot stripped stars.

The effect of the primary mass and metallicity on the mass transfer duration is also evident in Fig. 7.7, in which we take a slice through the grid of binary models selecting those with initial periods of $P_{ini} \approx 225$ days and varying the initial primary mass $M_1$. Above a certain primary mass, the low-Z donors retain a substantially larger fraction of their envelopes from the initial rapid interaction and experience episodes of slow mass transfer afterwards. Notably, LMC systems with $M_1 = 17\ M_\odot$ and $44\ M_\odot$ as well as the SMC model with $M_1 = 53\ M_\odot$ evolve through mostly rapid (thermal) mass transfer and yet they retain a higher envelope fraction compared to Solar metallicity models. Those model lead to the formation of long-lived partially stripped stars in detached binaries, similarly to the $M_1 = 30\ M_\odot$ LMC model with $P_{ini} \approx 22$ days shown earlier in detail in Fig. 7.4 and Fig. 7.5. In the next section we analyze the parameter space for this type of evolution as well as the properties of partially-stripped stars.

### 7.3.3 FORMATION AND PROPERTIES OF PARTIALLY-STRIPPED STARS IN DETACHED BINARIES

In this section we take a closer look at models that lead to formation of long-lived partially-stripped stars in detached binaries (e.g. Fig. 7.4 and Fig. 7.5). We define those as binaries in which a donor star spends at least 75% of its core-He burning lifetime as a post-interaction star that stays on the

cooler side of the ZAMS temperature in the HR diagram. Such donors are partially-stripped of their envelopes and overlap with single stellar tracks, as opposed to fully stripped stars that become hot helium stars (with $T_{\rm eff} >> T_{\rm ZAMS}$), see Fig. 7.5.

In Fig. 7.8, with hatches we mark which models in our grid lead to partially-stripped stars. It should be noted that various non-hatched magenta rectangles (representing models that evolve through nuclear-timescale mass transfer) can also produce partially-stripped donors but only for relatively short detachment phases (that do not make our $0.75\Delta T_{\rm He;burn}$ cut). For more details see Fig. 7.17 in the appendix. Importantly, in those cases the donor star never shrinks significantly with respect to its Roche lobe (usually $R_{\rm don}/R_{\rm RL} > 0.6$). [3]

Fig. 7.8 makes it clear that in the $M_1 - P_{\rm ini}$ plane models leading to partially- stripped stars are a intermediate stage between rapid mass transfer models and models experiencing nuclear-timescale mass transfer. Similarly to nuclear-timescale interaction models, we find that partial-envelope stripping is roughly associated with the primary mass range in which the HG expansion is halted at the blue/yellow supergiant stage. Additionally, for a given primary mass among the LMC and SMC models with $M_1 \geq 17\ M_\odot$, the type of mass transfer evolution depends on the orbital period, where long detachments with partially-stripped stars usually take place in binaries with relatively short orbital periods. This is because the shorter the orbital period, the more of the envelope is transferred in the initial mass transfer phase (which favors long detachments), see also Fig. 7.3. A similar effect would be observed in models with a more extreme mass ratio or a higher specific angular momentum of the non-accreted matter. We also find relatively fewer binaries with long detachment phases among the SMC models compared to the LMC grid.

With the next few figures, we discuss the basic properties of partially-stripped stars. Fig. 7.9 compares the distribution of donors stripped in the LMC metallicity models with their Solar metallicity counterparts in the HR diagram. In each panel, the coloured lines show donor tracks from a selection of binary models with different primary masses in which the mass transfer was initiated soon after the end of MS. Crosses indicate where a donor spends most of its core-He burning lifetime since the onset of RLOF (spaced by 50,000 yr). Grey lines show single-stellar models of the same masses. In addition, in greyscale we plot the distribution of post-interaction donors in a detached state with a Roche-lobe filling factor $R/R_{\rm RL} < 0.6$ from all our binary models. The 0.6 cut makes sure that we do not include most of binaries that evolve primarily through phases of nuclear-timescale mass transfer (and temporary detachments with $R/R_{\rm RL} > 0.6$) with blue or yellow supergiant donors at $\log(T_{\rm eff}/{\rm K}) < 4.0$. We discuss those in Sec. 7.5.4. We caution that the binary models used to construct the greyscale distribution were not weighted by either the initial mass function or the initial period distribution (for a weighted HRD distribution we refer to Fig. 7.14).

For Solar metallicity (left panel in Fig. 7.9), all the binary models evolve through thermal-timescale mass transfer which rapidly strips nearly the entire envelope of the donor. As a result,

[3]The detachment phases in nuclear-timescale mass transfer models are associated with changes in the H abundance in the moving location of the H-burning shell. Given the uncertainties in the detailed features of the H abundance profile of the bottom envelope layers, these detachments are not a robust prediction of evolutionary models.

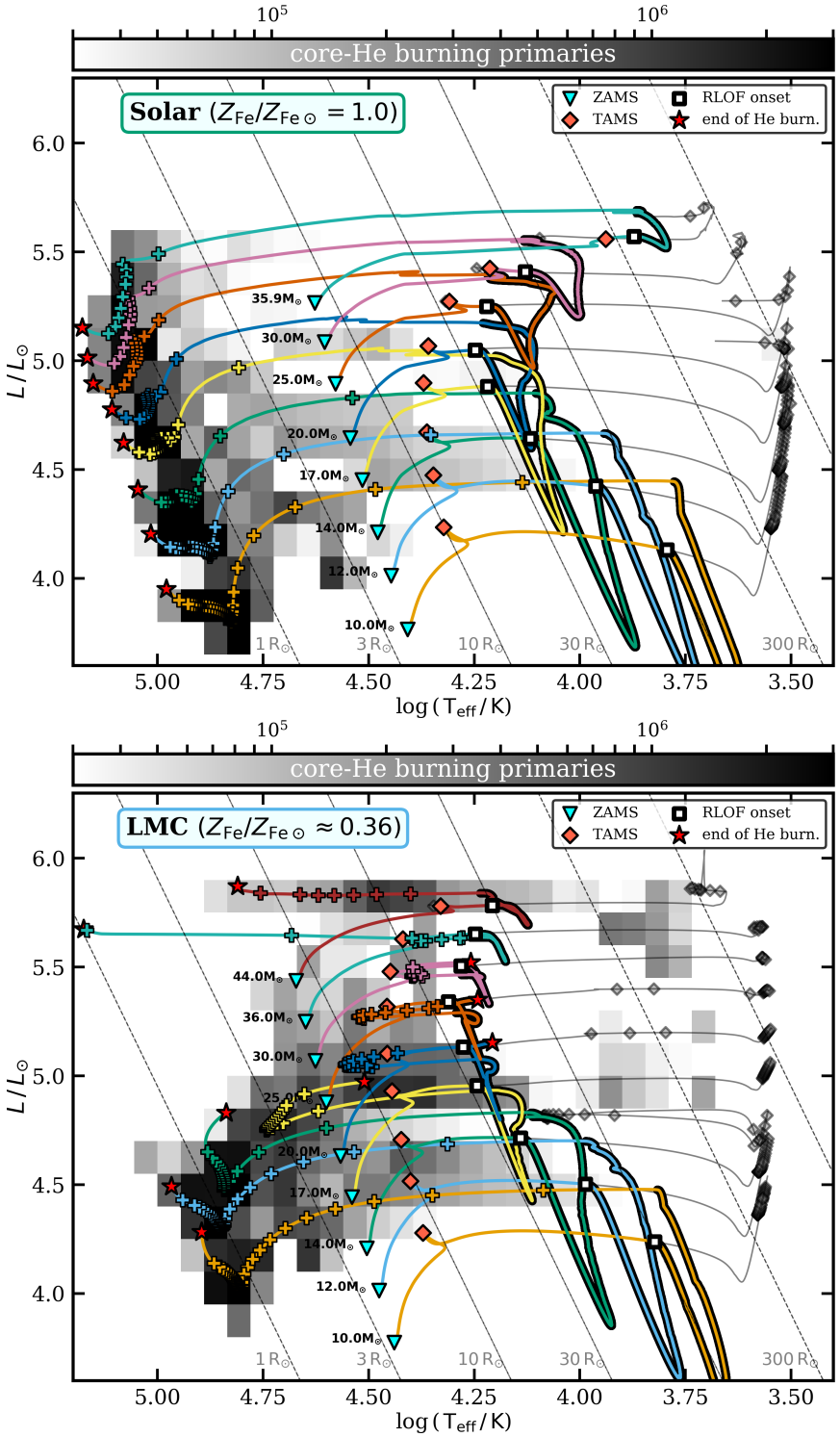


Figure 7.9: Distribution of post-interaction donors in detached binaries with Roche-lobe filling factors $< 0.6$ from all the grid models interacting after the end of MS (shown in greyscale), plotted for the Solar metallicity (left) and the LMC composition (right). Overplotted are several donor tracks from selected binary models (colored lines) as well as single stellar tracks for comparison (grey lines). The mass transfer phase is shown in bold. Crosses are spaced by 50,000 yr starting from the onset of RLOF. Note that models were not weighted by the initial-mass function or the initial period distribution to construct the distribution. In all the Solar metallicity models, thermal-timescale mass transfer leads to the formation of hot stripped stars. In the LMC models, primaries above the initial mass of $M_1 \geq 17\ M_\odot$ become only partially stripped and as post-interaction stars can largely overlap with single-stellar tracks.

most of the post-interaction lifetime of donors is spend in the hot region of stripped helium stars, to the left of the $T_{\rm eff}$ range of ZAMS. The only contribution of the post-interaction Solar-metallicity donors in the $T_{\rm eff} < T_{\rm eff;ZAMS}$ region comes from donors that have just detached from mass transfer and are rapidly contracting on the thermal timescale.

In the LMC case, models with primaries with $M_1 \geq 17\ M_\odot$ and a post-MS mass-transfer interaction no longer produce hot stripped stars. Instead, they lead to partially-stripped post-interaction donors that populate the HR diagram region with $T_{\rm eff} < T_{\rm eff;ZAMS}$ in which they occupy the same region as pre-interaction stars or single stars. Interestingly, we not only find post-interaction core-He burning stars in the region of MS (where, for most realistic star formation histories, they would be vastly outnumbered by core-H burning stars) but also in the $T_{\rm eff}$ range of the early post-MS stage ( $\log(T_{\rm eff}/{\rm K})$ between $\sim 4.2$ and 4.4), where single stellar tracks predict virtually not stars and a sharp gap in the HR diagram distribution, in contrast to observations (see Sec. 7.5.4).

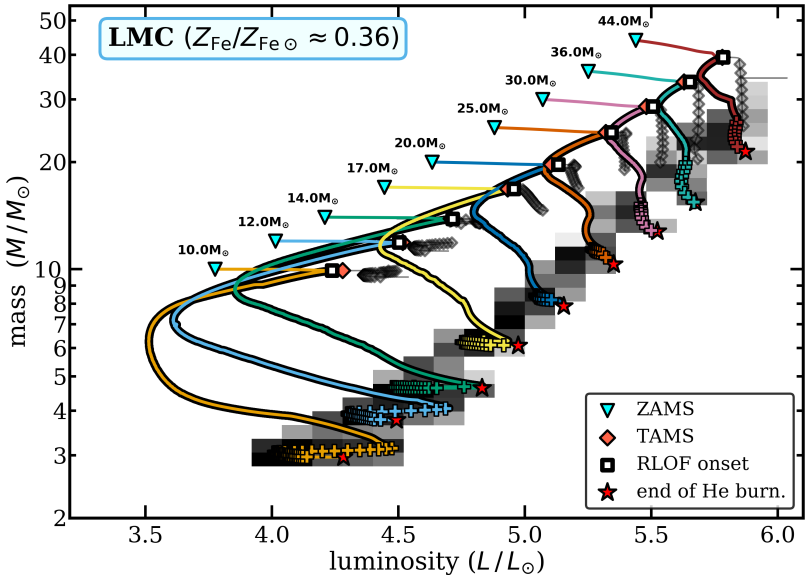


FIGURE 7.10: Luminosity-mass relation of post-interaction donor stars in detached binaries with $R/R_{\rm RL} < 0.6$ at the LMC metallicity. The colors correspond to the few selected donor tracks from binary models shown in the HR diagram in Fig. 7.9, with crosses (spaced by 50,000 yr) marking the position occupied for most of the evolution since the onset of RLOF. Grey lines show the evolution of single stars with the corresponding masses. Similarly to Fig. 7.9, in greyscale we plot the distribution of post-interaction stars in detached systems from all the grid models (except those interacting on MS). The figure demonstrates that mass transfer can produce partially-stripped stars that may appear significantly undermassive for their apparent evolutionary mass (as one would deduce from single tracks). Note, however, that models with $M_1 \leq 14\ M_\odot$ produce post-interaction stars that are hot stripped stars ($T_{\rm eff} > T_{\rm eff;ZAMS}$).

Partially-stripped stars, while potentially mixed with single or pre-interaction stars, have several distinctive characteristics. First, they are undermassive for they apparent luminosities compared to single stellar tracks. We illustrate this in Fig. 7.10 where, similarly to Fig. 7.9, in greyscale we plot

the mass-luminosity distribution of post-interaction stars in detached binaries from our entire grid of LMC models (excluding case A systems). With colored lines, we overplot donor tracks from a few selected binary models (the same as in Fig. 7.9), and with grey lines we show single stellar tracks for comparison. The figure demonstrates that mass transfer can produce partially-stripped stars that may appear significantly undermassive for their apparent evolutionary mass (as one would deduce from their luminosity and based on single tracks). Wind-mass loss can reduce the mass of post-MS single stars in a similar way only for the most massive stars in our grid ($\gtrsim 44\ M_\odot$).

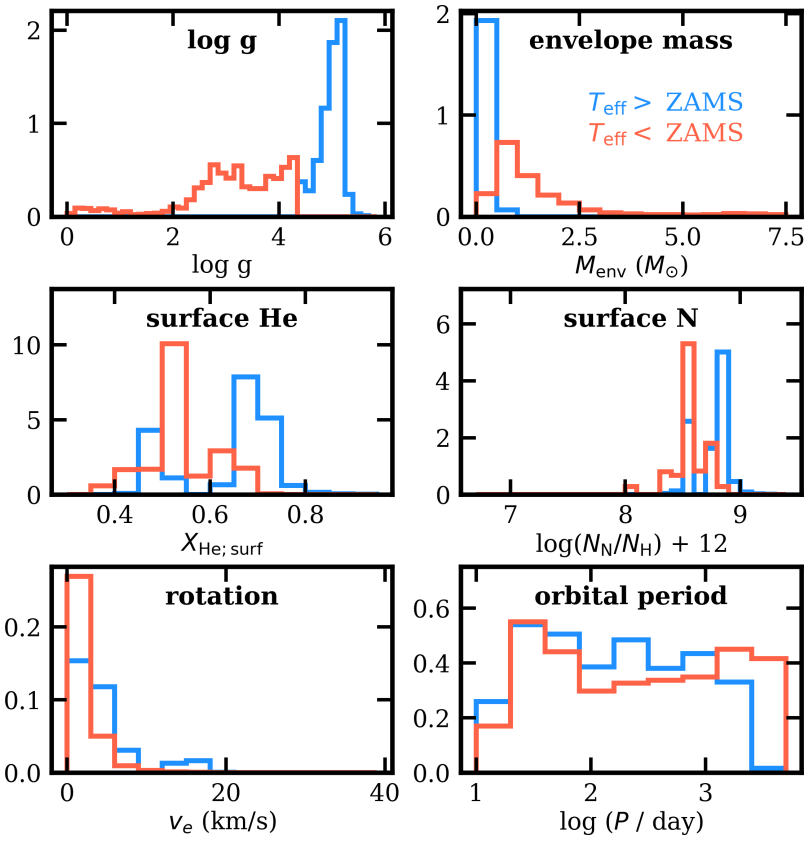


FIGURE 7.11: Properties of hot stripped stars ($T_{\rm eff} > T_{\rm eff;ZAMS}$, in red) compared to those of partially-stripped ($T_{\rm eff} < T_{\rm eff;ZAMS}$, in blue) in detached binaries with $R/R_{\rm RL} < 0.6$ (as in Fig. 7.9) based on LMC models with a post-MS mass transfer interaction (i.e. excluding case A models). Note that partially-stripped stars originate primarily from models with primary masses $M_1 > 17\ M_\odot$.

In Fig. 7.11, we illustrate several other basic properties of partially-stripped stars (in blue) compared to hot stripped stars (in red). In addition to their high luminosity-to-mass ratio, partially-stripped stars are also expected to be helium and nitrogen enriched on the surface, as prior mass loss has revealed deep envelope layers which have been mixed with products of CNO burning. At the same time, they are not expected to be fast rotators: they originate from wide binaries ($P_{\rm ini} > 10$ days) so that tidal synchronization leads to rotational velocities $\lesssim 10$ km/s. As we find them all across the HR diagram, they have surface gravities in a wide range, from $\sim 2$ to 4.3 (in log(g)), and can reside in systems with very different orbital periods (from tens to thousands of days).

In Sec. 7.5.4 we discuss those and other implications of our findings on the distribution and observables of core-He burning stars in the HR diagram.

## 7.4 WHY PARTIALLY STRIPPED? RADIAL RESPONSE OF STARS TO MASS LOSS

In the previous sections we found that in many low-Z massive binaries the post-MS mass transfer may include phases of long nuclear-timescale mass exchange ($\log(\dot{M}) \sim 10^{-5}\,\mathrm{M_\odot\,yr^{-1}}$, $\Delta T_{\rm MT} > 10^5$ yr) and produce post-interaction core-He burning supergiants that are only partially stripped of their envelopes. This is in stark contrast to Solar metallicity models, all of which predict the thermal-timescale mass transfer to strip nearly the entire donor envelope ($\log(\dot{M}) \sim 10^{-3}\,\mathrm{M_\odot\,yr^{-1}}$, $\Delta T_{\rm MT} \lesssim 10^4$ yr) and produce hot stripped stars. In this section, we seek to understand the origin of these canonically different types of post-MS mass transfer evolution. To do so, we study the behavior of donor stars of different metallicities in response to mass loss.

We define $R_{\rm th;eq}$ as the radius that a star needs to have in order to be in thermal equilibrium. In the case of singe-star evolution, most of the time $R_{\rm th;eq} = R$ where $R$ is the actual radius of a star. The exception are short-lived phases such as the HG expansion or a phase of He-shell burning right after the central He exhaustion. In the case of binary evolution, the radius of a star is restricted by the size of its Roche lobe ($R \lesssim R_{\rm RL}$), which may prevent it from reaching thermal equilibrium. For instance, during thermal-timescale mass transfer the donor star is thermally unstable having radius $R_{\rm don} \approx R_{\rm RL} << R_{\rm th;eq}$. Its continuous fast expansion in a futile attempt to equate $R_{\rm don} = R_{\rm th;eq}$ is what leads to high mass transfer rates.

Knowing $R_{\rm th;eq}$ of a donor star and how it changes over the course of mass transfer is the key to understand the transition from thermal-timescale mass transfer to detachment or to a nuclear-timescale mass exchange found in our SMC and LMC models. To obtain the evolution of $R_{\rm th;eq}$ as a function of the remaining donor mass $M_{\rm don}$, we proceed in a similar way to Quast et al. (2019). We begin by evolving a binary system until the onset of RLOF. Normally, from that point onwards, all of our binary models would enter a phase of thermal-timescale mass transfer (at least initially). Here, however, we terminate the binary model, extract the donor star, and subject it to the following mass-stripping experiment. We apply a constant mass-loss rate $10^{-5}\,\mathrm{M_\odot\,yr^{-1}}$ which is low enough to guarantee that the star remains at thermal equilibrium. At the same time, we switch off any composition changes due to nuclear burning. This mimics the rapid evolution through a phase of thermal-timescale mass transfer when there is no time for any significant burning to occur. The radius of a star that is being stripped in this way is a good representation of the equilibrium radius $R_{\rm th;eq}$ that a donor star would need to have in order to regain stability and stop the thermal-timescale mass transfer.

In Fig. 7.12, we plot the results for the case of 20 $M_\odot$ donors in binaries with an initial period of $P_{\rm ini} \approx 32$ days and three different metallicities. By the onset of RLOF ($R_{\rm RLOF} \approx 60\ R_\odot$), the SMC donor has nearly regained equilibrium from the HG phase as a core-He burning star, the LMC donor would still continue the HG expansion up to $R \approx 100\ R_\odot$ and the Solar donor up to $R \approx 1000\ R_\odot$. The panels are plotted as a function of the remaining donor mass, i.e. the time direction in the top and middle panel is to the left. The bottom panel shows the internal helium abundance ($X_{\rm He}$) profile of the donor at the onset of RLOF. The He profiles are characterized by a

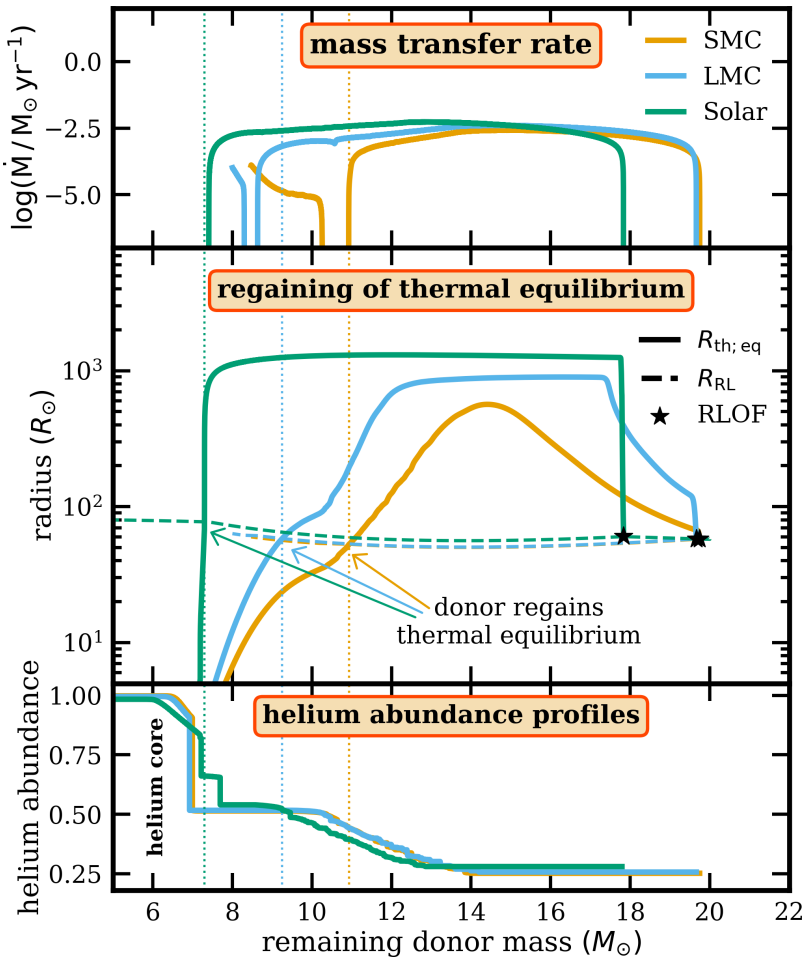


FIGURE 7.12: Origin of partial envelope stripping of the LMC and SMC models explained based on the response of donor stars to mass loss, using the 20 $M_\odot$ donor case as an example. Quantities are plotted as a function of the remaining donor mass $M_{\rm don}$, i.e. the time direction in the top two panels is to the left. Top panel: mass transfer rate from binary models ($P_{\rm ini} \approx 32$ days). Middle panel: equilibrium radius $R_{\rm th;eq}$ that the donor star would need to have in order to be in thermal equilibrium, compared with its Roche lobe size $R_{\rm RL}$. For as long as $R_{\rm th;eq} > R_{\rm RL}$, the thermal-timescale mass transfer continues to strip the envelope of the donor. Vertical dotted lines mark the points when $R_{\rm th;eq} = R_{\rm RL}$, the donor can regain equilibrium, and the mass transfer may stop or slow down to the nuclear timescale. Bottom panel: internal He abundance profile of the donor at the onset of RLOF.

plateau with a constant He abundance $X_{\rm He} \approx 0.5$ left by an intermediate convective zone and a constant $X_{\rm He}$ gradient above the plateau left by a retreating convective core during the MS (e.g. Langer et al., 1985; Langer, 1991). The middle panel shows the evolution of $R_{\rm th;eq}$ obtained from the mass-stripping experiment described above as well as the size of the donor's Roche lobe $R_{\rm RL}$ in the corresponding binary model (initial mass ratio $q = 0.6$). For as long as $R_{\rm th;eq} > R_{\rm RL} \approx R_{\rm don}$, the donor star is out-of-equilibrium and the mass transfer proceeds on the thermal timescale. Vertical dotted lines mark the donor mass when $R_{\rm th;eq} = R_{\rm RL}$. For comparison, in the top panel we plot the actual mass transfer rate evolution from the corresponding binary models. Note that beside the initial thermal phase with $\log(\dot{M}) \approx 10^{-2.5}\,{\rm M}_\odot\,{\rm yr}^{-1}$, the SMC model also experiences a nuclear-timescale mass transfer with $\log(\dot{M}) \approx 10^{-5}\,{\rm M}_\odot\,{\rm yr}^{-1}$.

The middle panel of Fig. 7.12 illustrates the key difference between the Solar-metallicity and

the low-Z donors. All throughout the mass transfer, the Solar-metallicity donor would need to expand to $R_{\rm th;eq} \approx 1000\ R_\odot$ (the size of a red supergiant) to regain thermal equilibrium. This is much larger than the size of the Roche lobe, not only in the $P_{\rm ini} \approx 32$ days and $q = 0.6$ example shown in Fig. 7.12 but in nearly all the possible orbital configurations in an interacting binary. Only when the donor is stripped of nearly its entire envelope ($M_{\rm don} \approx 7.5\ M_\odot$), does the $R_{\rm th;eq}$ begin to rapidly decrease towards the typical size of a fully-stripped helium star (a few $R_\odot$) and the binary detaches. The $R_{\rm th;eq}$ evolution of the Solar model in Fig. 7.12 is very well representative for all the post-MS donor stars that become fully stripped during thermal-timescale mass transfer, i.e. the entire Solar-metallicity grid as well as the 10-14 $M_\odot$ donors at SMC and LMC compositions.

The SMC and LMC donors in Fig. 7.12 behave in a distinctively different way. The initial increase of $R_{\rm th;eq}$ is slower, which leads to slightly smaller thermal $\dot{M}$ rates found in low-Z compared to Solar binary models. More importantly, $R_{\rm th;eq}$ begins to decrease much earlier, when the donors are still far from being fully stripped. [4] This allows the low-Z donors to regain thermal equilibrium and detach when only partially stripped, as seen in the binary models in the top panel (and found all throughout the low-Z grids of binary models). In addition, the fact that $R_{\rm th;eq}$ decreases gradually over a wide range of remaining donor masses is what leads to a large variety of envelope masses of partially stripped low-Z donors, depending on the orbital period and the mass ratio (e.g. Fig. 7.2 and Fig. 7.3).

One may notice that the moment when $R_{\rm th;eq} = R_{\rm RL}$ in the mass-stripping experiment is not always exactly aligned with the $\dot{M}$ drop in the binary model (top panel), e.g. the LMC model in Fig. 7.12. This is because as a the donor star relaxes to regain equilibrium at $R = R_{\rm th;eq}$, it may still continue to expand relative to its Roche lobe, leading to 'over-stripping'. We find that this is especially the case when the $R_{\rm th;eq} = R_{\rm RL}$ vertical line falls in the region of the He abundance plateau ($M_{\rm don}$ range between $\sim 7$ and $10\ M_\odot$ in the SMC and LMC models in Fig. 7.12).

Fig. 7.12 suggests that the equilibrium radius $R_{\rm th;eq}$ is to some extent affected by the underlying He abundance profile of the donor (as also found by Quast et al., 2019), in particular at the location of the already mentioned He plateau (where the $R_{\rm th;eq}$-$M_{\rm don}$ slope of the low-Z models temporarily flattens). We illustrate this better in Fig. 7.13, where we repeat the mass-stripping experiment for the case of a 25 $M_\odot$ donor at LMC metallicity and five different initial orbital periods. The corresponding binary models have led to various outcomes (hot stripped star, partially stripped star, or nuclear-timescale mass transfer), as explained in the legend. In the third panel we now show the mass-radius exponent $\zeta_{\rm th} = d\log R_{\rm th;eq}/d\log M_{\rm don}$. The value of $\zeta_{\rm th}$ is a useful magnifying glass to expose any changes in the $R_{\rm th;eq}$-$M_{\rm don}$ slope. For reference, with horizontal lines we show the mass-radius exponent of the donor's Roche lobe $\zeta_{\rm RL} = d\log R_{\rm RL}/d\log M_{\rm don}$ for a few different mass ratios and fully non-conservative mass transfer (Eqn. 16.25-26 from Tauris & van den Heuvel 2006).

The double-peaked behavior of $\zeta_{\rm th}$ in Fig. 7.13 can be linked to some of the features found in binary models throughout Sec. 7.3. In most binaries that evolve through phase(s) of nuclear-timescale mass transfer, the donor regains thermal-equilibrium when crossing the first peak of $\zeta_{\rm th}$

[4] In fact, the $R_{\rm th;eq}$ behavior of low-Z models in Fig. 7.12 is somewhat similar to that of MS donors.

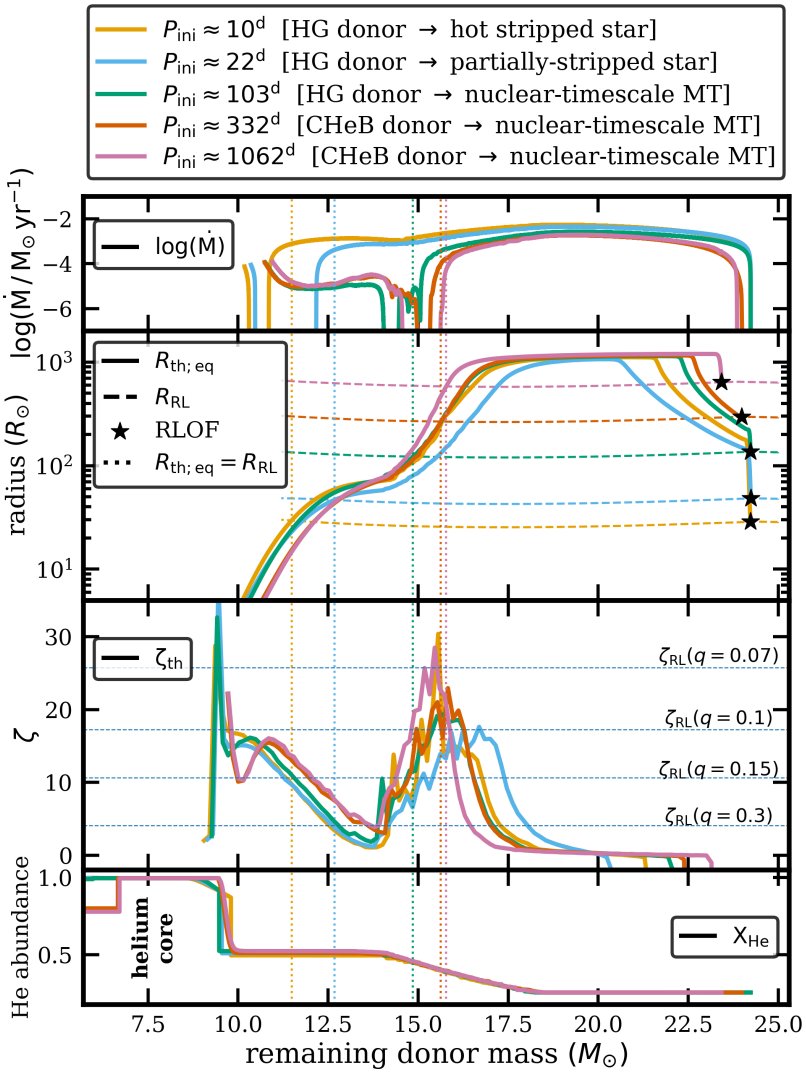


FIGURE 7.13: Similar to Fig. 7.12, but for the case of a 25 $M_\odot$ donor at LMC composition and five different initial orbital periods. The legend on top details what was the evolutionary state of the donor at the onset of RLOF (HG phase or core-He burning) as well as the main outcome of the mass transfer interaction (hot stripped star, partially stripped star, or nuclear-timescale mass transfer). The mass-radius exponent in the third panel is defined as $\zeta_{th} = d\log R_{th;eq}/d\log M_{don}$ as derives directly from the results in the second panel. Horizontal lines show the mass-radius exponent of the donor's Roche lobe $\zeta_{RL} = d\log R_{RL}/d\log M_{don}$ assuming a fully non-conservative mass transfer. The behavior of $\zeta_{th}$ as a function of the remaining donor mass can be linked to various features found in binary models, see text.

(between ~ 14 and 17.5 $M_\odot$ in Fig. 7.13). In turn, in binary models in which the donor remains detached for most of the core-He burning lifetime (either as hot- or partially-stripped star) the thermal-timescale mass transfer tends to strip the donor down to deeper layers of constant $X_{He}$ ($\lesssim$ 14 $M_\odot$ in Fig. 7.13). The abundance pattern of these layers sets the surface composition of partially-stripped stars discussed in Sec. 7.3.3.

We always find a $\zeta_{th}$ peak in layers above the He abundance plateau. Its saw-like shape is related to the step-like He abundance gradient above the region of He plateau. It manifests itself in oscillations of the mass transfer rate during the nuclear-timescale mass transfer phase when a donor is being stripped from those envelope layers (see e.g. the SMC models in Fig. 7.2). The local minimum of $\zeta_{th}$ around $M_{don} \sim 14\ M_\odot$ in Fig. 7.13, on the other hand, is responsible for the secondary major $\dot{M}$ peak that in some models is a very prominent feature (see Fig. 7.4 and Fig. 7.5, label 'D'). [5] Stripping through the bottom envelope layers of constant He abundance

[5] If the mass ratio is close to unity then $\zeta_{th}$ may temporarily become smaller than $\zeta_{RL}$, leading to a brief phase of another thermal-timescale mass transfer.

($M_{\rm don} \lesssim 14\ M_\odot$) leads to a smooth $\zeta_{\rm th}$ increase and also results in a smooth $\dot{M}$ behavior found in late phases of mass transfer in binary models. [6]

It is noteworthy that the values of $\zeta_{\rm th}$ found in the mid-envelope region can be very high, with $\zeta_{\rm th} > \zeta_{\rm RL}$ for even extreme mass ratios of $q < 0.1$. We discuss this in the context of ULX sources with NS accretors in Sec. 7.5.7.

In summary, we find that partial envelope stripping and nuclear-timescale mass transfer occurs in binary models when the donor can be in thermal equilibrium as a partially-stripped star of an intermediate size ($R_{\rm th;eq}$ of a few tens or hundreds $R_\odot$). Such donors, when evolved as single stars, are characterized by a relatively modest HG expansion and a long blue/yellow supergiant lifetime during the core-He burning phase. The post-MS expansion of a massive star is thus the key factor affecting its evolution in an interacting binary. A secondary role is played by detailed features of the He abundance profile, some of which may be causing small variations in the mass transfer rate or temporary detachments. The abundance profile in massive star envelopes is a particularly uncertain prediction of stellar models. Consequently, details of the nuclear-timescale mass transfer sequences should be treated with much caution.

## 7.5 DISCUSSION

### 7.5.1 THE IMPORTANCE OF POST-MS EXPANSION AND ITS UNCERTAINTY DUE TO MIXING

Throughout the paper, we have found that the course and outcome of stable mass transfer evolution initiated by a post-MS donor is closely related to the way in which massive stars expand after the end of MS when they transition to the core-He burning phase. Stars that rapidly expand all the way to the red (super)giant branch (i.e. the HG phase), when transferring mass in interacting binaries, become nearly fully stripped of their H envelopes in a short phase of thermal-timescale mass transfer ($\log(\dot{M}) \sim 10^{-3}\,{\rm M}_\odot\,{\rm yr}^{-1}$, $\Delta T_{\rm MT} \lesssim 10^4$ yr). In contrast, stars that remain relatively compact in the transition to the core-He burning phase and burn He as blue or yellow supergiants, when in binaries, remain only partially stripped of their H envelopes (at least by the end of core-He burning) and can evolve through phases of nuclear-timescale mass transfer ($\log(\dot{M}) \sim 10^{-5}\,{\rm M}_\odot\,{\rm yr}^{-1}$, $\Delta T_{\rm MT} > 10^5$ yr). Such a halted HG expansion of massive stars has been found in single low-Z models computed with different codes over the years (being more and more prominent the lower the metallicity, e.g. Brunish & Truran, 1982; Baraffe & El Eid, 1991; Langer, 1991; Georgy et al., 2013; Tang et al., 2014; Groh et al., 2019; Klencki et al., 2020). The fact that low-Z massive giants can remain much more compact compared to their high (Solar) metallicity counterparts is a result of a complicated interplay between at least two different Z-dependent factors: higher temperatures and densities of low-Z helium cores at TAMS as well as lower opacities of low-Z envelopes. It is

[6] We notice a slight shift in the values $\zeta_{\rm th}$ of those layers between the HG and more evolved core-He burning donors in Fig. 7.13. This is likely associated with changes in the H abundance and He/H gradient in the moving location of the H-burning shell, which has been found to affect the radii of core-He burning massive stars (Langer, 1991).

not until the current study that this phenomenon has gained special significance as the key factor affecting the evolution of stars through mass transfer in binaries.

It is essential to realize that the post-MS expansion of massive stars is notoriously model sensitive due to being highly dependent on the efficiency of internal mixing. This well-established fact (e.g. Langer et al., 1985; Langer & Maeder, 1995; Maeder & Meynet, 2001) is especially clear in the recent studies in which the increased computational power has allowed for a more comprehensive exploration of various mixing coefficients (Schootemeijer et al., 2019; Klencki et al., 2020; Kaiser et al., 2020; Higgins & Vink, 2020). Among the factors that were identified to play a role are convective-core overshooting during the MS (Stothers & Chin, 1992; Langer & Maeder, 1995), semiconvection (Langer et al., 1985; Langer, 1991), rotational mixing (Georgy et al., 2013), as well as past accretion phases (especially if the accretor is non-rejuvenated, see Hellings, 1984; Braun & Langer, 1995; Dray & Tout, 2007). We refer to an extensive discussion of the subject in Sec. 5.1 and App.B in Klencki et al. (2020). For example, if we were to compute our grids of binary models with lower efficiency of semiconvection ($\alpha_{\rm SC} = 1$ instead of $\alpha_{\rm SC} = 33$) then even the SMC-metallicity models would all experience a rapid HG expansion all the way until the red supergiant stage (and be subject to full envelope stripping through thermal-timescale mass transfer).

For the time being, the key piece of evidence in support of the models presented in this paper are large populations of blue and yellow supergiants identified in the LMC and the SMC (Hunter et al. 2008; Neugent et al. 2010, 2012; Urbaneja et al. 2017; Kalari et al. 2018, see also HR diagrams in Ramachandran et al. 2019; Gilkis et al. 2021). Their existence can only be reconciled with models that predict a significant fraction of core-He burning taking place in the middle of the HR diagram (Schootemeijer et al., 2019; Klencki et al., 2020) such as the models adopted here (with a halted HG expansion at the LMC and SMC compositions). A robust comparison between theory and observation to calibrate the post-MS expansion is challenged by the fact that the population of blue and yellow supergiants may also include stars in a post-red supergiant stage (either stripped in binaries or through cool-star winds, or stars experiencing blue-loops, e.g. Ekström et al., 2012; Meynet et al., 2015; Farrell et al., 2019) as well as potentially some of the accretors and mergers from past binary interaction phases (e.g. Podsiadlowski et al., 1992; Vanbeveren et al., 2013; Glebbeek et al., 2013; Justham et al., 2014). Extended grids of binary models, exploring various mixing assumptions and including the evolution of accretors, are likely necessary to further calibrate the post-MS expansion of LMC and SMC stars in the future studies.

Instead, a promising way to constrain the mass transfer evolution in low-Z binaries and verify our findings is to search for signatures of partial-envelope stripping and nuclear-timescale mass transfer among the populations of massive stars in metal-poor galaxies. We outline the main observational predictions from our models in Sec. 7.5.4.

Notably, while details of the post-MS expansion of massive stars at a given metallicity are very uncertain in stellar models, the overall trend with metallicity appears to be a robust prediction (Sec. 5.2 in Klencki et al., 2020). As such, we predict that at some sufficiently low metallicity (possibly already at the LMC composition), the thermal-timescale mass transfer and full envelope

stripping will yield ground to nuclear-timescale mass exchange and partial-envelope stripping of massive post-MS donors.

### 7.5.2 THE CASE OF STELLAR-ACCRETOR BINARIES

In this work, for simplicity, we treated the secondary star as a point mass and we set the accretion efficiency $\beta$ at the Eddington limit. This makes our models directly applicable to BH binaries (assuming that the Eddington limit is not substantially exceeded). However, as we argue below, we predict that most of our results and conclusions will also hold for the case of binaries with stellar accretors.

It is important to realize that Eddington-limited accretion in massive binaries is similar to the assumption of a fully non-conservative mass transfer (i.e. $\beta = 0$). For the default initial mass ratio $q = 0.6$, the accretor masses range from 6 to 31.8 $M_\odot$ across our models. The corresponding Eddington accretion rates for BHs (assumed as the accretion limit in our models) range from $\sim 1.3 \times 10^{-7}\,\mathrm{M_\odot\,yr^{-1}}$ to $\sim 7 \times 10^{-7}\,\mathrm{M_\odot\,yr^{-1}}$. Even during phases of slow nuclear-timescale mass transfer, with typical rates of $10^{-5}\,\mathrm{M_\odot\,yr^{-1}}$, this yields accretion efficiencies of only a few percent. We thus expect that a grid of binary models with stellar accretors and a small accretion efficiency would produce mass-transfer sequences very similar to our models.

As we discuss in Sec. 7.5.3, the true accretion efficiency in stellar-accretor binaries corresponding to our models is currently unknown and so ideally any $\beta$ value between 0 and 1 should be considered. Varying $\beta$, and similarly considering different values for the specific angular momentum of the non-accreted matter, would affect the evolution of binary separation during mass transfer and consequently the size of the donor's Roche lobe. These effects are degenerate with changing the mass ratio between the binary components. In Fig. 7.2, using the 25 $M_\odot$ donor example, we showed that for a wide range of initial mass ratios ($q$ between 0.25 and 1.5), the essential differences between the Solar and low-Z models remain unaffected. In particular, binaries in which thermal-timescale mass transfer produces fully stripped donors (the Solar-Z example) evolve towards the same outcome no matter the mass ratio. In the case of low-Z models with partial envelope stripping, variations in factors that affect the Roche lobe of the donor will likely affect the ratio between systems that remain primarily in the detached stage and those that maintain the nuclear-timescale mass transfer.

Besides the possibility of high accretion efficiencies, the presence of a stellar accretor could also lead to some of the binaries evolving towards a contact phase (Pols, 1994; Wellstein et al., 2001) and potentially dynamical instability and a merger (Marchant et al., 2016). Details of this process remain highly uncertain.

### 7.5.3 INCREASED ACCRETION EFFICIENCY IN LOW-Z BINARIES?

It is interesting to speculate about the impact of long and slow mass transfer phases in our low-Z models on the fraction of the transferred matter that gets accreted by the companion. A clear coherent picture of accretion efficiencies $\beta$ in binaries of different orbital periods and component

masses is still missing. Observational clues from double-lined eclipsing SMC binaries (de Mink et al., 2009a), WR-O star systems (Petrovic et al., 2005), the well studied sdO+Be binary system $\varphi$ Persei (Schootemeijer et al., 2018), or Be-X ray binaries in the SMC (Vinciguerra et al., 2020) yield very different accretion efficiencies, ranging from highly non-conservative ($\beta \approx 0$) to nearly fully conservative cases ($\beta \approx 1$).[7] Since the emergence of binary evolution models with rotation (Langer et al., 2003b), a promising way of obtaining $\beta$ self-consistently from models has been to assume that the material can be accreted conservatively up to the point when the accretor becomes spun-up to critical rotation, at which point $\beta$ drastically decreases and is further controlled by the timescale of internal angular momentum transport in the accretor (Langer et al., 2003a).[8] Because little mass accretion is needed to reach the critical rotation of the accretor (Packet, 1981), and the thermal timescale of mass transfer is typically much shorter than the timescale for angular momentum transport in the accretor, such models tend to predict a highly non-conservative post-MS mass transfer evolution (Petrovic et al., 2005; de Mink et al., 2013). The exception are cases with a close to equal mass ratio due to their relatively lower mass transfer rates (e.g. Cantiello et al., 2007). Based on those arguments, we expect that long nuclear-timescale mass transfer phases in low-Z binaries may result in considerably higher accretion efficiencies compared to systems evolving through only thermal-timescale mass transfer. This might possibly bring such models into agreement with $\beta \sim 0.5$ inferred from Be-X-ray binaries of the SMC composition (Vinciguerra et al., 2020), although a detailed study of the issue is certainty needed before any conclusions could be drawn. Longer mass transfer phases could potentially also extend the duration of the Be phenomenon in rapidly-rotating accretors, which might help in resolving the apparent overabundance of Be stars in the SMC compared to the Galactic environment (Dray, 2006).

### 7.5.4 Core-He burning primaries in the HR diagram

Here, we discuss one of the most interesting implications of binary evolution models: the predicted distribution of core-He burning stars in the HR diagram. In the current study, for each initial composition we computed only a single grid of models (with initial mass ratio $q = 0.6$) and evolved only the primary stars. For that reason, we are unable to construct a complete population model of massive stars and binaries. Even a single $q$ grid, however, is sufficient to showcase the main subpopulations of core-He burning primaries predicted by the binary models and discuss their main observational characteristics. To this end, we choose the LMC grid as the most illustrative example.

In order to construct a simple population model, we weight all our binary models by the initial mass function of massive stars $\mathrm{d}N/\mathrm{d}M_1 \propto M_1^{-2.3}$ (Bastian et al., 2010), making the usual assumption that it well describes the initial mass function of primaries (Kroupa et al., 2013). In addition, we weight each model according to an initial orbital period distribution $\mathrm{d}N/\mathrm{d}\log P_{\rm ini} \propto \log P_{\rm ini}^{-0.55}$ (Sana et al., 2012). We normalize the period distribution to the range

[7] Note that these different types of post-interaction systems are probing different mass transfer regimes, so the large spread in $\beta$ values is perhaps not unexpected.

[8] A model of efficient accretion at breakup rotation velocity has been proposed by (Popham & Narayan, 1991).

$\log P_{\rm ini} = [0.15, 5.5]$. While wider early-type binaries do exist, they are very rare for $q > 0.3$ (see Fig. 37 in Moe & Di Stefano, 2017). For simplicity, we only consider massive stars that are formed in binaries, which neglects that a significant fraction of early-type stars are formed in triples or higher order systems (see Fig. 39 in Moe & Di Stefano, 2017). For each primary mass, we use our widest binary model (i.e. the non-interacting one) to represent all the wide non-interacting binaries in the weighting procedure described above. Likewise, we extrapolate to the shortest orbital periods of very close binaries ($P_{\rm ini} \sim 1.41$ days) using the model with the shortest initial orbital period in our grid ($P_{\rm ini} \approx 3.16$ days), which is relevant for our estimates of the products of case A mass transfer evolution. We caution that this is a rather crude approximation: very close binaries will produce somewhat less massive and luminous stripped helium stars than our $P_{\rm ini} \approx 3.16$ days models. [9]

Based on these assumptions, we are able to estimate the distribution of core-He burning primaries at the LMC metallicity in the HR diagram. The result is shown in greyscale in Fig. 7.14. For comparison, we plot several single stellar tracks with diamonds spaced by 50,000 yr in the post-MS evolution (starting from TAMS). Core-He burning primaries from wide non-interacting binaries (around 30% of primaries) occupy regions in the HR diagram that would also be populated by single stellar tracks: primarily the red (super) giant branch at $\log(T_{\rm eff}/{\rm K}) \approx 3.6$ and the blue or yellow supergiant regions indicated by the diamonds (in particular at the location of the blue loop of the 14 $M_\odot$ model. Binary interaction products, on the other hand, can occupy nearly any location in the HR diagram (although in the region of the MS they would be a small minority compared to core-H burning objects). Below we describe four most prominent categories of post-interaction and interacting primaries, with Boxes I-IV marking regions where they can typically be found in Fig. 7.14.

Box I is populated by hot fully stripped stars originating from both the primaries that interacted already during the MS (case A mass transfer) as well as those that are stripped through post-MS mass transfer. As the case A mass transfer systems are not the focus of the paper and have not been presented as part of the results, we clarify that in each of our case A models the primary becomes a fully stripped helium star after a sequence of case A and case AB mass transfer phases. This is in agreement with all the previous detailed mass transfer models of such systems (e.g. Podsiadlowski et al., 1992; Pols, 1994; Wellstein et al., 2001; Petrovic et al., 2005; de Mink et al., 2007; Wang et al., 2020). In general, we find that stars stripped in case A (+ case AB) mass transfer are slightly hotter in our models compared to those fully stripped in post-MS mass transfer (by about 0.1 dex in $\log(T_{\rm eff}/{\rm K})$). A more detailed discussion of differences between the two classes, including potential surface abundance signatures (e.g. Schootemeijer & Langer, 2018), is beyond the scope of this paper. Notably, Box I is populated by primaries with initial masses $\leq 14\ M_\odot$ from our LMC grid, i.e. the mass range in which post-MS mass transfer always leads to full envelope stripping on the thermal timescale (see Fig. 7.8 for the summary of model outcomes).

[9] Additionally, their orbits would typically be synchronized at ZAMS, which could lead to chemically-homogeneous evolution of the most massive LMC or SMC cases in that period range (de Mink et al., 2009a).

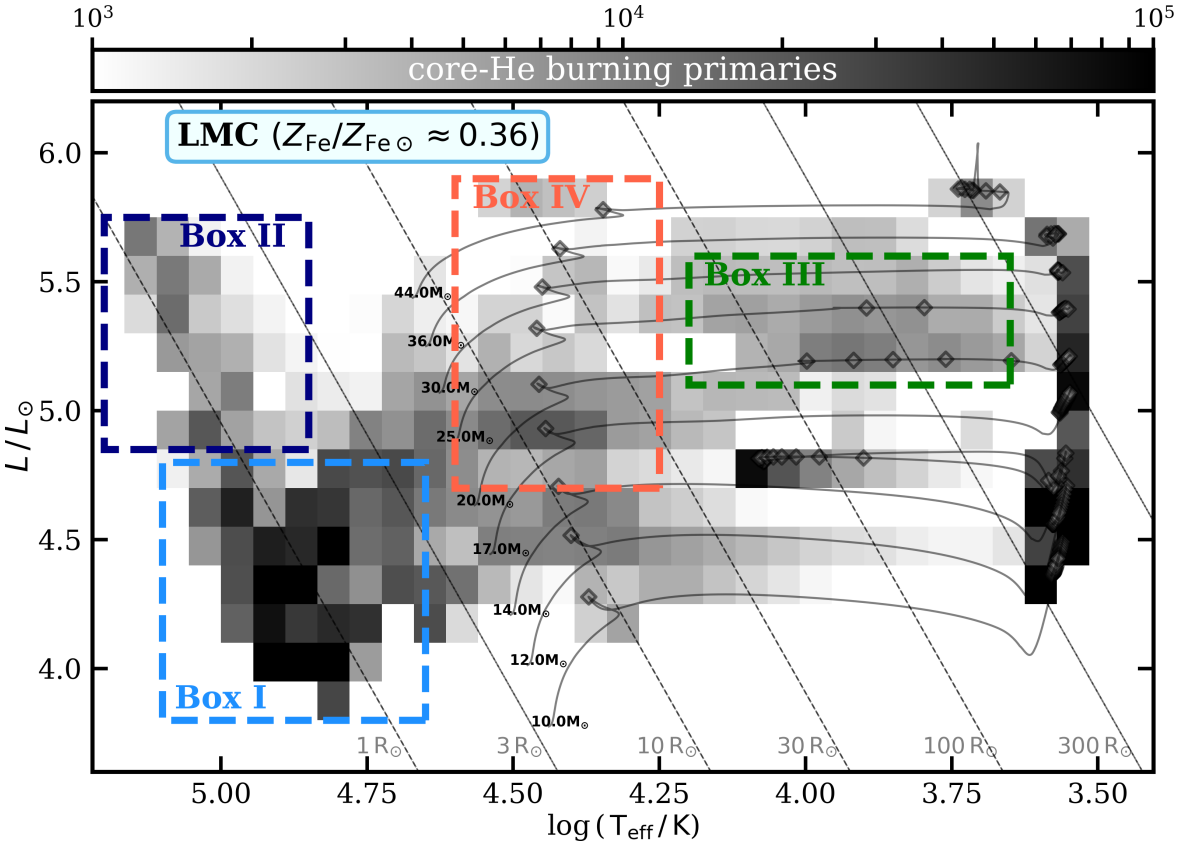


Figure 7.14: Distribution of core-He burning primary stars in the HR diagram inferred from the grid of $q = 0.6$ binary models at the LMC composition. Models have been weighted according to the initial mass function and initial orbital period distribution of early-type binaries (see text). The distribution also includes the contribution from wide non-interacting systems (around 30% of all primaries). Several single stellar tracks are plotted with solid lines for comparison. The four Boxes indicate four characteristic regions: hot stripped stars from both case A and post-MS mass transfer (Box I), hot stripped stars from case A mass transfer only (Box II), a region where most of the donors in mass-transferring systems reside (Box III), and finally a region where most of the long-lived partially-stripped stars in detached binaries are (Box IV).

In contrast to Box I, the hot stripped stars populating Box II (WR stars above a certain luminosity) are only formed in case A mass transfer systems (to compare, see the right-hand panel of Fig. 7.9 which excludes the case A systems). This is because in the $M_1 \geq 17\ M_\odot$ primary mass range the majority of LMC models evolve to either produce long-lived partially stripped stars or spend most of the core-He burning lifetime in nuclear-timescale mass transfer. This naturally leads to a prediction that the formation efficiency of hot stripped stars in interacting binaries decreases with increasing luminosity around $\log(L/L_\odot) \approx 4.8$ for the LMC composition relative to Solar metallicity models (which always lead to full envelope stripping in mass transfer). We discuss this further in Sec. 7.5.5.

Box III is where the majority of donors in nuclear-timescale mass transfer systems reside. They originate from systems with primaries in the mass range where single stellar models predict

a halted HG expansion and core-He burning blue or yellow supergiants ($M_1$ between $\sim$ 20 and 36 $M_\odot$ in our LMC grid). In fact, about 40% of stars in Box III are currently mass transferring, i.e. they are donors in semi-detached or contact systems. Their presence or absence in a population of blue/yellow supergiants in the LMC (or similarly SMC) will serve as a strong observational test to verify whether nuclear-timescale post-MS evolution can happen already at the LMC (or SMC) metallicity. The period distribution of mass-transferring systems in Box III is roughly flat in $\log(P)$ in the range between $\sim$ 50 and 1000 days. The long periods of these systems may make it challenging to assess their binary nature in spectroscopic surveys.

Finally, Box IV is largely populated by the class of long-lived partially-stripped core-He burning stars in detached binaries that is unique to our low-Z models, see also Sec. 7.3.3 for details about their formation.[10] The properties of stars in Box IV are quite interesting. First of all, they are under-massive for their luminosity when compared to single stellar tracks (by about a factor of 2, depending on luminosity, see Fig. 7.10). They are also helium and nitrogen enriched while being slow rotators (Fig. 7.11), which distinguishes them from fast rotators in which the surface enrichment is the result of rotational mixing in their interiors. These properties in principle make them similar to MS donors interacting in case A mass transfer binaries. However, in case A systems the donor spends most of its lifetime in a semi-detached or nearly Roche-lobe filling stage in a close orbit (Wang et al., 2020). Partially-stripped stars from the post-MS mass transfer models, on the other hand, can be found in binaries with much wider orbits, with their period distribution stretching from tens to thousands of days (Fig. 7.11). Together with the supposed presence of a rapidly-spinning companion (spun-up as a result of mass transfer), these set of characteristics makes them a unique class of objects.

It is tempting to view partially-stripped stars as a promising explanation for at least some of the puzzling nitrogen-enriched slowly-rotating B- and O-type (super)giants that have been identified in VLT-Flames spectroscopic surveys of the LMC (Hunter et al., 2008; McEvoy et al., 2015; Grin et al., 2017). Even more interestingly, Box IV stretches out to temperatures cooler than the TAMS, i.e. $\log(T_{\rm eff}/{\rm K}) < 4.35$. This is the region of the HR diagram that remains virtually unpopulated by single stellar tracks. In reality, a surprisingly large number of B (super)giants living apparently next to the MS have been found in the LMC (e.g. Evans et al., 2006), many of which being N-rich and with spectroscopic masses systematically lower than their evolutionary masses (McEvoy et al., 2015), i.e. with properties resembling those of partially-stripped stars. In the past, binary-interaction channels involving the accretors or stellar mergers have been put forth as a possible explanation of this population (Brott et al., 2011b; Glebbeek et al., 2013).

The elephant in the room of the discussion so far is the nature of the companion star. Mass losers that become hot stripped stars (Box I and Box II) emit most of the light in the UV, which is why irrespective of the relative bolometric luminosity of the components, the secondary (if a star and not a compact object) is nearly always the brighter source in optical bands (Götberg et al., 2018). This is no longer the case for the much cooler partially-stripped stars with $T_{\rm eff} < T_{\rm eff;ZAMS}$

[10]The grey region just below Box IV are stripped donors contracting on the thermal-timescale to become hot stripped stars.

produced in our LMC and SMC binary models (e.g. Box III and Box IV). Among those, depending on the initial mass ratio and the accretion efficiency, there could be systems in which the secondary becomes more massive and luminous than the primary as well as such in which the primary remains the brighter and more easily detectable component. In the first case, the partially-stripped companion may remain hidden in the presence of a (most likely) rapidly spinning companion with broad emission lines that make it challenging to detect orbital velocity variations. Such two components may be especially difficult to disentangle from their spectra in the case of the Box IV population, where both stars are likely to have a similar spectral type (type B). They may appear as more massive analogues of the recently reported LB-1 system (Liu et al., 2019), in which case the presence of a B- and Be-type components in the spectra has proven to be misleading and challenging to unravel without a dedicated technique (Shenar et al., 2020a). On the other hand, binaries in which the partially-stripped donor remains the more luminous of the two components are the most promising to explain some of the peculiar nitrogen-enriched (super)giants mentioned above.

### 7.5.5 Fewer stripped and WR stars from interacting binaries at low-Z?

Mass transfer interaction in binary systems is thought to be the main formation channel for stripped stars and, alongside the single-star channel in which the envelope is stripped through strong winds (Conti, 1975; Smith, 2014), one of the two main channels for their most luminous subclass: WR stars (Paczyński, 1967) [11]. While the single-star WR channel is expected to become less efficient the lower the metallicity (on the basis that line-driven mass loss decreases with metallicity, see Vink et al., 2001; Vink & de Koter, 2005), the mass-transfer channel has so far been predicted to have an efficiency that is roughly independent of metallicity (e.g. Maeder & Meynet, 1994).

The binary models computed in this work suggest something different. At LMC and SMC metallicities, most of our post-MS donors with masses above 17 $M_\odot$ never become fully stripped in mass transfer during the core-He burning phase (see Fig. 7.8 with the summary of model outcomes). As such, we predict the efficiency of the binary formation channel for stripped and WR stars to decrease at low metallicity. We illustrate this in Fig. 7.15, where for each metallicity, we estimate what fraction of primaries of a given initial mass will evolve to form a hot stripped star as a result of a mass-transfer interaction. While at Solar metallicity this fraction is nearly independent of the primary mass and very high (70% – 80%, with the remaining 20% – 30% being primaries in non-interacting wide systems), at lower LMC and SMC metallicities it drops down by a factor of two (to 30% – 40%) for stars with initial masses $\gtrsim 20\ M_\odot$, which corresponds to stripped-star luminosities $\log(L/L_\odot) \gtrsim 4.8$. For this calculation, similarly to that in Sec. 7.5.4, we assumed an initial mass function $\mathrm{d}N/\mathrm{d}M_1 \propto M_1^{-2.3}$ and an initial orbital period distribution $\mathrm{d}N/\mathrm{d}\log P_\mathrm{ini} \propto \log P_\mathrm{ini}^{-0.55}$ spanning the range $\log P_\mathrm{ini} = [0.15, 5.5]$. Based on the few case A mass

[11] WR stars are essentially stripped stars with high enough luminosity to mass ratio to launch strong optically-thick winds (e.g. Gräfener et al., 2011).

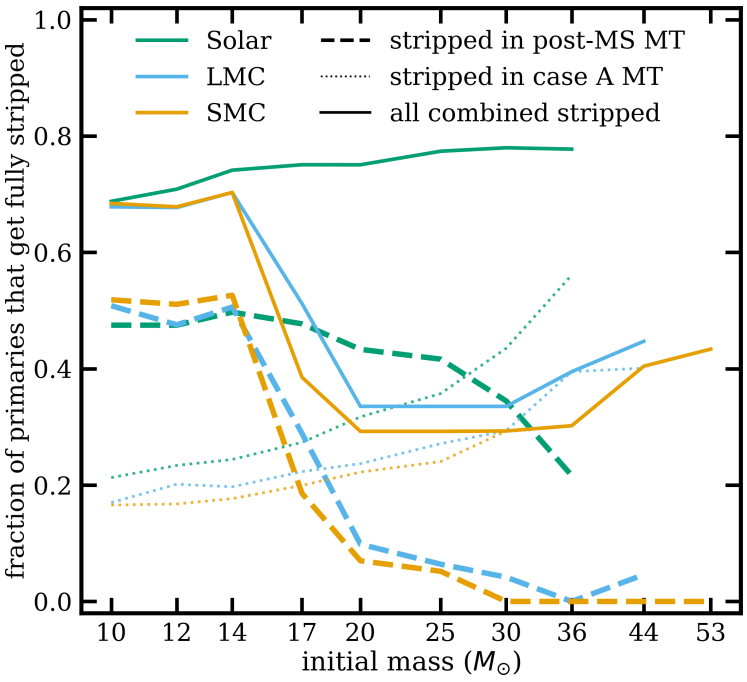


FIGURE 7.15: Fraction of primaries that become hot stripped stars as a result of a mass transfer interaction, estimated based on the results from binary models as well as the assumed distributions for initial masses and orbital periods (see text). At Solar metallicity, any primary in an interacting binary eventually becomes a hot stripped star (the remaining 20%-30% are in wide non-interacting systems). At LMC and SMC metallicities, post-MS donors with masses above $\gtrsim 17 - 20\ M_\odot$ become only partially rather than fully stripped in mass transfer, leading to a predicted decrease in the efficiency of formation of stripped stars from low-Z interacting binaries.

transfer models in our grid as well as previous detailed studies of case A binary evolution (e.g. Pols, 1994; Petrovic et al., 2005; Wang et al., 2020), we predict that all the primaries interacting during the MS will become hot stripped stars after an episode of case AB mass transfer. Note that the result in Fig. 7.15 is based on a single grid of binary models with the initial mass ratio $q = 0.6$. The relative fraction of case A compared to post-MS mass transfer systems is subject to uncertainty in the degree of envelope inflation of massive MS stars (Sanyal et al., 2015, 2017; Klencki et al., 2020), a phenomenon that occurs in some of the most massive primaries in our grid of models.

Fig. 7.15 constitutes a prediction that the number of stripped stars above a certain mass (and luminosity: $\log(L/L_\odot) \approx 4.8$ in the case of our models) should be lower in metal-poor galaxies compared to high-metallicity environments. An observational test may not be straightforward. Stripped stars that are not luminous enough to appear as WR stars ($\log(L/L_\odot) < 5.25$ in the LMC and $\log(L/L_\odot) < 5.6$ in the SMC case, following Shenar et al., 2020b) are difficult to detect in optical surveys. The most promising strategy so far has been far-UV spectroscopy targeting Galactic Be stars and it has recently led to a discovery of ten new subdwarfs (sdO), thus tripling the number of known Be+sdO systems (Wang et al., 2021). Future similar campaigns focused on the LMC and SMC could help verify the metallicity trend predicted by our binary models.

In the WR regime, the binary fraction of WR stars has long been predicted to increase with metallicity (due to the decreasing efficiency of the single-star channel, e.g. Maeder & Meynet, 1994). Surprisingly, this does not seem to be the case as the binary fractions of classical WRs is found to be about $\sim 40\%$ in the Milky Way and Magellanic Clouds alike (Bartzakos et al., 2001; van der Hucht, 2001; Foellmi et al., 2003a,b). Shenar et al. (2020b) has recently pointed out that this tension may be reduced taking into account the metallicity-dependent minimum luminosity

for the WR phenomenon. Our results, suggesting a metallicity-depended formation of WRs in binaries, may also help to solve this apparent discrepancy.

### 7.5.6 Implications for explodability and SN progenitors

In this section, we discuss the impact of the newly found partial envelope stripping of low-Z massive donors on their carbon-oxygen (CO) cores, pre-SN structure, and explodability. Whether a massive star loses its H-rich envelope shortly after the end of MS as a result of mass transfer (or strong winds) or still retains at least part of its envelope during the core-He burning phase has implications for the evolution of the core. In the first case, the naked helium core decreases in mass due to wind mass-loss. In the second case, the helium core grows in mass due to continuous H-shell burning. This effect was shown to lead to lower CO core masses ($M_{\rm CO}$) and higher carbon mass fractions ($X_{\rm C}$) in the CO cores of fully stripped stars, two factors that largely determine the further core evolution throughout the advanced burning stages until the core collapses (Timmes et al., 1996; Brown et al., 2001; Patton & Sukhbold, 2020).[12] Consequently, pre-SN stellar models computed from naked helium stars (Woosley et al., 1995; McClelland & Eldridge, 2016; Woosley, 2019; Ertl et al., 2020) and from fully stripped stars alike (Schneider et al., 2021; Laplace et al., 2021; Vartanyan et al., 2021) were found to have systematically smaller compactness and to be more prone to explode rather than to collapse into a BH. In particular, Schneider et al. (2021) argues that envelope loss due to mass transfer increases the minimum initial mass to form a BH from ∼20−25 $M_\odot$ up to ∼ 70 $M_\odot$. Among other implications, their work suggests a drastic reduction of the formation rate of binary BH and BH-NS systems from binary evolution. The only exception in Schneider et al. (2021) were cases of case C mass transfer, i.e. the RLOF initiated after the end of core-He burning, which the authors found to have very little effect on the pre-SN core structure with respect to single stellar models. However, in the case of massive stars with initial masses above 20−25 $M_\odot$, case C evolution is extremely rare except in very metal-poor environments ($Z \lesssim 0.04\ Z_\odot$ in Klencki et al., 2020).

Importantly, the key CO core properties ($M_{\rm CO}$ and $X_{\rm C}$) that were found to determine the compactness are set already at the end of core-He burning (when we terminate our models). By analyzing the final CO cores of donors from our binary models, we find that those that were only partially stripped have their CO core properties $M_{\rm CO}$ and $X_{\rm C}$ very close to those formed in single stars of the same mass. Based on that and the results of the above-mentioned studies, it is well-founded to expect that partially-stripped stars will produce pre-SN core structures that are similar to those of single stars: more compact and prone to BH formation compared to pre-SN cores of fully stripped stars. Partial envelope stripping is common among our models: the vast majority of low-Z donors with masses between ∼20 and 50 $M_\odot$ are never fully stripped in post-MS mass transfer (see Fig. 7.8) and we estimate that fully stripped stars are the minority in this mass range (originating mostly from case A mass transfer, see Fig. 7.15). Taken together with the results

[12] In particular whether or not carbon burning will trigger convection, which is especially consequential for the final compactness of the pre-SN core (e.g. Chieffi & Limongi, 2020).

of Schneider et al. (2021), this could mean that most of the BHs in close binaries in the LMC and SMC-like environments are formed from partially-stripped progenitors. This may also 'save' the binary BH and BH-NS formation scenario from low-Z massive binaries.

Finally, we point out that our binary models are terminated at the end of core-He burning and at that point, in most of the massive low-Z systems the mass transfer is still ongoing. This means that even though many of the low-Z primaries have not been fully stripped in our simulations, they could still lose the remaining hydrogen (or possibly also helium) in the short remaining evolution until the core collapse (several thousand yr, depending on mass). Such H-rich layers, if not-accreted by the companion, could still reside in the proximity of the star at the core collapse and the possible SN.

### 7.5.7 IMPLICATIONS FOR ULTRA-LUMINOUS X-RAY SOURCES

Here, we discuss the implications of our binary models assuming that the accretor is a compact object: a stellar-mass BH. For the default mass ratio $q = 0.6$, the BH mass would range from 6 to $\sim 32\ M_\odot$ with the corresponding Eddington accretion rates ranging from $\sim 1.3 \times 10^{-7}\,\mathrm{M_\odot\,yr^{-1}}$ to $\sim 7 \times 10^{-7}\,\mathrm{M_\odot\,yr^{-1}}$. This is much lower than the mass transfer rates found in models when they are at the RLOF stage (even during the phases of slow nuclear-timescale mass transfer, when $\dot{M} \sim 10^{-5}\,\mathrm{M_\odot\,yr^{-1}}$). Such BH binaries would thus be HMXBs with highly super-Eddington mass transfer rates. It was shown that in this supercritical regime the thin disk model is no longer valid (Shakura & Sunyaev, 1973). Instead, the accretion is thought to proceed through a thicker (slim) disk, possibly with a super-Eddington accretion rate and most of the energy being advected into the BH or used to power strong disk winds and jets (Lipunova, 1999; King et al., 2001; Poutanen et al., 2007; Lasota et al., 2016). The disk together with optically-thick outflows make the X-ray emission geometrically beamed. Depending on the viewing angle, such systems may appear as ULXs (defined as point X-ray sources with spherically-equivalent X-ray luminosity $L_\mathrm{X} > 10^{39}$ erg/s, see the review by Kaaret et al., 2017) or X-ray bright microquasars such as the Galactic SS433 system (Fabrika, 2004).

In this work, we found that a significant fraction of massive low-Z binaries evolve through nuclear-timescale post-MS mass transfer. In such models, the super-Eddington mass exchange phase lasts a few times $10^5$ yr, which is more than an order of magnitude longer than the thermal-timescale mass transfer phase found in the high-metallicity models ($\lesssim 10^4$ yr). This leads to a prediction that HMXBs and ULXs with BH accretors, post-MS donors (blue and yellow supergiants), and periods of at least a few tens of days should be much more common in metal-poor galaxies.

It is interesting to discuss whether that is indeed observed. At first glace, our results might seem in tension with the fact that no such BH-HMXB system is known in the LMC (the LMC X-1 BH binary contains a MS donor in a short-period orbit Orosz et al., 2009). However, the lack of such systems in the LMC may in fact be statistically consistent with our results. Based on detailed binary models, Langer et al. (2020) estimate that about 100 BH-OB star binaries should be present

in the LMC. Taking that the MS lasts for about 90% the stellar lifetime, this corresponds to $\sim 10$ BH binaries with post-MS companions. Roughly $1/3$ of BH binaries predicted by Langer et al. (2020) have companion masses of 20 $M_\odot$ and above and roughly $1/2$ have orbital periods above $\sim 50$ days (the minimum donor mass and orbital period for nuclear-timescale mass transfer in our LMC grid). This estimation leads to an approximate prediction of $10/6 \approx 1.7$ BH binaries with post-MS donors that are currently in a mass-transferring state: a number that is not inconsistent with no such systems being observed.

Instead, the effect of nuclear-timescale mass transfer on the number of ULX sources may be more evident when looking at larger scales, across more distant and diverse galaxies. The recent census of ULX sources in the Local Universe amounts to 629 ULX candidates in 309 galaxies with distance smaller than 40 Mpc (Kovlakas et al., 2020). Interestingly, the number of ULXs per unit of star formation rate is found to increase with decreasing metallicity of the host galaxy (as pointed out by Zampieri & Roberts 2009; Mapelli et al. 2009, see also observational studies of the ULX host galaxies by Walton et al. 2011; Swartz et al. 2011b). Qualitatively, this agrees with the results from out models. Unfortunately, the potential to use the observed number of ULXs to constrain our findings is at the moment hindered by the fact that in the vast majority of ULXs the nature of neither the accretor (whether a BH or a NS) nor the donor (whether or not a high-mass star) is known.

In the context of ULX systems, it is interesting to highlight that in Sec. 7.4 and Fig. 7.13 we found that low-Z donors can be characterized by very high $\zeta_{\rm th}$ values in the mid-envelope region (with $\zeta_{\rm th} > \zeta_{\rm RL}$ for even extreme mass ratios of $q < 0.1$). This means that mass transfer from a partially-stripped star could be thermally stable even in binaries with a NS accretor ($M_{\rm NS} \approx 1 - 2.5\ M_\odot$), provided that the mass transfer is also dynamically stable, i.e. $\zeta_{\rm ad} > \zeta_{\rm RL}$ (which may well be the case for radiative-envelope supergiants Ge et al. 2015). Quast et al. (2019) suggested this as a possible explanation for ultra-luminous X-ray sources with blue-supergiant donors and NS accretors such as the NGC 7793 P13 system (Israel et al., 2017). In their models, the high stability region could be reached after stripping most but not quite all of the donor envelope (up to the point with high $\zeta_{\rm th}$ values found near the helium core also in our models). Interestingly, in our stellar models we find another region of high $\zeta_{\rm th}$ located higher up inside the envelope, meaning that a smaller fraction of the outer envelope would have to be lost in previous evolution before reaching the high-stability regime. A possible agent for such prior stripping in systems with extreme mass radios could be common-envelope evolution with a partial-envelope ejection (see discussion in Sec. 4.6 in Klencki et al. 2021).

## 7.6 SUMMARY

In this paper, we studied the mass transfer evolution in massive binaries and the effect played by the metallicity of the donor star, as motivated by Klencki et al. (2020). To this end, using the MESA stellar evolution code, we computed grids of detailed binary models at three different metallicities (Solar, LMC, and SMC compositions) spanning a wide range of orbital periods (from $\sim 3$ to

5000 days) and initial primary masses (from 10 $M_\odot$ to 36-53 $M_\odot$, depending on metallicity). Our main focus was on the mass transfer initiated by a post-MS donor star. Due to the challenging numerical nature of such models, we treated the secondary as a point mass. Most of the models were computed with an initial mass ratio of $q = 0.6$ although we also explored the effect of varying $q$ for a few cases. Our conclusions can be summarized as follows.

– We reveal that metallicity has a substantial effect on the course and outcome of mass transfer evolution of massive binaries. While at high (Solar) metallicity a post-MS mass transfer is always a short-lived phase ($\Delta T_{\rm MT} \lesssim 10^4$ yr) of thermal-timescale mass transfer ($\log(\dot{M}) \sim 10^{-3}\,{\rm M}_\odot\,{\rm yr}^{-1}$) with the mass loser becoming a stripped helium star (in agreement with the long-standing paradigm, e.g. Paczyński, 1971; van den Heuvel, 1975; Podsiadlowski et al., 1992; Vanbeveren et al., 1998), this turns out to not be the case in our LMC and SMC models with donor masses $\gtrsim 17\ M_\odot$. For such massive low-Z donors, the post-MS mass transfer is much less violent: leading either to evolution through long nuclear-timescale mass exchange, that continues until the end of core-He burning ($\Delta T_{\rm MT} \gtrsim 10^5$ yr, $\log(\dot{M}) \sim 10^{-5}\,{\rm M}_\odot\,{\rm yr}^{-1}$), or to detached binaries with mass-losers that are only partially stripped of their envelopes.

– The origin of the metallicity effect found in the mass transfer models lies in the different response of low-Z donors to mass loss and their small equilibrium radii as partially-stripped core-He burning stars. This in turn is related to the post-MS expansion of massive stars when they transition to the core-He burning stage. Stars in which the rapid HG expansion continues until the red (super)giant branch (a common feature of high-Z models), when donors in binaries, become fully stripped in thermal-timescale mass transfer. Partial envelope stripping and slow mass transfer, on the other hand, occur in the mass range in which massive stars begin to burn He already as blue or yellow supergiants. Such a halted HG expansion is often found in low-Z models of massive stars. Although uncertain due to its sensitivity to mixing, it is supported observationally by the large populations of yellow supergiants in the LMC and the SMC.

– Based on a simple population model, we predict that at SMC and LMC metallicities, fewer (by a factor of ∼2−2.5) stripped (WR) stars with $4.8 < \log(L/L_\odot) < 6.0$ are produced by binary interactions compared to a Solar-metallicity environments. This is because among our LMC and SMC models, only ∼0−20% of post-MS donors with $M_1 \gtrsim 20\ M_\odot$ become hot stripped stars by the end of core-He burning (∼100% at Solar metallicity). Case A mass transfer evolution leads to full envelope stripping irrespective of metallicity.

– We find a significantly longer average duration of post-MS mass transfer in low-Z binary systems (by more than an order of magnitude). In the case of BH accretors, this implies longer lifetimes of high-mass X-ray binaries, which at face value agrees with the large numbers of ULXs found in metal-poor galaxies (although the nature of ULX accretors is usually unknown). This also suggests that the immediate progenitors of binary BH systems could be in the mass-transferring state rather than being detached BH-WRs. In the case of stellar accretors, our models provide a testable prediction that many of the blue and yellow supergiants with $\log(L/L_\odot) \gtrsim 5$ in the LMC and SMC should be in semi-detached binaries (∼30−40% from our $q = 0.6$ grid). We also speculate that lower mass transfer rates of low-Z models could lead to higher accretion efficiencies.

– We predict a population of partially-stripped stars in detached binaries in the LMC and SMC. Unlike stripped stars, such mass losers are relatively cool (typically $4.1 < \log(T_{\rm eff}/{\rm K}) < 4.5$ and $2.0 < \log(g) < 4.3$) and thus overlap with the MS and blue supergiants. They are expected to be undermassive for their luminosity (by a factor of ∼1.5−2), He and N rich, slowly rotating, and reside in binaries with a wide range of periods (from tens to thousands of days). Potentially, they could explain some of the puzzling N-rich slow rotators observed in the LMC (Hunter et al., 2008; McEvoy et al., 2015; Grin et al., 2017).

– Guided by the carbon-oxygen core properties, we expect the pre-SN core structure of most of the low-Z $\gtrsim 20\ M_\odot$ primaries to be similar to that of single stars in terms of their higher compactness (and lower explodability) compared to fully stripped binary interaction products. Our results therefore suggest that the recently obtained high initial masses needed for the BH formation in case A and case B binaries ($\gtrsim 70\ M_\odot$ Schneider et al., 2021), at low metallicity, could potentially be reduced to the often quoted $\sim 25\ M_\odot$ BH-formation threshold.

**Acknowledgements**

The authors acknowledge support from the Netherlands Organisation for Scientific Research (NWO). It is a pleasure to acknowledge valuable discussions and suggestions from Stephen Justham, Selma de Mink, Manos Zapartas, Lida Oskinova, Tomer Shenar, Julia Bodensteiner, Pablo Marchant, Ylva Götberg, Thomas Tauris, and David Aguilera-Dena.

## 7.A Additional figures

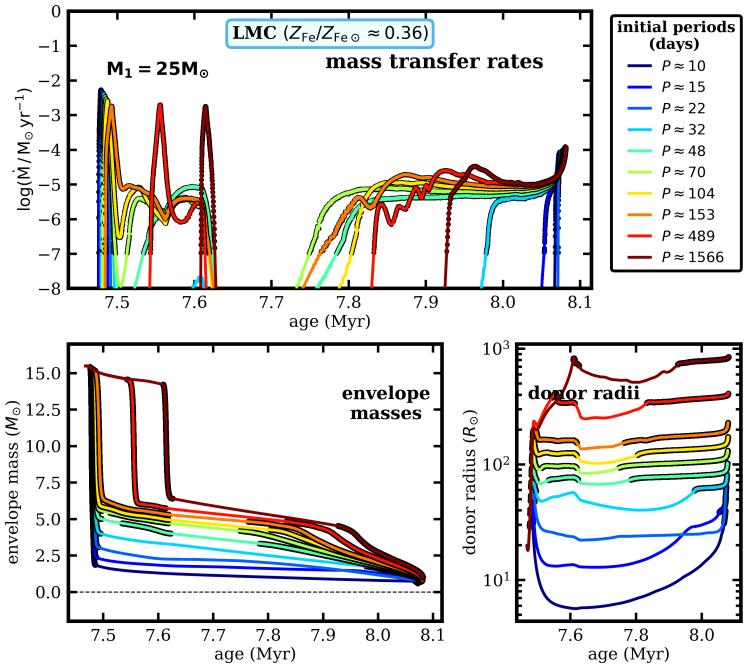


Figure 7.16: Same as Fig. 7.3 but for the LMC metallicity. Mass transfer evolution in binaries with a 25 $M_\odot$ primary (initial mass), LMC composition, and various initial orbital periods $P_{\rm ini}$.

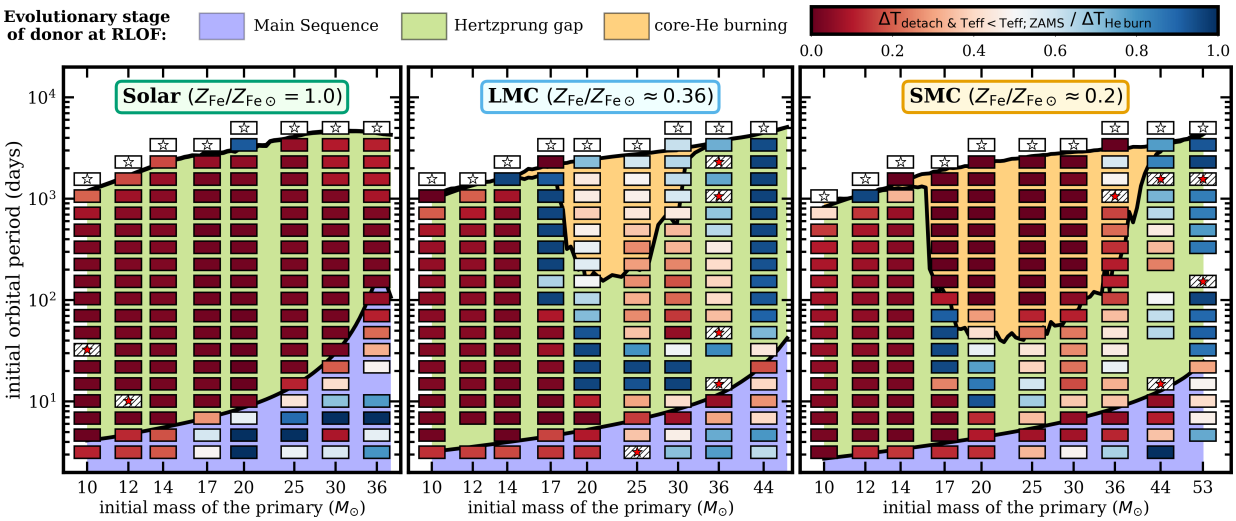


FIGURE 7.17: Similar to Fig. 7.6 but the rectangles representing the binary models are colored according to the integrated duration of a post-interaction detachment phase during which the mass loser remains on the cooler side of the ZAMS line in the HR diagram. Rectangles corresponding to models with post-MS donors (either at the Hertzprung gap or the core-He burning stage, see the background colors) that are colored in various shades of blue are models that produce partially-stripped long-lived stars in detached binaries (see Sec. 7.3.3 and Sec. 7.5.4 for a discussion of this population).

o

# Chapter 8

# Summary

*"Think, think, think"*
*Winnie the Pooh*

This thesis revolves around the subject of massive stars. During their lives – short but energetic and rarely without a companion – massive stars shine with extreme luminosities and blast through the surrounding medium with outflows of mass. They are the Cosmic engines, the beacons of star-forming galaxies both near and far, and seeds to some of the most energetic explosions observed out to the dawn of galaxies. In their afterlives, massive stars become neutron stars (NSs) or black holes (BHs): some of the most imagination provoking objects in the Universe, from the boundaries of known physics.

The evolution of massive stars and massive binary systems is full of mysteries. Among the major unsolved problems is the evolution through mass transfer phases, in particular the outcome of the enigmatic common-envelope in-spiral, as well as the final collapse of a massive star and the formation of a NS or a BH. In both cases, 3D hydrodynamic simulations are computationally challenging and current numerical tools are not sufficient to answer all the questions. Another method to tackle these puzzling evolutionary phases, a method we apply in this thesis, is by studying their products, such as BH X-ray binary systems and merging pairs of BHs or NSs. Observation of the latter has recently become possible with gravitational-wave (GW) detectors, opening a new window into the Universe and massive-star remnants.

We take a theoretical approach: by modeling the populations of massive binaries and their remnants in the Milky Way and across the Cosmic history, we link the observations of X-ray binaries and GW sources to the uncertain theory of massive binary evolution. In later chapters, we turn to detailed 1D stellar and binary models to scrutinize our understanding of the key mass transfer phases and the role played by the content of metals in massive stars (metallicity). We seek a direct confrontation between the stellar models and results from spectroscopic surveys of massive stars in nearby galaxies.

## Chapter II: BH X-ray binaries from fly-by encounters

The formation of the Galactic population of BH X-ray binaries with low-mass companions (BH-LMXBs) is a long-standing puzzle. If their progenitors are close binary systems then no evolutionary scenario involving a mass transfer phase is able to explain all their properties. Instead, we explore the evolution of ultra-wide non-interacting systems. Their large orbits make it so that dynamical interactions with fly-bys are non-negligible, even in the Galactic field. We modify the rapid binary evolution code StarTrack to include the effect of random three-body dynamical encounters on the binary orbit and carry out a population synthesis of massive binaries in the Milky Way field. Assuming that binaries perturbed to highly-eccentric orbits ($e \sim 0.99$) can be tidally circularized given a sufficiently close pericenter passage, we estimate that fly-by interactions can produce a current population of $\sim$60$-$220 BH-LMXBs in the Galactic field. Although the predicted donor mass distribution agrees well will the observed one, the fly-by channel contribution to the total population of BH-LMXBs is likely rather small. In any case, the assumption of efficient tidal circularization of highly-eccentric orbits needs to be scrutinized in the future studies of similar channels.

## Chapter III: Initial binary parameters for binary BH and NS mergers

Distributions of the initial binary parameters (mass, mass ratio, orbital period, eccentricity) are not independent from each other. However, their inter-correlations have only recently been quantified by Moe & Di Stefano (2017). Using the StarTrack rapid binary evolution code, we study the effect of these inter-correlations on the predicted population of binary BH and NS mergers (GW sources) from the isolated binary evolution channel involving a common-envelope (CE) phase. Our findings indicate that none of the changes to the initial binary distributions have a significant effect on the predicted population of GW events. We also argue that a similarly small effect would result from even extreme variations of the initial mass function because the number of massive stars is directly constrained by the empirically inferred cosmic star formation rate. Instead, we highlight the significant role of low-metallicity predicted by the models and suggest that our understanding of the evolution of metal-poor binaries as well as the cosmic star formation rate at low metallicities are the more important uncertainties to pin down in the future studies of GW progenitors. The former is the subject of chapters V and VII.

## Chapter IV: Effective spins of binary BH mergers

All ten binary BH mergers reported by the end of the second observing run of LIGO/Virgo were found to have small effective spins. The effective spin distribution is especially interesting in the context of distinguishing between various formation scenarios (Farr et al., 2018b). In this chapter, we investigate the range of effective spin distributions predicted within the CE formation channel. We use the StarTrack code to model the population of detectable GW sources and explore different prescriptions for the initial BH spin. Notably, we assume that the angular momentum of the core at the moment of the final collapse is preserved and determines the initial spin of the BH. We find that under the assumption that most of the binary BH mergers originate from

isolated binary evolution, their low effective spins strongly favor stellar models with relatively high efficiency of angular momentum transport in stellar interiors (transport via the Taylor-Spruit dynamo rather than meridional currents). In such models, even stellar cores that are initially rapidly rotating are eventually slowed down due to the angular momentum being transported into the envelope from which it is lost in stellar winds. The conclusion holds after considering the effect of tidal spin-up at the BH-Wolf Rayet binary stage. Among the considered model variation, we find such that simultaneously reproduce the merger rate, mass, and spin distribution of the binary BH mergers observed to date (at the time of writing). However, it is clear that degeneracies between the effect played by various uncertain factors make it impossible to constrain them or draw robust conclusions about the origin of the LIGO/Virgo sources.

## Chapter V: Metallicity and the onset of mass transfer in massive binaries

Metallicity is well-known to have a substantial effect on the evolution of massive stars due to its influence on the strength of line-driven winds. Lesser known is the fact that metallicity also strongly affects the radial expansion of massive stars, in particular during their post-main sequence evolution. While perhaps not crucial for the outcome of single-stellar evolution, the radial expansion of stars gains a special level of significance when considered in the context of binaries. We demonstrate this by estimating at what evolutionary stage, depending on metallicity, a massive star will overflow its Roche lobe in a binary system. To this end, using the MESA 1D stellar evolution code, we compute grids of single massive star models across several different metallicities. We consider several variations in factors known to influence the post-main sequence expansion of massive stars (e.g. overshooting, semiconvection) and confront the model predictions with the observed number of blue, yellow, and red supergiants in the Milky Way and in the Small Magellanic Cloud. We show that with decreasing metallicity, the parameter space for mass transfer initiated by a core-helium burning supergiant increases dramatically compared to the evolution at high (Solar) metallicity. This type of mass transfer evolution has not been studied before: we investigate it further with detailed binary models in chapter VII. In addition, we find that at very low metallicity (a few percent of the Solar value), a significant fraction of massive stars will engage in their first mass transfer episode only after central helium depletion, i.e. only $\lesssim 10^4$ yr before the core-collapse. This suggests that many metal-poor supernova progenitors could be exploding during or shortly after a mass transfer phase. We also point out that the parameter space for mass transfer from a convective donor is extremely small in the case of massive stars that are thought to be the progenitors of BHs. This raises concerns for the efficiency of the CE formation channel for binary BH mergers, as we study in-depth in the next chapter.

## Chapter VI: Common-envelope evolution in BH binaries

One of the most prominent channels for the formation of binary BH mergers (also considered in previous chapters of this thesis) is isolated binary evolution involving a CE phase. The CE in-spiral, being the key stage of the scenario, takes place when the first BH has already been formed. In this chapter, we set out to constrain the properties of companion stars in those BH

binaries that can evolve through and survive a CE phase. We use the MESA stellar-evolution code to compute envelope binding energies of massive supergiants of different metallicities. We also consider additional possible energy sources and discuss uncertainties. All this lets us scrutinize the predictions for the CE outcome in massive binaries based on the energy formalism. We show that successful CE ejection in BH binaries is only possible if the unstable mass transfer is initiated by a red supergiant (RSG) donor star. Observationally, for reasons that remain poorly understood, RSGs are missing among the most luminous and massive stars that are necessary to explain about half of the LIGO/Virgo events. Furthermore, we suggest ultra-lumionous X-ray sources with RSG companions such as NGC 300 ULX-1 as candidates for future GW sources (Heida et al., 2019). Their role as probes of binary evolution channels may become especially prominent with the results from the James Webb Space Telescope and Extremely Large Telescope (ELT). Our results also suggest that the efficiency of the CE channel for the formation of binary BH mergers has likely been severely overestimated in various population models. In the context of BH-LMXB systems, we show that envelope binding energies of massive stars in the post core-helium burning stage are sufficiently low to allow for a common-envelope ejection by even a low mass companion ($< 1\ M_{\odot}$). The significance of this finding in resolving the BH-LMXB formation puzzle will need to be tested with population models.

## Chapter VII: Stable mass transfer evolution from massive donors

In chapter V we found that metallicity has a significant influence on the evolutionary stage at which massive stars overflow their Roche lobes and become donors in interacting binary systems. This motivates us to perform a detailed study of mass transfer evolution in massive binary systems of different metallicities, using the MESA stellar evolution code. Among our high (Solar) metallicity models, mass transfer from a post-main sequence massive donor is always a short-lived event ($\lesssim 10^4$ yr) of rapid thermal-timescale mass transfer that strips the donor giant of its (nearly) entire hydrogen envelope, producing a stripped (~helium) star. This type of evolution is the canonical picture of what post-main sequence mass transfer evolution looks like. However, surprisingly, at low metallicity we obtain a significant number of models that evolve very differently, following either of the two newly-found types of evolution: (a) short-lived mass transfer phase leading to donors that are only partially stripped of their envelopes, or (b) rapid mass transfer followed by long phase of nuclear-timescale mass exchange that continues until the end of core-helium burning. We show that the three types of mass transfer evolution described above can be associated with the degree of rapid post-main sequence expansion of the massive donor. This association appears to be quite robust. Similarly, the connection between the post-main sequence expansion and metallicity is also well established. Our study thus suggests a strong link between metallicity and mass transfer evolution. However, the details of this relation, i.e. at what exact masses and metallicities the mass transfer evolution transitions between the different types discussed above, at the moment, should be considered uncertain. We discuss the implications of our findings for the formation of stripped stars from binary interactions, observational properties of post-interaction stars in massive star populations, pre-supernova properties of massive stars, as well as high-mass X-ray binary

populations in galaxies of different metallicities. We also suggest various observational tests of the binary models, which in the future will be the key to understand the evolution of metal-poor massive binaries. Given the importance of low-metallicity stellar evolution, in particular in the context of GW astrophysics, the results obtained in this thesis promise a lot of exciting work in the coming years.

## Looking into the future

Throughout this thesis, we have provided some answers and, unsurprisingly, formulated perhaps even more new questions.

The formation of the Galactic population of BH-LMXB systems remains a puzzle. The revised envelope binding energies of massive supergiants obtained in chapter VI give some hope for resolving the problems in the formation scenario involving a CE phase: this needs to be tested with population models. Quite possibly though, the BH-LMXB systems are an indication that we are missing something major in the CE evolution in massive binaries. I think that an interesting idea to pursue on theoretical grounds is the possibility of partial envelope ejection followed by stable mass transfer evolution (Quast et al., 2019, chapter VI-VII).

When it comes to our understanding of binary BH formation from isolated binary evolution, I would venture a guess that in the near future we will see a shift away from the so-called classical CE channel – labelling it as rather 'uncommon' – and perhaps towards its rising alternative, that is the formation through stable mass transfer evolution. This was suggested in chapter VI of this thesis and soon after also by the similar results obtained by Marchant et al. (2021), as well as indicated as a possibility in some of the population-synthesis model variations (Neijssel et al., 2019; Olejak et al., 2021). An important step in advancing our understanding of the binary BH formation will be results from 3D hydrodynamic simulations of massive CE evolution (including the radiative transfer; Ricker et al., 2019). On the observational side, thanks to the combination of Gaia and large-scale spectroscopic surveys such as LAMOST, in the near future we will likely see an increase in the number of non-interacting BH binary candidates in the Milky Way. Without a question, a growing sample of such systems will be a priceless test-bed of massive binary star evolution and prior mass transfer phases.

Detailed models of massive stars and binaries in chapters V and VII revealed that our understanding of mass transfer evolution in metal-poor environments is far from complete. The finding of partial envelope stripping from low-metallicity donors in especially significant. The next step is to confront a comprehensive set of detailed binary models with results from spectroscopic surveys in the Local Group, in particular the VLT-FLAMES multi-epoch survey of massive stars in the 30 Doradus star-forming region in the Large Magellanic Cloud (Evans et al., 2011). Similar complementary surveys in the Small Magellanic Clouds would allow for constraints at a regime of even lower metallicity, probing various effects predicted in this thesis. In addition, next generation telescopes, with ELT at the front, will open a long-awaited window into metal-poor environments of galaxies located $\sim 1$ Mpc away: Sextans A, SagDIG, and Leo P, with respective metallicities of about $\sim 1/10$, $1/20$, $1/30$ the Solar value (Garcia et al., 2019). Together, they will form the first

empirical cosmic metallicity ladder of massive star evolution.

On the frontier of GW astronomy, with increasing sensitivity of the current GW detectors (LIGO and Virgo, with the Japanese KAGRA about to join the detector network), the number of observed GW events of merging BH and NS pairs will continue to grow in the next years. This will allow to not only accurately measure the mass and spin distributions but also to start probing the population of binary BHs as a function of redshift. Ultimately, with future generations of GW detectors (such as Cosmic Explorer, Reitze et al. 2019, and Einstein Telescope, Maggiore et al. 2020), the properties of binary BH mergers will be mapped throughout the entire Cosmic history, making it the best constrained phase of massive star evolution. The challenge for theorists is to be well prepared on the side of models so that this wealth of observational results could be put to the best possible use.

# Chapter 9

# Samenvatting

*"Denk, denk, denk"*
*Winnie de Poeh*

Deze dissertatie draait om het onderwerp van massieve sterren. Tijdens hun leven - kort maar energiek en zelden zonder begeleide ster - schijnen zware sterren met extreme helderheden en blazen ze door het omringende medium met stromen van materie. Zij zijn de kosmische motoren, de bakens van stervormende sterrenstelsels dichtbij en ver weg, en de oorsprong van enkele van de meest energetische explosies die tot aan de oorsprong van de sterrenstelsels zijn waargenomen. Aan het einde van hun leven worden massieve sterren neutronensterren of zwarte gaten: enkele van de meest tot de verbeelding sprekende objecten in het heelal die de grenzen van de bekende fysica overschrijden.

De evolutie van massieve sterren en massieve dubbelstersystemen zit vol mysteries. Een van de belangrijkste onopgeloste problemen is de evolutie door fasen van massaoverdracht. In het bijzonder de uitkomst van de raadselachtige *common-envelope in-spiral* en eveneens de uiteindelijke ineenstorting van een massieve ster en de vorming van een neutronenster of een zwart gat. In beide gevallen zijn 3D hydrodynamische simulaties een rekenkundige uitdaging en de huidige numerieke hulpmiddelen zijn niet toereikend om alle vragen te beantwoorden. Een andere methode om deze raadselachtige evolutiefasen aan te pakken, een methode die we in dit proefschrift toepassen, is door hun overblijfselen te bestuderen. Bijvoorbeeld door röntgendubbelsystemen met zwarte gaten en fuserende paren van zwarte gaten of neutronensterren. Waarnemingen van deze laatste zijn sinds kort mogelijk met zwaartekrachtsgolfdetectoren. Dit opent een nieuwe blik op het heelal en de overblijfselen van massieve sterren.

We kiezen voor een theoretische benadering: door modellen te maken van de populaties van massieve dubbelsterren en hun overblijfselen in de Melkweg en in de kosmische geschiedenis, koppelen we de waarnemingen van röntgendubbelsystemen en bronnen van zwaartekrachtsgolven aan de onzekere theorieën van de evolutie van massieve dubbelsterren. In latere hoofdstukken gebruiken we gedetailleerde 1D stellaire en binaire modellen om ons begrip van de belangrijkste fasen van massaoverdracht en de rol van het metaalgehalte in massieve sterren (metalliciteit) onder

de loep te nemen. We zoeken een directe verband tussen de stellaire modellen en resultaten van spectroscopische onderzoeken van massieve sterren in nabije sterrenstelsels.

## Hoofdstuk II: Röntgendubbelsystemen met een zwart gat tijdens nauwe ontmoetingen

De vorming van de galactische populatie van röntgendubbelsystemen met een zwart gat en een lage-massa begeleider (ZG-LMXBs) is een lang bestaand raadsel. Als hun voorlopers nabije dubbelsystemen zijn, dan kan geen enkel evolutionair scenario met een fase van massaoverdracht al hun eigenschappen verklaren. In plaats daarvan onderzoeken we de evolutie van ultra-wijde dubbelsystemen die geen interactie hebben met elkaar. Hun grote banen maken het zo dat dynamische interacties met nabije sterren niet verwaarloosbaar zijn, zelfs in de minder drukke galactische schijf. We passen de snelle dubbelsysteem evolutiecode StarTrack aan om het effect van willekeurige dynamische ontmoetingen met drie lichamen op de baan van de dubbelsystemen op te nemen en we voeren een populatiesynthese uit van massieve dubbelsystemen in de schijf van de Melkweg. Ervan uitgaande dat dubbelsystemen die zijn verstoord tot zeer excentrische banen ($e \sim 0.99$) gecirculariseerd kunnen worden door getijdenkrachten bij een voldoende nauwe passage van het pericentrum, schatten we dat nauwe interacties een huidige populatie van $\sim$60$-$220 ZG-LMXBs in de Galactische schijf kunnen voortbrengen. Hoewel de voorspelde massaverdeling van de donorsterren goed overeenkomt met de waargenomen massaverdeling, is de bijdrage van de nauwe ontmoetingen aan de totale populatie van ZG-LMXBs waarschijnlijk vrij klein. In ieder geval moet de aanname van efficiënte circularisatie door getijdenkrachten van zeer excentrische banen nauwkeurig onderzocht worden in toekomstige studies van vergelijkbare systemen.

## Hoofdstuk III: Initiële parameters voor samensmeltingen van zwarte gaten en neutronensterren in dubbelsystemen

De verdelingen van de initiële parameters (massa, massaverhouding, omlooptijd, excentriciteit) van dubbelsystemen zijn niet onafhankelijk van elkaar. Hun onderlinge correlaties zijn echter pas recent gekwantificeerd door Moe & Di Stefano (2017). Met behulp van de snelle dubbelsysteemevolutiecode StarTrack bestuderen we het effect van deze onderlinge correlaties op de voorspelde populatie van fusies in dubbelsystemen met zwarte gaten en neutronensterren (zwaartekrachtsgolfbronnen) van het geïsoleerde dubbelsysteemevolutiekanaal met een common-envelope (CE) fase. Onze bevindingen tonen aan dat geen van de veranderingen in de initiële verdelingen van dubbelsystemen een significant effect heeft op de voorspelde populatie van bronnen van zwaartekrachtsgolven. We stellen ook dat zelfs extreme variaties van de initiële massafunctie een vergelijkbaar klein effect zouden hebben omdat het aantal massieve sterren direct wordt beperkt door de empirisch afgeleide kosmische stervormingssnelheid. In plaats daarvan benadrukken we de belangrijke rol van de lage metalliciteit die door de modellen wordt voorspeld en suggereren we dat ons begrip van de evolutie van metaal-arme dubbelsystemen en de kosmische stervormingssnelheid bij lage metalliciteiten de belangrijkste onzekerheden zijn om vast te stellen in de toekomstige studies van de voorlopers van zwaartekrachtsgolfbronnen. Dat eerste is het onderwerp van de

hoofdstukken V en VII.

## Hoofdstuk IV: Effectieve spin van fusies van dubbelsystemen van zwarte gaten

Alle tien fusies van dubbelsystemen van zwarte gaten, die aan het eind van de tweede waarnemingsronde van LIGO/Virgo waren gerapporteerd, bleken kleine effectieve spin te hebben. De effectieve spin-verdeling is vooral interessant in het kader van het onderscheid tussen verschillende formatiescenario's (Farr et al., 2018b). In dit hoofdstuk onderzoeken we verschillende effectieve spinverdelingen die voorspeld worden binnen het CE-vormingskanaal. We gebruiken de StarTrack code om de populatie van detecteerbare zwaartekrachtsgolfbronnen te modelleren en onderzoeken verschillende aannames voor de initiële spin van een zwart gat. In het bijzonder nemen we aan dat het impulsmoment van de kern van de ster op het moment van de uiteindelijke ineenstorting behouden blijft en de initiële spin van het zwarte gat bepaalt. We vinden dat onder de aanname dat de meeste zwarte gat dubbelsystemen fusies ontstaan uit geïsoleerde dubbelsysteemevolutie, dat hun lage effectieve spins sterk in het voordeel werken van stellaire modellen met relatief hoge efficiëntie van transport van impulsmoment binnen in de sterren (transport via de Taylor-Spruit dynamo in plaats van meridionale stromingen). In zulke modellen worden zelfs stellaire kernen die aanvankelijk snel roteren uiteindelijk afgeremd doordat het impulsmoment naar het omhulsel wordt getransporteerd vanwaar het verloren gaat in stellaire winden. Deze conclusie geldt ook als we rekening houden met het effect van opwinding van de spin door getijdenkrachten in het zwarte gat-Wolf Rayet dubbelsysteem stadium. Onder de beschouwde modelvariaties vinden we modellen die tegelijkertijd de fusiesnelheid, massa en spin verdeling van de tot nu toe waargenomen zwarte gaten dubbelsystemen fusies reproduceren (op het moment van schrijven). Het is echter duidelijk dat degeneraties tussen het effect van verschillende onzekere factoren het onmogelijk maken om limieten te stellen of robuuste conclusies te trekken over de oorsprong van de LIGO/Virgo bronnen.

## Hoofdstuk V: Metalliciteit en het begin van massaoverdracht in massieve dubbelstersystemen

Het is bekend dat metalliciteit een aanzienlijk effect heeft op de evolutie van massieve sterren vanwege de invloed ervan op de sterkte van de door winden aangedreven door spectraallijnen. Minder bekend is dat metalliciteit ook een sterke invloed heeft op de radiale uitzetting van zware sterren, vooral tijdens hun evolutie na de hoofdreeks. De radiale uitzetting van sterren is misschien niet cruciaal voor de evolutie van enkelsysteem sterren, maar wordt wel van bijzonder belang in de context van dubbelsystemen. Wij tonen dit aan door te schatten in welk evolutionair stadium, afhankelijk van de metalliciteit, een massieve ster groter wordt dan zijn Roche-lob in een dubbelsysteem. Daartoe berekenen we met de MESA 1D stellaire evolutiecode roosters van enkelvoudige massieve stermodellen met verschillende metalliciteiten. We beschouwen verschillende variaties in factoren waarvan bekend is dat ze de expansie van massieve sterren na de hoofdreeks beïnvloeden (bijvoorbeeld het doorschieten van convectie of semiconvectie) en vergelijken de modelvoorspellingen met het waargenomen aantal blauwe,

gele en rode superreuzen in de Melkweg en in de Kleine Magelhaense Wolk. We laten zien dat met afnemende metalliciteit, de parameterruimte voor massaoverdracht geïnitieerd door een kern-helium brandende superreus dramatisch toeneemt in vergelijking met de evolutie bij hoge (zonne-)metalliciteit. Dit type massaoverdrachtsevolutie is nog niet eerder bestudeerd: we onderzoeken het verder met gedetailleerde binaire modellen in hoofdstuk VII. Bovendien vinden we dat bij zeer lage metalliciteit (een paar procent van de waarde van de Zon) een significante fractie van de zware sterren pas na uitputting van helium in de kern, dus pas $\lesssim 10^4$ jaar voor de ineenstorting van de kern, aan hun eerste massaoverdrachtsevolutie beginnen. Dit suggereert dat veel metaalarme supernova-progenitors tijdens of kort na een massaoverdrachtsfase zouden kunnen exploderen. We wijzen er ook op dat de parameterruimte voor massaoverdracht van een convectieve donor extreem klein is in het geval van massieve sterren waarvan gedacht wordt dat ze de voorlopers van zwarte gaten zijn. Dit geeft reden tot bezorgdheid over de efficiëntie van het CE-vormingskanaal voor fusies van dubbelsystemen van zwarte gaten, zoals we in het volgende hoofdstuk diepgaand bestuderen.

## Hoofdstuk VI: Common-envelope in fusies van dubbelsystemen met een zwart gat

Een van de meest prominente kanalen voor de vorming van fusies van dubbelsystemen van zwarte gaten (ook beschouwd in eerdere hoofdstukken van dit proefschrift) is geïsoleerde dubbelsysteemevolutie met een CE fase. De inwaartse spiraal tijdens de CE fase, de belangrijkste fase van het scenario, vindt plaats als het eerste zwarte gat al gevormd is. In dit hoofdstuk proberen we de eigenschappen te bepalen van de begeleidende sterren in dubbelsystemen met een zwart gat die een CE-fase kunnen doormaken en daar kunnen overleven. We gebruiken de MESA stellaire-evolutiecode om bindingsenergieën van de buitenlagen van massieve sterren te berekenen voor verschillende metalliciteiten. We bekijken ook andere mogelijke energiebronnen en bespreken onzekerheden. Dit alles stelt ons in staat om de voorspellingen voor de uitstoting van de buitenlagen van de ster in de CE fase in massieve binaire superreuzen op basis van het energieformalisme nauwkeurig te onderzoeken. We tonen aan dat succesvolle CE-uitstoting in dubbelsystemen met een zwart gat alleen mogelijk is als de instabiele massaoverdracht geïnitieerd wordt door een rode superreus (RSR) donorster. Waargenomen is dat rode superreuzen ontbreken onder de heldere en massieve sterren die nodig zijn om ongeveer de helft van de LIGO/Virgo-metingen te verklaren. De redenen hiervoor worden nog steeds slecht begrepen. Verder suggereren wij dat ultra-heldere röntgenbronnen met RSR begeleiders zoals NGC 300 ULX-1 kandidaten zijn voor toekomstige zwaartekrachtsgolfbronnen (Heida et al., 2019). Hun rol als indicatie van dubbelsysteemevolutiekanalen zou wel eens bijzonder prominent kunnen worden met de resultaten van de James Webb ruimtetelescoop en de Extremely Large Telescope (ELT). Onze resultaten suggereren ook dat de efficiëntie van het CE-kanaal voor de vorming van fusies van dubbelsystemen van zwarte gaten in verschillende populatiemodellen waarschijnlijk ernstig overschat is. In de context van ZG-LMXB-systemen tonen we aan dat de bindingsenergie van massieve sterren in de fase na de heliumfusie in de kern voldoende laag is om zelfs een begeleider met lage massa

($< 1\ M_\odot$) in staat te stellen de buitenlagen van de ster uit te stoten. De betekenis van deze bevinding voor het oplossen van het ZG-LMXB-vormingsraadsel zal moeten worden getest met populatiemodellen.

## Hoofdstuk VII: Stabiele evolutie van de massaoverdracht van massieve donoren

In hoofdstuk V hebben we ontdekt dat de metalliciteit een significante invloed heeft op de evolutionaire fase waarin de Roche-lobben van massieve sterren overlopen waarbij deze donoren worden in dubbelsystemen. Dit motiveert ons om een gedetailleerde studie te maken van de evolutie van massaoverdracht in massieve dubbelsystemen van verschillende metalliciteiten, met behulp van de MESA stellaire evolutiecode. In onze hoge (zonne)metalliciteitsmodellen is massaoverdracht van een massieve donor na de hoofdreeks altijd een kortstondige gebeurtenis ($\lesssim 10^4$ jaar) van snelle massaoverdracht op de thermische-tijdschaal die de donorreus ontdoet van zijn (bijna) volledige laag van waterstof, waardoor een gestripte (~helium) ster ontstaat. Dit type evolutie is het canonieke beeld van hoe massaoverdrachtsevolutie na de hoofdreeks eruit ziet. Maar verrassend genoeg krijgen we bij lage metalliciteit een aanzienlijk aantal modellen die heel anders evolueren. Zij evolueren volgens één van de twee nieuw ontdekte evolutietypes: (a) kortstondige massaoverdrachtsfase die leidt tot donors die slechts gedeeltelijk van hun buitenlagen zijn ontdaan, of (b) snelle massaoverdracht gevolgd door een lange fase van massauitwisseling op de nucleaire tijdschaal die doorgaat tot het einde van heliumfusiefase in de kern. We laten zien dat de drie hierboven beschreven soorten massaoverdracht geassocieerd kunnen worden met de mate van snelle expansie van de massieve donor na de hoofdreeks. Dit verband blijkt vrij robuust te zijn. Ook het verband tussen de expansie na de hoofdreeks en de metalliciteit is duidelijk vastgesteld. Onze studie suggereert dus een sterk verband tussen metalliciteit en massaoverdrachtsevolutie. De details van dit verband, d.w.z. bij welke massa's en metalliciteiten de massaoverdrachtsevolutie precies overgaat tussen de verschillende hierboven besproken typen, moeten op dit moment echter als onzeker worden beschouwd. We bespreken de implicaties van onze bevindingen voor de vorming van gestripte sterren uit dubbelsysteem interacties, observationele eigenschappen sterren na massaoverdracht in populaties van massieve sterren, eigenschappen van massieve sterren voor deze supernova gaan, evenals populaties van röntgendubbelsystemen met hoge massa's in melkwegstelsels met verschillende metalliciteiten. We stellen ook verschillende observationele testen voor van de binaire modellen die in de toekomst belangrijk zullen zijn bij het begrijpen van de evolutie van metaal-arme massieve dubbelsystemen. Gezien het belang van sterevolutie met lage metalliciteit, in het bijzonder in de context van het vakgebied van de zwaartekrachtsgolven, beloven de resultaten van dit proefschrift veel interessant werk in de komende jaren.

## Een vooruitblik

In dit proefschrift hebben we enkele antwoorden gegeven en, niet verrassend, misschien nog meer nieuwe vragen geformuleerd.

De vorming van de galactische populatie van ZG-LMXB systemen blijft een raadsel. De

herziene bindingsenergieën van de buitenlagen van massieve superreuzen, verkregen in hoofdstuk VI, geven enige hoop op het oplossen van de problemen in het vormingsscenario met een CE-fase: dit moet worden getest met populatiemodellen. Het is echter heel goed mogelijk dat de ZG-LMXB systemen een aanwijzing zijn dat we iets belangrijks missen in de CE evolutie in massieve dubbelsystemen. Op theoretische gronden denk ik dat de mogelijkheid van gedeeltelijke ejectie van de buitenlagen gevolgd door stabiele massaoverdrachtsevolutie een interessant idee is (Quast et al., 2019, hoofdstuk VI-VII).

Als het gaat om ons begrip van de vorming van dubbelsysteem van zwarte gaten uit geïsoleerde dubbelsysteemevolutie, durf ik te gokken dat we in de nabije toekomst een verschuiving zullen zien weg van het zogenaamde klassieke CE-kanaal - dat als nogal 'ongewoon' wordt bestempeld - en misschien naar het interessanter wordende alternatief ervan: de vorming door stabiele massaoverdrachtsevolutie. Dit werd in hoofdstuk VI van dit proefschrift voorgesteld en kort daarna ook door de vergelijkbare resultaten van Marchant et al. (2021), alsmede aangegeven als een mogelijkheid in enkele populatie-synthese modelvariaties (Neijssel et al., 2019; Olejak et al., 2021). Een belangrijke stap voorwaarts in ons begrip van de vorming van dubbelsystemen van zwarte gaten zullen de resultaten zijn van 3D hydrodynamische simulaties van de evolutie van massieve zwarte gaten (inclusief stralingsoverdracht; Ricker et al., 2019). Wat de waarnemingen betreft zullen we dankzij de combinatie van Gaia en grootschalige spectroscopische onderzoeken zoals LAMOST, in de nabije toekomst waarschijnlijk een toename zien van het aantal kandidaten in de Melkweg voor niet-interagerende dubbelsystemen van zwarte gaten. Zonder twijfel zal dit leiden tot een groeiend aantal van zulke systemen. Dit zal van onschatbare waarde zijn om de evolutie van massieve dubbelstersystemen en de voorafgaande massaoverdrachtsfasen aan de test te ondervinden.

Gedetailleerde modellen van zware sterren en dubbelsystemen in hoofdstukken V en VII laten zien dat ons begrip van de evolutie van massaoverdracht in metaal-arme omgevingen nog lang niet compleet is. Vooral de ontdekking van de gedeeltelijke CE stripping van donoren met lage metalliciteit is belangrijk. De volgende stap is om een uitgebreide set van gedetailleerde dubbelsysteemmodellen te vergelijken met resultaten van spectroscopische onderzoeken in de Lokale Groep, in het bijzonder het VLT-FLAMES multi-epoch onderzoek van massieve sterren in het 30 Doradus stervormingsgebied in de Grote Magelhaense Wolk (Evans et al., 2011). Vergelijkbare aanvullende onderzoeken in de Kleine Magelhaense Wolk zouden limieten kunnen stellen voor nog lagere metalliciteit. De verschillende effecten die in dit proefschrift worden voorspeld, zouden daar kunnen worden onderzocht. Bovendien zullen de volgende generatie telescopen, vooral de ELT, een langverwacht nieuwe blik kunnen openen op metaalarme omgevingen van melkwegstelsels op $\sim 1$ Mpc afstand: Sextans A, SagDIG, en Leo P, met metalliciteiten van ongeveer $\sim 1/10, 1/20, 1/30$ van de zonnewaarde (Garcia et al., 2019). Samen vormen ze de eerste empirische kosmische metalliciteitsladder van de evolutie van massieve sterren.

Aan de grenzen van onze kennis in het vakgebied van de zwaartekrachtsgolven zal het aantal waargenomen zwaartekrachtsgolven van samensmeltende zwarte gaten en neutronensterren de komende jaren blijven toenemen. Dit is dankzij de toenemende gevoeligheid van de huidige

zwaartekrachtsgolfdetectoren (LIGO en Virgo, maar ook het Japanse KAGRA zal zich binnenkort bij het detectornetwerk aansluiten). Dit zal het niet alleen mogelijk maken om de massa en de spinverdeling nauwkeurig te meten, maar het zal het ook mogelijk maken te beginnen met het onderzoeken van de populatie van dubbelsystemen van zwarte gaten als functie van de roodverschuiving. Uiteindelijk zullen met toekomstige generaties zwaartekrachtsgolfdetectoren (zoals Cosmic Explorer, Reitze et al. 2019, en de Einstein Telescoop, Maggiore et al. 2020) de eigenschappen van fusies van dubbelsystemen van zwarte gaten door de hele kosmische geschiedenis in kaart worden gebracht. De uitdaging voor theoretisch onderzoek bestaat uit zich zo goed mogelijk voor te bereiden met modellen zodat de toekomstige waarnemingen zo goed mogelijk kunnen worden gebruikt.

# Bibliography


Abadie, J., Abbott, B. P., Abbott, R., et al. 2010, Classical and Quantum Gravity, 27, 173001

Abbott, B. P., Abbott, R., Abbott, T. D., et al. 2016a, Physical Review Letters, 116, 241103

Abbott, B. P., Abbott, R., Abbott, T. D., et al. 2016b, Phys. Rev. Lett., 116, 061102

Abbott, B. P., Abbott, R., Abbott, T. D., et al. 2016c, Physical Review Letters, 116, 241102

Abbott, B. P., Abbott, R., Abbott, T. D., et al. 2016d, Living Reviews in Relativity, 19, 1

Abbott, B. P., Abbott, R., Abbott, T. D., et al. 2018, Living Reviews in Relativity, 21, 3

Abbott, B. P., Abbott, R., Abbott, T. D., et al. 2019a, ApJ, 882, L24

Abbott, B. P., Abbott, R., Abbott, T. D., et al. 2019b, Physical Review X, 9, 031040

Abbott, B. P., Abbott, R., Abbott, T. D., et al. 2017a, Phys. Rev. Lett., 119, 161101

Abbott, B. P., Abbott, R., Abbott, T. D., et al. 2017b, Physical Review Letters, 118, 221101

Abbott, B. P., Abbott, R., Abbott, T. D., et al. 2017c, ApJ, 851, L35

Abbott, B. P., Abbott, R., Abbott, T. D., et al. 2017d, Physical Review Letters, 119, 141101

Abbott, B. P., Abbott, R., Abbott, T. D., et al. 2017e, ApJ, 848, L12

Abbott, B. P. et al. 2017, Phys. Rev. Lett., 118, 221101

Abbott, R., Abbott, T. D., Abraham, S., et al. 2020a, arXiv e-prints, arXiv:2010.14527

Abbott, R., Abbott, T. D., Abraham, S., et al. 2021, ApJ, 913, L7

Abbott, R., Abbott, T. D., Abraham, S., et al. 2020b, ApJ, 896, L44

Abbott, R., Abbott, T. D., Abraham, S., et al. 2020c, Phys. Rev. Lett., 125, 101102

Abolmasov, P., Karpov, S., & Kotani, T. 2009, PASJ, 61, 213

Abt, H. A. 1983, ARA&A, 21, 343

Abt, H. A., Gomez, A. E., & Levy, S. G. 1990, ApJS, 74, 551

Acernese, F., Agathos, M., Agatsuma, K., et al. 2015, Classical and Quantum Gravity, 32, 024001

Adams, F. C. & Fatuzzo, M. 1996, ApJ, 464, 256

Aldoretta, E. J., Caballero-Nieves, S. M., Gies, D. R., et al. 2015, AJ, 149, 26

Andrews, B. H. & Martini, P. 2013, ApJ, 765, 140

Andrews, J. J. & Zezas, A. 2019, MNRAS, 486, 3213

Antonini, F. & Rasio, F. A. 2016, ApJ, 831, 187

Antonini, F., Rodriguez, C. L., Petrovich, C., & Fischer, C. L. 2017a, ArXiv e-prints [[arXiv]1711.07142]

Antonini, F., Toonen, S., & Hamers, A. S. 2017b, ApJ, 841, 77
Arca-Sedda, M. & Capuzzo-Dolcetta, R. 2017, ArXiv e-prints [[arXiv]1709.05567]
Arca-Sedda, M. & Gualandris, A. 2018, MNRAS, 477, 4423
Armitage, P. J. & Livio, M. 2000, ApJ, 532, 540
Askar, A., Szkudlarek, M., Gondek-Rosińska, D., Giersz, M., & Bulik, T. 2017, MNRAS, 464, L36
Asplund, M. 1998, A&A, 330, 641
Bae, Y.-B., Kim, C., & Lee, H. M. 2014, MNRAS, 440, 2714
Bahcall, J. N., Hut, P., & Tremaine, S. 1985, ApJ, 290, 15
Baldry, I. K., Driver, S. P., Loveday, J., et al. 2012, MNRAS, 421, 621
Banerjee, S. 2018, MNRAS, 473, 909
Barack, L., Cardoso, V., Nissanke, S., et al. 2019, Classical and Quantum Gravity, 36, 143001
Baraffe, I. & El Eid, M. F. 1991, A&A, 245, 548
Barrett, J. W., Gaebel, S. M., Neijssel, C. J., et al. 2018, MNRAS, 477, 4685
Bartzakos, P., Moffat, A. F. J., & Niemela, V. S. 2001, MNRAS, 324, 18
Bastian, N., Covey, K. R., & Meyer, M. R. 2010, ARA&A, 48, 339
Bate, M. R. & Bonnell, I. A. 2005, MNRAS, 356, 1201
Baugh, C. M., Lacey, C. G., Frenk, C. S., et al. 2005, MNRAS, 356, 1191
Baumgardt, H., Kroupa, P., & Parmentier, G. 2008, MNRAS, 384, 1231
Bavera, S. S., Fragos, T., Qin, Y., et al. 2020, A&A, 635, A97
Begelman, M. C., King, A. R., & Pringle, J. E. 2006, MNRAS, 370, 399
Behroozi, P. S., Wechsler, R. H., & Conroy, C. 2013, ApJ, 770, 57
Belczynski, K., Askar, A., Arca-Sedda, M., et al. 2018, A&A, 615, A91
Belczynski, K. & Banerjee, S. 2020, arXiv e-prints, arXiv:2002.08050
Belczynski, K., Bulik, T., & Fryer, C. L. 2012a, ArXiv e-prints [[arXiv]1208.2422]
Belczynski, K., Bulik, T., Fryer, C. L., et al. 2010a, ApJ, 714, 1217
Belczynski, K., Bulik, T., Mandel, I., et al. 2013, ApJ, 764, 96
Belczynski, K., Buonanno, A., Cantiello, M., et al. 2014, ApJ, 789, 120
Belczynski, K., Dominik, M., Bulik, T., et al. 2010b, ApJ, 715, L138
Belczynski, K., Heger, A., Gladysz, W., et al. 2016a, A&A, 594, A97
Belczynski, K., Hirschi, R., Kaiser, E. A., et al. 2020a, ApJ, 890, 113
Belczynski, K., Holz, D. E., Bulik, T., & O'Shaughnessy, R. 2016b, Nature, 534, 512
Belczynski, K., Kalogera, V., & Bulik, T. 2002, ApJ, 572, 407
Belczynski, K., Kalogera, V., Rasio, F. A., et al. 2008a, ApJS, 174, 223
Belczynski, K., Klencki, J., Fields, C. E., et al. 2020b, A&A, 636, A104
Belczynski, K., Repetto, S., Holz, D. E., et al. 2016c, ApJ, 819, 108
Belczynski, K. & Taam, R. E. 2004, ApJ, 603, 690
Belczynski, K., Taam, R. E., Kalogera, V., Rasio, F. A., & Bulik, T. 2007, ApJ, 662, 504
Belczynski, K., Taam, R. E., Rantsiou, E., & van der Sluys, M. 2008b, ApJ, 682, 474
Belczynski, K., Wiktorowicz, G., Fryer, C. L., Holz, D. E., & Kalogera, V. 2012b, ApJ, 757, 91

Benacquista, M. J. & Downing, J. M. B. 2013, Living Reviews in Relativity, 16, 4
Benson, R. S. 1970, PhD thesis, UNIVERSITY OF CALIFORNIA, BERKELEY.
Berg, D. A., Skillman, E. D., Marble, A. R., et al. 2012, ApJ, 754, 98
Bertelli, G., Bressan, A., Chiosi, C., Fagotto, F., & Nasi, E. 1994, A&AS, 106
Bestenlehner, J. M., Gräfener, G., Vink, J. S., et al. 2014, A&A, 570, A38
Bethe, H. A. & Brown, G. E. 1998, ApJ, 506, 780
Blaauw, A. 1961, Bull. Astron. Inst. Netherlands, 15, 265
Blagorodnova, N., Kotak, R., Polshaw, J., et al. 2017, ApJ, 834, 107
Blondin, J. M. & Mezzacappa, A. 2007, Nature, 445, 58
Böhm-Vitense, E. 1958, ZAp, 46, 108
Bonanos, A. Z., Lennon, D. J., Köhlinger, F., et al. 2010, AJ, 140, 416
Bond, N. A., Ivezić, Ž., Sesar, B., et al. 2010, ApJ, 716, 1
Bonnell, I. A., Clarke, C. J., & Bate, M. R. 2006, MNRAS, 368, 1296
Boogaard, L. A., Brinchmann, J., Bouché, N., et al. 2018, ArXiv e-prints [[arXiv]1808.04900]
Bouret, J. C., Lanz, T., Hillier, D. J., et al. 2015, MNRAS, 449, 1545
Braun, H. & Langer, N. 1995, A&A, 297, 483
Breivik, K., Chatterjee, S., & Larson, S. L. 2017, ApJ, 850, L13
Breivik, K., Coughlin, S., Zevin, M., et al. 2020, ApJ, 898, 71
Bressan, A., Fagotto, F., Bertelli, G., & Chiosi, C. 1993, A&AS, 100, 647
Britavskiy, N. E., Bonanos, A. Z., Herrero, A., et al. 2019, A&A, 631, A95
Bromm, V., Coppi, P. S., & Larson, R. B. 1999, ApJ, 527, L5
Brorby, M., Kaaret, P., & Prestwich, A. 2014, MNRAS, 441, 2346
Brott, I., de Mink, S. E., Cantiello, M., et al. 2011a, A&A, 530, A115
Brott, I., Evans, C. J., Hunter, I., et al. 2011b, A&A, 530, A116
Brown, G. E., Heger, A., Langer, N., et al. 2001, New A, 6, 457
Brunish, W. M. & Truran, J. W. 1982, ApJS, 49, 447
Bulik, T., Belczynski, K., & Prestwich, A. 2011, ApJ, 730, 140
Caballero-Nieves, S. M., Nelan, E. P., Gies, D. R., et al. 2014, AJ, 147, 40
Cantiello, M., Langer, N., Brott, I., et al. 2009, A&A, 499, 279
Cantiello, M., Mankovich, C., Bildsten, L., Christensen-Dalsgaard, J., & Paxton, B. 2014, ApJ, 788, 93
Cantiello, M., Yoon, S. C., Langer, N., & Livio, M. 2007, A&A
Carpano, S., Pollock, A. M. T., Prestwich, A., et al. 2007, A&A, 466, L17
Casares, J., Charles, P. A., & Naylor, T. 1992, Nature, 355, 614
Casares, J. & Jonker, P. G. 2014, Space Sci. Rev., 183, 223
Castro, N., Fossati, L., Langer, N., et al. 2014, A&A, 570, L13
Chatterjee, S., Fregeau, J. M., Umbreit, S., & Rasio, F. A. 2010, ApJ, 719, 915
Chatterjee, S., Rodriguez, C. L., Kalogera, V., & Rasio, F. A. 2016, ArXiv e-prints [[arXiv]1609.06689]
Chen, H.-Y., Holz, D. E., Miller, J., et al. 2017, ArXiv e-prints [[arXiv]1709.08079]

Chen, W.-C. & Li, X.-D. 2006, MNRAS, 373, 305
Chen, X. & Han, Z. 2002, MNRAS, 335, 948
Chen, Y., Bressan, A., Girardi, L., et al. 2015, MNRAS, 452, 1068
Chieffi, A. & Limongi, M. 2013, ApJ, 764, 21
Chieffi, A. & Limongi, M. 2020, ApJ, 890, 43
Chini, R., Hoffmeister, V. H., Nasseri, A., Stahl, O., & Zinnecker, H. 2012, MNRAS, 424, 1925
Choi, J., Dotter, A., Conroy, C., et al. 2016, ApJ, 823, 102
Choksi, N., Volonteri, M., Colpi, M., Gnedin, O. Y., & Li, H. 2019, ApJ, 873, 100
Chrimes, A. A., Stanway, E. R., & Eldridge, J. J. 2020, MNRAS, 491, 3479
Chruslinska, M., Belczynski, K., Klencki, J., & Benacquista, M. 2018, MNRAS, 474, 2937
Chruslinska, M. & Nelemans, G. 2019a, MNRAS, 488, 5300
Chruslinska, M. & Nelemans, G. 2019b, MNRAS, 1974
Chruslinska, M., Nelemans, G., & Belczynski, K. 2019, MNRAS, 482, 5012
Chun, S.-H., Yoon, S.-C., Jung, M.-K., Kim, D. U., & Kim, J. 2018, ApJ, 853, 79
Claret, A. 2007, A&A, 467, 1389
Claret, A. & Torres, G. 2018, ApJ, 859, 100
Clark, G. W. 1975, ApJ, 199, L143
Clark, P. C., Glover, S. C. O., Klessen, R. S., & Bromm, V. 2011, ApJ, 727, 110
Clayton, M., Podsiadlowski, P., Ivanova, N., & Justham, S. 2017, MNRAS, 470, 1788
Conti, P. S. 1975, Memoires of the Societe Royale des Sciences de Liege, 9, 193
Corral-Santana, J. M., Casares, J., Muñoz-Darias, T., et al. 2016, A&A, 587, A61
Couch, S. M., Warren, M. L., & O'Connor, E. P. 2020, ApJ, 890, 127
Crowther, P. A., Schnurr, O., Hirschi, R., et al. 2010, MNRAS, 408, 731
Daflon, S. & Cunha, K. 2004, ApJ, 617, 1115
Daigne, F., Olive, K. A., Silk, J., Stoehr, F., & Vangioni, E. 2006, ApJ, 647, 773
Darwin, G. H. 1879, Proceedings of the Royal Society of London Series I, 29, 168
Davies, B., Crowther, P. A., & Beasor, E. R. 2018, MNRAS, 478, 3138
Davies, B. & Dessart, L. 2019, MNRAS, 483, 887
Davies, B., Kudritzki, R.-P., Gazak, Z., et al. 2015, ApJ, 806, 21
Davis, P. J., Kolb, U., & Knigge, C. 2012, MNRAS, 419, 287
De, S., MacLeod, M., Everson, R. W., et al. 2020, ApJ, 897, 130
de Kool, M. 1990, ApJ, 358, 189
de Kool, M., van den Heuvel, E. P. J., & Pylyser, E. 1987, A&A, 183, 47
De Loore, C. & De Greve, J. P. 1992, A&AS, 94, 453
De Marchi, G., Paresce, F., & Pulone, L. 2007, ApJ, 656, L65
De Marco, O., Passy, J.-C., Moe, M., et al. 2011, MNRAS, 411, 2277
de Mink, S. E. & Belczynski, K. 2015a, ApJ, 814, 58
de Mink, S. E. & Belczynski, K. 2015b, ApJ, 814, 58
de Mink, S. E., Cantiello, M., Langer, N., et al. 2009a, A&A, 497, 243
de Mink, S. E., Langer, N., Izzard, R. G., Sana, H., & de Koter, A. 2013, ApJ, 764, 166

de Mink, S. E. & Mandel, I. 2016, MNRAS, 460, 3545
de Mink, S. E., Pols, O. R., & Hilditch, R. W. 2007, A&A, 467, 1181
de Mink, S. E., Pols, O. R., Langer, N., & Izzard, R. G. 2009b, A&A, 507, L1
de Mink, S. E., Pols, O. R., & Yoon, S.-C. 2008, in American Institute of Physics Conference Series, Vol. 990, First Stars III, eds. B. W. O'Shea & A. Heger, 230–232
de Mink, S. E., Sana, H., Langer, N., Izzard, R. G., & Schneider, F. R. N. 2014, ApJ, 782, 7
Detmers, R. G., Langer, N., Podsiadlowski, P., & Izzard, R. G. 2008, A&A, 484, 831
Dewi, J. D. M., Podsiadlowski, P., & Sena, A. 2006, MNRAS, 368, 1742
Dewi, J. D. M. & Tauris, T. M. 2000, A&A, 360, 1043
Di Carlo, U. N., Giacobbo, N., Mapelli, M., et al. 2019, arXiv e-prints [[arXiv]1901.00863]
Djorgovski, S., Piotto, G., & Capaccioli, M. 1993, AJ, 105, 2148
Dominik, M., Belczynski, K., Fryer, C., et al. 2012, ApJ, 759, 52
Dominik, M., Belczynski, K., Fryer, C., et al. 2013, ApJ, 779, 72
Dominik, M., Berti, E., O'Shaughnessy, R., et al. 2015, ApJ, 806, 263
Downing, J. M. B., Benacquista, M. J., Giersz, M., & Spurzem, R. 2010, MNRAS, 407, 1946
Dray, L. M. 2006, MNRAS, 370, 2079
Dray, L. M. & Tout, C. A. 2007, MNRAS, 376, 61
Drout, M. R., Massey, P., Meynet, G., Tokarz, S., & Caldwell, N. 2009, ApJ, 703, 441
Duchêne, G. & Kraus, A. 2013, ARA&A, 51, 269
Dvorkin, I., Silk, J., Vangioni, E., Petitjean, P., & Olive, K. A. 2015, MNRAS, 452, L36
Edgar, R. 2004, New A Rev., 48, 843
Eggenberger, P., Meynet, G., & Maeder, A. 2002, A&A, 386, 576
Eggenberger, P., Meynet, G., Maeder, A., et al. 2008, Ap&SS, 316, 43
Eggleton, P. P. 1983, ApJ, 268, 368
Eggleton, P. P. & Kiseleva-Eggleton, L. 2001, ApJ, 562, 1012
Ekström, S., Georgy, C., Eggenberger, P., et al. 2012, A&A, 537, A146
Elbert, O. D., Bullock, J. S., & Kaplinghat, M. 2018, MNRAS, 473, 1186
Eldridge, J. J., Izzard, R. G., & Tout, C. A. 2008, MNRAS, 384, 1109
Eldridge, J. J. & Stanway, E. R. 2016, MNRAS, 462, 3302
Eldridge, J. J., Stanway, E. R., Xiao, L., et al. 2017, PASA, 34, e058
Ertl, T., Janka, H. T., Woosley, S. E., Sukhbold, T., & Ugliano, M. 2016, ApJ, 818, 124
Ertl, T., Woosley, S. E., Sukhbold, T., & Janka, H. T. 2020, ApJ, 890, 51
Evans, C. J., Lennon, D. J., Smartt, S. J., & Trundle, C. 2006, A&A, 456, 623
Evans, C. J., Taylor, W. D., Hénault-Brunet, V., et al. 2011, A&A, 530, A108
Evans, F. A., Renzo, M., & Rossi, E. M. 2020, MNRAS, 497, 5344
Event Horizon Telescope Collaboration, Akiyama, K., Alberdi, A., et al. 2019, ApJ, 875, L1
Fabian, A. C., Pringle, J. E., & Rees, M. J. 1975, MNRAS, 172, 15p
Fabrika, S. 2004, Astrophys. Space Phys. Res., 12, 1
Fagotto, F., Bressan, A., Bertelli, G., & Chiosi, C. 1994, A&AS, 105, 29
Fang, T. & Cen, R. 2004, ApJ, 616, L87

Farmer, R., Fields, C. E., Petermann, I., et al. 2016, ApJS, 227, 22
Farmer, R., Renzo, M., de Mink, S. E., Marchant, P., & Justham, S. 2019, ApJ, 887, 53
Farr, B., Holz, D. E., & Farr, W. M. 2018a, ApJ, 854, L9
Farr, B., Holz, D. E., & Farr, W. M. 2018b, ApJ, 854, L9
Farr, W. M. & Mandel, I. 2018, ArXiv e-prints [[arXiv]1807.09772]
Farr, W. M., Stevenson, S., Miller, M. C., et al. 2017, Nature, 548, 426
Farrell, E. J., Groh, J. H., Meynet, G., et al. 2019, A&A, 621, A22
Faucher-Giguère, C.-A. & Kaspi, V. M. 2006, ApJ, 643, 332
Ferrario, L., Pringle, J. E., Tout, C. A., & Wickramasinghe, D. T. 2009, MNRAS, 400, L71
Fields, C. E., Timmes, F. X., Farmer, R., et al. 2018, ApJS, 234, 19
Finke, J. D. & Razzaque, S. 2017, MNRAS, 472, 3683
Fishbach, M. & Holz, D. E. 2017a, ApJ, 851, L25
Fishbach, M. & Holz, D. E. 2017b, ApJ, 851
Fishbach, M., Holz, D. E., & Farr, B. 2017, ApJ, 840, L24
Flynn, C., Sommer-Larsen, J., & Christensen, P. R. 1996, MNRAS, 281, 1027
Foellmi, C., Moffat, A. F. J., & Guerrero, M. A. 2003a, MNRAS, 338, 360
Foellmi, C., Moffat, A. F. J., & Guerrero, M. A. 2003b, MNRAS, 338, 1025
Foglizzo, T., Guilet, J., & Sato, J. 2009, in SF2A-2009: Proceedings of the Annual meeting of the French Society of Astronomy and Astrophysics, eds. M. Heydari-Malayeri, C. Reyl'E, & R. Samadi, 143
Fragione, G., Grishin, E., Leigh, N. W. C., Perets, H. B., & Perna, R. 2019, MNRAS, 488, 47
Fragione, G. & Kocsis, B. 2018, Phys. Rev. Lett., 121, 161103
Fragione, G. & Kocsis, B. 2019, MNRAS, 486, 4781
Fragos, T., Andrews, J. J., Ramirez-Ruiz, E., et al. 2019, ApJ, 883, L45
Fregeau, J. M., Cheung, P., Portegies Zwart, S. F., & Rasio, F. A. 2004, MNRAS, 352, 1
Freytag, B., Ludwig, H. G., & Steffen, M. 1996, A&A, 313, 497
Fruchter, A. S., Levan, A. J., Strolger, L., et al. 2006, Nature, 441, 463
Fryer, C. L. 1999, ApJ, 522, 413
Fryer, C. L., Belczynski, K., Wiktorowicz, G., et al. 2012, ApJ, 749, 91
Fryer, C. L. & Heger, A. 2000, ApJ, 541, 1033
Fryer, C. L. & Kalogera, V. 2001, ApJ, 554, 548
Fryer, C. L. & Kusenko, A. 2006, ApJS, 163, 335
Fryer, C. L., Lloyd-Ronning, N., Wollaeger, R., et al. 2019, arXiv e-prints [[arXiv]1904.10008]
Fryer, C. L., Woosley, S. E., & Hartmann, D. H. 1999, ApJ, 526, 152
Fryer, C. L. & Young, P. A. 2007, ApJ, 659, 1438
Fuller, J. & Ma, L. 2019, ApJ, 881, L1
Fuller, J., Piro, A. L., & Jermyn, A. S. 2019, MNRAS[[arXiv]1902.08227]
Gal-Yam, A. 2012, Science, 337, 927
Garcia, M., Evans, C. J., Bestenlehner, J. M., et al. 2019, arXiv e-prints, arXiv:1908.04687
Ge, H., Hjellming, M. S., Webbink, R. F., Chen, X., & Han, Z. 2010, ApJ, 717, 724

Ge, H., Webbink, R. F., Chen, X., & Han, Z. 2015, ApJ, 812, 40
Genzel, R., Eisenhauer, F., & Gillessen, S. 2010, Reviews of Modern Physics, 82, 3121
Georgy, C., Ekström, S., Eggenberger, P., et al. 2013, A&A, 558, A103
Georgy, C., Ekström, S., Meynet, G., et al. 2012, A&A, 542, A29
Gerosa, D. & Berti, E. 2017, Phys. Rev., D95, 124046
Gerosa, D., Berti, E., O'Shaughnessy, R., et al. 2018, Phys. Rev. D, 98, 084036
Gerosa, D., Kesden, M., Berti, E., O'Shaughnessy, R., & Sperhake, U. 2013, Phys. Rev. D, 87, 104028
Gerosa, D., Kesden, M., Sperhake, U., Berti, E., & O'Shaughnessy, R. 2015, Phys. Rev. D, 92, 064016
Ghez, A. M., Salim, S., Hornstein, S. D., et al. 2005, ApJ, 620, 744
Ghez, A. M., Salim, S., Weinberg, N. N., et al. 2008, ApJ, 689, 1044
Giacobbo, N. & Mapelli, M. 2018, MNRAS[[arXiv]1806.00001]
Giacobbo, N. & Mapelli, M. 2020, ApJ, 891, 141
Giacobbo, N., Mapelli, M., & Spera, M. 2018, MNRAS, 474, 2959
Giersz, M., Heggie, D. C., Hurley, J. R., & Hypki, A. 2013, MNRAS, 431, 2184
Gilkis, A., Shenar, T., Ramachandran, V., et al. 2021, MNRAS, 503, 1884
Gilmore, G. & Reid, N. 1983, MNRAS, 202, 1025
Ginat, Y. B., Glanz, H., Perets, H. B., Grishin, E., & Desjacques, V. 2020, MNRAS, 493, 4861
Glatzel, W. & Kiriakidis, M. 1993, MNRAS, 263, 375
Glebbeek, E., Gaburov, E., de Mink, S. E., Pols, O. R., & Portegies Zwart, S. F. 2009, A&A, 497, 255
Glebbeek, E., Gaburov, E., Portegies Zwart, S., & Pols, O. R. 2013, MNRAS, 434, 3497
Götberg, Y., de Mink, S. E., & Groh, J. H. 2017, A&A, 608, A11
Götberg, Y., de Mink, S. E., Groh, J. H., et al. 2018, A&A, 615, A78
Götberg, Y., de Mink, S. E., McQuinn, M., et al. 2020, A&A, 634, A134
Gräfener, G. & Hamann, W. R. 2008, A&A, 482, 945
Gräfener, G., Owocki, S. P., & Vink, J. S. 2012, A&A, 538, A40
Gräfener, G., Vink, J. S., de Koter, A., & Langer, N. 2011, A&A, 535, A56
Graham, J. F. & Fruchter, A. S. 2013, ApJ, 774, 119
Graziani, L., Schneider, R., Marassi, S., et al. 2020, MNRAS, 495, L81
Green, A. M. 2017, ArXiv e-prints [[arXiv]1705.10818]
Greif, T. H., Glover, S. C. O., Bromm, V., & Klessen, R. S. 2010, ApJ, 716, 510
Greif, T. H., Schleicher, D. R. G., Johnson, J. L., et al. 2008, in IAU Symposium, Vol. 255, Low-Metallicity Star Formation: From the First Stars to Dwarf Galaxies, eds. L. K. Hunt, S. C. Madden, & R. Schneider, 33–48
Grevesse, N., Noels, A., & Sauval, A. J. 1996, in Astronomical Society of the Pacific Conference Series, Vol. 99, Cosmic Abundances, eds. S. S. Holt & G. Sonneborn, 117
Grevesse, N. & Sauval, A. J. 1998, Space Sci. Rev., 85, 161
Grin, N. J., Ramírez-Agudelo, O. H., de Koter, A., et al. 2017, A&A, 600, A82

Groh, J. H., Ekström, S., Georgy, C., et al. 2019, A&A, 627, A24
Gültekin, K., Miller, M. C., & Hamilton, D. P. 2004, ApJ, 616, 221
Gültekin, K., Miller, M. C., & Hamilton, D. P. 2006, ApJ, 640, 156
Hainich, R., Oskinova, L. M., Shenar, T., et al. 2018, A&A, 609, A94
Hainich, R., Rühling, U., Todt, H., et al. 2014, A&A, 565, A27
Hamann, W.-R. & Koesterke, L. 1998, A&A, 335, 1003
Hamann, W. R., Koesterke, L., & Wessolowski, U. 1995, A&A, 299, 151
Hamers, A. S. & Thompson, T. A. 2019, ApJ, 883, 23
Hamilton, A. J. S. & Sarazin, G. L. 1982, MNRAS, 198, 59
Han, Z. 1998, MNRAS, 296, 1019
Han, Z., Podsiadlowski, P., & Eggleton, P. P. 1994, MNRAS, 270, 121
Heger, A., Fryer, C. L., Woosley, S. E., Langer, N., & Hartmann, D. H. 2003, ApJ, 591, 288
Heger, A., Langer, N., & Woosley, S. E. 2000, ApJ, 528, 368
Heger, A. & Woosley, S. E. 2002, ApJ, 567, 532
Heger, A., Woosley, S. E., & Spruit, H. C. 2005, ApJ, 626, 350
Heggie, D. C. 1975, MNRAS, 173, 729
Heggie, D. C. & Rasio, F. A. 1996, MNRAS, 282, 1064
Heida, M., Jonker, P. G., Torres, M. A. P., et al. 2016, MNRAS, 459, 771
Heida, M., Lau, R. M., Davies, B., et al. 2019, ApJ, 883, L34
Heida, M., Torres, M. A. P., Jonker, P. G., et al. 2015, MNRAS, 453, 3510
Hellings, P. 1983, Ap&SS, 96, 37
Hellings, P. 1984, Ap&SS, 104, 83
Herwig, F. 2000, A&A, 360, 952
Higgins, E. R. & Vink, J. S. 2019, A&A, 622, A50
Higgins, E. R. & Vink, J. S. 2020, A&A, 635, A175
Hills, J. G. 1981, AJ, 86, 1730
Hillwig, T. C. & Gies, D. R. 2008, ApJ, 676, L37
Hirano, S., Hosokawa, T., Yoshida, N., Omukai, K., & Yorke, H. W. 2015, MNRAS, 448, 568
Hjellming, M. S. & Webbink, R. F. 1987, ApJ, 318, 794
Hobbs, G., Lorimer, D. R., Lyne, A. G., & Kramer, M. 2005, MNRAS, 360, 974
Holgado, A. M., Ricker, P. M., & Huerta, E. A. 2017, ArXiv e-prints [[arXiv]1706.09413]
Hong, J., Vesperini, E., Askar, A., et al. 2018, MNRAS, 480, 5645
Hotokezaka, K. & Piran, T. 2017a, arXiv e-prints, arXiv:1707.08978
Hotokezaka, K. & Piran, T. 2017b, ApJ, 842, 111
Hotokezaka, K. & Piran, T. 2017c, ArXiv e-prints [[arXiv]1702.03952]
Houck, J. C. & Chevalier, R. A. 1991, ApJ, 376, 234
Howitt, G., Stevenson, S., Vigna-Gómez, A. r., et al. 2020, MNRAS, 492, 3229
Hulse, R. A. & Taylor, J. H. 1975, ApJ, 195, L51
Humphreys, R. M. & Davidson, K. 1979, ApJ, 232, 409
Humphreys, R. M. & Davidson, K. 1994, PASP, 106, 1025

Hunter, I., Lennon, D. J., Dufton, P. L., et al. 2008, A&A, 479, 541
Hurley, J. R., Pols, O. R., & Tout, C. A. 2000, MNRAS, 315, 543
Hurley, J. R., Sippel, A. C., Tout, C. A., & Aarseth, S. J. 2016, PASA, 33, e036
Hurley, J. R., Tout, C. A., & Pols, O. R. 2002, MNRAS, 329, 897
Husa, S., Khan, S., Hannam, M., et al. 2016, Phys. Rev. D, 93, 044006
Iben, I., J. & Tutukov, A. V. 1984, ApJ, 284, 719
Iben, Icko, J. & Livio, M. 1993, PASP, 105, 1373
Iglesias, C. A. & Rogers, F. J. 1996, ApJ, 464, 943
Igoshev, A. P. & Popov, S. B. 2013, MNRAS, 432, 967
Inoue, Y., Tanaka, Y. T., & Isobe, N. 2016, MNRAS, 461, 4329
Irwin, J. A. 2005, ApJ, 631, 511
Israel, G. L., Papitto, A., Esposito, P., et al. 2017, MNRAS, 466, L48
Ivanova, N. 2006, ApJ, 653, L137
Ivanova, N. 2011a, ApJ, 730, 76
Ivanova, N. 2011b, in Astronomical Society of the Pacific Conference Series, Vol. 447, Evolution of Compact Binaries, eds. L. Schmidtobreick, M. R. Schreiber, & C. Tappert, 91
Ivanova, N. 2015, Binary Evolution: Roche Lobe Overflow and Blue Stragglers, eds. H. M. J. Boffin, G. Carraro, & G. Beccari, 179
Ivanova, N. & Chaichenets, S. 2011, ApJ, 731, L36
Ivanova, N., Justham, S., Avendano Nandez, J. L., & Lombardi, J. C. 2013a, Science, 339, 433
Ivanova, N., Justham, S., Chen, X., et al. 2013b, A&A Rev., 21, 59
Ivanova, N. & Podsiadlowski, P. 2003, in From Twilight to Highlight: The Physics of Supernovae, eds. W. Hillebrandt & B. Leibundgut, 19
Ivanova, N. & Taam, R. E. 2004, ApJ, 601, 1058
Janiuk, A. 2017, ApJ, 837, 39
Janka, H.-T. 2013, MNRAS, 434, 1355
Janka, H.-T. 2017, Neutrino-Driven Explosions, eds. A. W. Alsabti & P. Murdin, 1095
Janka, H.-T., Melson, T., & Summa, A. 2016, Annual Review of Nuclear and Particle Science, 66, 341
Jeans, J. H. 1902, Philosophical Transactions of the Royal Society of London Series A, 199, 1
Jiang, Y.-F., Cantiello, M., Bildsten, L., Quataert, E., & Blaes, O. 2015, ApJ, 813, 74
Jiang, Y.-F., Cantiello, M., Bildsten, L., et al. 2018, Nature, 561, 498
Johnston, K. B., Oswalt, T. D., & Valls-Gabaud, D. 2012, New A, 17, 458
Jones, S., Hirschi, R., Pignatari, M., et al. 2015, MNRAS, 447, 3115
Jurić, M., Ivezić, Ž., Brooks, A., et al. 2008, ApJ, 673, 864
Justham, S., Podsiadlowski, P., & Vink, J. S. 2014, ApJ, 796, 121
Justham, S., Rappaport, S., & Podsiadlowski, P. 2006, MNRAS, 366, 1415
Kaaret, P., Feng, H., & Roberts, T. P. 2017, ARA&A, 55, 303
Kaib, N. A. & Raymond, S. N. 2014, ApJ, 782, 60
Kaiser, E. A., Hirschi, R., Arnett, W. D., et al. 2020, MNRAS, 496, 1967

Kalari, V. M., Vink, J. S., Dufton, P. L., & Fraser, M. 2018, A&A, 618, A17
Kalogera, V. 1999, ApJ, 521, 723
Kato, M. 1985, PASJ, 37, 311
Kazeroni, R., Guilet, J., & Foglizzo, T. 2016, MNRAS, 456, 126
Khan, S., Husa, S., Hannam, M., et al. 2016, Phys. Rev. D, 93, 044007
King, A. R. 1988, QJRAS, 29, 1
King, A. R. 2004, Nuclear Physics B Proceedings Supplements, 132, 376
King, A. R., Davies, M. B., Ward, M. J., Fabbiano, G., & Elvis, M. 2001, ApJ, 552, L109
King, A. R. & Ritter, H. 1999, MNRAS, 309, 253
King, A. R., Taam, R. E., & Begelman, M. C. 2000, ApJ, 530, L25
Kippenhahn, R. & Weigert, A. 1967, ZAp, 65, 251
Kippenhahn, R. & Weigert, A. 1990, Stellar Structure and Evolution
Klencki, J., Moe, M., Gladysz, W., et al. 2018, A&A, 619, A77
Klencki, J. & Nelemans, G. 2019, in IAU Symposium, Vol. 346, IAU Symposium, eds. L. M. Oskinova, E. Bozzo, T. Bulik, & D. R. Gies, 417–425
Klencki, J., Nelemans, G., Istrate, A. G., & Chruslinska, M. 2021, A&A, 645, A54
Klencki, J., Nelemans, G., Istrate, A. G., & Pols, O. 2020, A&A, 638, A55
Klencki, J., Wiktorowicz, G., Gładysz, W., & Belczynski, K. 2017, MNRAS, 469, 3088
Kobayashi, C., Karakas, A. I., & Lugaro, M. 2020, ApJ, 900, 179
Kobulnicky, H. A., Fryer, C. L., & Kiminki, D. C. 2006, ArXiv Astrophysics e-prints [astro-ph/0605069]
Kochanek, C. S. 2014, ApJ, 785, 28
Kokkotas, K. D. 2008, Reviews in Modern Astronomy, 20, 140
Kolb, U. & Ritter, H. 1990, A&A, 236, 385
Korn, A. J., Becker, S. R., Gummersbach, C. A., & Wolf, B. 2000, A&A, 353, 655
Kovlakas, K., Zezas, A., Andrews, J. J., et al. 2020, MNRAS, 498, 4790
Kratter, K. M. & Matzner, C. D. 2006, MNRAS, 373, 1563
Kratter, K. M., Matzner, C. D., & Krumholz, M. R. 2008, ApJ, 681, 375
Kratter, K. M., Matzner, C. D., Krumholz, M. R., & Klein, R. I. 2010, ApJ, 708, 1585
Kreidberg, L., Bailyn, C. D., Farr, W. M., & Kalogera, V. 2012, ApJ, 757, 36
Kroupa, P. 2001, MNRAS, 322, 231
Kroupa, P., Tout, C. A., & Gilmore, G. 1993, MNRAS, 262, 545
Kroupa, P., Weidner, C., Pflamm-Altenburg, J., et al. 2013, The Stellar and Sub-Stellar Initial Mass Function of Simple and Composite Populations, eds. T. D. Oswalt & G. Gilmore, 115
Kruckow, M. U., Tauris, T. M., Langer, N., Kramer, M., & Izzard, R. G. 2018, ArXiv e-prints [[arXiv]1801.05433]
Kruckow, M. U., Tauris, T. M., Langer, N., et al. 2016, A&A, 596, A58
Kulkarni, S. R., Ofek, E. O., Rau, A., et al. 2007, Nature, 447, 458
Kumar, P. & Goodman, J. 1996, ApJ, 466, 946
Kusenko, A. & Segrè, G. 1996, Physical Review Letters, 77, 4872

Kushnir, D., Zaldarriaga, M., Kollmeier, J. A., & Waldman, R. 2016, MNRAS, 462, 844
Kushnir, D., Zaldarriaga, M., Kollmeier, J. A., & Waldman, R. 2017, MNRAS, 467, 2146
Lai, D. & Qian, Y.-Z. 1998, ApJ, 495, L103
Lamberts, A., Garrison-Kimmel, S., Clausen, D. R., & Hopkins, P. F. 2016, MNRAS, 463, L31
Langer, N. 1991, A&A, 252, 669
Langer, N. 1998, A&A, 329, 551
Langer, N. 2012, ARA&A, 50, 107
Langer, N., El Eid, M. F., & Baraffe, I. 1989, A&A, 224, L17
Langer, N., El Eid, M. F., & Fricke, K. J. 1985, A&A, 145, 179
Langer, N., Fricke, K. J., & Sugimoto, D. 1983, A&A, 126, 207
Langer, N. & Kudritzki, R. P. 2014, A&A, 564, A52
Langer, N. & Maeder, A. 1995, A&A, 295, 685
Langer, N., Schürmann, C., Stoll, K., et al. 2020, A&A, 638, A39
Langer, N., Wellstein, S., & Petrovic, J. 2003a, in A Massive Star Odyssey: From Main Sequence to Supernova, eds. K. van der Hucht, A. Herrero, & C. Esteban, Vol. 212, 275
Langer, N., Yoon, S. C., Petrovic, J., & Heger, A. 2003b, arXiv e-prints, astro
Laplace, E., Götberg, Y., de Mink, S. E., Justham, S., & Farmer, R. 2020, A&A, 637, A6
Laplace, E., Justham, S., Renzo, M., et al. 2021, arXiv e-prints, arXiv:2102.05036
Lara-López, M. A., Hopkins, A. M., López-Sánchez, A. R., et al. 2013, MNRAS, 434, 451
Larson, R. B. 1998, MNRAS, 301, 569
Lasota, J.-P. 2001, New A Rev., 45, 449
Lasota, J.-P. 2015, ArXiv e-prints [[arXiv]1505.02172]
Lasota, J.-P., Vieira, R. S. S., Sadowski, A., Narayan, R., & Abramowicz, M. A. 2016, A&A, 587, A13
Lau, R. M., Heida, M., Walton, D. J., et al. 2019, ApJ, 878, 71
Law-Smith, J. A. P., Everson, R. W., Ramirez-Ruiz, E., et al. 2020, arXiv e-prints, arXiv:2011.06630
Lee, H. M. & Ostriker, J. P. 1986, ApJ, 310, 176
Leitherer, C., Ekström, S., Meynet, G., et al. 2014, ApJS, 212, 14
Leitherer, C., Schaerer, D., Goldader, J. D., et al. 1999, ApJS, 123, 3
Leung, S.-C., Nomoto, K., & Blinnikov, S. 2019, ApJ, 887, 72
Levesque, E. M., Massey, P., Olsen, K. A. G., et al. 2006, ApJ, 645, 1102
Li, X.-D. 2015, New A Rev., 64, 1
LIGO Scientific Collaboration, Aasi, J., Abbott, B. P., et al. 2015, Classical and Quantum Gravity, 32, 074001
Limongi, M. & Chieffi, A. 2018, ApJS, 237, 13
Lipunov, V. M., Postnov, K. A., & Prokhorov, M. E. 1997, Astronomy Letters, 23, 492
Lipunova, G. V. 1999, Astronomy Letters, 25, 508
Liu, J., Zhang, H., Howard, A. W., et al. 2019, Nature, 575, 618
Liu, J.-F., Bregman, J. N., Bai, Y., Justham, S., & Crowther, P. 2013, Nature, 503, 500
Livio, M. & Soker, N. 1988, ApJ, 329, 764

Lommen, D., Yungelson, L., van den Heuvel, E., Nelemans, G., & Portegies Zwart, S. 2005, A&A, 443, 231
López, K. M., Heida, M., Jonker, P. G., et al. 2020, MNRAS, 497, 917
Loveridge, A. J., van der Sluys, M. V., & Kalogera, V. 2011, ApJ, 743, 49
Lubow, S. H. & Shu, F. H. 1975, ApJ, 198, 383
LVC. 2019a, GCN Circ. 25324
LVC. 2019b, GCN Circ. 25333
Ma, L. & Fuller, J. 2019, arXiv e-prints [[arXiv]1907.03713]
Mac Low, M.-M. & Klessen, R. S. 2004, Reviews of Modern Physics, 76, 125
MacLeod, M., Antoni, A., Murguia-Berthier, A., Macias, P., & Ramirez-Ruiz, E. 2017, ApJ, 838, 56
MacLeod, M. & Loeb, A. 2020a, ApJ, 895, 29
MacLeod, M. & Loeb, A. 2020b, ApJ, 893, 106
MacLeod, M., Ostriker, E. C., & Stone, J. M. 2018a, ApJ, 868, 136
MacLeod, M., Ostriker, E. C., & Stone, J. M. 2018b, ApJ, 863, 5
MacLeod, M. & Ramirez-Ruiz, E. 2015a, ApJ, 803, 41
MacLeod, M. & Ramirez-Ruiz, E. 2015b, ApJ, 803, 41
Madau, P. & Dickinson, M. 2014, ARA&A, 52, 415
Madau, P. & Fragos, T. 2017, ApJ, 840, 39
Maeder, A. 1987, A&A, 178, 159
Maeder, A. & Meynet, G. 1994, A&A, 287, 803
Maeder, A. & Meynet, G. 2000, A&A, 361, 159
Maeder, A. & Meynet, G. 2001, A&A, 373, 555
Maggiore, M., Van Den Broeck, C., Bartolo, N., et al. 2020, J. Cosmology Astropart. Phys., 2020, 050
Magic, Z., Serenelli, A., Weiss, A., & Chaboyer, B. 2010, ApJ, 718, 1378
Maiolino, R., Nagao, T., Grazian, A., et al. 2008, A&A, 488, 463
Manchester, R. N. & Taylor, J. H. 1977, Pulsars
Mandel, I. 2016, MNRAS, 456, 578
Mandel, I. & de Mink, S. E. 2016, MNRAS, 458, 2634
Mandel, I. & Farmer, A. 2018, arXiv e-prints, arXiv:1806.05820
Mandel, I., Farr, W. M., Colonna, A., et al. 2017, MNRAS, 465, 3254
Mandel, I. & Fragos, T. 2020, ApJ, 895, L28
Mandel, I., Haster, C.-J., Dominik, M., & Belczynski, K. 2015, MNRAS, 450, L85
Mandel, I. & O'Shaughnessy, R. 2010, Classical and Quantum Gravity, 27, 114007
Mapelli, M. 2016, MNRAS, 459, 3432
Mapelli, M., Colpi, M., & Zampieri, L. 2009, MNRAS, 395, L71
Mapelli, M., Dall'Amico, M., Bouffanais, Y., et al. 2021, MNRAS[[arXiv]2103.05016]
Mapelli, M. & Giacobbo, N. 2018, MNRAS, 479, 4391
Mapelli, M., Giacobbo, N., Ripamonti, E., & Spera, M. 2017, MNRAS, 472, 2422

Mapelli, M., Giacobbo, N., Santoliquido, F., & Artale, M. C. 2019, MNRAS, 487, 2
Marchant, P., Langer, N., Podsiadlowski, P., et al. 2017, A&A, 604, A55
Marchant, P., Langer, N., Podsiadlowski, P., Tauris, T. M., & Moriya, T. J. 2016, A&A, 588, A50
Marchant, P., Pappas, K. M. W., Gallegos-Garcia, M., et al. 2021, arXiv e-prints, arXiv:2103.09243
Marchant, P., Renzo, M., Farmer, R., et al. 2018, arXiv e-prints [[arXiv]1810.13412]
Mardling, R. A. 1995, ApJ, 450, 732
Marigo, P., Girardi, L., Chiosi, C., & Wood, P. R. 2001, A&A, 371, 152
Marks, M. & Kroupa, P. 2010, MNRAS, 406, 2000
Marks, M. & Kroupa, P. 2012, A&A, 543, A8
Marks, M., Kroupa, P., & Baumgardt, H. 2008, MNRAS, 386, 2047
Marks, M., Kroupa, P., Dabringhausen, J., & Pawlowski, M. S. 2012, MNRAS, 422, 2246
Massey, P. 2003, ARA&A, 41, 15
Mauerhan, J. C., Van Dyk, S. D., Johansson, J., et al. 2018, MNRAS, 473, 3765
McClelland, L. A. S. & Eldridge, J. J. 2016, MNRAS, 459, 1505
McCrea, W. H. 1964, MNRAS, 128, 147
McEvoy, C. M., Dufton, P. L., Evans, C. J., et al. 2015, A&A, 575, A70
McKernan, B., Ford, K. E. S., Bellovary, J., et al. 2018, ApJ, 866, 66
McKernan, B., Ford, K. E. S., Kocsis, B., Lyra, W., & Winter, L. M. 2014, MNRAS, 441, 900
McKernan, B., Ford, K. E. S., Lyra, W., & Perets, H. B. 2012, MNRAS, 425, 460
Mennekens, N. & Vanbeveren, D. 2014, A&A, 564, A134
Meurs, E. J. A. & van den Heuvel, E. P. J. 1989, A&A, 226, 88
Meyer, F. & Meyer-Hofmeister, E. 1979, A&A, 78, 167
Meynet, G., Chomienne, V., Ekström, S., et al. 2015, A&A, 575, A60
Meynet, G., Ekstrom, S., Maeder, A., et al. 2013, Models of Rotating Massive Stars: Impacts of Various Prescriptions, eds. M. Goupil, K. Belkacem, C. Neiner, F. Lignières, & J. J. Green, Vol. 865, 3
Meynet, G. & Maeder, A. 1997, A&A, 321, 465
Michaely, E. & Perets, H. B. 2016, MNRAS, 458, 4188
Miller, M. C. & Hamilton, D. P. 2002a, ApJ, 576, 894
Miller, M. C. & Hamilton, D. P. 2002b, MNRAS, 330, 232
Miller, M. C. & Lauburg, V. M. 2009, ApJ, 692, 917
Miller, M. C. & Miller, J. M. 2015, Phys. Rep., 548, 1
Misra, D., Fragos, T., Tauris, T., Zapartas, E., & Aguilera-Dena, D. R. 2020, arXiv e-prints, arXiv:2004.01205
Miyamoto, M. & Nagai, R. 1975, PASJ, 27, 533
Modjaz, M., Kewley, L., Bloom, J. S., et al. 2011, ApJ, 731, L4
Moe, M. & Di Stefano, R. 2013, ApJ, 778, 95
Moe, M. & Di Stefano, R. 2017, ApJS, 230, 15
Moe, M., Kratter, K. M., & Badenes, C. 2018, ArXiv e-prints [[arXiv]1808.02116]

Mondal, S., Belczyński, K., Wiktorowicz, G., Lasota, J.-P., & King, A. R. 2020, MNRAS, 491, 2747
Morawski, J., Giersz, M., Askar, A., & Belczynski, K. 2018, ArXiv e-prints [[arXiv]1802.01192]
Morris, T. & Podsiadlowski, P. 2007, Science, 315, 1103
Murguia-Berthier, A., MacLeod, M., Ramirez-Ruiz, E., Antoni, A., & Macias, P. 2017a, ArXiv e-prints [[arXiv]1705.04698]
Murguia-Berthier, A., MacLeod, M., Ramirez-Ruiz, E., Antoni, A., & Macias, P. 2017b, ApJ, 845, 173
Nagashima, M., Lacey, C. G., Baugh, C. M., Frenk, C. S., & Cole, S. 2005, MNRAS, 358, 1247
Nandez, J. L. A. & Ivanova, N. 2016, MNRAS, 460, 3992
Nandez, J. L. A., Ivanova, N., & Lombardi, J. C. J. 2015, MNRAS, 450, L39
Naoz, S. 2016, ARA&A, 54, 441
Naoz, S., Fragos, T., Geller, A., Stephan, A. P., & Rasio, F. A. 2016, ApJ, 822, L24
Neijssel, C. J., Vigna-Gómez, A., Stevenson, S., et al. 2019, MNRAS, 490, 3740
Nelemans, G., Tauris, T. M., & van den Heuvel, E. P. J. 1999, A&A, 352, L87
Nelemans, G., Verbunt, F., Yungelson, L. R., & Portegies Zwart, S. F. 2000, A&A, 360, 1011
Nelemans, G., Yungelson, L. R., & Portegies Zwart, S. F. 2001, A&A, 375, 890
Nelson, D., Pillepich, A., Genel, S., et al. 2015, Astronomy and Computing, 13, 12
Neo, S., Miyaji, S., Nomoto, K., & Sugimoto, D. 1977, PASJ, 29, 249
Neugent, K. F., Massey, P., Georgy, C., et al. 2020, ApJ, 889, 44
Neugent, K. F., Massey, P., Skiff, B., et al. 2010, ApJ, 719, 1784
Neugent, K. F., Massey, P., Skiff, B., & Meynet, G. 2012, ApJ, 749, 177
Nieuwenhuijzen, H. & de Jager, C. 1990a, A&A, 231, 134
Nieuwenhuijzen, H. & de Jager, C. 1990b, A&A, 231, 134
Noutsos, A., Schnitzeler, D. H. F. M., Keane, E. F., Kramer, M., & Johnston, S. 2013, MNRAS, 430, 2281
Nugis, T. & Lamers, H. J. G. L. M. 2000a, A&A, 360, 227
Nugis, T. & Lamers, H. J. G. L. M. 2000b, A&A, 360, 227
O'Connor, E. & Ott, C. D. 2011, ApJ, 730, 70
Ohlmann, S. T., Röpke, F. K., Pakmor, R., & Springel, V. 2016, ApJ, 816, L9
Ohsuga, K. 2007, ApJ, 659, 205
O'Leary, R. M., O'Shaughnessy, R., & Rasio, F. A. 2007, Phys. Rev. D, 76, 061504
Olejak, A., Belczynski, K., & Ivanova, N. 2021, arXiv e-prints, arXiv:2102.05649
Öpik, E. 1924, Publications of the Tartu Astrofizica Observatory, 25
Orosz, J. A., Steeghs, D., McClintock, J. E., et al. 2009, ApJ, 697, 573
O'Shaughnessy, R., Gerosa, D., & Wysocki, D. 2017a, ArXiv e-prints [[arXiv]1704.03879]
O'Shaughnessy, R., Gerosa, D., & Wysocki, D. 2017b, Phys. Rev. Lett., 119, 011101
Oskinova, L. M., Sun, W., Evans, C. J., et al. 2013, ApJ, 765, 73
Oskinova, L. M., Todt, H., Ignace, R., et al. 2011, MNRAS, 416, 1456
Owocki, S. P., Gayley, K. G., & Shaviv, N. J. 2004, ApJ, 616, 525

Packet, W. 1981, A&A, 102, 17
Paczyński, B. 1967, Acta Astron., 17, 355
Paczyński, B. 1971, ARA&A, 9, 183
Paczynski, B. 1976, in IAU Symposium, Vol. 73, Structure and Evolution of Close Binary Systems, eds. P. Eggleton, S. Mitton, & J. Whelan, 75
Paczynski, B. 1986, ApJ, 304, 1
Pagel, B. E. J. 1989, in Evolutionary Phenomena in Galaxies, eds. J. E. Beckman & B. E. J. Pagel, 201–223
Pakull, M. W. & Mirioni, L. 2003, in Revista Mexicana de Astronomia y Astrofisica Conference Series, Vol. 15, Revista Mexicana de Astronomia y Astrofisica Conference Series, eds. J. Arthur & W. J. Henney, 197–199
Park, D., Kim, C., Lee, H. M., Bae, Y.-B., & Belczynski, C. 2017, ArXiv e-prints [[arXiv]1703.01568]
Passy, J.-C., Herwig, F., & Paxton, B. 2012, ApJ, 760, 90
Patrick, L. R., Evans, C. J., Davies, B., et al. 2015, ApJ, 803, 14
Patton, R. A. & Sukhbold, T. 2020, arXiv e-prints, arXiv:2005.03055
Pavlovskii, K. & Ivanova, N. 2015, MNRAS, 449, 4415
Pavlovskii, K., Ivanova, N., Belczynski, K., & Van, K. X. 2017, MNRAS, 465, 2092
Paxton, B., Bildsten, L., Dotter, A., et al. 2011, ApJS, 192, 3
Paxton, B., Cantiello, M., Arras, P., et al. 2013, ApJS, 208, 4
Paxton, B., Marchant, P., Schwab, J., et al. 2015, ApJS, 220, 15
Paxton, B., Schwab, J., Bauer, E. B., et al. 2018, ApJS, 234, 34
Paxton, B., Smolec, R., Schwab, J., et al. 2019, ApJS, 243, 10
Perets, H. B. & Kouwenhoven, M. B. N. 2012, ApJ, 750, 83
Perets, H. B. & Kratter, K. M. 2012, ApJ, 760, 99
Perna, R., Wang, Y.-H., Farr, W. M., Leigh, N., & Cantiello, M. 2019, ApJ, 878, L1
Peter, D., Feldt, M., Henning, T., & Hormuth, F. 2012, A&A, 538, A74
Peters, P. C. 1964, Physical Review, 136, 1224
Petrovic, J., Langer, N., & van der Hucht, K. A. 2005, A&A, 435, 1013
Petrovic, J., Pols, O., & Langer, N. 2006, A&A, 450, 219
Piran, T. & Hotokezaka, K. 2018, arXiv e-prints, arXiv:1807.01336
Planck Collaboration, Ade, P. A. R., Aghanim, N., et al. 2016, A&A, 594, A13
Podsiadlowski, P. 1996, MNRAS, 279, 1104
Podsiadlowski, P. 2001, Astronomical Society of the Pacific Conference Series, Vol. 229, Common-Envelope Evolution and Stellar Mergers, eds. P. Podsiadlowski, S. Rappaport, A. R. King, F. D'Antona, & L. Burderi, 239
Podsiadlowski, P., Ivanova, N., Justham, S., & Rappaport, S. 2010, MNRAS, 406, 840
Podsiadlowski, P., Joss, P. C., & Hsu, J. J. L. 1992, ApJ, 391, 246
Podsiadlowski, P., Joss, P. C., & Rappaport, S. 1990, A&A, 227, L9
Podsiadlowski, P., Rappaport, S., & Han, Z. 2003, MNRAS, 341, 385

Pols, O. R. 1994, A&A, 290, 119
Pols, O. R., Cote, J., Waters, L. B. F. M., & Heise, J. 1991, A&A, 241, 419
Pols, O. R., Schröder, K.-P., Hurley, J. R., Tout, C. A., & Eggleton, P. P. 1998, MNRAS, 298, 525
Popham, R. & Narayan, R. 1991, ApJ, 370, 604
Popov, S. B. & Turolla, R. 2012, Ap&SS, 341, 457
Portegies Zwart, S. 2013, MNRAS, 429, L45
Portegies Zwart, S. F., Baumgardt, H., Hut, P., Makino, J., & McMillan, S. L. W. 2004, Nature, 428, 724
Portegies Zwart, S. F. & McMillan, S. L. W. 2000, ApJ, 528, L17
Portegies Zwart, S. F. & Verbunt, F. 1996, A&A, 309, 179
Portegies Zwart, S. F., Verbunt, F., & Ergma, E. 1997, A&A, 321, 207
Portegies Zwart, S. F. & Yungelson, L. R. 1998, A&A, 332, 173
Poutanen, J., Lipunova, G., Fabrika, S., Butkevich, A. G., & Abolmasov, P. 2007, MNRAS, 377, 1187
Poveda, A., Allen, C., & Hernández-Alcántara, A. 2007, in IAU Symposium, Vol. 240, Binary Stars as Critical Tools & Tests in Contemporary Astrophysics, eds. W. I. Hartkopf, P. Harmanec, & E. F. Guinan, 417–425
Press, W. H. & Teukolsky, S. A. 1977, ApJ, 213, 183
Puls, J., Kudritzki, R. P., Herrero, A., et al. 1996, A&A, 305, 171
Puls, J., Vink, J. S., & Najarro, F. 2008, A&A Rev., 16, 209
Qin, Y., Fragos, T., Meynet, G., et al. 2018, A&A, 616, A28
Qin, Y., Marchant, P., Fragos, T., Meynet, G., & Kalogera, V. 2019, ApJ, 870, L18
Quast, M., Langer, N., & Tauris, T. M. 2019, A&A, 628, A19
Quataert, E., Fernández, R., Kasen, D., Klion, H., & Paxton, B. 2016, MNRAS, 458, 1214
Raghavan, D., McAlister, H. A., Henry, T. J., et al. 2010, ApJS, 190, 1
Ramachandran, V., Hamann, W. R., Oskinova, L. M., et al. 2019, A&A, 625, A104
Ramírez-Agudelo, O. H., Simón-Díaz, S., Sana, H., et al. 2013, A&A, 560, A29
Rantsiou, E., Burrows, A., Nordhaus, J., & Almgren, A. 2011, ApJ, 732, 57
Rappaport, S., Verbunt, F., & Joss, P. C. 1983, ApJ, 275, 713
Rasio, F. A. 1995, ApJ, 444, L41
Ray, A., Kembhavi, A. K., & Antia, H. M. 1987, A&A, 184, 164
Reitze, D., Adhikari, R. X., Ballmer, S., et al. 2019, in Bulletin of the American Astronomical Society, Vol. 51, 35
Remillard, R. A. & McClintock, J. E. 2006, ARA&A, 44, 49
Renzo, M., Farmer, R. J., Justham, S., et al. 2020, MNRAS, 493, 4333
Renzo, M., Ott, C. D., Shore, S. N., & de Mink, S. E. 2017, A&A, 603, A118
Repetto, S., Davies, M. B., & Sigurdsson, S. 2012, MNRAS, 425, 2799
Repetto, S., Igoshev, A. P., & Nelemans, G. 2017, MNRAS, 467, 298
Repetto, S. & Nelemans, G. 2015, MNRAS, 453, 3341
Ricker, P. M. & Taam, R. E. 2008, ApJ, 672, L41

Ricker, P. M. & Taam, R. E. 2012, ApJ, 746, 74
Ricker, P. M., Timmes, F. X., Taam, R. E., & Webbink, R. F. 2019, in IAU Symposium, Vol. 346, IAU Symposium, eds. L. M. Oskinova, E. Bozzo, T. Bulik, & D. R. Gies, 449–454
Rivinius, T., Baade, D., Hadrava, P., Heida, M., & Klement, R. 2020, A&A, 637, L3
Rodriguez, C. L., Amaro-Seoane, P., Chatterjee, S., et al. 2018a, Phys. Rev. D, 98, 123005
Rodriguez, C. L., Amaro-Seoane, P., Chatterjee, S., & Rasio, F. A. 2018b, Phys. Rev. Lett., 120, 151101
Rodriguez, C. L., Chatterjee, S., & Rasio, F. A. 2016a, Phys. Rev. D, 93, 084029
Rodriguez, C. L., Haster, C.-J., Chatterjee, S., Kalogera, V., & Rasio, F. A. 2016b, ApJ, 824, L8
Rodriguez, C. L., Zevin, M., Pankow, C., Kalogera, V., & Rasio, F. A. 2016c, ApJ, 832, L2
Romani, R. W. 1998, A&A, 333, 583
Sadowski, A., Belczynski, K., Bulik, T., et al. 2008, ApJ, 676, 1162
Salpeter, E. E. 1955, ApJ, 121, 161
Samsing, J. 2017, ArXiv e-prints [[arXiv]1711.07452]
Sana, H., de Koter, A., de Mink, S. E., et al. 2013, A&A, 550, A107
Sana, H., de Mink, S. E., de Koter, A., et al. 2012, Science, 337, 444
Sana, H., Le Bouquin, J.-B., Lacour, S., et al. 2014, ApJS, 215, 15
Sand, C., Ohlmann, S. T., Schneider, F. R. N., Pakmor, R., & Röpke, F. K. 2020, A&A, 644, A60
Sander, A. A. C., Vink, J. S., & Hamann, W. R. 2020, MNRAS, 491, 4406
Sanyal, D., Grassitelli, L., Langer, N., & Bestenlehner, J. M. 2015, A&A, 580, A20
Sanyal, D., Langer, N., Szécsi, D., -C Yoon, S., & Grassitelli, L. 2017, A&A, 597, A71
Sathyaprakash, B. S. & Schutz, B. F. 2009, Living Reviews in Relativity, 12, 2
Schneider, F. R. N., Izzard, R. G., Langer, N., & de Mink, S. E. 2015, ApJ, 805, 20
Schneider, F. R. N., Ohlmann, S. T., Podsiadlowski, P., et al. 2019, Nature, 574, 211
Schneider, F. R. N., Podsiadlowski, P., & Müller, B. 2021, A&A, 645, A5
Schneider, F. R. N., Sana, H., Evans, C. J., et al. 2018, Science, 359, 69
Schneider, R., Graziani, L., Marassi, S., et al. 2017, MNRAS, 471, L105
Schootemeijer, A., Götberg, Y., de Mink, S. E., Gies, D., & Zapartas, E. 2018, A&A, 615, A30
Schootemeijer, A. & Langer, N. 2018, A&A, 611, A75
Schootemeijer, A., Langer, N., Grin, N. J., & Wang, C. 2019, A&A, 625, A132
Shakura, N. I. & Sunyaev, R. A. 1973, A&A, 500, 33
Shao, Y. & Li, X.-D. 2014, ApJ, 796, 37
Shenar, T., Bodensteiner, J., Abdul-Masih, M., et al. 2020a, A&A, 639, L6
Shenar, T., Gilkis, A., Vink, J. S., Sana, H., & Sand er, A. A. C. 2020b, A&A, 634, A79
Shiber, S., Iaconi, R., De Marco, O., & Soker, N. 2019, MNRAS, 488, 5615
Shu, F. H. & Lubow, S. H. 1981, ARA&A, 19, 277
Sądowski, A., Lasota, J.-P., Abramowicz, M. A., & Narayan, R. 2016, MNRAS, 456, 3915
Smith, N. 2014, ARA&A, 52, 487
Smith, N., Andrews, J. E., Van Dyk, S. D., et al. 2016, MNRAS, 458, 950

Smith, N., Li, W., Silverman, J. M., Ganeshalingam, M., & Filippenko, A. V. 2011, MNRAS, 415, 773
Soberman, G. E., Phinney, E. S., & van den Heuvel, E. P. J. 1997, A&A, 327, 620
Socrates, A., Blaes, O., Hungerford, A., & Fryer, C. L. 2005, ApJ, 632, 531
Soker, N. 2015, ApJ, 800, 114
Soker, N. & Tylenda, R. 2003, ApJ, 582, L105
Spera, M., Mapelli, M., & Bressan, A. 2015, MNRAS, 451, 4086
Spera, M., Mapelli, M., Giacobbo, N., et al. 2019, MNRAS, 485, 889
Spruit, H. C. 1999, A&A, 349, 189
Spruit, H. C. 2002, A&A, 381, 923
Stanway, E. R., Eldridge, J. J., & Becker, G. D. 2016, MNRAS, 456, 485
Stevenson, S., Berry, C. P. L., & Mandel, I. 2017a, ArXiv e-prints [[arXiv]1703.06873]
Stevenson, S., Ohme, F., & Fairhurst, S. 2015, ApJ, 810, 58
Stevenson, S., Sampson, M., Powell, J., et al. 2019, arXiv e-prints [[arXiv]1904.02821]
Stevenson, S., Vigna-Gómez, A., Mandel, I., et al. 2017b, Nature Communications, 8, 14906
Stone, N. C., Metzger, B. D., & Haiman, Z. 2017, MNRAS, 464, 946
Stothers, R. & Chin, C.-W. 1973, ApJ, 179, 555
Stothers, R. B. & Chin, C.-W. 1992, ApJ, 390, 136
Sun, N.-C., Maund, J. R., & Crowther, P. A. 2020, arXiv e-prints, arXiv:2003.09325
Surman, R., McLaughlin, G. C., & Hix, W. R. 2006, ApJ, 643, 1057
Swartz, D. A., Soria, R., Tennant, A. F., & Yukita, M. 2011a, ApJ, 741, 49
Swartz, D. A., Soria, R., Tennant, A. F., & Yukita, M. 2011b, ApJ, 741, 49
Tabernero, H. M., Dorda, R., Negueruela, I., & González-Fernández, C. 2018, MNRAS, 476, 3106
Tamborra, I., Hanke, F., Janka, H.-T., et al. 2014, Astrophys. J., 792, 96
Tanaka, K. E. I. & Omukai, K. 2014, MNRAS, 439, 1884
Tang, J., Bressan, A., Rosenfield, P., et al. 2014, MNRAS, 445, 4287
Tauris, T. M. & Dewi, J. D. M. 2001, A&A, 369, 170
Tauris, T. M., Kramer, M., Freire, P. C. C., et al. 2017, ApJ, 846, 170
Tauris, T. M., Langer, N., & Podsiadlowski, P. 2015, MNRAS, 451, 2123
Tauris, T. M. & van den Heuvel, E. P. J. 2006, Formation and evolution of compact stellar X-ray sources, Vol. 39, 623–665
Tauris, T. M., van den Heuvel, E. P. J., & Savonije, G. J. 2000, ApJ, 530, L93
Tayar, J., Somers, G., Pinsonneault, M. H., et al. 2017, ApJ, 840, 17
Taylor, J. H. & Weisberg, J. M. 1982, ApJ, 253, 908
Tetarenko, B. E., Bahramian, A., Arnason, R. M., et al. 2016a, ApJ, 825, 10
Tetarenko, B. E., Sivakoff, G. R., Heinke, C. O., & Gladstone, J. C. 2016b, ApJS, 222, 15
Tetarenko, B. E., Sivakoff, G. R., Heinke, C. O., & Gladstone, J. C. 2016c, ApJS, 222, 15
The LIGO Scientific Collaboration, the Virgo Collaboration, Abbott, R., et al. 2020a, arXiv e-prints, arXiv:2004.08342

The LIGO Scientific Collaboration, the Virgo Collaboration, Abbott, R., et al. 2020b, arXiv e-prints, arXiv:2009.01075
Thompson, T. A., Kochanek, C. S., Stanek, K. Z., et al. 2020, Science, 368, eaba4356
Thompson, T. A., Kochanek, C. S., Stanek, K. Z., et al. 2019, Science, 366, 637
Timmes, F. X., Woosley, S. E., & Weaver, T. A. 1995, ApJS, 98, 617
Timmes, F. X., Woosley, S. E., & Weaver, T. A. 1996, ApJ, 457, 834
Toonen, S., Hollands, M., Gaensicke, B. T., & Boekholt, T. 2017, ArXiv e-prints [[arXiv]1703.06893]
Tornatore, L., Borgani, S., Dolag, K., & Matteucci, F. 2007, MNRAS, 382, 1050
Tout, C. A., Aarseth, S. J., Pols, O. R., & Eggleton, P. P. 1997, MNRAS, 291, 732
Tramper, F., Sana, H., & de Koter, A. 2016, ApJ, 833, 133
Tremonti, C. A., Heckman, T. M., Kauffmann, G., et al. 2004, ApJ, 613, 898
Tutukov, A. & Yungelson, L. 1979, in IAU Symposium, Vol. 83, Mass Loss and Evolution of O-Type Stars, eds. P. S. Conti & C. W. H. De Loore, 401–406
Tutukov, A. V. & Yungelson, L. R. 1993, MNRAS, 260, 675
Tylenda, R., Hajduk, M., Kamiński, T., et al. 2011, A&A, 528, A114
Ugliano, M., Janka, H.-T., Marek, A., & Arcones, A. 2012, ApJ, 757, 69
Ulmer, A. & Fitzpatrick, E. L. 1998, ApJ, 504, 200
Urbaneja, M. A., Kudritzki, R. P., Gieren, W., et al. 2017, AJ, 154, 102
Vagnozzi, S. 2017, arXiv e-prints [[arXiv]1703.10834]
Valsecchi, F., Glebbeek, E., Farr, W. M., et al. 2010, Nature, 468, 77
van den Heuvel, E. P. J. 1975, ApJ, 198, L109
van den Heuvel, E. P. J. 1976, in IAU Symposium, Vol. 73, Structure and Evolution of Close Binary Systems, eds. P. Eggleton, S. Mitton, & J. Whelan, 35
van den Heuvel, E. P. J. 1994, A&A, 291, L39
van den Heuvel, E. P. J. & De Loore, C. 1973, A&A, 25, 387
van den Heuvel, E. P. J., Portegies Zwart, S. F., & de Mink, S. E. 2017, MNRAS, 471, 4256
van den Heuvel, E. P. J. & Tauris, T. M. 2020, Science, 368, eaba3282
van der Hucht, K. A. 2001, VizieR Online Data Catalog, 3215
van Marle, A. J., Owocki, S. P., & Shaviv, N. J. 2008, MNRAS, 389, 1353
van Son, L. A. C., De Mink, S. E., Broekgaarden, F. S., et al. 2020, ApJ, 897, 100
Vanbeveren, D. 1982, A&A, 105, 260
Vanbeveren, D. 1991, A&A, 252, 159
Vanbeveren, D., De Loore, C., & Van Rensbergen, W. 1998, A&A Rev., 9, 63
Vanbeveren, D., Mennekens, N., Shara, M. M., & Moffat, A. F. J. 2018, A&A, 615, A65
Vanbeveren, D., Mennekens, N., Van Rensbergen, W., & De Loore, C. 2013, A&A, 552, A105
Vangioni, E., Olive, K. A., Prestegard, T., et al. 2015, MNRAS, 447, 2575
VanLandingham, J. H., Miller, M. C., Hamilton, D. P., & Richardson, D. C. 2016, ApJ, 828, 77
Vartanyan, D., Laplace, E., Renzo, M., et al. 2021, arXiv e-prints, arXiv:2104.03317
Vázquez, G. A. & Leitherer, C. 2005, ApJ, 621, 695

Venn, K. A. 1999, ApJ, 518, 405
Venumadhav, T., Zackay, B., Roulet, J., Dai, L., & Zaldarriaga, M. 2019, arXiv e-prints [[arXiv]1904.07214]
Veras, D., Wyatt, M. C., Mustill, A. J., Bonsor, A., & Eldridge, J. J. 2011, MNRAS, 417, 2104
Verbunt, F. 1993, ARA&A, 31, 93
Verbunt, F., Igoshev, A., & Cator, E. 2017, A&A, 608, A57
Verbunt, F. & Zwaan, C. 1981, A&A, 100, L7
Verlet, L. 1967, Physical Review, 159, 98
Vigna-Gómez, A., MacLeod, M., Neijssel, C. J., et al. 2020, arXiv e-prints, arXiv:2001.09829
Vigna-Gómez, A., Neijssel, C. J., Stevenson, S., et al. 2018, MNRAS, 481, 4009
Villante, F. L., Serenelli, A. M., Delahaye, F., & Pinsonneault, M. H. 2014, ApJ, 787, 13
Vinciguerra, S., Neijssel, C. J., Vigna-Gómez, A., et al. 2020, MNRAS, 498, 4705
Vink, J. S. 2017, A&A, 607, L8
Vink, J. S. & de Koter, A. 2005, A&A, 442, 587
Vink, J. S., de Koter, A., & Lamers, H. J. G. L. M. 2000, A&A, 362, 295
Vink, J. S., de Koter, A., & Lamers, H. J. G. L. M. 2001, A&A, 369, 574
Vink, J. S., Higgins, E. R., Sander, A. A. C., & Sabhahit, G. N. 2021, MNRAS, 504, 146
Vink, J. S., Muijres, L. E., Anthonisse, B., et al. 2011, A&A, 531, A132
Virtanen, P., Gommers, R., Oliphant, T. E., et al. 2019, arXiv e-prints, arXiv:1907.10121
Vitale, S., Gerosa, D., Haster, C.-J., Chatziioannou, K., & Zimmerman, A. 2017a, Physical Review Letters, 119, 251103
Vitale, S., Lynch, R., Sturani, R., & Graff, P. 2017b, Classical and Quantum Gravity, 34, 03LT01
Vlahakis, N. & Königl, A. 2001, ApJ, 563, L129
Voss, R. & Gilfanov, M. 2007, MNRAS, 380, 1685
Voss, R. & Tauris, T. M. 2003, MNRAS, 342, 1169
Walton, D. J., Roberts, T. P., Mateos, S., & Heard, V. 2011, MNRAS, 416, 1844
Wang, C., Jia, K., & Li, X.-D. 2016, MNRAS, 457, 1015
Wang, C., Langer, N., Schootemeijer, A., et al. 2020, ApJ, 888, L12
Wang, L., Gies, D. R., Peters, G. J., et al. 2021, AJ, 161, 248
Webb, J. J. & Leigh, N. W. C. 2015, MNRAS, 453, 3278
Webbink, R. F. 1984, ApJ, 277, 355
Wellstein, S., Langer, N., & Braun, H. 2001, A&A, 369, 939
Wiktorowicz, G., Belczynski, K., & Maccarone, T. 2014, in Binary Systems, their Evolution and Environments, eds. R. de Grijs, 37
Wiktorowicz, G., Lu, Y., Wyrzykowski, Ł., et al. 2020, ApJ, 905, 134
Wiktorowicz, G., Sobolewska, M., Lasota, J.-P., & Belczynski, K. 2017, ApJ, 846, 17
Wiktorowicz, G., Wyrzykowski, Ł., Chruslinska, M., et al. 2019, ApJ, 885, 1
Wilkins, S. M., Hopkins, A. M., Trentham, N., & Tojeiro, R. 2008, MNRAS, 391, 363
Williamson, A. R., Lange, J., O'Shaughnessy, R., et al. 2017, ArXiv e-prints [[arXiv]1709.03095]
Wolf, C. & Podsiadlowski, P. 2007, MNRAS, 375, 1049

Woods, T. E. & Ivanova, N. 2011, ApJ, 739, L48
Woosley, S. E. 1993, ApJ, 405, 273
Woosley, S. E. 2016, ApJ, 824, L10
Woosley, S. E. 2017, ApJ, 836, 244
Woosley, S. E. 2019, ApJ, 878, 49
Woosley, S. E., Langer, N., & Weaver, T. A. 1995, ApJ, 448, 315
Woosley, S. E. & Weaver, T. A. 1995, ApJS, 101, 181
Worley, A., Krastev, P. G., & Li, B.-A. 2008, ApJ, 685, 390
Wyrzykowski, Ł., Kostrzewa-Rutkowska, Z., Skowron, J., et al. 2016, MNRAS, 458, 3012
Wyrzykowski, Ł. & Mandel, I. 2020, A&A, 636, A20
Wysocki, D., Gerosa, D., O'Shaughnessy, R., et al. 2018, Phys. Rev. D, 97, 043014
Xu, X.-J. & Li, X.-D. 2010, ApJ, 716, 114
Ye, C. S., Fong, W.-f., Kremer, K., et al. 2020, ApJ, 888, L10
Yoon, S.-C. 2017, MNRAS, 470, 3970
Yoon, S.-C., Langer, N., & Norman, C. 2006, A&A, 460, 199
Yoshida, N., Oh, S. P., Kitayama, T., & Hernquist, L. 2007, ApJ, 663, 687
Yoshida, N., Omukai, K., Hernquist, L., & Abel, T. 2006, ApJ, 652, 6
Yungelson, L. R. & Lasota, J. P. 2008, A&A, 488, 257
Yungelson, L. R., Lasota, J.-P., Nelemans, G., et al. 2006, A&A, 454, 559
Yusof, N., Hirschi, R., Meynet, G., et al. 2013, MNRAS, 433, 1114
Zackay, B., Venumadhav, T., Dai, L., Roulet, J., & Zaldarriaga, M. 2019, arXiv e-prints [[arXiv]1902.10331]
Zahid, H. J., Dima, G. I., Kudritzki, R.-P., et al. 2014, ApJ, 791, 130
Zahn, J.-P. 1977, A&A, 57, 383
Zahn, J.-P. 1989, A&A, 220, 112
Zahn, J. P. 1992, A&A, 265, 115
Zaldarriaga, M., Kushnir, D., & Kollmeier, J. A. 2017, ArXiv e-prints [[arXiv]1702.00885]
Zaldarriaga, M., Kushnir, D., & Kollmeier, J. A. 2018, MNRAS, 473, 4174
Zampieri, L. & Roberts, T. P. 2009, MNRAS, 400, 677
Zevin, M., Kremer, K., Siegel, D. M., et al. 2019, ApJ, 886, 4
Zhang, W., Woosley, S. E., & Heger, A. 2008, ApJ, 679, 639
Ziosi, B. M., Mapelli, M., Branchesi, M., & Tormen, G. 2014, MNRAS, 441, 3703
Zorotovic, M., Schreiber, M. R., & Gänsicke, B. T. 2011, A&A, 536, A42
Zorotovic, M., Schreiber, M. R., Gänsicke, B. T., & Nebot Gómez-Morán, A. 2010, A&A, 520, A86

# About the author

I was born in Łódź, a city in central Poland in which countless remnants of rich industrial past mix with the modern and yet somehow nostalgic spirit of art and creativity. The result is a unique and polarizing blend: you either love it or hate it. I have always been drawn to numbers, problem solving, and science in general, with much of this interest being sparked and patiently fueled by my parents.

My adventures with astronomy began when as a sixteen-year-old I first attended a summer camp organized by the polish astronomical club 'Almukantarat'. There I discovered a whole new world of slightly crazy individuals who all seemed to be pationate about something in their lives, science in particular. I got equally intimidated, intrigued, and inspired, which I think is just the right mix. I got hooked (up) and made friends for life. From this point on, I would return many times over the next ten years to attend or co-organize 'Almukantarat' meetings and outreach events, first as a student, later as a lecturer. Throughout high school, I was very fortunate to have multiple other opportunities to interact with science enthusiasts at various workshops, institute visits, training camps, and olympiads. All largely thanks to the activity of the Polish Children's Fund and its volunteers. Without even noticing, I quickly became a part of vibrant and inspiring community and felt right at home in the world of academia. There was no isolated moment when I decided to work to become a scientist: it simply felt like the natural thing to do. Looking back, it is humbling to realize how much we are shaped and directed in life by the amazing people who surround us.

In 2012, I enrolled into an inter-faculty program at the University of Warsaw. My main trajectory and bachelor's degree was in physics, I took additional classes in computer science, but my passion has always been astronomy. This combination resulted in a bachelor's thesis in which I applied machine learning to improve transient detection in the OGLE photometric survey (prepared under the supervision of Łukasz Wyrzykowski). Around that time, I was not yet sure what to focus on next, so I found myself trying various things. I was a summer intern at the Interdisciplinary Centre for Mathematical and Computational Modelling, which turned out to be a strictly programming job. Together with a few fellow students, we obtained funding to kick-start a small lab for team student competitions in experimental physics (such as the International Physicists' Tournament). Thanks to Łukasz, I undertook several observing trips to Loiano, Italy, to

follow-up on transient candidates from the Gaia Science Alert Network. This experience reinforced my commitment to astronomy (as well as taught me to have a great deal of respect for observational astronomers).

One of the first master courses I took was stellar evolution, lectured by Chris Belczynski. I remember being fascinated by the elegant tales of how stars are born, live their lives, and fade away into afterlives as dark remnants. I immediately became sucked in. Chris agreed to take me under his wings and I began to work with him, Grzegorz Wiktorowicz, and the rest of the group. A few months in, in the early 2016, the news of the first gravitational-wave detection from a binary black hole merger went public. I remember that the level of excitement and motivation was going through the roof, also among us students, and I suddenly found myself involved in several different projects. Around that time, I got rejections from various internship programs in Europe and in the USA, which was quite a big blow. In July 2016, I got the opportunity to attend and present a poster at my first international meeting, the "Binary Stars" conference in Cambridge. It was, in a way, a similar experience to that at the first summer camp with 'Almukantarat': intimidating but intriguing, and very inspiring. The sense of a worldwide astronomical community was growing on me and I was determined to become a part of it. Upon finishing my master thesis, I told Chris that I would like to expand into new territories and pursue a PhD degree abroad. On his suggestion, I contacted Gijs Nelemans who happened to have an opening for a PhD position at Radboud University.

Gijs decided to give me a go and in September 2017 I started as a PhD candidate at Radboud. My work continued to revolve around the subject of gravitational-wave sources and their origin: we had a number of different ideas and Gijs was patient enough to let me try out a fair number of those, even if that meant having to go back to start anew. This gave me a sense of independence and certainly shaped me to be more mature as a researcher. Throughout my PhD, I ventured into the vast world of detailed stellar evolution computations, on a path that would never be possible without the supervision of Alina Istrate and Onno Pols. I had the wonderful opportunity to attend multiple conferences, workshops, and schools, both in the Netherlands, abroad, and (most recently) in the virtual environment of Zoom presentations, thanks to the support from Gijs and NOVA. I gave talks at invited seminars and various informal meetings, many of which resulted in fruitful discussions and collaborations. During my PhD, I served as a teaching assistant to several different astronomy and physics courses and I co-supervised a master thesis project. I attended a summer school 'Gravitational Waves' in Les Houches as well as the NOVA Fall school in Dwingeloo. I was occasionally involved with the public outreach of the Astronomy Department and I co-organized the Dutch Astronomy Olympiad in Nijmegen. I have met a lot of amazing and inspiring people, quite reminiscent of that first astronomy camp with 'Almukantarat'. Apart from doing science, I enjoy playing various sports (without being very good at any), in particular squash and chess. Traveling is my constant source of excitement, especially when exploring new cultures or reaching for the mountain peaks.

In October, I will be starting as an ESO Fellow at the European Southern Observatory headquarters in Garching, Germany.

# Acknowledgments

The first one has got to go to Gijs.

I am hugely grateful to my supervisor, Gijs Nelemens, for taking me under his wings and guiding me in this pursuit of a PhD. Gijs, many thanks for your wisdom and calmness, for always having a solution no matter what the problem, and for being patient and understanding of my occasional (frequent?) foolishness. I very much enjoyed every one of our meetings, especially those that had left me with more questions than I had bargained for: thank you for always pushing and challenging me to gain a deeper understanding of things. Your ideas flow quickly and you often seem to know what I am after better than I do. Thank you for always finding the time to meet, despite your ever busy schedule, and especially during the hectic times of job application and thesis writing. It has been a privilege and a joy to call you a supervisor.

Alina, I could never thank you enough, for being a supervisor and for being a friend. You are a truly amazing person who always cares for others and their well-being more than you think about yourself. Thank you for being so relentless and rigorous in teaching me how to properly do science with MESA, I hope that I can make you proud. Hats off to you bringing for the kickers frenzy into the department and for making sure that our competitive nature is always fed (defense is the best form of attack!)

Many thanks to Onno Pols, my co-advisor and mentor in understanding of how stars work. Our careful and long discussions of various intricacies of stellar interiors have been an eye opener. Even more so, you made me realize that things may often be difficult to understand not because of my incapabilities but because they are inherently very complex and unexplained.

Chris Belczynski, you truly are unmatched in generating enthusiasm among your students. Thank you for your constant energy, sharp critical thinking, and for being so down to earth. It has been a great fun to work together. If anyone ever complains about me sticking my nose into academia, blame it on Chris!

Selma de Mink, thank you for your hospitality, excellent discussions, and words of encouragement during my visit at UvA and elsewhere. It has been a recurring source of motivation. I recall that our first encounter was at the 'Binary Star' conference in Cambridge in 2016 when I was a master student. I remember vividly the energetic explanation of the role of binaries in element enrichment in globular clusters that you gave on our way from breakfast to the conference

venue. I think I did not understand a thing back then (that is on me, I was not at my brightest) but I sure kept nodding nonetheless. Somehow, that experience made me feel more welcome into the community, thank you.

Ilya Mandel, thank you for being always up for a discussion and for patiently entertaining my curiosity and naive ideas with illuminating explanations and eloquent yet lighthearted criticism. Alejandro, for making sure we never go off track too much and that we get things done. Michelle, for bearing with me and my sometimes chaotic explanations.

I am very grateful to my thesis reading committee for agreeing to evaluate my thesis.

The Astrophysics Department at Radboud is the most amazing, vibrant, and truly welcoming place, made so by the people who inhabit it. Thank you to our amazing secretaries and management, Marja, Monique, Merijn, Katharina, and Amanda, for making ru-astro such a pleasant place to work in.

Thank you to all my past and present officemates. Bjarni: for showing up with a three-player chessboard all of a sudden, always keeping it calm, cool, and collected, and for sharing that evening with a questionable but somewhat heartwarming fun-made spin-off of the Witcher series. Fiore: for the ever-present smile (even when I mix up what language I am speaking) and for kindly allowing me to overtake you in the kickers ranking. Alina (and Lee): for... way too many things. Most of all, for always being there and looking out for us, especially during the lockdowns. But the coffee machine you brought to the office was really rather crappy. Emma: for being there to have a chat with at times when nobody else was around. And for giving us the impression that we are somewhat useful in helping you organize the Olympiad. Roque and Jan: for welcoming me into the office on my first day and for making me feel right at home.

Thank you to the entire astro-football squad – Glenn, Ala'a, Sukanth, Irene, Deepak, Hamid, Shinsuke, Bjarni, Fio, and others – for all the crazy matches, not only in football. I think we all got a bit better eventually, right Glenn? Cheers to all the squash enthusiasts (thanks for showing us how it is done, Christiaan!). Martha: congratz on winning the World Cup prediction contest! Never before have I been so engaged in following the matches, haha

Salut to the frequent visitors of the kickers chamber! We have shared triumphs and defeats, frustrations and reliefs, self-goals and clean sweeps ;-) The atmosphere up there was really something special. Antonio, I do not know how you do it, you are the champ.

Martha, Glenn, and Karel: for organizing the weekly stellar evolution meetings and patiently dealing with our complaints about the schedule. Karel, your presentations are simply the best. Nadia, it has been a pleasure to work on a fun project together and to combine our different expertises (say hello to Matt and Kai!)

Sjoerd, Frederike, Steven, Valentina, Sukanth: thanks for getting together for remote boardgaming in times when we had to stay isolated. Christiaan, your knowledge in seemingly any topic can only be topped by your ability to always ask an interesting question. It might just be that these two are related, who knows... Irene & Gieljan, you guys rock, that is all I wanted to say. Leon, your creativity is uncanny. Anastasia, I think we did well fiddling with that camera stand! Next time our shots will make the final cut, surely... Jordy, you are an inspiration. Sjoerd, please keep

building things. And this includes delicious food. Oh, and thanks to all the good souls who kept bringing puzzles to the kitchen table!

To all the Friday drinks regulars (you know who you are), proost! Special thanks to Andrei, Svea, Glenn, Steven, Valentina, and Sukanth for passing the torch of keeping the tradition alive.

Thank you to my parents for their patience, wisdom, always having my back, and teaching me not to take myself too seriously. The path that you have been on together in the world of academia is an inspiration! My sister, for sharing the moments of foolishness. With you it's the best type of party! My grandmother, for many words of encouragement. And for all the hot chocolate!

For everything else, including the unnoticed, thank you to M. We've got here together and you made it feel like smooth sailing. Let's keep going and explore that oyster!

# Research Data Management

This thesis research has been carried out under the institute research data management policy of the *Institute for Mathematics Astrophysics and Particle Physics* (IMAPP), as documented in https://www.ru.nl/publish/pages/868512/imapp_rdm_policy.pdf (last accessed on 06/2021).

- Results of the population synthesis simulations discussed in chapter II and chapter III are publicly available on: https://ftp.science.ru.nl/astro/jklencki/.
  Population synthesis models presented in chapter IV are publicly available on:
  https://www.syntheticuniverse.org/
  The code used to obtain those results is developed and maintained by the Synthetic Universe team (PI: Krzysztof Belczyński).

- Stellar and binary models presented in chapters V, VI, and VII were computed using the publicly available code MESA (version r11554), see http://mesa.sourceforge.net/ for documentation and http://mesa.sourceforge.net/release/2019/03/15/r11554.html for the code release r11554.

- Input files (so-called MESA inlists) as well as the computed models from chapters V and VI are publicly availabe on https://zenodo.org/record/3740578#.YMjNqSaxVSk.

- Results of the envelope binding energy computations from chapter VI are publicly available on: https://ftp.science.ru.nl/astro/jklencki/

- Results of the simulations discussed in chapter VII will be made publicly available on: https://ftp.science.ru.nl/astro/jklencki/